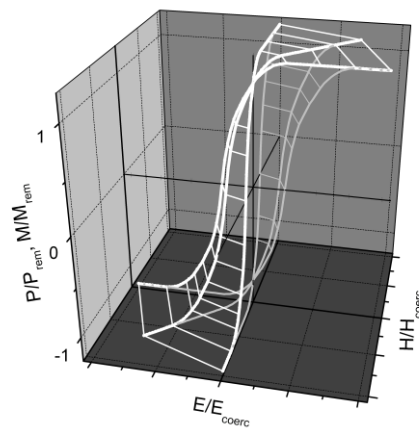




FÁBIO GABRIEL
NAZÁRIO FIGUEIRAS

STUDY OF MULTIFERROIC MATERIALS
ESTUDO DE MATERIAIS MULTIFERROICOS





**FÁBIO GABRIEL
NAZÁRIO FIGUEIRAS**

**STUDY OF MULTIFERROIC MATERIAIS
ESTUDO DE MATERIAIS MULTIFERROICOS**

Dissertação apresentada à Universidade de Aveiro para cumprimento dos requisitos necessários à obtenção do grau de Doutor em Física, realizada sob a orientação científica do Professor Doutor Vitor Brás de Sequeira Amaral, Professor Catedrático do Departamento de Física da Universidade de Aveiro e co-orientação do Professor Doutor Pedro Manuel de Melo Bandeira Tavares Professor Associado do Departamento de Química da Universidade de Trás-os-Montes e Alto Douro.

Apoio financeiro da FCT
no âmbito da Bolsa de Doutoramento:
SFRH / BD / 25011 / 2005



Jury

President

Supervisor

Doutor Vítor Brás de Sequeira Amaral
Professor Catedrático, Departamento de Física da Universidade de Aveiro

Invited

Doutor Andrei Leonidovitch Kholkin
Investigador Coordenador, Laboratório Associado CICECO – Centro de Investigação em Materiais Cerâmicos e Compósitos da Universidade de Aveiro

Invited

Doutor Joaquim Agostinho Gomes Moreira
Professor Auxiliar, Departamento de Física da Faculdade de Ciências da Universidade do Porto

Invited

Doutor Bernardo Gonçalves Almeida
Professor Auxiliar, Departamento de Física da Universidade do Minho

Co-Supervisor

Doutor Pedro Manuel de Melo Bandeira Tavares
Professor Associado, Departamento de Química da Universidade de Trás-os-Montes e Alto Douro

Invited

Doutor Armando António Cardoso dos Santos Lourenço
Professor Auxiliar, Departamento de Física da Universidade de Aveiro

Acknowledgments

My parents Dina and Lando

Ana Venâncio

André and Sandra and all true friends.

We thank the excellent supervision and friendship of Professor Dr. Vitor Brás de Sequeira Amaral and of Professor Dr. Pedro Manuel de Melo Bandeira Tavares.

The research primarily made use of the available infrastructures at the Department of Physics and the CICECO Associated Laboratory from Aveiro University and the Chemistry Centre – Vila Real from UTAD, for which we thank the assistance of all the professional staff and research colleagues.

To Marco Peres for implementing *NI Labview* control software for the Magneto-Resistance and Magneto-electric measurement systems and his assistance in performing graze angle XRD measurements of thin films.

To Soma Das for her assistance in VSM and Magneto-Resistance measurements and participation in Magneto-impedance measurements performed at ITT -Kharagpur, India.

To Narciso Soares for his collaboration, namely in the construction and development of the O¹⁸ annealing system and in the final stage of the Magneto-Resistance system.

Part of the work was undertaken within the scope of a collaboration in the European project “MULTICERAL” (STREP NMP3-CT-2006-032616) coordinated by Doctor Andrei Kholkin (CICECO), aiming for the development of multiferroic sensor devices based on thin films of Ni₂MnGa onto Piezoelectric substrates.

To Nikolay Vyshatko for our team work performed at IEMN - Lille, France, in RF sputtering deposition of the first series of Ni₂MnGa alloy thin films and respective characterization.

To Igor Bdikin for his participation in Piezo Force and Magnetic Force Microscopy measurements of samples as well as Dmitry Karpinski for also performing Neutron powder Diffraction of a LuMn_{1-d}O₃ sample at BENSC - Berlin, Germany

To Prof. Dr. Agostinho Moreira support to perform Raman spectroscopy of manganite samples; and to prof. Dr. João Pedro Araújo, Dr. João Ventura, and research team at IFIMUP for assisting in complementary Magneto-Resistance and SQUID measurements.

To Dr. João Guilherme Correia, for his supervision for PAC measurements at CERN ISOLDE – Switzerland.

To Dr. Carlos Moreira Sá at CEMUP - Porto for his expertise in XPS.

To Dr. Eduardo Alves at ITN - Sacavém for the RBS results;

To Dr. Sergei V. Kalinin and the research team at CNMS ORNL -TN, USA for the course and measurements of SPM and BEPS.

**FÁBIO GABRIEL
NAZÁRIO FIGUEIRAS**

STUDY OF MULTIFERROIC MATERIAIS ESTUDO DE MATERIAIS MULTIFERROICOS

Key words

Multiferroic materials, Manganites, Magnetoresistance, Magnetoelectric effect, Magnetization, Probe Microscopy,

Abstract

The present PhD work aims the research and development of materials that exhibit multiferroic properties, in particular having a significant interaction between ferromagnetism and ferroelectricity; either directly within an intrinsic single phase or by combining extrinsic materials, achieving the coupling of properties through mechanic phenomena of the respective magnetostriction and piezoelectricity.

These hybrid properties will allow the cross modification of magnetic and electric polarization states by the application of cross external magnetic and/or electric fields, giving way to a vast area for scientific investigation and potential technological applications in a new generation of electronic devices, such as computer memories, signal processing, transducers, sensors, etc.

Initial experimental work consisted in chemical synthesis of nano powders oxides by urea pyrolysis method: A series of ceramic bulk composites with potential multiferroic properties comprised: of LuMnO_3 with $\text{La}_{0.7}\text{Sr}_{0.3}\text{MnO}_3$ and BaTiO_3 with $\text{La}_{0.7}\text{Ba}_{0.3}\text{MnO}_3$; and a series based on the intrinsic multiferroic $\text{LuMn}_{1-z}\text{O}_3$ phase modified with of Manganese vacancies.

The acquisition of a new magnetron RF sputtering deposition system, in the Physics Department of Aveiro University, contributed to the proposal of an analogous experimental study in multiferroic thin films and multilayer samples. Besides the operational debut of this equipment several technical upgrades were completed like: the design and construction of the heater electrical contacts; specific shutters and supports for the magnetrons and for the substrate holder and; the addition of mass flow controllers, which allowed the introduction of N_2 or O_2 active atmosphere in the chamber; and the addition of a second RF generator, enabling co-deposition of different targets.

Base study of the deposition conditions and resulting thin films characteristics in different substrates was made from an extensive list of targets. Particular attention was given to thin film deposition of magnetic phases $\text{La}_{1-x}\text{Sr}_x\text{MnO}_3$, $\text{La}_{1-x}\text{Ba}_x\text{MnO}_3$ and $\text{Ni}_{2+x-y}\text{Mn}_{1-x}\text{Ga}_{1+y}$ alloy, from the respective targets: $\text{La}_{0.7}\text{Sr}_{0.3}\text{MnO}_3$, $\text{La}_{0.7}\text{Ba}_{0.3}\text{MnO}_3$; and NiGa with NiMn.

Main structural characterization of samples was performed by conventional and high resolution X-Ray Diffraction (XRD); chemical composition was determined by Electron Dispersion Spectroscopy (EDS); magnetization measurements recur to a Vibrating Sample Magnetometer (VSM) prototype; and surface probing (SPM) using Magnetic-Force (MFM) and Piezo-Response (PFM) Microscopy.

(continue on back page)

Abstract (cont.)

Results clearly show that the composite bulk samples (LuM+LSM and BTO+LBM) feat the intended quality objectives in terms of phase composition and purity, having spurious contents below 0.5 %. SEM images confirm compact grain packaging and size distribution around the 50 nm scale. Electric conductivity, magnetization intensity and magneto impedance spreading response are coherent with the relative amount of magnetic phase in the sample. The existence of coupling between the functional phases is confirmed by the Magnetoelectric effect measurements of the sample “78%LuM+22%LSM” reaching 300% of electric response for 1 T at 100 kHz; while in the “78%BTO+22%LBM” sample the structural transitions of the magnetic phase at ~350 K result in a inversion of ME coefficient the behavior.

A functional Magneto-Resistance measurement system was assembled from the concept stage until the, development and operational status; it enabled to test samples from 77 to 350 K, under an applied magnetic field up to 1 Tesla with 360° horizontal rotation; this system was also designed to measure Hall effect and has the potential to be further upgraded.

Under collaboration protocols established with national and international institutions, complementary courses and sample characterization studies were performed using Magneto-Resistance (MR), Magneto-Impedance (MZ) and Magneto-Electric (ME) measurements; Raman and X-ray Photoelectron Spectroscopy (XPS); SQUID and VSM magnetization; Scanning Electron Microscopy (SEM) and Rutherford Back Scattering (RBS); Scan Probe Microscopy (SPM) with Band Excitation Probe Spectroscopy (BEPS); Neutron Powder Diffraction (NPD) and Perturbed Angular Correlations (PAC).

Additional collaboration in research projects outside the scope of multiferroic materials provided further experience in sample preparation and characterization techniques, namely VSM and XPS measurements were performed in cubane molecular complex compounds and enable to identify the oxidation state of the integrating cluster of Ru ions; also, XRD and EDS/SEM analysis of the acquired targets and substrates implied the devolution of some items not in conformity with the specifications.

Direct cooperation with parallel research projects regarding multiferroic materials, enable the assess to supplementary samples, namely a preliminary series of nanopowder $Y_{1-x-y}Ca_xO_yMn_1O_3$ and of $Eu_{0.8}Y_{0.2}MnO_3$, a series of micropowder composites of $LuMnO_3$ with $La_{0.625}Sr_{0.375}MnO_3$ and of $BaTiO_3$ with hexagonal ferrites; mono and polycrystalline samples of $Pr_{1-x}Ca_xMnO_3$, $La_{1-x}Sr_xMnO_3$ and $La_{1-x}Ca_xMnO_3$.

**FÁBIO GABRIEL
NAZÁRIO FIGUEIRAS**

STUDY OF MULTIFERROIC MATERIAIS

ESTUDO DE MATERIAIS MULTIFERROICOS

Palavras Chave

Materiais Multiferroicos, Efeito Magnetoelectrico, Magneto-resistência, microscopia de ponta,

Resumo

O trabalho de doutoramento presente tem por objectivo a pesquisa e desenvolvimento de materiais que manifestem propriedades multiferróicas, em particular com uma significativa interacção entre os fenómenos de ferromagnetismo e ferroelectricidade; seja de forma intrínseca em determinados materiais singulares, ou extrínseca ao combinar materiais que apresentam respectivamente fenómenos magnetoestritivo e de piezoelectricidade e em que geralmente o acoplamento se processa mecanicamente entre as fases.

Esta hibridação de propriedades permite a modificação dos estados de polarização magnética ou eléctrica por aplicação dos campos externos complementares (eléctricos e/ou magnéticos), dando origem a uma vasta área de investigação científica e potenciais aplicações tecnológicas numa nova geração de dispositivos electrónicos como memórias, processadores, transdutores, sensores, etc.

O trabalho experimental inicial consistiu na síntese química de óxidos sob a forma de pós nanométricos, pelo método de pirólise da ureia; As séries de compósitos maciços com potenciais propriedades multiferróicas compreendem: LuMnO_3 com $\text{La}_{0.7}\text{Sr}_{0.3}\text{MnO}_3$ e BaTiO_3 com $\text{La}_{0.7}\text{Ba}_{0.3}\text{MnO}_3$; e uma série baseada na modificação com lacunas de Manganésio da fase multiferróica intrínseca $\text{LuMn}_{1-z}\text{O}_3$.

A aquisição de um novo sistema de deposição por *RF sputtering*, no Departamento de Física da Universidade de Aveiro, contribuiu para a proposta de estudo análogo de amostras multiferróicas sob a forma de filmes finos e multicamadas. Além da estreia operacional do equipamento foram efectuadas algumas melhorias técnicas e funcionais de que se destacam: o desenho e construção das ligações eléctricas do aquecedor; de portadas, protecções e respectivos suportes para os magnetrons e para o "porta substratos"; a adição de dois controladores de fluxo de gás permitindo a introdução controlada de Árgon e de atmosfera activa de O_2 ou N_2 durante a deposição; e a adição de uma segunda fonte e controlador RF permitindo a co-deposição simultânea de filmes a partir de dois alvos diferentes.

O estudo base sobre as condições de deposição e das características dos filmes finos resultantes em diferentes substratos foi efectuada a partir de uma extensa lista de alvos. Atenção particular foi dada à deposição de filmes finos das fases magnéticas de $\text{La}_{1-x}\text{Sr}_x\text{MnO}_3$, $\text{La}_{1-x}\text{Ba}_x\text{MnO}_3$ e da liga $\text{Ni}_{2+x-y}\text{Mn}_{1-x}\text{Ga}_{1+y}$ a partir dos correspondentes alvos $\text{La}_{0.7}\text{Sr}_{0.3}\text{MnO}_3$; $\text{La}_{0.7}\text{Ba}_{0.3}\text{MnO}_3$ e NiGa com NiMn.

(continua na página seguinte)

Resumo (cont.)

A caracterização estrutural das amostras foi efectuada com Difractometria por Raios-X (XRD) convencional e de elevada resolução; determinação da composição química foi essencialmente realizada por Espectroscopia de Dispersão de Electrões (EDS); medidas de magnetização foram executadas com recurso a um protótipo de Magnetometro por Vibração da Amostra (VSM) e as medidas de análise de superfície utilizaram Microscopia de Ponta (SPM) nas vertentes de piezo resposta (PFM) e de força magnética (MFM).

Os resultados obtidos nos compósitos maciços (LuM+LSM e BTO+LBM) demonstram claramente que as amostras satisfazem os objectivos propostos em termos de composição pureza das fases, com eventual conteúdo em óxidos espúrios inferior a 0.5%. Imagens obtidas por SEM confirmam a compactação dos grãos e distribuição de tamanhos em torno dos 50 nm. Condutividade eléctrica, intensidade da magnetização e a dispersão da resposta em Magneto-Impedância são coerentes com a proporção relativa da fase magnética em cada amostra. A existência de um acoplamento entre as fases funcionais é evidenciada por medidas de efeito Magneto-Eléctrico na amostra “78%LuM+22%LSM” que apresenta uma resposta eléctrica de ~300% para 1 Tesla a 100 kHz; enquanto que na amostra “78%BTO+22%LBM” se assinala a transição estrutural da fase magnética a ~350 K resulta na inversão do comportamento do coeficiente ME.

Um sistema de Medidas de Magneto-Resistência foi totalmente desenvolvido e montado desde a fase conceptual até ao estado operacional; permite testar amostras de 77 a 350 K em função do campo magnético até 1 Tesla, e rotação horizontal de 360°; o sistema foi também desenhado para poder efectuar medidas de efeito de Hall e permitir upgrades.

Ao abrigo de protocolos de colaboração estabelecidos com diversas instituições nacionais e internacionais, foram realizados cursos de formação complementar e caracterização de amostras em técnicas como Magneto Resistência (MR), Magneto Impedância (MZ) e efeito Magneto Eléctrico (ME); Espectroscopia Raman e Foelectrónica de Raios-X (XPS); Magnetização via sistemas SQUID e VSM; Microscopia de Ponta em Piezo resposta (PFM) e Espectroscopia de excitação em largura de banda (BEPS); Espectroscopia de Rutherford por Retro dispersão (RBS); Difracção de Neutrões em pós (NPD) e Correlações de Perturbação Angular (PAC)

Colaboração em projectos de investigação fora do âmbito dos materiais multiferróicos permitiu ampliar e versatilizar experiencia em técnicas de preparação e caracterização de amostras, nomeadamente medidas de VSM e XPS permitiram identificar os estados de oxidação dos clusters de iões de Ruténio que integram complexos moleculares utilizados em catalisadores; A certificação por XRD e SEM/EDS do conjunto dos alvos e amostragem dos substratos adquiridos implicou a devolução de alguns itens com por falta de conformidade com as especificações.

Cooperação directa em projectos de investigação paralelos sobre materiais multiferróicos permitiu o acesso a amostras suplementares, nomeadamente a uma série nano pós de $Y_{1-x-y}Ca_xO_yMn_1O_3$ e de $Eu_{0.8}Y_{0.2}MnO_3$; a series de compósitos microestruturados de $LuMnO_3$ com $La_{0.625}Sr_{0.375}MnO_3$ e de $BaTiO_3$ com ferrites hexagonais; e a diversas amostras poli- e mono-cristalinas de $Pr_{1-x}Ca_xMnO_3$, $La_{1-x}Sr_xMnO_3$ e $La_{1-x}Ca_xMnO_3$.

PREFACE

The role of science and technology is, beyond any doubt, of ever growing importance in human life, to the point that the advances in the field of information technologies have made possible the development of what we now call the “information society”.

The need for faster, smaller and lighter devices with better performance in data storage and processing has now driven the scientific and engineering research to downscale such functional devices into the nanometer range. Concurrently, the expansion of computer simulation models, the resolution enhancements of several characterization systems and improvements in the quality of materials open the possibility to study and manufacture sophisticated materials at nearly molecular scales. At such nanometric dimensions, the physical properties of materials change dramatically when compared to those of their macroscopic counterparts; in fact, they exhibit new or crossover phenomena connected with quantum size effects.

The intensive interest in understanding and manipulating “in deep” the nano-structured materials in regard to their interacting electric, magnetic and structural properties has led the scientific community to greatly focus in the research of their design, synthesis, characterization and potential applications, supported by a great expectation in industry that these exciting scientific breakthroughs can be exploited in a new generation of high-technology devices.

Relatively recent science fields and terminologies have been introduced to refer to these new phenomenological aspects: magneto-electronics, spintronics, spin-valve, magneto-resistance, magneto-electric, multiferroics, tunneling effect, exchange bias, oscillatory magnetic coupling, etc.; in fact, many of these fields have already found applications in magneto sensors, electronics, data storage, computer hard disk heads, single electron devices, microwave electronic devices, RAM chips, etc.

Thus, this generic nanotechnology will inevitably have great impact on a wide range of industrial sectors and on the everyday human lives. In other words, one of the pillars of industry in the 21st century involves the field of nanoscale materials [0.0.1].

CONTENTS

	DISSERTATION	3
	JURY	5
	ACKNOWLEDGMENTS	7
	ABSTRACT	9
	PREFACE	13
	OBJECTIVES	16
	MOTIVATION	17
	THESIS STRUCTURE	18
	SYMBOLS AND ACRONYMS	19
I	INTRODUCTION	25
	1. Materials Structure	27
	2. Electrical properties	31
	2.1. Conductors	33
	2.2. Semiconductors	35
	2.3. Dielectrics	36
	3. Magnetic properties	44
	3.1. Magnetic States	48
	3.2. Magnetoelastic effect	54
	3.3. Magnetism Units	56
	4. State of the Art	57
	4.1. Multiferroic Materials	57
	4.2. Perovskite Manganites	62
	4.3. Ferroelectric Perovskites:	65
	4.4. Ferroelectric Hexagonal Manganites	68
	4.5. Magnetostrictive Ni_2MnGa Heusler alloy	70
II	EXPERIMENTAL METHODS	73
	5. Samples preparation Methods	73
	5.1. Ceramics Powders Sintering	74
	5.1.1. Solid State Synthesis	75
	5.1.2. Coprecipitation Synthesis	76
	5.1.3. Sol-Gel Synthesis	76
	5.1.4. Combustion Synthesis	77
	5.2. Thin Films	78
	5.2.1. Film growth	78
	5.2.2. Deposition Processes	80
	5.2.3. Deposition by RF Magnetron Sputtering	83

6.	Characterization Methods	85
6.1.	Scanning electron Microscopy - SEM	86
6.2.	Energy Dispersive X-Ray Spectroscopy – EDS	87
6.3.	Scanning Probe Microscopy – SPM (PFM, MFM, BEPS)	89
6.4.	X-Ray Diffraction – XRD and Reflectometry – XRR	92
6.5.	Neutron Powder Diffraction – NPD	94
6.6.	Rietveld Refinement	95
6.7.	Raman Spectroscopy	97
6.8.	Magneto-Resistance – MR	99
6.9.	Magneto-Electric – ME	101
6.10.	Magneto-Impedance – MZ	102
6.11.	Vibrating Sample Magnetometer – VSM	102
6.12.	Superconductor Quantum Interference Device – SQUID	103
6.13.	X-Ray Photoelectron Spectroscopy – XPS	105
6.14.	Rutherford Backscattering Spectroscopy – RBS	106
III	EXPERIMENTAL WORK	107
7.	Experimental Systems Development	107
7.1.	Magneto Resistance measurements system	107
7.2.	RF Sputtering System	119
8.	Powders synthesis	123
8.1.	2 inch Targets manufacture	123
8.2.	BaTiO ₃ + La _{0.7} Ba _{0.3} MnO ₃ series	126
8.3.	LuMnO ₃ + La _{0.7} Sr _{0.3} MnO ₃ series	127
8.4.	LuMn _{1-z} O ₃ Intrinsic Multiferroic series	128
9.	Thin Film Deposition by Magnetron RF Sputtering System	129
9.1.	La _{0.7} Sr _{0.3} MnO ₃ phase series	134
9.2.	Ni ₂ MnGa phase series	134
10.	Samples Measurements, Conditions and Parameters	138
IV	EXPERIMENTAL RESULTS AND ANALYSIS	149
11.	Powder samples	149
11.1.	LuMnO ₃ + La _{0.7} Sr _{0.3} MnO ₃ composites series	151
11.2.	Bulk LuMn _{1-z} O ₃ Intrinsic Multiferroic series	172
11.3.	BaTiO ₃ + La _{0.7} Ba _{0.3} MnO ₃ composites series	184
11.4.	SPM study of Induced Ferroelectricity in C.O. Manganites	196
12.	Thin Film samples	212
12.1.	La _{0.7} Sr _{0.3} MnO ₃ phase series	212
12.2.	Ni ₂ MnGa phase series @ IENM	227
12.3.	Ni ₂ MnGa phase series @ UA	239
IV	CONCLUSIONS	257
V	FURTHER WORK	265
VI	REFERENCES	267
VII	COMMUNICATIONS AND PUBLICATIONS LIST	275
VIII	ATTACHMENTS	279

OBJECTIVES

With the main objective of achieving and measure potential magneto-electric coupling effects, compositions and structure of the samples were preferably sought in order to attain systems exhibiting appreciable magnetic and ferroelectric properties with relevant transitions near room temperature, making possible to broaden the diversity of characterization techniques applicable enabling to measure the complementary properties that may describe the potential conditions to obtain multiferroic composites.

- Research and development of experimental tools as well as interpretation models that make it possible to design, manufacture and characterize functional multiferroic materials and devices.
- To apply different manufacturing methods for nano-structured materials envisaging functional magneto-electric properties; in particular, nano powders Sol-gel synthesis and thin film deposition by RF Sputtering.
- To understand and make use of several characterization techniques: Structural (XRD XRR and HR-XRD, Raman, TEM, NPD), Chemical (EDS, RBS, ICP, XPS), Magnetic (VSM, SQUID), Electric (MR, ME, MZ), Surface (SEM, SPM, PFM, MFM, V-I, BEPS).
- Conception, design, construction and assembly of experimental hardware setups for:
 - Magneto-resistance and Hall Effect measurements
 - Magnetron RF Sputtering system

MOTIVATION

The scientific work expressed within this thesis, while focused on multiferroic materials, represents only a part of the personal and professional experience attained during the PhD graduation period; in these four years, there has been a long list of activities and collaborations in complementary scientific projects, as part of the intricacy of working in a dynamic research group in a Physics Department belonging to a forceful network laboratory like CICECO and within an active academic institution like the University of Aveiro.

The previous scientific and technical background acquired during the Physics graduate course specializing on solid state matter, as well as during a Masters' course, investigating doping and thermal manipulation effects on the properties of CMR manganites, was proven relevant when selecting a topic to progress on PhD studies. Further participation in some national and international congresses and courses was significant in meeting research colleagues and recognizing our group scientific and technical work as being comparable to the state of the art worldwide.

Given the wide spectra of their structural and functional phases, manganites became among the selected materials to further explore, modify and combine for their versatility and potential to attain magneto-electric coupling properties.

Besides the preceding know-how in sample preparation by solid-state sintering, *Sol-Gel* nano-powder oxides synthesis by *Pechini* and *coprecipitation* methods along with thin film deposition using PLD and MOCVD systems, it was possible to extend technical knowledge to new experimental techniques, samples were prepared using a nano powder oxides synthesis by *Sol-Gel Urea Combustion* method, while thin film deposition was performed using by *Magnetron RF sputtering*.

Adding to the former capabilities with characterization methods including XRD, RBS, EDS, SEM, TEM, SQUID and MR, further training was implemented regarding also several other measurement techniques: Raman spectroscopy, magneto impedance (MZ), magneto-electric effect (ME) and scanning probe microscopy (PFM, MFM, BEPS), special concern was given to magnetization using a new VSM system prototype and the development of a Magneto Resistance (MR) measurements setup. There was also the

opportunity to perform hyperfine interactions (PAC) [0.0.2] and X-Ray Photoelectron Spectroscopy (XPS) measurements in complementary samples.

Based on the support given by supervisors, colleagues and academic institutions alike, there's a firm expectation to be able to give a valid contribution to the R&D of multiferroic materials. In addition, to be of assistance in the supervision of several academic students in their Bachelor's and Master's courses was a gratifying pedagogical opportunity, validating the personal scientific background.

STRUCTURE

This work begins by introducing some physics background concerning structural, electric and magnetic properties of materials, then follows a more specific discussion about the state of the art regarding multiferroics in particular and of materials having extrinsic properties which combined may lead to potential magneto-electric coupling. The principles behind the experimental techniques for both preparation and characterization of nano-sized materials are described, focusing on the methods employed during this research work.

The experimental work is expressed into the samples synthesis procedures, technical developments performed in specific instrumental systems and the different characterization methods used. The experimental results are organized according to each series of samples, enabling to compare and analyze the observations from different characterization methods. The conclusions reached are complemented by some trends for future research and mention for some potential technical applications of multiferroic systems. Finally, a comprehensive list of the completed publications and communications illustrates some of the complementary work performed in the context of PhD project.

The chapters' configuration was selected in order to establish a direct relation between the identification number of each section and the respective figures, tables, notes and references, thus avoiding the conventional long list of sequential entries detached from the respective context.

SYMBOLS AND ACRONYMS

This section provides a coherent summary of symbols, units, constants, some conversion factors and acronyms, which will be used within this work [0.0.3].

<u>Symbol</u>	<u>Definition</u>	<u>Type</u>	<u>Usual Value and Units</u>
\emptyset	Vacancy, empty	stoichiometric	--
A	Amplitude, Intensity	scalar	--
A	Ampere	electric current unit	$1 \text{ A} = 1 \text{ C.s}^{-1}$
a, b, c	Cell parameters length	scalar	\AA
a_0	Bohr Radius	constant	$5.29177 \cdot 10^{-11} \text{ m}$
\AA	Angstrom	length unit	$1 \text{\AA} = 10^{-10} \text{ m}$
α, β, γ	proportion coefficients	general	--
α_e	(Electric) polarizability	scalar, tensor	$\text{C.m}^2.\text{V}^{-1} = \text{A}^2.\text{s}^4.\text{kg}^{-1}$
B	Magnetic Induction	vector	T
β	Gain	scalar	--
c	Speed of light	constant	$2.9992458 \cdot 10^8 \text{ m.s}^{-1}$
C	Coulomb	charge unit	$1 \text{ C} = 1 \text{ A.s}$
C	Capacitance	scalar	F
C	Curie Constant	materials'	K
$^{\circ}\text{C}$	Celsius	temperature unit	$^{\circ}\text{C} = \text{K} + 273.15$
\dots°	Degree	angle unit	$2.\pi \text{ rd} = 360^{\circ}$
d	Diameter, distance	scalar	m
d_{ij}	Piezoelectric coefficient	tensor	m.V^{-1}
d_{hkl}	Distance between crystalline planes	scalar	\AA
D	Electric flux density or displacement	vector	C.m^{-2}
$\Delta \dots$	variation, difference, change	operator	--
$\partial \dots$	differential, derivative	operator	--
δ	small change, skin depth, loss	general	--
$\nabla \dots$	Nabla: $u_x.\partial \dots / \partial x + u_y.\partial \dots / \partial y + u_z.\partial \dots / \partial z$	operator	--
E	Energy	scalar	J
E_p, E_k	Potential, Kinetic Energy	scalar	J
E_F, E_C, E_V	Fermi, Conduction, Valence Energy levels	materials'	J
E	Electric Field	vector	V.m^{-1}
e	Napier base	constant	$2.71828182846 \dots$
$e^{(\dots)}, \exp(\dots)$	Exponential of base e	operator	--
e^-	Electron charge	constant	$-1.602177 \cdot 10^{-19} \text{ C}$
emu	Electro-magnetic unit	CGS unit	$1 \text{ emu} = 10^{-3} \text{ A.m}^2$
ϵ	Electric permittivity	materials'	$\text{J}^{-1}.\text{C}^2.\text{m}^{-1} = \text{C.V}^{-1}.\text{m}^{-1}$
ϵ_0	Vacuum electric permittivity	constant	$8.854 \cdot 10^{-12} \text{ J}^{-1}.\text{C}^2.\text{m}^{-1}$
ϵ_r	relative electric permittivity	materials'	$\epsilon_r = \epsilon / \epsilon_0$
f	Frequency	scalar	s^{-1}
F	Force	vector	$1 \text{ N} = \text{Kg.m.s}^{-2}$

<u>Symbol</u>	<u>Definition</u>	<u>Type</u>	<u>Usual Value and Units</u>
F	Faraday	capacitance unit	1 F = 1 C.V ⁻¹
φ	phase angle	scalar	rd
g	gram	mass unit	1 g = 10 ⁻³ kg
G	Gauss (magnetic induction)	CGS unit	1 G = 10 ⁻⁴ T
g_e	Electron gyromagnetic factor	constant	2.00232
g_J	Landé factor	scalar	--
h	Plank Constant	constant	6.62608*10 ⁻³⁴ J.s
\hbar	Plank Constant (dashed)	constant	$\hbar = h/2.\pi$
h	Height	scalar (vertical)	m
H	Magnetic Field	vector	A.m ⁻¹ (or kOe in CGS)
Hz	Hertz	frequency unit	1 Hz = 1 s ⁻¹
i, j	Indexes, integer variable	general	--
i	Imaginary unit (i ² = -1)	complex number	i = $\sqrt{-1}$
i	Instantaneous current	vector	A
I	Nucleus total moment	vector (quantum)	--
J	Joule	energy unit	1 J = 1 kg.m ² .s ⁻²
J_e	Current density	vector	A.m ⁻²
J	Total angular moment	vector (quantum)	$J = L + S$
($h k l$)	Crystallography Miller notation planes	vector	integers
k...	kilo	prefix unit	10 ⁺³
k_B	Boltzmann Constant	constant	1.38065*10 ⁻²³ J.K ⁻¹
K	Kelvin	temperature unit	--
K_{em}	Electro-mechanic energy conversion factor	materials'	--
kg	kilogram	mass unit	--
l	Length	scalar (longitudinal)	m
L	Total angular moment	vector (quantum)	--
λ	wavelength	scalar	m
lg(...), log(...)	logarithm base 10	operator	
ln(...)	logarithm base e	operator	
m	meter	length unit	--
m	Mass	scalar	kg
m_e	Electron mass	constant	9.10939*10 ⁻³¹ kg
m_n	Neutron mass	constant	1.67493*10 ⁻²⁷ kg
m_p	Proton mass	constant	1.67262*10 ⁻²⁷ kg
M...	mega	prefix unit	10 ⁺⁶
M	Magnetization (Volume)	vector	A.m ⁻¹
M_{rem}	Remanent Magnetization	scalar	A.m ⁻¹
M_{sat}	Saturation Magnetization	scalar	A.m ⁻¹
$M(...)$	specific atomic or molecular mass	scalar	g.mol ⁻¹
mol	mole	quantity unit	6.02214*10 ²³
m_l, m_s	angular, spin, moment projection	scalar (quantum)	--
m_z	magnetic moment projection	scalar (quantum)	--
$\mu...$	micro	prefix unit	10 ⁻⁶

<u>Symbol</u>	<u>Definition</u>	<u>Type</u>	<u>Usual Value and Units</u>
μ	magnetic permeability	materials'	$\text{J.s}^2.\text{C}^{-2}.\text{m}^{-1}$
μ_0	absolute permeability	constant	$4.\pi * 10^{-7} \text{ J.s}^2.\text{C}^{-2}.\text{m}^{-1}$
μ_r	relative permeability	materials'	$\mu_r = \mu/\mu_0$
μ_B	Bohr magneton	constant	$9.2732*10^{-24} \text{ J.T}^{-1}$
μ_m	magnetic dipole moment	vector	A.m^2
n...	nano	prefix unit	10^{-9}
n	number of mol	scalar	mol
N	Quantity, total number of entities	scalar	--
N	Newton	force unit	$1 \text{ N} = 1 \text{ kg.m.s}^{-2}$
n^0	Neutron charge	constant	0
\tilde{n}	Wave number	scalar	$10^{-2}/\lambda \text{ cm}^{-1}$
N_A	Avogadro constant	constant	$6.02214*10^{23} \text{ mol}^{-1}$
η	efficiency	scalar	--
Oe	Oersted (magnetic field)	CGS unit	$1 \text{ Oe} = 10^3/4\pi \text{ A.m}^{-1}$
P	Pressure (force perpendicular to surface)	vector	Pa
P	Polarization ($P = \sum p/V$)	vector	C.m^{-2}
p	Electric dipole moment	vector	C.m
P	Power	scalar	W
p^+	Proton charge	constant	$1.602177*10^{-19} \text{ C}$
Pa	Pascal	pressure unit	$1 \text{ Pa} = 1 \text{ N.m}^{-2}$
π	pi	constant	$3.14159265359\dots$
q	Charge	scalar	C
Q	Quality factor	scalar	--
r	radius distance	scalar	m
r	position vector	vector	m, rd
(r, φ, θ)	Spherical position coordinates	vector	m, rd, rd
R	Resistance (real component of Z)	scalar	Ω
R'	Reactance (imaginary component of Z)	scalar	Ω
rd	radians	angle unit	--
ρ	Electrical resistivity ($\rho = R.S/I$)	scalar	$\Omega.\text{m}$
ρ	Density, specific mass	scalar	kg.m^{-3}
ρ_e	Charge density	scalar	C.m^{-3}
(ρ, φ, z)	cylindrical position coordinates	vector	M, rd, m
s	second	time unit	--
s	Strain ($s = \delta l/l$) (deformation)	vector	--
S	section, surface area	scalar	m^2
$\sum\dots$	Sum	operator	--
$\int\dots$	Integral	operator	--
S	total Spin moment	vector (quantum)	--
σ	Electric conductivity ($\sigma = 1/\rho$)	scalar, tensor	$\Omega^{-1}.\text{m}^{-1}$
t	Time	scalar	s
T	Tesla	magnetic unit	$1 \text{ T} = 1 \text{ N.A}^{-1}.\text{m}^{-1}$
T	Stress (force parallel to surface, Tension)	vector	$\text{Pa} = \text{N.m}^{-2}$

<u>Symbol</u>	<u>Definition</u>	<u>Type</u>	<u>Value and Units</u>
T	Absolute Temperature	scalar	K
T_c	Critical transition Temperature	materials'	K
T_C	Curie temperature	materials'	K
T_N	Neel temperature	materials'	K
θ	angle	scalar	Rd
τ	time constant	scalar	S
v	velocity, speed	vector	m.s ⁻¹
V	Volt	voltage unit	--
V	Voltage, electric potential	scalar	V
V	Volume	scalar	m ³
x, y, z	arbitrary variables	general	--
(x, y, z)	Cartesian position coordinates	vector	m
xx, yy, zz	Cartesian longitudinal, lateral, vertical	axis	m
u_x, u_y, u_z	Cartesian versors	vectors	1
χ	Magnetic susceptibility (volume)	materials'	--
χ_m	Mass magnetic susceptibility	materials'	A.m ² .kg ⁻¹
χ_e	electric susceptibility	materials'	--
χ_{ij}	Magnetoelectric susceptibility coupling	materials'	--
w	wide	scalar (lateral)	m
ω	angular frequency	vector	rd.s ⁻¹
W	Watt	power unit	1 W = 1 J.s ⁻¹
$\Psi(...)$	wave function, orbital	operator	--
Y	Young's Elastic Modulus ($T = Y.s$)	material's	Pa
Z	Atomic number, proton number	scalar	--
Z	Impedance $Z = R + i.R'$	Complex number	Ω
Ω	Ohm	resistance unit	$\Omega = V.A^{-1} = Kg.m^2.s^{-3}.A^{-2}$

<u>Abbreviations</u>	<u>Meaning</u>
a.c.	Alternating current
AFM	Antiferromagnetic (phase)
... [©]	Copyright (software)
BEPS	Band Excitation Probe Spectroscopy
CEMUP	Centre of Materials of Universidade of Porto (Portugal)
CERN	European Laboratory for Particle Physics (Genève, Switzerland)
CICECO	Centre for Research in Ceramics and Composite Materials (Aveiro, Portugal)
CNMS	Center for Nanophase Materials Sciences (TN, USA)
CVD	Chemical Vapor Deposition
C.O.	Charge Order
d.c.	Direct current
EDS	Energy Dispersive Spectroscopy
... ^{eff}	Effective, efficient
FE	Ferroelectric (phase)
FI	Ferrimagnetic (phase)
FM	Ferromagnetic (phase)
GPIO	General Purpose Interface Bus (IEEE-488)
IEMN	Institute of Electronics, Microelectronics and Nanotechnology (Lille, France)
IFIMUP	Institute of Materials Physics, University of Porto (Portugal)
ISOLDE	Isotope Separator On Line (CERN, Genève, Switzerland)
ITN	Nuclear and Technological Institute (Lisbon, Portugal)
JT	Jahn-Teller (electronic 3d level degeneracy, MnO ₆ distortion)
ME	Magneto-Electric
MFM	Magnetic Force Microscopy
M-I	Metal-Insulator (transition)
MOCVD	Metallic Organic Chemical Vapor Deposition
MR	Magneto-Resistance
MZ	Magneto-Impedance
n.a.	Non applicable, non available
NPD	Neutron Powder Diffraction
O.O.	Orbital Order
ORNL	Oak Ridge National Laboratory (TN, USA)
PFM	Piezo Force Microscopy
PM	Paramagnetic (phase)
... [®]	registered trademark or service mark tag
R&D	Research and Development
RF	Radio Frequency (GHz band)
RKKY	Ruderman-Kittel-Kasuya-Yoshida (magnetic model)
SC	Spin canted
SEM	Scanning Electron Microscopy
S.I.	International System (m, kg, s, A, K, cd, mol)
S.G.	Space Group (Crystallographic Symmetry)
SPM	Scanning Probe Microscopy

TEM	Transmission Electron Microscopy
... TM	Unregistered trade mark tag
UA	University of Aveiro (Portugal)
UP	University of Porto (Portugal)
UTAD	University of Trás-os-Montes e Alto Douro (Vila Real, Portugal)
UHV	Ultra High Vacuum
XPS	X-Ray Photo-electron Spectroscopy
XRD	X-Ray Diffraction Spectroscopy
XRR	X-Ray Reflectometry

I INTRODUCTION

This chapter provides a resume of the most relevant concepts, theories, terms and units that are essential for understanding the scientific background of multiferroic materials; although some aspects of the presented models are rather simplistic with limited applicability, when used in an adequate context, they provide a basis and a phenomenological description of the mechanisms involved in particular aspects of the materials.

Following the boom of semiconductors microelectronics, electron-charge-based information processing systems have become victims of their own success; as the downscaling process has further advanced, the ability to pack more transistors and to operate them at higher speeds has given rise to circuits approaching a power density ~ 100 W/cm²; besides that, heat dissipation problems at channel lengths below 5 nm, quantum effects like tunneling and over-barrier transitions result in atypical behavior for conventional electronics.

If we start from the basic physics and chemistry subjacent to the structural, electric and magnetic properties of materials on the macroscopic scale, we will find that, once the dimensions decrease down to the nanometer scale, materials start to exhibit additional phenomena, mainly due to quantum size effects. Actually, even the intrinsic properties of the materials become extrinsic (size dependent) and some parameters can be tailored, which virtually allows for a wide range of values for them; moreover, the possibility to combine several nano-structured elements in a single electronic component can further complement some physical functionalities, which could not be achieved by using macroscopic materials alone [I.0.1].

There are endless possibilities for scientists to research new phenomena and develop high-technology devices by understanding the complex effects on these systems and reducing their size to the nanometric scale, cutting down the dimensional layout from the “3D” bulk materials particularly to “2D” (films, quantum wells), but also to “1D” (wires) and even “0D” (quantum dots).

Inherent to the nano-scale of the systems, minor imperfections, like chemical inhomogeneity or impurities, crystalline structural defects, interfaces and external morphology, etc., have significant effects upon the physical properties; therefore, very high quality materials should be designed and implemented in order to get a device with the desired characteristics.

Research and development of new materials for alternative vectors in information processing has to achieve at least performances one order of magnitude higher than the established in order to progress to a new technological paradigm shift. In any case, it must be perceptive to five essential and integrated aspects [I.0.2]:

- Distinguishability between logic states (materials having asymmetric states)
- Thermodynamic stability (store, noise, life cycle, switching energy and speed between states)
- Information assessment and transport (data transfer process)
- Thermal management (energy consumption and dissipation in the nano scale)
- Manufacturing costs (use of widespread materials and preference for self assembly systems)

In fact, nanotechnology research has advanced rapidly over the last decades; the structural, electric and magnetic properties of materials have been shown to become controllable in such low dimensions as well. Part of this research is directed at using “spin” in some form as the information vector; under the general heading of “spintronics” [I.0.3], one may find areas like correlated spin systems, magnetic domains, single-spin logic, and particularly a class of materials labeled as multiferroics that can conjugate magneto-electric-elastic coupling properties.

1 Materials Structure

The fundamental concept about matter is that it is made of atoms. An atom is the basic unit of an element that can undergo a chemical change; in the simplest model, it consists of a nucleus about 10^{-14} m in diameter, accounting for almost all the mass of the atom, with a Z number of protons (p^+) and an approximate number of neutrons (n^0).

The volume of the atom, typically in the order of 10^{-10} m, is imposed by the cloud of Z electrons (e^-). The electrons are arranged in a spatial distributions (x, y, z) configuration and quantified energy (E) described by wave functions represented in figure 1.0.1, that are solutions of the Schrödinger equation Ψ . a)

$$\nabla^2 \Psi(x, y, z) + \frac{2m_e}{\hbar^2} (E - E_p) \Psi(x, y, z) = 0 \quad (\text{Schrödinger equation})$$

The electrons states are described by the quantum mechanics theory in a set of four quantum numbers: principal or shell ($n = 1, 2, 3, \dots$), orbital ($l = 0, 1, 2, \dots, n-1$), orbital magnetic ($m = -l, -l+1, \dots, 0, \dots, l-1, l$) and spin ($s = -1/2$ or $+1/2$), arranged in rising energy levels that cannot be repeated (Pauli's exclusion principle) while spreading the spatial distribution within the same orbital (Hund's rule) [1.0.1]. b)

The valence electrons, occupying the outer shell, play the most important role in defining the substance chemical behavior and most of its physical properties; in fact, the different columns in the periodic table of elements are arranged according to the number and orbital disposition of valence electrons, whilst the rows are linked to the total number of shells, as depicted in figure 1.0.2.

The atoms tend to bond with each other forming more stable energy configurations as molecules; some kind of bonds can be relatively strong, in the case that electrons are shared or transferred between neighboring atoms, forming three different classes of solids: covalent, metallic or ionic. As a result, there is a redistribution of electrons near each atom, modifying its properties in relation to the isolated state [1.0.2]. c)

a) Ψ As developed by Erwin Schrodinger (1887–1961)

b) A letter has been assigned to each orbital quantum number " l ": $1 \equiv s$, $2 \equiv p$, $3 \equiv d$ and $4 \equiv f$

c) Although there are weaker bonds due to permanent or fluctuating polarization of the electron clouds in the atoms or molecules, the present work is mainly concerned with the stronger and more stable bonds responsible for solid state materials.

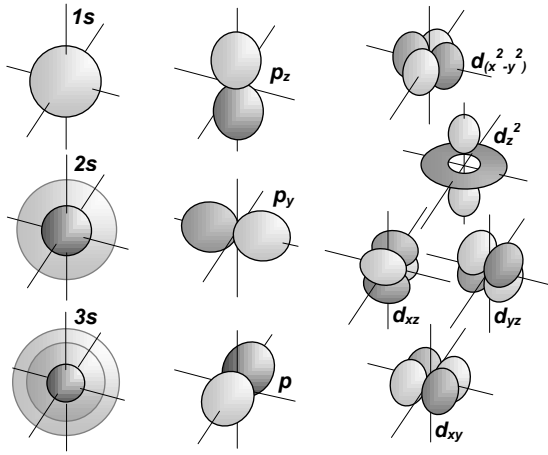


Fig. 1.0.1: Schematics of $|\Psi|^2$ and labels of electrons' orbitals in the Hydrogen atom.

Fig. 1.0.2: The Periodic Table is an indispensable tool in materials research (from NIST).

In the solid state, the atoms or molecules will be spatially arranged according to their relative amount and forces between them; if there is a repeating pattern, we are in the presence of a crystalline structure. When describing the periodic entities as points in a 3D network, there are a limited number of possibilities for their relative disposition, leading to seven distinct crystal systems [1.0.3], as represented in figure 1.0.3.

Many of the properties of materials depend directly on the crystallographic symmetries, directions and distances between particular planes of atoms; in order to identify these features, we use the Miller Indices' convention:

Taking a , b and c cell parameters and the respective axis of the crystal system as a referential, we represent, by the set of normalized integer numbers, the vector $[h \ k \ l]$ perpendicular to the family of planes $(h \ k \ l)$ that intercepts the framework; this is exemplified in figure 1.0.4. The separation between planes (d_{hkl}) and the angle (α) between two directions $[h_1 \ k_1 \ l_1]$ and $[h_2 \ k_2 \ l_2]$ can be found by the expressions [1.0.3]:

$$\frac{1}{d_{(hkl)}^2} = \frac{h^2}{a^2} + \frac{k^2}{b^2} + \frac{l^2}{c^2} \quad (\text{Separation between planes})$$

$$\cos \alpha = \frac{h_1 h_2 + k_1 k_2 + l_1 l_2}{\sqrt{h_1^2 + k_1^2 + l_1^2} \sqrt{h_2^2 + k_2^2 + l_2^2}} \quad (\text{Angle between planes})$$

However, there is no such thing as a perfect crystal; the periodicity can be affected by several types of point and line defects that generate strain field distortions in the matrix, as represented in figures 1.0.5 and 1.0.6. These also have a strong influence in modifying the materials' properties [1.0.3].

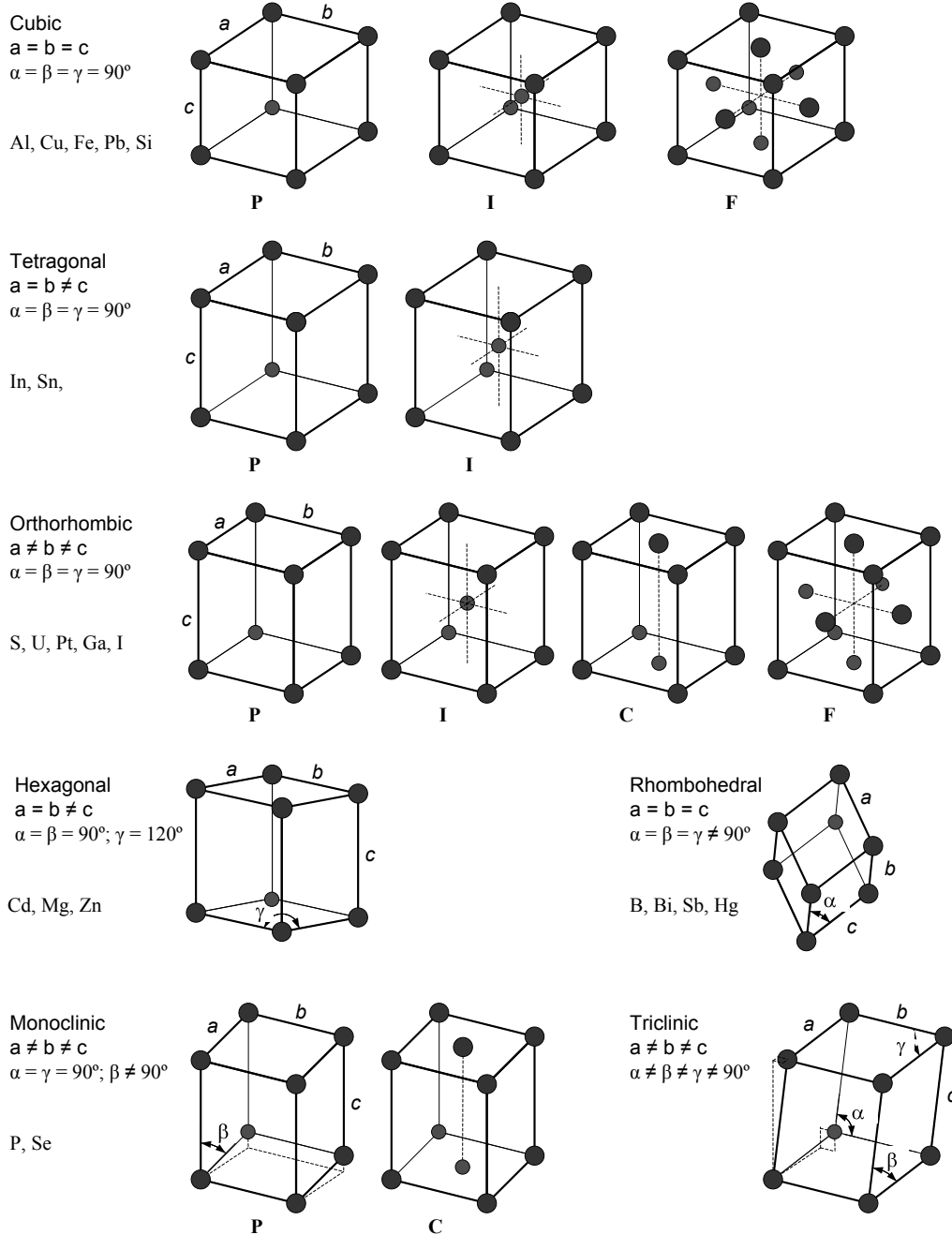


Fig. 1.0.3: The seven crystal systems, their respective symmetry relations and some typical examples of elements that are structured in such geometry. The fourteen Bravais Lattices are designated: P as primitive, I as body-centered, F as face-centered and C (or A or B) as opposite sides centered unit cells.

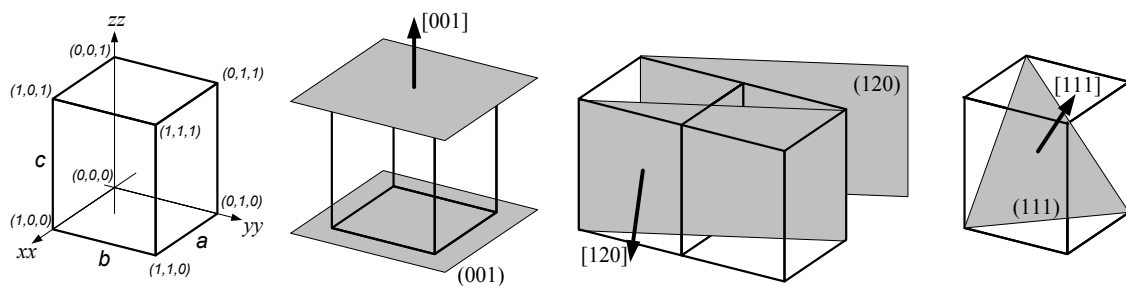


Fig. 1.0.4: Examples for defining directions $[h k l]$ and family of planes $(h k l)$ in a crystallographic system.

In effect, the crystals' surfaces represent the most radical break of periodicity, leaving partially unbounded atoms able to adsorb and absorb other atoms or molecules or even to be corroded or dislodged from the matrix; as such, usually the surfaces are covered with various imperfections, impurities and rearrangements that usually lead to local changes in the material's properties in relation to the bulk. Moreover, most solid materials are polycrystalline, i.e., an aggregate of many micro or nano-sized crystallites with random orientations, resulting in a sequence of mismatches and defects all across the grain boundaries due to the drastic changes in crystallographic directions in adjacent grains.

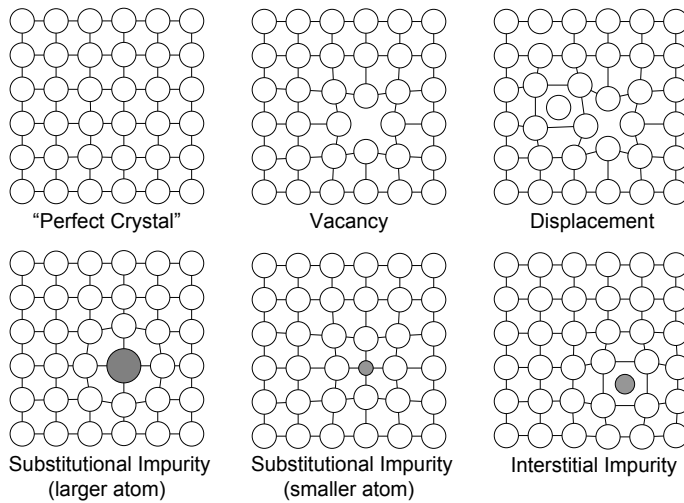


Fig. 1.0.5: Schematics of a "perfect crystal" and point defects

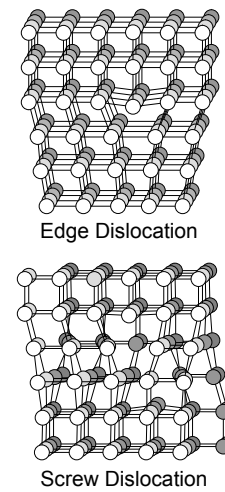


Fig. 1.0.6: Schematics of line defects

Single and polycrystalline solids exhibit a particular phase if the structure and properties are homogeneous all over the material. When different materials come to contact, there can be thermodynamic conditions to merge in a solid solution and generate a new phase, or else to be immiscible and produce a mixture keeping the individual phases separate, though some relevant interface phenomena may be established. The specific state and phases of a material system are usually expressed in terms of phase diagrams as function of parameters like microstructure, composition, temperature and pressure under equilibrium conditions.

An important aspect about mixtures and composites is the connectivity between the different fractions: if it assumes a 0D (dots), 1D (lines), 2D (layers) or 3D (powders) distribution, if there are percolation patterns for each phase and if there is an epitaxial connection between the different phases; these factors are fundamental in defining both how the phases interact and the conjugated properties of the composite [1.0.4].

2 Electrical Properties

Starting from the indispensable electromagnetism equations proposed in 1864 by James Clerk Maxwell [2.0.1]:

$$\nabla \times \mathbf{H} = \mathbf{J}_e + \frac{\partial \mathbf{D}}{\partial t} \quad (\text{Ampère's law})$$

$$\nabla \cdot \mathbf{D} = \rho_e \quad (\text{Gauss' law})$$

$$\nabla \times \mathbf{E} = -\frac{\partial \mathbf{B}}{\partial t} \quad (\text{Faraday's law})$$

$$\nabla \cdot \mathbf{B} = 0 \quad (\text{Gauss's law for Magnetism})$$

The merit of Maxwell's equations is that a wide range of electromagnetic phenomena can be described using only a few variables:

- Ampere's law states that an external magnetic field (\mathbf{H}) can be generated by a free electric current density (\mathbf{J}_e) or a variation in the electric flux density (\mathbf{D});
- Gauss' law states that a charge density (ρ_e) generates a electric flux density (\mathbf{D}) gradient;
- Faraday's law states that a variation in the magnetic flux density (\mathbf{B}) will induce an external electric field (\mathbf{E});
- The fourth law states that the magnetic flux lines form closed loops thus no magnetic monopoles have yet been discovered.

We postpone the discussion of magnetic properties for the next chapter, and proceed by further describing some of the electric principles governing the properties of materials:

Materials can be basically classified as conductors, semiconductors or insulators, (whereas the particular case of superconductors is out of the scope of this work), each exhibiting particular and extensive phenomena and possessing their own interpretative models; some select theories are introduced in this chapter as indispensable tools to understand the context of the thesis work.

All types of electronic systems are made from a complex assemblage of these three kinds of materials, each performing a specific function according to the motion behavior of charges under the influence of an applied electric field, for instance: conductors for current feeding, semiconductors in diodes and amplifiers, and dielectrics for insulation or capacitor fillings, optical media, etc.

Although valuable, the absolute value of conductivity, exemplified in figure 2.0.1, is not the only criterion used to distinguish between materials' electrical character or transitions [2.0.2]; in fact, the structural mechanisms that affect carrier's mobility and its temperature dependence become fundamental to understand the electrical properties and respective applications for each material. In the case of "free atoms", the available states for electrons have discrete energies, whereas for solid materials the superimposition of the electrons wave functions result in a distribution of energy states in the form of bands (figure 2.02). The electrons can belong to the valence band and be "trapped" in ionic or covalent bonds, or be excited to the conduction band, available for electric conduction complemented by the vacancies left at the valence band (figure 2.0.3) or for metallic bonding.

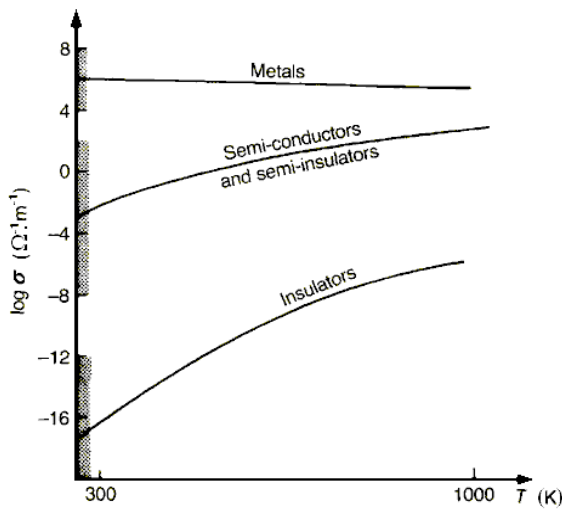


Fig. 2.0.1: Example of typical conductivity (σ) ranges for several classes of electrical materials [2.0.2]

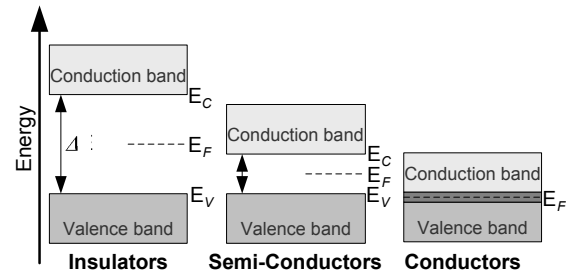


Fig. 2.0.2: Energy band diagrams for solids

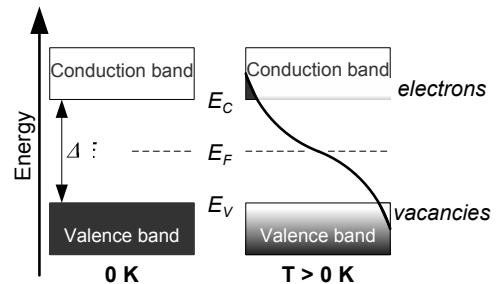


Fig. 2.0.3: Fermi distribution for $T = 0$ K and $T > 0$ K

In insulators, the valence band are separated by a relatively large gap from the conduction band ($\Delta E > 4$ eV), while in semiconductors the difference is small enough that thermal or other excitations can bridge the gap easily at room temperature ($k_B \cdot T = 0.026$

eV); in conductors, like metals, the valence band overlaps the conduction band as represented in figure 2.0.2.

The concept of the Fermi energy (E_F) and chemical potential is also important for understanding the electrical and thermal properties of solids. At absolute zero the electrons pack into the lowest available energy states up to the Fermi level, while at higher temperatures a certain fraction $f(E)$ will exist above and transfer to the conduction band (figure 2.0.3).

$$f(E) = \frac{1}{e^{\frac{E - E_F}{k_B T}} + 1} \quad (\text{Fermi function})$$

2.1. Conductors

Typical conductors like metals contain a large number of “free” electrons per volume (N/V) that are able to move within the material when accelerated by an electric field (E), attaining an average “drift” velocity (v_d) which is limited by the mean free time (τ) between collisions of the electrons with the lattice vibrations, defects, impurities, etc., as represented in figure 2.1.1. The free current density (J_e) as explained by Drude’s theory [2.1.1] under a d.c. electric field (E):

$$J_e = \frac{\Delta}{S \Delta} = \frac{N_e}{V} v_d = \frac{N_e e^2 \tau}{V m_e} E \quad (\text{Drude's Theory})$$

$$J_e = \tau E \text{ or } J_e = \mathcal{J} / \rho \quad (\text{Ohm's law})$$

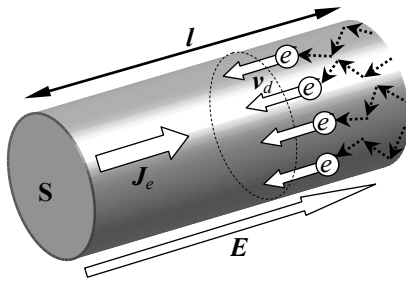


Fig. 2.1.1: Schematics of charge flow (J_e) in a conductor due to electrons mobility (e^-) in the presence of an applied electric field (E).

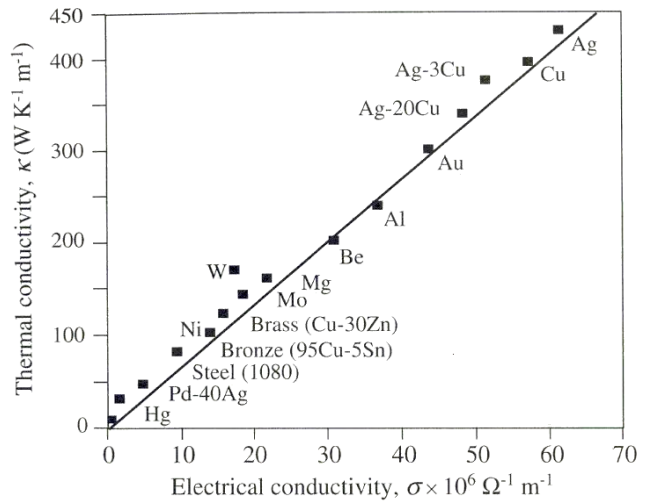


Fig. 2.1.2: Thermal conductivity vs. conductivity for some metals at 20°C. The solid line represents the WFL law [2.0.2].

Given that the amplitude of the lattice vibrations increases with the thermal energy available, the resistivity (ρ) is temperature (T) dependent, approximately by the equation:

$$\rho = \rho_0 [1 + \alpha_0 (T - T_0)] \quad (\text{Metals' resistivity})$$

Within limited temperature range, above 100 K and below fusion and magnetic phase transitions, the thermal coefficient α_0 is of the order of $10^{-2}/\text{K}$ for most pure metals, where the reference resistivity ρ_0 is usually defined at $T_0 = 273 \text{ K}$. Within this simplified model, electrons also govern the process of heat transport in metals and the electronic thermal conductivity (κ) is given by the Wiedemann-Franz-Lorenz law [2.0.2]:

$$\kappa = \frac{\pi^2 k_B^2}{3e^2} \sigma T \quad (\text{WFL law}),$$

$$\text{With } \frac{\pi^2 k_B^2}{3e^2} = 2.45 \times 10^{-8} \text{ W} \cdot \Omega \cdot \text{K}^{-2} \quad (\text{Lorenz number})$$

For a metallic material with length l and cross section S , this result is equivalent expressions for electrical Ohm's law ($i = \Delta V/R$) and heat (E) thermal conductivity:

$$\frac{\partial i}{\partial t} = \frac{S}{l} \cdot \frac{\Delta V}{\rho} \quad \text{and} \quad \frac{\partial E}{\partial t} = \frac{S}{l} \cdot \frac{\Delta T}{\kappa} \quad (\text{Similarity between Ohm's and Fourier's laws})$$

The resistivity decreases more rapidly below 100 K in a $\rho = \alpha_r T^5 + \rho_r$ dependence, where α_r is a constant and ρ_r is the residual resistivity which in the exceptional case of superconductors can vanish.

For a conductor under a.c. excitation, most of the current flows in the surface region of depth δ (of the order of μm) defined as a function of conductivity (σ), angular frequency (ω) of the applied field and absolute permeability (μ):

$$\delta = \left(\frac{1}{2} \cdot \frac{1}{\omega \cdot \mu \cdot \sigma} \right)^{1/2} \quad (\text{Normal Conduction depth})$$

In the case of thin films, the thickness (δ) is smaller than the mean free path of the electrons ($v_d \cdot \tau$) in the bulk material. Consequently, in polycrystalline films, the additional scattering from the surfaces and a more significant contribution from scattering effects due to the morphology (grain size, stress, etc.) may lead to an increased resistivity, whereas high quality films with epitaxial or preferred orientation structure usually show higher conductivity [2.0.2].

2.2. Semiconductors

As mentioned before, semiconductors constitute the backbone of conventional electronics, due to the high flexibility they exhibit regarding the manipulation of their conductive behavior. This very same characteristic also renders them very sensitive to impurities and crystal defects, making necessary a level of extreme chemical purity, precise chemical doping and high crystalline perfection in order to achieve predictable and reliable electrical properties.

At the normal ranges of temperature and pressure, the dominant charge carriers in an intrinsic semiconductor are mainly generated by thermal excitation in the bulk, because the semiconductor has a relatively small energy band gap ($\Delta E = E_c - E_v$); hence, a small amount of energy is sufficient to excite electrons from full valence band to an upper empty conduction band, leaving behind a broken bond (or hole) with a localized positive charge.

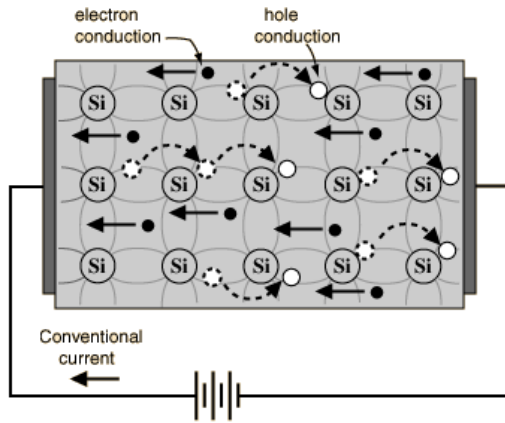


Fig. 2.2.1: Schematics of electron and hole conduction for an intrinsic semiconductor.

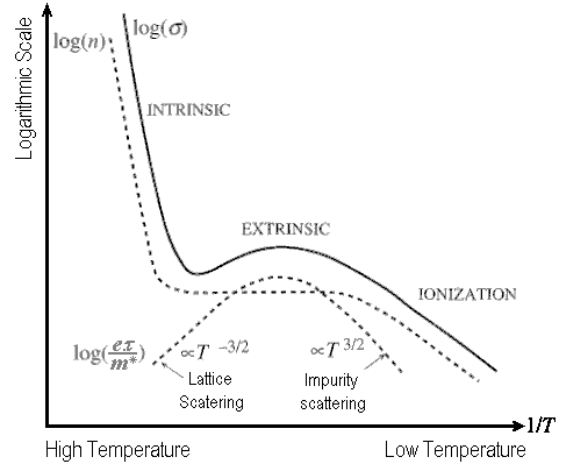


Fig. 2.2.2: Conductivity (σ) vs. inverse temperature dependence for n-type semiconductor [2.2.1], highlighting the most important regimes.

Both the conduction electrons and the holes displacements (by tunneling electrons from neighboring bonds) contribute to electric conduction in presence of an applied field (figure 2.2.1). The effective concentration of electrons in the conduction band (n), which corresponds to an equal number of holes (p) in the valence band, is temperature dependent [2.0.2]:

$$n.p = n_i^2 = 4 \cdot \pi \cdot k_B \cdot T \cdot h^2 \cdot \left(\frac{m_h^* \cdot m_e^*}{2\pi \hbar^2} \right)^{3/2} \cdot e^{-\frac{E_g}{k_B \cdot T}} \quad (\text{Mass action law})$$

In extrinsic semiconductors, doping elements are added to the matrix material: “donors” to contribute to excess electrons (n-type) or “acceptors” to produce excess holes (p-type), resulting in a dislocation of the Fermi energy level and imposing the electrical work performed by each kind of carrier under conduction regime.

The conductivity of extrinsic semiconductors has three distinct regimes as a function of temperature as exemplified in figure 2.2.2: at low temperature range ($T < T_s$), is dominated by the progressive ionization of the donor (or acceptor) elements up to the respective saturation at T_s ; for intermediate temperature ranges ($T_s < T < T_i$), the system becomes more stable (extrinsic); for temperatures above the intrinsic limit (T_i), the conduction is dominated by electron excitation of the matrix semiconductor, overcoming the dopant contribution [2.2.1].

2.3. Dielectrics

As the electrons are strongly bound to the respective atoms or molecules, external fields, such as electromagnetic fields, mechanical stress, or temperature gradients, only result in a local distortion of the charge cloud. Eventual charge carriers are mainly injected from electrical contacts or other external sources or result from the dielectric breakdown [2.3.1]. Under linear response to an electric field (E), the centers of distribution of positive ($+q$) and negative charges ($-q$) are displaced from their equilibrium position and become separate by a finite distance (l), inducing an electric dipole moment:

$$p = \underline{l} = \chi \underline{E} \quad \text{(Electric dipole moment)}$$

$$\text{with: } \alpha_e = \frac{Z \cdot e^2}{m_e \cdot \omega} \quad \text{(Electronic polarizability)}$$

Given that the electrostatic restoring force is proportional to the displaced charge (Z) and the distance (l), after the removal of the field, the electronic cloud executes a simple harmonic motion about the nucleus with a characteristic angular frequency (ω_0).

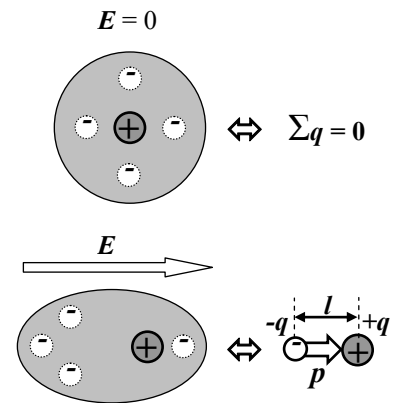


Fig. 2.3.1: Electronic polarization under electric field and dipole moment definition.

$$\text{Making } \chi_e = \frac{N \cdot \alpha_e}{V \cdot \epsilon_0} \quad (\text{Electronic dipole susceptibility})$$

$$\text{and } \epsilon_r = 1 + \chi_e \quad (\text{Relative permittivity})$$

$$\text{where } \epsilon_0 = 8.854 \cdot 10^{-12} \text{ J}^{-1} \cdot \text{C}^2 \cdot \text{m}^{-1} \text{ (or } \text{F} \cdot \text{m}^{-1}) \quad (\text{Vacuum permittivity})$$

This allows the calculation of the macroscopic property ϵ_r from the microscopic electronic or ionic polarization (α_e) phenomena:

$$\text{thus yielding } \frac{\epsilon_r + 1}{\epsilon_r + 2} = \frac{1}{3} \frac{N}{V} \frac{\alpha_e}{\epsilon_0} \quad (\text{Clausius-Mossotti equation})$$

In the case of molecules with permanent dipole moments (p_0), like for example liquid crystals, there is orientational polarization under the effect of an electric field, with:

$$\alpha_e = \frac{1}{3} \frac{p_0^2}{k_e \cdot T} \quad (\text{Orientational polarizability})$$

Other polarization mechanisms may comprise accumulation of charge at interfaces between two regions, like at the contact area between the dielectric and the electrodes or within the material itself (α_i) such as the case of grain boundaries, defects, impurities, etc.

The total linear response polarization (P) will be the sum of all existing contributions, with dependencies on the dielectric material's geometry, microstructure, temperature, mobility and electronic bonds of the molecules, etc:

$$P = \frac{1}{V} \sum_{i=1}^N = \frac{1}{V} \cdot \sum_{i=1}^N \alpha_i E_i^{local} \quad (\text{Total polarization})$$

Or the bulk:

$$P = \epsilon_0 \cdot \epsilon_r \cdot E \quad (\text{Polarization})$$

Defining the overall electrical susceptibility as:

$$\chi_e = \frac{P}{\epsilon_0 \cdot E} \quad (\text{Electric susceptibility}) \quad \text{a)}$$

One of the most common uses of polarization is to enhance capacitance (C_0 to C) due to the rise of the electric displacement (D) in the medium, resulting in a higher charge accumulation (q_0 to q) between electrode plates for the same voltage (ΔV), area (S) and distance (d) conditions, as represented in figure 2.3.2.

a) In practice, for $\chi_e \gg 1$: $\epsilon_r \approx \chi_e \approx \chi_e + 1$

$$D = \epsilon_0 E + P = \epsilon_0 (1 + \epsilon_r) E = \epsilon E \quad (\text{Electric displacement})$$

$$C_0 = \epsilon_0 / \Delta = \epsilon_0 S / d \quad (\text{Capacitance in free space})$$

$$\epsilon = \frac{D}{E} = \epsilon_0 \frac{C}{C_0} = \epsilon_0 \frac{q}{q_0} = \epsilon_0 \epsilon_r \quad (\text{Medium dielectric permittivity})$$

The polarization generates a depolarizing field (E_{dep}) that depends on the shape factor (N_{dep}) of the dielectric, reducing the effective electric field inside the material:

$$E_{dep} = N_{dep} \cdot P / \epsilon \quad (\text{Polarization for dc field})$$

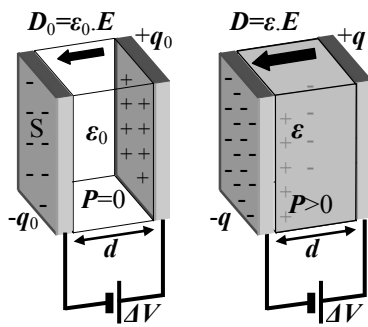


Fig. 2.3.2: Polarization contribution for capacitance enhancement.

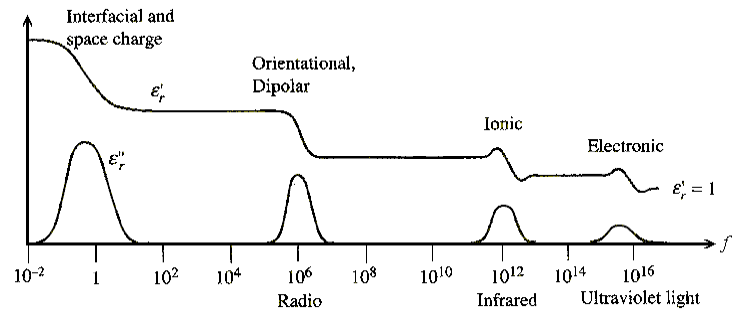


Fig. 2.3.3: Frequency dependence of real and imaginary parts of the dielectric constant in the presence of different polarization mechanisms [2.2.1].

Due to damping factors like the materials lattice thermal agitation, the dielectric material responds with some delay to the alignment or formation of the dipoles as a result of an applied field variation and assumes a more general frequency dependent form:

$$P(\omega) = \epsilon_e(\omega) \epsilon_0 E(\omega) \quad (\text{Polarization vector for a.c. field})$$

For ideal non-interacting dipoles, the permittivity (ϵ) is expressed as a complex number ($\epsilon = \epsilon' + i\epsilon''$) function of the field frequency (ω), as exemplified in figure 2.3.3.

$$\epsilon(\omega) = \epsilon(\omega_\infty) + \frac{\epsilon(\omega_0) - \epsilon(\omega_\infty)}{1 + \omega^2 \tau^2} \quad (\text{Debye dielectric relaxation model})$$

Where τ is the characteristic relaxation time of the medium, $\epsilon(\omega_\infty)$ is the permittivity at the high frequency limit and $\epsilon(\omega_0)$ at the static condition. The influence of $\epsilon(\omega)$ in voltage and current amplitude and relative phases is described in terms of impedance (Z); for the plain capacitor example, it introduces pure reactive impedance inversely proportional to the signal frequency and a $\pi/2$ delay between voltage and current:

$$Z_C(\omega) = \frac{1}{i\omega C} \quad (\text{Capacitor impedance})$$

Thus, the electric polarization leads to the occurrence of resonance, relaxation, energy storage, energy dissipation phenomena, and extends to a panoply of thermal, mechanical, and optical effects and their interrelations. On the other hand, to mention a few limitations, dielectric materials can suffer electrical aging and destructive breakdown, especially when used as insulators or capacitor fillers under high power a.c. fields.

Dielectric materials may be classified into two major categories according to the presence or not of a concomitant (ferroic) polarization order, as seen in figure 2.3.4:

Non-ferroic dielectrics are also known as normal dielectrics or paraelectrics, can be found either in gas, liquid or solid phases and may be divided into three classes: nonpolar (that have only electronic polarization), polar (have both electronic and ionic polarization) and dipolar (have all three fundamental polarizations: electronic, ionic, and orientational).

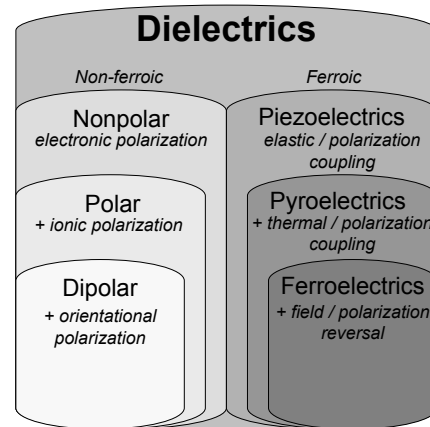


Fig. 2.3.4: Dielectrics classification

Ferroic dielectrics have spontaneous polarization and must be in single crystalline or polycrystalline form; when subjected to an external field, undergo a change in electric polarization that also result in a small change in unit cell dimensions, depending on the specific symmetry of the unit cells, determines whether the crystal exhibits piezoelectric, pyroelectric, ferroelectric, electro-optic or even non linear effects [2.3.2].

Piezoelectric crystals become strained when an electric field is applied and conversely, while for a pyroelectric crystal a change in temperature produces a change in polarization and specific ferroelectric crystals possess a reversible spontaneous polarization over a certain temperature range.

a)

a) The term “ferroelectrics” can also be used to designate the “ferroic dielectrics” category of materials when understood in the broad context of ferroic phenomena in analogy to ferromagnetism, in opposition to the specific properties of “ferroelectric materials” with reversible spontaneous polarization, meaning that the polarization has a nonzero value in the absence of an applied electric field, and that the direction of the spontaneous polarization can be reversed by applying a field in opposite direction.

On the basis of crystallographic symmetry elements there are 230 space groups, these break down into 32 classes, from which 21 are non-centrosymmetric and of these 20 can exhibit piezoelectric effect and only 10 can be pyroelectric with a subgroup also ferroelectric. Materials exhibiting these effects imply that phase transitions involve asymmetric displacements of atoms inside the crystal arrangement, albeit the cubic system possesses symmetry characteristics which can combine to give no piezoelectric effect.

2.3.1. Ferroelectrics

The most prominent properties of ferroelectrics are the hysteresis and nonlinearity in the relation between the polarization (\mathbf{P}) and the applied electric field (\mathbf{E}), as scheme in figure 2.3.5; and anomalously high dielectric constants (ϵ_r up to 10^5), especially near the critical Curie temperature (T_C), as examples in figure 2.3.6; while at $T > T_C$ the behavior of the electric susceptibility (χ_e) follows the Curie-Weiss law mean field approximation:

$$\chi_e = \frac{C}{T - T_C} \quad (\text{Curie-Weiss law})$$

The transition to a polarized state also induces a mechanical strain, tending to change the volume and the shape of the material body. The direction of spontaneous polarization, also referred to as the ferroelectric polar axis, is along the direction of the unit cell's elongation. The direction of the polarization (\mathbf{P}) can be reversed by a sufficiently high electric field (\mathbf{E}) of opposite polarity, distinguishing it as a ferroelectric material. This possibility makes it also capable of piezoelectric, pyroelectric and electro-optic behavior. Because a ceramic is composed of a large number of randomly oriented crystallites, it is normally observed an isotropic response whereas single crystals have anisotropic responses.

The conventional poling process, which is reversible, consists in forcing the polar axis as near to the field direction as possible, within the mechanical and electric breakdown limits of the material, by the application of an external static electric field for some time, enough to bring the specimen to the saturation polarization and then allowed to relax back to the remanent condition. Poling is usually carried out at temperatures as high as the Curie threshold temperature allows. It should be noted that a poling process is often necessary even with single-crystal ferroelectric bodies because they contain randomly oriented domains.

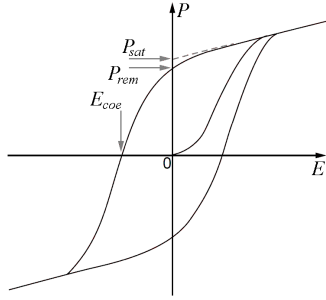


Fig. 2.3.5: Schematic diagram of a typical ferroelectric hysteresis loop.

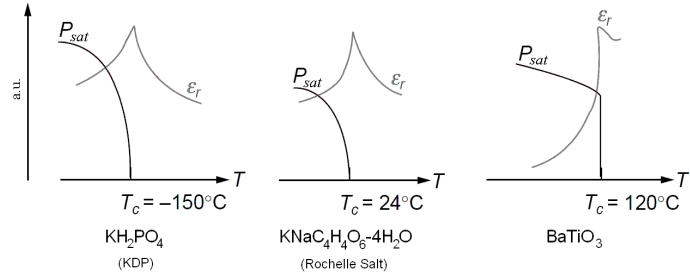


Fig. 2.3.6: Schematics of the dielectric constant ϵ_r and the spontaneous polarization P_{sat} with the temperature for three typical FE crystals [2.2.1].

Ferroelectrics have been traditionally divided into 2 different types of transitions:

- *Displacive ferroelectrics* where the discrete symmetry group is broken at T_C and the ferroelectric transition can be described as the result instability of the anharmonic crystal lattice against soft polar lattice vibration (e.g., BaTiO_3).
- *Order-disorder-type ferroelectrics* where a discrete symmetry group is broken due to the ordering of the ions or molecules in a rigid lattice potential (e.g., KH_2PO_4).

The extensive diversity of phases can be classified as:

- *Ferroelectric liquid crystals* where a continuous symmetry group is broken at T_C and the relaxational soft mode of the high-temperature phase splits below T_C .
- *Relaxors* where there is no macroscopic symmetry breaking and where, in view of “site” and “charge” disorder, there is an extremely broad distribution of correlation times. The longest correlation time diverges at the freezing transition whereas other correlation times are still finite (e.g., $\text{PbMg}_{1/3}\text{Nb}_{2/3}\text{O}_3$).
- *Ferrielectrics* behavior is related to the relative spatial distribution of entire polar molecules and can be found for example in quiral liquid crystals.
- *Antiferroelectrics* do not show a net spontaneous polarization below T_N , but are characterized by the existence of a superstructure described in terms of two sublattices having equal but opposite polarization; practically show a paraelectric response to fields and the dielectric constant is considerably low. Some antiferroelectric materials may also be induced to become ferroelectric under the application of a suitable electric field.

It is worth mentioning that upon repeated switching of the polarization of the crystals, spontaneous polarization becomes clamped or decreases, and the coercive field increases. This phenomenon is referred to as the fatigue or decay of the crystal and it has been attributed to the build-up of the space charge near the crystal surfaces and the interaction of this space charge with domain walls.

2.3.2. Piezoelectric phenomena

The direct effect of the piezoelectricity is the generation of electric polarization by a mechanical stress, while the converse effect is the mechanical displacement actuated by an electric field. The effects are reversible and convertible in relation to the direction of the electric field (\mathbf{E}) and the mechanical distortion ($\mathbf{s} = \Delta l/l$); whereas the electrostriction phenomenon is not inversive and the resulting strain is proportional to the square of the field. Combining the polarization ($\mathbf{P} = \chi_e \cdot \epsilon \cdot \mathbf{E}$) and Hooke's law ($\mathbf{T} = \mathbf{Y} \cdot \mathbf{s}$) we define the piezoelectric coefficient tensor (\mathbf{d}_{ij})

$$P_i = d_{ij} \cdot T_j \quad \Leftrightarrow \quad s_i = d_{ij} \cdot E_j \quad (\text{Piezoelectric coefficient definition})$$

The tensor \mathbf{d}_{ij} assumes maximum value for \mathbf{d}_{33} when the relation between polarization and stress or strain and electric field are considered in the same direction, as represented in figure 2.3.7.

The electro-mechanic energy conversion factor (K_{em}) is given by:

$$K_{em}^2 = \frac{\oint_{\text{cycle}} \frac{dW_{mech}}{dW_{elec}}}{\oint_{\text{cycle}} \frac{dW_{elec}}{dW_{mech}}} \quad \Leftrightarrow \quad (\text{Electro-mechanic energy conversion factor})$$

Crystal	d_{33} $10^{-12} \cdot \text{m} \cdot \text{V}^{-1}$	K_{em} \sim	ρ $\text{g} \cdot \text{cm}^{-3}$
Quartz (SiO_2)	2.3	0.1	2.65
Rochelle Salt	350	0.8	1.77
BaTiO_3	190	0.4	5.70
NaNbO_3	49	0.4	4.45
PZT ($\text{PbTi}_{0.5}\text{Zr}_{0.5}\text{O}_3$)	480	0.7	7.70
KH_2PO_4 (KDP)	107	0.1	2.31
Kynar (PVDF)	4	0.1	1.78

Table 2.3.1: Some examples of materials and typical values of \mathbf{d}_{ij} and K_{em} . [2.3.2]

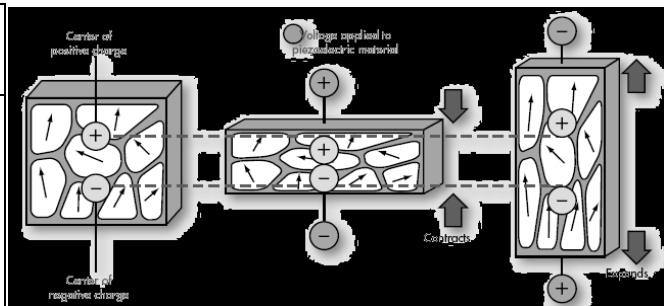


Fig.2.3.7: Illustration of the piezoelectric effect

There are two principal mechanisms for piezoelectricity.

- The *linear piezoelectric effect* may occur, in first approximation, if the crystal has no center of symmetry and when under the unstrained condition the dipole moments of the material mutually cancel each other.
- For *ferroelectric piezoelectricity*, the variation of the mechanical strain with the applied electric field follows the change of polarization in the hysteresis loop shown in Figure 2.3.5. The dipole moment memory effect adds to the resulting moment along a polar axis of the unit cell, so the occurrence of piezoelectricity is accompanied by pyroelectricity, involving spontaneous polarization.

During the poling process, there is a small expansion of the material along the poling direction and a contraction in perpendicular directions as examples in figure 2.3.8.

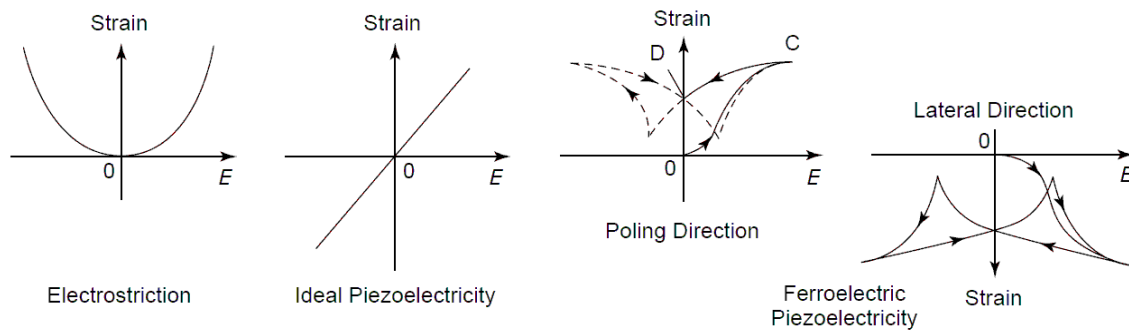


Fig. 2.3.8: Schematic illustration of the variation of mechanical strain with electric field for electrostriction, ideal piezoelectricity and ferroelectric piezoelectricity in poling and lateral directions [2.2.1].

3 Magnetic Properties

One of the simplest models [3.0.1] to describe the magnetic dipole moment (μ_m) is the perpendicular vector generated by an electric current (i) looping the surface (S), as shown in figure 3.0.1.

$$\mu = S u_z \quad (\text{Classic magnetic moment model})$$

Given that the atoms in a material are composed of protons (p^+) and neutrons (n^0) in the nucleus, having overall quantum angular momentum (I), and electrons (e^-), each with orbital (L) and intrinsic spin (S) moments, represented in figure 3.0.2, it follows that the entire atom responds to an external magnetic field with a net magnetic moment (μ_F):

$$\mu = \sum_i \frac{\mu}{\hbar} [\mathbf{g}_L \cdot L_i + \mathbf{g}_S \cdot S_i] + \sum_i \frac{\mu}{\hbar} [\mathbf{g}_I \cdot I_i] \quad (\text{Atom's magnetic moment})$$

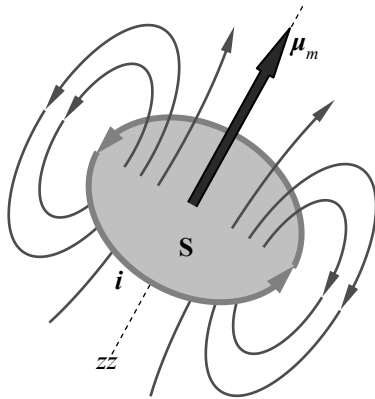


Fig. 3.0.1: Magnetic dipole moment concept

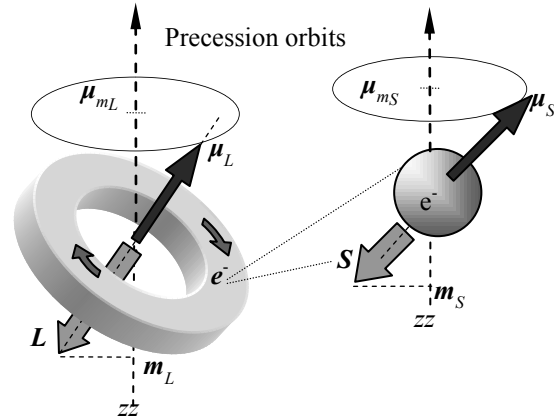


Fig. 3.0.2: Orbiting electron and spinning electron

The comparatively higher mass of protons and neutrons implies that the magnitude of the nucleus' momentum is 1000 times smaller than that of the electrons; for specific isotopes, the sum over the electrons magnetic moments is nul, whereas the nuclear moment is present and can be detected by Nuclear Magnetic Resonance (NMR) systems. Under most circumstances, it is possible to consider mainly the electrons' contribution and the total angular momentum [3.0.2]:

$$\mathbf{J} = \mathbf{L} + \mathbf{S} \quad (\text{Russell-Saunders coupling})$$

Calculated according Hund's rule and Pauli's principle, usually $\mathbf{J} = \mathbf{L} - \mathbf{S}$ for less than half filled shells (like most lanthanide elements) or $\mathbf{J} = \mathbf{L} + \mathbf{S}$ for more than half full shells.

The Landé factor (g_J) relates \mathbf{J} and μ_m and is a function of the quantum numbers L and S with respective gyromagnetic factors ($g_L \approx 1$) and ($g_S \approx 2$), as described by Alfred Landé in 1921.

$$g_J \approx 1 + \frac{J(J+1) + S(S+1) - L(L+1)}{2J(J+1)} \quad (\text{Landé factor})$$

For transition metals, due to quenching in a crystal, L usually takes the minimum allowed values and, in general, $L \approx 0$, $J \approx S$, $g_J \approx 2$. The respective precession of the projection μ_m along the direction of an external field is given by:

$$\mu = \sum_i \frac{\gamma}{\hbar} \cdot g_J \cdot J_i = \gamma \cdot g_J \cdot m_z \quad (\text{Quantified magnetic moment})$$

Where $m_z = -J, -J+1, \dots, 0, \dots, J-1, J$, with m_z taking $(2J+1)$ possible integral values. The resulting magnetization per unit volume (M) is

$$M = \frac{1}{\Delta} \sum_{i=1}^N \mu_i = \frac{N}{\Delta} \cdot \langle \mu \rangle \quad (\text{Magnetization per volume})$$

Considering that the magnetostatic dipole interactions are very weak ($\mu_B/k_B = 0.672$ K/T) and temperatures of the order of 1K are sufficient to destroy the established ferromagnetic order, the main forces responsible for the magnetization are the quantum mechanic exchange interactions between the moments of the nearest neighbor atoms (S_j). This can be written as resulting from local magnetic field (H_i) acting on the i -th spin, described by the Heisenberg Hamiltonian:

$$H = -2 \sum_{i < j} J_{ij} \cdot S_i \cdot S_j - g \cdot \mu_B \cdot \sum_i H_i \cdot S_i \quad (\text{Heisenberg Hamiltonian})$$

When applicable, the total spins interaction sum can be approximated to an average molecular field (H_m) proportional to the magnetization:

$$H_m = \chi_M \cdot M \quad (\text{Weiss molecular mean field})$$

The total “field” experienced by the magnetic moments comprises the external field (H_{ext}) and the internal Weiss field (H_m):

$$H = H_{ext} + H_m \quad (\text{Total Magnetic Field})$$

At high temperatures, above the critical asymptotic paramagnetic Curie temperature (Θ_{PM} or T_C) the expression for the magnetization can be approximated by:

$$M = \chi H = \frac{C}{T - T_w} (H_{ext} + N_w M) \quad (\text{Magnetization})$$

$$\text{or} \quad \chi = \frac{M}{H} = \frac{C}{T - T_w} = \frac{C}{T - \Theta_M} \quad (\text{Curie-Weiss Law})$$

$$\text{Where} \quad C = \frac{N \cdot g_J^2 \cdot J(J+1) \mu_B^2}{3k_B} = \frac{N \cdot \mu_{eff}^2}{3k_B} \quad (\text{Curie's constant})$$

$$\text{and} \quad N_w = \frac{T}{C} = \lim_{H \rightarrow 0} \frac{M}{H} \quad (\text{Weiss constant})$$

When $T = \Theta_{PM}$, the susceptibility diverges, and there may be a spontaneous magnetization for $T < \Theta_{PM}$ even under no external magnetic field.

To determine the magnetization between 0 and T_C , we introduce the concept of magnetic induction or flux density (\mathbf{B}), which results from the external field (\mathbf{H}_{ext}) in free space and the respective magnetization (\mathbf{M}) in the material, and is a measure of the effective force (\mathbf{F}) exerted on charge (q) moving at the velocity \mathbf{v} inside the effectual field:

$$\mathbf{B} = \mu_0 (\mathbf{H}_{ext} + \mathbf{M}) = \mu_0 (1 + \chi) \mathbf{H}_{ext} = \mu_0 \mu_r \mathbf{H}_{ext} \quad (\text{Magnetic induction})$$

$$\mathbf{F} = q \mathbf{v} \otimes \mathbf{B} \quad (\text{Magnetic force})$$

Hence, the magnetic interaction energy (E_m) between the total angular momentum of an atom (μ_m) and the surrounding average magnetic field (\mathbf{B}) tends to be minimized and align the vectors μ_m with \mathbf{B} , whilst the thermal energy ($k_B T$) tends to randomize it:

$$E_m = -\mu_m \cdot \mathbf{B} = -\mu_B g_J m_z B \quad (\text{Magnetostatic Energy})$$

$$\text{Making: } x = \frac{\mu_B g_J B}{k_B T} \quad (\text{Partition function variable})$$

$$\text{becomes: } \langle \mu_z \rangle = \frac{\sum_{m=-J}^J \mu_B g_J m B e^{m x}}{\sum_{m=-J}^J e^{m x}} = \mu_B g_J J B_J \left(\frac{x}{J} \right) \quad (\text{Average moment})$$

$$\text{with} \quad B_J \left(\frac{x}{J} \right) = \frac{1}{J} \left[\left(J + \frac{1}{2} \right) \coth \left(\left(J + \frac{1}{2} \right) x \right) - \frac{1}{2} \coth \left(\frac{1}{2} x \right) \right] \quad (\text{Brillouin function})$$

These calculations assume particular simplifications under certain limits. At very high fields, the Brillouin function goes to 1 and the magnetization saturates, with the magnetic moments completely aligned with the applied field as the temperature tends to zero.

$$\langle \mu \rangle_{sat} = \mu_B g_J J \quad (\text{Saturation moment})$$

giving $\mu_{eff} = \mu_B g_J \sqrt{J(J+1)} = \sqrt{\frac{3Ck_B}{N}}$ (Effective moment)

3.0.1. Demagnetizing Field Correction

The formal linear magnetization equation $\mathbf{M} = \chi \mathbf{H}$ yields a classification into paramagnets ($\chi > 0$) and diamagnets ($\chi < 0$) for small values of \mathbf{M} and \mathbf{H} ; however, for most materials the relationship between \mathbf{M} and \mathbf{H} is generally nonlinear, therefore a more precise definition of the susceptibility is the tensor form $\chi_{ij} = \partial M_i / \partial H_j$, measured at $\mathbf{H} \rightarrow 0$.

Due to magnetostatic dipolar effects depending on the sample's finite size shape and susceptibility, the actual internal field inside the material (\mathbf{H}) is distorted:

$$\mathbf{H} = \mathbf{H}_{ext} - N_d \mathbf{M} \quad (\text{Internal magnetic field correction})$$

And the actual magnetization is found by:

$$\mathbf{M} = \chi \mathbf{H} = \frac{\chi}{1 + \chi N_d} \mathbf{H}_{ext} \quad (\text{Demagnetizing field correction})$$

Where N_d is the demagnetizing coefficient that depends of the sample geometry; in relation to the \mathbf{H}_{ext} direction; for very elongated rod or toroid forms N_d is $< 10^{-2}$; but if χ assumes very high values ($> 10^3$) like in the case of ideal ferromagnets, the magnetization tends to depend only on the geometry:

$$\lim_{\chi \rightarrow \infty} \mathbf{M} = \frac{1}{N_d} \mathbf{H}_{ext} \quad (\text{Extrinsic magnetization in strong ferromagnets})$$

3.1. Magnetic States

Given that the magnetic moments are intrinsic to the orbital and spin motions of electrons, all materials have magnetic properties; the main distinctions lie in how the electrons are ordered and interact collectively according to the exchange interaction principle [3.1.1] and how this affects the materials' response to magnetic fields.

In compounds, the interatomic bonding results in the dislocation or hybridization of the electrons' orbitals; from the competition between the electrons exchange coupling and the Coulomb repulsion, the spins become interactively oriented depending on parameters such as the interatomic distance, the geometry and the number of electrons per atom accounting for the Pauli's exclusion principle, that imposes an antiparallel ($\uparrow\downarrow$) spin structure within a single double-electron ground-state, or the Hund's rule that favors the parallel ($\uparrow\uparrow$) spin distribution of electrons occupying one-electron excited states.

For many metals, and for some nano-composites, interactions between local moments are fairly well approximated by the RKKY model [3.1.2], which yields an oscillatory exchange mediated by conduction electrons; such as a) Nano-composites consisting of low dimensional systems that may include arrangements of magnetic molecules or nanosized objects; such as, metal-based dots, wires or layers distributed within a paramagnetic matrix, which are in the forefront in the development of high TC ferromagnets in particular for the design of spin electronics, magnetic sensors and magnetic recording media.

In oxides, indirect exchange mechanisms are mediated by the 2p electrons of the O^{2-} anions separating transition metal ions: one is the "super-exchange" between identical ions; another is the "double-exchange" mechanism, which can be interpreted as electron hopping with spin memory between mixed valence ions (further detailed in chapter 4). Although the exchange-coupling usually dominates neighboring atoms magnetic interaction, a key role in the nature of the magnetic ordering results from the long range magnetostatic (dipolar) and the anisotropic effects on the material.

The origin, size, and relative orientation of the magnetic moments can translate into cooperative alignment order in ferromagnetics (FM) or the formation of magnetic sublattices, which may balance in antiferromagnetic (AFM) or involve nonequivalent

crystallographic sites with uncompensated moments in ferrimagnetics (FI). There can be also noncollinear spin structures due to competing exchange interactions resulting in more complex spins arrangements, some of which can be comensurated and other turn to be incommensurate, like helical configurations (HS), spin canted (SC), or even disordered spin glass (SG), as illustrated in figure 3.1.0 and briefly summarized below [3.1.3]:

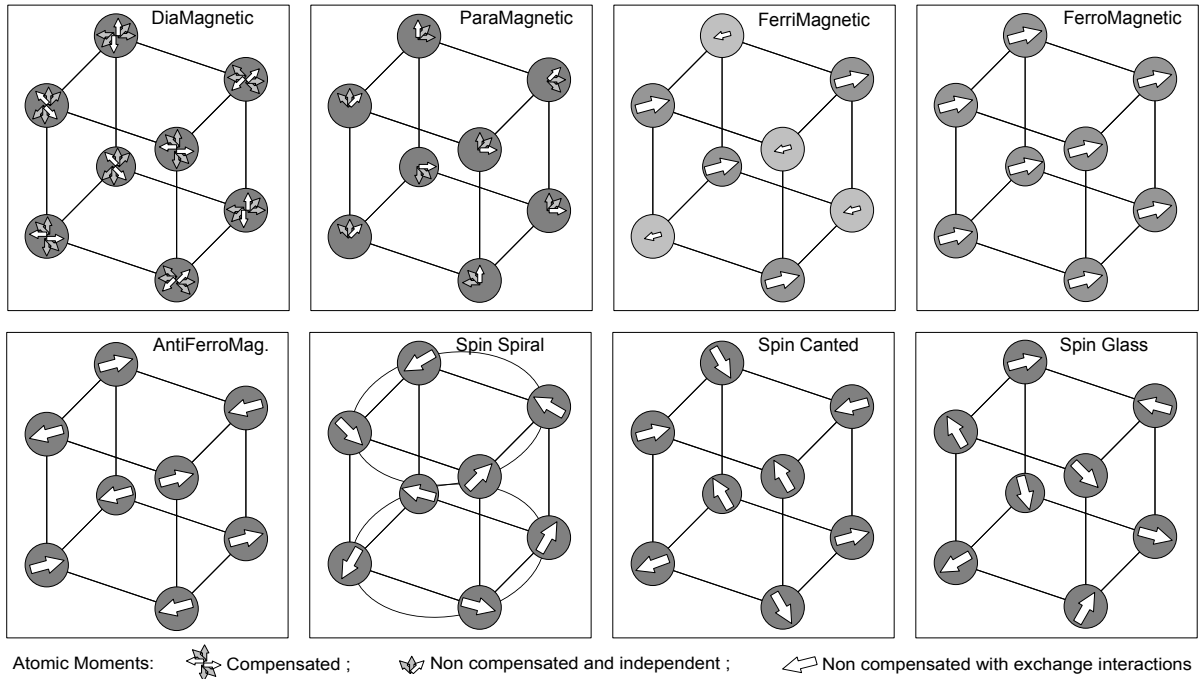


Fig. 3.1.0: Conceptual illustrations of magnetic moments arrangements for some different magnetic states.

3.1.1. Diamagnetism

Usually mistaken as non-magnetic, most materials that don't seem to react to magnetic fields, are in fact diamagnetic, composed of atoms or molecules where the moment contributions of electrons tend to cancel each other (i.e. all the orbital shells are filled and there are no unpaired electrons). Due to the non-cooperative behavior of orbiting electrons when exposed to an applied magnetic field, a very weak negative magnetization is produced, and therefore the materials become in fact repelled by magnetic field gradient in opposition to the case of PM or FM materials. Except for the extreme case of superconductors that assume a true diamagnetic behavior with $\chi = -1$, the characteristic susceptibility (χ) of materials is negative, generally small (of the order of 10^{-5} to 10^{-4}) and temperature independent. Some examples are presented in table 3.1.1 and figures 3.1.1.

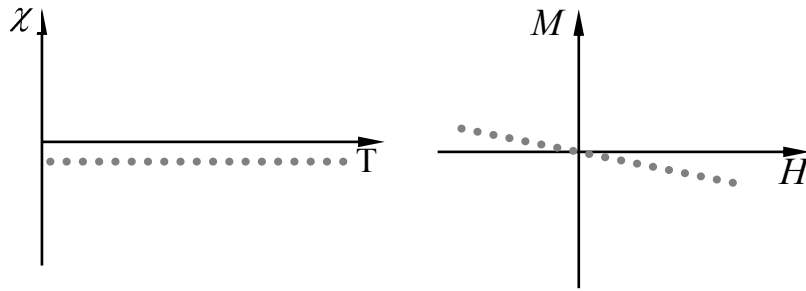


Fig. 3.1.1: Typical behavior of diamagnetic materials

Material	χ
Bismuth	-16.7
Copper	-1.0
Graphite	-1.6
SiO ₂ (quartz)	-0.62
Water	-0.91

Table 3.1.1: Examples of diamagnetic materials in 10^{-5} m³/kg units.

3.1.2. Paramagnetism

If some of the atoms or ions in the material have a net magnetic moment due to unpaired electrons in partially filled orbitals, there is now a progressive alignment of the atomic magnetic moments in the direction of an external magnetic field, although these do not interact with each other and are highly susceptible to the randomizing effects of temperature. The net positive magnetization and the temperature dependent susceptibility are known as Curie's Law described previously. Unless the temperature is very low ($\ll 100$ K) or the field is very high, the paramagnetic susceptibility is relatively small and independent of the applied field (figure 3.1.2). Some examples are presented in table 3.1.2:

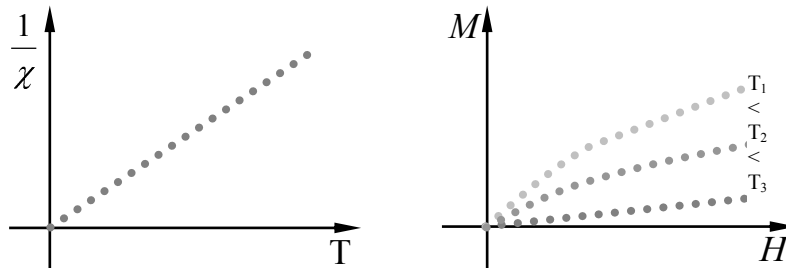


Fig. 3.1.2: Typical behaviour of paramagnetic materials

Material	χ
Aluminum	2.2
Lithium	1.4
Magnesium	1.2
Oxygen	0.19
Platinum	26

Table 3.1.2: Examples of paramagnetic materials in 10^{-8} m³/kg units.

3.1.3. Ferromagnetism

Ferromagnetic materials exhibit parallel alignment of moments, resulting in large spontaneous magnetization even in the absence of a magnetic field. The most representative magnetic materials, like iron, nickel or cobalt and many of their alloys, exhibit very strong interactions between atomic moments, resulting from intense electronic

exchange forces due to the relative orientation of the spins of electrons. The magnetism of the iron-series transition-metal elements is caused by extended, delocalized, or itinerant electrons owned by all atoms, so that the moment per atom is not necessarily an integer, such as the $2.2 \mu_B$ for Fe, $1.7 \mu_B$ for Co, and $0.6 \mu_B$ for Ni. Rare-earth transition-metal intermetallics such as SmCo_5 and $\text{Nd}_2\text{Fe}_{14}\text{B}$ exhibit both itinerant ($3d$) and localized ($4f$) features and reflect RKKY-type interactions.

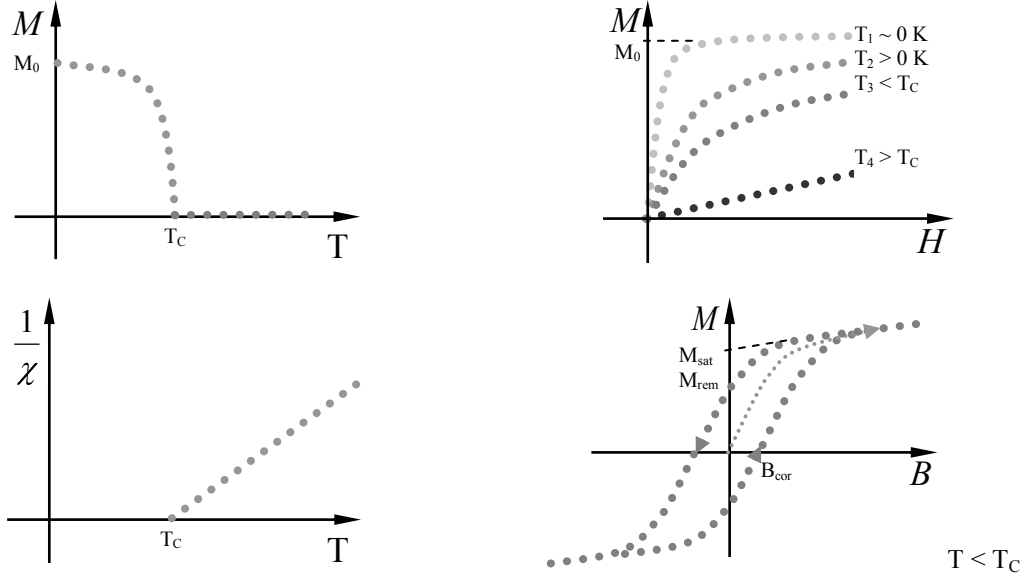


Fig. 3.1.3: Typical behavior of ferromagnetic materials

The saturation magnetization (M_{sat}) is the maximum limit of magnetic moment that can be obtained; this is an intrinsic property, independent of particle size but dependent on temperature. In addition, ferromagnets can retain a memory or remanence (M_{rem}) of the applied field even after its removal. This hysteresis implies that a coercive field (H_{cor} or B_{cor}) must be applied to reduce the magnetization to zero. Hysteresis is a complex nonlinear, nonequilibrium, and extrinsic phenomenon dependent of the magnetization process history, caused by magnetic anisotropy energy barriers and metastable magnetostatic energy minima (E_{K1}) associated with real-structure features, such as metallurgical and chemical inhomogeneities, grain size, domain state distribution, stresses and temperature factors.

In order to reduce the magnetostatic energy, ferromagnetic and ferrimagnetic materials adopt a magnetic domain structure separated by domain walls, reflecting the competition between exchange and anisotropy and leading to zero net magnetization in the demagnetized state:

$$\delta = \tau (E_{\text{ex}} / E_{\text{Kl}})^{1/2} \quad (\text{Domain wall width})$$

If the particle size is smaller than the critical threshold of a single domain range, at high temperatures the particles become superparamagnetic. Analogous to paramagnetism, instead of a single atom, nanometric particles have a net magnetic moment in zero field and at $T > 0$ K, which averages to zero. In an applied field, there will be a net statistical alignment of magnetic moments, revealing a much higher susceptibility than simple paramagnetism. Under such particular circumstances the Brillouin function can be simplified into:

$$L(x) = \coth(x) - \frac{1}{x} \quad \text{with } x = \frac{\mu \cdot g_J \cdot B}{k_B \cdot T} \quad (\text{Langevin function})$$

3.1.4 Antiferromagnetism

The appearance of an antiparallel arrangement of the magnetic moments below T_N shows as a maximum in thermal variation of susceptibility; in the simplest cases the magnetic frustration is distributed into two compensating sublattices, having equal and opposite magnetization. Due to negative exchange interactions between neighboring atoms results zero magnetization in the absence of magnetic field. At high temperature, thermal agitation overcomes interaction effects, and the system transit to a paramagnet above T_N ; typical behavior examples are presented in figure 3.1.4.

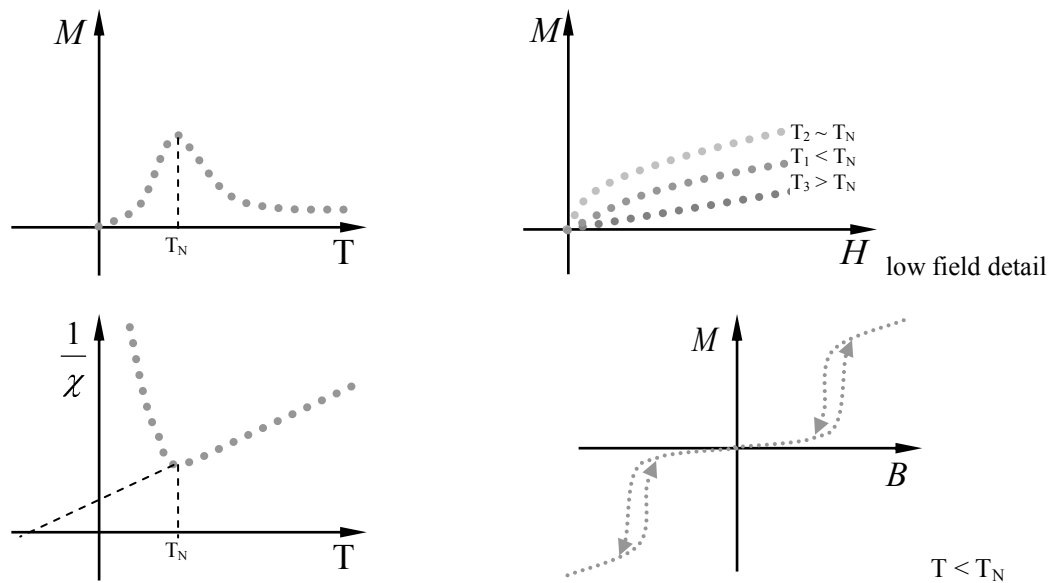


Fig. 3.1.4: Typical behaviour of antiferromagnetic materials

In fact many antiferromagnetic substances feature more complex magnetic structures, especially compensated non collinear structures; also no global moment result in the extreme case of the frustrated configurations where the magnetic moments will freeze with random orientations below a characteristic temperature, since no long-range order occurs, it is said to behave like a spin glass.

3.1.5 Ferrimagnetism

More complex forms of magnetic ordering can occur in oxides and ionic compounds as a result of the crystal structure. Typically the magnetic structure can be composed of two magnetic sublattices (A and B) where the super-exchange interactions result in an antiparallel alignment of spins; however, the magnetic moments are not equal like in the antiferromagnetic case and result in a net magnetic moment. Therefore ferrimagnetism exhibits all the hallmarks of ferromagnetism like Curie temperature and remanence; though hysteresis cycles and susceptibility thermal variation usually exhibit much less monotonous behavior (figure 3.1.5). A large number of materials which exhibit non collinear magnetic structures, and/or which are made of several types of magnetic atoms with different values of moments, can be classified as ferrimagnets.

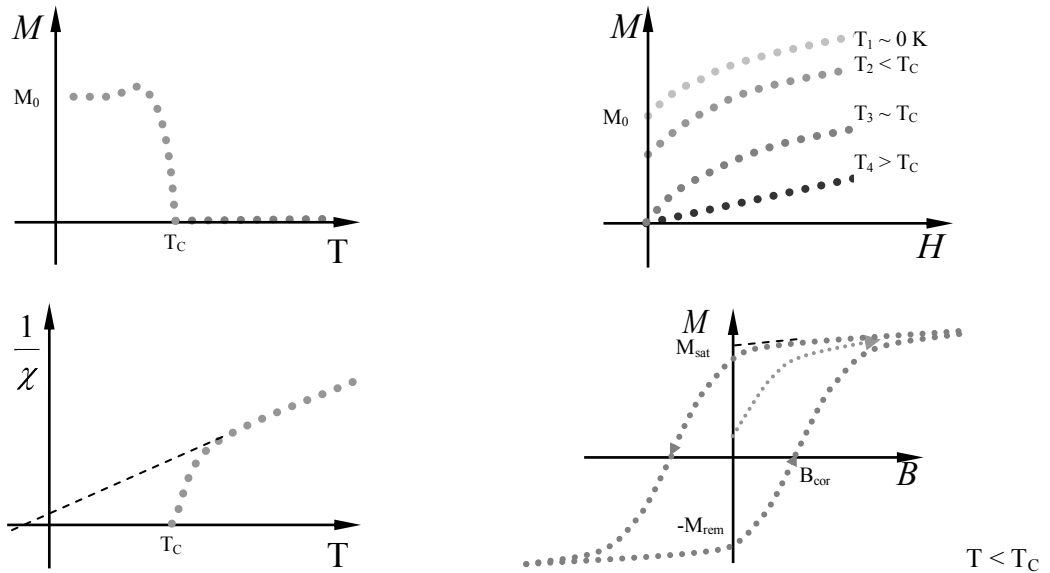


Fig. 3.1.5: Typical behaviour of ferrimagnetic materials

3.2. Magnetoelastic Effect

In a magnetic material, the interatomic distances can vary with the intensity and the orientation of magnetization this direct magnetoelastic effect is also called magnetostriction. Conversely, in the inverse magnetoelastic effect, the magnetic state of the material is sensitive to mechanical influences, leading for example, to the distortion of hysteresis loops under mechanical stress.

Magnetostrictive materials have an advantage in sensor and actuators applications over piezo-electric ceramics, principally because of the possibility to detect the signals from a distance and without wires.

The most common effect, called Joule magnetostriction, occurs when the dimensional change is associated with a distribution of distorted magnetic domains present in the magnetically ordered material, leading to dimensional changes when an external field causes a rotation of the magnetization direction within a domain, and/or a growth of domains and depending on the initial and final direction of the magnetization as well as the anisotropic properties of the material.

$$\Delta l = \lambda H \quad (\text{Magnetostriction effect})$$

When a magnetic field H is applied to a sphere having compensated magnetic domains ($\Sigma \mathbf{M}_s = 0$) it suffers an anisotropic deformation at constant volume and changes into an ellipsoid of revolution along the field axis. The relative variation in length measured along the field direction is determined by $\lambda_{//}$, while λ_{\perp} occurs perpendicularly, as represented in figure 3.2.1. The saturation magnetostriction constant (λ_s) is defined:

$$\lambda_s = \lambda_{//} = -2\lambda_{\perp} \quad (\text{Isotropic saturation magnetostriction constant})$$

Below saturation, anisotropic magnetostriction is very sensitive to the magnetic field. Beyond saturation, a small variation $\partial \lambda_s / \partial H$ is sometimes observed. Magnetostrictive characteristics vary with magnetic field as represented in figure 3.2.2, and analog to magnetization with temperature collapse near T_C .

The microscopic origin of magnetostrictive effects is not only related to the dependencies of the exchange or dipolar energies with the variation of interatomic spacing; it can also arise from the relation between magnetocrystalline anisotropy and crystal-field-induced anisotropy, resulting that the spontaneous straining of the lattice lowers the magnetic energy more than it raises the elastic.

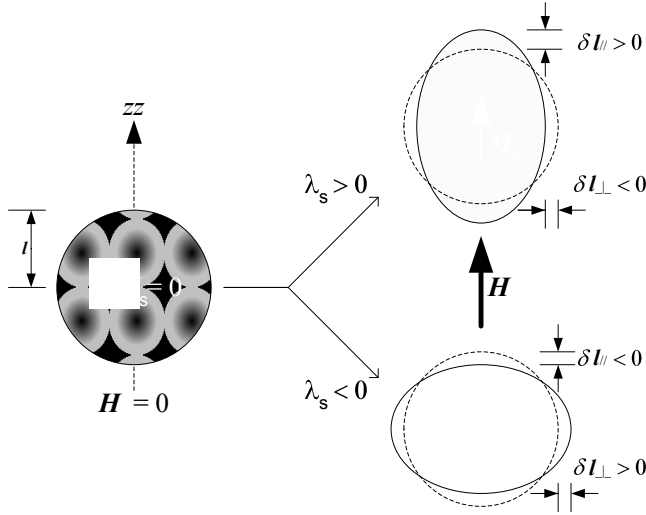


Fig. 3.2.1: The magnetostriction constant sign for an isotropic sphere leads to a prolate or oblate ellipsoid deformation.

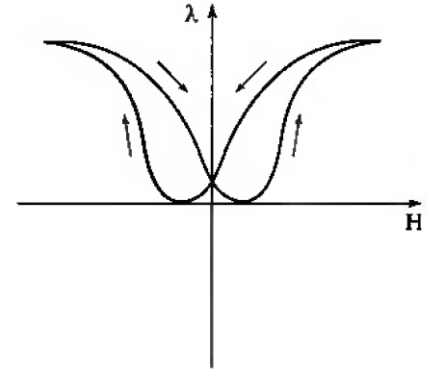


Fig. 3.2.2: Butterfly shape of $\lambda_{//}$ dependence with H .

Magnetostriction is very sensitive to a material's symmetry and the effects depend on the relative orientation of the crystalline axis, magnetization and applied field:

- In polycrystalline materials although isotropic, i.e. as aggregates or randomly oriented grains, due to the local anisotropic character of each crystallite the variations in magnetostriction with magnetic field or temperature can involve anomalies; hence it cannot be correctly described by a single λ_s value and should be calculated from the average deformation for each grain.
- In thin films the contribution from the surface symmetry break superimposes on the bulk magnetostriction; in epitaxially grown thin film over substrates this generally leads to the existence of huge stresses (GPa), a change in the magneto-elastic-crystalline anisotropy coefficients and magnetization easy direction. The application of a magnetic field will lead to a complex deformation of the bimorph coupled system of the film and its substrate.

3.3. Magnetism Units

No other scientific discipline as electromagnetism generates such endless discussion and confusion on the topic of units. Until the 1970's, numerous scientific literature used the Gaussian (*cgs*) system of units. Like all systems of units and dimensions, it is totally arbitrary. It uses three base units: centimeter, gram, and second; and a combination of two subsets: the electrostatic units (*esu*) and electromagnetic units (*emu*). As a result, the permeability of free space (μ_0) and the permittivity of free space (ϵ_0) become dimensionless, equal to unity, and often ignored, while the velocity of light in vacuum (c) appeared explicitly in some equations dealing with magnetic and electric effects. This resulted in a cumbersome set of units with “inconvenient” magnitudes for practical electrical units such as the Volt, Ohm, and Ampere. Even if it is now common ground to use the SI system units, that uses four base units: meter, kilogram, second, and Ampere (MKSA), ϵ_0 , μ_0 now take on dimensions and numerical values much different from unity. A summary of terms, units and conversion factors is presented in table 3.3.1.

Quantity	Symbol	Comment	SI units	CGS Units	Conversion
Magnetic Induction	\mathbf{B}	Generates a force on a moving charge: $\mathbf{F} = q.\mathbf{v} \otimes \mathbf{B}$	T (Tesla) = $\text{N.A}^{-1}.\text{m}^{-1}$	G (Gauss)	$1 \text{ T} = 10^4 \text{ G}$
Magnetic Field	\mathbf{H}	Due to external field or currents only	A.m^{-1}	Oe (Oersted)	$1 \text{ A.m}^{-1} = 4\pi \cdot 10^{-3} \text{ Oe}$
Magnetic Moment	$\boldsymbol{\mu}_m$	In general, generated by a moving charge: $\boldsymbol{\mu}_m = q.\mathbf{v} \otimes \mathbf{r}$	$\text{A.m}^2 = \text{J.T}^{-1}$	emu	$1 \text{ A.m}^2 = 10^3 \text{ emu}$
(Volume) Magnetization	\mathbf{M}	$\mathbf{M} = \Sigma \langle \boldsymbol{\mu}_m \rangle / \mathbf{V}$, Within the material	A.m^{-1}	emu.cm^{-3}	$1 \text{ A.m}^{-1} = 10^{-3} \text{ emu.cm}^{-3}$
(Volume) Susceptibility	χ	$\mathbf{M} = \chi.\mathbf{H} \Leftrightarrow \chi = \mathbf{M}/\mathbf{H}$	none	none	$1 \text{ (SI)} = 1/4\pi \text{ (CGS)}$
Mass Magnetization	\mathbf{M}_m	related to mass: $\mathbf{M}_m = \chi_m \mathbf{H}$	$\text{A.m}^2.\text{kg}^{-1}$	emu.g^{-1}	$1 \text{ A.m}^2.\text{kg}^{-1} = 1 \text{ emu.g}^{-1}$
Mass Susceptibility	χ_m	$\chi_m = \chi.\rho^{-1}$	$\text{m}^3.\text{kg}^{-1}$	$\text{emu.Oe}^{-1}.\text{g}^{-1}$	$4\pi.\text{m}^3.\text{kg}^{-1} = 10^3 \text{ emu.Oe}^{-1}.\text{g}^{-1}$
Vacuum permeability	μ_0	$\mu_0 = \mathbf{B}_0/\mathbf{H} = 4\pi \cdot 10^{-7} \text{ N.A}^{-2}$	$\text{N.A}^{-2} = \text{kg.m.s}^{-2}.\text{A}^{-2}$	G.Oe^{-1}	$1 \text{ N.A}^{-2} = 10^7/4\pi \text{ G.Oe}^{-1}$
Absolute permeability	$\boldsymbol{\mu}$	$\boldsymbol{\mu} = \mu_0.(1+\chi) \Leftrightarrow \boldsymbol{\mu} = \mathbf{B}/\mathbf{H} \Leftrightarrow$	$\text{N.A}^{-2} = \text{kg.m.s}^{-2}.\text{A}^{-2}$	G.Oe^{-1}	$1 \text{ N.A}^{-2} = 10^7/4\pi \text{ G.Oe}^{-1}$
Relative permeability	μ_r	Depends on the material $\mu_r = 1+\chi = \boldsymbol{\mu}/\mu_0$	none	none	none
Bohr magneton	μ_B	Due to intrinsic electron spin: $\mu_B = 9.27402 \cdot 10^{-24} \text{ J.T}^{-1}$	A.m^2	emu	$1 \text{ A.m}^2 = 10^3 \text{ emu}$
Nuclear magneton	μ_N	Due to intrinsic proton spin: $\mu_N = 5.05079 \cdot 10^{-27} \text{ J.T}^{-1}$	A.m^2	emu	$\text{A.m}^2 = 10^3 \text{ emu}$
Magnetostatic Energy	\mathbf{E}_m	Interaction between moment and field: $\mathbf{E}_m = \langle \boldsymbol{\mu}_m \rangle . \mathbf{B}$	J	erg	$1 \text{ J} = 10^7 \text{ erg}$

Table 3.3.1: Summary of terms, units and conversion factors used in magnetism

4 State of the Art on Relevant materials research

4.1. Multiferroic Materials

Multiferroics represent an exceptional class of multifunctional materials that simultaneously exhibit at least two ferroic orders, such as ferroelasticity, ferroelectricity and ferromagnetism, suggesting that even a weak strictive-magneto-electric interaction can lead to extraordinary cross-coupling effects; hence it is expected to bring about novel physical phenomena models and potential technological applications in sensors, transducers, information storing and processing. In addition to the essential ferroelectricity and ferromagnetism dependences with the respective fields, the underlying scientific and technological relevance of multiferroic materials focus in a supplementary traverse control and modeling level provided via conjugated applied fields due to the magnetoelectric (ME) coupling, that may occur directly between the two order parameters or indirectly via strain [4.1.1], as illustrated in figure 4.1.1. a)

Whereas the relativistic magnetoelectric interaction is a discrete but intrinsic phenomenon of matter in the response to electromagnetic fields also the magnetoelectric susceptibility is supposed to be small to most materials; considering the phenomenological free energy expansion approximately:

$$- \mathcal{F}(E, H) = \mathcal{F}_0 + \varepsilon_j P_i E_j + \mu_j M_i H_j + \frac{1}{2} \varepsilon_j \varepsilon_j E_i E_j + \frac{1}{2} \mu_j \mu_j H_i H_j + \chi_{ij} E_i H_j + \dots$$

Ignoring higher-order terms and considering stable phase and temperature conditions, a large linear ME coupling (χ_{ij}) is expected to occur in some multiferroics having both strong ferroelectric (large ε) and ferri-ferromagnetic (large μ) properties [4.1.2]:

$$\begin{cases} - \mathcal{F} / \partial E = P \\ - \mathcal{F} / \partial H = M \end{cases} \Rightarrow \begin{cases} P_i = \chi_{ij} \varepsilon_j E_j + \chi_{ij} H_j + \dots \\ M_i = \chi_{ij} E_j + \chi_{ij} H_j + \dots \end{cases} \quad (\text{Linear magnetoelectric coupling})$$

$$\chi_{ij}^2 \leq \varepsilon_0 \mu_0 \varepsilon_j \mu_j \quad (\text{linear ME relation to } \varepsilon \text{ and } \mu)$$

a) Higher-order nonlinear ME couplings can become relevant if ε and μ have small values, under this circumstances reducing the dimensionality of the material promotes the persistence of magnetic order up to higher temperatures than in 3D systems.

The respective cross susceptibilities tensors χ_{ij} and χ_{ji} must follow the symmetry rules of each ferroic properties:

$$\begin{aligned}
 M|t^{-1}\rangle &= -M & (\text{Time reversal of magnetization}) \\
 P|r^{-1}\rangle &= -P & (\text{Spatial inversion of polarization}) \\
 \begin{cases} \chi_{ij}|t^{-1}\rangle = -\chi_{ij} \\ \chi_{ji}|r^{-1}\rangle = -\chi_{ji} \end{cases} \Rightarrow \langle r^{-1}|\chi_{ij}|t^{-1}\rangle = \langle t^{-1}|\chi_{ji}|r^{-1}\rangle & \quad (\text{Multiferroics symmetry rule})
 \end{aligned}$$

As suggested in figure 4.1.2, electric polarization and a magnetically ordered state rarely coexist in a single phase material; essentially because the most suitable molecular, electronic and structural conditions that enhance one particular ferroic order tend to discard the counterpart mechanisms that originate the complementary ferroic effect [4.1.3]. However, the possible combinations of elements, structures and fundamental physics studies provide a wide range of theoretical and experimental areas still uncharted.

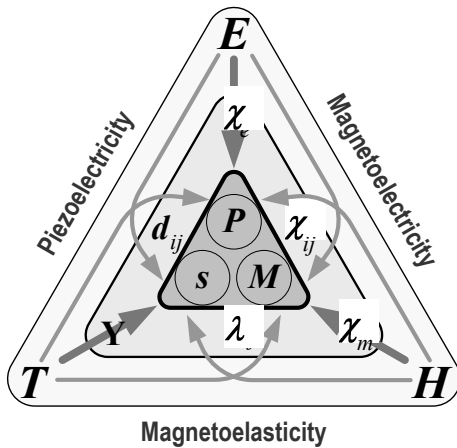


Fig. 4.1.1: Schematic interaction between properties and fields in materials.

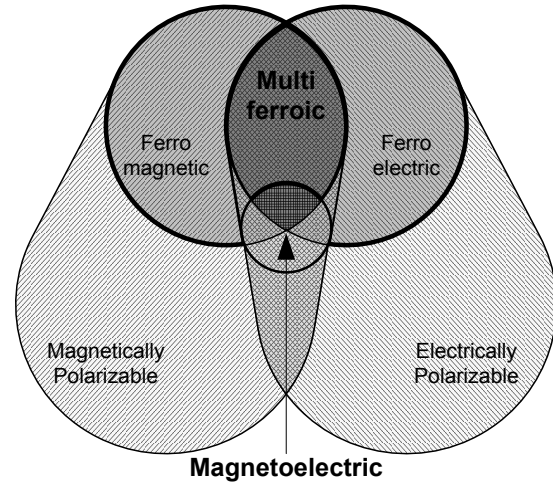


Fig. 4.1.2: Schematic relation between multiferroic and magnetoelectric materials.

Given that the magnetization order is systematically based upon the exchange interaction between localized electrons (and respective unpaired spins) on partially filled d or f shells of transition metals or rare earth elements; multiferroic materials are usually categorized according to table 4.1.1 by the different phenomenological origin of the ferroelectric behavior [4.1.4].

Among relevant results, the most studied intrinsic multiferroic systems basically include compounds based on the perovskite structure specially BiFeO_3 that has FE and AFM order at room temperature [4.1.5]; on the other hand, The RMnO_3 manganites with $R = \text{La, Pr, Bi, Y, Tb, Dy, Ho, Eu, ...}$ [4.1.6] possess magnetic order at temperatures

typically below 150 K and recurring to doping by other rare earths or metallic elements like Ca, Sr, Ba, Fe, etc, it is possible to promote limited piezo- or ferroelectric response.

In particular, based upon existing studies for manganite systems, with Mn^{4+} doping below 0.5, having charge and bond ordering mechanisms leading to a breaking of the inversion symmetry [4.1.7], it becomes possible to strengthen these dipolar polaronic states coupling with the magnetic ordering thus generating multiferroic properties [4.1.8], as represented in figure 4.1.3.

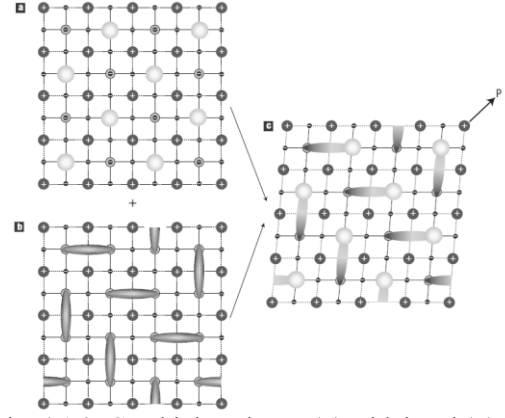


Fig. 4.1.3: Combining charge (a) with bond (b) orders may lead to polarization (c) [4.1.8].

Of related composition, the hexagonal manganites with $R = \text{Sc, Y, In, Ho, Er, Tm, Yb, Lu}$ [4.1.9] due to the coexistence of ferroelectric and multiple antiferromagnetic ordering, reveal magnetoelectric bulk effects by the interplay of magnetic exchange, wall magnetization, and ferroelectric distortion.

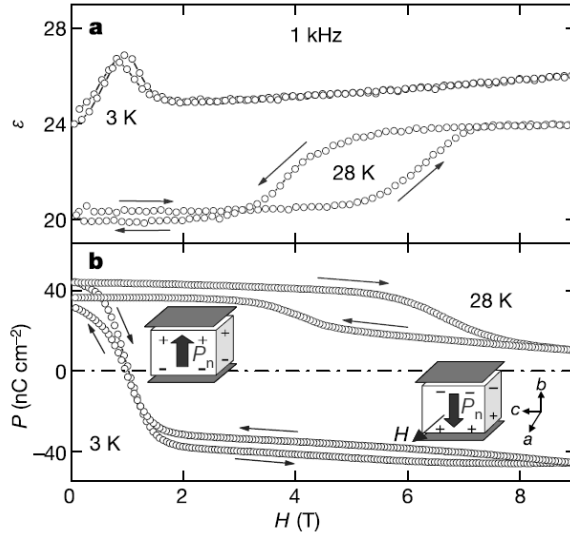


Fig. 4.1.4: Magnetic field dependence of ϵ (a) and P (b) as function of the in TbMn_2O_5 [4.1.10].

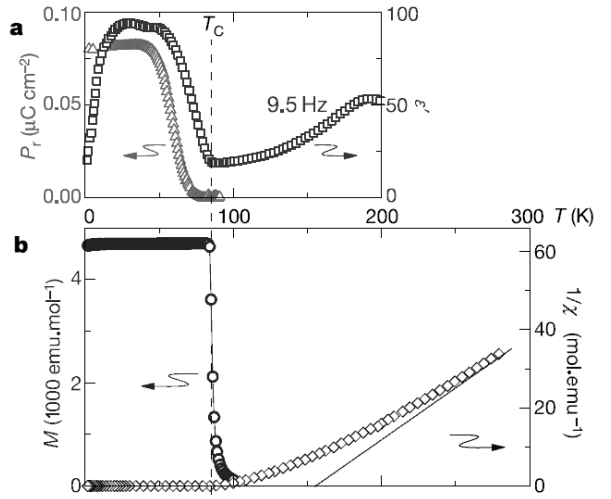


Fig. 4.1.5: Temperature dependence of P and ϵ' (a) and the M and $1/\chi$ (b) of CdCr_2S_4 [4.1.13].

Alternative structures such as TbMn_2O_5 , demonstrated a highly reproducible electric polarization reversal and permanent polarization imprint actuated by an applied magnetic field, as illustrated in figure 4.1.4 [4.1.10]; Other RMn_2O_5 systems with ($R = \text{Y, Tb, Ho, Er, Tm, Dy, Lu}$) [4.1.11], [4.1.12] show simultaneous magnetic and dielectric ordering phase transitions, suggesting that the long-range commensurate order of Mn^{3+} and

Mn^{4+} in a transverse spiral spin structure propagating along the c-axis induces a ferroelectric moment through a cooperative packaging of the neighboring asymmetric Jahn–Teller Mn^{3+}O_6 . Other studies reveal the coexistence of FM and proper FE in the CdCr_2S_4 spinel [4.1.13] producing a colossal magnetocapacitive effect ($\sim 500\%$) below $T_C \sim 100$ K, as exemplified in figure 4.1.5. Among other intrinsic compounds, worth mention that also display some significant ME effects at low temperatures are the RFe_2O_4 system ($\text{R} = \text{Y, In, Sc and Dy to Lu}$), MnWO_4 , $\text{Bi}_2\text{FeCrO}_6$, $\text{Ni}_3\text{V}_2\text{O}_8$, BaNiF_4 , etc [4.1.14].

Indirect ME coupling via strain can be significant or even the dominant effect. For example, the contribution of piezoelectricity/electrostriction (d_{ij}) and piezomagnetism/magnetostriction (λ_{ij}) generate additional mixed terms in the free energy expression proportional to strain that may vary linearly or quadratically with H_i or E_i .

Type:	Mechanism:	Ferroelectricity origin description:	Examples:	$\partial E/\partial H$ (mV/cm.Oe)
I	“lone pair order”	In perovskite type ABO_3 , the A ion has a pair polarizable electrons.	BiFeO_3 [4.1.5], BiMnO_3 [4.1.6]	
	“charge order”	Non-centrosymmetric arrangement of charge and bond ordered sites.	TbMn_2O_5 [4.1.10] LuMn_2O_4 [4.1.12]	3E-6 @ 4 K
	“geometric order”	Cooperative dipolar interactions in the structure.	YMnO_3 LuMnO_3 [4.1.9]	
II	“magnetic order”	Non-centrosymmetric arrangement of spins structure.	TbMnO_3 , $\text{Ni}_3\text{V}_2\text{O}_8$, MnWO_4 [4.1.14]	
III	“composites”	Combinations of FE phase with FM phase having ME effect via strain propagation.	$\text{BaTiO}_3+\text{CoFe}_2\text{O}_4$ [4.1.15] $\text{PZT}+\text{NiFe}_2\text{O}_4$ [4.1.16]	2500 @ RT 1500 @ RT

Table 4.1.1: Classification of multiferroics

Special attention should be given to the combination of two materials having each an enhanced ferroelectric/piezoelectric or ferromagnetic/magnetostrictive property. Complex multiferroic systems can be achieved from the interaction between extrinsic materials in the form of nanometric granular composites [4.1.15], columnar, laminated heterostructures or epitaxial multilayers [4.1.16], [4.1.17], as depicted in figure 4.1.6.

It becomes possible to take advantage of field induced structural transitions enhancing the resulting materials strain and conjugated ferroic property; for example, some Permendur–PZT laminated layers, as an external magnetic fields induce the reorientation of ferromagnetic domains which in turn mechanically drive the ferroelectric compound structure, it is possible to achieve ME voltage coefficient in the vicinity of electromechanical resonances of $\sim 90 \text{ V.cm}^{-1}.\text{Oe}^{-1}$ which largely exceeds the responses of any single-phase compounds [4.1.18]. Composites can conjugate a variety of piezoelectric

materials, as shown in section 4.3 and magnetostrictive alloys, like in particular Ni_2MnGa [4.1.19] which is further detailed in section 4.5.

The effectiveness of such indirect coupling is not only related to the respective piezoelectric or piezomagnetic strength of each phase but mostly how the two phases entwine and how efficient the mechanical expansion/contraction is propagated from one component to the other, consequently dependent on the frequency of the a.c. electric or magnetic field applied. It becomes essential in the design to account for adequate electrodes insertion and to avoid short circuiting over the ferroelectric component. Although heterostructures are very sensitive to substrate clamping and damping from size or texture effects, under the suitable design, the ME coupling can surpass that of single-phase systems by several orders of magnitude (from 5 to 5000 $\text{mV}\cdot\text{cm}^{-1}\cdot\text{Oe}^{-1}$) [4.1.1] and achieve above room temperature performances.

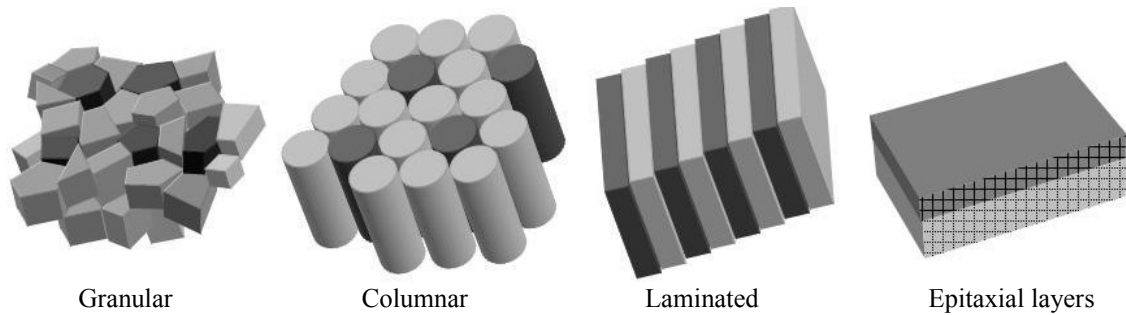


Fig. 4.1.6: Some representative construction geometries for composites combining two functional phases.

While multiferroic intrinsic single-phase systems are essential for understanding the several fundamental mechanisms behind the magnetoelectric effect, composites systems, combining a FE and a FM phase, present a more promising approach to achieve a synergy of properties, as figure 4.1.7 may suggest, and a relevant technological proof of concept.

Multiferroic materials that show two independent hysteresis behaviors, may allow 4 distinct logic states (P^+M^+ ; P^+M^- ; P^-M^+ ; P^-M^-) in a single element, eventually leading to a whole new range of innovative information processing functions and devices. In the case the two order parameters are directly coupled, in principle this would can be used to increase the quality of data storing and to explore independent processes for an electrical data writing and magnetic data reading of the same memory bit, taking advantage of the best features of the ferroelectric random access memory (FeRAMs) and the magnetic data storage devices.

4.2. Perovskite Manganites

At present, the perovskite manganites are the most representative materials system which can show versatile unconventional electronic-lattice structural changes or insulator–metal transitions, including CMR, upon external stimulation, not only by magnetic field but also by pressure, light, x-rays irradiation as well as current injection.

In the parent LnMnO_3 pseudo perovskite represented in figure 4.2.1, the “Ln” represents a rare earth element such as La, Pr, Nd, Sm, etc. with 12 O^{2-} ions coordination (A site); while the Mn^{3+} ion has an enclosing configuration of 6 oxygen ions (B site). Each Mn^{3+} ion has an electronic configuration $[\text{Ar}]3d^4$, the crystal-field splits the five-fold degenerate atomic 3d levels into three electrons in the t_{2g} -state and one electron in the e_g -state; due to Hund’s rule the spins are coupled ferromagnetically ($S = 2$); a Jahn–Teller effect further lifts the orbital degeneracy giving rise to the apical distortion of the octahedron (MnO_6) [4.2.1], as represented in figure 4.2.2.

Stoichiometric LaMnO_3 is insulator and antiferromagnetic ($T_N \sim 150$ K) due to the super-exchange interaction mediated by the O^{2-} between two adjacent Mn^{3+} ions. When the compound is doped either by replacing some of La^{3+} ions with divalent (Sr^{2+} , Ca^{2+} , Ba^{2+} , ...) or monovalent (Na^{1+} , Ag^{1+} , ...) ions, or by introducing excess Mn, leaving cationic “A site” vacancies (O_A^0), or else by reducing Mn content leaving “B site” vacancies (O_B^0) a correspondent amount of Mn^{4+} ions are formed and an e_g -electron from a neighboring Mn^{3+} can hop by double-exchange hopping under strong Hund’s rule coupling. These electronic states become highly mobile above a percolation threshold and are usually termed as polarons because in addition to the intrinsic charge and spin transport, there are interrelated effects of strong electron-correlation and electron–lattice coupling.

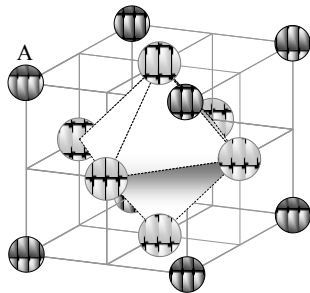


Fig. 4.2.1: Two equivalent representations of the perovskite.

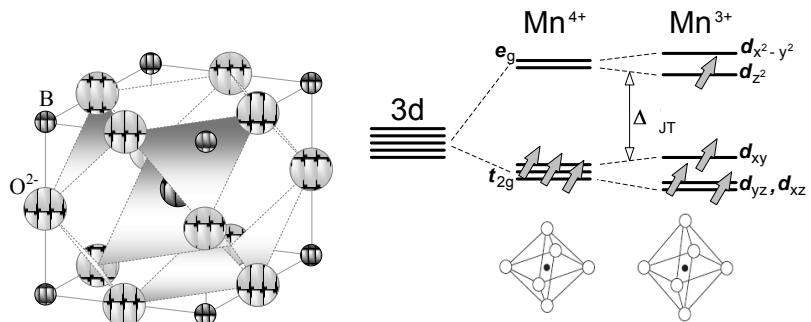


Fig. 4.2.2: Crystal-field splitting of 3d levels into lower t_{2g} triplet and e_g doublet and the JT distortion of the MnO_6 octahedra [4.2.1].

Besides the two important electronic parameters, bandwidth and band-filling that can be finely controlled with the crystal chemistry, the collective Jahn–Teller interaction promotes the orbital ordering through the displacement of oxygen in a cooperative manner and induces properties anisotropy and lattice distortion, as exemplified in figure 4.2.3. The packing of MnO_6 octahedra and the resulting perovskite distortion can be interpreted by the tolerance factor t_f :

$$t_f = \frac{\langle r_A \rangle + \langle r_O \rangle}{\sqrt{2} \cdot \langle r_B \rangle + \langle r_O \rangle} \quad (\text{Tolerance factor})$$

Where $\langle r_A \rangle$, $\langle r_B \rangle$, $\langle r_O \rangle$, are the average ionic radii of each element in the respective site of the perovskite structure, as listed in table 4.2.1. The cubic perovskite structure is observed when $t_f \sim 1$; as $\langle r_A \rangle$ decreases, the lattice structure transforms to the rhombohedral ($0.96 < t_f < 1$) and then to the orthorhombic structure ($t_f < 0.96$), as progressively the Mn–O–Mn bond angle (θ) bents from 180° . This bond angle distortion also affects the relative spin orientation between neighboring Mn ions and the electron transfer process via O^{2-} 2p state is decreased from the ideal perovskite situation (t_0) [4.2.1]:

$$t_\theta = \frac{1}{2} \cdot \cos \theta \quad (\text{Transfer integral})$$

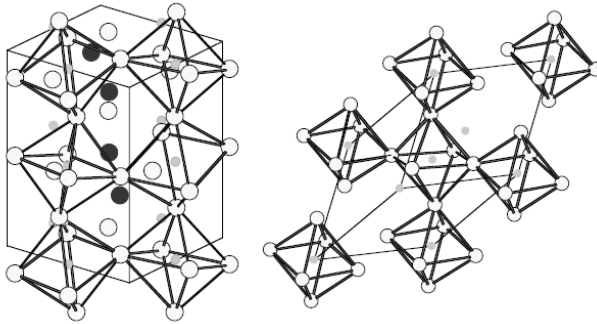


Fig. 4.2.3: Structures of distorted perovskites of manganites: orthorhombic $Pnma$ (left) and rhombohedral $R-3c$ (right).

A site	La^{3+}	Pr^{3+}	Nd^{3+}	Sm^{3+}	Eu^{3+}	Gd^{3+}
$\langle r_A \rangle$	1.36	1.29	1.27	1.24	1.23	1.21
A site	Ba^{2+}	Pb^{2+}	Sr^{2+}	Ca^{2+}	Y^{3+}	Bi^{3+}
$\langle r_A \rangle$	1.61	1.49	1.44	1.34	1.18	0.96
B site	Mn^{3+}	Mn^{4+}	Ti^{4+}	Fe^{3+}	Ga^{3+}	Al^{3+}
$\langle r_B \rangle$	0.645	0.53	0.605	0.645	0.62	0.535
O site	O^{2-}					
$\langle r_O \rangle$	1.40					

Table 4.2.1: Ionic radii (in Å) for some ions involved in manganites [4.2.1].

The phase diagrams of figure 4.2.4 and 4.2.5 are representative of how the successive transport, magnetic and structural phases can be organized according to the filling of the e_g electrons (which mediate the ferromagnetic double-exchange interaction), the tolerance factor (which influence the charge transfer bandwidth) [4.2.2] and the temperature [4.2.3]. The possibility of phase inhomogeneities and phases competition, i.e. in terms of separation/percolation of clusters in a matrix, should also be considered as one of the inherent features for understanding the physics of manganites properties and transitions. All these versatility at structural, magnetic ordering and transport behavior in such simple perovskite system can produce a rich variety of phases and phenomena.

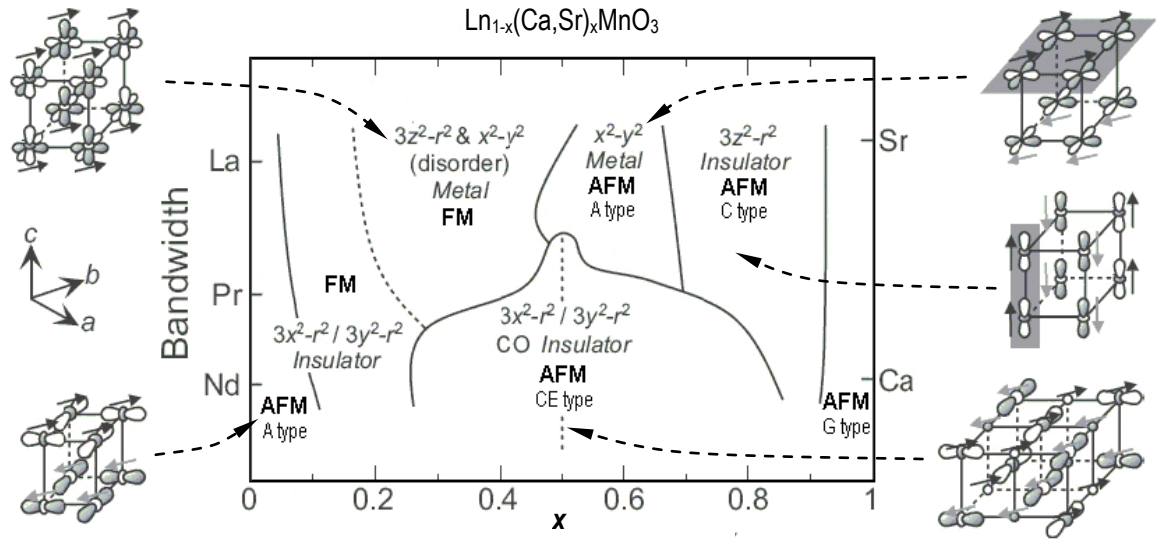


Fig. 4.2.4: Bandwidth versus hole concentration phase diagram at the ground state of $\text{Ln}_{1-x}(\text{Ca,Sr})_x\text{MnO}_3$ and schematic views of the e_g orbitals (lobes) and spins (arrows) on Mn sites for the respective phases [4.2.2].

Of particular relevance became the Rhombohedral La manganites doped with $\sim 1/3$ of Sr [4.2.4] or Ba [4.2.5] having FM and CMR behavior above room temperature, as shown by the respective phase diagrams of figure 4.2.6.

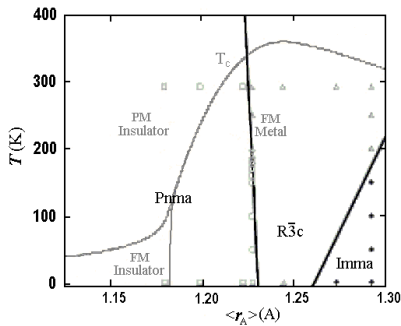


Fig. 4.2.5: Generic manganites phase diagram of as function of A site radii and T [4.2.3].

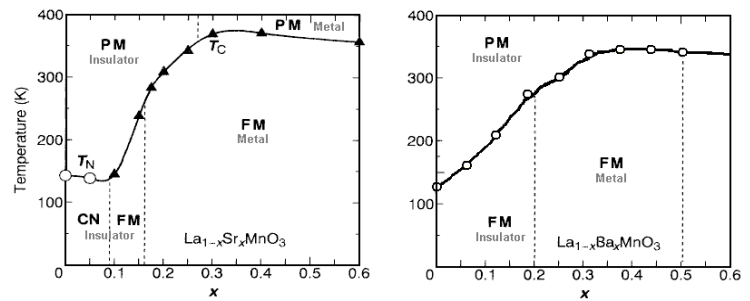


Fig. 4.2.6: Magnetic and conductivity phase diagrams as function of doping (x) and temperature for: $\text{La}_{1-x}\text{Sr}_x\text{MnO}_3$ [4.2.4] (left) and $\text{La}_{1-x}\text{Ba}_x\text{MnO}_3$ [4.2.5] (right).

4.3. Ferroelectric Perovskites: BaTiO₃, PZT and PMN-PT

4.3.1. BaTiO₃

BaTiO₃ belongs to the ABO₃ Perovskite family, described in the previous chapter, with Ti⁴⁺ forming octahedral cages with the O²⁻ ions as represented in figure 4.3.1. BaTiO₃ shows three relevant structural phase transitions with temperature also affecting the dielectric constant ϵ_r and respective frequency dependences as represented in figure 4.3.2 [4.3.1]; also the dielectric behavior, which is isotropic in the cubic nonpolarized phase, becomes strongly anisotropic in the polarized phases.

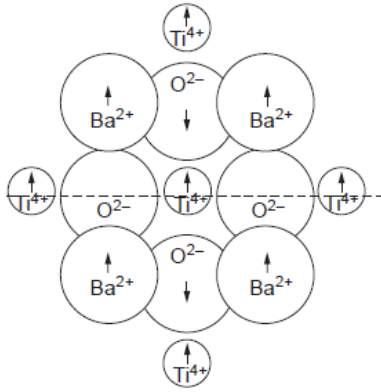


Fig. 4.3.1: Cubic-tetragonal ion displacements of BaTiO₃ [2.3.2].

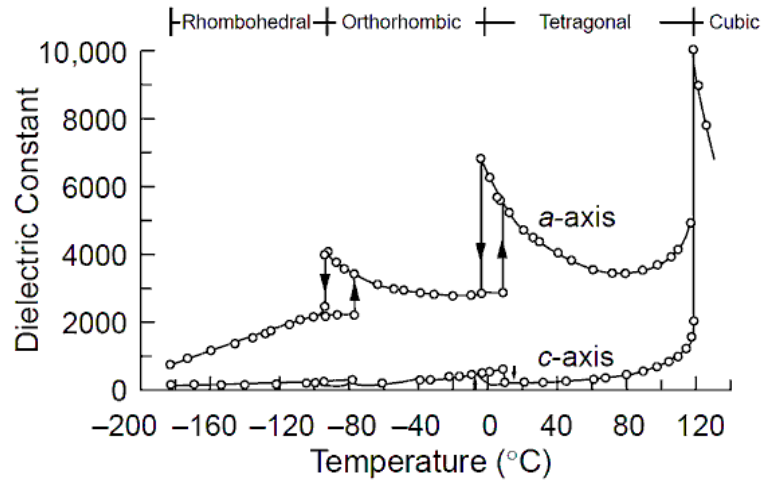


Fig. 4.3.2: *a* and *c* axis and dielectric constant of BaTiO₃ [4.3.1].

In the high temperature cubic $Pm\bar{3}m$ paraelectric state, the Ti ions are dynamically disordered and off-center the O₆ octahedra. At around $T_C = 408$ K it undergoes to ferroelectric transition to the tetragonal $P4mm$: the Ba²⁺ ions shift 0.05 Å upward from their original position, the Ti⁴⁺ ions shift upward by 0.1 Å, and the O²⁻ ions downward by 0.04 Å. As a result of the ion shifts, the centroids of the positive and negative charges no longer coincide, spontaneously forming permanent dipoles, therefore, the unit cells become permanently polarized, as shown in figure 4.3.1. Within the ferroelectric state two further structural transitions occur with temperature, at 278 K the structure becomes orthorhombic, $C2mm$; and at 183 K a transition into the rhombohedral low-temperature $R\bar{3}m$ phase occurs as exemplified in figure 4.3.3.

The hysteresis loop of BaTiO₃ single crystals with a single domain is a square loop, having a spontaneous polarization $P_{sat} \sim 26$ mC.cm⁻² and a coercive field $E_{coe} \sim 1$ kV.cm⁻¹ at room temperature. Depending to a great extent on the preparation of the ceramic

specimens, polycrystalline BaTiO₃ has random directions of the crystallographic axes, internal strains and other defects that limit the motion of domain walls and the extent to which spontaneous polarization can be developed. The hysteresis loop more rounded, having P_{sat} of about 7 mC.cm⁻² and E_{coe} of about 4 kV.cm⁻¹.

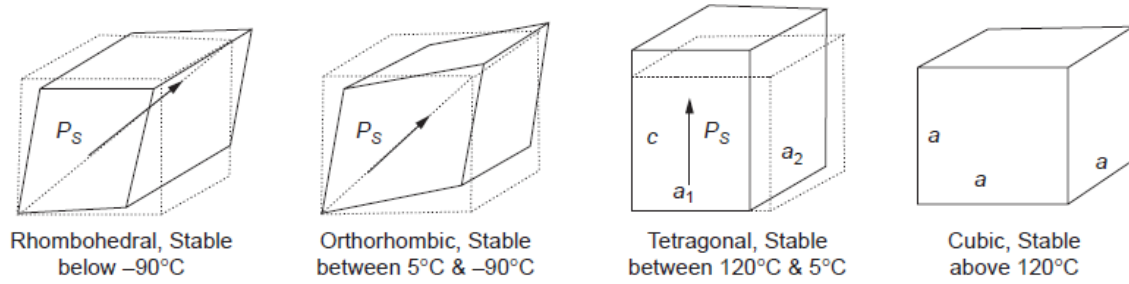


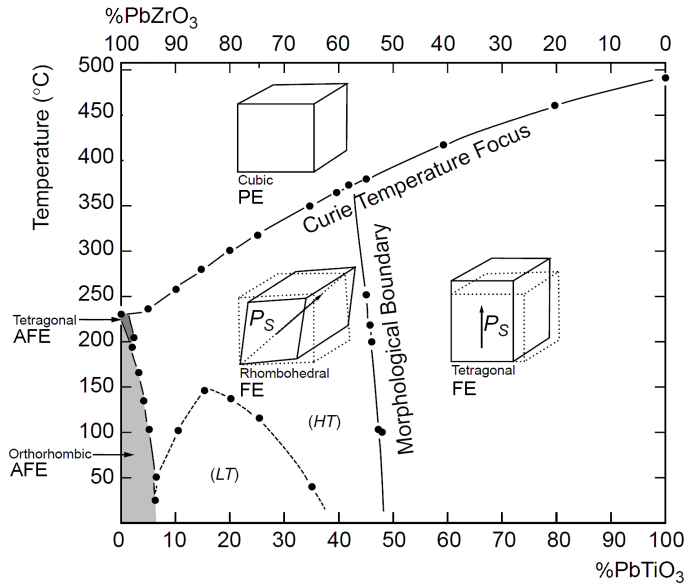
Fig. 4.3.3: The temperature dependence of the structure of the unit cell [2.3.2]

4.3.2. PZT

PZT ceramics are in fact a solid solution of two components: PbZrO₃ and PbTiO₃ that belong to the perovskite family; similar to BaTiO₃ in their structure and ferroelectric properties, by controlling the composition and microstructure of the PZT, it is possible to tailor their properties to suit particular applications [2.3.2]. The PZT system is used mostly in piezoelectric devices taking advantage of these crystal morphology transitions and high T_C . The Curie temperature (T_C) depends on the composition of the system but is notably higher than that of BaTiO₃; the main reason is that the Pb²⁺ ion has two more outer electrons beyond the last full shell of Ba²⁺, which contribute to covalent bonding with neighboring oxygen ions, thus a greater thermal energy is required to convert the polarized state into an unpolarized state. A typical equilibrium phase diagram for the Pb(Zr_{1-x}Ti_x)O₃ system is shown in figure 4.3.4, it has some prominent features worth mentioning:

- The rich Zr region has a low T_C and an interesting antiferroelectric (AFE) structure.
- The rhombohedral phase has two different directions of polarization according to the high (*HT*) or low (*LT*) temperature region.
- The cubic paraelectric phase can be distorted and transit from the unpolarized to the polarized state by application of a suitable electric field.

- At $x \sim 0.5$ occurs a morphological boundary between the rhombohedral and tetragonal phases, also a local maximum in the piezoelectric coupling coefficient due to the easier transformation between the two structures and the conformation from 6 to 8 easy directions of polarization.



Property	Value
Coupling coefficient, k_{31}	0.35
Coupling coefficient, k_{33}	0.69
Density	7.5 to 7.6 g/cm ³
Dielectric constant, ϵ_r	1700
Strain coefficient, d_{31}	1.8E-10 m/V
Strain coefficient, d_{33}	3.6E-10 m/V
Strain constant	1.1E-10 m/V
Voltage coefficient, g_{31}	0.011V.m/N
Voltage coefficient, g_{33}	0.025 V.m/N
Young's Modulus, Y_{11}	63 GPa
Young's Modulus, Y_{33}	49 GPa

Table: 4.3.1: Typical values Piezoelectric properties of $\text{Pb}(\text{Zr}_{55}\text{Ti}_{45})\text{O}_3$ single crystal [4.3.2].

Fig. 4.3.4: The equilibrium phase diagram of the PZT system and the unit cell for different phases [2.3.2].

4.3.3. PMN-PT Relaxors

Classical relaxors are perovskite solid solutions like $\text{Pb}(\text{Mg}_{1/3}\text{Nb}_{2/3})\text{O}_3$ (PMN) and PbTiO_3 (PT), which exhibit the presence of site and charge disorder that merge into a broad correlation resulting in a distribution of the dipole moments forming clusters of nanometric size [4.3.3].

The enhanced ferroelectric interactions [4.3.4] may be explained by the presence of A site polar ions, like Pb^{2+} in the relatively random environment, contributing to increase the required bias for the transition between states. The Pb^{2+} also establish a closer coupling to the usually larger ferroelectrically inactive B' cations through oxygen bonding, leaving the ferroelectrically active B'' cations relatively free for further ferroelectric coupling. Instead of relatively “stable” polar tetragonal cells, PMN remains pseudo-cubic to the lowest temperatures measured, however the hopping times of the various constitutive ions between different off-center sites is much shorter than the lifetime of the polar nanoclusters

determining the dynamical ferroelectric properties of relaxors. There is convincing evidence that in the relaxor two or more types of polar clusters coexist [4.3.5]:

- Low-frequency ($1-10^5$ Hz) contribution to the broad ϵ -maximum that usually is interpreted as “reorientation of dipole moments of polar nanoregions”, accounted for a strong electromechanical coupling which electrostriction to piezoelectric effect.
- High-frequency (10^8-10^{10} Hz) contribution to the ϵ -maximum that commonly is explained as a motion of the “frozen paraelectricity” in the nanoregions boundaries, due to the multidomain structure.

Relaxors are used as low or non-hysteresis actuator materials applied in micro-mechanics and as microdrivers for microwave mechanically tunable filters and phase shifters. The strain energy density is 6 to 10 times that of PZT, peak d_{33} is of the order of 1 nm/V [4.3.6]. The response characteristics of relaxor-based devices is determined by its size and the sound speed in the relaxor material imposed by the electromechanical coupling of polar clusters

4.4. Ferroelectric Hexagonal Manganites

Manganites of the LnMnO_3 formula with $\text{Ln} = \text{Ho, Er, Tm, Yb, Lu, Y and Sc}$, which have smaller ionic radius, crystallize in a hexagonal structure [4.4.1]. Each Mn^{3+} is surrounded by 5 O^{2-} forming a bipyramid and having at least 3 non-equivalent Mn-O bonds and in-plane angles Mn-O-Mn close to 120° ; the bipyramids are stacked in alternated directions in each layer and sandwiched between distorted planes of Ln ions, as represented in figure 4.4.1.

As example, in the LuMnO_3 compound the non-centrosymmetric space group $P6_3cm$, makes it possible to find ferroelectric ordering up to very high temperatures ($T_C > 800$ K) [4.4.2]. Large local dipole moments are originated from the two non equivalent LuO_7 coordination sites, nonetheless a 0.02 Å difference between the apical Mn-O1 and Mn-O2 bonds lengths can create a less significant local dipole moment, parallel to the c axis [4.4.3] as can be observed in figure 4.4.1.

Typical FE properties at 2400 V are a maximum polarization $P_{\text{sat}} = 0.189 \text{ mC/cm}^2$, remnant polarization $P_{\text{rem}} = 0.096 \text{ mC/cm}^2$ and coercive field $E_{\text{coe}} = 12.13 \text{ kV/cm}$.

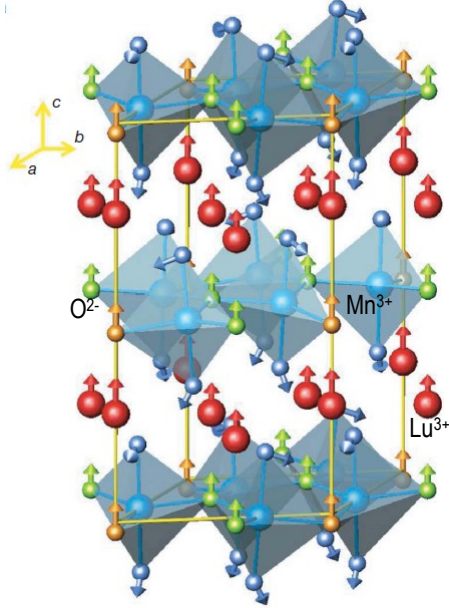


Fig. 4.4.1: The unit cell of hexagonal manganite. The ions displacements are represented by arrows [4.4.2].

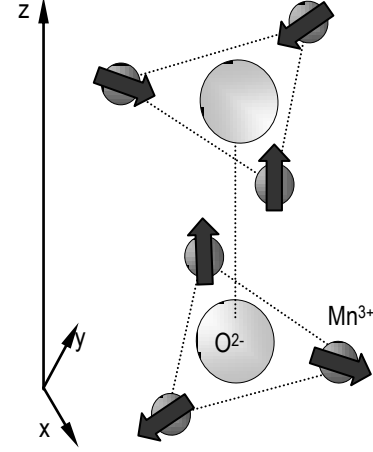


Fig. 4.4.2: Representation of a dual plane having triangular magnetic frustration in the $P6_3cm$ system.

The coexistence of the two order parameters is a rarity in oxides and opens up the possibility for electric–magnetic interactions. Particularly for $T < T_N$ ($\sim 90 \text{ K}$), as indication in figure 4.4.3, the triangular frustrated antiferromagnetic ordering of Mn^{3+} ions spins [4.4.4] represented in figure 4.4.2, may be also associated with a magnetostrictive effect and involve the ferroelectric structure or the domain wall mobility [4.4.5], as evidenced in figure 4.4.4.

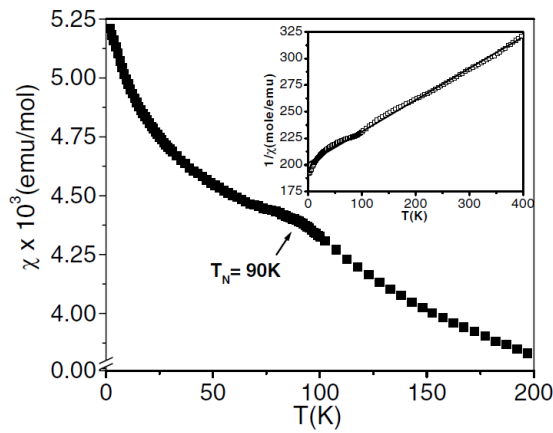


Fig. 4.4.3: Magnetic susceptibility χ of LuMnO_3 . Inset: $1/\chi$ and respective High- T Curie-Weiss fit.

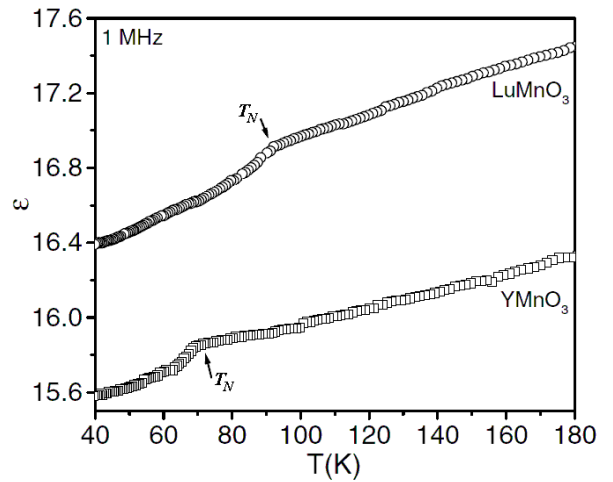


Fig. 4.4.4: Dielectric constant of YMnO_3 and LuMnO_3 at 1 MHz, the arrows point the respective T_N [4.4.5].

4.5. Magnetostrictive $\text{Ni}_{2+x}\text{Mn}_{1-x}\text{Ga}$ Heussler Alloy

Ni_2MnGa alloy is one of the most extensively studied ferromagnetic shape memory compounds; some of the most relevant phases and transitions of this compound is complex phase diagram are described [4.5.1], [4.5.2]; at 400 K the compound has the austenitic cubic $L2_1$ structure having $a = 5.825 \text{ \AA}$ (figure 4.5.1), it orders ferromagnetically at $T_C \approx 370 \text{ K}$. Specific magnetization at 265 K is 58 emu/g; given its mass density of 8.3 g/cm^3 , this translates to a saturation flux density of $4\pi M_s$ 56 kG. On cooling below 260 K appears a pre-martensitic phase. Another structural phase transition occur at $T_M \approx 200 \text{ K}$ consisting in $\sim 1\%$ decrease in cell volume ($c/a \approx 0.94$) and an increase in the magnetic anisotropy, changing to the “5M” martensitic tetragonal (I_4/mmm) which exhibits giant field-induced strain of near 6%, or even at $\sim 100 \text{ K}$ the “7M” orthorhombic ($Pnnm$) unit cell that can reach $\sim 10\%$ field-induced strain [4.5.3].

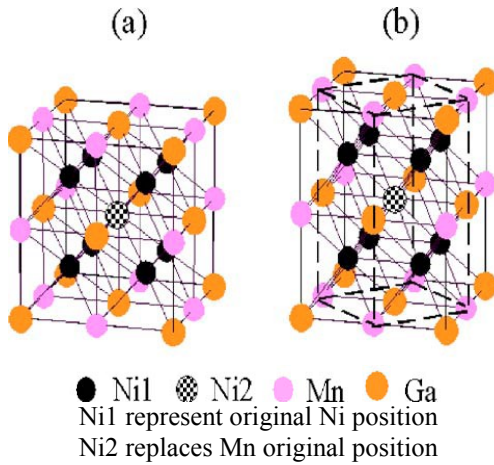


Fig. 4.5.1: Unit cell of $\text{Ni}_{2.25}\text{Mn}_{0.75}\text{Ga}$, austenitic cubic phase (a) and tetragonal martensitic phase (b) in face centered or body centered (dash) representations [4.5.4].

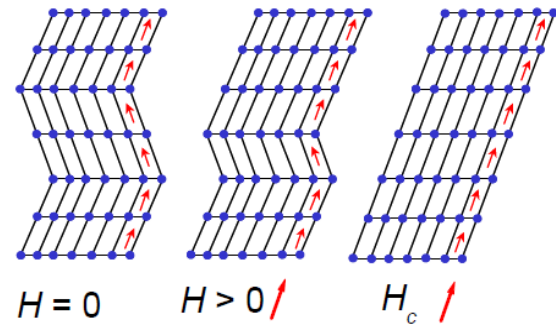


Fig. 4.5.2: Magnetic Shape Memory effect due to the redistribution of martensitic variants with the magnetic field [4.5.5].

The Ni_2MnGa Heusler alloy magnetic shape memory effect (MSM) can be described within the martensitic phase as a reversible macroscopic deformation resultant from the redistribution of the self-accommodated martensitic variants coincident with magnetic domains aligning with an external magnetic field as represented in figure 4.5.2 [4.5.5], [4.5.6]. Also if the material is plastically deformed in the low temperature martensitic phase and the external load removed it will regain its original shape when heated above the transition temperature.

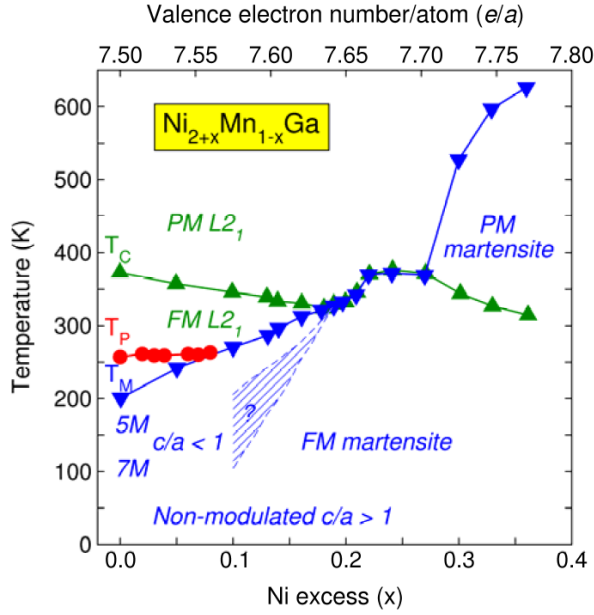


Fig. 4.5.3: Phase diagram of $\text{Ni}_{2+x}\text{Mn}_{1-x}\text{Ga}$ Heuler alloy showing critical temperatures dependence with composition for martensitic (T_m), Curie (T_c) and pre-martensitic transitions (T_p) [4.5.8].

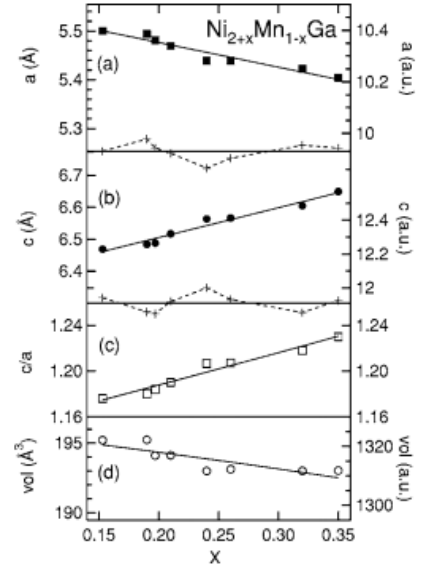


Fig. 4.5.4: Lattice parameters a , c , a/c ratio and volume for $\text{Ni}_{2+x}\text{Mn}_{1-x}\text{Ga}$ with $0.15 \leq x \leq 0.35$ in the martensitic tetragonal phase [4.5.4].

Bulk Ni_2MnGa can be prepared by melting high purity elements in an arc furnace. In order to obtain volume homogeneity, the ingot can be remelted, annealed at 1300 K up to 48 hr preferably in Argon atmosphere and then slowly cooled [4.5.1], [4.5.2]. In this basic form is too brittle and its transition temperature T_M too low for convenient use; it's possible to maximize the magnetostrictive potential of these material and optimize the magnetization properties by changing the stoichiometry either by controlled substitution for other elements like Fe, Co, Al [4.5.7], or most important, by self doping as in the case $\text{Ni}_{2+x}\text{Mn}_{1-x}\text{Ga}$ [4.5.4], [4.5.8], exemplified in figure 4.5.3 and 4.5.4 and table 4.5.1.

Composition	x	a (Å)	c (Å)	T_M (K)	T_C (K)	Space group
$\text{Ni}_2\text{Mn}_{1.05}\text{Ga}_{0.95}$	0	5.820	5.820	207	360	$Fm\bar{3}m$
$\text{Ni}_{2.01}\text{Mn}_{0.99}\text{Ga}$	0.01	5.820	5.820	205	365	$Fm\bar{3}m$
$\text{Ni}_{2.03}\text{Mn}_{0.96}\text{Ga}$	0.03	5.821	5.821	205	376	$Fm\bar{3}m$
$\text{Ni}_{2.07}\text{Mn}_{0.91}\text{Ga}_{1.02}$	0.07	5.826	5.826			$Fm\bar{3}m$
$\text{Ni}_{2.1}\text{Mn}_{0.9}\text{Ga}$	0.1	5.813	5.813	276	344	$Fm\bar{3}m, 14/mmm$
$\text{Ni}_{2.13}\text{Mn}_{0.87}\text{Ga}_{1.02}$	0.13	5.811	5.811	292	339	$Fm\bar{3}m, 14/mmm$
$\text{Ni}_{2.15}\text{Mn}_{0.84}\text{Ga}$	0.15	5.795, 5.501	5.795, 6.469			$Fm\bar{3}m, 14/mmm$
$\text{Ni}_{2.19}\text{Mn}_{0.82}\text{Ga}$	0.19	5.494	6.484	329	331	$14/mmm$
$\text{Ni}_{2.20}\text{Mn}_{0.8}\text{Ga}$	0.2	5.482	6.488	334	334	$14/mmm$
$\text{Ni}_{2.24}\text{Mn}_{0.75}\text{Ga}_{1.02}$	0.24	5.439	6.563	434	351	$14/mmm$
$\text{Ni}_{2.26}\text{Mn}_{0.73}\text{Ga}_{1.02}$	0.26	5.440	6.566			$14/mmm$
$\text{Ni}_{2.32}\text{Mn}_{0.67}\text{Ga}_{1.02}$	0.32	5.422	6.605	508	331	$14/mmm$
$\text{Ni}_{2.35}\text{Mn}_{0.66}\text{Ga}_{0.98}$	0.35	5.404	6.649	537	320	$14/mmm$

Table. 4.5.1: SG and a , c lattice parameters at 293 K, T_M and T_C of $\text{Ni}_{2+x}\text{Mn}_{1-x}\text{Ga}$ for $0.15 \leq x \leq 0.35$ [4.5.4]

The electronic states near the Fermi-level are associated to the Ni ions, making the most influent contribution to the magnetostrictive performance of the system; the Mn-states are at lower energies making Mn less important concerning both structural and transition properties, although the magnetic moment are mainly originated from the Mn ions, Mn excess atoms substituted at Ga or Ni sites will couple antiferromagnetically to the normal Mn sites. [4.5.9]. The magnetization behaviour as function of $\text{Ni}_{2+x}\text{Mn}_{1-x}\text{Ga}$ composition and temperature can be illustrated in figure 4.5.5:

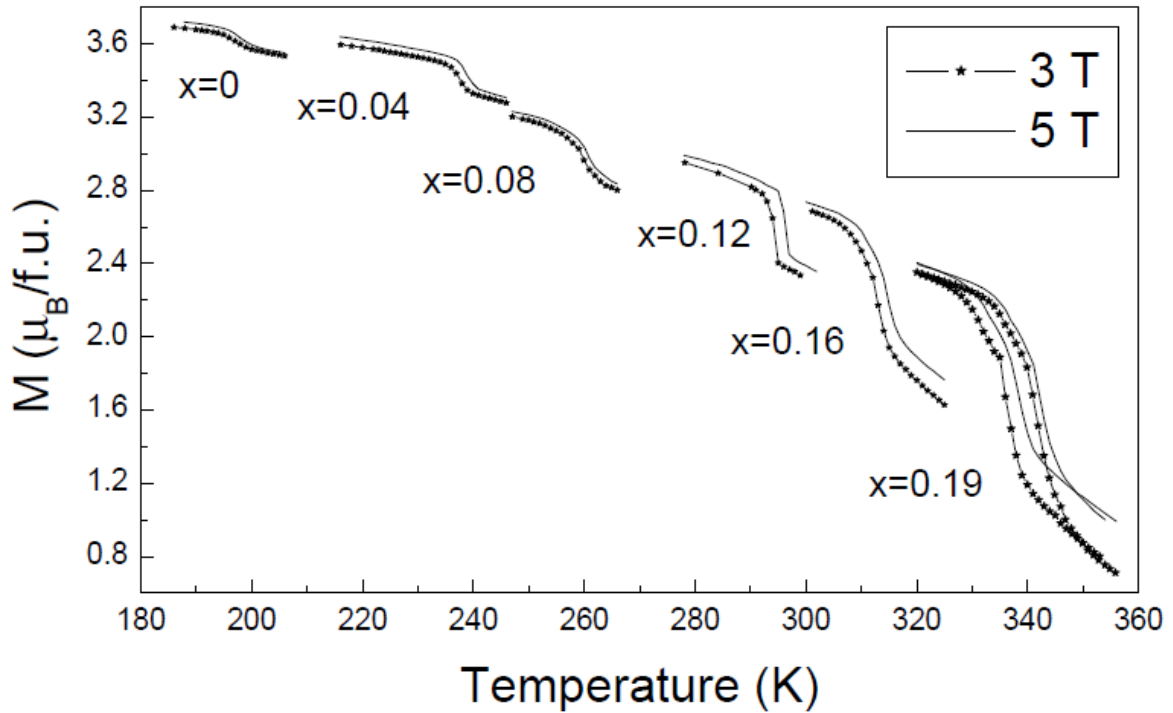


Fig. 4.5.5: Magnetization jumps at the martensitic transition in magnetic fields of 3 T (stared line) and 5 T (solid line). For compositions $\text{Ni}_{2+x}\text{Mn}_{1-x}\text{Ga}$ $0 \leq x \leq 0.16$ measured upon heating. For the composition. For $x = 0.19$ a temperature hysteresis loop of the magnetization observed upon cooling [4.5.10].

II EXPERIMENTAL METHODS

5 Samples Preparation Methods

Starting with the objective of producing samples with particular properties, it is indispensable to understand the respective material's phase's formation diagrams, which describe the relations between a particular equilibrium state, structure, and other fundamental characteristics of the compound, as function of the thermodynamic parameters: composition, temperature, atmosphere, hydraulic pressure, to refer the most common. The sample properties will depend also on other essential features, like shape and mechanical stability, chemical homogeneity, crystalline growth, grain size distribution, surface texture, epitaxy, among other aspects, which are strongly dictated by the mechanisms and limitations of the synthesis process; in its turn the selection of a determined preparation technique depends on the available experimental capabilities to achieve the suitable thermodynamic conditions necessary for the formation of the intended phase and sample characteristics.

In order to achieve successful scientific research and eventual practical applications based on a sample results, it is also fundamental to assure reproducibility of the preparation conditions, leading to a controlled stoichiometry, microstructure and properties of the material. In fact, the preparation techniques themselves become a subject of research and development: the discover of a new synthesis method that enable the access to new material phases usually become a relevant scientific breakthrough; pertinent simplification or modification of a conventional routes may have laboratorial or industrial production impact; and frequently, extensive studies are carried out to understand and control each of the processes variables to the resulting sample properties.

Bearing in mind that the advantages or disadvantages of each technique are evaluated in terms of the objectives proposed for the resulting samples properties, the main issue becomes to swiftly recognize the limitations and inadequacy of some routes and to focus on methods that not only can reach the right conditions to achieve the intended material's phase, but also the potential to further explore innovative aspects of the material or of the method itself.

This section provides a brief description of some experimental methods used in this work to manufacture bulk and thin film samples, for which there is practical technical access and expertise in the context of this thesis:

- Micro-powder oxides by *Solid-State* sintering route;
- Nano-powder oxides synthesis by *Co-precipitation*; by *Pechini Sol-Gel* and by *Sol-Gel urea combustion* methods;
- Thin films deposition by *Magnetron Radio Frequency Sputtering Physical Vapor Deposition* (PVD)

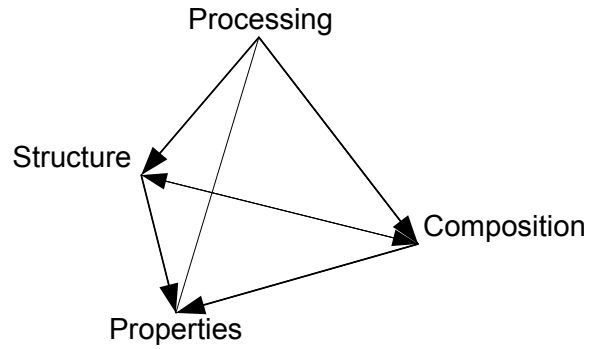


Figure 5.0.1: Correlation between materials' processing and resulting structure, composition and properties.

5.1 Ceramics Powders Sintering

In the preparation of pure or composite materials in the form of powders or bulk pieces, all methods go through stages at very high temperature in vacuum or in the presence of air or some pure gas atmosphere (Ar, O₂, N₂, etc.).

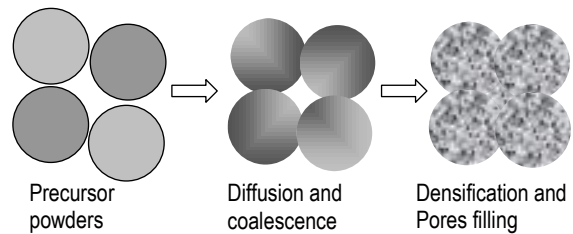


Fig. 5.1.1: Schematic of the sintering evolution.

This essential sintering process, can be undertaken below (<60-70%) the melting temperature of the elements composing the precursors matrix, preferably preventing the full segregation of any liquid phase; it is also essential to achieve a tight contact between the precursor particles, by starting from a compact and/or applying pressure during the sintering procedure, in order to promote the exchange of elements across the grains surfaces that ensures diffusion and homogeneous distribution of the components, as well resulting into the coalescence of the original agglomerates into larger grains (figure 5.1.1).

Once reaching the thermodynamic conditions for the formation of the equilibrium phase the system can be frozen in a metastable state by performing a rapid cooling to room or even lower temperature (quenching), or else allow gradual cooling down, achieving equilibrium with environment conditions.

Further heat treatments (or annealing) involve in summary the same physical mechanisms present in the sintering process, although already within the intended ceramic phase; the controlled high temperature stage can be used to enhance grain growth; densification; to recover or further enhance crystalline or chemical homogeneity of the sample; or yet, to modify the oxidation state of the compound cations: either increasing the Oxygen content by using limited temperatures (from 400° to 800° C) in air or O₂ atmosphere or reducing it by applying higher temperatures (above 1000° C) under vacuum, Argon or even in air [5.1.1].

5.1.1 Solid State Synthesis

In this process simple compounds or granular composites are usually directly prepared from laboratorial reagents powders [5.1.1]; in some cases it may become necessary use a binder or to perform a preliminary step to alter the chemical composition of a reagent to some other precursor form, more suited to form a solid solution with the other components (or for safety reasons), in general the procedure has few simple steps:

- Weighting the reagents;
- Grinding, disperse and mixing the powders in ethanol (or other appropriate dispersant) by manual or mechanical balls milling process;
- Calcination stage at ~600° to 700° C in air for at least 2 hours to eliminate all carbonated contends.
- Intermediate grinding, sieving and pressing into pellets;
- Successive sintering stages at raising temperatures ~900°, ~1200°, ~1500° C, etc. under the selected atmosphere, according to the material intended composition and phase, usually for periods of ~24 hours or more (the higher the temperature less time is required), until achieving the desired oxidation state, grain size and densification.

This process has the advantage of comprising straightforward routines and the most basic laboratorial material, nevertheless to achieve good degree of chemical homogeneity in the samples it becomes necessary to perform repetitive grinding steps, extended sintering time and raising temperatures above 1200° C to enhance elements diffusion; under these conditions there is a considerable grain growth typically in the 1 to 10 µm range that compromises oxygen stoichiometry between the grains surface and core.

5.1.2 Coprecipitation Synthesis

The coprecipitation method [5.1.2] is a wet chemical technique that has three main variants: a) direct solution-coprecipitation route; b) reverse solution-coprecipitation route and c) pH controlled reverse solution-coprecipitation route, as indicated in figure 5.1.2. The resulting precipitated salts have in principle a good distribution of chemical species in amorphous agglomerates of nanometric size, which are then dried and calcinated. The starting precursors small size ensures an easier sintering/densification process requiring lower temperatures and time than the solid-state route, resulting better chemical homogeneity, control over Oxygen stoichiometry, and an important management of the grain size growth (from ~5 nm for limited sintering at ~700° C; up to ~500 nm for extensive sintering under pressure above 1100° C)

5.1.3 Sol-Gel Synthesis

Introduced by Pechini in 1967 [5.1.3] this method for producing nano-sized oxides powders, and its many subsequent modifications, is focused on dissolving the reagent salts in suitable solvents; addition of an organic compounds (citric acid plus ethylene glycol and ethanol mix) that will form polymerizable complex precursors with the cationic elements in solution; heating to allow the solvent evaporation and the polyesterification resulting in a amorphous gel; this intermediary resin is later calcinated and transformed into fine powder oxides (figure 5.1.3). Chemical homogeneity and grain size distribution results are comparable to the previous coprecipitation method.

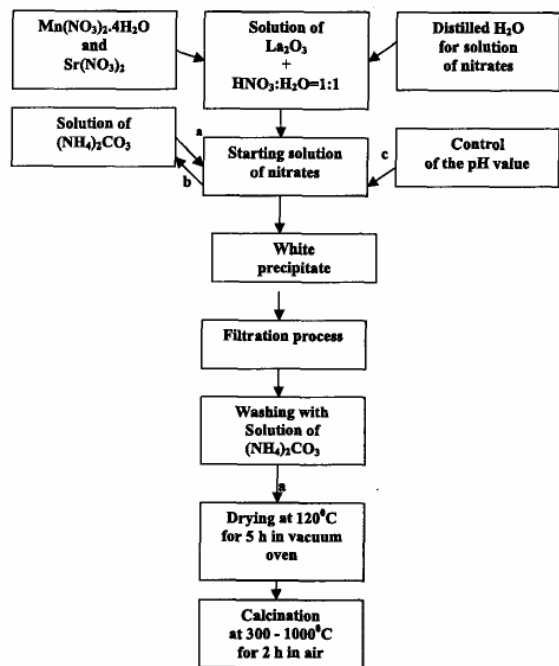


Fig. 5.1.2: Coprecipitation method procedure [5.1.3].

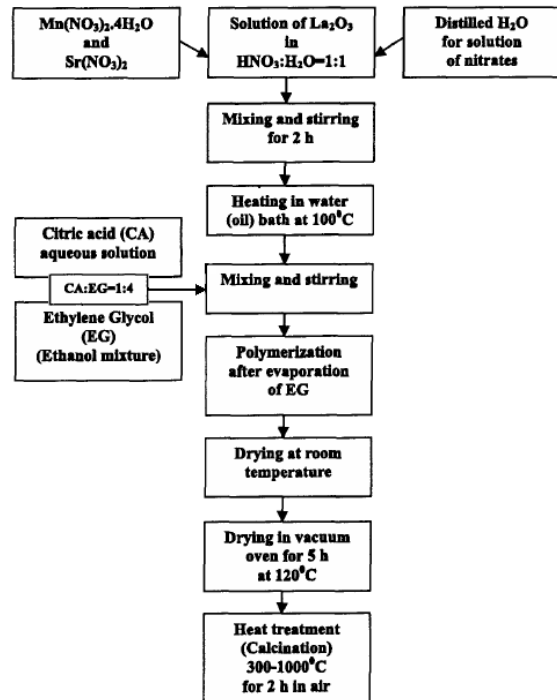


Fig. 5.1.3: Pechini method procedure [5.1.3].

5.1.4 Combustion Synthesis

An alternative chemical process uses *urea* as combustible gel precursor to synthesize the metallic oxides, since it is known to produce powders with grain size distribution between 10 and 50 nm [5.1.4] [5.1.5]. This method presents the benefit of comprising an extended stage of homogenous aqueous solution of the metallic salts; the ions remain dispersed until the solvent full evaporation, followed by the decomposition and auto combustion of the deposit into the ceramic pre-product. Effective formation/segregation of the ceramic phases is achieved after calcination and sintering stages. A more detailed description of this technique application can be found in section 7.1.

5.2 Thin Films Preparation

Thin film technology may find its roots to the ancient craft of gold leaf beating since Egyptians time almost four thousands years ago. Gold can be beaten by a skilled craftsman down to 0.05 micron leaf, and even at this extraordinary thinness, its beauty and resistance to chemical degradation have earmarked its use for durable ornamentation and protection purposes [5.2.1].

The study of thin films is focused in $2D$ aspect materials, usually having a thickness below $1\ \mu\text{m}$ down to 1 atomic layer, thin films can be either continuous or patterned, bonded to relatively thick substrates, stacked as multilayers, or even as free-standing; all became nowadays a crucial component for the new generation of technological devices.

The special interest of ultrathin films is that they make it possible to research and develop new science and applications making use of properties coupling (optical-electro-magneto-elastic) in new artificial structures, consisting of thin layers of different, sometimes non-miscible compounds, This “clamped” growth of a thin films typically results in internal stress that also modify the original properties of the material in bulk form.

5.2.1. Thin Film growth

The most important stage in thin film deposition is the desired material growth mechanism onto the substrate which will dictate the thin film outcome characteristics. The normal course of action for film formation is represented in figure 5.2.1.

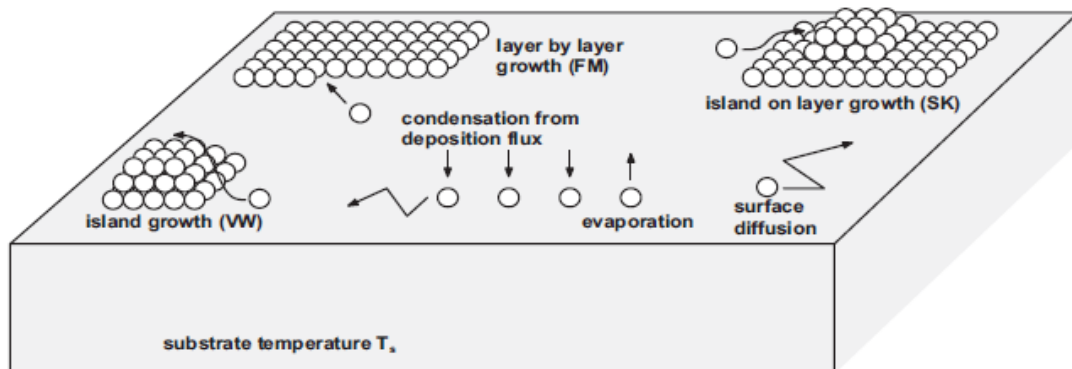


Figure 5.2.1: Schematic showing the atomistic formation of a film onto a substrate [5.2.2].

The atomic species arriving to the substrate may have enough energy to be adsorbed, otherwise can re-evaporate; suitable substrate temperature improves atoms diffusion on the surface, as the number of atoms rises, there are collisions and merging that develop into nucleation sites which grow into islands and as coalescence occurs all surface is covered and the film thickens.

According to the growth progression, the thin film outcome:

- Chemical composition can directly transpose the targets (or precursors) and atmosphere nominal composition, or reflect the distinct incorporation behavior into film of different elements.
- Microstructure onto the substrate can range from single crystal, bilayer of epitaxial and relaxed phase; preferable orientation growth in columnar or twined grains; random polycrystalline with varied kind of grain size and shape; or a basically amorphous layer.
- Surface can have a smooth vitreous or mirror like aspect, to have regular patterns or rough granular texture, to present porosity or show irregularities, have defects or even to detach from substrate.
- The thin film material can form in the expected phase and present the suitable properties, but it's also possible to develop other metastable phases.

In order to achieve the intended thin film characteristics, it is necessary to conjugate the most suitable deposition process and conditions that promote the adequate thin film growth. Although the bulk materials' phase diagrams may reveal some guide lines in terms of temperature and pressure for the formation of a selected phase, it is not directly applicable to the specific aspects of thin film formation, epitaxy and substrate induced stress; for that reason thin film deposition usually goes through an extensive preliminary empirical procedure. A series of experimental depositions are performed with controlled variation of operational parameters and the produced samples are characterized in the respective pertinent features, in order to estimate the appropriate deposition conditions that will lead to the final thin film properties.

5.2.2. Thin Film Deposition processes

The surface growth of a film being deposited onto a substrate is achieved by transference of the material in the vapor form or liquid dispersion from a precursor source; the deposition process is normally carried out in a vacuum chamber to enable control of the vapor composition. The way in which the film is formed classifies the method as:

- Chemical Deposition a vapor (CVD) or a volatile liquid precursor (CLD) undergoes a chemical reaction on the surface of substrate (combustion or reduction).
- Physical Vapor Deposition (PVD) the atoms are directly transported from source to the substrate through gas or plasma phase.

The route how the vapor is created and transported from the precursor target subdivides these two basic methods into several different processes, most relevant are presented in table 5.2.1 and figure 5.2.2, each having advantages and disadvantages according to the specific purpose of the thin film application, in terms of reproducibility, reliability, atmosphere and temperature constrains, production velocity, and of course, cost ratios.

Method	Process designation		Operational principle	Vacuum	Vapor Kinetic Energy
CD	L	Direct injection (DLI)	Precursor solution is sprayed by injectors.	$>10^{-3}$ mbar	Very low
		Spin Coating	Precursor solution is spread by centrifugation.	~ 1 bar	Very low
		Dip Coating	Substrate is temporarily immersed in the solution	~ 1 bar	Very low
		Screen Printing	Lithography (use of templates over substrates)	~ 1 bar	Very low
	V	Metal-Organic (MOCVD)	Ultrasonic evaporation of liquid metal-organic precursor and aerosol transport by inert gas flux.	Reactive $>10^{-3}$ mbar	Very low
		Combustion (CCVD)	Vapor derived from flame-based technique at open-atmosphere.	Reactive ~ 1 bar	High
		Plasma-Enhanced (PECVD) - variant -	Plasma discharge near substrate enhances chemical reaction of precursors.	Reactive $>10^{-3}$ mbar	High
PVD	Evaporation	Thermal	Resistive heating of target, evaporation from melting or sublimation results in high vapor pressure.	High $<10^{-5}$ mbar	Low
		E-beam	Target heating by electron bombardment.	Ultra High $<10^{-8}$ mbar	High
	Sputtering	DC	Plasma discharge and bias voltage drives Argon ions bombardment and atoms ejection from target.	Ultra High $<10^{-8}$ mbar	Very high
		RF Magnetron	Electrons plasma confinement near target improves Argon ions acceleration to target.	+ Argon $>10^{-3}$ mbar	
	Pulsed Laser Deposition(PLD)		High power laser ablates material from the target into a plasma plume.	Ultra High $<10^{-8}$ mbar	Very high
	Reactive PVD - variant -		Introduction of a reactive gas in chamber (O_2 , N_2 , F_2 , ...) to deposit oxides, nitrides, fluorides, etc.	Reactive $>10^{-3}$ mbar	High

Table 5.2.1: Basic aspects of most used thin film deposition processes.

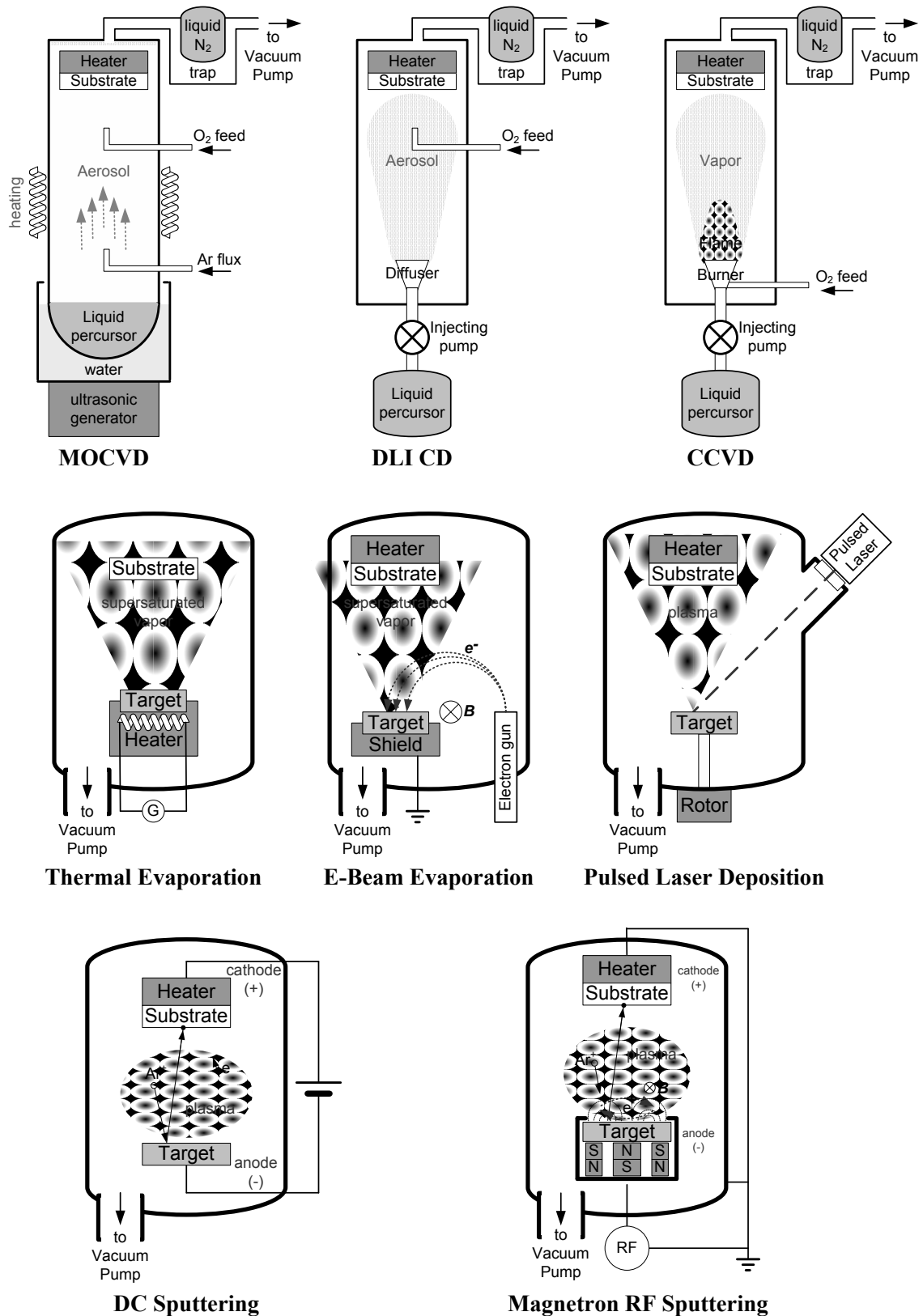


Figure 5.2.2: Diagrams showing the basic components of the several thin film deposition processes.

Each of these processes enables some degree of control over the following factors:

- The architecture between target, substrate and vapor flow relates to film homogeneity.
- The generated vapor pressure affects the nucleation progress of the film.
- The vapor particles energy arriving on substrate is essential for the formation of the intended film phase.
- The substrate temperature influences atoms diffusion and rate of film growth.
- The compatibility of substrate crystallographic parameters and orientation with the deposited film phase induces the epitaxial growth.
- The appropriate reactive atmosphere pressure during deposition imposes the film stoichiometry.
- The deposition chamber and vacuum quality affects the presence of impurities in the film that may include incorporation of the inert gas used in plasma discharge.
- In situ annealing is advisable in order to, promote re-crystallization, adjust stoichiometry and reduce defects and stress.

The most important limitations associated with the several thin film deposition processes are generally:

- CVD methods usually result in polycrystalline or amorphous structured films due to the high rate of deposition, hence are normally employed in industrial production. Special concerns should be given about the efficient exhaust of the reaction byproducts.
- Thermal evaporation is typically only applicable to relatively low melting/sublimation temperature materials ($<1500^{\circ}\text{C}$), slow deposition rates and very low kinetic energy of the vapor ($\sim 0.1\text{ eV/atom}$) results poor crystalline formation of films there is also the possibility of contamination due to the simultaneous heating of the crucible sustaining the target.
- Target Ablation by Pulsed Laser generates high energy plasma, the point source and high deposition rates compromise the good uniformity and crystalline formation of the film; in addition, ballistic droplets can eject from the target and splat in the substrate.

- E-Beam evaporation has not so many limitations as the previous described processes; it enables some management of deposition rate and vapors kinetic energy within a restricted range; never the less, distinct elements evaporate at different rates and complex composition films usually present poor stoichiometry and uniformity.
- DC bias sputtering can only be used in conductive targets in order to close the plasma discharge circuit; dc magnetron sputtering can provide high deposition rates since power supplies can be built up to 20 kW.
- Conventional RF sputtering has the risk of re-sputtering the film.

5.2.3 Magnetron RF Sputtering PVD

Magnetron RF Sputtering turns to be one of the most versatile PVD techniques because it enables an ample control of the conditions and parameters that lead to the successful deposition of all kind of elements and compounds in a variety of thin films phases. Most systems allow reactive deposition, by introducing an oxidizing (O_2 , N_2 , S_2 ,...) or even a reducer (CO , H_2 ,...) gas which combines with the sputtered material and deposits as compound films.

Sputter deposition is performed at moderately low pressures ($>10^{-3}$, $<10^{-1}$ mbar) in an inert gas (generally Argon) atmosphere. The plasma is sustained by RF current with densities between 10 - 100 mA/cm²; the Argon positive ions are generated by collisions of the neutral atoms with the plasma electrons.

The magnetron consist of a configuration of permanent magnets behind the planar target that create a magnetic field with flux lines (***B***) parallel to the target surface while the RF electric field (***E***) is perpendicular; this conjunction establishing a continuous path for the trapped "hopping" electrons. Even if RF power supplies are limited to <3 kW, the magnetron increases the plasma density near the target surface by confining the electrons which cause ionizing collisions; due to the induced bias voltage resulting from the electrons spatial gradient across the plasma, that can reach a few hundred volts; the Argon ions suffer additional acceleration towards the target resulting in a more efficient sputtering process.

The highly energetic Argon ions bombard the target and dislodge (sputter) atoms or molecules which are ejected with considerable kinetic energy (up to 10^2 eV/atom), contributing to better adhesion and denser crystalline films; hence thin film formation can occur even when substrate is kept at normal room temperature; however, heating is widely used.

Most elements are sputtered with similar rates, favoring direct thin film stoichiometry to target nominal composition. Planar and parallel geometry of target and substrate and broad directionality of the sputtered atoms offers a better control of the thin film uniformity and step coverage. Thin film purity is minimized by ensuring previous quality of vacuum ($<10^{-8}$ mbar) and by recurring to a pre-sputtering procedure that cleans eventual contaminants adsorbed by the target surface, nevertheless Argon gas can be implanted in the film.

6 Characterization Methods

There is a wide range of experimental techniques to characterize most kind of sample's properties, depending on the nature of the qualitative or quantitative information to access and the degree of accuracy necessary for the research objectives.

Most characterization methods involve a probing process, usually can be either: ions, electrons or photons which interact directly or indirectly with the material to be analyzed resulting in some aspects of the probing to be modified, for example: momentum, frequency, angle, polarization, etc. and then monitored with a specific acquisition system; the information is correlated to a particular property according an appropriate calibration, systematization and observation of the data. More conclusive analysis may require the use of complementary techniques or combination of several measurements.

Technique	Main information	depth probed	min. area probed	Accuracy resolution	Operational range	Operational requirements	Typical sample requirements
SEM	surface imaging	< 1 μm	< 5 nm^2	> 1 nm	room T	High vacuum	conductive surface or coating
EDS	composition mapping	$\sim 1 \mu\text{m}$	10 nm^2	> 0.1% $\sim 0.2 \mu\text{m}$	room T	High vacuum liquid N_2	$Z > 3$
XRD	structure phases	$\sim 1 \mu\text{m}$	> mm^2	> 0.001°	77-600 K or room T	vacuum, liquid N_2 or nothing	> 20 mm^2
HR-XRD	structure phases profile	< 1 μm	> mm^2	> 0.001°	room T	careful alignment	Thin films > 20 mm^2
XRR	Film thickness	< 1 μm	> mm^2	> 0.001° $\sim 1 \text{ nm}$	room T	careful alignment	Thin films > 20 mm^2
NPD	structure magnetic phase	> 1 μm	> cm^2	> 0.001°	4-300 K	High vacuum	Bulk, crystalline > 50 g
RAMAN	structure phases	$\sim 1 \mu\text{m}$	> mm^2	$\sim 0.5 \text{ cm}^{-1}$	4-300 K	Vacuum, liquid N_2	> 20 mm^2
PFM BEPS	dielectric phase mapping	< 1 μm	10 nm^2	< 20 nm	room T	Mechanical stability	smooth surfaces
MFM	magnetic phase mapping	< 1 μm	10 nm^2	< 20 nm	room T	Mechanical stability	smooth surfaces
XPS	Composition Bond energy	< 0.1 μm	> mm^2	$\sim 0.5 \text{ cm}^{-1}$	room T	High vacuum	> 20 mm^2
RBS	composition depth profile	< 2 μm	$\sim \text{mm}^2$	$\sim 0.01\%$ $\sim 10 \text{ nm}$	room T	High vacuum	> 20 mm^2
VSM	magnetic moment	> cm	> mm^2	0.001 T > 10^{-5} emu	4-310 K	vacuum, He	< 1 cm long > 0.05 g
SQUID	Magnetic moment	> cm	> mm^2	0.001 T < 10^{-7} emu	4-310 K	vacuum, He	< 1 cm long > 0.05 g
MR	magneto-resistance	> 1 μm	5 mm^2	$\sim 100 \text{ nV}$	4-320 K 77-400 K	vacuum, He or liquid N_2	> 20 mm^2
MZ	magneto-impedance	> mm	5 mm^2	$\sim 100 \text{ nV}$	4-310 K	vacuum, He	> 20 mm^2
ME	magneto-electric effect	> mm	5 mm^2	$\sim 100 \text{ nV}$	4-310 K 100-500K	vacuum, He or liquid N_2	> 20 mm^2

Table 6.0.1: Summary of the basic functions of the measurement systems utilized.

Many microanalytical techniques specialize in very fine dimensions, like interfaces and thin films where there is often very low quantity of material to analyze; though the practical distinction of “surface” from “bulk” or “thin” from “thick” depends on the properties and applications of interest in the sample [6.0.1]. In thin-film technology requirements can range to layers some μm thick, which for the majority of analytical techniques constitute like bulk material, whereas only a few techniques have suitable depths ranges to examine layers thinner than 10 \AA or even the detail of epitaxial relationship between the last atomic layers of single crystal material interfaces.

The table 6.0.1 summarizes and compares the features of the several measurement systems operated during the present research.

6.1 Scanning Electron Microscope – SEM

To observe features that are beyond the resolution of the human eye (about $100 \mu\text{m}$), and require far superior spatial resolution and depth of focus than the optical microscope, the Scanning Electron Microscope (SEM) is one of the most versatile analytical instruments and is often the preferred starting tool for materials studies [6.0.1].

The mechanism is based on a vacuum chamber, an electron source and a system of focusing condensers and deflection coils to raster the probe beam of electrons over the surface of the sample. The output can be almost directly used to modulate the brightness of a cathode ray tube (CRT) and correlated to the sample’s surface mapping; the magnification can be easily adjusted by the ratio between the voltages applied to the deflection amplifiers and the CRT; the resolution can reach the nm scale.

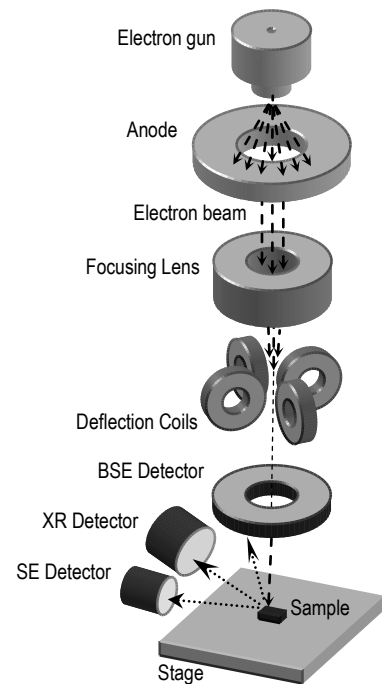


Fig. 6.1.1: Basic SEM schematics

Most SEM equipments usually require sample's compatibility with vacuum and preferably clean and conductive surfaces, in case the material is insulator it can be coated with a DC sputtered carbon or gold film (~10 nm).

The SEM images can be separated into secondary electron images, backscattered electron images, and elemental X-ray maps; each is collected by appropriate detectors:

Emitted secondary electrons (SE) are produced from inelastic scattering with atomic electrons, have much lower energy (<50 eV) and result from the first few nm of the sample's surface, providing excellent topographical contrast. Backscattered electrons (BSE) are considered to be the electrons that undergo elastic scattering with the atomic nucleus and exit the specimen with an energy comparable to the energy of the primary beam (>50 eV). The higher the atomic number of a material, the more likely it is that backscattering will occur, thus image contrast is caused by elemental differences.

An additional electron interaction of major importance occurs when the primary electron collides and ejects a core electron from an atom in the solid. The excited atom will decay to its ground state by emitting a characteristic X-ray photon and sorted by energy in an energy dispersive X-ray detector. These signals can be used to trace the spatial distribution of particular elements in the image, although the resolution of this type of image will rarely be better than 0.5 μm .

6.2. Energy Dispersive X-Ray Spectroscopy – EDS

When an inner shell electron is removed from an atom, to recover to an ionized ground state, an electron from a higher energy outer shell fills the vacant inner shell and, in the process, releases an amount of quantified energy as an X-ray photon equal to the potential energy difference between the two shells, each transition or cascade transitions are specific for element [6.0.1].

The energy-dispersive X-ray detectors used for elemental detection in the SEM maps can also produce an output signal proportional to the number of X-ray photons in the area under electron bombardment. With an EDS the output is displayed as a histogram of counts versus X-ray energy. With modern detectors and electronics most EDS systems can

detect X rays from all the elements in the periodic table above beryllium, $Z = 4$, if present in sufficient quantity. In practice the minimum detection limit (MDL) is ~ 200 ppm for most elements ($Z > 11$) under ideal conditions; however, because of a high background count and overlapped broad peaks, the accuracy may be generally 1-2% wt.

For bulk samples it is more important to maximize X-ray production and use an acceleration voltage of the electron beam ~ 2.5 greater than the critical ionization voltage (E_i) for the X-ray line of interest, while in the study of thin films it is usually desirable to minimize the electron penetration in the sample and use a moderate voltage of 5 to 15 keV, ultimately being able to detect even a monolayer of metal film on a substrate using $K\alpha$ lines.

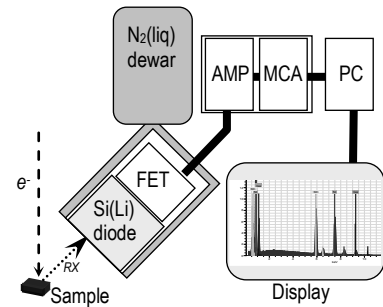


Fig. 6.2.1: Basic EDS schematics

The heart of the energy-dispersive spectrometer is usually a diode made from a silicon crystal with diffused lithium atoms, having thin layers of gold evaporated onto the front and back surface of the diode. Detectors are maintained under vacuum at liquid nitrogen temperature to reduce electronic noise and to inhibit diffusion of the lithium when a bias voltage is applied. When an X-ray photon enters the intrinsic region of the detector through the p type end, there is a high probability that it will ionize a silicon atom through the photoelectric effect. The cascade outcome will produce a particular number of electron-hole pairs that are drawn to the detector contacts under the action of an applied reverse bias field (100-1000 V). The signal acquisition is made at the gate of a specially designed field effect transistor (FET) mounted directly behind the detector crystal; then the signal is amplified (AMP) and filtered to a level that can be processed by a multi-channel analyzer (MCA), as represented in figure 6.2.1.

EDS systems are easy to use and controlled by computer (PC), the basic operations include spectrum collection, peak identification, and background subtraction, while peaks deconvolution and quantitative analysis is software processed.

6.3. Scanning Probe Microscopy – SPM

The expanding family of instruments commonly termed Scanning Probe Microscopes (SPMs) started in 1981 when Gerd Binnig and Heinrich Rohrer invented the Scanning Tunneling Microscopy (STM) at IBM, Zurich, for which they earned the Nobel Prize for Physics in 1986. This powerful real-space imaging technique can produce topographic images within atomic resolution in all three dimensions; it measures a quantum-mechanical tunneling current between the tip within a few Å distance of a conducting surface; therefore is more suitable to study conductive materials under ultrahigh-vacuum condition since any surface oxide or other contaminant will complicate operation under ambient conditions.

The derived Scanning Force Microscopy (SFM) has much more flexibility, able to operate under normal environments and measure any type of samples, minimizing system setup, samples' preparation and acquisition time; further reducing the cost and complexity of the microscope. With vertical sub-Å resolution and fields of view ranging from 10 nm features recognition to greater than 250 x 250 µm scans this research tools become of increasing importance for atomic-imaging applications in surface science.

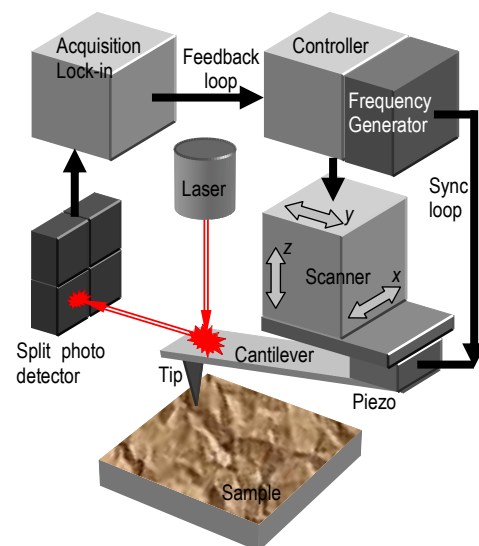


Fig. 6.3.1: Basic SFM' schematics

Scanning Force Microscopes use a sharp tip mounted on a flexible cantilever; when the tip comes within a few Å of the sample's surface it establishes electric, magnetic or *Van der Waals* forces between the atoms of the tip and those on the sample, causing the cantilever to deflect in a power law dependence on the tip-to-sample distance (d). SFM employs a beam-bounce detection system, using the light from a laser diode reflected from the back of the cantilever into a very position-sensitive (about 0.1 Å) photodiode; a piezoelectric transducer operating in feedback loop ensures the constant distance between the tip and the sample and the accurate scan across the surface, as depicted in figure 6.3.1.

In the Piezo-response Force Microscopy (PFM) [6.3.1] a conductive AFM tip is brought into contact with the surface of ferroelectric or piezoelectric material; by applying a pre-set voltage (< 1 V) through the tip the sample stimulated region expands or contracts (inverse piezoelectric effect) according to the relation between the local piezoelectric properties and the electric field. The deformation provokes the cantilever deflection, as schematized in figure 6.3.2.

The use of a small modulated a.c. field ($|E_{in}(\omega)| < E_{coerc.}$), close to the electro-mechanic resonance of the system, enables to trace the correlated response in amplitude $A_{out}(\omega)$ and phase $\phi_{out}(\omega)$ correlated to the sample local polarization, whilst the cantilever deflection associated with the topographic features of the sample surface are distinguished as crossing $E_{in}(\omega) = 0$.

Typically there can be three images modes for PFM: *Out-of-plane* polarization as a direct measure of the tip vertical deflection, *In-plane* polarization detected as lateral motion of the tip and finally the *Vectorial*, integrating the 3 orthogonal components of the polarization and topological information making possible to charter the correlation between grain size, location and shape with the polarization domains. PFM can also be used for micro *lithography* applications, since by forcing at the tip a bias electric field higher than the local coercive field of a ferroelectric sample it is possible to write single domains and even complex patterns; under certain limitations, the control of mechanical pressure can even be used to dig topographic changes in the sample surface if required.

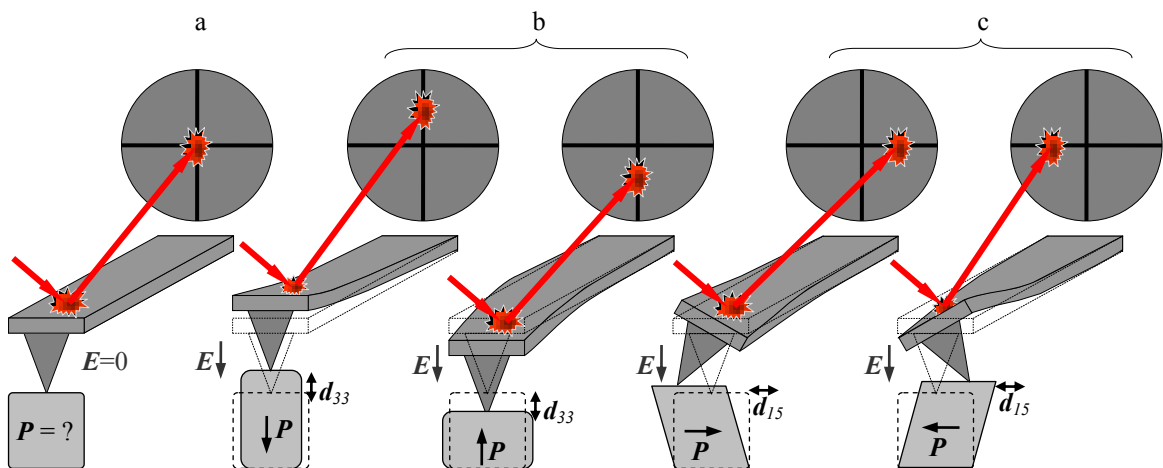


Fig. 6.3.2: Diagram of PFM operation principle a) topographic default at $E = 0$, b) *out-of-plane* and c) *in-plane* local polarization measurement at $E < E_{coerc.}$.

Magnetic Force Microscopy (MFM) use similar operating principles though changing the tip function to be in off-contact mode and sensitive to the magnetic moment coupling between the tip and the area of the sample under measurement.

Information on local ferroelectric behavior such as imprint, switching work, nucleation biases, etc, can be obtained as function of the local hysteresis loops generated by PFM *Spectroscopy Mapping* mode; however technical limitations related to tip positioning and drift restrain the number of points and acquisition time in the sample. A particular option developed by ORNL and *Asylum Research*TM Company is *Band Excitation Piezo-Response Spectroscopy* (BEPS) [6.3.2], able to monitor responses simultaneously at a wide and continuous band of frequencies, improving acquisition time and scope of parameters as function of frequency. BEPS mode requires a modulated waveform ($V_{in} = V_{dc} + V_{ac}.sin(\omega.t)$), as exemplified in figure 6.3.3; high-speed data acquisition and FFT signal processing hardware as well as specially developed software. The resulting data array has terms of amplitude, phase, voltage, resonance and dissipation response to each frequency bin at each mapped point, as represented in figure 6.3.4; data processing and conversion reveals maps of local hysteresis loops and most significant ferroelectric parameters (figure 6.3.4), as well as mapping FE domains and respective nucleation, imprint, switching polarization and work.

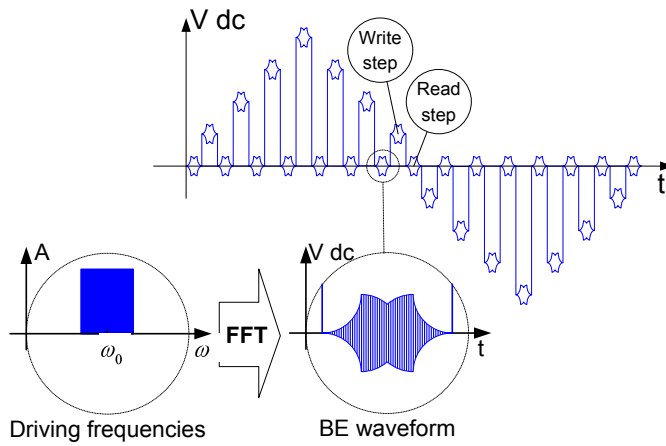


Fig. 6.3.3: Typical BEPS driving signal.

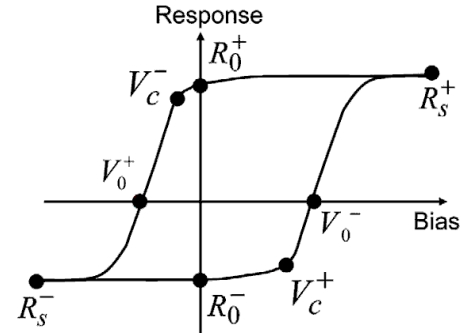


Fig. 6.3.4: Fitting model for piezo-response cycle with BEPS parameters determined at each point for each frequency bin and voltage bias step [6.3.2].

6.4. X-ray Diffraction – XRD and Reflectometry – XRR

XRD is the most widely used technique for general crystalline material characterization; it has the advantage to be a powerful noncontact and nondestructive technique that can be used in most environments and is comparatively less expensive and practical to operate than other techniques that provide structural information, namely: Extended X-ray Absorption Fine-Structure (EXAFS), Low-Energy Electron Diffraction (LEED), Reflection High-Energy Electron Diffraction (RHEED), X-ray Photoelectron Diffraction (XPD), Neutron Powder Diffraction (NPD), Transmission Electron Microscopy (TEM), etc.

Owing to the huge data bank available covering practically every phase of every known material (powder diffraction patterns), from XRD patterns it becomes possible to routinely identify phases in polycrystalline bulk material and to quantify the respective fraction present in material. The diffractogram peaks positions enables to resolve the long-range order information like space group symmetries and determine average unit cell dimensions, atomic positions and theoretical unit cell density; by further analyzing the broadening and splitting of peaks other structural informations like strain state, grain size, epitaxy, preferred orientation, and even defect structure can be accessed [6.0.1].

XRD does not allow identifying directly atoms composing the individual crystalline phases present on a sample, but enables to evaluate the correlation between the structure and the expected chemical composition of a phase. In their “usual” form, XRD is used for bulk samples, since X rays can probe many microns deep; however, there are ways to make XRD more surface sensitive. Since it offers unparalleled accuracy in the measurement of atomic spacing it can also be used to resolve atomic arrangements in amorphous materials (including polymers) and at interfaces and is the technique of choice for determining strain states and particle size in thin films (both produce distinguishable peak broadenings).

For completely random polycrystalline thin films down to thicknesses of 100 Å, phase identification and relative amounts are also easily determined, using standard equipment and diffraction geometries. Once preferred orientations occur (texturing) it requires the collection of much more data or the introduction of more sophisticated equipment with different diffraction geometries so that the orientations can be “seen”

effectively. These diffraction geometries include Grazing Incidence XRD (GIXRD), in which case the X-ray probing depth is greatly reduced greatly improving surface sensitivity and allowing a depth profiling mode (50 Å to microns) by varying the incidence angle. Because of small diffracted intensities, thin-film XRD generally requires large specimens ($>20 \text{ mm}^2$) and the information acquired is an average over a large area.

The fundamental principle of XRD is the constructive interference from X-rays scattered by the atomic planes in a crystal; the diffracted intensity is measured as a function of 2θ (angle between the incident and diffracted X-rays) and the orientation of the specimen as illustrated in figure 6.4.1. The condition for constructive interference from planes with spacing d_{hkl} (from Eq. 1.0.1) is given by Bragg's law:

$$\lambda = 2 \cdot d_{hkl} \cdot \sin\theta \quad (\text{Bragg's law})$$

The X-ray wavelength λ is normally 0.7-2 Å, (corresponding to energies of 8.7 - 24.8 keV) and the most used is the monochromatic $\lambda(\text{Cu}_{K\alpha 1}) = 1.5405980 \text{ Å}$.

The degree of crystallite orientation in a thin film can vary from epitaxial, to complete fiber texture, to preferred orientation, to randomly distributed (powder); this not only influences the thin-film properties but also has important consequences on the method of measurement and on the difficulty of identifying the phases present. For a single crystal or an epitaxial thin film, there is only one specimen orientation for each (hkl) plane where these diffraction conditions are satisfied. The crystal must be oriented so that the normal to the diffracting plane is coplanar with the incident and diffracted X-rays and so that the angle between the diffracting plane and the incident X rays is equal to the Bragg angle. Polycrystalline thin films or bulk samples consist of many grains or crystallites having a random distribution of orientations; then diffraction occurs from any crystallite that happens to have the proper orientation to satisfy the diffraction conditions. The diffracted X-rays emerge as cones about the incident beam with an opening angle of $2\theta_{hkl}$ creating a “powder” diffraction pattern.

The X-ray Reflectometry (XRR) mode is a highly accurate method for determining the layer thickness of thin films (preferably $< 200 \text{ nm}$) deposited in plain substrates. Very similar to the Bragg-Brentano configuration but with less geometry restrictions in order to adjust the incident beam to the sample critical angle and the measurement is performed within a grazing angle of $0.01 < \theta < 6^\circ$.

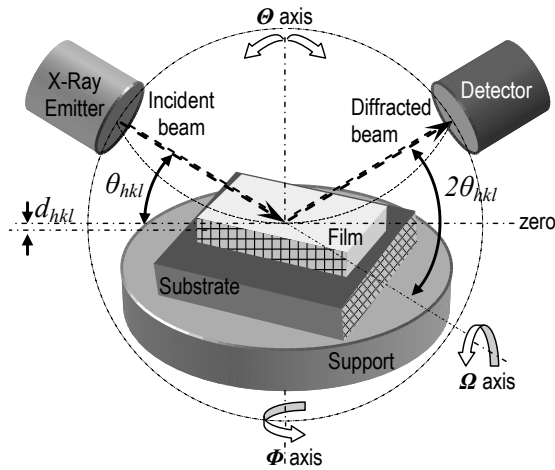


Fig. 6.4.1: Basic schematics of Bragg-Brentano XRD configuration and goniometry movements

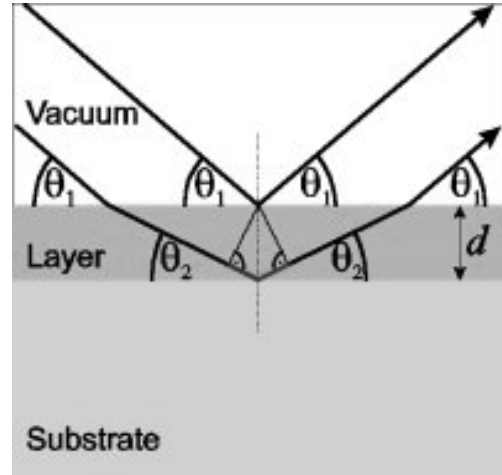


Fig. 6.4.2: Reflectivity and interference effect due to the interfaces of different materials.

In this technique, the reflectance of the sample is measured as a function of the grazing incidence angle of the X-rays. Due to interference effects of the radiation reflected at the two interfaces as illustrated in figure 6.4.2, oscillations occur in the reflectance curve and are correlated with thickness according to the Bragg equation. While the oscillation amplitude (at fixed photon energy) depends on the densities and the surface and interface roughness, the oscillation period is mainly determined by the layer thickness.

6.5. Neutron Powder Diffraction – NPD

Neutron diffraction is a nondestructive technique that can be used to determine the positions of atoms in crystalline materials (similar to X-ray and electron techniques but with enhanced sensitivities). Other uses are phase identification and quantification, residual stress measurements, and average particle-size estimations for crystalline materials.

Major advantages of neutron diffraction comprise: sensitivity to the special arrangement of magnetically active atoms, since neutrons possess a magnetic moment; detailed structural information averaged over thousands of Å (up to 50 μm) due to the extraordinarily greater penetrating nature of the neutron; and structural analysis with distinction of materials containing atoms of widely varying atomic number, such as heavy metal oxides, due to the specific interaction of neutrons with different nuclei.

The greater penetration of neutrons may allow to study larger samples and to use thick ancillary devices, such as furnaces or pressure cells, without seriously affecting the quality of diffraction data; the main consequence become to ensure health and safety requirements by shielding neutron sources and instruments with several meters of absorbing material (usually steel, concrete, or boron-containing materials), implying installations and investments orders of magnitude larger than the corresponding X-ray devices [6.5.1].

6.6. Rietveld Refinement

The standard method for analyzing the diffractograms results (intensity vs. scattering angle 2θ) of a neutron powder or X-ray diffraction experiments is known as "Rietveld profile refinement", developed by Hugo M. Rietveld in 1969. This mathematical process is based on a non-linear minimization algorithm of least squares in order to obtain the best fit of a crystalline structure model and the acquisition conditions simulation (y_{calc}), to the experimental measured diffraction pattern (y_{obs}). The practical application of this method only became viable due to the modern increase in computing power.

$$y_{i,calc} = y_{i,back} + \sum_p \sum_{k_1}^{k_2} G_{ik} \cdot I_k \quad (\text{Rietveld method equation})$$

Where $y_{i,calc}$ the net intensity calculated at point i in the pattern, $y_{i,back}$ is the background intensity, G_{ik} is a normalized peak profile function, I_k is the intensity of the k^{th} Bragg reflection, $k_1 \dots k_2$ are the reflections contributing to the intensity at point i , and the superscript p corresponds to the possible phases present in the sample.

The number of adjusted model parameters (P) most common in a Rietveld refinement software analysis can be divided into several categories; the user selects the fitting strategy, the order, variables and parts of the model should be refined:

- Fundamental experimental features like radiation source, wavelengths (λ), system geometry and presence of beam adjustment devices, acquisition range ($2\theta_i$ - $2\theta_f$) and step ($\Delta\theta$), instrument alignment, sample height, surface roughness among other factors.
- Description of the peaks' profile shape function (G_{ik}), relative line broadening, presence of asymmetries, corrections and polarization.

- Number of expected phases, respective symmetry group (SG) and unit cell parameters ($a, b, c, \alpha, \beta, \gamma$); determining the allowed reflections and consequently the positions and relative intensities of the Bragg peaks.
- Atom positions within the unit cell (x, y, z), magnetic moments components (M_x, M_y, M_z), site occupancies factor (SOF) as well as anisotropic (U_{ij}) and isotropic (B) temperature factors responsible for atoms displacements, collectively determine the atomic scattering factors (F_{hkl}) and the integrated intensities of peaks.
- Change of peaks relative intensity due to sample aspect (bulk, film, wire, dots) and eventual preferable crystalline orientation due to epitaxial growth.
- Contributions to the peaks broadening due to small grain size and strain effects
- Description of the relatively smooth "background" scattering that lies between and below the Bragg peaks, that may include coherent and/or incoherent contributions from the sample and its environment, electronic noise, and other unwanted sources.
- The method only works well if the starting model is close enough to the samples characteristics, sometimes restrain of bond distances or bond angles and constrains in phase composition are necessary to avoid divergence.

The minimization is undertaken over all data points contributing to the peaks and (when refined) the background.

$$R = \sum_i w_i (y_{i,obs} - y_{i,calc})^2 \quad (\text{Least square Newton-Raphson algorithm})$$

Where w_i is the weight assigned to each observation; having N as the number of acquisition points. The agreement between the observations and the model can be assessed during the course of the refinement by the ratios:

$$R_p = \frac{\sum_i |y_{i,obs} - y_{i,calc}|}{\sum_i y_{i,obs}} \quad (\text{Profile R-factor})$$

$$R_{wp} = \left[\frac{\sum_i w_i (y_{i,obs} - y_{i,calc})^2}{\sum_i w_i y_{i,obs}^2} \right]^{1/2} \quad (\text{Weighted profile R-factor})$$

$$R_{\text{EXP}} = \left[\sum_i \frac{N - \mu}{i \cdot \sigma_{i,obs}^2} \right]^{-1/2} \quad (\text{Expected R-factor})$$

$$\chi = \left[\frac{\chi_{\text{WP}}}{\chi_{\text{EXP}}} \right]^{-1} \quad (\text{Fit quality})$$

The most important judgment is in all cases the visual judgment of the diffractograms and residues, low indices mean nothing if the fit does not look convincingly similar to the original data [6.6.1].

6.7. Raman Spectroscopy

The molecular and crystal mechanical vibrations (phonons) occur at frequencies ranges 10^{12} - 10^{14} Hz, which is in the infrared (IR) region of the electromagnetic spectrum. The Raman spectrum arises from an indirect coupling of high frequency radiation (ultraviolet, visible or near infrared) with the energy levels of the phonons, whereas direct coupling to incident infrared radiation produces the infrared absorption spectrum (FTIR). Both spectroscopies measure the vibrational spectra of materials and should be considered complementary given that the physical processes and the selection rules that determine which of the vibrational modes are excited are different. Raman spectroscopy is primarily a structural characterization tool more sensitive to the lengths, strengths, and arrangement of bonds in a material than it is to the chemical composition.

When monochromatic radiation is incident upon a sample it interacts with the electron clouds and may be reflected, absorbed or scattered: The main scattering process occurs without a change of frequency (Rayleigh scattering), however, in the order of 10^{-7} of these photons have some change in the frequency (Raman scattering) shifted either to higher (Anti-Stokes) or lower (Stokes) frequencies, as illustrated in figure 6.7.1.

Unless circumstances such as materials' fluorescence, specific absorption edge or photodecomposition of the sample, it's standard to use high frequency laser lines to perform Raman spectroscopy, commonly continuous gas laser like the Argon ion laser (488 nm or 514.5 nm), He-Ne lasers (632.8 nm) and the Krypton laser (647.1 nm).

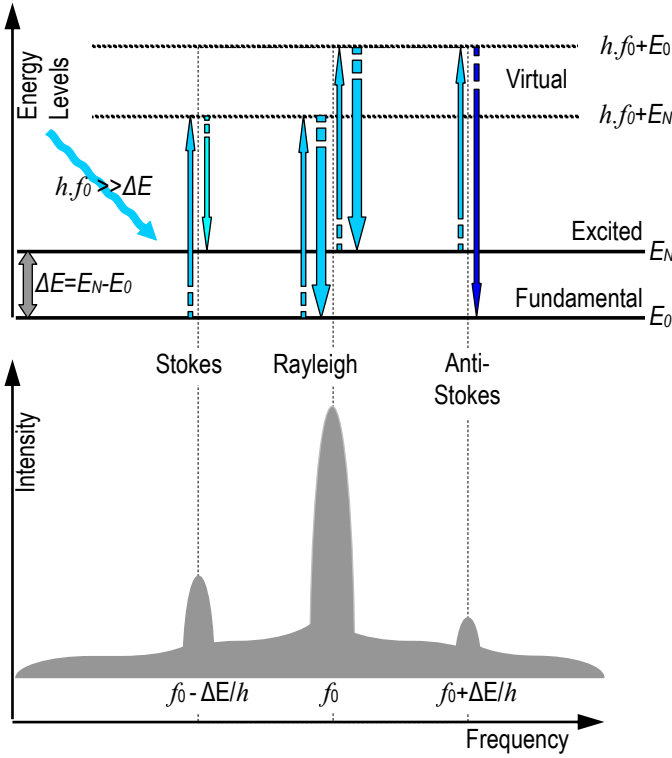
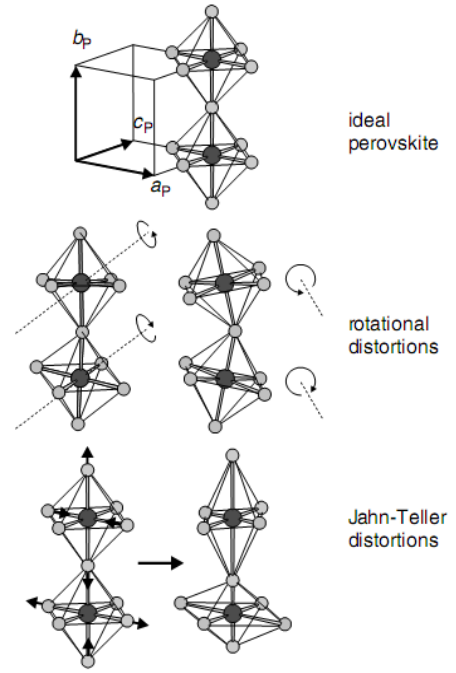


Fig. 6.7.1: Basic diagram of Raman' scattering effect.


 Fig. 6.7.2: Examples of MnO₆ octahedra distortions in perovskite like structure that may confer Raman active modes [6.7.2].

The system geometrical arrangement and assembly of focusing optics and slits, direct the laser spot to the sample surface and collect the scattered light at 90° angle; since Raman spectra is extremely dim, the system must be protected from stray light entering the detectors. Photomultipliers are used in single-channel instruments, whilst array detectors either linear diodes or charge-coupled devices allow partial or the entire spectrum to be captured at one time, although with limited resolution. The Raman spectrum consists of a plot of intensity of scattered light versus energy shift, typically in cm⁻¹ wave number ($\tilde{\nu} = 10^2/\lambda$) units.

The relative intensity of Stokes and Anti-Stokes lines depends on the thermodynamic distribution and degeneracy (g_i) of the fundamental and excited energy states of the molecules:

$$\frac{I_S}{I_{AS}} = \frac{g_0}{g_N} e^{-\frac{\Delta E}{k_B \cdot T}} \quad (\text{Stokes and Anti-Stokes lines relative intensity})$$

From Heisenberg uncertainty principle ($\delta E = \hbar/\tau$), the band broadening ($\delta\tilde{\nu}$) is inversely proportional to the lifetime (τ) of the energy states involved:

$$\delta\tilde{\nu} \approx \frac{5.3}{\tau / 10^{-12} \text{ s}} \text{ cm}^{-1} \quad (\text{Raman band broadening})$$

The scattered radiation occurs over all directions and may also have observable changes in polarization along with its wavelength; the separation from the Rayleigh line is a direct measure of the vibrational state and electronic level transitions of the molecules from which it is possible to infer the respective structural and chemical information [6.0.1]. The fundamental selection rule for Raman transitions is that the molecules must be anisotropically polarizable ($\alpha_{\perp} \neq \alpha_{\parallel}$), i.e. the structural distortion depends on the direction of the electric field from the incident photon. In structural terms, the species have a quadratic (x^2 , xy , etc) form or no symmetric inversion centre.

Of particular interests is the pseudocubic structure of perovskite manganites which shows some Raman active modes related to the orientational disorder of Mn-O bonds intrinsic to the Jahn-Teller (JT) displacements and on rotations of the MnO_6 octahedra as represented in figure 6.7.2; these distortions and lattice dynamics are allowed within a range of the phase diagrams of some manganites (Not considering eventual spurious phases that may confuse the spectra.), displaying ferromagnetic, antiferromagnetic, charge-ordering and metal-insulator transitions [6.7.2]. a)

6.8. Magneto-Resistance – MR

Magneto-resistance (MR) is a term widely used to mean the change in the electric resistance due to the presence of a magnetic field, having different characteristics in metallic, semiconducting and insulating materials [6.8.1]; commonly defined by the coefficient:

$$\text{MR} = \frac{R(H) - R(0)}{R(0)} \quad (\text{Magneto resistance})$$

Where $R(H)$ is the materials resistance under magnetic field and $R(0)$ without.

Conventional anisotropic magneto-resistance (AMR) effect can be found in ferromagnetic materials with metallic conductance. The dependence of conductance on the relative angle between the electric current and magnetization is fairly small, a few percent for $\text{Ni}_{0.8}\text{Fe}_{0.2}$ (permalloy) at room temperature, nevertheless very useful in some technical applications like sensors. On ferromagnetic thin films a small resistance change is generally observed in the vicinity of the magnetization reversal field where domain walls

spin directions are deviated from the easy direction and the non-collinear spin structure formed acts as electron scattering centers influencing on conductance [6.8.2].

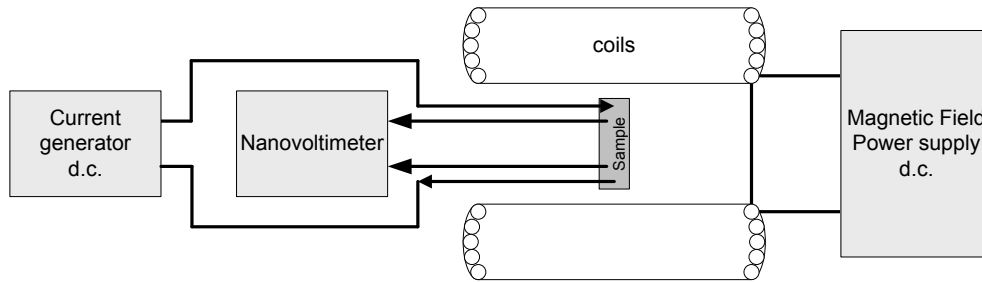


Fig. 6.8.1: Simplified Diagram of a MR measurement setup.

Giant magneto-resistance (GMR) was first observed in Fe/Cr multilayers by the group of Fert in 1988 [6.8.3], subsequent to the work Grünberg et al. [6.8.4]. The GMR mechanism can be explained by considering the spin-dependent scattering of conduction electrons at the interface of the ferromagnetic layers. When an external magnetic field overcomes the existence of a strong antiferromagnetic interlayer coupling between Fe layers (separated by the Cr spacer), the collinear spin electrons will have a long mean-free path in the magnetic aligned layers resulting in a higher conductance. The key behind the discovery of GMR is to utilize spin structure manipulation. The anti-parallel alignment of Fe layers' magnetizations at zero fields and the reorientation into parallel alignment by an increase in the external field, that is, the resistance in anti-ferromagnetic state can be 20-30% larger than that in ferromagnetic state. In only 10 years, through the studies on the oscillatory interlayer coupling behavior, between the FM layers and spacer thickness our understanding of the electronic structure of thin metal films has advanced remarkably, given rise to hard disks and read devices based on GMR.

In tunneling magneto-resistance, (TMR) two magnetic electrodes are separated by an insulating barrier and the difference of conductance can surpass 100% [6.8.5] between the states of parallel and anti-parallel magnetizations as the electrons tunnel through the barrier or are blocked by the spacer.

Colossal magneto-resistance (CMR) phenomena can be observed in the perovskite-type hole-doped manganites in which the charge-orbital ordered antiferromagnetic phase and the double-exchange ferromagnetic metal phase compete with each other, giving rise to insulator-metal transitions induced by the magnetic field [4.2.2].

6.9. Magneto-Electric Effect – ME

The dynamic Magneto-Electric effect (ME) method measures the electric voltage signal ($V_{a.c.}^{out}$) generated between the sample electrodes (d) due to the polarization induced by a weak a.c. magnetic field ($H_{a.c.}$) oscillating in the presence of a strong magnetic bias field ($H_{a.c.} \ll H_{d.c.}$) [6.9.1], as represented in figure 6.9.1.

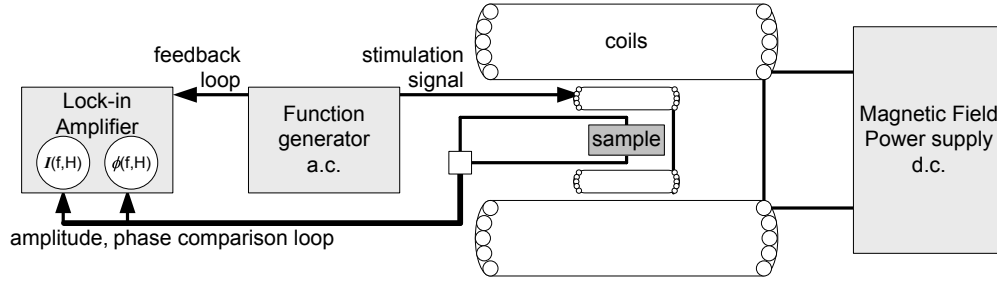


Fig. 6.9.1: Simplified Diagram of the ME measurement setup.

$$\text{ME coefficient} = \frac{\partial \mathcal{I}}{\partial \mathcal{I}} = \frac{1}{d} \frac{\partial \mathcal{V}}{\partial \mathcal{I}} = \frac{1}{d} \frac{V_{a.c.}^{out}}{H_{a.c.}} \quad (\text{Magneto-Electric coefficient})$$

By recurring to a well-defined frequency and a lock-in amplifier working in differential mode, the noise is dramatically reduced and the calibration problem is avoided. A weak point of this method is the eventual charge accumulation or electrical discharging through the sample, either due to resistive or capacitive process, depending on the frequency used.

ME behavior may include higher order manifestations, including second harmonic generation that can be used to further investigate the coupling between electric and magnetic domain structures; although with this kind of setup only one of the facets ($\partial \mathbf{E} / \partial \mathbf{H}$) of the ME effect, it can be evaluated under different time scale responses of the magnetostrictive component by changing the frequency of the AC field and explore different working points of the sample by changing the DC magnetic bias field.

Other means of studying the ME effect may use static or quasi-static methods, the induced linear or nonlinear optical polarization and dispersion effects due to the complex changes in the electric and magnetic susceptibilities of the material subject to magnetic or electric fields.

6.10. Magneto-Impedance – MZ

Magneto-Impedance (MZ) is a general technique related to the previous described magneto-resistance (MR); by measuring the dissipative effects of resistance (\mathbf{R}) and the phase shift due to the reactance (\mathbf{R}') of a sample as function of applied a.c. voltage frequency (f) and d.c. external magnetic field (\mathbf{H}); the analogous definition:

$$MZ_f(H) = \frac{Z_f(H) - Z_f(0)}{Z_f(0)} \quad (\text{Magneto-Impedance})$$

Where $Z = R + jR'$ making $|Z| = \sqrt{R^2 + R'^2}$ (Impedance)

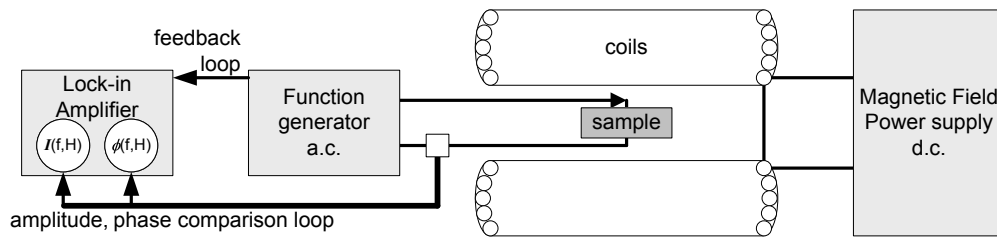


Fig. 6.10.1: Simplified Diagram of the MZ measurement setup.

The origin of the MZ effect can be understood in a context of classical electrodynamics on the basis of the impedance dependence on classic skin penetration depth $\delta = (\pi f \sigma \mu)^{-1/2}$ as referred in section 2.1, where all the relevant parameters are directly involved: frequency, conductivity and magnetic permeability [6.10.1].

Giant MZ is also a promising effect for developing sensors highly sensitive to magnetic fields, like CMR, with the addition of being frequency discriminatory, with potential applications as selective detectors and transducers in communication technology.

6.11. Vibrating Sample Magnetometer – VSM

The basic principle of the VSM for measuring the magnetic moment of a sample can be summarized as the sample placed inside a uniform magnetic field (\mathbf{H}_0) is magnetized, and subjected to a sinusoidal oscillation (f) by means of a piezoelectric transducer. The induced voltage (V) in a couple of calibrated pickup coils (n turns, S section) is proportional to the sample's magnetic moment (M) and independent of the magnetic field, being measured through the use of a lock-in amplifier using the vibration

frequency as reference signal; figure 6.9.1 gives a schematic representation of a VSM setup.

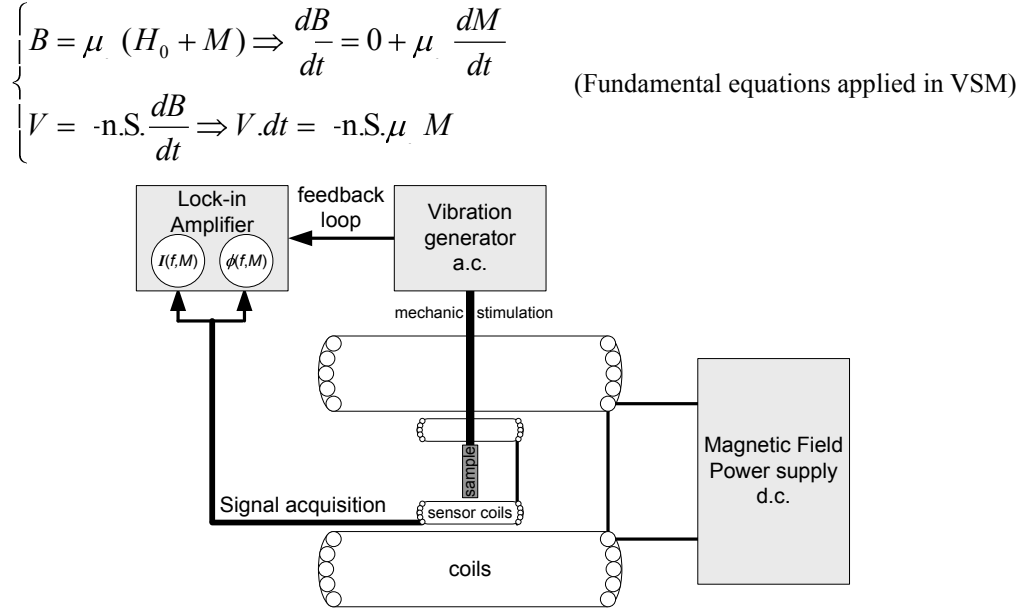


Fig. 6.11.1: Simplified Diagram of the ME measurement setup.

This experimental technique was patented in 1956 by Simon Foner (1925-2007) [6.11.1], VSM can perform susceptibility and magnetization studies, common measurements are: hysteresis loops, susceptibility or saturation magnetization as a function of temperature (thermo magnetic analysis), magnetization curves as a function of angle (anisotropy), and as a function of time.

Magnetic moment sensitivity is usually $\geq 5 \cdot 10^{-5}$ emu, since the acquired signal is susceptible to drifts due to minor shifts in frequency or amplitude of the vibrations and usually implies complex hardware/software corrections to minimize errors sources.

6.12. Superconducting Quantum Interference Device – SQUID

The basic element in a SQUID magnetometer is a ring of superconducting material having one or two Josephson junctions that are highly sensitive to variations in the magnetic flux ($\oint \mathbf{B} \cdot d\mathbf{S}$) associated to the Meissner effect. As result of interference effects of cooper electron-pairs wave functions, the critical current in an array of these devices become periodic and quantified in $h/2.e$ field units ($= 2.0679 \times 10^{-15}$ Tesla.m²).

$$S.dB = \pm h/2.e \quad \text{(Magnetic flux quantum)}$$

SQUID magnetometers usually use the extremely sensitive current-to-voltage-conversion occurring at the Josephson junctions, as represented in figure 6.12.1.

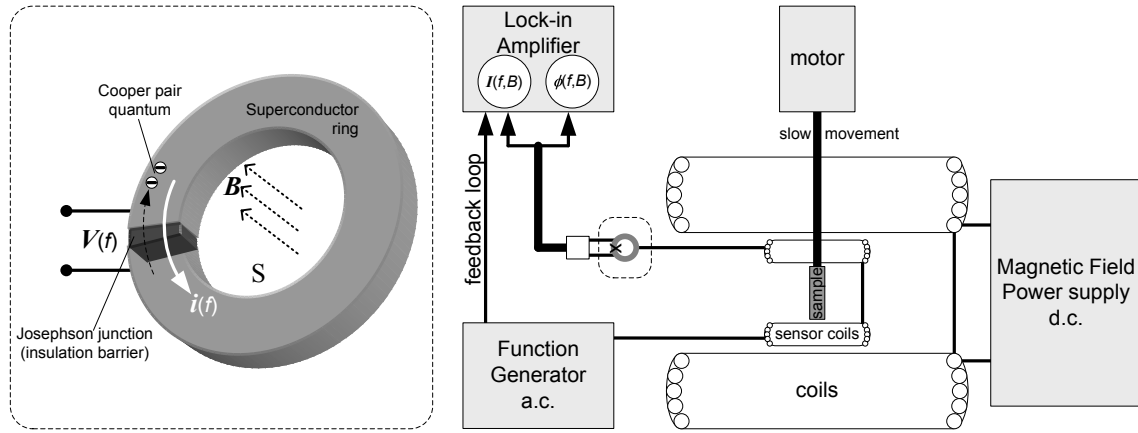


Fig. 6.12.1: Simplified diagram of the Josephson junction (left) and of the a.c. SQUID magnetometer system (right).

As the sample moves through the superconducting detection coils (second-order gradiometer), the flux variation induces an electric current that is converted by the coupled SQUID detection circuit into an output voltage proportional the magnetic moment of sample. The SQUID high sensitivity can reach 10^{-8} emu or detect magnetic fields as small as 10^{-15} Tesla. There are two main versions of this principle [6.12.1]:

- The d.c. SQUID is based on a pair of Josephson junctions having a d.c. current applied; using a modulated RF field enables to correlate the minimal magnetic flux variations to the changes in the persistent current.
- The a.c. SQUID is based on a simple ring with only one Josephson junction, it is coupled with a sensitive resonator circuit that undergo a change in impedance due to any variation in the magnetic flux. Driven by a RF current source also feeding-back a lock-in amplifier that will detect and compare the minimal frequency and amplitude variation and measure the respective magnetic flux.

$$f = \frac{2eV}{h} \quad (\text{a.c. Josephson effect})$$

This phenomenon is adopted to define the standard for 1 Volt across a Josephson junction corresponding to a RF current of $= 483.5979$ THz, independent on the nature of the superconductor material [2.2.1].

6.13. X-ray Photoelectron Spectroscopy – XPS

The photoelectric process, discovered by Heinrich Hertz in 1887 and explained by Albert Einstein in 1905 was only developed for analytical purposes by Kai Siegbahn's group in the 1960s.

$$E_{\text{Kinetic}} = h \cdot f_{\text{RX}} - \epsilon_{\text{Binding}} \quad (\text{Photoelectric effect})$$

The kinetic energy (E_{Kinetic}) of the photoelectrons emitted is exactly the energy of the incident photon $h \cdot f$ minus the material's binding energy (E_{Binding}); the coherent light source can be a UV laser, a XR discharge tube, or an adjustable high frequency radiation from a synchrotron source.

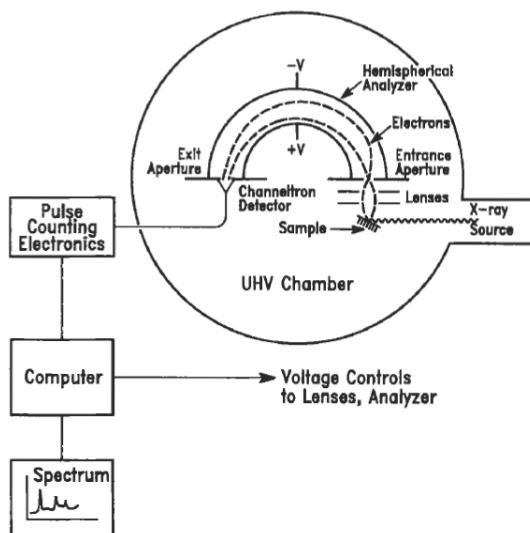


Fig. 6.13.1: Schematic of a typical XPS spectrometer showing also a hemispherical electrostatic electron energy analyzer [6.0.1].

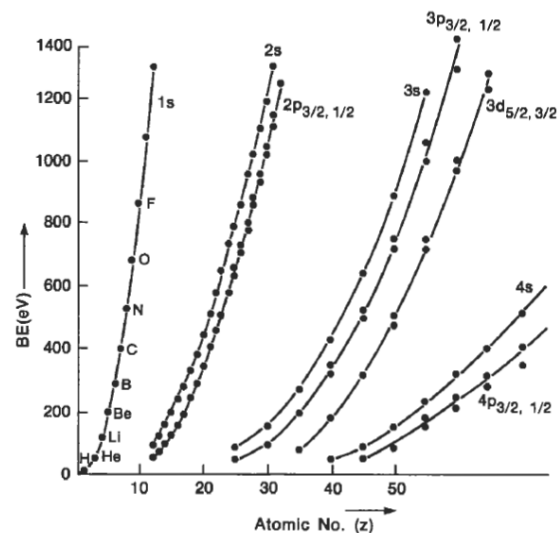


Fig. 6.13.2: Approximate Binding Energies of the different electron shells as a function of atomic number up to the Al K α radiation of 1486.6 eV [6.0.1].

A typical electron energy analyzer uses an electric field to change the directions of photo emitted electrons depending on their kinetic energies (figure 6.13.1). In a simplified approximation the resulting spectrogram has a number of peaks corresponding to the number of occupied energy levels in the atoms whose $E_{\text{Binding}} < h \cdot f$, the position of the peaks directly measures the E_{Binding} of the electrons in the orbitals and identifies the atom concerned; the intensities of the peaks depend on the number of atoms present and on the orbital concerned (figure 6.13.2). The emitted electrons can travel only short distances through gas or solids before being scattered and losing energy in collisions with atoms; for this reason XPS is a technique basically sensitive to the materials surface and is necessarily performed in a high-vacuum environment [6.0.1].

6.14. Rutherford Backscattering Spectroscopy- RBS

RBS is a nondestructive characterization technique that typically uses high-energy He or H ions (usually 1-3.4 MeV energies) which penetrate well into the sample (up to 2 μm for He^{2+} ions; 20 μm for H^+) [6.0.1]. As the incident ions (mass \mathbf{M}_i) go through the sample, a part loses initial energy (\mathbf{E}_i) in a continuous manner through a series of electronic scattering events dependent on the depth traveled; eventually some ions are back scattered, at angle θ , from “frontal” collisions with the sample atoms’ nucleus, and the large energy loss (\mathbf{E}_f) is atom specific (\mathbf{M}_a) due to the discrete momentum transfer.

$$\frac{E_f}{E_i} = \left(\frac{\sqrt{1 - \left(\frac{M_i}{M_a}\right)^2 \sin^2 \theta} + \frac{M_i}{M_a} \cos \theta}{\frac{M_i}{M_a}} \right)^2 \quad (\text{RBS energy loss})$$

RBS has much better mass resolution for light elements than for heavy elements, because as the mass of the target atom increases, less momentum is transferred from the incident particle and the energy of the backscattered particle asymptotically approaches the energy (\mathbf{E}_i). The backscattering cross section is essentially proportional to \mathbf{Z}^2 and therefore heavy elements have much better detection limits:

$$\frac{\partial \sigma}{\partial \Omega} = \left(\frac{Z_i Z_a e^2}{4 E_i} \right)^2 \frac{4 \left(\sqrt{1 - \left(\frac{M_i}{M_a}\right)^2 \sin^2 \theta} + \cos \theta \right)}{\sin^4 \theta \sqrt{1 - \left(\frac{M_i}{M_a}\right)^2 \sin^2 \theta}} \quad (\text{Diff. scatt. cross section})$$

By measuring the height of different peaks and normalizing by the scattering cross section of the respective element, the ratio of elements can be obtained for a given depth in the film. A particle that backscatters from some depth in a sample will have measurably less energy (>100 eV/nm) than a particle that backscatters from the same element on the sample's surface. The depth-resolution can go from 2 to 20 nm depending on ion energy, angle of incidence and depth below the surface. The overall energy spectrum of the emerging backscattered ions reveals both the elemental composition and the depth distribution of those elements. RBS channeling works by aligning the ion beam with a crystallographic direction in a single crystal sample, the first few surface layers shadow bulk atoms below and the resulting signal can be used to determine the extent of crystalline defects. RBS systems are extremely expensive, requiring an ion accelerator and take up large laboratories.

II EXPERIMENTAL WORK

Section 7 provides a detailed description of the most relevant work developed in the concept and assembly of new instrumental/mechanical laboratorial support systems and their specific use.

The following sections 8 and 9 refer to the specific experimental methods and conditions used in the preparation of samples.

Section 10 describes the specific characterization systems employed.

7 Experimental systems development

7.1 Magneto-resistance Measurement System

7.1.1. Background

The study of the electric transport behavior as a function of temperature and magnetic field is essential to characterize and understand the properties of materials of areas such as multiferroics, superconductivity, spintronics, magnetoelectric, magnetocaloric and magnetoresistance effects, among other.

The University of Aveiro hosts research workgroups actively studying a wide range of materials exhibiting magnetic functionalities; however, it did not possess a magneto-resistance (MR) measurement system. To provide the Department of Physics and CICECO with an autonomous magneto-resistance measurement system, the project took in consideration a few points:

- To employ a previously existing *Multimag®* - *Magnetic Solutions* magnetic field generation system which comprises a computer control subsystem and a motorized arrangement of NdFeB permanent magnets able to be geometrically combined to generate a continuous magnetic field of up to 1 Tesla intensity and a 360° horizontal orientation. This system has the advantage of being able to produce an autonomous

magnetic field, without electric powering or cooling needs. The effective field is approximately situated 20 cm high from base of the magnet, at the center of a 52 mm diameter by ~30 cm long tube.

- Making the system versatile enough so that it can subsequently be further enhanced with the capability to perform measurements of dielectric properties as function of temperature and magnetic field, allowing also for the reversion between both types of measurements.
- Coordinating the design and use of this new system in order to meet the needs arising not only from the immediate work, but also from future projects and other research workgroups.
- To maximize the effective temperature range available for measurements. Presently ranging from 77 K (liquid nitrogen) up to 400 K.
- To simplify sample holders design and construction to provide a sufficient number of interchangeable operational units and enable expedite thermal, mechanic and electric contact setting up in the cryostat.
- To consider that the resistance for different samples can comprise values below 1 Ω up to $10^5 \Omega$.

7.1.2. Course of action

A first year period was dedicated to the concept, design and selection of equipment; once the available hardware was identified, several studies were made in order to determine the necessary components to complete an optimal MR measurement system, having in consideration cost/benefits compromises and some budget limitations. An extensive research took place in order to identify the adequate equipment and materials and chose the most suitable suppliers according to price/quality criteria. Most electrical and mechanical components were build or modify in the Physics Department workshops facilities.

The First project approach consisted in designing the MR measurement system as an “add on” setup on an existing closed cycle Helium cryostat able to reach 4 to 300 K, currently used as part of a dielectric measurements setup, making use of the installed temperature controller and vacuum systems, most part of the measuring instruments and adapting the control and acquisition software. Complementary equipment consisted in designing a sample holder able to match the cold tip configuration (figure 7.1.2) and assembling the respective electric cabling; designing the necessary thermal and vacuum shields customized to fit the magnetic source equipment internal dimensions (figure 7.1.1); furthermore, to acquire a winch and propose a mechanical support to positioning the ~40 kg magnetic source box over the cryostat. Since it was not possible to access or acquire another closed cycle Helium cryostat, there were no conditions to proceed in this line of concept; although the designed components may provide a reference for a future application.

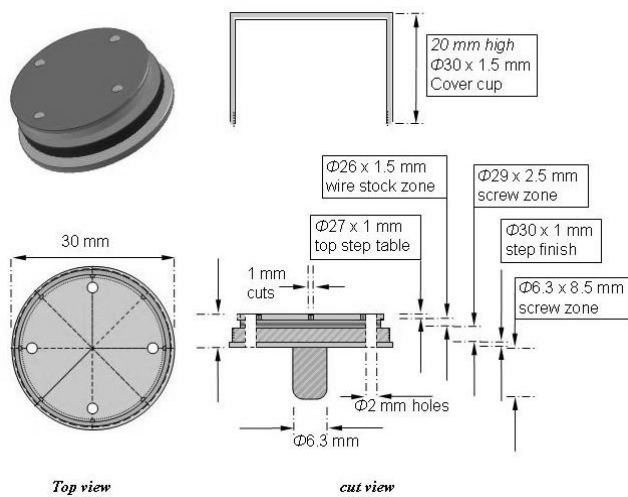


Fig 7.1.1: Design of the copper sample holder adapted to the close cycle He Cryostat.

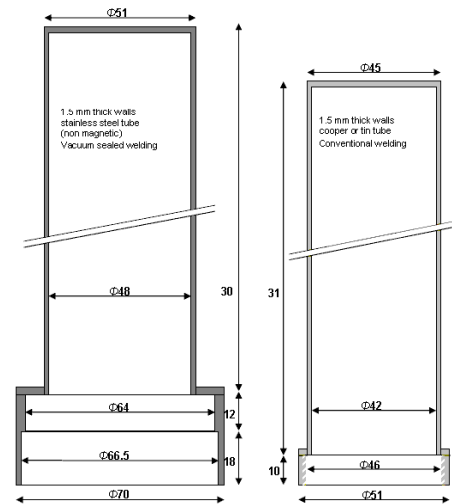


Fig 7.1.2: Design of the vacuum and thermal shields customized for the He cryostat and magnetic source equipment

The project was reformulated based now on a liquid N₂ “open cryostat”, required to extend the list of necessary equipment and to design more complex support components and introduce some innovative solutions:

- The MR setup used high precision measurement instruments previously available within the research group: an *Agilent 34420A 7½® Nanovolt/Micro-ohm Meter* and a *Keithley 6221®* stabilized electric current source.

- It became necessary to acquire a *Lakeshore 325®* temperature controller: capable of 0.001 K precision, dual temperature reading from a thermo-couple and a platinum gauge with internal references and function to feed a heater element up to 1 A, 24 V dc.
- Standard *IEEE-488 GPIB* was used to connect to the instruments to a computer for control and data registration.
- A custom made dewar flask with reference *LN2 9-SI®* from *KGW-Isotherm* (figure 7.1.3) was acquired, having the suitable dimensions to fit the space inside the magnet source system and to carry an adequate volume liquid N₂. The available diameter for the sample holder and shields became constrained to <32 mm, while lengthening the respective armrest to ~70 cm.
- The vacuum shielding was made using a 31 mm diameter glass tube, with 1 mm wall thick and 80 cm long, closed at one end and able to fit the dewar center line; a specific sealing adaptor made from Aluminum was custom designed and built at the *Criolab Lda.* (figure 7.1.5), connecting the open top of the glass tube to a four way *ISO KF40* nylon cross used for connecting subsystems to top and used as mechanical support.
- Expecting regular assembly and disassembly of components that require a practical and reusable interfacing method, the *ISO KF* connections vacuum system was chosen since it employs metric interface dimensions (figure 7.1.4) which have been defined by the International Standards Organization (ISO). This ensures a high degree of compatibility between commonly used components obtained from different sources and standard dimensions references to design and machine the necessary custom fittings, feed-through and accessories. Each vacuum seal is made by compression of an O-ring on a centering ring between mating flanges. The seal is made in seconds by finger-closure of a wing nut on the all-metal hinged aluminum clamp. Assemblies are usable to 10⁻⁸ mbar and maximum temperature for sustained use is 150° C (figure 7.1.4).

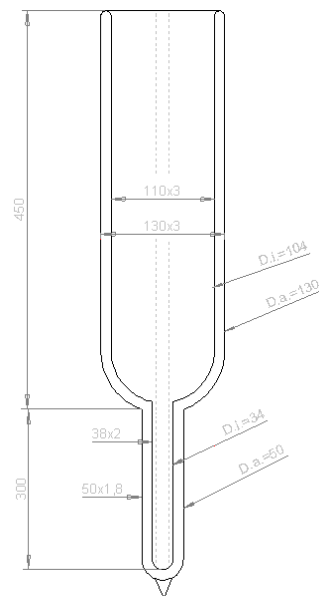


Fig. 7.1.3: DIN/ISO 3585 compliance LN2 bath cryostats made from *DURAN* borosilicate glass 3.3 from *KGW-Isotherm*

- An additional four way *ISO KF40 to KF25* reducing nylon cross was placed on top of the previous, to allow a more balanced mass distribution of the connected subsystems, although extending by more 9 cm the armrest of the sample holder.
- A 20 mm long by 55 mm diameter non magnetic steel disk was machined to comply with *KF40* dimensions in one side, also welded in the center to a 10 mm diameter by 855 mm long steel tube serving as support to the sample holder at the end; the external side is fitted with two 9 mm screw openings, one for fitting a security exhaust valve and other for an electric cabling feed-through (figure 7.1.5).
- To safely install and vertically drive the fragile glass shield inside the dewar, and this, inside the magnet cavity, it was necessary to build a set of vertical rails and support table firmly attach and aligned to the magnet block. The respective hauler was made from aluminum plates providing alignment and rigidity staked between foam blocks carved to serve as mechanical and thermal protection for the dewar and also as support to align the glass shield group (figure 7.1.6).

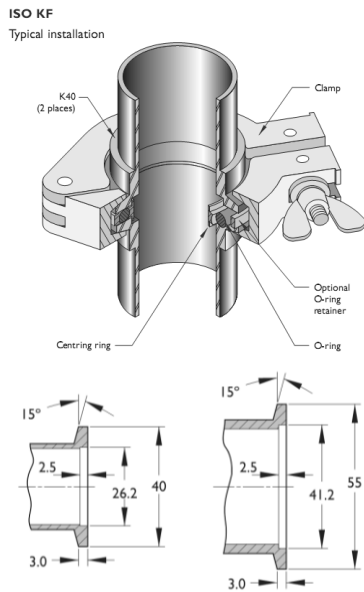


Fig. 7.1.4: *ISO KF* typical installation seal (top) and standard dimensions for *KF25* (left) and *KF40* (right) flanges.

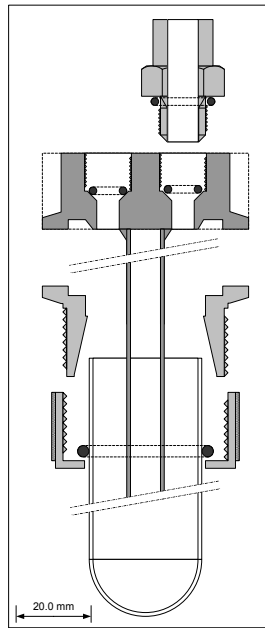


Fig. 7.1.5: Scale $\frac{1}{2}$ sketches of the wires feed-through and *KF40* crown support (top), and adaptor (center) for sealing the glass shield (bottom).

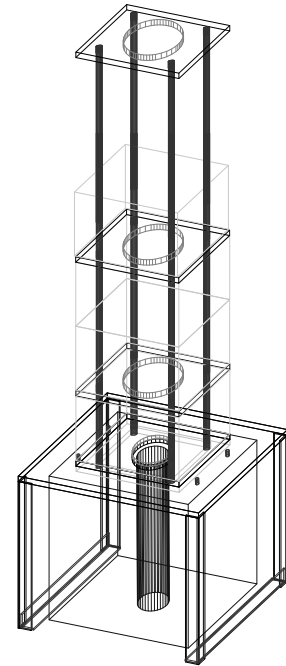


Fig. 7.1.6: Frame schematics of the support table, rails and hauler.

- A *Vacuumbrand MD1®* diaphragm vacuum pump able to reach 1.5 mbar is used to drain the air inside the glass shield tube, either to prevent ice or water condensing at lower temperatures, that can reach ~ 77 K due to the liquid N_2 bath in the cryostat; or,

on the other hand, to avoid eventual over pressure or hot vapor damage of any installed components, when raising temperature up to ~ 400 K security limit.

- *KF25* blank flanges were custom modified to interface with the 8 mm internal diameter flexible hose connecting to the vacuum pump and a 5 dm³ He gas balloon; each hose branch has a respective *butterfly* sealing type valve.
- To perform the heat exchange between the N₂ bath and the sample holder heater it is also necessary to use Helium gas inside the glass shield tube.
- To permanently verify the air or He pressure inside the MR system we recur to a *Pirani Alcatel PA101*® manometer able to measure from 10² to 10⁻³ mbar, having the respective sensor probe fitted to a *KF25* blank flange.
- Stable vacuum links are appropriately reinforced with *Teflon*TM tape, whereas for non-permanent connections is applied *Apiezon*® vacuum grease to interfaces and *Viton*TM O-rings.
- The main electric cabling is composed of five pairs of 0.4 mm copper wire with varnish insulation; the wires are twisted together and run the top feed-through sealed by vacuum wax and then introduced along the interior of the steel tube. The couplings are made by soldering the wires to standard male/female *crimp* contacts then cased and tagged by PVC thermal sleeves. In the interior, the connectors are organized in a top and bottom 25 mm diameter *Teflon*TM ring that also have the function of lining up the steel tube inside the glass shield; the thermocouple wires and the specific plugs are fixed outside the steel tube.
- Externally, another thermocouple plug was placed adjacent to a standard *DA-15 socket D-Sub* female connector used for terminating the wires coming out from the top feed-through; whereas, from the respective male connector emerge the independent coaxial cables relaying to the measurement instruments (figure 7.1.7).
- The sample carrier head is constrained to less than 25 mm diameter; besides the conventional installation of three pairs of electrical wires for sample current feed and voltage assessment, the prototype had also to carry all the necessary temperature management elements consisting of: a heat sink body to stabilize the temperature;

provision to install a *K* type thermo-couple; an additional temperature platinum gauge (for calibration procedures); a heating resistance and all the respective electric cabling.



Fig. 7.1.7: Male and female standard connectors: from left to right: Thermocouple plugs; 15 socket *D-Sub* connectors, *D-Sub* crimps and a *IC* socket.

- As an alternative to using a conventional copper mass, the heat sink volume was made from a 20 mm diameter by 50 mm long cylinder of *Shapal-M*TM ceramic, purchased from *Ceramic Substrates CO*. With a basic composition of Aluminium Nitride (AlN), this advanced material has a very good thermal conductivity ($\sim 100 \text{ W.m}^{-1}.\text{K}^{-1}$) and low thermal expansion ($4.4 \times 10^{-4} \text{ C}^{-1}$) with the advantage of being insulating ($10^{12} \Omega.\text{m}$), diamagnetic and chemical stable up to 1000 K (even in hazardous environments); besides, it is also ductile enough to be machined like a common steel piece, enabling to insert and insulate the electric wires and contacts by directly drill holes or cut grooves in the ceramic.
- The heating resistance intended to have $\sim 35 \Omega$ was hand made from $\sim 50 \text{ cm}$ manganine wire covered with fiber glass insulation, glued with *GE-varnish*TM around a *M5* x 45 mm brass screw; the head of this screw is also used as support for connecting the current feeding wires protected with fiber-glass sleeve. The element is then positioned and fixed with more *GE-varnish*TM in a 7 mm diameter x 45 mm hole drilled in the center of the ceramic cylinder body (figure 7.1.8).
- The electric pins geometry is based on the arrangement of two crossing 2x8 way *IC DILP* sockets used as chip carriers in printed circuit boards (*PCB*) (figure 7.1.7).
- The interchangeable sample holders are made from 20 mm diameter by 2 mm thick *Shapal-M*TM disks with sets of *IC* pins glued with *M-Bond*TM adhesive, matching respective the pins holes located in the face of the heat sink cylinder, (figure 7.1.9).
- One of the holders has a specific designed for Hall Effect measurements, with perpendicular 20x10x2 mm *Shapal-M*TM slab fixed with *M-Bond*TM, (figure 7.1.9).

- A 20 mm diameter by 5 mm thick *Shapal-M*TM disks was adapted for carrying a *Pt100* resistance temperature gauge (size 15 x 2 mm) in a central groove, (figure 7.1.9).
- Samples are fixed to the holder using *GE-varnish*TM, and electric contacts are made through thin 0.1 mm copper wires and *Silver paint* from the connectors; size is limited to ~15x15 mm.
- From a 25 mm diameter brass rod were milled two components: a terminal support to align and fasten the ceramic cylinder to the steel tube and feed-through the electric wires; and a cover for thermal homogeneity of the sample holder group (figure 7.1.8).

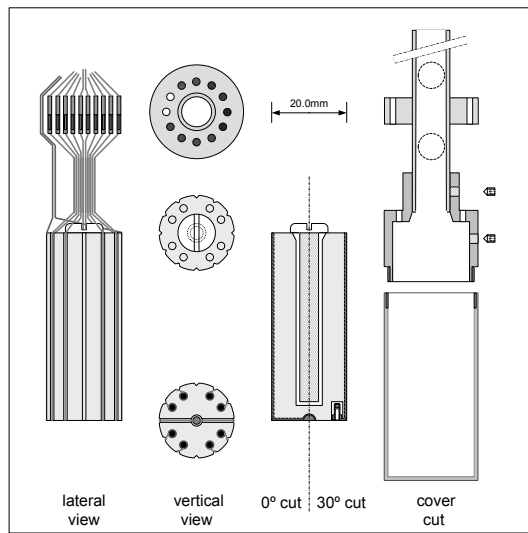


Fig. 7.1.8: Scale ½ sketches for the heater body (left), *Teflon*TM ring and connectors (top), terminal support and cover (right).

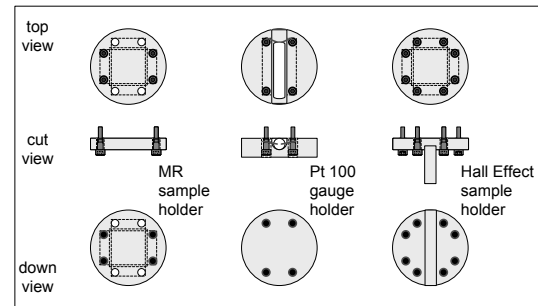


Fig. 7.1.9: Scale ½ sketches for the MR sample holder (left), support for the Pt 100 temperature gauge (center) and Hall Effect sample holder (right).

During the second year, parts of the necessary materials were acquired and most components were under manufacturing/assembly phase. Having most of the system ready by the third year, some substantial setbacks delayed the system operational come through:

- Non compliance of a first contractor to deliver a suitable *NI Labview*[®] custom software application of control a data acquisition for the MR system;
- Shipment delay of the manganine wire and the *Lakeshore* temperature controller;
- The *Magnetic Solutions* Company only provided a default control software and did not develop drivers for any other O.S.; hence it was necessary to find a competent collaboration to write a specific software emulation program that virtually commands the *Multimag*[®] system by a *NI Labview*[®] application and to employ a specific *NI* adaptor interfacing a *RS-232* connector signals to an *USB* port.

7.1.3. Operational set

The system was completely assembled during the end of third year (figure 7.1.11), yielding the integration of all the measurement devices with a desktop personal computer running O.S. *Microsoft Windows XP*®, and the development of an integrated, coherent and original *NI Labview*® application able to address and control the indispensable devices functions and with the adequate versatility to perform several modes of data acquisition:

- V vs. i : ($-100 \text{ mA} < i < +100 \text{ mA}$) with T , θ_B and B set;
- V vs. θ_B : ($0 < \theta_B < 360^\circ$) in horizontal plane, with i , T and B set;
- V vs. B : ($-1 \text{ T} < H < +1 \text{ T}$) with i , θ_B and T set;
- V vs. T : ($77 \text{ K} < T < 400 \text{ K}$) with i , θ_B and B set at 0 or 1 tesla.

First operational tests of the MR measurement system were successful, nonetheless some technical improvements in the system were performed, namely: debugging the developed *NI Labview*® software application; revising and replacing some of the electrical cabling feeding the sample holder; securing the support components and repositioning vacuum connectors and valves; manufacturing more sample holders and spare heating resistances; acquiring indispensable support and maintenance material; carry out temperature calibration tests; a specific transport bench was made and the installation was assigned to a dedicated laboratory room in CICECO building.

The system became fully operational during the end of the fourth year and some specific safety and efficiency procedures were established:

- 1) To engage and disengage the glass shield inside the dewar or the dewar inside the magnet by using the support hauler and the vertical rails only.
- 2) Before remove or installing any sample verify if the heater is at room temperature and if the shield is at room air pressure; confirm if the dewar is empty of liquid N_2 and turn off the electric feed of all devices.
- 3) Verify the conductivity quality of the electric contact pins, if necessary clean eventual oxidation or dirt accumulated on the pins.

- 4) Measure sample dimensions (l , w , h), mount it in the center of the sample holder and apply a four probe linear disposition as depicted in figure 7.1.10; measure the distance (d) between the internal Voltage contacts.
- 5) Verify and register the sample and contacts alignment in relation to the heater support direction.
- 6) Before performing a V vs. T mode measurements, previously run a set of experiments at room temperature and room pressure to validate the sample correct mounting:

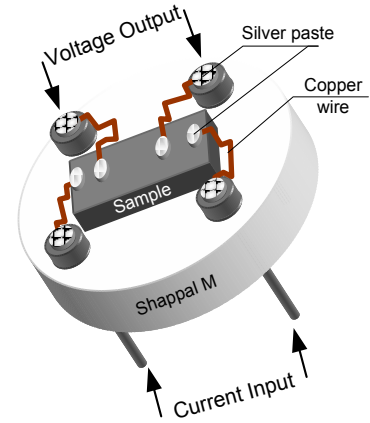


Fig. 7.1.10: Sample holder layout.

- 6.1) By running a V vs. i at $B = 0$; chose a suited current for the sample minimizing Joule heating and checking voltage signal output preferably below 1 volt dc.
- 6.2) Adjust the default angle of magnetic field in relation to the alignment of the sample contacts by running a V vs. θ_B 360° cycle at the suitable i , stable T and B set at 1 Tesla;
- 6.3) Observe (if relevant at room T) the MR response running a few V vs. B cycles from -1 to + 1 tesla with i , θ_B and T set.
- 7) To perform measurements above 300 K implies having the dewar empty of liquid N_2 and constant vacuum pumping ~ 2 mbar.
- 8) To achieve stable measurements as function of temperature imply heating rates ≤ 0.5 K/min.
- 9) Before filling the dewar with liquid N_2 , in order to perform measurements below 300 K, implies previously reaching ~ 2 mbar pumping minimum, turning off the heater, perform a He purge and use a He gas pressure near 2 to 5 mbar and do not surpass ~ 200 mbar inside the glass shield.



Fig. 7.1.11: Photograph of the complete and operational MR measurement system at CICECO's Laboratory of Aveiro University.

Further details of cited companies and respective products specifications can be found in the respective Internet sites:

Agilent 34401A 6½®: <http://cp.literature.agilent.com/litweb/pdf/5968-0162EN.pdf>

Apiezon® Vacuum Grease: <http://www.apiezon.com/document-library.htm>

Ceramic Substrates CO: www.ceramic-substrates.co.uk

Criolab: Equipamento Criogénico e de Laboratório, Lda.

D-Sub connector: <http://en.wikipedia.org/wiki/D-sub>

GE-varnish™: GE/IMI 7031 from CMR: <http://www.cmr-direct.com/images/products/02-33-001/gespecs.pdf>

IEEE-488 GPIB: <http://en.wikipedia.org/wiki/GPIB>

Keithley 6221®: <http://www.keithley.com/products/dcac/currentsource/highperfor/?mn=6221>

KF (Klein Flange) ISO standard: <http://www.caburn.com/resources/downloads/pdfs/sec1.2.pdf>

ISO (International Standards Organization): www.iso.org/

LN2 9-S1® KGW-Isotherm: <http://www.kgw-isotherm.com/produkte/kryostat/ln2eng.html>

Lakeshore 325® temperature controller: <http://www.lakeshore.com/temp/cn/325po.html>

Multimag® - Magnetic Solutions: <http://www.magnetic-solutions.com/varfld.html>

M-Bond™ adhesive: http://www.2spi.com/catalog/spec_prep/glue.shtml

NI Labview® software: <http://www.ni.com/labview/>

PCB DILP IC sockets: http://en.wikipedia.org/wiki/Dual_in-line_package

Pirani manometer: A. Ellett and R. M. Zabel, Phys. Rev. 37, Issue 9, (1931) 1102–1111

Pt100 temperature sensor: <http://www.iqinstruments.com/iqshop/technical/pt100.html>

Alcatel PA101®: <http://www.adixen.com/>

Shapal-M™: <http://www.bilact.ru/new/pdf/shapal.pdf>

Silver Paint: http://www.2spi.com/catalog/spec_prep/silver-paint.shtml#2

Teflon™: <http://en.wikipedia.org/wiki/Teflon>

Vacuubrand MD1® diaphragm vacuum pump: <http://www.vacuubrand.net/pages/MD1.html>

Viton™: <http://en.wikipedia.org/wiki/Viton>

7.2 Magnetron RF Sputtering System for Thin Films Deposition

The RF Sputtering system in the Physics Department of Aveiro University was custom built from the technical specifications proposed by Professor Armando Lourenço. Since the project first designs throughout suppliers selection, shipments of the acquired components (figure 7.2.1) and constructing some specific elements recurring to the mechanics workshop in the Physics Department of Aveiro University, a period of almost 4 years was necessary until the system could become operational (figure 7.2.2).

Special consideration was given to the UHV chamber design; envisage a more homogeneous distribution of eventual charge accumulation, gas pressure and temperature in a spherical symmetry, when compared to conventional cylindrical chambers. Other advantages become from the alignment of the access ports to the chamber geometric center and the leveled dimensions of the perpendicular walls for all ports, simplifying the design and movement of components.

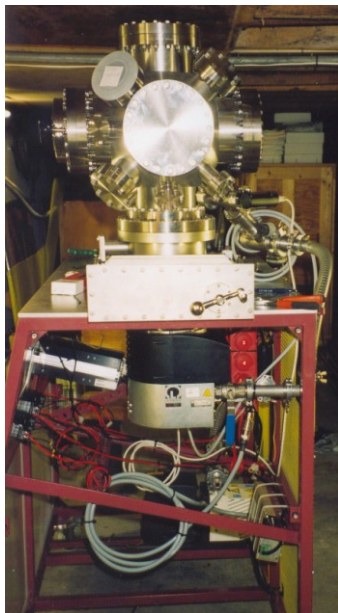


Fig. 7.2.1: Vacuum pumps and electrical systems installation.

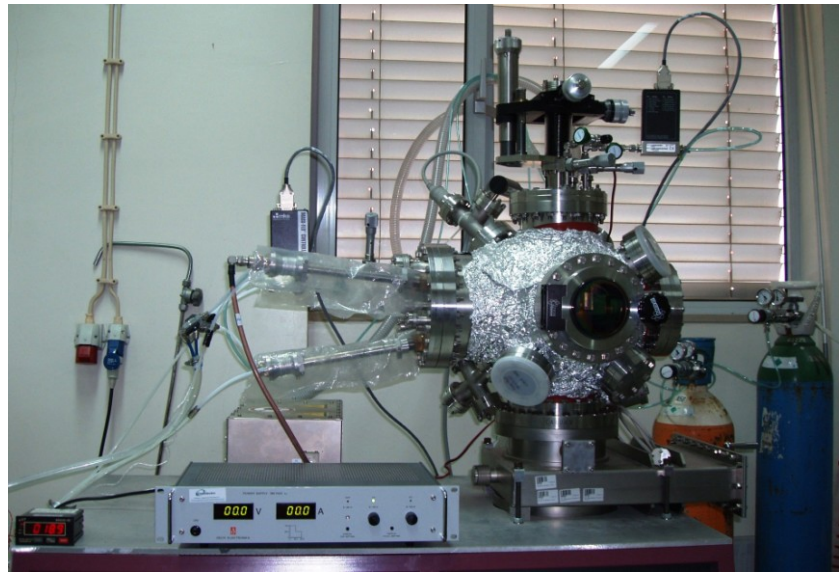


Fig.7.2.2: Image of the 1st operational setup of the RF sputtering system for thin film deposition.

Main components consist of:

- An ultra high vacuum (UHV) 30 cm diameter spherical main chamber custom made by *CABURN MDC*, with 14 access ports, based in a 6 way cross main ports and 8 diagonal secondary ports;

- Installation for three 2" diameter RF sputtering planar magnetrons in a co-focal configuration pointing at 10° to 420 mm from flange center, enabling independent adjustment of the distance to the substrate; two *ION'X-2" 9027* designed to work with ferromagnetic targets and one *ION'X-2" 9020* for conventional targets;
- Two RF generators *PF3-300-RF* operating at a nominal frequency of 13.56 MHz up to 300 Watt and two respective *PFM-1500-A* matchboxes for impedance matching to plasma load, both supplied by *HÜTTINGER Elektronik GmbH*. These two independent magnetron feeds enable to perform co-deposition from two independent magnetrons/targets: by operating the magnetrons power ratio it becomes possible to adjust the composition of the thin films; or by alternate deposition implement the deposition of buffer layers or multilayers films.
- A close cycle water cooling system for magnetrons refrigeration feeding 3 l/min to each magnetron;
- A 2" substrate heater *SU200HH* supplied by *US Inc.* able to operate up to 950° C under reactive O₂ or N₂ atmosphere. Positioned at 270 mm from magnetrons port, it is connected to a xyz positioning stage and can be mounted either on-axis or off-axis geometry;
- A *SM 7020-D* d.c. power supply from *DELTA ELEKTRONIKA BV* able to reach 700 Watt ranging 70 V and 10 A to feed the substrate heater and a *EUROTHERM model 2216e* temperature controller;
- A combined system of vacuum pumps consisting in a conventional rotary pump and a *TURBOVAC TW 701* turbo molecular pump (visible in figure 7.2.1) able to reach ~10⁻⁸ mbar vacuum quality;
- Dual manometer system based in a *959 Hot Cathode Controller* from *MKS Instruments, Inc.* capable of monitoring between 10⁻¹⁰ to 10⁻³ mbar and Pirani gauges used to check the internal atmosphere from 10⁻³ to 10⁺³ mbar.
- Two sets of *MKS type 1179A Mass-Flo®* controller connected to a respective leak valve and a *MKS type 246C single channel Power Supply/Readout* unit enables to adjust Argon and O₂ (or N₂) gas flow up to 100 cm³/min and down to 0.5 cm³/min min.

- Four UHV rotary motion feed-through systems, three *E-BRM-133* from *CABURN MDC* in order to control independently the shutters at each magnetron face (figure 7.2.3) and one *E-MBR-133* from *CABURN MDC* to control the movement of the shutter for the substrate heater front (figure 7.2.4).



Fig 7.2.3: Front view of the 3 co-focal magnetron guns assembly and one of the shutters installation.

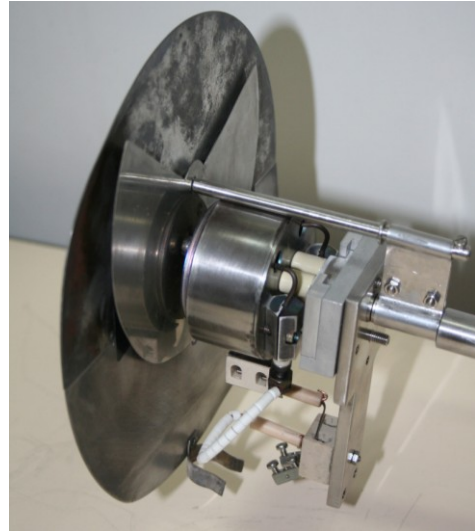


Fig 7.2.3: Back view of the heater installation, showing the bearing for the shield and shutter and the supports for electrical connectors.

Note: Most of the components were acquired through intermediation of *Criolab Lda*.

Page intentionally left blank

8 Nano-powders synthesis

The synthesis of pure and composite materials of $\text{LuMn}_{1-z}\text{O}_3$, $\text{La}_{0.7}\text{Sr}_{0.3}\text{MnO}_3$ and $\text{La}_{0.7}\text{Ba}_{0.3}\text{MnO}_3$ was made by the *urea* combustion process previously described. BaTiO_3 was prepared from the reagents powders by solid state sintering route.

Information about the molar mass of the elements, products as well as supplier and purity of reagents used in the experimental work are listed in table 8.0.1. The detailed quantity of reagents and specific preparation process for each manufactured sample is explained in the respective entries.

Elements	Z	M_r (g/mol)	Chemical Reagents	M_r (g/mol)	Supplier	Purity	Compounds Products	M_r (g/mol)
H	1	1.008	HNO_3	62.02	Riedel-deHaën	65% a.r.	H_2O	18.02
C	6	12.01	$(\text{NH}_2)_2\text{CO}_3$ (<i>Urea</i>)	60.06	Panreac	> 99.0%	CO_2	46.01
N	7	14.01	NH_3	17.03	Merck	Min. 25% p.a.	N_2	28.02
O	8	16.00	TiO_2	79.87	Merck	>99%		
Ti	22	47.87	La_2O_3	325.81	CERAC	99.999%		
Mn	25	54.94	SrCO_3	147.63	Merck	> 99% p.a.	BaTiO_3	233.21
Sr	38	87.62	BaCO_3	197.35	Merck	> 99% p.a.	$\text{La}_{0.7}\text{Sr}_{0.3}\text{MnO}_3$	226.46
Ba	56	137.34	MnCO_3	115.04	Aldrich	> 99.9%	$\text{La}_{0.7}\text{Ba}_{0.3}\text{MnO}_3$	241.38
La	57	138.06	$\text{Mn}(\text{NO}_3)_4 \cdot 4\text{H}_2\text{O}$	251.01	ABCR	> 98%	$\text{LuMn}_{0.94}\text{O}_3$	274.61
Lu	71	174.97	$\text{Lu}(\text{NO}_3)_3 \cdot 3.6\text{H}_2\text{O}$	425.84	Aldrich	99.999	LuMnO_3	277.91

Table 8.0.1: Molar mass of the elements and compounds intervening in the synthesis experimental work.

8.1. Manufacture of 2" circular planar targets for RF sputtering

A series of compounds were prepared with the specific aim to manufacture ceramic disks with 2 inches (~51 mm) diameter and only 4 to 5 mm thick intended to be applied subsequently as targets for thin film deposition by means of a magnetron RF sputtering system. The approximate volume of a target is $\sim 10 \text{ cm}^3$ implying a minimum estimated mass of > 60 g for each powder. The respective reagents, synthesis route used and products nominal compositions and calculated mass are listed in table 8.1.1.

The $\text{La}_{0.7}\text{Sr}_{0.3}\text{MnO}_3$ and the $\text{La}_{0.7}\text{Ba}_{0.3}\text{MnO}_3$ compounds were prepared by the *Urea* combustion route represented in figure 8.1.1; the equipment is listed in table 8.1.3 and the procedure steps described in table 8.1.2.

Nominal composition:	Estimated density (g/cm ³)	Synthesis route:	Specific reagents used:	Reagents mass (g):	Cations presence (mol)	Final product mass (g):
La _{0.7} Sr _{0.3} MnO ₃	6.32	Urea combustion	MnCO ₃ La ₂ O ₃ SrCO ₃ (NH ₂) ₂ CO ₃ (Urea)	67.302(7) 66.767(0) 25.929(6) 210.990	[Mn]= 0.5850(4) [La]= 0.4098(5) [Sr]= 0.1756(4) [Urea]= 3.51(3)	~ 131.7 g
La _{0.7} Ba _{0.3} MnO ₃	6.60	Urea combustion	Mn(NO ₃) ₄ ·4H ₂ O La ₂ O ₃ BaCO ₃ (NH ₂) ₂ CO ₃ (Urea)	71.000 32.255 16.746 101.93	[Mn]= 0.2828(6) [La]= 0.1980(0) [Ba]= 0.0848(5) [Urea]= 1.69(7)	~ 68.1 g
BaTiO ₃	5.99	Solid state	BaCO ₃ TiO ₂	85.426 34.574	[Ba]= 0.4328(7) [Ti]= 0.4328(7)	~ 100.9 g

Table 8.1.1: Molar mass of the elements and compounds intervening in the synthesis experimental work.

Basic Material
<ul style="list-style-type: none"> - Exhaust chamber - Microgram scale - Goblets - Thermometer - Glass steering rod - Oven with magnetic steering - magnetic steering rod - pH meter - Pipettes - Crucibles - Programmable Furnace - Mortar and pestle, - Sieves - Hydraulic press - Molds
Basic Reagents:
<ul style="list-style-type: none"> - H₂O (Desionized water), - HNO₃ (Nitric acid aqueous solution) - NH₃ (Ammonia aqueous solution) - (NH₂)₂CO₃ (Urea)

Table 8.1.2: Basic material and reagents required for ceramics synthesis by urea combustion method.

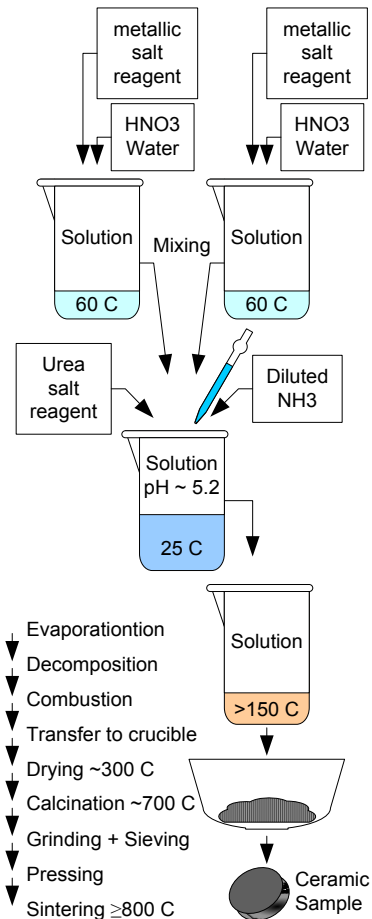


Fig. 8.1.1: Basic schematics of the ceramics synthesis by urea combustion method.

The specific solid state sintering procedure used for the BaTiO₃ compound can be summarized in table 8.1.4:

- Define the mass and molecular composition of ceramic sample to synthesize;
- Calculate the respective molar number of the metallic elements;
- Precise weight each metallic salt reagent taking in account purity and hydration factors;
- Precise weight the urea reagent equivalent to 3 times the molar number of the metallic ions;
- Dissolve each metallic salt quantity separately in a goblet at $\sim 60^\circ \text{C}$, adding the necessary desionized water and HNO_3 solution;
- Mix the previous solutions into a single goblet, keep stirring and temperature within 25°C ;
- Add the Urea mass to the solution, verifying full solubility and pH level;
- Correct the pH to ~ 5.2 by adding (NH_3) aqueous solution, avoiding the formation of precipitates;
- Raise the temperature to $\sim 110^\circ \text{C}$ to achieve water evaporation;
- Raise the temperature to $\sim 150\text{-}200^\circ \text{C}$ and wait for the urea decomposition, ignition and full combustion;
- Remove the powder to an alumina crucible and perform calcination at $600 - 700^\circ \text{C}$ for ~ 2 hours in the a furnace at air;
- Grinding with a mortar and pestle;
- Sieving of the calcinated power through a $38 \mu\text{m}$ mesh sieve;
- For samples processing: Further grinding and sieving; molding and pressing into 20 mm pellets (300 MPa) and thermal treatment at $800\text{-}900^\circ \text{C}$ for 48 h or more;
- Cut the pellet into samples approximately $\sim 10 \times 5 \times 2 \text{ mm}$
- For targets processing: Molding to 60 mm targets, pressing and sintering at $1300\text{-}1400^\circ \text{C}$.
- Storage the samples in a desiccator or muffle ($>60^\circ$ to $<200^\circ \text{C}$).

Table 8.1.3: Procedure steps used for ceramics synthesis by urea combustion method.

- Disperse and mixing the reagents powders in ethanol
- Heating at $\sim 90^\circ \text{C}$ to dry the mix from the ethanol
- Calcination stage at $\sim 700^\circ \text{C}$ for 24 hours
- Grinding, sieving with a $108 \mu\text{m}$ mesh and pressing into pellets
- Second calcination stage at $\sim 900^\circ \text{C}$ for 16 hours to completely remove carbonates
- Grinding, sieving and pressing into pellets
- Thermal treatment stage at $\sim 1100^\circ \text{C}$ for 40 hours
- Grinding, sieving and pressing into pellets
- Slow heating to sintering stage at $\sim 1300^\circ \text{C}$ for 20 h.
- Grinding and sieving

Table 8.1.4: Procedure steps used for the synthesis of BaTiO_3 ceramic by solid state method.

Given that the sintering process reduces the initial volume of the molded material in about 20%, a suitable fraction of each synthesized powder was pressed at about 10 MPa into an appropriate 60 mm diameter mold with a maximum thickness of 6 mm. It was indispensable to mix some droplets of polyvinyl alcohol solution (2% PVA in water) to the powder, to make possible to hold the disk together and transfer it to a custom made alumina crucible, as illustrated in figure 8.1.2. To prevent buckling of the targets' shape, the sintering procedure was programmed through a series of stages with slow heating/cooling rates and intermediate long steps of uniform temperature as depicted table 8.1.5 and in figure 8.1.3.

Due to the extreme shape factor of such disk it tends to be brittle, that's why the BaTiO_3 and $\text{La}_{0.7}\text{Ba}_{0.3}\text{MnO}_3$ targets were not successfully employed; these targets presented some fissures and shattered when trying to install them onto the magnetrons.

- 6 hour stage at 150° C to allow all moist to evaporate
- 6 hours heating ramp to 800° C to avoid temperature gradients in the target
- 24 hour threshold at 800° C to promote oxygen incorporation
- Slow heating during 6 hours up to 1400° C
- 24 hour threshold at 1400° C to promote grain growth and hardening of the target
- 6 hours slow cooling down to 800° C
- 12 hour threshold at 800° C to recover oxygen incorporation
- 12 hours slow cooling down to room temperature

Table 8.1.5: Procedure steps used for the preparation of the 5 cm diameter RF targets .

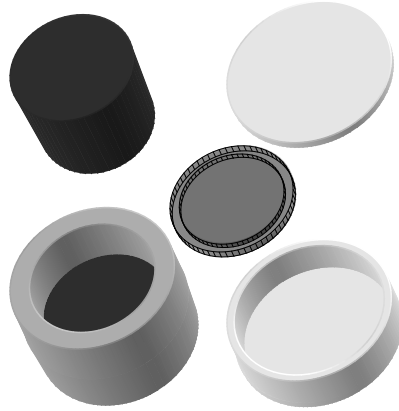


Fig. 8.1.2: scaled representation of the mold (left) and alumina crucible used (right); target size before and after sintering (center)

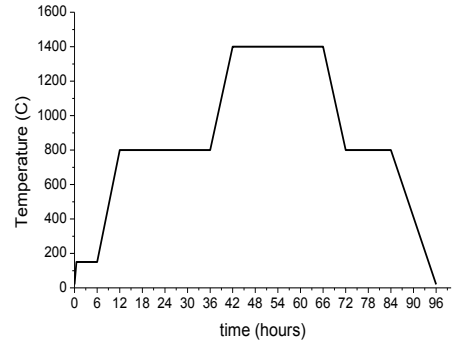


Fig. 8.1.3: Sintering procedure diagram used for the targets manufacture.

8.2. Bulk $\text{BaTiO}_3 + \text{La}_{0.7}\text{Ba}_{0.3}\text{MnO}_3$ Multiferroic composites series

Since the targets manufacture did not employ all the existing BaTiO_3 (BTO) and $\text{La}_{0.7}\text{Ba}_{0.3}\text{MnO}_3$ (LBM) powders, part of the surplus was used to perform the experimental preparation of potential multiferroic composite samples based on simple mixing and solid-state sintering process according to the list presented in table 8.2.1:

Sample Designation	Nominal Composition	Compound mass (g):		Final mass (g):	Query:
		LBM	BTO		
BTO100	BaTiO_3	0	5.00	5.00	Reference sample
BTO89LBM "T89"	$0.89\text{BaTiO}_3 + 0.11\text{La}_{0.7}\text{Ba}_{0.3}\text{MnO}_3$	0.5310	4.1516	4.68 g	Isolation of the LBM phase in BTO
BTO78LBM "T78"	$0.78\text{BaTiO}_3 + 0.22\text{La}_{0.7}\text{Ba}_{0.3}\text{MnO}_3$	1.0620	3.6385	4.69 g	Below percolation of the LBM phase in BTO
BTO50LBM "T50"	$0.50\text{BaTiO}_3 + 0.50\text{La}_{0.7}\text{Ba}_{0.3}\text{MnO}_3$	2.4138	2.3324	4.74 g	Above percolation of the LBM phase in BTO
LBM100	$\text{La}_{0.7}\text{Ba}_{0.3}\text{MnO}_3$	5.00	0	5.00	Reference sample

Table 8.2.1: List of samples prepared by solid state mixing of $\text{BaTiO}_3 + \text{La}_{0.7}\text{Ba}_{0.3}\text{MnO}_3$ composites.

Even expecting total immiscibility of these two phases, the preparation procedure listed in table 8.2.2 intends to mechanically maximize the dispersion and tight contact of the two compounds; the long annealing at $\sim 900^\circ\text{C}$ was chosen in order to prevent further grains growth or segregation, yet ensuring some diffusion of elements, intended to promote partial merging between the two phase's grains boundaries:

- | |
|--|
| <ul style="list-style-type: none"> - Transfer the precursor powders to a 150ml glass balloon; - Add 50 ml ethanol plus ~ 20 ml dionized water; - Mixing under ultrasonic bath for ~ 10 min; - Mixing until drying in a heater at $\sim 80^\circ\text{C}$; - Transfer the mix to a crucible and dry it in oven at $\sim 150^\circ\text{C}$; - Pressing the mixture in 20 mm diameter pellets under 15 ton; - Thermal treatment stage at $\sim 800^\circ\text{C}$ in air for 72 hours; - Grinding, sieving and pressing into pellets; - 6 hours heating ramp up to a sintering stage at $\sim 900^\circ\text{C}$ in air for 90 hours; - Quenching to room temperature ~ 10 min; - Cutting the pellets into several samples approximately $10 \times 5 \times 2$ mm size. |
|--|

Table 8.2.2: Procedure steps used for nano-powder oxides synthesis by solid state method.

8.3. Bulk LuMnO_3 + $\text{La}_{0.7}\text{Sr}_{0.3}\text{MnO}_3$ Multiferroic Composites

The synthesis of pure, doped and composite ceramics of the $\text{LuMn}_{1-z}\text{O}_3$ hexagonal FE manganite (LuM) and the $\text{La}_{0.7}\text{Sr}_{0.3}\text{MnO}_3$ rhombohedric FM manganite (LSM) was performed via the *urea combustion* procedure previously described. Instead of recurring to the amalgamation of the two independent powders, like the one used for the BTO+LBM composites, the mixing of the several precursors was perform in the solubility stage of the synthesis process; this innovative approach relies on the immiscible character of the two distinct phases, expecting the efficient segregation into distinct grains for each phase during the subsequent heat treatments stages at temperatures of 800 and 900°C , as described in table 8.3.1. This limited temperature were preferred in order to avoid prominent grain growth, yet promoting elements diffusion to enhance segregation and homogeneity within each phase while ensuring a close contact between grain boundaries in order to achieve a high degree of interpenetration of the mixed powders

The quantity of this first series of samples was determined by the limited amount of Lu reagent available, whereas composition was established in order to contribute to answer the objectives mentioned in table 8.3.2.

- Calcination for 21 hours at 600 °C plus 3 hours at 700 °C
- Grinding procedures and passage of the powder through sieves of successive smaller mesh,
- Pressing the powder in 13 mm diameter pellets under 2 ton;
- Sintering stage at ~800 C in air for 98 hours;
- Quenching to room temperature ~10 min;
- Grinding, sieving and pressing the mixture in 13 mm diameter pellets under 3 ton;
- Sintering stage at ~900 C in air for 90 hours;
- Cutting the pellets into several samples approximately 8 x 4 x 1 mm size.

Table 8.3.1: Procedure steps used for nano-powder oxides synthesis by solid state method.

Sample Designation	Nominal Composition	Element/reagent molar proportion:					Final mass	Query:
		Lu	La	Sr	Mn	Urea		
Lu96LSM	0.96 LuMnO ₃ + 0.04 La _{0.7} Sr _{0.3} MnO ₃	0.96	0.028	0.012	1	6	1.5 g	Study of LSM solubility in LuMnO ₃
Lu89LSM	0.89 LuMnO ₃ + 0.11 La _{0.7} Sr _{0.3} MnO ₃	0.89	0.077	0.033	1	6	1.7 g	Isolation of the LSM phase in Lu
Lu78LSM	0.78 LuMnO ₃ + 0.22 La _{0.7} Sr _{0.3} MnO ₃	0.78	0.154	0.066	1	6	2.0 g	Below percolation of LSM phase in Lu
Lu04LSM	0.04 LuMnO ₃ + 0.96 La _{0.7} Sr _{0.3} MnO ₃	0.04	0.672	0.288	1	6	2.0 g	Study of Lu solubility in LSM

Table 8.3.2: List of samples prepared by Urea combustion based on LuMnO₃ + La_{0.7}Sr_{0.3}MnO₃ composites.

8.4. Bulk LuMn_{1-z}O₃ Intrinsic Multiferroic series

With the purpose to study controlled modifications into the parent LuMnO₃ compound that may lead to enhancements of its multiferroic properties, in particular by frustrating the former antiferromagnetic behavior by introducing some Mn⁴⁺ cations, while trying to keep the structure and ferroelectric properties unharmed; It was proposed to synthesize samples with a limited amount of Manganese vacancies. The preparation method for the first series of samples was similar to the described in the previous section. The second series sample identified as “LuM098” was prepared specially to be measured in NPD and had to be made in more substantial quantity as listed in table 8.4.1.

Sample	z	Nominal Composition:	Elements molar proportion:			Final mass:	Query:
			Lu	Mn	Urea		
LuM100 (1 st series)	0.00	LuMnO ₃	1	1	6.00	1.5 g	Reference sample
LuM094 (1 st series)	0.06	LuMn _{0.94} O ₃	1	0.94	5.88	1.5 g	Study of 6% Mn vacancies effect
LuM098 (2 nd series)	0.02	LuMn _{0.98} O ₃	1	0.98	5.94	6.7 g	NPD study of Mn vacancies effect

Table 8.4.1: List of samples prepared by Urea combustion based on LuMn_{1-z}O₃

9. Thin Film Depositions by Magnetron RF Sputtering

9.0.1. Targets

Since March 2006 the RF Magnetron Sputtering system achieved operational capability. Throughout the years of 2007 and 2008 it was used for several projects under the scope of collaboration protocols held by CICECO associated Laboratory. The preliminary experimental research works were mostly dedicated to accompanying the depositions of thin films from targets of ZnO semiconductor, MgB_2 superconductor and the BN compound for structural reinforcement of steel tools.

According to the work plan concerning the study of potential multiferroic thin films composites, the RF Sputtering deposition system was then used to obtain and develop thin films and multilayers from targets of the ferroelectric BaTiO_3 ; $\text{La}_{0.7}\text{Ba}_{0.3}\text{MnO}_3$ or $\text{La}_{0.7}\text{Sr}_{0.3}\text{MnO}_3$ manganites and Ni-Mn-Ga alloys. From the first batch of prepared targets (as described in section 8.1): a $\text{La}_{0.7}\text{Sr}_{0.3}\text{MnO}_3$ target was successfully employed in a deposition series, until the disks broken due to plasma exposure, becoming unviable further utilization. In order to expedite the experimental work it was preferred to proceed to the acquisition of commercial targets as listed in table 9.0.1:

Designation Composition	Supplier	Purity	Thickness (")
BaTiO_3	<i>Kurt J. Lesker Co.</i>	99.9	0.125
$\text{La}_{0.7}\text{Ba}_{0.3}\text{MnO}_3$	<i>Kurt J. Lesker Co.</i>	99.9	0.125
$\text{Ni}_{50}\text{Mn}_{50}$	<i>Testbourne Ltd</i>	99.9	0.125
$\text{Ni}_{60}\text{Mn}_{40}$	<i>Testbourne Ltd</i>	99.9	0.125
$\text{Ni}_{50}\text{Ga}_{50}$	<i>ACI Alloys, Inc</i>	99.9	0.125

Table 9.0.1: List of targets and respective parameters

All the targets went through a certification procedure by XRD, SEM and EDS to attest the phase, surface and composition of the targets and further comparison with the respective resulting films. First batch of acquired $\text{La}_{0.7}\text{Ba}_{0.3}\text{MnO}_3$ and BaTiO_3 , $\text{Ni}_{50}\text{Mn}_{50}$ and $\text{Ni}_{60}\text{Mn}_{40}$ targets was returned to suppliers due to non conformity with the declared chemical composition. Suitable new $\text{La}_{0.7}\text{Ba}_{0.3}\text{MnO}_3$ and BaTiO_3 targets were not available in useful time to be included in this work.

9.0.2. Substrates

Preliminary depositions tests were usually made onto 30x30x1 mm³ laminated glass substrates, in order to establish the basic conditions that verify the correct phase and composition of the film.

The principal criterion to select the composition and orientation of substrates is the lattice matching to the crystalline structure of film phase to be deposited, in order to promote the epitaxial growth of the thin film. Commercial substrates are usually cut to 10x10x0.5 or 10x5x0.5 mm³. Table 9.0.2 summarizes some of the substrates available.

Designation Orientations	Supplier	SG	ρ g/cm ³	Crystalline Parameters:					
				a (Å)	b (Å)	c (Å)	α (°)	β (°)	γ (°)
MgO (100)	Crystec	Cubic Fm3m (225)	3.585	4.212	4.212	4.212	90	90	90
SrTiO ₃ (100), (110)	Crystec	Cubic Pm-3m (221)	5.175	3.905	3.905	3.905	90	90	90
LaAlO ₃ (100) _c	Crystec	Hexagonal R-3c (167)	6.518	5.365	5.365	13.111	90	90	120
Al ₂ O ₃ (0001) _H	Crystec	Hexagonal R-3c (167)	3.69	4.757	4.757	12.983	90	90	120
Si (100)	Crystec	Cubic Fd-3m (227)	2.329	5.431	5.431	5.431	90	90	90
PMN-PT (100)	Crystec	Cubic Pm-3m (221)	7.5	4.04	4.04	4.04	90	90	90

Table 9.0.2: List of substrates and respective parameters

Precautions should be taken for the correct storing in a dry and clean environment and a careful handling to prevent touching or scratching the polished oriented surface. Most common inconvenients detected in thin films related to substrates, arise from inappropriate cleaning. Nevertheless some substrates are particularly sensitive to loose their features:

- Water adsorption into MgO can form bulges and roughness stains in the surface, due to the formation of hydroxides and carbonates; long storage periods will increase this problem [9.1.1];
- Air adsorption creates a thin layer of amorphous SiO₂ on top of Si substrates; when required, it is possible to eliminate this layer by performing HF last etching or >10 min of reversed sputtering in the substrate, although the substrate surface quality becomes compromised.
- In the case of LaAlO₃ a structural phase transitions to Cubic *Pm-3m* at ~544° C [9.1.2] leaves maculae or twins in the substrate surface; hence films deposited above this temperature may encompass additional defects.

9.0.3. Deposition Operational Procedures

1. Substrate cleaning is performed in ultrasonic bath in three sequential stages of 15 min in acetone and ethanol; direct dry under pure N₂ gas; careful handling and positioning the substrates in the frame at heater front, (minimal use of silver paste when necessary) and tight fixing of the masks.
2. Previous to sputtering procedure, the heater is set at 600-700° C for 60 to 90 min to evaporate any residual water in substrates, while proceeding to pumping the chamber.
3. The effective substrates temperature chosen during deposition procedure is calculated according to the calibration shown in figure 9.0.1, within $\pm 5^\circ$ C
4. At the present, magnetrons have a co-focal disposition with 10° inclination, as seen in figure 7.2.3, facing the heater front where the substrate are fixed (figure 7.2.5). Distance is usually set to 100 mm for a single targets employ, and constrained to 125 mm for dual (or triple) targets use.

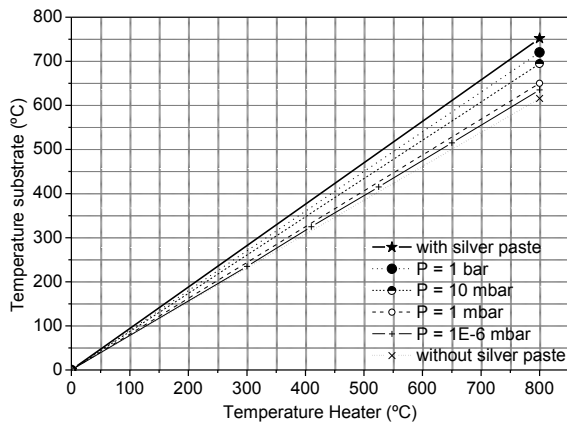


Fig. 9.0.1: Substrate temperature vs. heater temperature for different conditions.

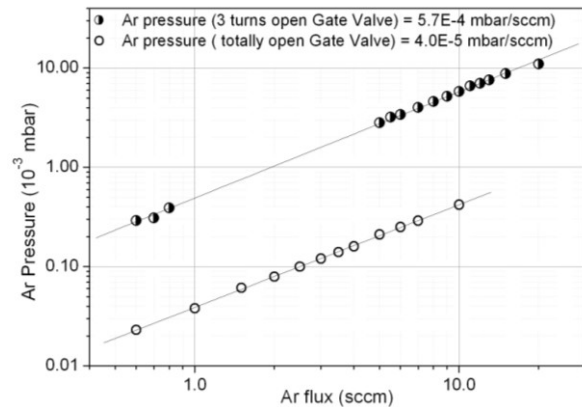


Fig. 9.0.2: Chamber Ar pressure vs. flux for gate valve apertures.

5. First stage for performing vacuum inside the chamber starts by using the rotary pump up to $\sim 10^{-2}$ mbar and then turning the turbo pump at 100 % performance for reaching at least $\sim 10^{-7}$ mbar.
6. The chamber Ar pressure is managed by controlling the turbo pump at 75 % from full power, positioning the gate valve dish before sealing (open at 3 handle turns), in order to reduce the gas load on the turbine front;
7. The stabilized Ar admission and pressure is achieved by adjusting the leak valves and mass flow controllers (respectively O₂ or N₂ when applicable), as graph in figure 9.0.2.

8. Pirani manometer reading of Ar pressure (and other monatomic gases) is 1/2 of the real pressure, while for O₂, N₂ or Air the scaling is direct,
9. For most targets plasma ignition is typically achieved at ~5 watt power and ~5x10⁻² mbar of Ar, pre-sputtering and deposition is usually performed at ~5x10⁻³ mbar of Ar.
10. Pre-sputtering is undertaken for at least 15 min having all shields closed, under the same power and Argon pressure parameters as the subsequent deposition process itself.
11. Deposition time is accounted during plasma exposure when both shutters from targets and substrates are in the opening position. It is essential to keep continuous monitoring of magnetron power feeding, Argon (and other gases) pressure and heater temperature, confirming stabilized parameters or registering eventual alterations.
12. Non oxidizing in-situ annealing can be performed up to 950° C usually in vacuum, whereas Oxidizing in-situ annealing is usually performed under ~10⁻² mbar of O₂ limiting the temperature set up to 850° C due to additional heat generated by the oxygen presence.
13. Cooling time is constrained by the chamber venting.

Laboratorial work concerning thin films deposition was focused in finding the experimental conditions to achieve high quality films that have the adequate composition, functional properties and structural epitaxy with the substrate or buffers, which enables the strictive-magneto-electric interaction between layers leading to magnetoelectric effect properties. As the system becomes technically improved by incorporating new devices and capabilities, also the management of deposition conditions progressed, making possible to undertake more complex thin films compositions and architectures, validating further investment in a broad selection of targets with different compositions and in a widespread of high quality and functional substrates.

The corresponding experimental characterization of these thin films was performed using several complementary techniques, namely XRD, SEM, TEM, EDS, RBS, VSM, MR and RAMAN, aiming to understand most pertinent features:

- Surface quality and homogeneity;
- Thickness and growth rate;
- Adhesion to substrate;
- Crystalline structure;
- Substrate induced epitaxial growth;
- Chemical composition.
- Related functional properties (electrical, magnetic, optical or mechanical).

With the systematization and analysis of the characterization results it becomes possible to interactively optimize the succeeding deposition conditions, enhancing the quality and respective parameters intended for each series of thin films produced. The most relevant adjustable configurations and conditions applicable to the system concern:

- Ensuring correct substrates quality, cleaning and drying.
- Positioning of substrates in heater (use or not of thermal paste)
- Alignment and distance from targets to substrates
- Achieving the lowest possible vacuum in chamber previous to deposition
- Suiting the heater temperature for each kind of target, substrate and intended thin film.
- Defining pre-sputtering period and stipulating the deposition time
- Finding a suitable Argon pressure to achieve plasma stability during deposition.
- Selecting each magnetron power feed and resulting plasma energy.
- Setting chamber active O₂ (or N₂) flux and pressure during film growth (when applicable).
- Deciding the in-situ treatment after deposition (annealing temperature and time; Ar, O₂ or N₂ pressure; cooling rate or rapid quenching).

9.1. $\text{La}_{0.7}\text{Sr}_{0.3}\text{MnO}_3$ phase Thin Film series

The initial series of thin films were deposited using the prepared 51 mm $\text{La}_{0.7}\text{Sr}_{0.3}\text{MnO}_3$ target, under supervision of Prof. Dr. Armando Lourenço. The prepared samples and respective conditions are listed in table 9.1.1:

Samples	Substrate	Orientation	Initial Vacuum (10^{-8} mbar)	Argon (10^{-3} mbar)	O_2 (10^{-3} mbar)	RF Power (Watt)	DC bias (Volt)	Distance (mm)	Time (min.)	Temperature Substrate ($^{\circ}\text{C}$)	In situ Annealing O_2 (mbar)
LSM1a	SrTiO ₃	(100)	7.8	9.8	0.7	75	215	75	90	687	300
LSM1b	MgO	(100)	7.8	9.8	0.7	75	215	75	90	687	300
LSM2a	SrTiO ₃	(100)	29.0	7.0	0.5	70	207	75	90	711	390
LSM2b	MgO	(100)	29.0	7.0	0.5	70	207	75	90	711	390
LSM3a	SrTiO ₃	(110)	6.9	8.0	0.4	71	201	75	90	697	510
LSM3b	MgO	(100)	6.9	8.0	0.4	71	201	75	90	697	510
LSM4a	MgO	(100)	4.8	6.8	0.4	70	200	75	90	697	510
LSM4b	SrTiO ₃	(100)	4.8	6.8	0.4	70	200	75	90	697	510
LSM5a	ITO	n.a.	3.6	5.0	0.4	74	196	100	70	668	74
LSM5b	Glass	n.a.	3.6	5.0	0.4	74	196	100	70	668	74
LSM6a	MgO	(100)	6.2	5.0	2.0	73	200	100	70	697	520
LSM6b	LaAlO ₃	(100) _c	6.2	5.0	2.0	73	200	100	70	697	520
LSM6c	SrTiO ₃	(100)	6.2	5.0	2.0	73	200	100	70	697	520
LSM6d	Al ₂ O ₃	(0001) _h	6.2	5.0	2.0	73	200	100	70	697	520

Table 9.1.1: List of samples deposited by RF Magnetron Sputtering from $\text{La}_{0.7}\text{Sr}_{0.3}\text{MnO}_3$ target.

9.2. Ni_2MnGa phase Thin Film series

The second part of this experimental work became focused on the deposition and characterization of the magnetoelastic Ni_2MnGa phase-like alloy.

An extensive roll of thin film samples was prepared at the IEMN, University of Lille, France using a standard "Plassys MP 600" RF Sputtering deposition system. This system has six magnetrons, three of which in a co-focal geometry that can be operated independently by three RF generators.

Deposition process was performed from preparatory pressures below 10^{-7} mbar in the vacuum chamber. Then the Ar pressure in the chamber was adjusted between 2.5 and 70×10^{-3} mbar range. The RF power applied to the magnetrons ranges from 50 up to 300 W

(maximum). Pre-sputtering treatment was done during 15 minutes, the axis distance to substrate holder was 8 cm, and deposition procedure took from 30 up to 90 minutes. The substrate temperature was maintained at approximately 10 °C, using a cooling water circuit holder, or left to rise under plasma heating effect (up to 100 °C), as monitored by thermocouple.

The first set of test samples was deposited using a single 76.2 mm target with a nominal alloy composition of $\text{Ni}_{0.5}\text{Mn}_{0.33}\text{Ga}_{0.17}$ in order to optimize the deposition conditions of this type of alloy onto bare Si (100) substrates and onto PZT layer deposited onto a LaNiO_3 buffer on Si(100) substrates, as listed in table 9.2.1.

Samples	Substrate	Orientation	Substrate Off center position (mm)	Argon (10^{-3} mbar)	RF Power (Watt)	Time (min.)	Temperature Substrate (°C)	Anneal Temperature (°C)	Anneal Time (min.)
NMG01	Si	(100)	0	13.3	100	90	10	NO	
NMG02	Si	(100)	0	13.3	200	90	10	NO	
NMG03	Si	(100)	0	66.5	100	90	10	NO	
NMG04	Si	(100)	0	13.3	100	90	420	NO	
NMG05	Si	(100)	0	13.3	200	90	420	NO	
NMG06	Si	(100)	0	13.3	300	90	10	NO	
NMG07	Si	(100)	0	2.66	200	60	10	NO	
NMG08	Si	(100)	0	6.65	300	90	10	NO	
NMG09	Si	(100)	0	6.65	100	90	68	510	120
NMG10	Si	(100)	0	6.65	200	90	86	640	60
NMG11	Si	(100)	0	13.3	300	90	94	NO	
NMG12	Si	(100)	35	13.3	300	90	94	NO	
NMG13	Si	(100)	75	13.3	300	90	94	NO	
NMG14	Si	(100)	43	13.3	300	45	77	NO	
NMG15	Si	(100)	43	13.3	300	45	77	NO	
NMG16	Si	(100)	0	13.3	300	45	77	NO	
NMG17	Si	(100)	0	13.3	300	45	77	NO	
NMG18	Si	(100)	0	13.3	300	45	77	NO	
NMG19	Si	(100)	0	66.5	200	45	60	NO	
NMG20	Si	(100)	43	66.5	200	45	60	NO	
NMG21	Si	(100)	0	39.9	200	45	61	NO	
NMG22	Si	(100)	43	39.9	200	45	61	NO	
NMG23	Si	(100)	0	13.3	50	90	43	NO	
NMG24	Si	(100)	43	13.3	50	90	43	NO	
PZTNMG1	Si/LNO/PZT	(100)	0	13.3	300	45	77	NO	
PZTNMG2	Si/LNO/PZT	(100)	43	13.3	300	45	77	NO	
PZTNMG3	Si/LNO/PZT	(100)	0	39.9	200	45	61	NO	
PZTNMG4	Si/LNO/PZT	(100)	43	39.9	200	45	61	NO	
PZTNMG5	Si/LNO/PZT	(100)	0	13.3	50	90	43	NO	
PZTNMG6	Si/LNO/PZT	(100)	43	13.3	50	90	43	NO	

Table 9.2.1: List of samples deposited by RF Magnetron Sputtering from $\text{Ni}_{0.50}\text{Mn}_{0.33}\text{Ga}_{0.17}$ target.

The procedure to deposit the perovskite PZT layer make use of an *Addax* magnetron sputtering machine and is described in reference [8.2.1]. The LaNiO_3 thin film grown on the top of the Si (100) substrate serves both as bottom electrode and also as buffer for the growth of (100) oriented PZT film.

The second set of films was also deposited onto bare Si (100) substrates and onto $\text{LaNiO}_3/\text{PZT}$ buffered Si (100) substrates, using con-focal sputtering of three independent targets configuration (100% Ni, 100% Mn and 50:50% NiGa alloy) allowing power ratio variation for targets as listed in table 9.2.2.

Samples	Substrate	Orientation	RF Power Ni (Watt)	RF Power Mn (Watt)	RF Power NiGa (Watt)	Argon (10^{-3} mbar)	Substrate Off center position (mm)	Time (min.)	Temperature Substrate ($^{\circ}\text{C}$)
NMG25	Si	(100)	50	50	100	13.3	0	30	59
NMG26	Si	(100)	50	50	100	13.3	35	30	59
NMG27	Si	(100)	100	100	200	13.3	0	30	74
NMG28	Si	(100)	100	100	200	13.3	35	30	74
NMG29	Si	(100)	150	150	300	13.3	0	30	98
NMG30	Si	(100)	150	150	300	13.3	35	30	98
NMG31	Si	(100)	200	200	200	13.3	0	30	102
NMG32	Si	(100)	200	200	200	13.3	35	30	102
NMG33	Si	(100)	50	50	100	66.5	0	30	51
NMG34	Si	(100)	50	50	100	66.5	35	30	51
NMG35	Si	(100)	87	163	200	13.3	0	30	86
NMG36	Si	(100)	87	163	200	13.3	0	30	86
NMG37	Si	(100)	87	163	200	13.3	35	30	86
NMG38	Si	(100)	130	244	300	13.3	0	30	113
NMG39	Si	(100)	130	244	300	13.3	0	30	113
NMG40	Si	(100)	130	244	300	13.3	0	30	113
NMG41	Si	(100)	130	244	300	13.3	0	30	113
NMG42	Si	(100)	43	82	100	66.5	0	30	55
NMG43	Si	(100)	43	82	100	66.5	0	30	55
NMG44	Si	(100)	43	82	100	66.5	0	30	55
NMG45	Si	(100)	43	82	100	66.5	0	30	55
PZTNMG6	Si/LNO/PZT	(100)	100	100	200	13.3	0	30	77
PZTNMG8	Si/LNO/PZT	(100)	100	100	200	13.3	35	30	77
PZTNMG9	Si/LNO/PZT	(100)	87	163	200	13.3	0	30	79
PZTNMG10	Si/LNO/PZT	(100)	87	163	200	13.3	0	30	79

Table 9.2.2: List of samples deposited by RF Magnetron co-Sputtering from Ni, Mn and $\text{Ni}_{50}\text{Ga}_{50}$ targets.

Taking advantage of the know-how gathered in the two previous series results, a third series of depositions was performed in the Physics Dep. of Aveiro University using the magnetron RF sputtering deposition system described in section 8.1. Co-sputtering conditions from a $\text{Ni}_{50}\text{Mn}_{50}$ and a $\text{Ni}_{50}\text{Ga}_{50}$ targets onto several different substrates as listed in table 9.2.3:

Sample	Substrate (orientation)	Substrate Temperature (°C)	Argon pressure (10^{-3} mbar)	$\text{Ni}_{50}\text{Mn}_{50}$ (W) Target power	$\text{Ni}_{50}\text{Ga}_{50}$ (W) Target power	Time deposition (min.)
NG1g	glass	124	5.0	0	25	15
NG2g	glass	124	5.0	0	25	30
NG3g	glass	45	5.0	0	25	10
NM1g	glass	293	5.0	71	0	60
NM2g	glass	43	5.0	50	0	20
NM3g	glass	157	5.0	50	0	15
NM4g	glass	125	5.0	25	0	15
NMG01g	glass	120	5.0	23	22	30
NMG02g	glass	200	5.0	21	20	35
NMG03g	glass	290	5.0	23	20	49
NMG04g	glass	370	5.0	19	16	40
NMG05g	glass	370	5.0	16	11	60
NMG06g	glass	450	5.0	16	11	90
NMG07g	glass	150	7.0	16	12	120
NMG08g	glass	450	7.0	13	10	120
NMG09a	Al_2O_3 (0001)	540	7.0	10	8	102
NMG09b	Si (100)					
NMG09c	SrTiO_3 (100)					
NMG09d	MgO (100)					
NMG10a	Al_2O_3 (0001)	400	5.0	12	10	102
NMG10b	Si (100)					
NMG10c	SrTiO_3 (100)					
NMG10d	MgO (100)					
NMG11a	Al_2O_3 (0001)	420	5.0	16	14	90
NMG11b	Si (100)					
NMG11c	SrTiO_3 (100)					
NMG11d	MgO (100)					
NMG12a	Al_2O_3 (0001)	400	2.5	16	14	90
NMG12b	Si (100)					
NMG12c	SrTiO_3 (100)					
NMG12d	MgO (100)					
NMG13a	Al_2O_3 (0001)	420	5.0	14	14	17
NMG13b	MgO (100)					
NMG13c	SrTiO_3 (100)					
NMG13d	Si (100)					

Table 9.2.3: List of samples deposited by RF Magnetron co-Sputtering from $\text{Ni}_{50}\text{Mn}_{50}$ and $\text{Ni}_{50}\text{Ga}_{50}$ targets.

10. Experimental Measurements Conditions

SEM and EDS

An extensive number of bulk and thin film samples were analyzed by SEM with respective composition measured by EDS; samples are usually attached with carbon tape to aluminum holders ensuring conductive samples short-circuit to the holder in order to avoid charge accumulation, while non-conductive samples need a nanometric layer of carbon (deposited by DC sputtering)

High resolution analytic SEM model *Hitachi SU-70*[®], using Schottky emission (SE) with acceleration voltages from 0.1 up to 30 kV, fitted with secondary and backscattering electrons detectors, X-Ray/EDS micro analysis system *Bruker Quantax 400*[®] with detector *XFlash 4010*[®] of 133 eV resolution was used at the Ceramics and Glass Engineering Department of Aveiro University.

Philips-FEI/Quanta 400[®] system was used at the University of Trás-os-Montes e Alto-Douro, Vila Real.



Fig. 10.0.1: Photo of the *Hitachi SU-70*[®] system.



Fig. 10.0.2: Photo of a *Philips-FEI*[®] system.

XRD, HRXRD, XRR

X-ray diffraction (XRD XRR and HRXRD) measurements were made at Central Analysis Labs (LCA) from Aveiro University and at UTAD facilities, comprising a *Siemens D5000*, *Rigaku Geigerflex D/MAX-B[®]*, a *Philips X'Pert MPD[®]* and *Philips X'Pert 4-circles MRD[®]* diffractometers systems from *PANALYTICAL* all using standard Cu-K α_1 radiation = 1.540598 Å, tension of 40 kV and current of 50 mA, conventional XRD measurements range 2θ from 10° to 120° and Ω from 10° to 80°, with step size $\Delta\theta = 0.02$; while XRR and HRXRD can use low 2θ angles from 0 to 6° and $\Delta\theta = 0.01$ °.



Fig. 10.0.3: XRD system from X'Pert PRO[®] image.

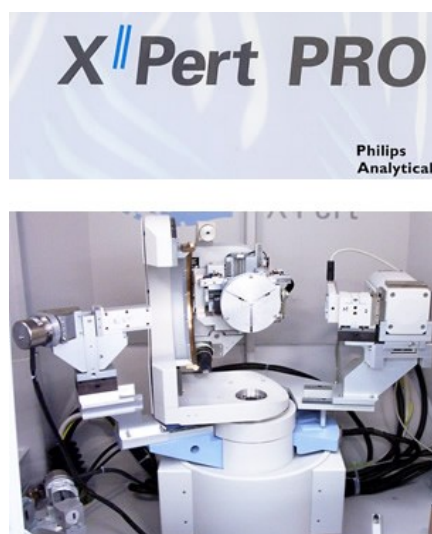


Fig. 10.0.4: detail of the goniometric system.

Rietveld analysis is performed using open source software like *Rietica* and *PowderCell*; whereas XRR is processed using *X'Pert Epitaxy[®]* licensed to U.A.

NPD

Neutron diffraction measurements were carried out by D. Karpinsky on a high resolution *E9[®] (FIREPOD)* powder neutron diffractometer of the *BERII* research reactor at the Berlin Neutron Diffraction Center (BENSC), HZB (*Helmholtz-Zentrum Berlin für Materialien und Energie GmbH*). The neutron wavelength was $\lambda = 1.797$ Å (reflection (511) of vertical focusing Ge monochromator). The sample was placed in a cylindrical vanadium container 8 mm in diameter. Neutron diffraction patterns were recorded in the range $10^\circ < 2\theta < 150^\circ$. The neutron diffraction data was processed using the *FullProf Suite[®]* software [10.0.1].

Raman Spectroscopy

Raman-scattering studies were done at IFIMUP under supervision of Prof. A. Moreira. Measurements in a series of thin film samples deposited by the RF sputtering technique from the $\text{La}_{0.7}\text{Sr}_{0.3}\text{MnO}_3$ target were performed at room temperature; while for the series of bulk samples comprising LuMnO_3 and $\text{La}_{0.7}\text{Sr}_{0.3}\text{MnO}_3$ compounds were measured as function of temperature; in this case pellets maximum size cannot surpass 3x4x5 mm, the exposed surface is polished with silk fabric, secured to the sample holder with silver paste and enclosed with a cooper mask setup in order to ensure temperature homogeneity.

The closed-cycle helium cryostat operates in the 10–300 K temperature range with a temperature stability <0.2 K. The temperature of the sample was estimated to differ by less than 1 K from the temperature measured with a silicon diode attached to the sample holder.

The 632.8 nm polarized red line of a He-Ne laser was used for excitation with an incident power of about 5 mW impinging on the sample. The unpolarized Raman spectra are measured in the pseudo backscattering geometry. The scattered light is analyzed using a *T64000 Jobin-Yvon*[®] spectrometer, illustrated in figure 10.0.5, operating in triple subtractive mode with a resolution $<1\text{ cm}^{-1}$; it is equipped with liquid nitrogen cooled charge-coupled and photon-counting devices.

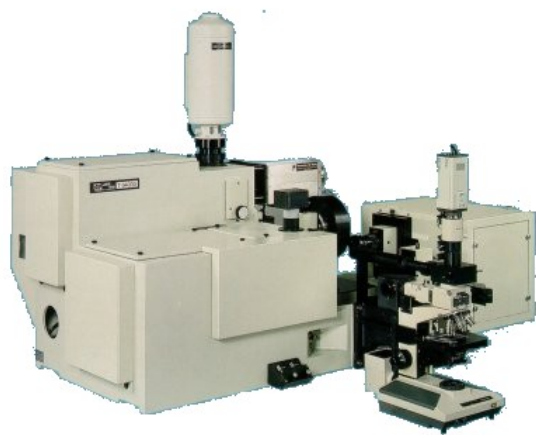


Fig. 10.0.5: image of the *T64000 Jobin-Yvon*[®] spectrometer system.

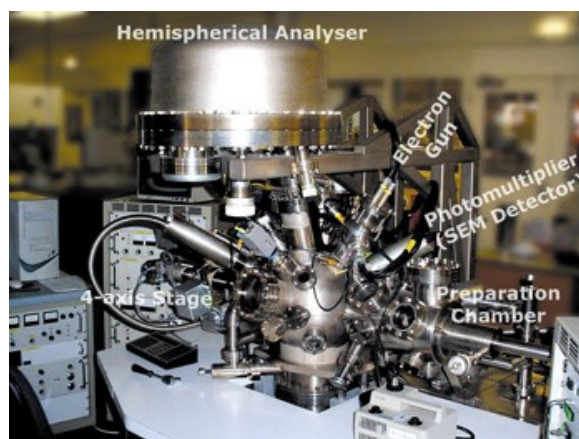


Fig. 10.0.6: Image of the *ESCALAB 200A*[®] from *VG Scientific* XPS system.

XPS

The XPS analysis was performed at CEMUP by Dr. Carlos Sá, using an *ESCALAB 200A*[®] from *VG Scientific* (UK), illustrated in figure 10.0.6, with *PISCES*[®] software for data acquisition and analysis. For the analysis, an achromatic Al (K_{α}) X-ray source operating at 15kV (300 W) was used, and the spectrometer, calibrated with reference to Ag 3d^{5/2} (368.27 eV), was operated in CAE mode with 20eV pass energy. Spectra analysis was performed using peak fitting with Gaussian-Lorentzian peak shape and Shirley type background subtraction (or linear taking in account the data).

Peak reference data was taken from: Handbook of X-Ray Photoelectron Spectroscopy [10.0.2]; specific application and results of this characterization method were subject of publication in the article [10.0.3].

RBS

A restricted number of thin film samples Deposited by RF Magnetron Sputtering from La_{0.7}Sr_{0.3}MnO₃ target onto several substrates, were measured by RBS at the Physics Department of the Nuclear Technologic Institute, Lisbon under supervision of Dr. Carlos P. Marques and Dr. Eduardo Alves.

RBS studies were performed with a 2.0 MeV He⁺ beam at normal and tilted incidences, to characterize the composition of the samples. The backscattered particles were detected at 140° (standard) and close to 180° (annular) using silicon surface barrier detectors with resolutions of 13 and 18 keV respectively. The beam current was measured on target and kept below 4 nA in order to minimize the effects of charge accumulation at the surface during analysis. No attempt to measure the hydrogen content was made.

The data were analyzed with the *IBA DataFurnace NDF v8.0 x*[®]. All spectra of a given sample were analyzed simultaneously in a self-consistent manner, to ensure all information is properly taken into account to obtain the final result. *ZBL 2000*[®] *stopping powers* were used [10.0.4], [10.0.5].

VSM

An extensive roll of magnetization measurements, as function of temperature from 2 up to 320 K and applied field up to 10 tesla, were performed in a vibrating sample magnetometer (VSM) prototype equipment from *CRYOGENIC Limited*[®] installed at the Physics Dep. labs of Aveiro University. The sample cavity and of superconducting coils responsible for the magnetic field are refrigerated system by means of a close cycle He cryostat. Samples were positioned with the longer axis in plane to the magnetic field.

The fact that this equipment was still in the prototype stage implied that some of its functionalities were not operational or did not comply supplier specifications; several technical bugs were detected during experimental measurements, namely:

- Although the technical specifications announce a resolution near 10^{-6} emu, the equipment was far from corresponding with any precision bellow 10^{-5} emu.
- The “high temperature” sample carrier oven measurement subsystem (~ 300 to 700 K) was never functional.
- The amplification subsystem introduced additional noise and significant noise and jumps were also found to be introduced by the automatic scale selection function during magnetization signal acquisition particularly during external magnetic field crossing over the “zero”.
- The superconductor magnet can generate up to 0.02 Tesla at the supposed “zero” field depending on the previous use, there is no automatic protocol to compensate this bias. The “zero” magnetic field is only attainable above 23 K once the coils go through a forced transition to normal conductor.
- The inductive detection coils were found not to be properly shielded introducing an additional magnetization bias proportional to $\mathbf{M} \cdot \mathbf{B}$, as exemplified in figure 10.0.7.
- Sample temperature uniformity was detected only to be reliable below variation rates of <0.5 K/min. implying that a standard \mathbf{M} vs. \mathbf{T} measurements from 5 to >300 K could take more than 10 hours.

For most of these problems it was necessary to implement time consuming empirical diagnostic procedures, report and request to the supplier suitable software or

even hardware rectifications, consequently it was usually needed to implement new calibration procedures and even to repeat many samples' measurements.

A relevant example of how the original signal can appear distorted by noise and deviations picked up at the detector coil or due to problems in hardware/software processing can be observed in the sequence of figure 10.0.7; the graphs were obtained from the measurements of a polycrystalline manganite sample of $\text{Eu}_{0.8}\text{Y}_{0.2}\text{MnO}_3$ and is elucidative of the experimental data processing necessary to detect some of the VSM system acquisition shortcomings. In fact, the raw data obtained can mask the true behavior of a magnetic phase in the sample.

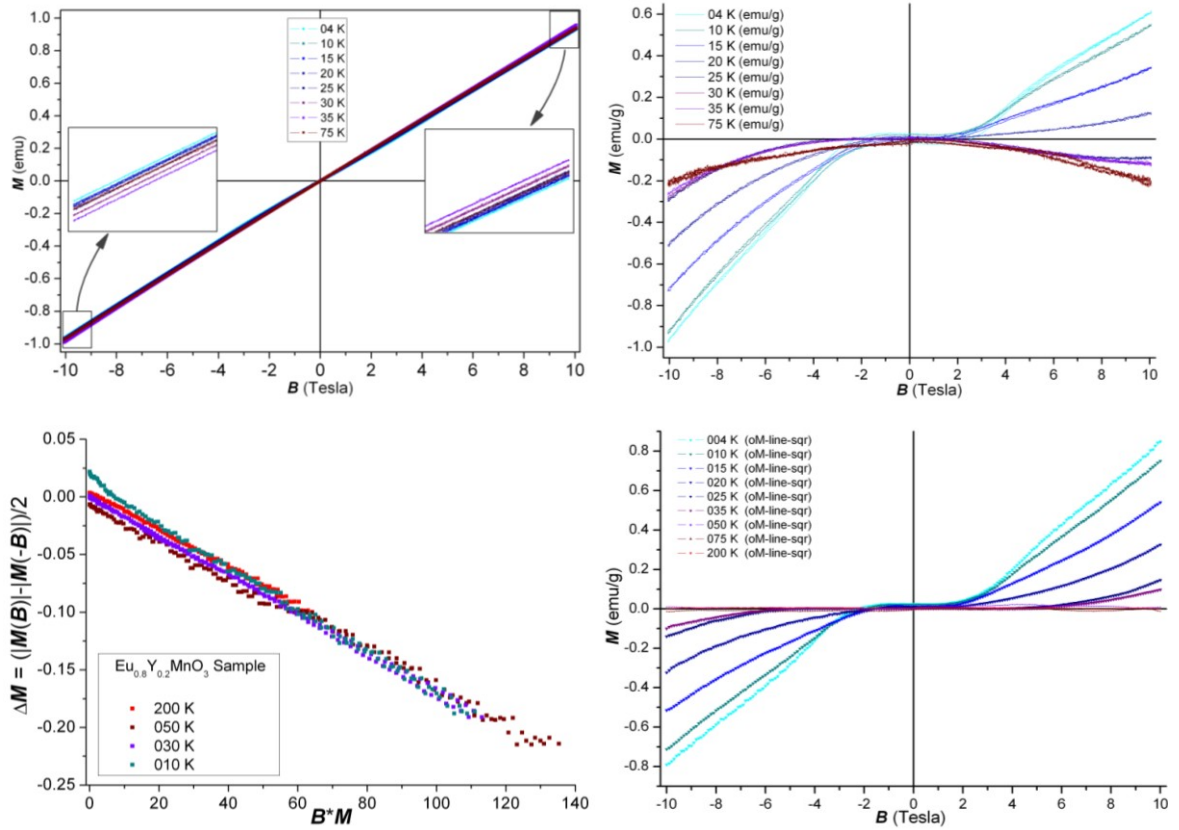


Fig. 10.0.7: Graphs representing VSM measurements and necessary corrections: Original data (top left); asymmetry detected after subtraction of the PM contribution (top right); systematic error proportional to the moment and the field (bottom left); effective AFM response of the sample.

The analysis of the magnetization as function magnetic field or temperature should account for the several phases composing the samples, like the case of powder composites or thin films and substrates; generally PM, DM or AFM phases introduce a constant magnetic moment contribution clearly visible as a slope over the saturation of the FM phase which alone has a horizontal behavior.

$$M_{FM_{phase}} = M_{sample} - \chi_{FM_{phase}} \cdot H \quad (\text{Magnetization correction})$$

When applicable, *Microcal Origin*® software was also used to implement fitting procedures (in S.I. units). High temperature M vs. T curves can be simulated using the Curie-Weiss model given by the formulation:

$$y = M_d + (C_0 \cdot H) / (x - T_C);$$

Where: $y = M$, $x = T$, M_d = Diamagnetic contribution, C_0 = Curie constant, H = Magnetic field, T_C = Curie temperature Whereas the M vs. B curves can be approximated by the Brilluoin model:

$$y = (C_1 \cdot x) + (C_2 \cdot x^2) + M_1 \cdot (1/S_1) \cdot ((S_1 + 0.5) \cdot (\cosh((S_1 + 0.5) \cdot G_2 \cdot x) / \sinh((S_1 + 0.5) \cdot G_2 \cdot x)) - 0.5 \cdot (\cosh(G_2 \cdot x / 2) / \sinh(G_2 \cdot x / 2)));$$

Where: $y = M$, $x = (\mu_B \cdot B / k_B \cdot T)$, $S_1 = J$, $G_2 = g$, $M_1 = N \cdot \mu_B \cdot J \cdot g = M_{sat}$, C_1 = Diamagnetic factor, C_2 = quadratic calibration factor.

Specific application and results of these methods was subject of publication also in the article [10.0.3].



Fig. 10.0.8: VSM system from *Cryogenic Limited*®.



Fig. 10.0.9: SQUID MPMS from *Quantum Design*®

SQUID Magnetometer

In some cases when the samples do not have enough magnetic moment to be detected by the VSM system, it was possible to recur to the Quantum Interference Device Magnetometer (SQUID) *MPMS* from *Quantum Design* at IFIMUP. This system illustrated in figure 10.0.9 can operate in the temperature range from 2 to 400 K and under magnetic fields up to 5.5 Tesla and a sensitivity reaching 10^{-8} emu.

MZ

Magneto-impedance measurements were carried out by Dr. Soma Das in the Thermophysical Properties Measurements Laboratory, Cryogenic Engineering Centre, Indian Institute of Technology, Kharagpur, India. The set up uses the impedance analyzer of *Wayne-Kerr model 6520A*[®] in the frequency range from 1 kHz to 15 MHz and an electromagnet to get the biasing dc field up to 4 kOe. The technique used is non-inductive and an approximate cylindrical-shaped sample is used for measurement of impedance. A signal coil of 25 turns was wound over the midpoint of the sample (diameter = 3 mm, length = 10 mm) and the impedance of the coil with and without the sample is measured with the impedance analyzer. The sample impedance is obtained after correcting it with respect to empty coil impedance. The biasing dc field up to 4 kOe is applied parallel to the exciting ac field. The resistive and reactive components of impedance are measured up to 15 MHz. All measurements are performed using excitation voltage of 0.5 V resulting in an ac field of ~ 0.09 T.

ME

The measurement of the voltage generated between the sample electrodes is performed by lock-in technique in a feed back loop with a wave generator operating in a frequency range of 1 to 100 kHz which feeds the small coils that produce a probe a.c. field (H_{ac}) of 10 Oe in amplitude, superimposed onto a magnetic bias field generated by the main electromagnets up to 15 kOe, checked by a Hall probe, The custom made setup is

based in an *Bruker ESP 300E*[®] system at the Physics Department of UA operated under supervision of Dr. N. Sobolev.

The sample can be rotated in relation to the field direction, in order to obtain the longitudinal and transverse components of the M effect. The magnetoelectric voltage across sample (V_{out}) is measured in the lock-in amplifier using an input resistance of 100 M Ω and transferred to a computer with *NI Labview*[®] software using a specific data acquisition interface also developed by M. Peres.

SFM

AFM, PFM and MFM measurements were performed by I. Bdikin and D. Karpinsky at CICECO labs UA under supervision of Dr. A. Kholkin using *VEECO*[®], *PicoPlus*[™], *Agilent*[®] SFM systems.

A specific set of mono and poly crystalline manganites bulk samples was selected to be measured at CNMS ORNL Labs under supervision of Dr. S. Kalinin, using the *Asylum MFP-3D*[®] SPM system represented in figure 10.0.10; this system enables to perform experimental measurements on samples surfaces like conventional topographic scan, PFM, micro lithography, BEPS, and *I-V* curves. The system handling comprise delicate hardware procedures that include selecting and assemble a suitable conductive tip in the holder, mount the *MFP-3D*[®] head unit in support table and with the aid of a optical microscope perform the laser alignment with the cantilever and engage the tip in the sample surface; system management and conventional PFM scans acquisition is performed via “*Igor Pro*[®]” software interface; whereas configuration of the wave function generator, lock-in amplifier and BEPS data acquisition is performed via specially developed interface with *NI LabView*[®] software.

The topographic, deflection and piezo-response amplitude and phase images can be visualized and compared via *Nanotec WSxM*[®] software; a specific program was under development using *MathLab*[®] software, in order to convert the complex multidimensional data resulting from BEPS measurements and present it in the form of maps showing the several polarization parameters accessed.

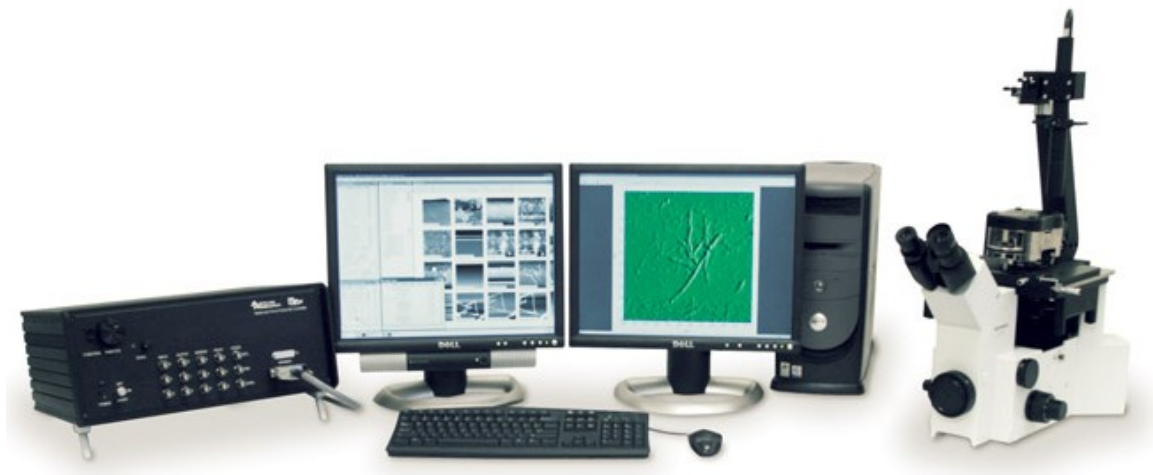


Fig. 10.0.10: Asylum MFP-3D® SPM system

Experimental course of action on samples began with a conventional topographic scan over a $20 \times 20 \mu\text{m}$ area from which a $5 \times 5 \mu\text{m}$ region with the most regular topology is selected, successive scans are necessary in order to adjust the resonance frequency and bias voltage of the tip to the sample surface stiffness in order to achieve some amplitude and phase contrast during the scans.

Lithographic frame was based on close pairs of $1 \mu\text{m}$ length lines at different bias voltages (± 5 , ± 10 , ± 15 , $\pm 20 \text{ V}$) each at $\sim 0.5 \mu\text{m}$ distance; further PFM scan enable to trace the sample surface reaction to the electrical stimulus. A representative area within the stimulated region is selected to performing BEPS grid measurements with respective resonance frequency and applied a.c. voltage in the limits of the observed threshold d.c. voltage based on the previous results ($< 20 \text{ V}$).



Fig. 10.0.11: Asylum MFP-3D specific ORCA® sample mount (left) and cantilever holder (right)

Some limited I - V curves probing tests were performed using the more sensitive *TUNA*® contact mode setup from a *VEECO*® Atomic Force Microscope system, the results were sufficient inspiring to proceed to more systematic measures using the *ORCA*® contact mode setup from the *MFP-3D*® system; some complementary hardware, shown in figure 10.0.11, system calibration and software adjustments were necessary to perform these experiments. This sub system can operate up to $\pm 10 \text{ V}$ in a ramp or cycle mode from 0.01 to 10 Hz, has a sensitivity of 0.2 nA and noise level around 1 pA.

Page intentionally left blank

III EXPERIMENTAL RESULTS AND ANALYSIS

11 Powder samples

Results of structural, chemical, magnetic and electric properties characterization of the prepared bulk ceramic samples are presented and commented through this section 11.

In the framework of multiferroic materials research performed in Aveiro University it was possible to participate directly in preceding and parallel experimental works which resulted in overall relevant information useful for this thesis work, shortly summarized:

- Preceding studies on nano powder manganite based on a series of $\text{La}_{0.85}\text{Ca}_{0.15}\text{Mn}_{1+z}\text{O}_{3-\delta}$ with $z = 0.00, 0.18, 0.24, 0.44, 0.56, 0.88$; samples were prepared by coprecipitation method which underwent systematic heat treatments as function of temperature and time. TEM and nano gauge EDS was used in order to understand the chemical and structural uniformity of the system; XRD was used to trace grain size and formation of spurious phases; and thermal gravimetry (TG) to understand Oxygen intake in the system. Main results and conclusions were relevant to advise long annealing procedures (>96 h) between 800° C to 900° C in air, adequate to increase the Oxygen content and to promote sufficient elements diffusion within the manganite compounds while constraining grain growth bellow 50 nm [11.0.1].
- Studies on composite samples of $(x)\text{La}_{0.625}\text{Sr}_{0.375}\text{MnO}_3 + (1-x)\text{LuMnO}_3$ prepared by the conventional solid state route from La_2O_3 , Lu_2O_3 , SrCO_3 , and Mn_2O_3 powder precursors [11.0.2] validate that there is a very limited solubility ~2% of Lu in the perovskite phase. Repeated milling and sintering at 1300° C steps are necessary for successful formation and segregation of the two different hexagonal and rhombohedral phases [11.0.3], [11.0.4]; the grain average size was comprised around ~5 μm distribution, preventing efficient oxygen diffusion and reducing surface contact between the different phases.

- Composites based on the hexagonal ferrites $\text{BaFe}_{12}\text{O}_{19}$ (BaM), $\text{SrFe}_{12}\text{O}_{19}$, $\text{Ba}_3\text{Co}_2\text{Fe}_{24}\text{O}_{41}$ and the ferroelectric perovskite BaTiO_3 (BTO), also prepared by solid state route [11.0.5], shown grain size between 0.5 to 5 μm , some incidence of impurities (<5%) and likely deficient oxygen stoichiometry for the magnetic phase. A faint magnetoelectric coupling localized between grain boundaries of the different phases was detected by means of piezoresponse force microscopy [11.0.6], [11.0.7]; confirming the multiferroic potential of these composites, even though the magnetoelectric coupling for such micrometer sized grains becomes marginal.

Overall these two processes involved extensive effort in multiple grinding, sintering and analysis steps to confirm the intended ceramic composite. The grains overgrown morphology also renders the thermodynamic diffusion of ions more difficult, contributing to the appearance of spurious phases and delaying the formation/segregation of the immiscible phases.

- *Pechini* and *Co-precipitation Sol-Gel* routes [5.1.2] were tried in the synthesis of nano-structured ceramic samples with nominal composition YMnO_3 , $\text{Y}_{0.86}\text{Ca}_{0.14}\text{MnO}_3$, $\text{Y}_{0.86}\text{MnO}_3$, intended for testing the effectiveness of these methods in achieving typical Yttrium manganites' hexagonal structure and properties. The resulting grain size distribution was in the order of 50 nm as expected; however XRD and Raman [11.0.8] characterization studies revealed also a high amount of Y_2O_3 spurious phase [11.0.9], even after repeated milling and sintering procedures, rendering this samples unsuitable for the proposes of this thesis research.

The former results and respective analysis and conclusions represent valuable data that lead to some of the approaches and improvements selected in the preparation of new materials and implement of new characterization techniques used in this thesis work.

11.1. Nano Powder Composites of LuMnO_3 + $\text{La}_{0.7}\text{Sr}_{0.3}\text{MnO}_3$

The single compounds LSM100 and LuM100 and the series of samples LuM+LSM synthesized by the *Urea* Combustion method described in table 8.3.2, were measured by XRD and EDS –SEM after heat treatment in air at 800 °C during 98 hours; In order to understand the limits of miscibility between the two phases and the eventual role such fraction of material may have in the properties of the composite.

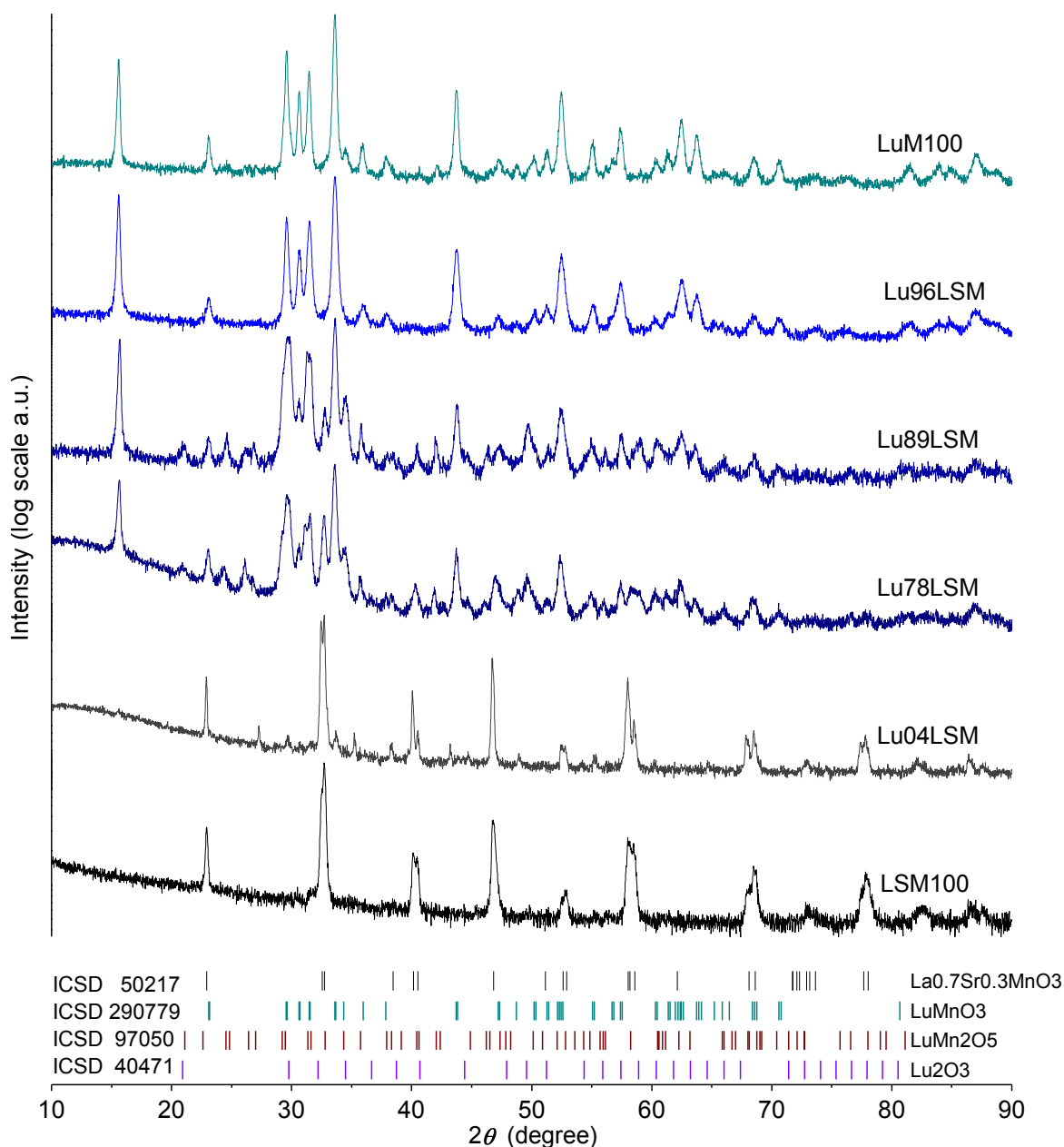


Fig. 11.1.1: Comparative XRD patterns for “LuM+LSM” samples series after 98 h heat treatment at 800C.

θ - 2θ powder diffractograms are shown in figure 11.1.1 and respective Rietveld refinement results presented in table 11.1.1, which overall confirm the hexagonal $P6_3cm$ (185) structure of LuMnO_3 indexed to the ICSD file #280779 [4.4.2]; the $\text{La}_{0.7}\text{Sr}_{0.3}\text{MnO}_3$ hexagonal $R-3c$ (167) phase is indexed to ICSD file #50217 [11.1.2], having $a = 5.52$ and $c = 13.37$ Å; In the composites a reduced presence of spurious phases was detected, with possible indexations to LuMn_2O_5 <4 % [11.1.2] and to Lu_2O_3 <<1 % [11.1.3].

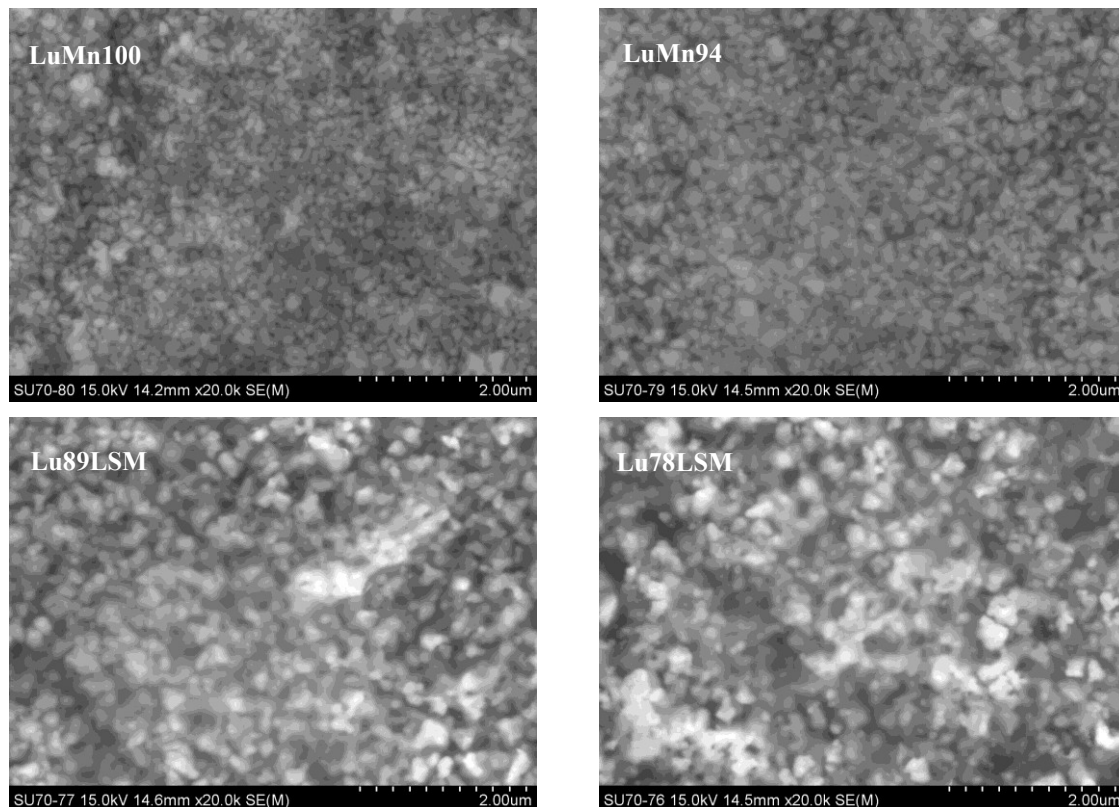
Sample Lu96LSM shows that La and Sr had substantial solubility in the dominant LuMnO_3 phase; in the other extreme, sample Lu04LSM, a segregation of ~5% of the LuMnO_3 phase from the $\text{La}_{0.7}\text{Sr}_{0.3}\text{MnO}_3$ matrix was identified which is within the margin error of the method, considering a intended nominal composition of 4% Lu.

Phases: Sample:	LuMnO_3 $P6_3cm$ %	$\text{La}_{0.7}\text{Sr}_{0.3}$ MnO_3 $R-3c$ %	LuMn_2O_5 $Pbam$ %	Lu_2O_3 $I213$ %	S.G.	a (Å)	b (Å)	c (Å)	grain (nm)	R_p	R_{wp}	χ^2
LSM100	0	100	n.a.	n.a.	$R-3c$	5.51	5.51	13.37	33	6.51	8.67	0.06
Lu04LSM	5.1	94.9	n.a.	n.a.	$P6_3cm$	6.039	6.039	11.374	66	3.50	4.65	0.25
	5.1	94.9	n.a.	n.a.	$R-3c$	5.524	5.524	13.374	33			
	3.5	96.4	n.a.	0.1	$I213$	10.398	10.398	10.398	98	3.74	4.96	1.80
Lu78LSM	~81	~19	n.a.	n.a.	$P6_3cm$	6.058	6.058	11.373	67	2.41	3.08	0.83
	~81	~19	n.a.	n.a.	$R-3c$	5.509	5.509	13.402	32			
	>75	>18	<4	n.a.	$Pbam$	7.315	8.665	5.774	162	2.92	3.78	1.22
	>75	>18	<4	<1	$I213$	10.404	10.404	10.404	98	4.51	5.98	0.34
Lu89LSM	~92	~8	n.a.	n.a.	$P6_3cm$	6.059	6.059	11.446	49	8.51	11.7	0.14
	~92	~8	n.a.	n.a.	$R-3c$	5.528	5.528	13.443	n.a.			
	>85	>9	<4	<1	$Pbam$	7.39	8.665	5.736	n.a.	2.87	3.72	1.18
	>85	>9	<4	<1	$I213$	10.404	10.404	10.404	n.a.			
Lu96LSM	~100	n.a.	n.a.	n.a.	$P6_3cm$	6.042	6.042	11.373	67	4.19	5.71	0.67
	99.8	0.2	n.a.	n.a.	$R-3c$	5.552	5.552	13.038	n.a.	2.67	3.39	0.87
LuM100	~100	n.a.	n.a.	n.a.	$P6_3cm$	6.048	6.048	11.389	56	4.83	6.35	0.10

Table 11.1.1: Rietveld Refinement Results for “LuM+LSM” samples series after 98 h, 800°C heat treatment.

Additional grinding and annealing is expected to further reduce their presence [11.1.4], nevertheless these composite samples exhibit a definite level of crystallization and phase's segregation to be able to develop potential magnetoelectric effects.

Representative examples of SEM images of the samples series are presented in figures 11.1.2 and the outcome of EDS measurements using *Philips-FEI/Quanta 400* system and recalibrated composition values for samples are presented in table 11.1.2.



Figs. 11.1.2: SEM images of samples surface for series “LuM+LSM” after sintering stage at 800C for 98 h

Surface survey of samples found reduced presence of precipitates ($\ll 1/100 \mu\text{m}^2$) having 0.2 to 0.5 μm size; correlated EDS probing of some of these scattered particles reveals partial deviation from the nominal composition of the main expected phases, indicating the presence of the spurious LuMn_2O_5 phase previously detected by XRD indexation, in particular for samples Lu78LSM and Lu89LSM.

EDS probing over μm^2 area reveal a higher degree of error in Lu parameterization ($>2\%$) compared to the other metallic elements ($\sim 0.5\%$); in fact, alternative measurements using SEM model *Hitachi SU-70* and EDS analysis system *Bruker Quantax 400*, also show a discrepancy of ~ 0.64 between Lu to Mn ratio for sample LuMn100. In order to find coherent values, plausible with the samples nominal composition, a renormalization criterion was based on the high reliability of the LuMnO_3 stoichiometry on the LuMn100 sample, assuming Lu/Mn ~ 1 rate.

The consistency of the recalibrated composition values found for all samples enable to trust these results within a 3% error margin; a critical case became the LuMn98 sample; like the LuMn94 sample was also intentionally prepared to have Mn deficit, hence the composition $\text{LuMn}_{0.98}\text{O}_3$ is more plausible than a composition of $\text{Lu}_{0.99}\text{MnO}_3$ obtained previously to calibration. Still according to this model, sample Lu04LSM may have ~50% more Lu than the originally intended, corresponding actually to a composition of $\text{Lu}_{0.06}(\text{La}_{0.66}\text{Sr}_{0.34})_{0.94}\text{MnO}_3$; this is clearly compatible with the ~5% of the LuMnO_3 phase results previously referred from XRD Rietveld refinement, denoting that the solubility of Lu within the LSM pseudo perovskite phase could be within a ~1%.

Sample:	LuMn100	LuMn94	LuMn98	Lu96LSM	Lu89LSM	Lu78LSM	Lu04LSM
Element (label):	At. %	At. %	At. %	At. %	At. %	At. %	At. %
O (K)	54.58	53.34	62.42	52.99	53.89	53.98	51.07
Mn (K)	23.01	22.91	18.89	24.75	23.025	22.78	23.37
Lu (L)	22.41	23.745	18.69	22.27	19.88	17.46	1.36
La (L)					1.86	3.57	15.77
Sr (K)					1.34	2.22	8.45
relative Lu/Mn	0.974	1.036	0.989	0.900	0.863	0.766	0.058
Mn/[Lu+La+Sr]	1.027	0.965	1.011	1.112	0.998	0.980	0.914
if Lu/Mn \equiv 1 @ LuMn100	Recalibration assuming 1/0.974 correction factor for Lu/Mn						
recalibrated Lu/Mn	\equiv 1	1.06	1.02	0.93	0.89	0.78	0.06
renorm Mn/[Lu+La+Sr]	\equiv 1	0.94	0.98	1.08	0.98	1.00	0.94

Table 11.1.2: EDS results obtained by *Philips-FEI/Quanta 400* SEM system for “LuM+LSM” series and renormalization assuming Mn/Lu ~1 for the stoichiometric composition LuMnO_3 of sample LuMn100.

The typical $\text{La}_{0.7}\text{Sr}_{0.3}\text{MnO}_3$ $R\bar{3}c$ symmetry result in a rather poor Raman spectra, as observed on the left graph of figure 11.1.3, with a group of peaks at $\sim 200\text{ cm}^{-1}$ and a relevant peak at $\sim 420\text{ cm}^{-1}$ corresponding to an A_{1g} mode [11.1.5].

The hexagonal LuMnO_3 in its ferroelectric phase $P6_3cm$ contains six formula units and can have up to 38 Raman active phonon modes ($9A_1 + 14E_1 + 15E_2$) some of them have substantial frequency shifts around the Néel temperature $\sim 90\text{ K}$ at $\sim 119 (A_1)$, $\sim 226 (A_1)$, $\sim 382 (E_1)$, $\sim 482 (A_1)$ and specially at $\sim 697 (A_1)\text{ cm}^{-1}$ [11.1.6]. A typical example of a Raman spectrogram of LuMnO_3 can be observed on the right graph of figure 11.1.3.

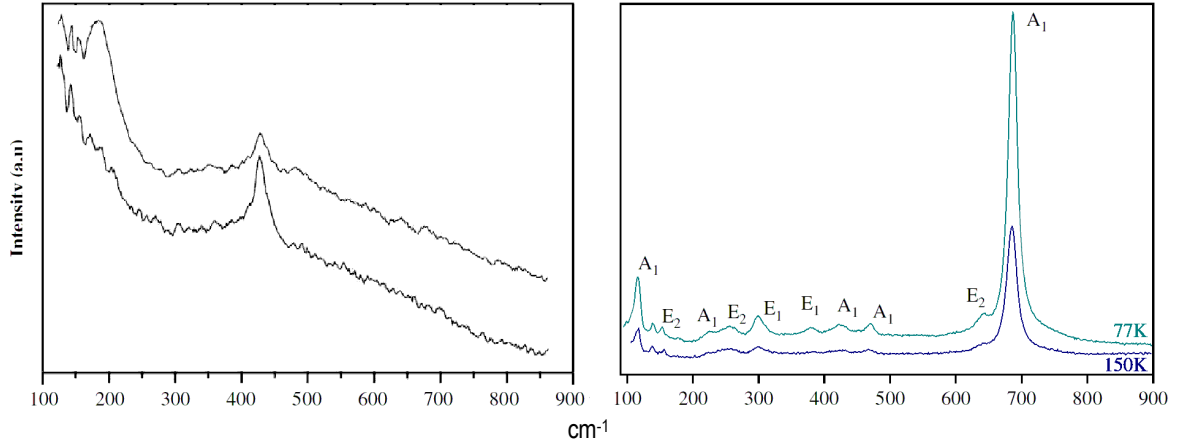


Fig.11.1.3: Left graph: Raman spectra of $\text{La}_{0.7}\text{Sr}_{0.3}\text{MnO}_3$ at room temperature in parallel (top line) and perpendicular (lower line) polarized geometry [11.1.5]. Right graph: Raman spectra of LuMnO_3 at 77 K (top line) and at 150 K (lower line) [11.1.6].

The rather poor Raman response of sample LuM100 essentially composed of LuMnO_3 and of sample Lu04LSM having $\text{La}_{0.7}\text{Sr}_{0.3}\text{MnO}_3$ as main phase, can be observed in figure 11.1.4. The most characteristic A_{1g} mode of the $\text{La}_{0.7}\text{Sr}_{0.3}\text{MnO}_3$ main phase can be identified at $\sim 439 \text{ cm}^{-1}$, whereas the peaks found near 650 cm^{-1} can belong to the LuMnO_3 phase; the systematic peak observed at $\sim 188 \text{ cm}^{-1}$ can be attributed to a laser line resonance.

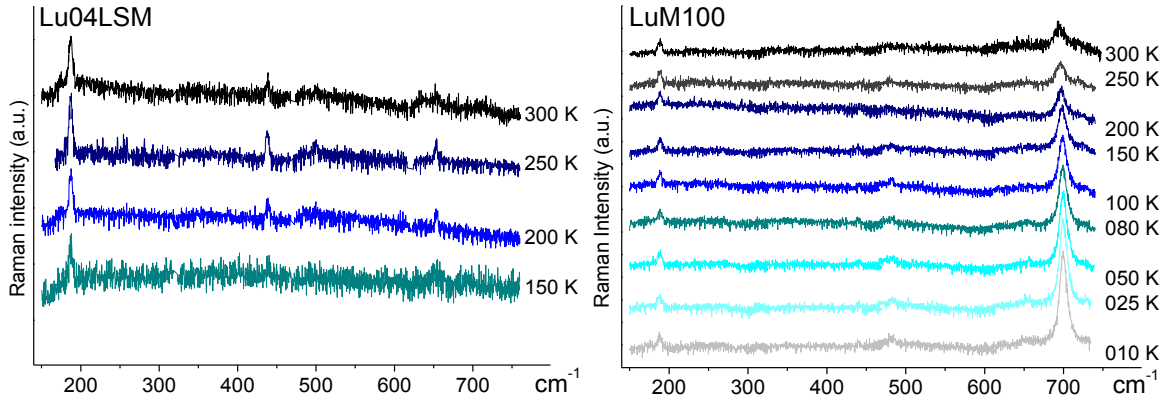


Fig.11.1.4: Raman spectrograms for sample Lu04LSM (left) and LuM100 (right) for several temperatures.

In the spectra from sample LuM100 are perceptible the A_1 modes at ~ 440 and $\sim 480 \text{ cm}^{-1}$, E_2 at $\sim 650 \text{ cm}^{-1}$ and particularly relevant is the A_1 mode peak near 699 cm^{-1} whose behavior with temperature suffers a patent deviation from the original trend from 300 to 100 K, as can be observed in figure 11.1.5 (guiding black line fitted according to the models discussed in [11.1.7]), to a $\sim 1 \text{ cm}^{-1}$ higher frequency from 100 to 0 K which can be explained by additional stiffness of the structure due to the appearance of the AFM order.

This shift [11.1.7] below Néel temperature confirms the typical PM-AFM transition at ~ 90 K expected for the stoichiometric LuMnO_3 phase present in the sample.

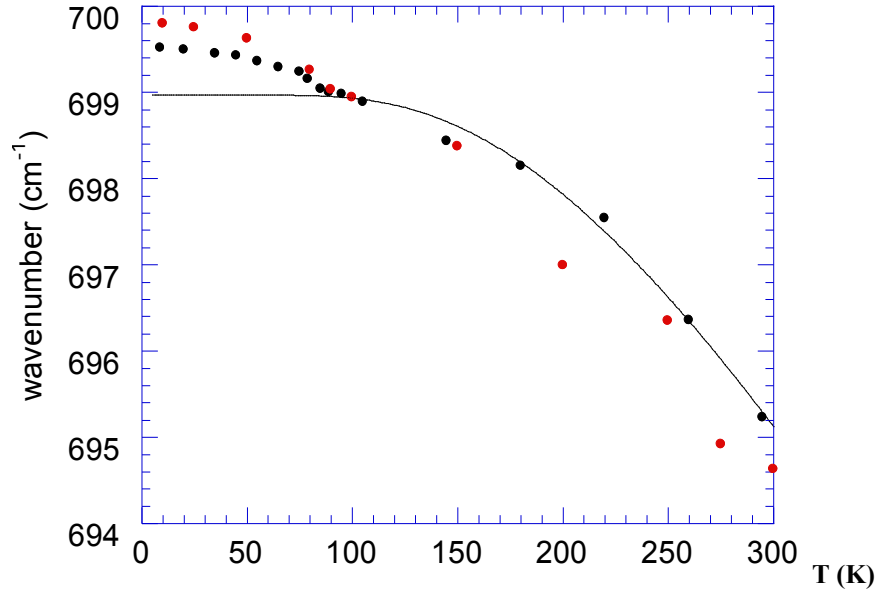


Fig.11.1.5: Dependence of the A_1 Raman mode with temperature for sample LuM100. Different color dots correspond to independent measurements.

Raman spectroscopy measurements of the composite samples Lu78LSM and Lu89LSM, reveal a surprising enrichment of the spectrogram, in particularly below 100 K with the manifestation of many new peaks and unfolding modes, observed in figure 11.1.6.

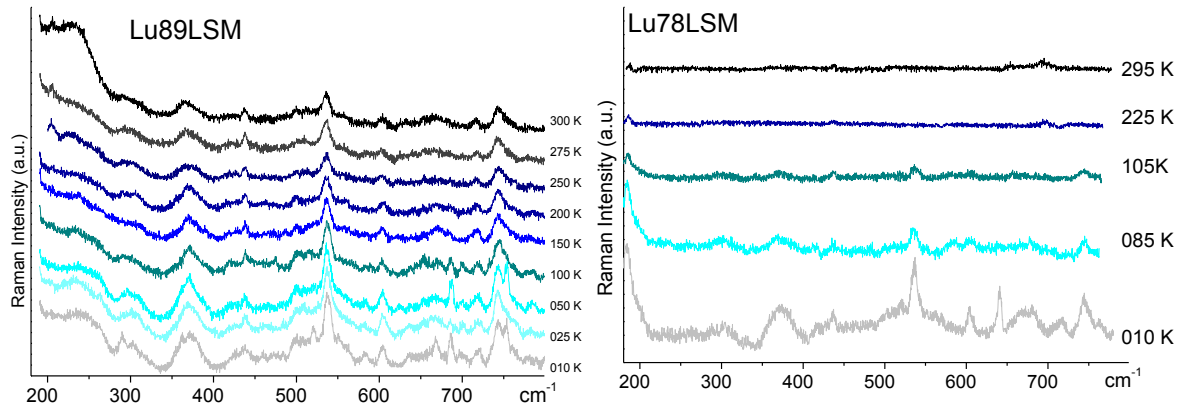


Fig.11.1.6: Raman spectra for composites Lu89LSM (left) and Lu78LSM (right) at several temperatures.

The possible contribution of the very small percentage ($<2\%$) of solid solution phase of Lu in $\text{La}_{0.7}\text{Sr}_{0.3}\text{MnO}_3$ or La and Sr in LuMnO_3 can result in broadening of the dominant phase peaks. The $\text{La}_{0.7}\text{Sr}_{0.3}\text{MnO}_3$ phase A_1 mode is relatively stable at ~ 439 cm^{-1} with temperature, but is clearly broader than that seen for sample Lu04LSM.

Considering the typical Lu_2O_3 phase cubic $Ia3$ structure no Raman response is expected; on the other hand, it is possible that small traces of orthorhombic LuMn_2O_5 *Pbam* phase may appear in the Raman diffractograms, similar to other RMn_2O_5 compounds patterns [11.1.8], [11.1.9]; nonetheless, this phase most relevant FE transition occurring at 34 K [11.1.10] was not noticeable and considering the XRD indexation results and the relatively low amount of such contaminant, it seems insufficient to justify the overrated appearance of so numerous and explicit unidentified modes.

In its turn, most modes related to the LuMnO_3 phase that were not detected in sample LuM100 can be recognized in the composite samples principally for measurements below 100 K (identified with light blue arrows in figure 11.1.7). These peaks also suffer relative shifts, broadening and convolutions with new unidentified modes, as can be observed in the left graph of figure 11.1.7. The Raman spectral distribution of the LuMnO_3 phase seems altered particularly in relation to the previously predominant A_1 mode close to 700 cm^{-1} that appears only below 100 K and is very faint when compared to overgrown and unfolded peaks coincident with E modes near 299, 379 and 642 cm^{-1} .

The emergence of new modes can be seen especially between 500 to 600 cm^{-1} and above 700 cm^{-1} , outlined (red arrows) in the left graph of figure 11.1.7. Most of these unidentified peaks also show relevant shifts and unfolding modes evolution with temperature as can be observed in figure 11.1.6. Some of these unknown peaks seem to follow the behaviour of the peaks indexed to the LuMnO_3 phase only appearing or unfolding below 100 K as the case of the modes at ~ 583 , ~ 687 and $\sim 753\text{ cm}^{-1}$.

In the sequence of diffractograms of the composite sample Lu89LSM shown in figure 11.1.6 it is possible to discriminate about 24 distinct modes. In order to trace the evolution of some representative peaks with temperature we used a Lorentz peak shape function fit performed at each peak. As can be seen in the examples of figure 11.1.7 (bottom), in general we observe at each mode the normal decrease in peak area and intensity, as temperature rises; the estimated peaks half width remains overall regular and some peaks have relevant position variation between 50 to 100 K.

Since the XRD patterns indexations exclude the presence of any other unpredicted crystalline phase, one of the possible justifications for the rich Raman spectra found for the sample Lu89LSM and Lu78LSM could be attributed to a more efficient refraction and

detection of the comprehensive Raman spectra formerly attributed to the LuMnO_3 phase found in sample LuM100 and eventually to some LuMn_2O_5 . In fact one of the factors affecting the acquisition sensitivity for Raman measurements is the sample surface characteristics which impose the conditions for the observable reflection/ absorption/ refraction of the laser line. Although the experimental preparation procedure for the surfaces was identical for all samples, the near single phase samples seem to impose substantial absorption upon the incident laser, whereas the composites samples surface having heterogeneous grains and interfaces may present more favorable conditions to the laser refraction.

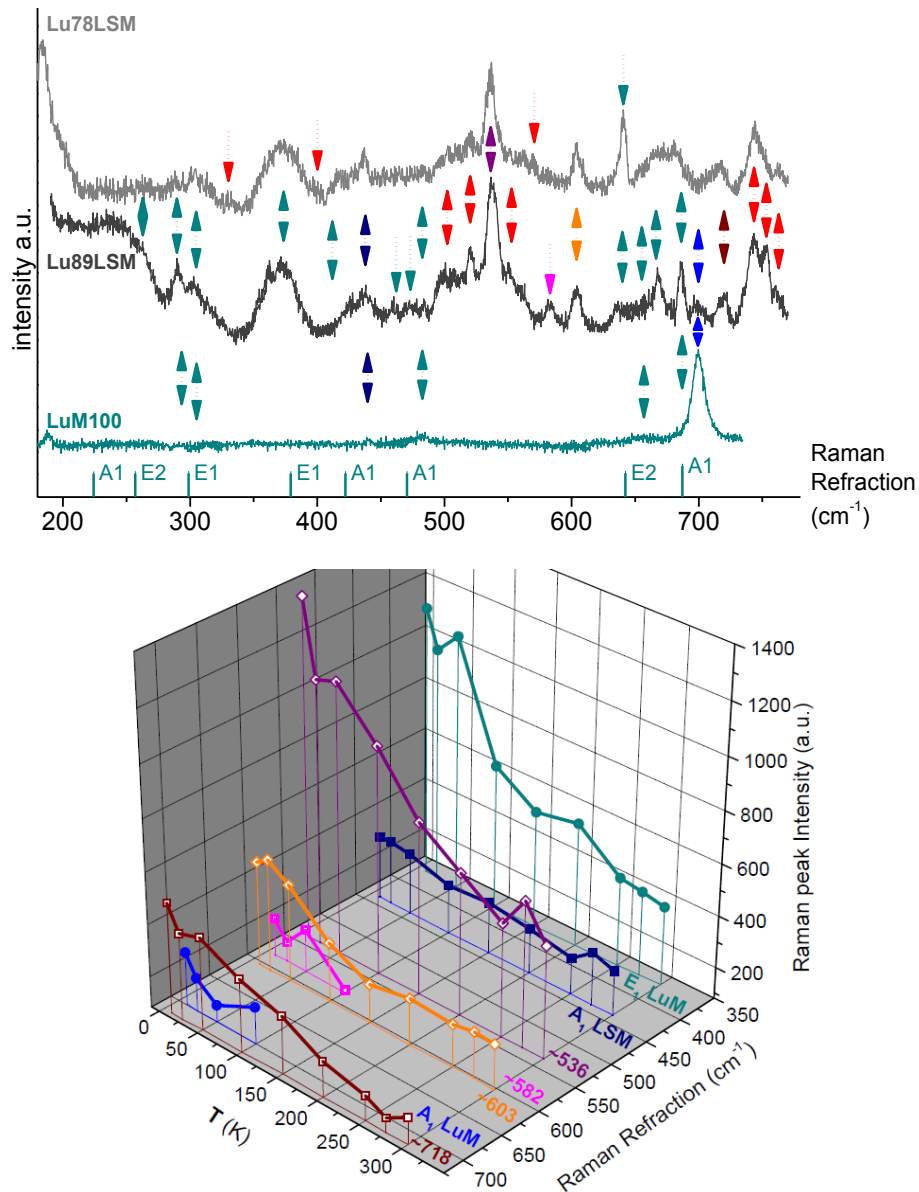


Fig.11.1.7: Comparative Raman spectra at 10 K of samples LuM100, Lu89LSM and Lu78LSM (top); Examples of the evolution of some peaks position and intensity with temperature (bottom).

Under this scope, it is possible that the particular environment of the surface at the interfaces between grains of the two different structural phase's may concentrate metastable atomic arrangements linking the two distinct lattices; this interstitial layer has small expression in volume as a phase itself, but its presence is expected to be disseminated over most of the LSM minority phase grains surface and can contribute to new active Raman modes.

In the $\text{La}_{0.7}\text{Sr}_{0.3}\text{MnO}_3$ plus LuMnO_3 composite samples the two distinct perovskite and hexagonal crystalline structures turn out to be in contact at the grains interfaces; the entanglement of the two different phases may suggest linking MnO_6 and MnO_5 groups sharing a common O^{2-} ion, as illustrated in figure 11.1.8, these metastable arrangements do not necessarily form a new structural phase, but constitute locally obvious non centre-symmetric molecular configurations which can originate specific Raman-active vibrational modes not found in the single parent phases.

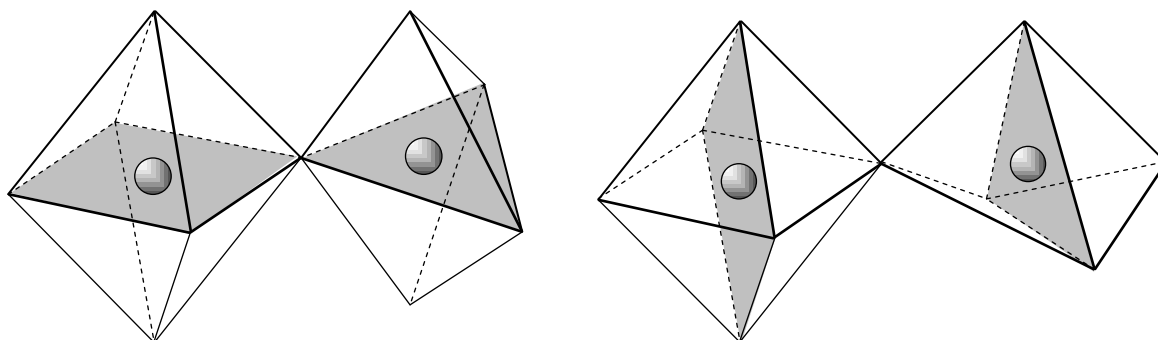


Fig.11.1.8: Schematics of possible in-plane (left) and apical (right) connections for MnO_6 Octahedra and MnO_5 bipyramid groups (angular variants and multiple dispositions of Jahn-Teller's distortion not shown).

Although the relative amount of such atypical $\text{O}_5\text{Mn—O—MnO}_4$ arrangements can be very small, they have a privileged spatial distribution at the surface of the $\text{La}_{0.7}\text{Sr}_{0.3}\text{MnO}_3$ grains, since it composes a minority phase enclosed by the dominant LuMnO_3 phase, as happens in samples Lu78LSM and Lu89LSM, hence a considerable part of the sample surface (roughly estimated $>10\%$) may exhibit these special arrangements that became exposed to the laser stimulation, revealing active Raman modes and contributing to the rich spectra found in these samples, not found in the single phase's perovskite or hexagonal compounds.

A deeper insight about these possible structural arrangements and properties would require a more extended and specific research to substantiate this hypothesis.

VSM measurements of the magnetic moment as function of temperature (M vs. T) for three of the composite samples and the single phase LSM100 and LuM100 samples are presented in figure 11.1.9. The AFM-PM transition of the LuMnO_3 phase can be easily recognized and enhanced in graph (c) by subtraction from the original M vs. T curve the linear fit found in the range from 85 to 95 K. Samples Lu78LSM and Lu89LSM also exhibit patent perturbations in the range 80 to 100 K, respectively zoomed in graphs (a) and (b) of same figure. These amplified disturbances can be attributed to the high susceptibility of the dispersed $\text{La}_{0.7}\text{Sr}_{0.3}\text{MnO}_3$ phase (under low magnetic field) easily responsive to local changes in the magnetic environment originated in the neighboring LuMnO_3 phase matrix. Sample Lu96LSM and sample LSM100 reveal the presence of a small magnetic transition near 40 K possibly due to a marginal contamination of Mn_3O_4 phase [11.1.11], although not perceptible in the XRD diffractograms indexations.

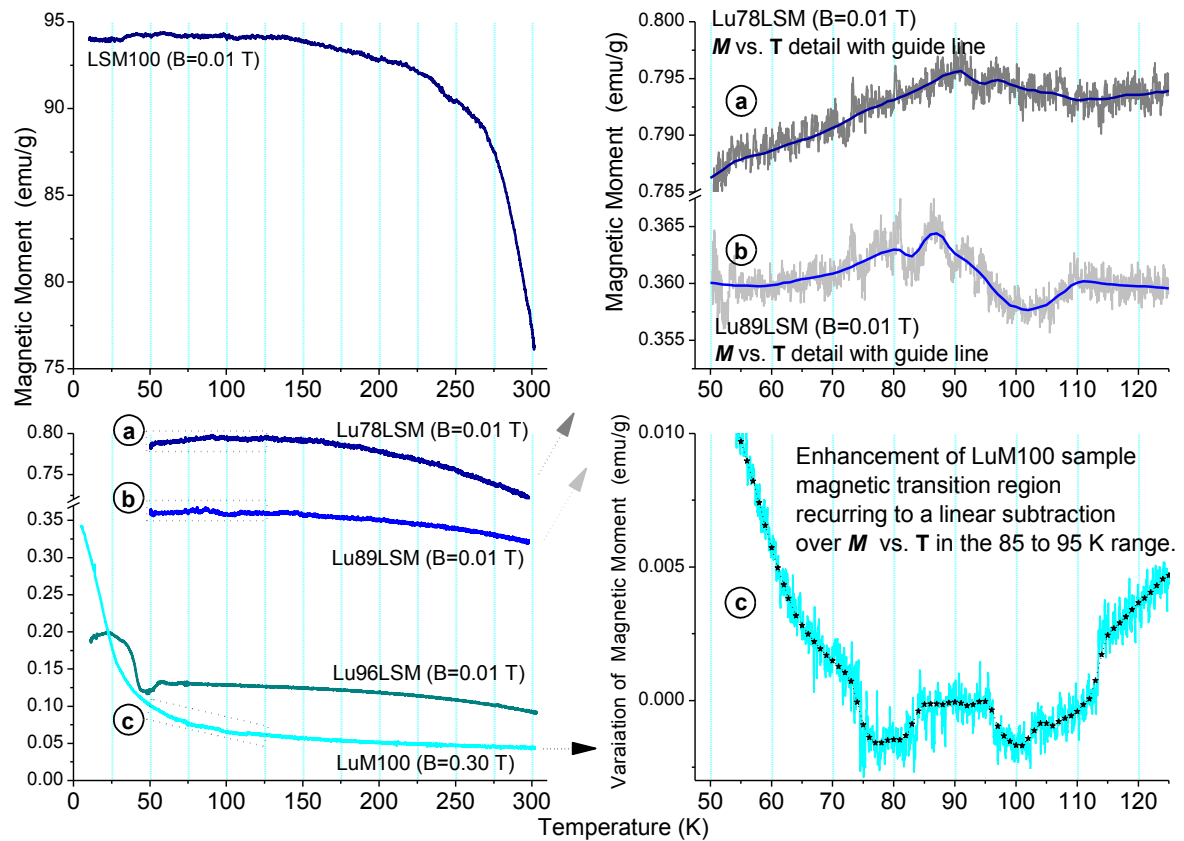


Fig.11.1.9: Magnetization (in emu/g) as function of temperature (at low B) Sample LSM100 (top left), composites and LuM100 samples (bottom left). Detail of M vs. T over region 50 to 125 K (right) for Lu78LSM (a), Lu89LSM (b) samples and enhancement of AFM transition at ~90 K for LuM100 sample (c).

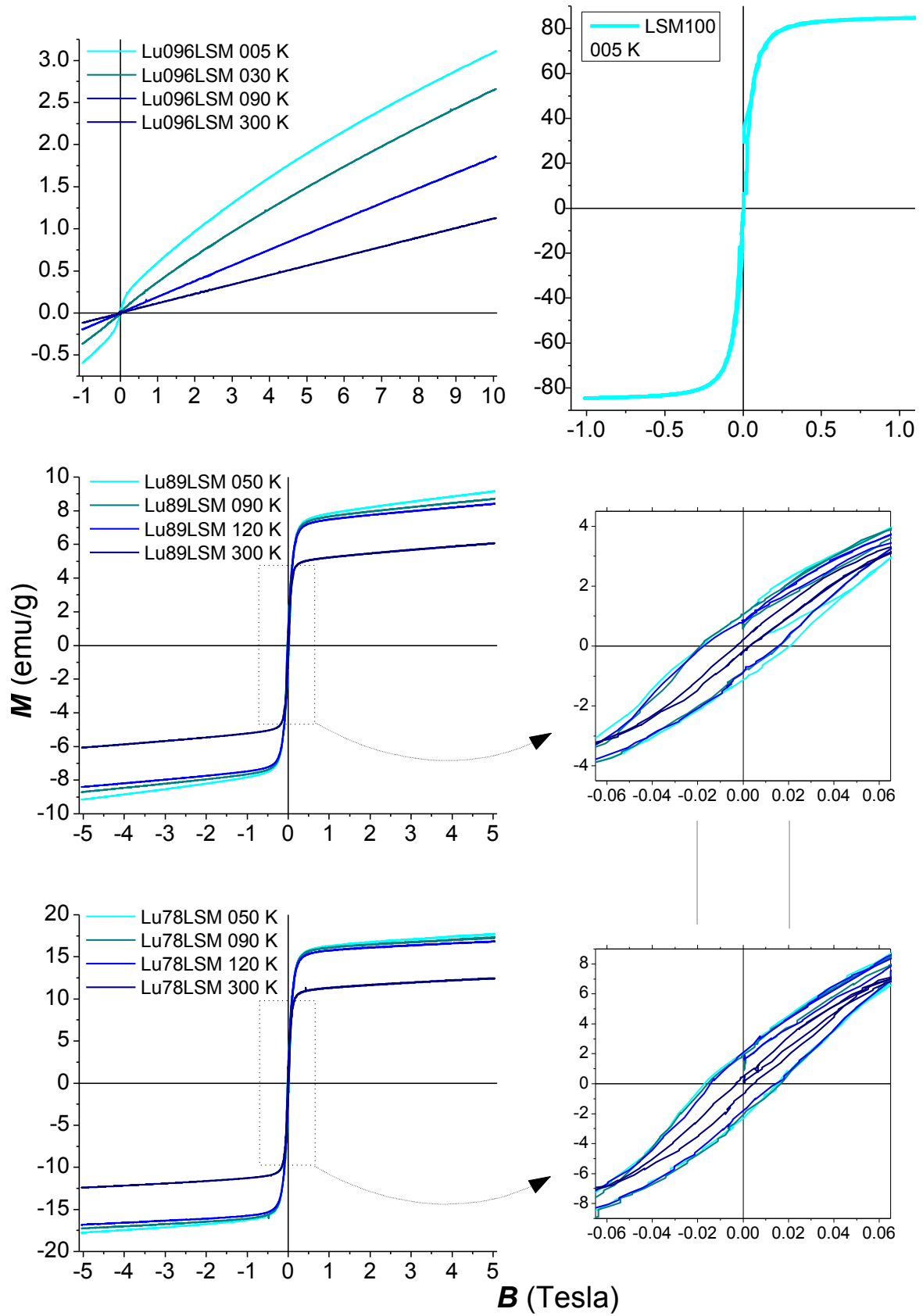


Fig.11.1.10: M (in emu/g) as function of external field B (in Tesla) for several temperatures: Lu96LSM (top left), LSM100 (top right); Lu89LSM (center) and Lu78LSM (bottom) with respective hysteresis loop details.

From \mathbf{M} vs. \mathbf{B} measurements shown in figure 11.1.10 it is possible to observe that the increasing ferromagnetic moment in each sample is directly proportional to the $\text{La}_{0.7}\text{Sr}_{0.3}\text{MnO}_3$ phase present in each sample and fully compatible with the nominal composition sequence of these samples series.

The saturation magnetic moment obtained at 90 K under 1 Tesla for sample Lu78LSM is ~ 16 emu/g and for sample Lu89LSM is ~ 8 emu/g; these values are coherent with the estimated mass ($\sim 22\%$ and $\sim 11\%$ respectively) presence of the $\text{La}_{0.7}\text{Sr}_{0.3}\text{MnO}_3$ phase, which in the plain LSM100 sample reaches the expected ~ 90 emu/g [11.1.12]. The non percolative distribution and some isolated nano particles of this ferromagnetic phase inside the paramagnetic matrix (above 100 K) could explain the (super)paramagnetic contribution found at higher magnetic fields in the composite samples.

VSM measurements of magnetic moment as function of field (\mathbf{M} vs. \mathbf{B}) for the same three composite samples and the single phase LSM100 sample (only at 5 K) are compared in figure 11.1.10. The presence and proportion of the LuMnO_3 phase is detected either by the PM (above 100 K) or AFM (below ~ 100 K) response, both adding a linear contribution in \mathbf{M} proportional to \mathbf{B} , clearly visible over the typical ferromagnetic behavior of the LSM phase. In its turn, from the hysteresis loops also detailed in figure 11.1.10, it is possible to observe equivalent coercive fields ($\mathbf{B}_{\text{coer.}}$) for the same temperatures in each sample. These details corroborate the similarity of the $\text{La}_{0.7}\text{Sr}_{0.3}\text{MnO}_3$ phase in both samples.

Only the two samples of this series which are mainly composed by the $\text{La}_{0.7}\text{Sr}_{0.3}\text{MnO}_3$ phase, have sufficiently low resistivity to perform magneto-resistance measurements (MR) in the available setup. The set of measurements performed in sample LSM100 are presented in figure 11.1.11; and for sample Lu04LSM in figure 11.1.12.

From figure 11.1.11 $\mathbf{R}(\mathbf{B})$ vs. \mathbf{T} graph it is possible to recognize the M-I transition at ~ 291 K and a subtle rise in resistivity trend above 330 K due to the regular PM transition without magnetic field, whereas under 1 Tesla field the long range FM order endures up to ~ 380 K keeping the former resistivity trend, which originate an accessional trend in MR up to 380 K. The room temperature MR $\sim 2\%$ at 1 T falls within the expected CMR performance for the $\text{La}_{0.7}\text{Sr}_{0.3}\text{MnO}_3$ phase [11.1.13].

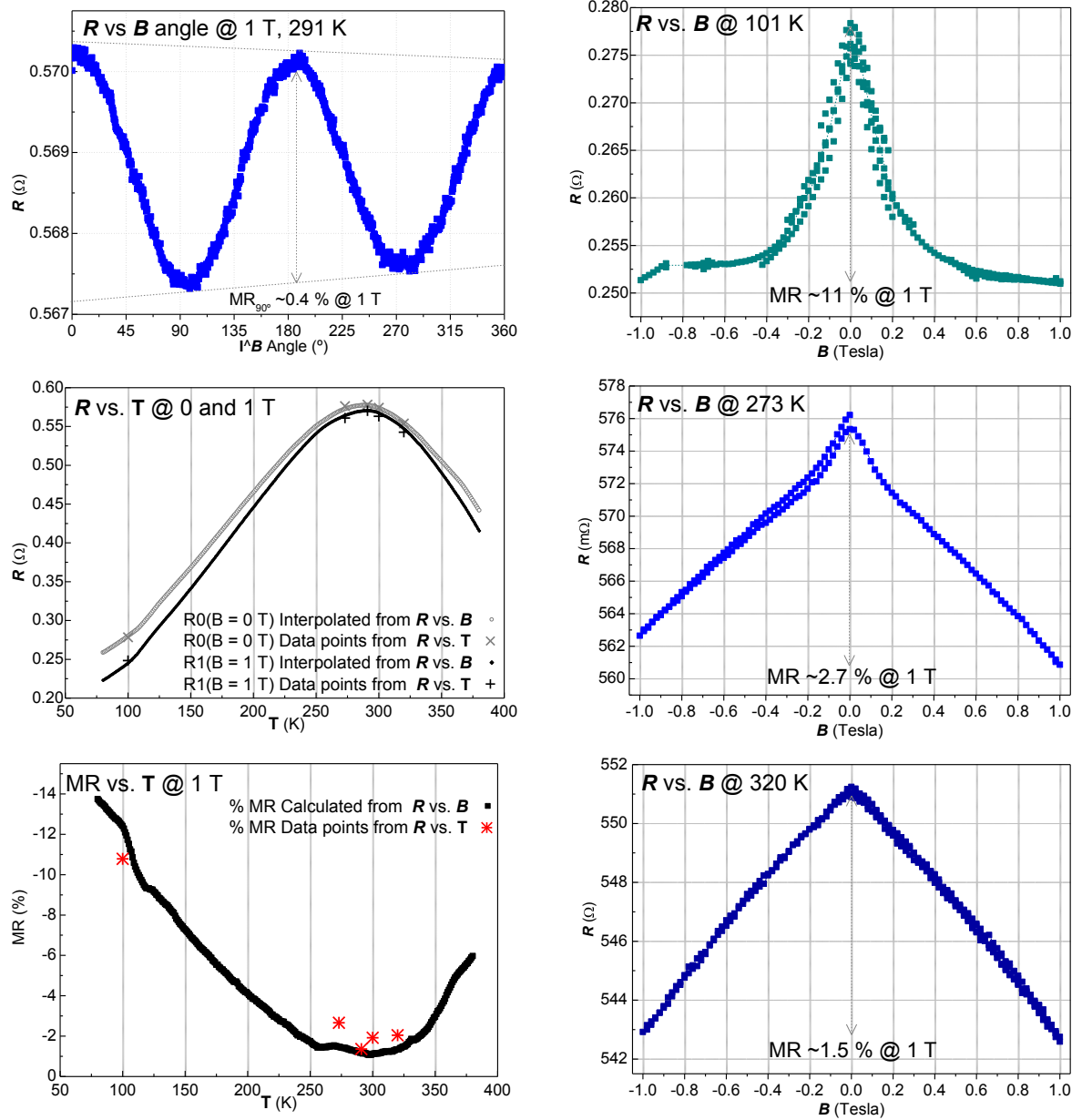


Fig.11.1.11: Magneto-Resistance measurements performed for sample LSM100: R as function of the angle between the magnetic field and the d.c. current going through the sample (top left); R as function of T at 0 and under 1 Tesla field (center left) and respective graph of MR as function of temperature (low left); R as function of B at 101 K (top right), 273 K (center right) and 320 K (low right).

For sample Lu04LSM the $R(B)$ vs. T graph clearly shows two relative maxima, one at ~ 238 K corresponding also to a relative increase in MR associated to the M-I transition and another at ~ 342 K associated to the PM transition. The resistivity increase relatively to the single phase sample is justified by the additional scattering introduced by the dispersion of dielectric LuMnO_3 nanometric grains in the $\text{La}_{0.7}\text{Sr}_{0.3}\text{MnO}_3$ matrix; in its turn, this may contribute to localized inhomogeneities in the manganite main phase and explain the appearance of two resistivity peaks.

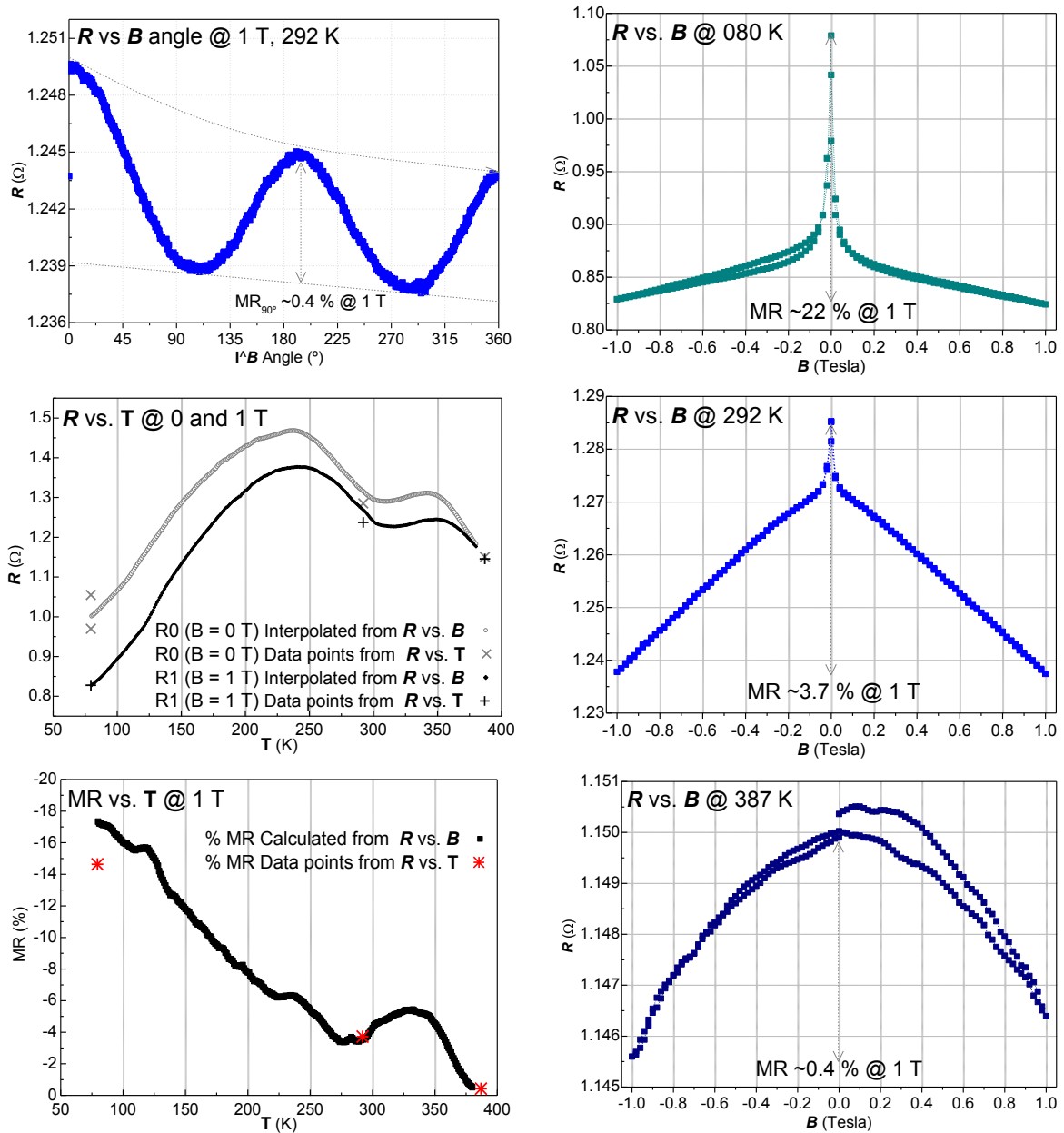


Fig.11.1.12: Magneto-Resistance measurements performed for sample Lu04LSM: R as function of the angle between the magnetic field and the d.c. current going through the sample (top left); R as function of T at 0 and under 1 Tesla field (center left) and respective graph of MR as function of temperature (low left); R as function of B at 80 K (top right), 292 K (center right) and 387 K (low right).

Comparing both samples graphs of MR vs. T , we observe that the ripples detected at 100-120 K can be attributed to noise originated by the beginning of liquid N_2 bath evaporation during measurements; it is patent that both samples' present a regular MR drop from low temperature reaching the relative minima at ~ 280 K, then keeping a smooth variation up to ~ 330 K, after which there is a stronger change in the MR trend suggesting the occurrence of the FM-PM transition.

These results substantiate the endurance of the FM state beyond the 300 K measured with the VSM system and is in close agreement with a Curie temperature above 330 K [11.1.14] intended for the $\text{La}_{0.7}\text{Sr}_{0.3}\text{MnO}_3$ nominal composition, as recognized in the respective $\text{La}_{1-x}\text{Sr}_x\text{MnO}_3$ phase diagram described in section 4.2.

As the samples are cycled through -1 to +1 tesla, either in angle (R vs. θ graphs showing approximately an anisotropic MR of ~ 0.4 % at room temperature) or in intensity (R vs. B graphs), a progressive drop in resistivity can be observed; this memory effect is a natural result of the magnetic hysteresis, magnetostriction and structural anisotropies mechanisms of the material, leading to a non reproducible history of the Bloch Walls displacements, enhancing the cumulative percolation of the magnetic domains which volume distribution is correlated to the electrical conduction paths, eventually stabilizing after some cycles.

Different magneto-resistance mechanisms operating in the $\text{La}_{0.7}\text{Sr}_{0.3}\text{MnO}_3$ phase can be observed in the succession of R vs. B graphs obtained at different temperatures, present in figures 11.1.11 and 11.1.12. Besides the intrinsic double-exchange model that explains the conductivity by means of electron hopping dependency on the alignment of neighboring Mn ions spins, there is also the role of the electron-phonon coupling (polaron), mediated by the Jahn-Teller splitting, giving rise to additional structural interactions that modify the charge carriers mobility and justify the more complex behavior of the resistivity as function of temperature or magnetic field [11.1.15].

For T below the Curie transition, and for polycrystalline samples, the MR response is strongly influenced by the tunneling effect through the grains boundaries barrier and mediated by the charge carries spin and the relative orientation of the magnetic moment of each grain [11.1.16]. The progressive alignment of the grains magnetic moment gives rise to a sharp MR response at low magnetic fields; then as the grains reach a common alignment the MR tends to stabilize near a linear relation to the external magnetic field dominated by the intrinsic mechanisms described above.

For T above the paramagnetic transition (~ 330 K) the cooperative spin mediated mechanisms disappear and the MR follows a quadratic dependence with the B field characteristic of the conventional paramagnetic scattering mechanism described in section 6.8.

Magneto-Impedance (MZ) measurements performed at room temperature as function of the applied electric field frequency and the external magnetic field for the four composite samples and the single phase LSM100 and LuM100 samples are presented in figure 11.1.13.

In table 11.1.3 are represented some illustrative impedance measurements performed on samples' at 10^3 , 10^5 and 10^7 Hz for 0 and 0.5 Tesla, plus the resulting MZ value; at 10^3 Hz under zero magnetic field the values were calibrated/normalized to resistance (R) $\sim 0.262 \Omega$ and reactance (R') $\sim 0.01 \Omega$. As for the magnetization, it becomes possible to trace a pattern for the magneto-impedance response along the series of samples, coherent with the series nominal composition sequence.

Samples LSM100 and Lu04LSM have equivalent behaviors since the similar $\text{La}_{0.7}\text{Sr}_{0.3}\text{MnO}_3$ bulk phase is governed both samples response; the MZ increases in relation to the applied magnetic field from 3 kHz up to 100 kHz, and then stabilizes up to 10 MHz. The most significant enhancement of the MZ variation with frequency is obtained at moderated fields up to 0.1 Tesla, consistent with the respective susceptibility behavior inferred from the figure 11.1.10; whereas the convergence of the MZ response at higher fields is a result of reaching the material magnetic saturation as can be observed in figure 11.1.14.

Sample:	Frequency (s ⁻¹)	$R(B=0)$ (Ω)	$R'(B=0)$ (Ω)	$Z(B=0)$ (Ω)	$R(B=.5 \text{ T})$ (Ω)	$R'(B=.5 \text{ T})$ (Ω)	$Z(B=.5 \text{ T})$ (Ω)	MZ %
LSM100	10^3	0.264	0.010	0.264	0.264	0.008	0.264	0.050
	10^5	0.273	1.207	1.238	0.271	0.969	1.006	18.735
	10^7	36.354	114.591	120.220	28.761	91.985	96.376	19.833
Lu04LSM	10^3	0.262	0.011	0.262	0.262	0.008	0.262	0.049
	10^5	0.271	1.330	1.357	0.269	0.967	1.003	26.073
	10^7	40.342	127.396	133.631	28.655	91.984	96.344	27.903
Lu78LSM	10^3	0.262	0.008	0.262	0.262	0.008	0.262	0.006
	10^5	0.272	1.008	1.044	0.271	0.980	1.017	2.631
	10^7	36.240	105.924	111.952	35.387	103.241	109.137	2.598
Lu89LSM	10^3	0.261	0.008	0.261	0.261	0.008	0.261	0.021
	10^5	0.269	0.972	1.009	0.268	0.958	0.995	1.348
	10^7	31.230	90.062	95.323	30.835	89.002	94.192	1.186
Lu96LSM	10^3	0.262	0.008	0.262	0.262	0.008	0.262	0.002
	10^5	0.270	0.967	1.004	0.269	0.961	0.998	0.588
	10^7	25.314	80.331	84.225	25.256	80.118	84.005	0.261
LuM100	10^3	0.261	0.007	0.261	0.261	0.008	0.261	0.014
	10^5	0.269	0.963	1.000	0.268	0.959	0.996	0.407
	10^7	31.484	88.598	94.026	31.376	88.562	93.956	0.074

Table 11.1.3: Illustrative values of MZ measurements at room temperature for the LuM+LSM samples series.

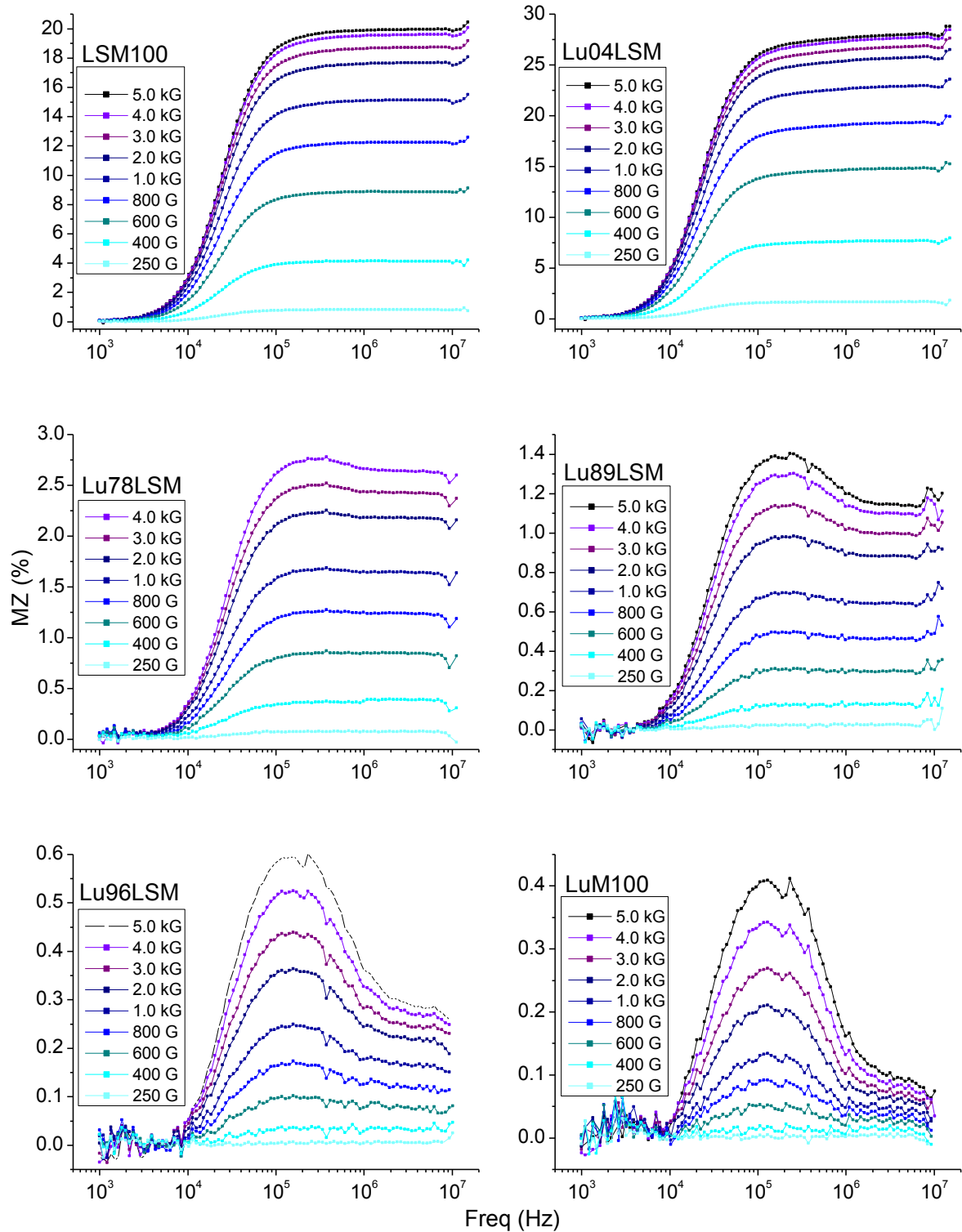


Fig.11.1.13: Graphs of Magneto-Impedance response with frequency and magnetic field at room temperature, for the LuM+LSM samples' series.

Sample Lu04LSM MZ response is ~40% superior to that of LSM100 under equivalent magnetic fields, owing mostly to the small presence of the LuMnO_3 dielectric phase which contributes to higher electrical impedance at ground magnetic field. In the other range of compositions the sample's MZ response is dominated by the preponderance of the LuMnO_3 dielectric/paramagnetic phase; for sample LuM100, MZ grows proportionally to the external magnetic field from 10 kHz up to 100 KHz then inflects and drops to $\sim 1/4^{\text{th}}$ of the maximum value previously reached until 1 MHz, then the decay slows down to $\sim 1/6^{\text{th}}$ until 10 MHz. The paramagnetic nature of the bulk LuMnO_3 phase is consistent with the regular spacing between successive MZ curves obtained for increasing magnetic fields, since the sample doesn't reach magnetic saturation. This paramagnetism has asufficient susceptibility to the bias magnetic field contributing to the real component of magneto-impedance response ($\sim 0.3\%$ at 10^5 Hz, 5 kG as seen in figure 11.1.13 for sample LuM100 MZ graph), the strong frequency dependent electrical response effect arises from the ferroelectric nature of the material, in this case, the circuits established tend to resonate near $\sim 10^5$ Hz.

The analysis of the MZ behavior of samples Lu96LSM, Lu89LSM and Lu78LSM can be summarized as the sum of the two distinct MZ curves obtained for sample LSM100 and LuM100, in relation to the phase's proportion found in each sample.

Due to the typical magneto-resistive manganites' character of the pseudo perovskite $\text{La}_{0.7}\text{Sr}_{0.3}\text{MnO}_3$ phase, a significant decrease in samples' resistance under the effect of an external magnetic field was expected. The outcome of applying an a.c. electrical field follows similar explanation, within a given frequency, as the material's electrons spins align with the bias magnetic field, the overall resistance lowers (as explained in section 6.8 and 6.8 and 6.10), due to the conductive behavior the reactance also drops, and hence the impedance.

The composite sample Lu78LSM was selected to undergo more specific analysis, considering upon the lack of electric conductivity (d.c.) and previous MZ results which proven the overall dielectric behavior of sample implying a non percolated distribution of the $\text{La}_{0.7}\text{Sr}_{0.3}\text{MnO}_3$ phase in the LuMnO_3 matrix; VSM also confirms the higher content in this FM phase; in addition SEM-EDS and Raman spectroscopy suggest an homogeneous dispersion and close contact between grains surfaces.

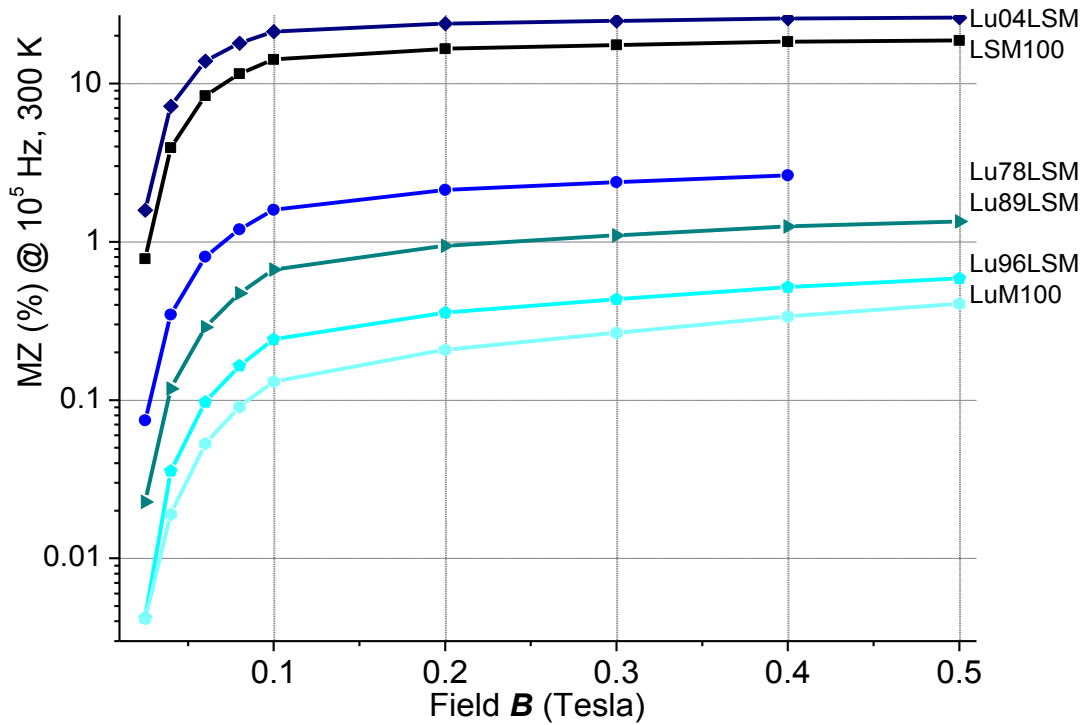


Fig.11.1.14: Magneto-Impedance response for the LuM+LSM samples' series with magnetic field at 10^5 Hz and room temperature

Magneto-impedance becomes a complementary measurement to magneto-resistance since measurements can be performed in non conductive samples and has the advantage not to depend on setting a bias electrical current through the sample, on the other hand, the acquired data only makes sense for frequencies above 10^3 or 10^4 Hz.

Magnetic Force Microscopy surface measurements performed in sample Lu78LSM are depicted in figure 11.1.15. In a rather smooth surface region of $5 \times 5 \mu\text{m}$, as can be observed by the deflection scan, it is possible to identify by the magnetic amplitude scan small group of independent magnetic domains; considering the relative size of these domains in the order of ~ 0.5 to $1 \mu\text{m}$, in principle each one is constituted by a small cluster of grains resulting from the segregation of the $\text{La}_{0.7}\text{Sr}_{0.3}\text{MnO}_3$ phase from the LuMnO_3 matrix.

The neighboring LuMnO_3 region of one of the magnetic clusters was subjected to a 20 V bias electric field; the expected electrostriction had a direct influence in the cluster magnetic easy direction, forcing the original domain orientation by $\sim 0.8^\circ$; as can prove the phase measurements performed on the region cross section going through two independent domains.

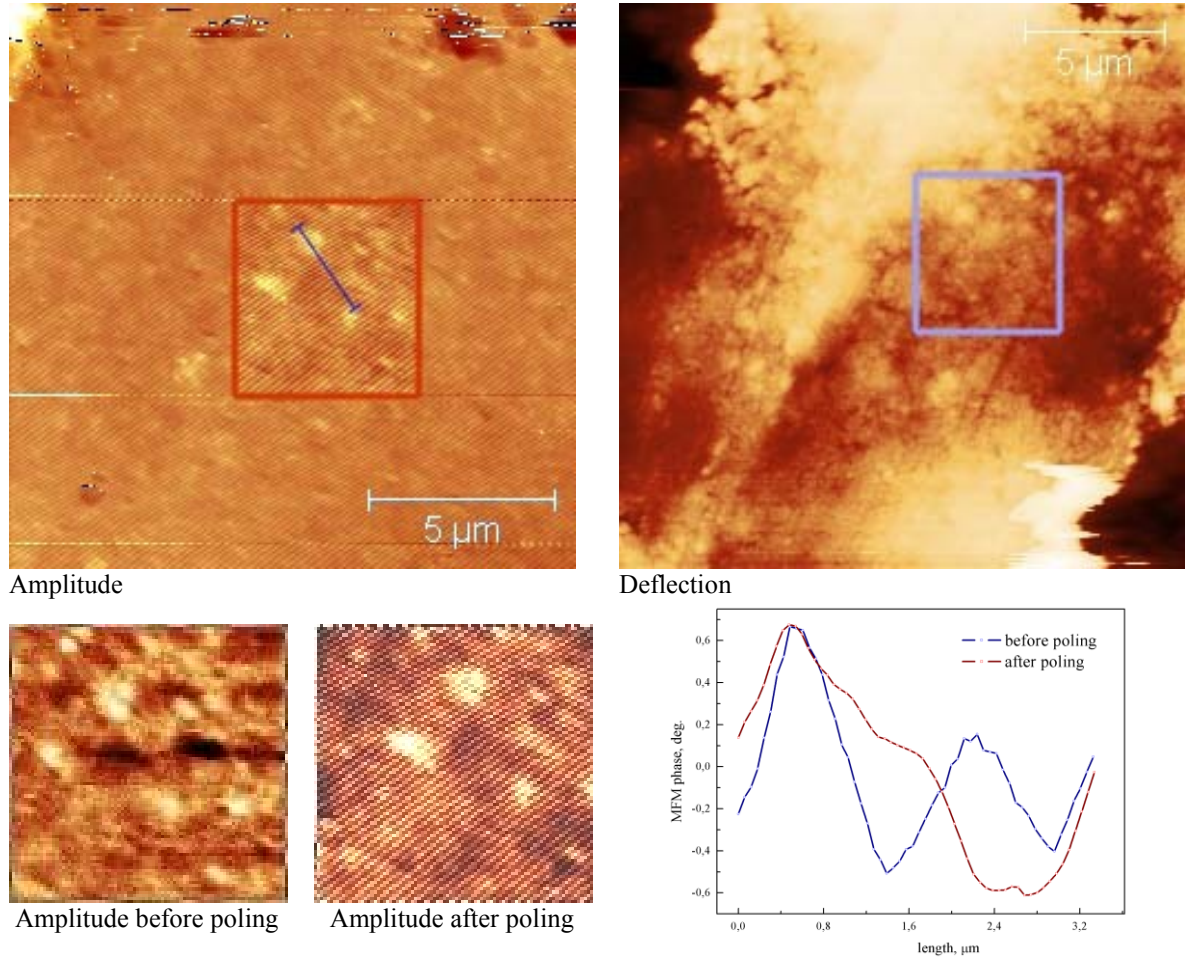


Fig. 11.1.15: Magnetic Force Microscopy of sample LuM78LSM at 25° C: Magnetic amplitude (top left) and respective tip deflection (top right); detail of region before and after being subject to electric poling: amplitude (bottom left) and cross section phase measurement (bottom right).

It was also only possible to perform magneto-electric effect measurements at room temperature in this sample. The graphical results of the experimental ME effect measurements are presented in figure 11.1.16. The initial drop in the electric response for small bias magnetic field, <0.3 Tesla at 25 and 50 kHz and for <0.2 Tesla at 100 kHz, is likely influenced by the incomplete magnetization of the $\text{La}_{0.7}\text{Sr}_{0.3}\text{MnO}_3$, in close relation to the previous VSM magnetic measurements, only when this phase becomes magnetically saturated, there can be a cooperative effect of the modulation imposed by the small a.c. magnetic field stimulation, augmenting with the bias external magnetic field intensity.

These results validate that the composite sample Lu78LSM has in fact magneto-electric effect properties reaching ~150 mV/m.Oe; the material stimulated with 10^5 Hz magnetic field of only 10 Gauss amplitude, can generate a correlated a.c. electric field ~300% higher under a bias external field of 1 Tesla than without the field.

This ME coefficient was validated by an independent measurement system, obtaining 113 mV/m.Oe at 10^5 Hz and using a bias Magnetic field of only 500 Oe.

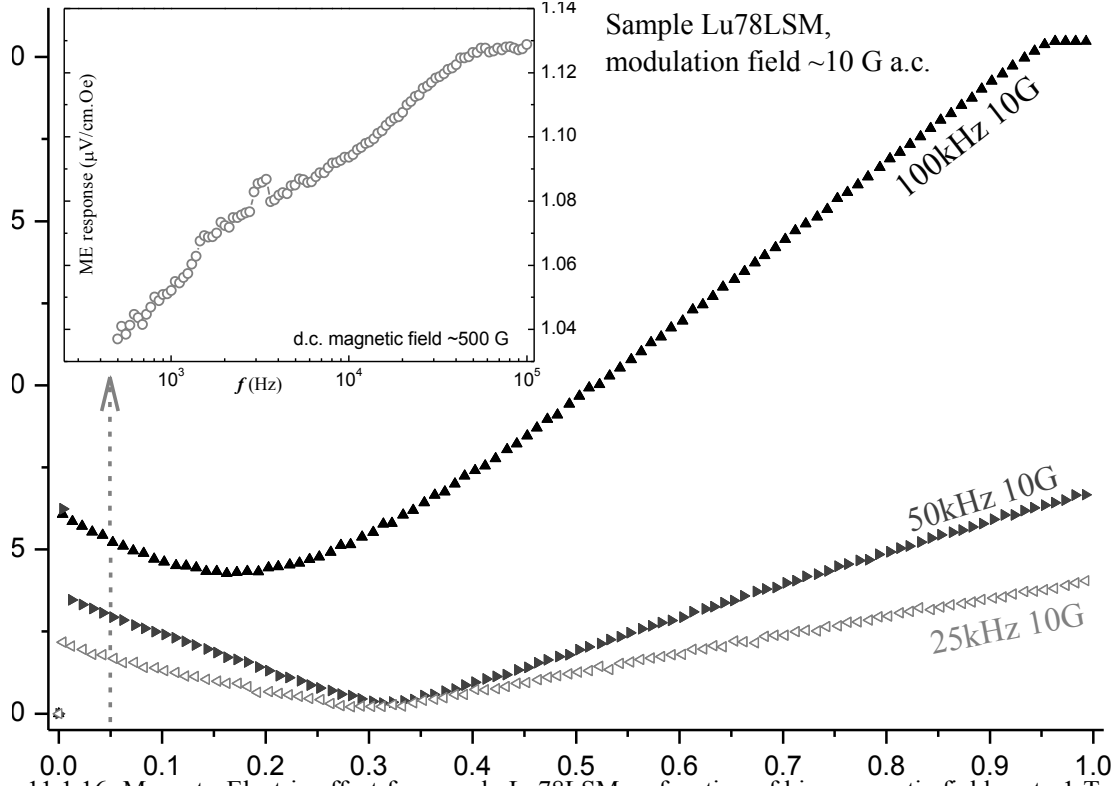


Fig. 11.1.16: Magneto-Electric effect for sample Lu78LSM as function of bias magnetic field up to 1 Tesla, for 3 frequencies at 10 Gauss a.c. stimulation field. Inset: ME coefficient as function of frequency at 500 Oe.

Most studies performed on analogous LuMnO_3 and $\text{La}_{1-x}\text{Sr}_x\text{MnO}_3$ composites are incipient when concerning the investigation of magnetoelectric effects in such potential multiferroic system. The previously referred [11.0.2], [11.0.3], [11.0.4] and also [11.1.17], [11.1.18] are mainly concerned with structural aspects, some relevant transport and magnetic measurements can be found in [11.1.19], where the authors consider an improbable $\text{Lu}_{0.7}\text{Sr}_{0.3}\text{MnO}_3$ hexagonal phase without any evidence to sustain such claim; on the other hand in [4.1.17], the influence of the LuMnO_3 phase transition at ~ 90 K is clearly visible in the resistivity vs. temperature response, but the authors state that such composite system seems "chemically unfeasible in the bulk" which we hereby prove otherwise.

11.2. Self doped $\text{LuMn}_{1-z}\text{O}_{3-\delta}$ ($z = 0.00, 0.02, 0.06$) Nano Powders

In the sequence of the previous studies on non-stoichiometric manganites [11.2.1], the relevance of self-doping has been proven useful for modifying specific characteristics like magneto-resistive response, critical temperature, conductive behavior, magnetic structure, etc.; as well minimizing the need for introducing extrinsic elements.

The LuMnO_3 compound presents intrinsic multiferroic proprieties below the Néel temperature ($T_N \sim 90$ K), where the ferroelectric behavior coexists with the canted antiferromagnetic ordering; further investigation on Mn deficient $\text{LuMn}_{1-z}\text{O}_{3-\delta}$ was carried out in order to study the role of the competing interactions between the Mn ions moments in complex magnetic orders. In order to keep the overall crystalline structure and to preserve the fundamental ferroelectric mechanisms from the parent LuMnO_3 compound, only a minor percentage of Manganese atoms are removed; the accommodation of such low Mn vacancies ($z \ll 10\%$) should not have major implication in the compound Oxygen stoichiometry, hence it is estimated the presence of a correlated number ($3z$) of Mn^{4+} ions which will locally shift the regular AFM ($\text{Mn}^{3+}\text{--O--Mn}^{3+}$) “super-exchange” coupling to a FM ($\text{Mn}^{3+}\text{--O--Mn}^{4+}$) “double-exchange”. Thus the Mn^{4+} magnetic moment tends to align with a neighboring Mn^{3+} , although the triangular disposition ($\theta \sim 120^\circ$) result a weaker electron transfer integral compared to the ($150^\circ < \theta < 180^\circ$) found on perovskite manganites.

In addition, according to the model described in [11.2.2], the triangular spins geometry, found in such hexagonal manganites, induces an electric dipole given by the correlation:

$$\begin{cases} P_x \propto S_1 \cdot (S_2 + S_3) - 2 \cdot S_2 \cdot S_3 \\ P_y \propto S_1 \cdot (S_2 - S_3) \end{cases} \quad (\text{Polarization from spins in triangular geometry})$$

The vacancies and particularly the presence of Mn^{4+} ions will tend to hamper the magnetic frustration of the former Mn^{3+} ions triangular lattice; the new spins configuration is also expected to have a direct impact into the intrinsic magneto-electric coupling of the material; besides, eventual long range coordination of the resulting magnetic moments modifies the material magnetic susceptibility; hence new multiferroic phases may be anticipated in the self doped system. In order to support this thesis, a more specific study of samples LuMn100 , LuMn098 and LuMn094 was carried out, comparing experimental results with referenced data on the LuMnO_3 manganite.

XRD diffractograms and respective Rietveld refinement results are presented in figure 11.2.1 and table 11.2.1:

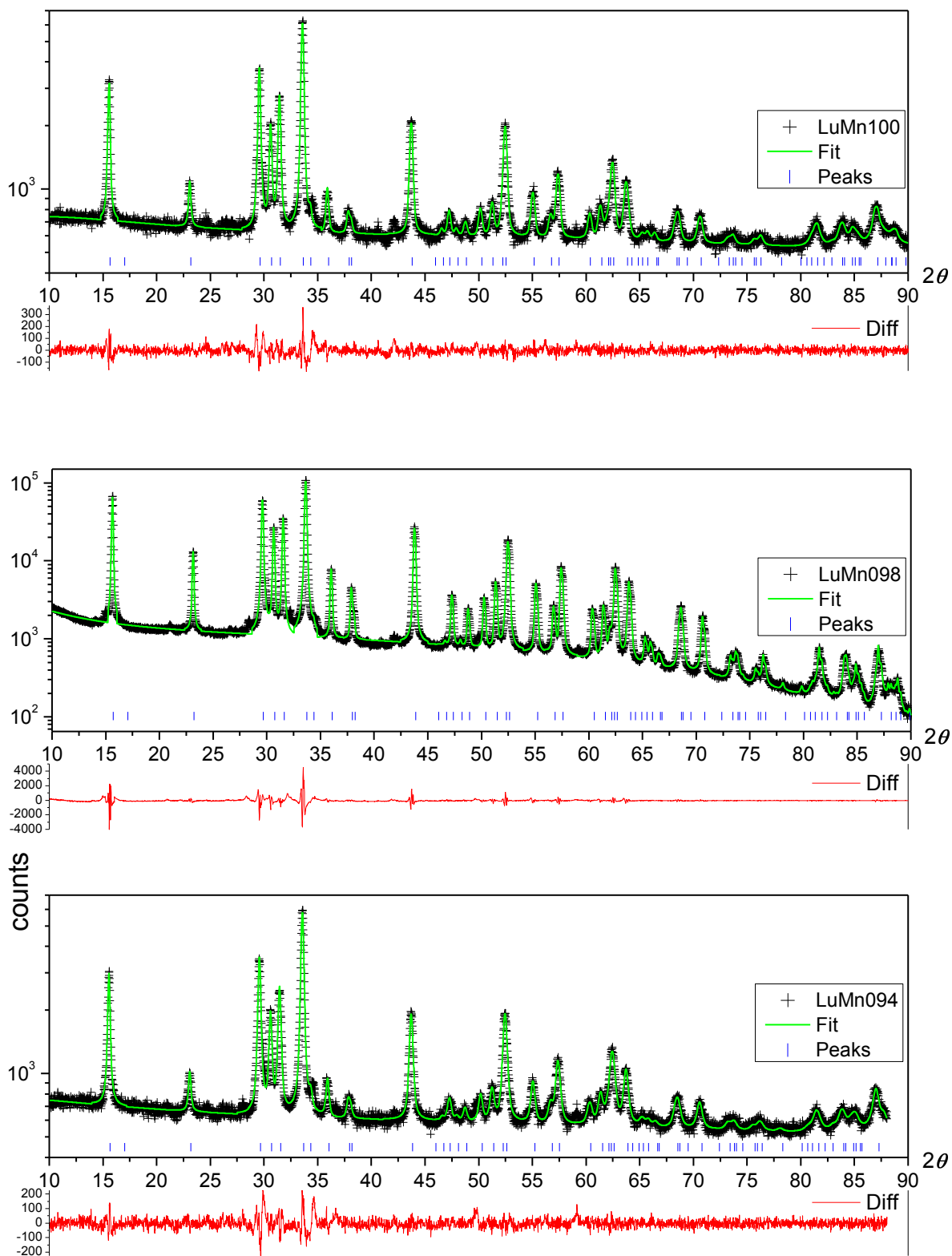


Fig. 11.2.1: XRD patterns and Rietveld refinements for the series of samples $\text{LuMn}_{1-x}\text{O}_3$.

It is possible to discriminate a small volume contraction as the number of Mn vacancies increase, although this tendency can be less significant when only three experimental samples are considered and these cell parameters found are consistent and comprised within the LuMnO_3 referenced data variance, as described in table 11.2.1. Having in mind that for a system with identical nominal composition the resulting structure can have deviations on the purity, homogeneity, grain size, and Oxygen incorporation, depending on the sample preparation method and thermal treatments.

sample	Synthesis method	Sintering-anneal T/C	<crystal> type	a, b Å	c Å	Volume Å ³	χ^2	H field kOe	T K	M emu/g	PM: μ_B/Mn^{3+}
LuMnO ₃ [4.4.1]	Solid State	1000-1300	poly >>1 μm^3	6.038	11.361	358.70	--			--	
LuMnO ₃ [4.4.2]	Flux in Bi ₂ O ₃	1250-1450	single >>1 mm ³	6.042	11.362	359.21	--			--	
LuMnO ₃ [4.4.5]	Solid State	1100-1400	poly >>1 μm^3					1	5	0.02	4.8
LuMnO ₃ [11.2.3]	Floating-zone	1200-1350	single >>1 mm ³	6.048	11.411	361.47	--	1	5	0.02	
LuMnO ₃ [11.2.4]	Solid State	1400- 800	poly >>1 μm^3	6.039	11.367	359.01	--	0.1	5	0.02	
LuMnO ₃ [11.2.5]	Solid State	1300-1300	poly >>1 μm^3	6.044	11.371	359.73	--	1	5	0.02	4.9
LuMnO ₃ [11.2.6]	Floating-zone	1300-1300	single >>1 mm ³	6.05	11.4	361.37	--	1	5	0.02	
LuMnO ₃ [11.2.7]	Solid State	1100-1400	poly >>1 μm^3	6.053	11.3704	360.76		1	5	0.02	
LuMnO ₃ [11.2.8]	EDTA	1000-1300	poly >>1 μm^3	6.047	11.372	360.08	--	1	5	0.02	
LuMnO ₃ [11.2.9]	Solid State	1200-1350	poly >>1 μm^3	6.046	11.407	361.11	--				3.1
LuMnO ₃ [11.2.10]	Flux in Bi ₂ O ₃	1250-1450	single >>1 mm ³	6.042	11.370	359.46	--			--	
LuMnO ₃ [11.2.11]	Solid State	1100-1100	poly < 1 μm^3	6.087	11.384	365.29	--	5	5	0.13	3.2
LuMnO ₃ [11.2.12]	Solid State	900-1300	poly >1 μm^3	6.046	11.370	359.896	--	1	40	0.11	--
LuMnO ₃ [11.2.13]	hydrothermal	250- 80	40x400 nm	6.055	11.389	361.61	--				
LuMnO ₃ [11.2.14]	hydrothermal	750 - 750	32 nm				--	0.01	5	0.16	--
LuMn100	Sol-Gel Urea Combustion	800 - 900	56 nm	6.048	11.389	360.79	0.2	3	5	0.34	4.70
LuMn098	Sol-Gel Urea Combustion	1200- 900	92 nm	6.046	11.366	359.82	3.4	3	5	0.07	5.27
LuMn094	Sol-Gel Urea Combustion	800- 900	46 nm	6.040	11.374	359.38	0.3	3	5	0.14	5.04

Table 11.2.1: Comparison of P6₃cm S.G. cell parameters at 300 K and Magnetization at ~5 K for LuMnO₃ compounds in referenced data and for the 3 LuMn_{1-z}O_{3- δ} samples.

Most pertinent modification on the original LuMnO_3 magnetic behavior is put in evidence by VSM measurements as shown in figure 11.2.2:

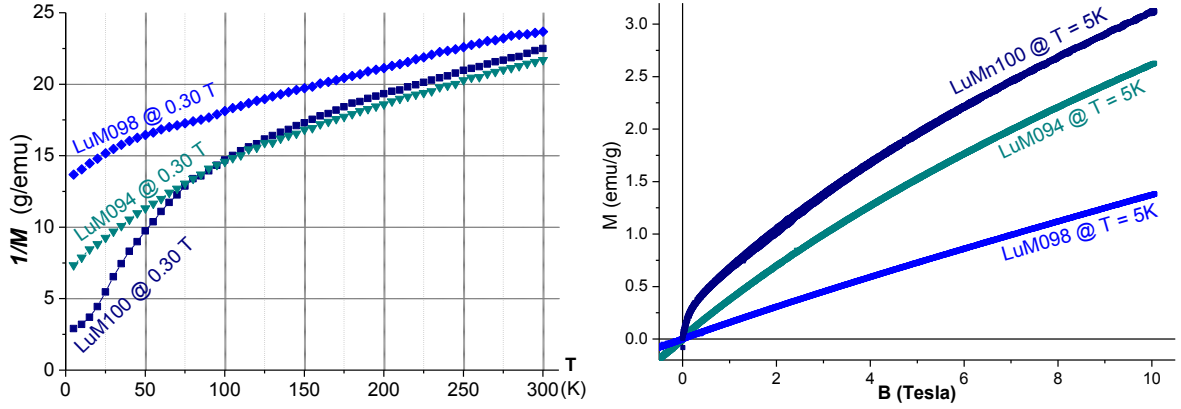


Fig. 11.2.2: VSM measurements of the $\text{LuMn}_{1-x}\text{O}_3$ samples $1/M$ vs. T at 0.03 T (left), M vs. B at 5 K (right).

VSM M vs. T measurements obtained at 0.3 tesla, expressed as $1/M$ vs. T in left graph of figure 11.2.2, clearly reveal a magnetic anomaly at ~ 90 K typically recognized as the characteristic PM to AFM transition LuMnO_3 phase.

This set of experimental samples $\text{LuMn}_{1-x}\text{O}_{1-\delta}$ exhibits a net paramagnetic moment listed in table 11.2.1 calculated by applying the Curie-Weiss model above 150 K. For the LuM100 sample the magnetic moment by Mn ion is $\sim 4.7 \mu_B$ in close agreement to the LuMnO_3 phase referenced in [4.4.5] and [11.2.5]. The two self-doped samples show a significant increase in the effective magnetization surpassing $5 \mu_B$; this higher value could be explained by the presence of Mn^{4+} ions, although with a lower magnetic moment, the preferential/instantaneous FM coupling with a neighboring Mn^{3+} magnetic moment promotes a higher average alignment with the small external magnetic field even in the paramagnetic regime.

A higher mass magnetization below the Néel transition can also be traced to LuMnO_3 nanopowders reported in [11.2.11] and [11.2.14]; these samples were synthesized at lower temperatures, resulting smaller grain size and implying a wider specific surface; in addition, the phase diagram of manganites synthesis [11.1.4], [11.2.15], also attest that relatively low annealing temperature ($< 1000^\circ \text{C}$) promotes Oxygen intake while the small grain size facilitates the diffusion. Such factors generates localized Mn^{4+} ions which can couple ferromagnetically to neighboring Mn^{3+} ions, hence contributing to the higher overall magnetization of LuMnO_3 AFM phase nano-powders in relation to micron sized powders, as reported in [4.4.5] and [11.2.3 to 11.2.8]; as summarized in table 11.2.1.

The dominant antiferromagnetic ordering state can be also observed in the discrete mass magnetic moment exhibited, not achieving saturation even at 10 T in the M vs. B measurements at ~ 5 K, shown in right graph of figure 11.2.2. While samples LuM094 and LuM098 show a weak and rather linear magnetic susceptibility, the LuM100 sample reveals at low B field (<0.5 Tesla) a higher susceptibility trend suggesting an additional and distinct magnetic order state in the structure; this feature is also substantiated by the small anomalies detected at ~ 25 K and ~ 65 K in M vs. T response obtained below the conventional $T_{\text{Néel}}$ at ~ 90 K, as attest the derivatives in the left graph of figure 11.2.3. In comparison, similar magnetic anomalies on nanometric LuMnO_3 powders were detected at ~ 40 K [11.2.12] and at ~ 12 and ~ 44 K [11.2.14] as depicted in the example of the right graph of figure 12.2.3.

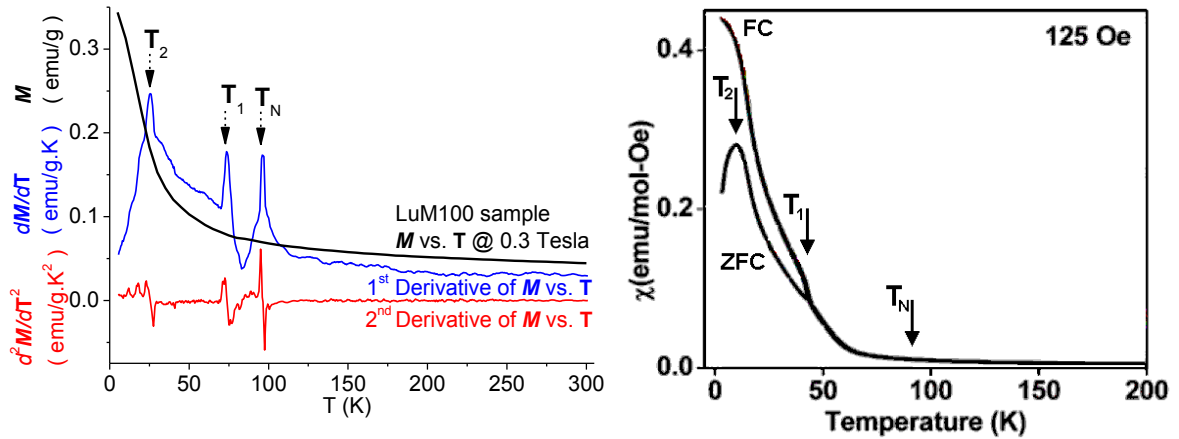


Fig. 11.2.3: Sample LuM100 M vs. T and derivatives (left); sample LuMnO_3 M vs. T from [12.2.14] (right).

Besides the grain size and surface thermodynamics aspects affecting magnetization, the anomalies observed below $T_{\text{Néel}}$ suggest rearrangements of the antiferromagnetic ordering structure in particularly under low magnetic fields, concurrent with the original and more conventional AFM phase that dominates at higher magnetic fields (>1000 Oe) [12.2.14].

The hexagonal LuMnO_3 structure allows various analogous triangular ordered antiferromagnetic arrangements. As temperature decreases the differences and adjustments in the basal and apical Mn--O--Mn bond lengths and angles lead to the appearance of subtle variations in Mn^{3+} --O-- Mn^{3+} super-exchange interactions highly sensitive to low applied magnetic field, but which are damped at higher fields.

In order to investigate this aspect, sample LuM098 was measured by NPD performed at 2 and 300 K as described in section 10, represented in figure 11.2.4:

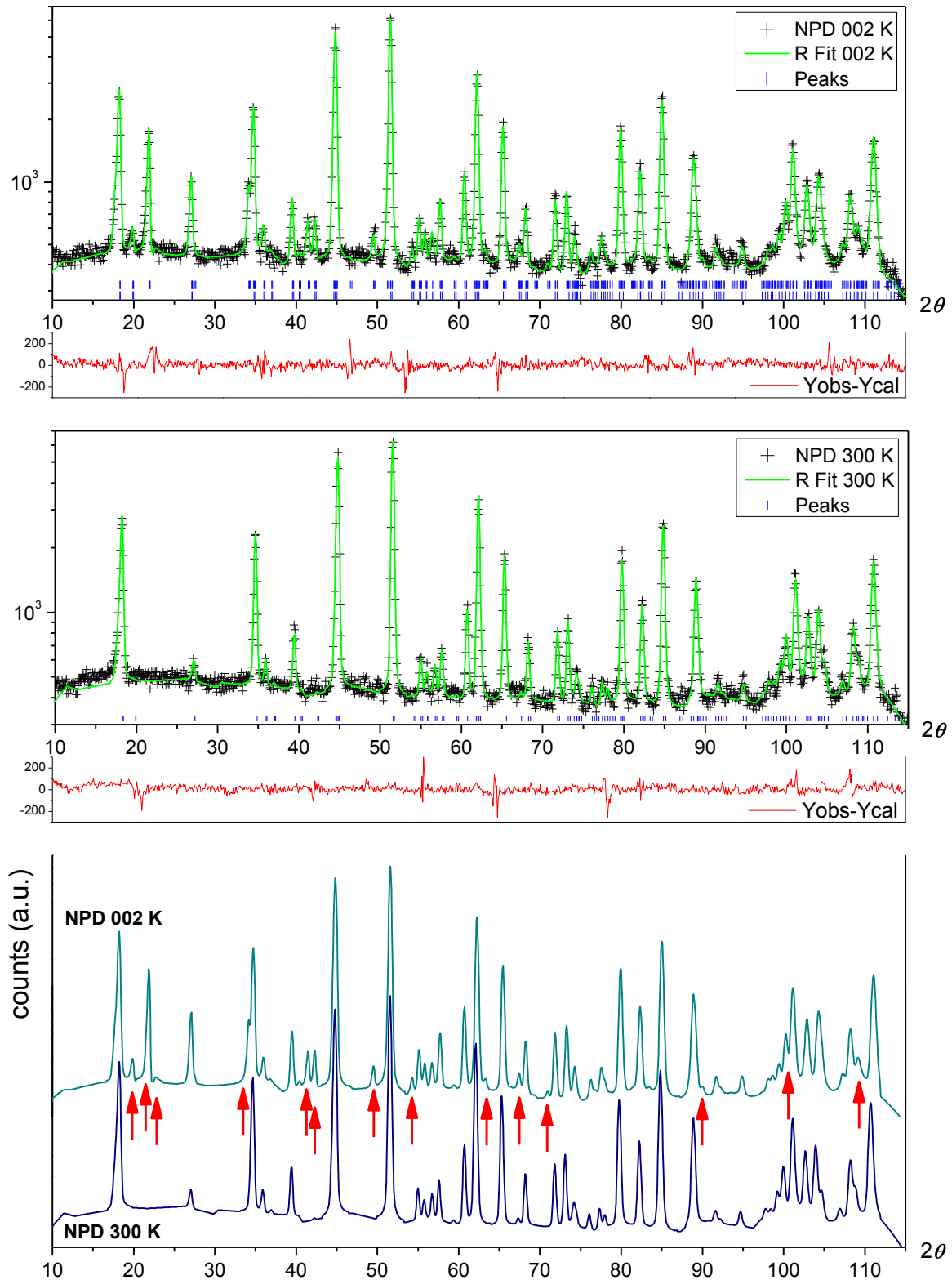
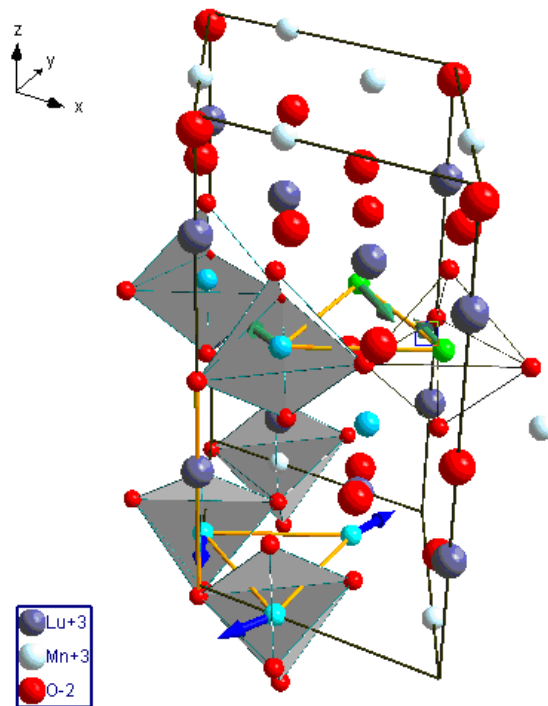


Fig. 11.2.4: NPD measurements of LuM098 sample performed 2 K (top) and at 300 K (center) with respective Rietveld refinements; comparison between the two diffractograms (bottom) marking the appearance of reflections from magnetic ordering (arrows).

Like in XRD, NPD measurements of sample LuM098 performed at ~ 300 K do not show distinctive features when compared to the parent stoichiometric LuMnO_3 paramagnetic phase [11.2.11]. At 2 K, a close inspection of the NPD diffractogram reveals the appearance a set of reflections related to magnetic neutron scattering not consistent with the crystal unit cell contributions; the dominant AFM coupling between adjacent Mn ions is confirmed by the strong intensity of the peaks (111), (103), (201) peculiar for antiferromagnetic order; in addition some peaks characteristic of ferromagnetic interactions (012), (112), (110) appear or become effectively amplified in comparison with the stoichiometric compound.

The presence of a small amount of Mn^{4+} ions in sample LuM098 justifies the discrepancy between the magnetic moment mean value of $\sim 2.84 \mu_B \pm 0.1$ per Mn ion calculated for the NPD diffractogram performed at 2 K, in relation to the $\sim 3.1 \mu_B$ measured by NPD described for the stoichiometric compound [11.2.9].

The calculated magnetic moments differentiated for each of the 6 Mn sites in the unit cell are illustrated in figure 11.2.5 alongside the structural lattice, and parameters described in table 11.2.2.



Formula	LuMnO_3		Z	6		
M (g/mol)	277.9 g/mol		ρ (g/cm ³)	7.708		
System	Hexagonal		S.G.	$P6_3cm$ (185)		
Cell (Å)	a = 6.02794		Volume (Å ³)	357.53		
	c = 11.36182					
label	type	Wyck.	<i>x/a</i>	<i>y/b</i>	<i>z/c</i>	S.O.F.
Lu1	Lu ⁺³	2a	0	0	0.2723	1
Lu2	Lu ⁺³	4b	1/3	2/3	0.2297	1
Mn1	Mn ⁺³	6c	0.3157	0	0	1
O1	O ⁻²	6c	0.3086	0	0.1665	1
O2	O ⁻²	6c	0.6383	0	0.3388	1
O3	O ⁻²	2a	0	0	0.4754	1
O4	O ⁻²	4b	1/3	2/3	0.0217	1
label	<i>x/a</i>	<i>y/b</i>	<i>z/c</i>	<i>M_x</i>	<i>M_y</i>	<i>M_z</i>
Mn1	0.3320	0	0	-2.779	-3.038	0.101
Mn2	0	0.3320	0	-0.011	-2.877	0.101
Mn3	0.6680	0.6680	0	2.299	3.055	0.104
Mn4	0.3320	0.3320	0.5	-1.887	1.261	0.104
Mn5	0.6680	1.0000	0.5	1.246	-2.035	0.101
Mn6	1.0000	0.6680	0.5	-1.246	2.03	0.101
ΣM_i				-2.378	-1.604	0.612

Fig. 11.2.5: Unit cell structure and Mn magnetic moments orientation determined for LuM098 sample from NPD measurements performed 2 K

Table 11.2.2: Unit cell and Mn magnetic moments parameters determined for LuM098 sample from NPD measurements performed 2 K.

Both XRD and NPD Rietveld refinements were not conclusive in determining preferential structural positions for vacancies or Mn^{4+} ions, neither to precise Manganese or Oxygen vacancies correspondent to the expected nominal composition of LuM098 sample. Nevertheless, cell volume is $\sim 0.8\%$ smaller relatively to the average cells present in table 11.2.1, pointing to eventual vacancies. The particular periodic distribution (long range coupling) of a non-compensated Mn ion magnetic moment is decisive to explain the anomalous ferromagnetic coupling detected in NPD diffractogram of the LuM098 sample at low temperatures. This distortion of the original magnetic frustration found in the LuMnO_3 stoichiometric phase could be interpreted either as a periodic distribution of Mn^{4+} ions within the system; or result of a small deformation in the bipyramids structures due to the combined effect of Manganese and Oxygen vacancies.

As consequence of this asymmetric and non-compensated new disposition of magnetic moments a significant enhancement of the anisotropic electric polarization in the basal (*ab*) plane is expected, at least 3-4 times, when compared to magnetic frustrated configurations, as elucidate the sketches and values indicated in figure 11.2.6.

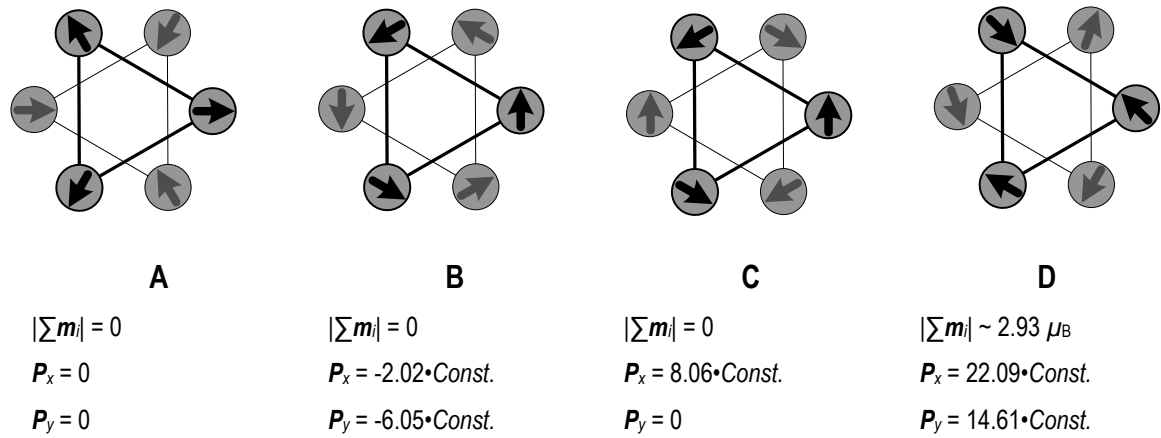


Fig. 11.2.6: Sketches of the Mn ions planes present in the LuMnO_3 in the $P6_3\text{cm}$ unit cell and respective planar polarization due to the triangular disposition of moments, considering an average magnetization for each Mn ion $\sim 2.84 \mu_B$. **A**, **B** and **C** represent possible magnetic frustration configurations [11.2.9], [11.2.16], [11.2.17]; **D** represents the configuration determined by NPD for the LuMn098 sample.

The polycrystalline LuM100 sample was used as an essay to perform experimental PFM measurements and use the innovative BEPS technique developed at CNMS-ORNL labs. Although the LuMnO_3 phase a relatively weak FE compared to PZT or PMN-PT, from the conventional PFM scan depicted in figure 11.2.7 it is possible to recognize in the surface some regions with piezoresponse amplitude and phase shift. Localized poling experiments up to 40 V offset bias reveled no lithographic effects; these regions are not necessarily fully polarized domains and may also result of the grains orientation, presenting easy or hard polarization axis relatively to the stimulation electric field.

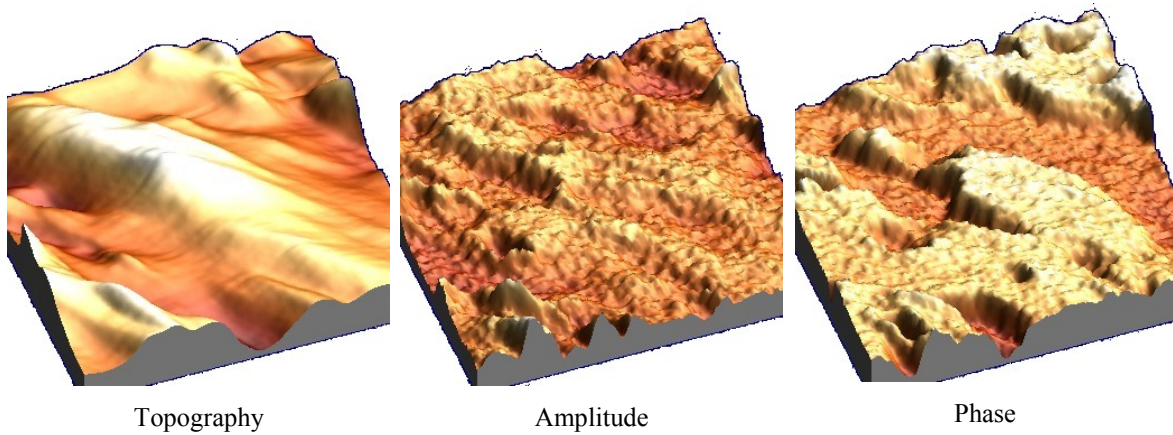


Fig. 11.2.7: PFM scan over a $5 \times 5 \mu\text{m}$ region of LuM100 sample' surface.

More thorough measurements by BEPS method sustain this hypothesis; in figure 11.2.8 it is possible to observe examples of scans showing that distinct regions have different resonant frequency dependence, implying different structural/elastic response. The respective local piezoresponse loops obtained are far from reaching full cycle in saturation and remanence reversal, even when subjecting the sample up to 80 V bias.

The system asymmetrical response in amplitude and phase delay to the external bias voltage signal is result of the relative orientation to the local polarization state; whereas the local resonance frequency dependence and loop energy dissipation results essentially of generating and switching the small polarization precession relatively to the easy and hard directions on the local structure orientation.

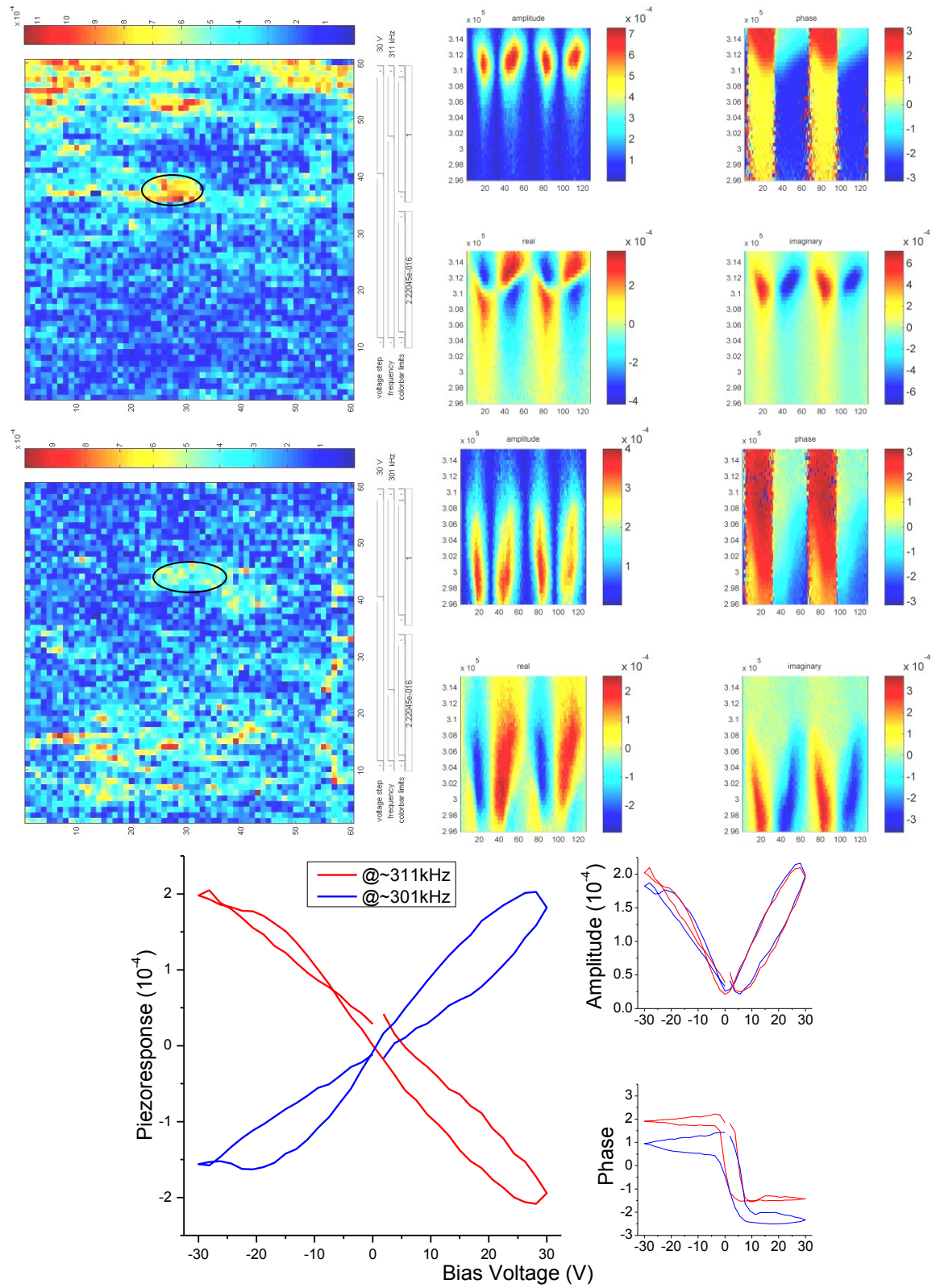


Fig. 11.2.8: Examples of BEPS scans of LuM100 sample. Each pixel corresponds to the local piezoresponse under the applied frequency and bias voltage: $5 \times 5 \mu\text{m}$ surface piezoresponse at $+30 \text{ V}_{\text{dc}}$ and 311 kHz (top left) and piezoresponse at $+30 \text{ V}_{\text{dc}}$ and 301 kHz (center left). Respective delimited regions (black encircles) averaged piezoresponse, amplitude and phase dependence to frequency (right) and loops as function of bias voltage (bottom).

Although the characterization is not complete because it was not possible to force polarization saturation during BEPS experiments, data processing presented in figure 11.2.9 confirms that sample LuM100 has in fact ferroelectric properties, with a small piezoresponse of the order $\sim 10^{-4}$ nm/V. The “V+”, “V-”, “imprint” and “switching polarization” maps of figure 11.2.8 also confirm the multidomain state (although not necessarily full saturated) of the polycrystalline system.

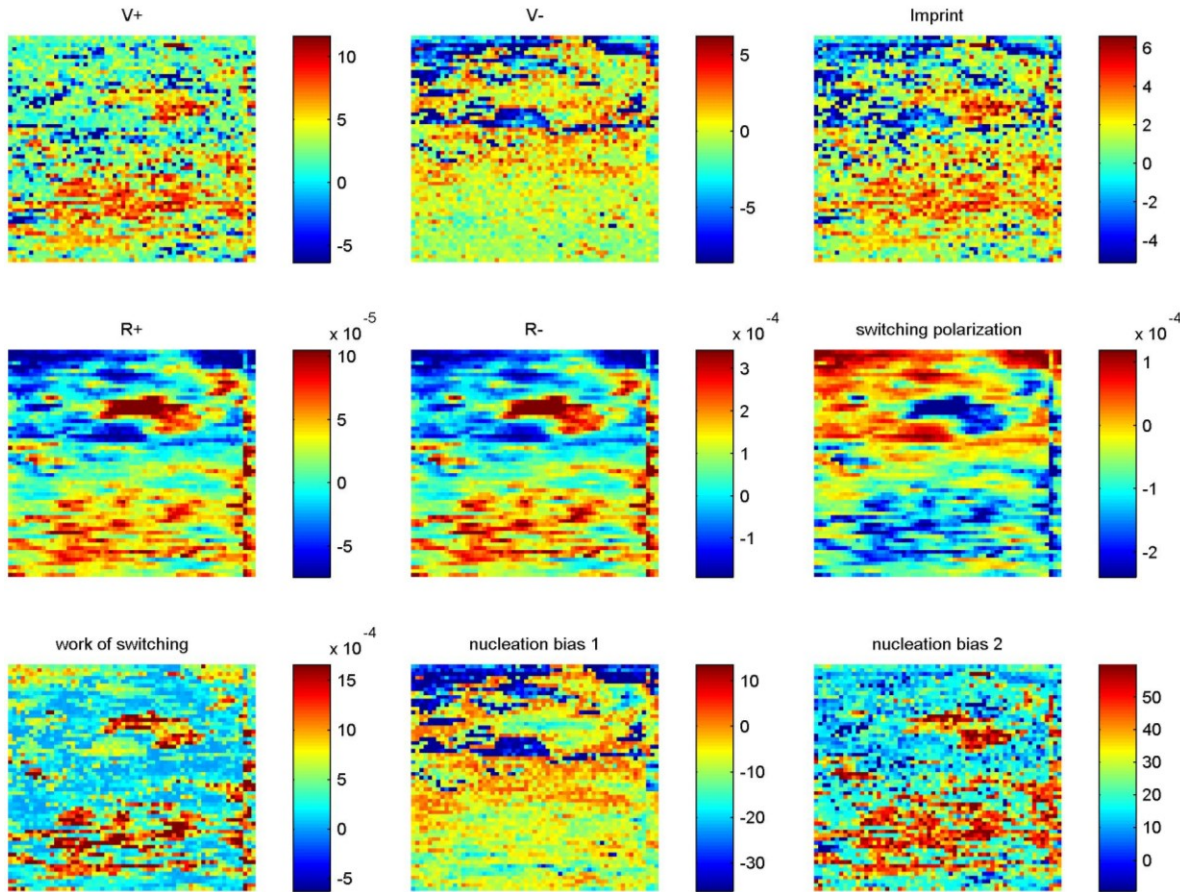


Fig. 11.2.9: PFM BEPS fitted piezoresponse coefficients maps over LuM100 5x5 μm sample surface.

It was not possible to access such comprehensive BEPS characterization for samples LuM098 or LuM094. Results of conventional PFM measurements performed in sample LuM094 at 50 kHz and ~ 10 V_{ac} are shown in figure 11.2.10. Like sample LuM100, this sample also reveals a weak piezoresponse with amplitude and phase contrast coincident with crystallites both before and after subjecting the region to a ± 50 V_{dc} cycle. In the experimental hysteresis loop obtained the system seems to saturate at 20 V bias.

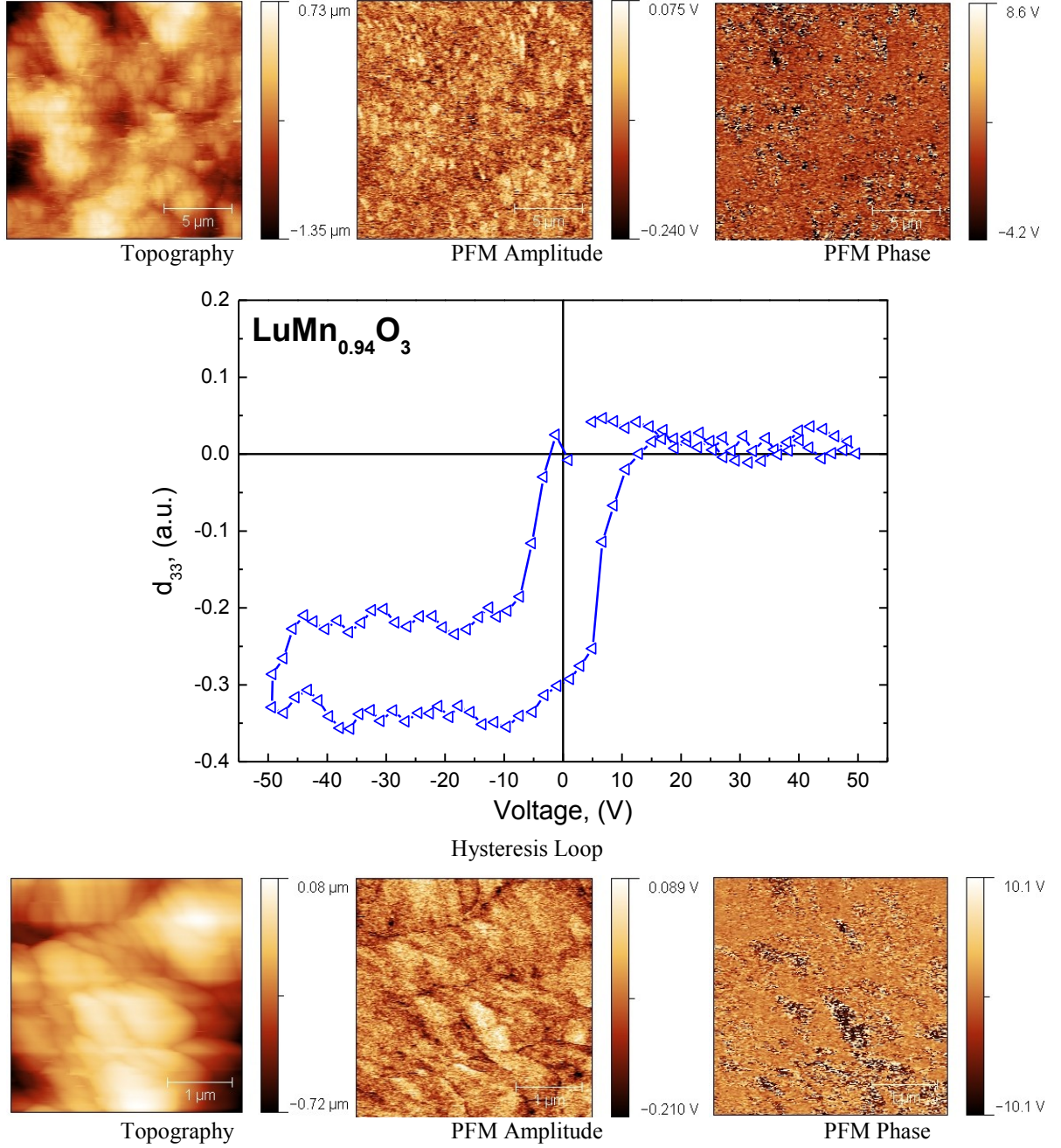


Fig. 11.2.10: PFM scans over LuM094 sample $17 \times 17 \mu\text{m}$ surface (top); local hysteresis loop at $0.1 \text{ Hz } \pm 50 \text{ V}$ cycle (center); PFM scans over a $5 \times 5 \mu\text{m}$ area after subjecting the region to the hysteresis loop (bottom).

PFM measurements in sample LuM094 confirm that the small Mn vacancy doping did not destroy the ferroelectric properties of the phase. In order to confirm this observation it is necessary to perform macroscopic polarization measurements

As expected from the hexagonal structure symmetry, preferential polarization axis are imposed by the crystallites orientation, hence grain boundaries delimit polarization domains.

11.3. Bulk Composites series of BaTiO₃ + La_{0.7}Ba_{0.3}MnO₃

Most research on composite multiferroics has been focused on FE perovskites like BaTiO₃ or PZT and FM spinels (Co,Ni,Zn)Fe₂O₄, taking advantage of the insulating electrical properties of these oxides [11.3.1]. Among the first research works on magnetoelectric coupling effects between two perovskite ferroic materials was the bulk composites (1-x)BaTiO₃+(x)LaMnO₃ [11.3.2], [11.3.3] prepared by solid state method above 1100 °C; by keeping the conductive phase bellow percolation threshold; this system demonstrated the coexistence of ferroelectricity and ferromagnetism at room temperature and the potential to achieve an electric field-induced magnetization change due to the emergent formation of the CMR La_{1-x}Ba_xMnO₃ phase. The authors defend that the composites ME performance improves when the diffusion of Ba ions into the LaMnO₃ phase conveniently reaches the La_{0.7}Ba_{0.3}MnO₃ composition ($T_{\text{Curie}} \sim 350$ K), noticing partial degradation of the FE properties of the BaTiO₃ phase due to the La-Ba and ions exchange.

Taking into consideration these results, we sought to investigate the properties of nano powders composites by mixing BaTiO₃ with the optimized La_{0.7}Ba_{0.3}MnO₃ composition, not recurring to high temperature synthesis or thermal treatments procedures in order to prevent inter phases' ions diffusion and extensive grain growth, yet taking advantage of the favourable phases interpenetration and inter connectivity namely by means of sharing an Oxygen ion between the different phases (O₅Ti—O—MnO₅) octahedrons along the grain boundaries.

The BTO+LBM series of samples, listed in table 8.2.1 and prepared as described in table 8.2.2, were measured by XRD, respective θ - 2θ powder diffractograms are shown in figure 11.3.1 and Rietveld refinements are summarized in table 11.3.1. Structural results present excellent overall reliability ($\chi^2 < 1$) confirming the tetragonal $P4mm$ (99) structure of BaTiO₃ phase indexed to the ICSD file #73643 [4.3.1], having cell parameters $a = b = 3.993$ and $c = 4.036$ Å, average crystallites size estimate 100 to 120 nm; the La_{0.7}Ba_{0.3}MnO₃ hexagonal $R-3c$ (167) phase is indexed to ICSD file #91185 [11.3.4], having $a = b = 5.532$ and $c = 13.489$ Å with average crystallites size between 40 to 50 nm.

No specific traces of BaO [11.3.5], TiO [11.3.6], TiO₂ (neither in the *Rutile*, *Anatase* [11.3.6] or *Brookite* [11.3.8] phases) or Ti₂O₃ [11.3.9] were detected in the series of diffractograms; also no Mn₃O₄ [11.3.10] or other spurious phases due to miscibility of the BaTiO₃ and the La_{0.7}Ba_{0.3}MnO₃ compounds were detected.

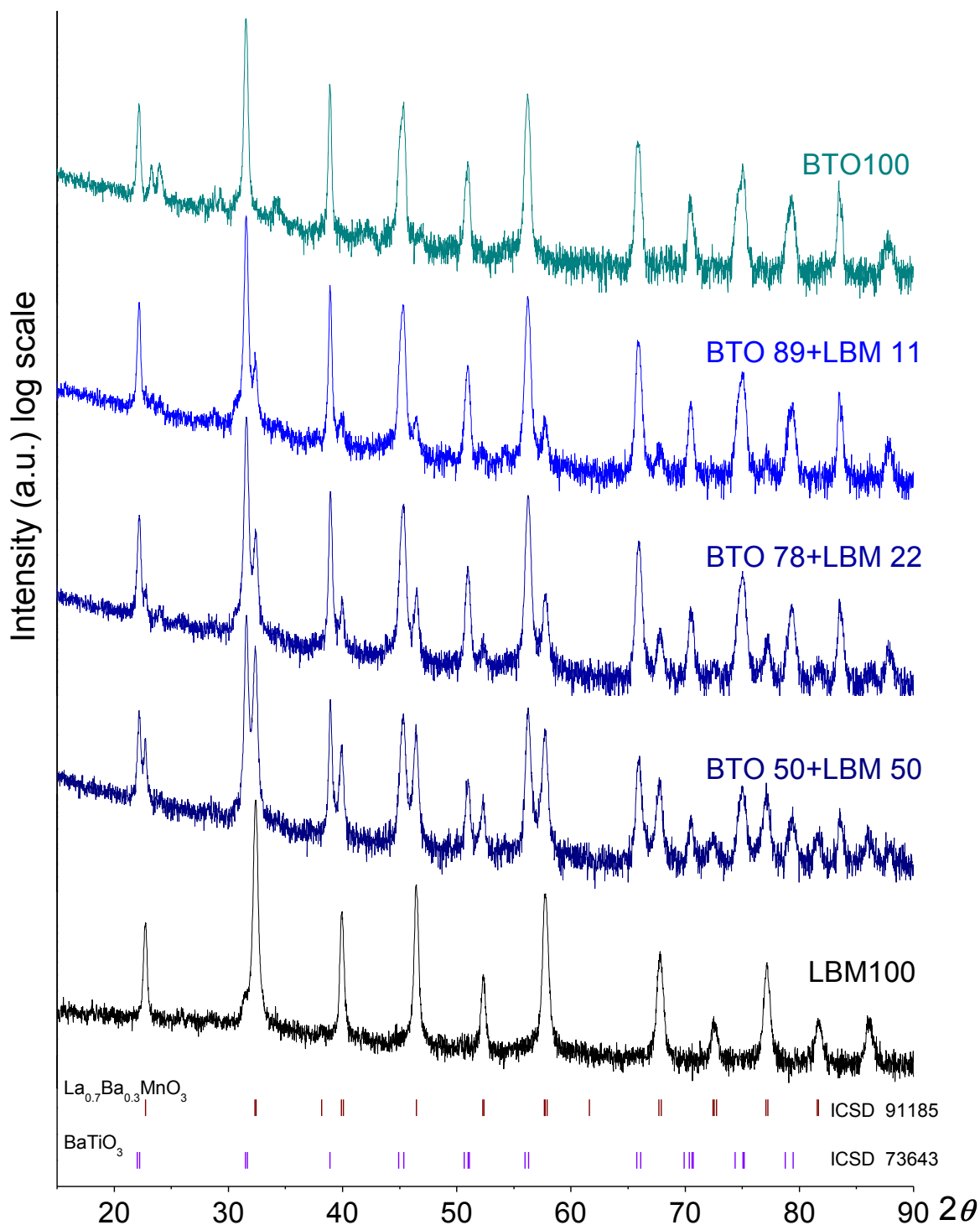


Fig. 11.3.1: XRD patterns for the series of samples BTO+LBM

Phase: Sample:	BaTiO ₃					La _{0.7} Ba _{0.3} MnO ₃					R _p	R _{wp}	R _{exp}
	<i>a</i>	<i>b</i>	ρ	scf	% Vol	<i>a</i>	<i>b</i>	ρ	scf	% Vol			
LBM100	--	--	--	--	0%	5.526	13.448	6.605	2.574	~100%	8.16	10.49	0.76
BTO50LBM50	3.998	4.017	6.031	1.3398	~62%	5.534	13.539	6.604	0.7996	~38%	6.64	8.84	0.14
BTO78LBM22	3.999	4.019	5.996	1.0132	~88%	5.535	13.498	6.605	0.1356	~12%	6.85	9.17	0.29
BTO89LBM11	3.999	4.019	5.995	1.1183	~95%	5.531	13.509	6.581	0.062	~5%	7.48	10.07	0.30
BTO100	3.999	4.023	5.989	1.114	~100%	--	--	--	--	0%	8.89	12.52	0.23

Table 11.3.1: Rietveld refinements results for the series of samples BTO+LBM.

Some minor unidentified peaks can be found at $2\theta \sim 23^\circ$ and $\sim 24^\circ$ in the BTO100 sample diffractogram, this eventual contamination has less relevance for the composite samples; also EDS-SEM measurements, exemplified in figure 11.3.2 and listed in table 11.3.2, do not detect other elements than the anticipated.

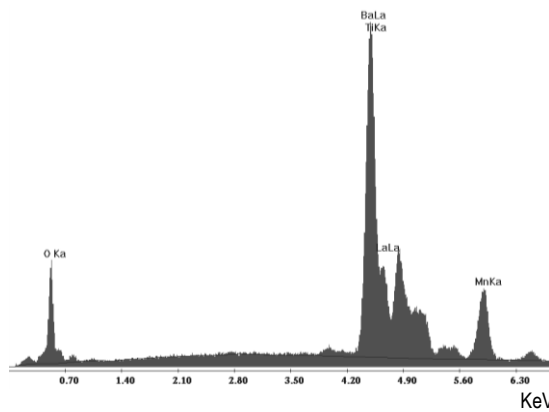


Fig. 11.3.2: Example of the EDS-SEM spectrogram obtained for sample BTO50LBM50.

Sample:	LBM100	BTO50 LBM50	BTO78 LBM22	BTO89 LBM11	BTO100
EDS @ 30 keV					
Element:	% atm.	% atm.	% atm.	% atm.	% atm.
O (K)	56.96	57.12	56.63	56.43	57.39
Ba (L)	6.88	14.60	19.12	20.45	22.18
Ti (K)	--	12.91	18.28	19.66	20.43
La (L)	14.79	6.48	2.65	1.49	--
Mn (K)	21.37	8.89	3.33	1.98	--
Normalized:	phase %	phase %	phase %	phase %	phase %
BaTiO ₃	--	~59	~84	~91	≡100
(LaBa)MnO ₃	≡100	~41	~16	~9	--

Table 11.3.2: EDS results and samples composition normalization.

The EDS results have a typical error of $\sim 1\%$ for each element; for the LBM100 compound was found an adequate proportion for La:Ba:Mn of 0.69/0.32/1.00, for the BTO100 sample there is a $\sim 10\%$ discrepancy of Ba over Ti, whereas for the composites the Mn:Ti normalization indicates that the fraction of La_{0.7}Ba_{0.3}MnO₃ compound is $\sim 80\%$ of the projected nominal composition; These statistics have correspondence to the respective scale factors estimated by XRD Rietveld refinement; consequently it becomes evident that the composites mixtures contain a small excess of the BaTiO₃ phase than the initially intended, nevertheless this does not alter the percolative distribution envisaged for the La_{0.7}Ba_{0.3}MnO₃ phase in sample BTO50LBM50, while for samples BTO78LBM22 and BTO89LBM11 this phase fraction is below percolation limit as it is further confirmed by MR measurements.

SEM images shown in figure 11.3.3, obtained following a fresh fracture of samples, confirm the submicron dimensions of both phases' grains, thus not permitting sufficient contrast to perform an EDS mapping; it is possible to observe only sparse porosity indicating that the selected pressing and thermal treatments procedures resulted in perceptible sintering phenomenon which promoted each phase densification and inter phase's close packing.

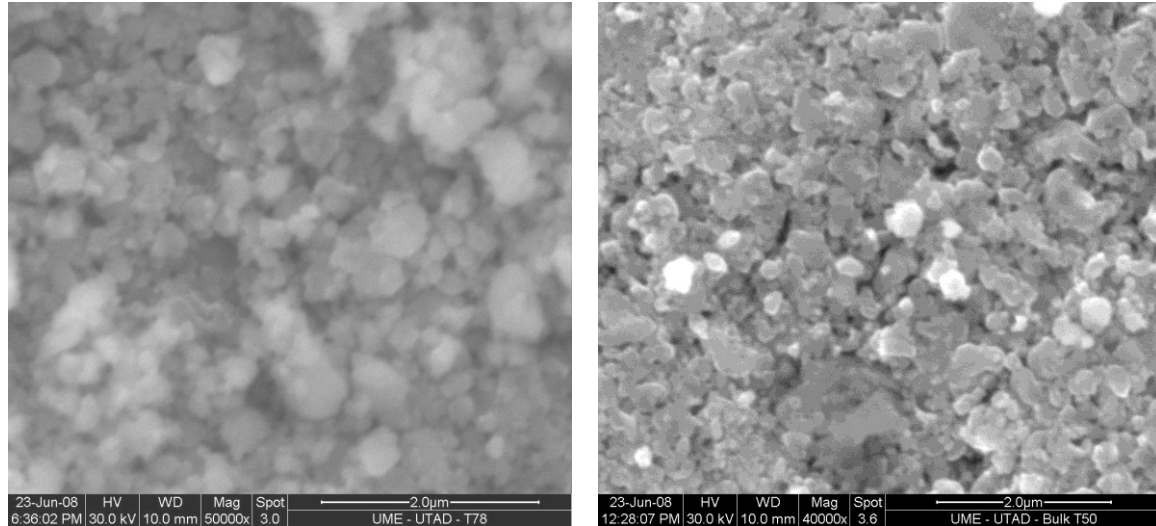


Fig. 11.3.3: SEM surface image for sample BTO78LBM22 (left) and BTO50LBM50 (right).

Isothermal magnetic moment measurements as function of the external field (M vs. B), performed by VSM are presented in figure 11.3.4. The conventional FM behavior of the $\text{La}_{0.7}\text{Ba}_{0.3}\text{MnO}_3$ bulk compound has the typical saturation ~ 100 emu/g at 5 K and although the critical PM transition is beyond 300 K (not possible to access with VSM measurements), the magnetization at room temperature was ~ 4 times lower than anticipated [11.3.12]. The smooth paramagnetic contribution observed for the composite samples BTO78LBM22 (~ 0.2 emu/g.T) and BTO50LBM50 (~ 0.5 emu/g.T) after the normal FM saturation behavior can be attributed to a dispersion in the BaTiO_3 matrix of independent nanometric grains of $\text{La}_{0.7}\text{Ba}_{0.3}\text{MnO}_3$ phase with anisotropic magnetization axis anchored to the aleatory crystallite orientation in relation to the magnetic field.

The small ferromagnetic contribution of ~ 0.04 emu/g.T at low magnetic fields (< 0.1 Tesla) detected in the BaTiO_3 nanopowders can be explained by the off-balance oxidation state of some Ti^{4+} to Ti^{3+} at the grain boundaries [11.3.11], [11.3.12], [11.3.13]; at higher fields it becomes masked by the common diamagnetic behavior (~ 0.008 emu/g.T) of the bulk compound.

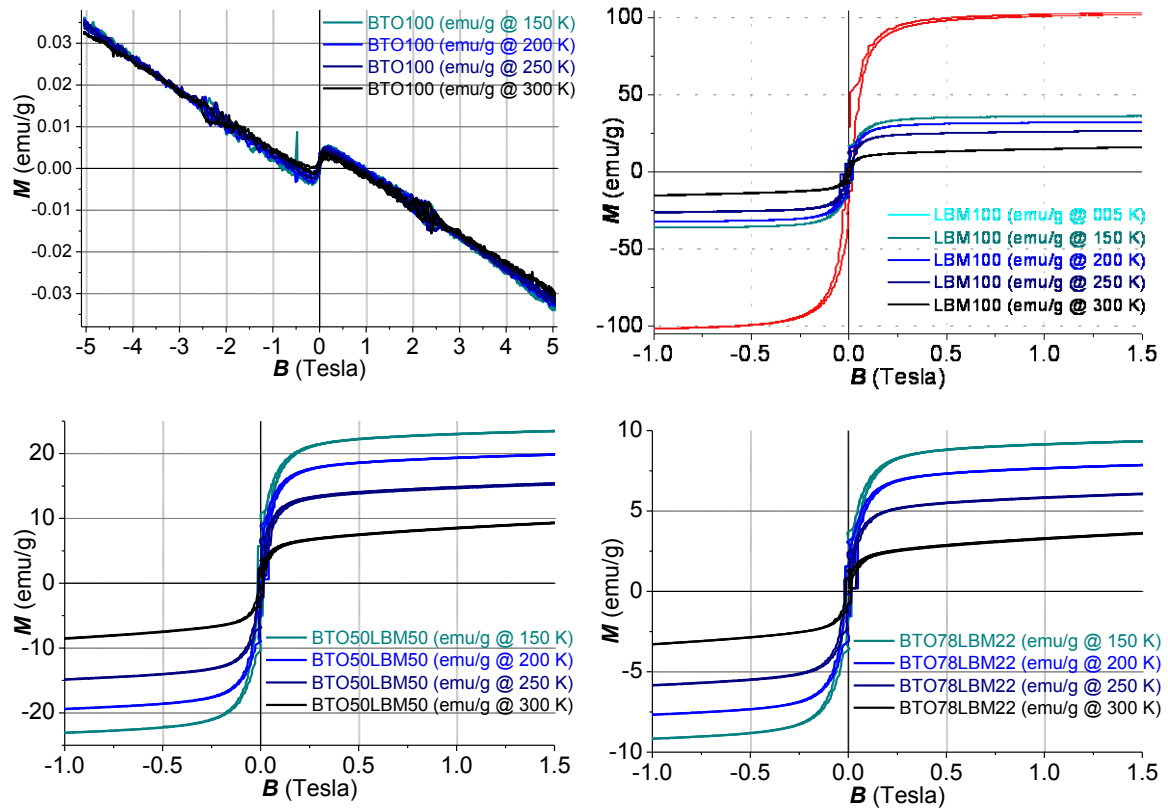


Fig.11.3.4: Samples' isothermal magnetization as function of external field: BTO100 (top left), LBM100 (top right), BTO50LBM50 (bottom left), BTO78LBM22 (bottom right).

Also witnessed in figure 11.3.5, the excess of magnetic moment found in the composite samples in relation to the one expected from the simple presence of the bulk $\text{La}_{0.7}\text{Ba}_{0.3}\text{MnO}_3$ phase, can be explained by the contribution of the superparamagnetism of isolated nanometric grains of $\text{La}_{0.7}\text{Ba}_{0.3}\text{MnO}_3$ phase, and in less extent the role of uncompensated Ti^{4+} at the grain boundaries of the BaTiO_3 nanometric phase that clearly registers $\sim 3.5 \times 10^{-3}$ emu/g at 300 K under 0.1 T.

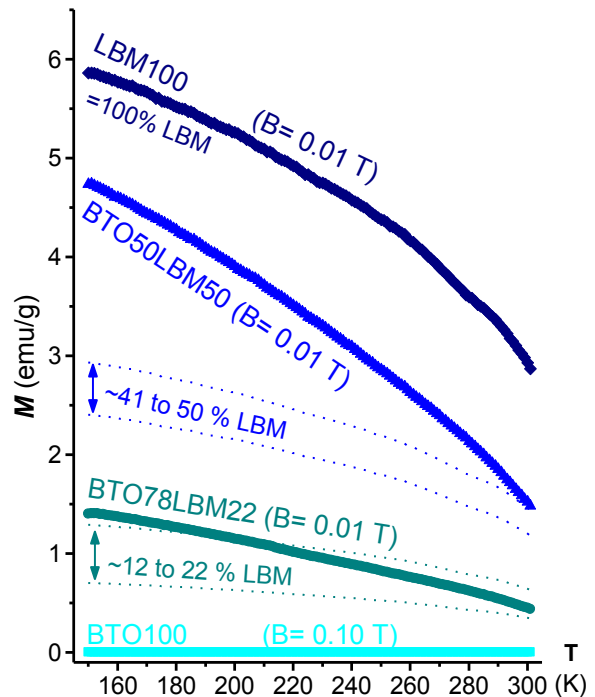


Fig.11.3.5: Samples' M as function of T .

Magneto-resistance d.c. measurements could only be performed in samples LBM100 and BTO50LBM50 which have sufficient $\text{La}_{0.7}\text{Ba}_{0.3}\text{MnO}_3$ conductive phase to ensure percolative paths for the current.

The LBM100 sample resistance and MR responses as function of temperature are presented in figure 11.3.6. The MR at 100 K under 1 Tesla reaches $\sim 11\%$, which is within the estimated order of magnitude, falling rapidly to $\sim 7\%$ at 150 K (neglecting the noise introduced by the liquid nitrogen evaporation at ~ 120 K). The critical I-M transition occurs at ~ 240 K is marginally observable in the MR by a small dive from ~ 4 to $\sim 3\%$ at ~ 250 K; further declining to $\sim 2\%$ at room temperature differs from the expected CMR behavior [11.3.14] and the MR endurance only to ~ 325 K points to the critical T_{Curie} below the estimated 340 K. Comparable results described in references [11.3.15] and [11.3.16] allow us to evaluate the bare manganite $\text{La}_{0.7}\text{Ba}_{0.3}\text{MnO}_3$ phase that constitutes this sample; suggesting that the incidence of Mn^{4+} could differ from the intended 30%, since the thermal treatments at $\sim 900^\circ\text{C}$ performed in these series of samples exclude the possibility of Oxygen deficiency [11.3.17], it is most probable that the Mn^{4+} surpass 40%. Eventual improvement of the MR performance could be reached by a slight reduction in Oxygen content in the sample, by means of further thermal treatments at higher temperature (1000 to 1200°C) or at $800\text{--}900^\circ\text{C}$ under vacuum or Ar atmosphere.

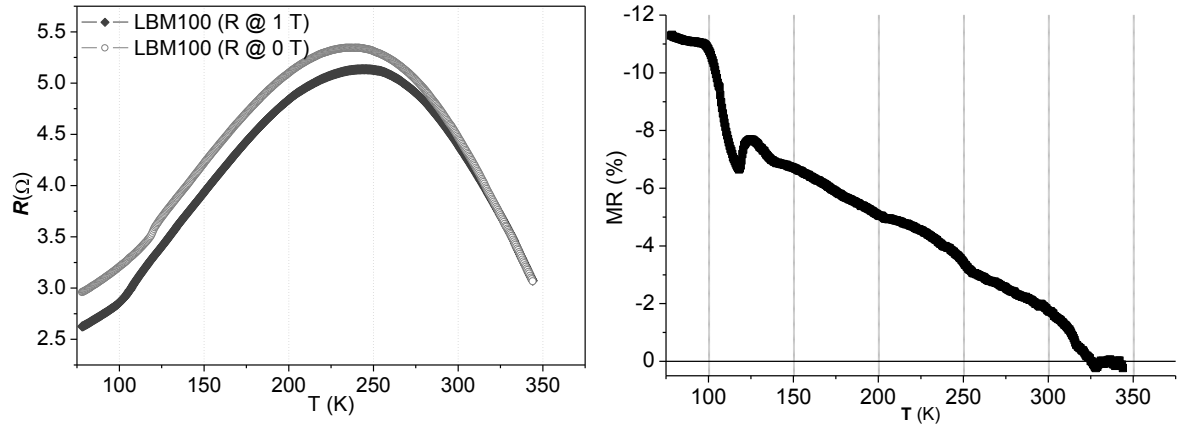


Fig.11.3.6: Magneto-Resistance measurements for sample LBM100 as function of temperature for 0 and 1 T.

In figure 11.3.7 are shown the MR measurements performed in sample BTO50LBM50. The overall sample M-I resistance transition seems to fall to ~ 110 K; although masked in the resistance measurements, the influence of the specific M-I transition from the $\text{La}_{0.7}\text{Ba}_{0.3}\text{MnO}_3$ phase is patent in the faster decrease of MR near ~ 250 K. The regular decline of MR with temperature has a patent slump around ~ 160 K consistent with the structural rhombohedral-orthorhombic [4.3.1] transition of the BaTiO_3 phase that partially composes the sample. In its turn, the BaTiO_3 tetragonal-cubic structural transition explains the sudden drop in resistivity above ~ 380 K, showing in the top-right graph of figure 11.3.7, leading to the total failure of polarization at ~ 391 K and consequently to a drastic change in the dielectric response, promoting current losses of previously accumulated charge and partially contributing to the drop in resistivity.

The MR also survives at least up to ~ 320 K pointing to some weakening of the long range magnetic order due to the dispersion in diamagnetic BaTiO_3 matrix.

The MR as function of field shown in the top left and center of figure 11.3.7 respectively changes from a typical sharp response dominated by inter grain polarized tunneling effect at low T , to a smooth magnetization dependency above T_{I-M} , as described previously in section 11.1.

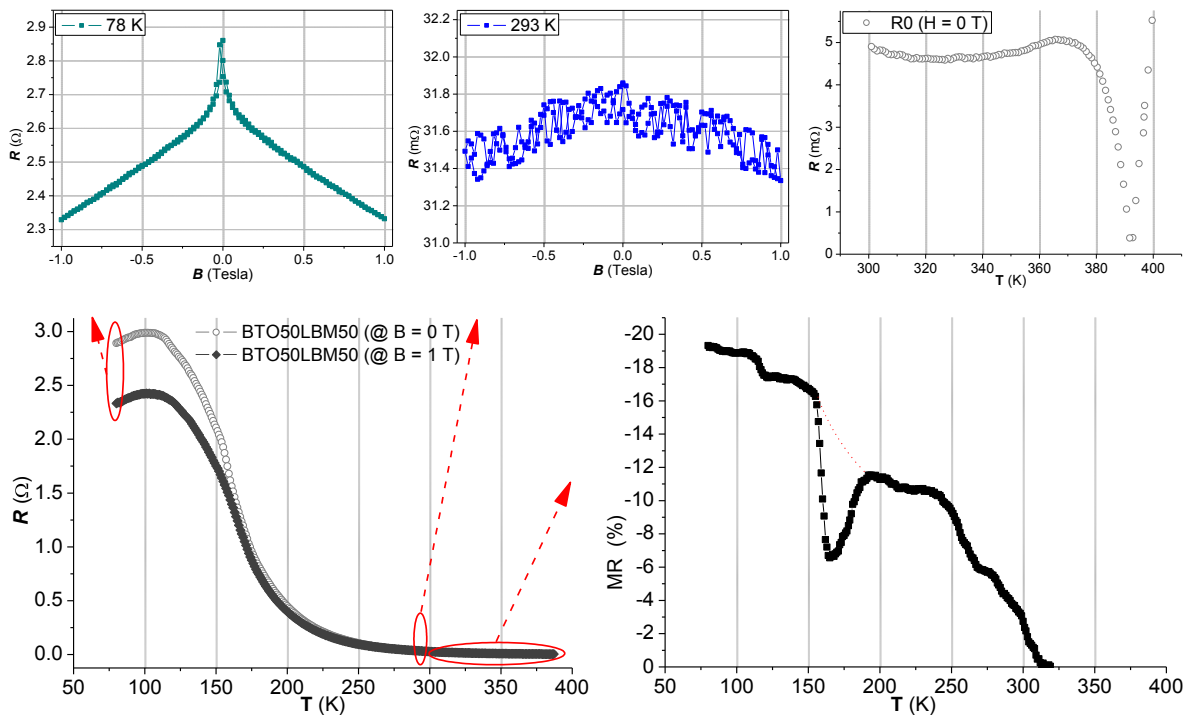


Fig.11.3.7: MR measurements for sample BTO50LBM50 as function of temperature up to 1 Tesla.

Magneto impedance measurements at room temperature of the BTO+LBM samples series shown in figure 11.3.8 follow the overall pattern previously found for the LuM+LSM series described in section 11.1, since the two manganites compounds have analogous properties.

The MZ profile increases rapidly with frequency from 3 kHz up to 100 kHz reaching the maximum near 10 MHz; beyond this frequency it is progressively attenuated in relation to the percentage of ferroelectric phase in each composite sample.

When the plain manganite reaches the magnetic saturation at higher fields (>0.3 T) the MZ response converge to a maximum $\sim 16\%$ under 10^5 Hz; whereas for the three composite samples the super-paramagnetic contribution spreads the MZ more regularly beyond 0.2 T. Although the percolation of the conductive $\text{La}_{0.7}\text{Ba}_{0.3}\text{MnO}_3$ phase, due to the presence of the ferroelectric BaTiO_3 phase sample BTO50LBM50 has a drastic decrease in MZ response to 1/4 of that found in sample LBM100, in opposition to the d.c. MR behavior.

The simple diamagnetic response of the BaTiO_3 bulk compound cannot explain the relative variation of the magneto impedance by 3 orders of magnitude, from $<10^{-4}$ to $\sim 10^{-1}$ %, between 0.025 to 0.1 Tesla for the of the BTO100 sample. The fact that the BaTiO_3 grain boundaries also play a pertinent role in the charge accumulation under polarization or electric field stimulation makes these localized environments more sensitive to the influence of the small positive magnetic susceptibility at low magnetic fields as can be observed in figure 11.3.8 (bottom right). By comparison, this effect is less visible for the LuMnO_3 compound (MZ varies $<10^{-2}$ to $\sim 10^{-1}$ % as can be observed in figure 11.1.14) since the preferential AFM or PM behavior dilutes such intrinsic MZ coupling.

Besides the MR and MZ responses the $\text{La}_{0.7}\text{Ba}_{0.3}\text{MnO}_3$ phase can also exhibit the ferromagnetic antiresonance (FMAR) phenomenon which can also induce large changes in surface resistivity upon moderate applied fields [11.3.18].

ME effect measurements obtained for sample BTO78LBM22, at low stimulation and low bias \mathbf{B} field, are represented in figure 11.3.9. Both transitions of the $\text{La}_{0.7}\text{Ba}_{0.3}\text{MnO}_3$ phase previously found (I-M at ~ 250 K and FM-PM at ~ 340 K) can be recognized independently in ME amplitude or ME phase measurements by clear changes of the respective graphical profiles.

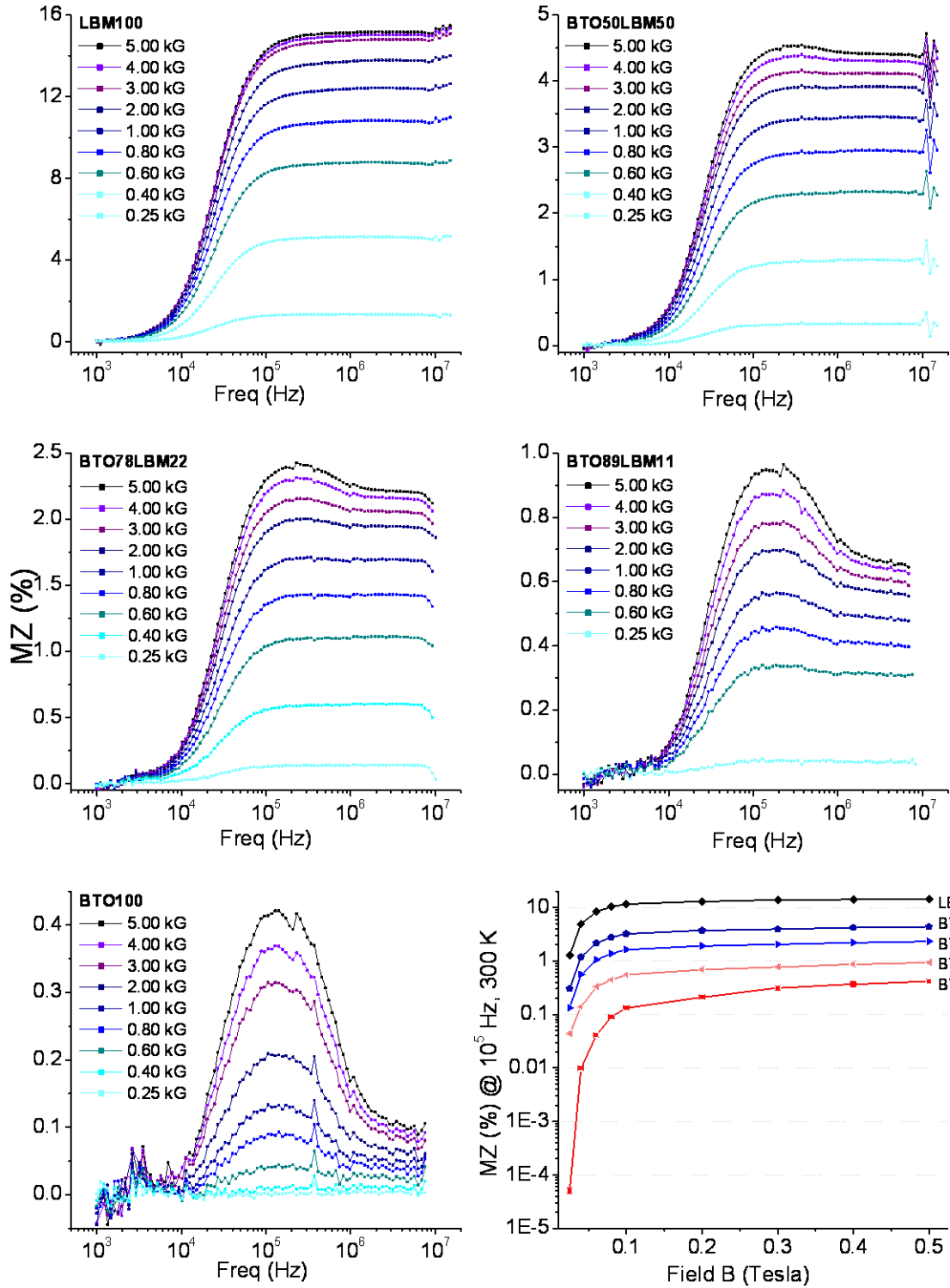


Fig.11.3.8: Magneto-Impedance measurements as function of applied a.c. electric field and bias magnetic field for the series BTO+LBM at room temperature. Comparison of ME response at 10^5 Hz (bottom-right).

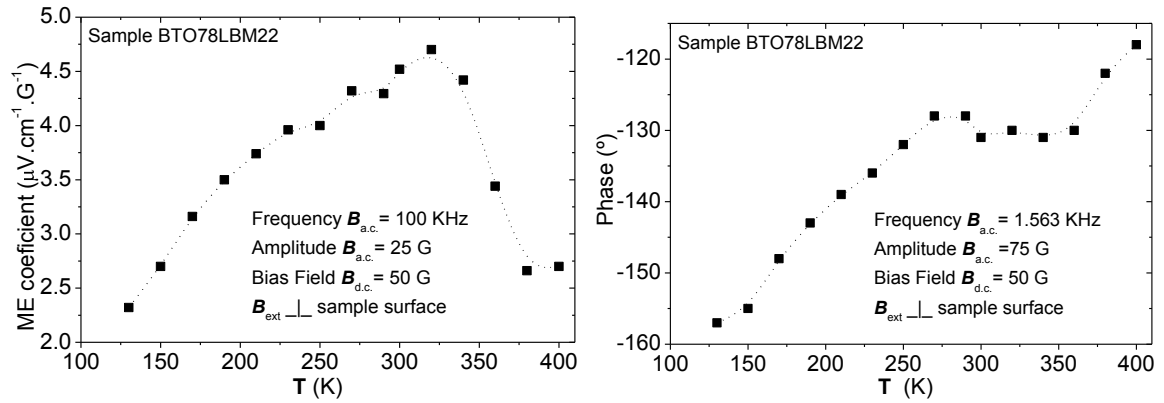


Fig. 11.3.9: Magneto-Electric effect amplitude (top) and phase difference (low) for sample BTO78LBM as function of temperature under low d.c. and a.c. magnetic field stimulation.

MFM measurements of sample BTO50LBM50 presented in figure 11.3.10, confirm that the $\text{La}_{0.7}\text{Ba}_{0.3}\text{MnO}_3$ phase is clearly ferromagnetic at room temperature, whereas for scans performed at above 328 K most FM contrast is lost in particular for the bigger clusters of the phase, while the smaller clusters or isolated grains keep the some remanent magnetization.

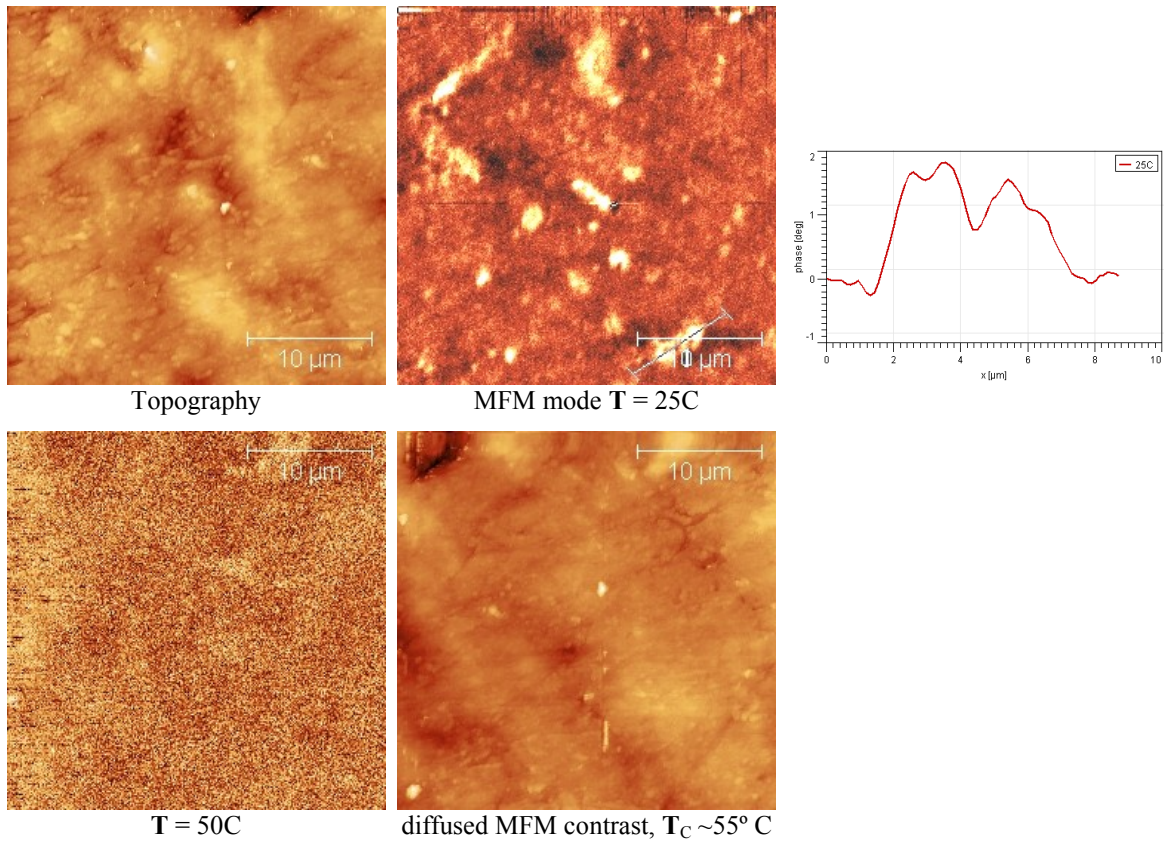


Fig. 11.3.10: Force Microscopy Topographic (left) and Magnetic scans of sample BTO50LBM50 surface performed at 25 C (top) and 55 C (bottom); detail of MFM cross-section signal for a LBM cluster.

In figure 11.3.11 are illustrated some lithographic experiments and MFM scans performed at room temperature, that are elucidative of the topographic and magnetic modifications on the BTO78LBM22 sample surface under electric field bias stimulation. The strong mechanical distortion experienced by the BaTiO₃ matrix is transmitted to the La_{0.7}Ba_{0.3}MnO₃ cluster altering its shape and partially the magnetization axis. Due to the irregular geometry of the grains and non uniform electric stimulation, the deformation of the surface it is not reproducible over a bias field cycle. Whereas application of a low electric field under $|V_{d.c.}| < 5$ V have restricted effect over the composite, under stronger fields the surface reacts and deforms irreversibly and part of the phase contrast obtained from the MFM scan is in fact cross talk due to the local BaTiO₃ polarization.

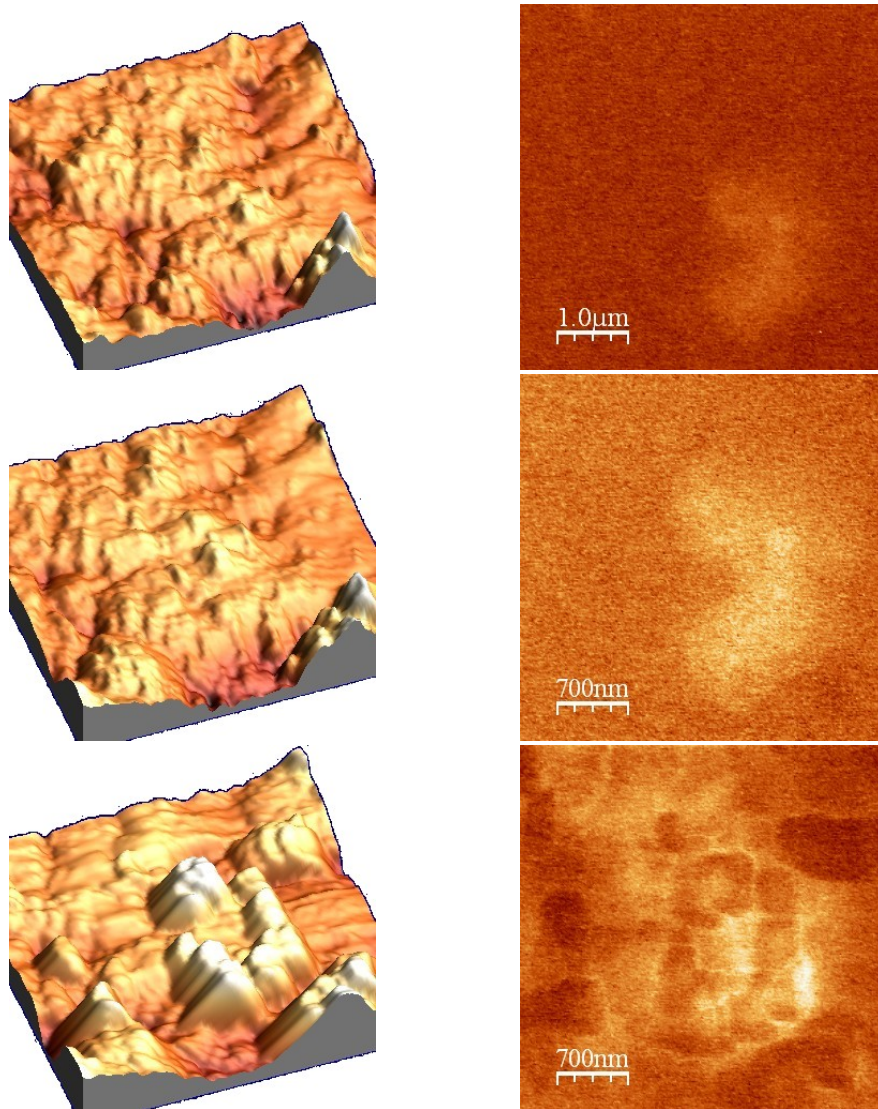


Fig. 11.3.11: MFM measurements BTO78LBM22 composite sample: Topography (left) and respective phase (right) near a LBM phase cluster. Before lithographic tests (right), after bias stimulation with 50 nm spaced 10x10 points grid at +5 V_{d.c.} (center) and then -9 V_{d.c.} (bottom).

Subsequent to the relevant work reported in 2007 by W. Eerenstein et al. [11.3.19] on BaTiO₃ and CMR manganites composites systems based in thin film layers, several authors [11.3.20], [11.3.21], [11.3.22] and [11.3.23] study similar systems without bringing yet any deeper insight on the magnetoelectric effect measurements or the strictive mechanisms mediating the multiferroic properties of such composites, which still deserve further research.

As overall conclusion, the widespread characterization of this BTO+LBM samples series exposed hereby are indicative that besides the predicted strictive interaction channel between the two phases, the discrete FM character of the BaTiO₃ grain boundaries have themselves local multiferroic properties and can couple directly with the magnetic moment orientation of neighboring La_{0.7}Ba_{0.3}MnO₃ grains, favoring a supplementary magnetoelectric effect route.

11.4. PFM studies of Induced Ferroelectricity in C.O. Manganites

Manganites present a wide spectrum of structural and functional phases, and so they become excellent test ground for materials modification R&D. In addition to chemical doping and thermal manipulation, phase transitions can also be induced by means of external fields; under certain circumstances, localized bias magnetic or electrical fields should induce ferroelectricity in magnetic manganites mediated by charge order mechanisms. Theoretically under certain circumstances C.O. may result in simultaneous inequivalent sites and bond dimerization which can break inversion symmetry, resulting in FE. Although the calculated phase diagram may allow such coexistence CO states, the energy levels are in general very close to one another [4.1.7], [11.4.1].

As illustrated in figure 11.4.1 for the respective phase diagrams of $\text{Pr}_{1-x}\text{Ca}_x\text{MnO}_3$, $\text{La}_{1-x}\text{Sr}_x\text{MnO}_3$ and $\text{La}_{1-x}\text{Ca}_x\text{MnO}_3$ manganites, each system presents a particular doping composition (x) corresponding to regions having rich transition thresholds between insulating and/or C.O. properties states (enhanced with red strips). The sensitive C.O. states are also correlated to Insulating-Metal conductivity and magnetic order phases and transitions; these can be also easily affected by external perturbations like pressure or temperature variation and external magnetic or electric fields, which could give rise to colossal dielectric response behaviors [4.2.2], [11.4.2].

However the finite conductivity of these materials in the bulk form renders difficult to observe directly the latent FE response by conventional dielectric/polarization measurement methods. On the other hand, FE localized phenomena can be studied via PFM techniques and may also is an important scientific promise for creating artificial multiferroic materials and memory states.

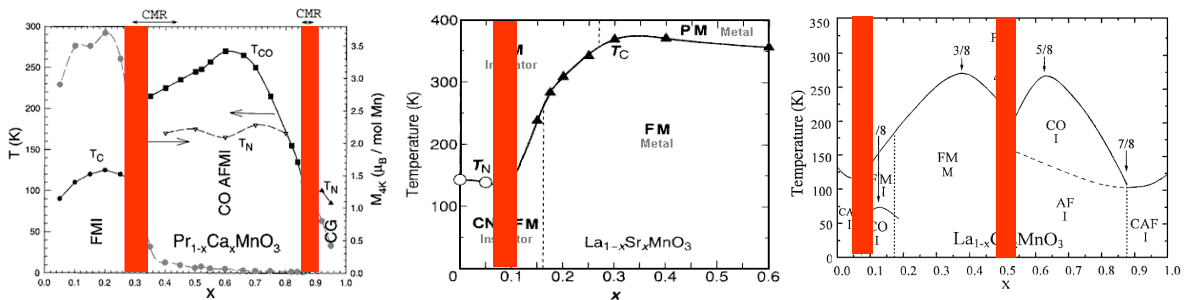


Fig. 11.4.1: Phase diagrams as function of doping (x) and temperature for Manganites: $\text{Pr}_{1-x}\text{Ca}_x\text{MnO}_3$ [11.4.3] (left) $\text{La}_{1-x}\text{Sr}_x\text{MnO}_3$ [4.2.4] (center) and $\text{La}_{1-x}\text{Ca}_x\text{MnO}_3$ [11.4.4] (right), showing sensitive phase transition C.O. regions (shadowed).

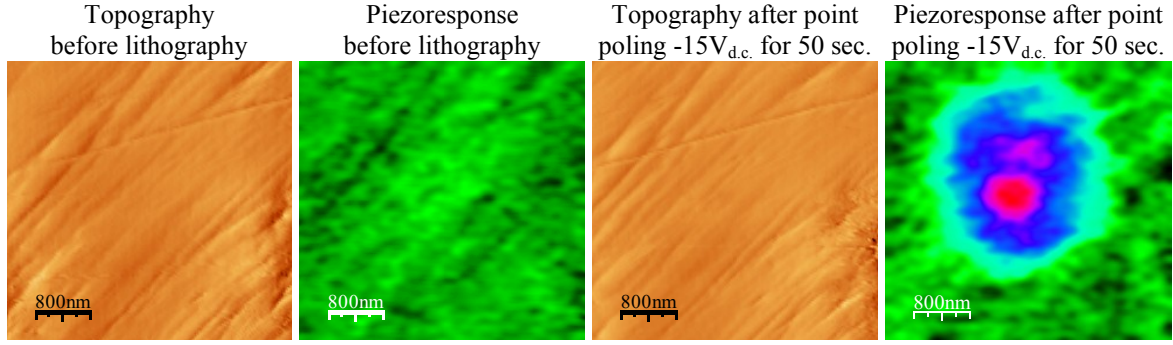
Inspiring research studies can be found in the works of Tomioka et al. [11.4.5] for magnetic field induced phase transitions, and especially of Jooss et al. [11.4.6], which identifies localized bias induced structural transitions and introduces a further insight of the $\text{Pr}_{1-x}\text{Ca}_x\text{MnO}_3$ system, having C.O. phases extending for $0.3 < x < 0.85$ (with a commensurate ordering at $x < 0.5$) and magnetic order only setting below C.O. transition temperature, can be classified as a type I multiferroic. In addition, electric field gradient (EFG) studies of A. Lopes et al. [11.4.7] across the $\text{Pr}_{1-x}\text{Ca}_x\text{MnO}_3$ phase diagram, using PAC measurements with ^{111}mCd , revealed typical signatures of a phase transition involving long-range ordering of local dipoles over the entire C.O./O.O. region.

Exploratory and preceding work performed at Aveiro University in the framework of multiferroic materials research was able to create and detect local bias induced charged states in manganites using Piezoresponse Force Microscopy (PFM) *PicoPlus*TM, *Agilent*[®] and *Veeco*[®] systems, patent in figures 11.4.2 through 11.4.5.

For the particular composition $\text{Pr}_{0.6}\text{Ca}_{0.4}\text{MnO}_3$, the C.O. and AFM orders prevents electron hopping, the magnetic correlations can survive locally as “Zener polarons” up to $T_{\text{CO}} = 235$ K (even if $T_{\text{N}} = 160$ K); under this circumstances Mn ions and Mn--Mn bonds become inequivalent and in fact the space group is the non-centrosymmetric *P11m*, for those reasons it should be an intrinsic multiferroic, making it one of the best candidates to prove the model of induced FE effects in manganites.

In figure 11.4.2 are shown PFM scans performed in a single crystal $\text{Pr}_{0.6}\text{Ca}_{0.4}\text{MnO}_3$ manganite measured at room temperature in the paramagnetic phase and above the CO transition. Experimental lithographic bias point poling at -15 V_{d.c.} during 50 seconds gave rise to a patent piezoelectric contrast evidencing the formation of a local polar state, without visible effects on the sample' surface topology. The polarization relaxes after a few hours, a time scale much longer than the expected for transient trapped charges.

Displayed in figure 11.4.3 are examples of the PFM measures performed in the surface of a $\text{Pr}_{0.6}\text{Ca}_{0.4}\text{MnO}_3$ polycrystalline sample; opposite polarization responses are observed from the lithographic lines made at positive or negative 10 V_{d.c.} biases, without visible topological effects.



Temporal sequence showing the piezoresponse decay after point poling $-15V_{d.c.}$ for 50 sec.

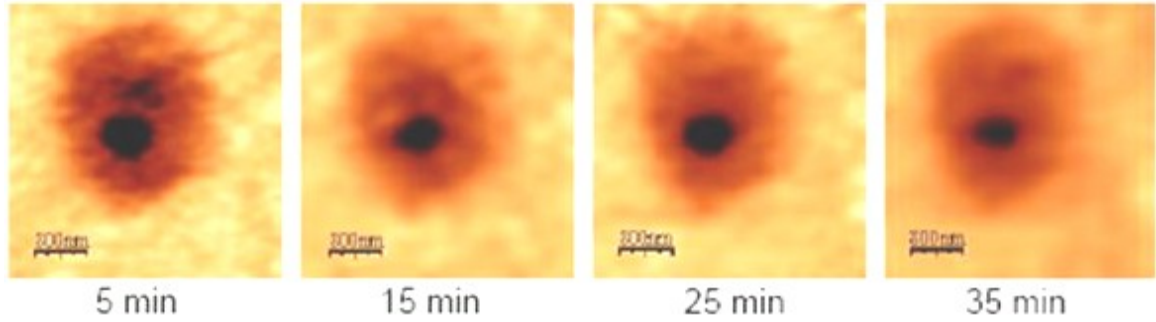


Fig. 11.4.2: Topographic and piezoresponse image (top) of a $3 \times 3 \mu m$ region of a $Pr_{0.60}Ca_{0.40}MnO_3$ monocrystalline sample before (left) and after (right) point poling lithography at $-15V_{d.c.}$ for 50 sec. Temporal sequence of piezoresponse images (low) showing the decay of the induced polarization.

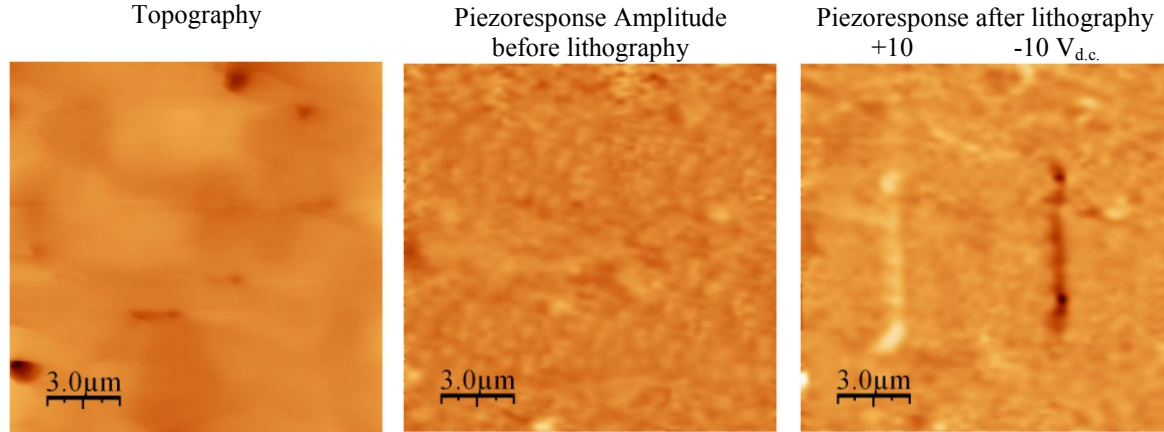


Fig. 11.4.3: Topographic (left) and piezoresponse image (center) of a $10 \times 10 \mu m$ region of a $Pr_{0.60}Ca_{0.40}MnO_3$ polycrystalline sample; PFM map after performing a lithographic frame of $\pm 10 V_{d.c.}$ (right).

Similar procedure was tested in $La_{0.89}Sr_{0.11}MnO_3$ single crystals at room temperature [11.4.8]. Although a non charge-ordered manganite, the insulating properties and the proximity to a spin canted state transition allows to display local ferroelectric states and hysteresis like response induced by the bias lithographic paths with piezoelectric contrast reversed by the applied field. The lifetime of these non-equilibrium states exceeded 100 hours, as illustrated in figure 11.4.4.

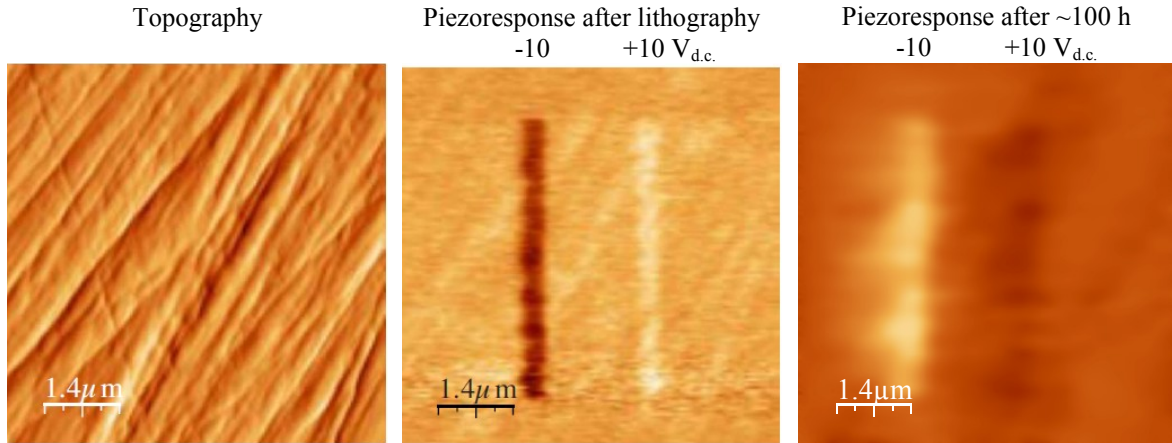


Fig. 11.4.4: Topographic (left) and PFM scans of the $\text{La}_{0.89}\text{Sr}_{0.11}\text{MnO}_3$ monocrystalline sample after lithographic paths of $\pm 10 \text{ V}_{\text{d.c.}}$ (center) and decay of the induced polarization after ~ 100 hours (right).

In figure 11.4.5 are shown some measurements performed in a $\text{La}_{0.50}\text{Ca}_{0.50}\text{MnO}_3$ polycrystalline sample. In the sequence it is possible to observe a Mn_3O_4 spurious grain that does not react to the lithographic stimulation in contrast to the manganite matrix which exhibit a definitive piezocontrast for the region subjected to a strong positive bias electric field ($+30 \text{ V}$), while the region subjected to negative bias has marginal response. The induced polarization also revealed time dependence decay in the order of hours.

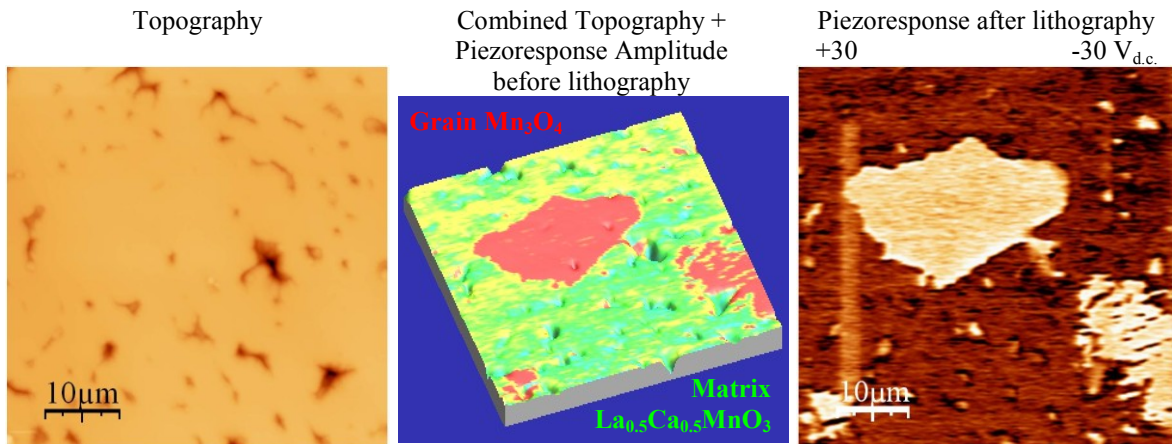


Fig. 11.4.5: Conventional topographic (left) and combined PFM image (center) of a $50 \times 50 \mu\text{m}$ region of the $\text{La}_{0.50}\text{Ca}_{0.50}\text{MnO}_3$ monocrystalline sample; PFM map after performing a lithographic frame of $\pm 30 \text{ V}_{\text{d.c.}}$ (right) showing a Mn_3O_4 grain having nil piezoresponse.

This particular experiment reveals important evidences supporting the model for bias induced polarization in C.O. manganites; the asymmetric poling and strong piezo contrast under positive bias stimulation points to a phase transition into the $|\text{Mn}^{4+}| > 50\%$ doping of the $\text{La}_{1-x}\text{Ca}_x\text{MnO}_3$ phase diagram, inside the C.O. region [11.4.9]; whereas the negative bias stimulation can form more Mn^{3+} polarons bringing the material into the metallic conductive phase preventing charge accumulation and polarization phenomena.

The presented preliminary results obtained at room temperature showed a clear piezocontrast which can be associated with the presence of nanoscopic C.O. regions, well above the C.O. transition, evidencing that the bias-induced ferroelectricity studied via PFM may also be an important for creating artificial multiferroic materials and memory cells. In this experimental work we propose to artificially induce the appearance of localized metastable nanoscopic C.O. regions at room temperature (above the C.O. transition) in the samples surface using localized bias voltage stimulation by means of a PFM lithographic mode.

The set of mono and polycrystalline manganites samples of $\text{La}_{1-x}\text{Sr}_x\text{MnO}_3$ ($x = 0.11, 0.40$), $\text{Pr}_{1-x}\text{Ca}_x\text{MnO}_3$ ($x = 0.11, 0.35, 0.40, 0.85$) and $\text{La}_{1-x}\text{Ca}_x\text{MnO}_3$ ($x = 0.05$ [11.4.10]; 0.33; 0.50), that also include some non-C.O. control samples, was gathered under the scope of these previous research works, and were specially selected for their potential to undergo localized phase transitions under the effect of a bias electric field applied by means of lithographic experiments performed by scanning probe microscopy performing PFM and BEPS scans [11.4.11] using an *Asylum MFP-3D*[®] SPM system at CNMS ORNL labs.

We expect that the dielectric nature of these materials metaphases may locally expose some ferroelectric behavior, that can be measured by the PFM and which may reveal latent multiferroic phenomena. The experimental course of action, previously described in section 10, goes through an initial survey of the sample surface, afterward the lithographic frame procedure and further PFM scan to enable to trace the sample surface reaction to the localized d.c. electrical stimulus. A representative area enclosing the stimulated region was selected to perform BEPS grid measurements in a ~60 kHz band of the respective resonance frequency up to a maximum a.c. voltage of 20 V.

Some elucidative examples of the measurements performed in the $\text{Pr}_{0.60}\text{Ca}_{0.40}\text{MnO}_3$ monocrystalline sample are detailed in figures 11.4.6 through 11.4.10; the surface response to the lithographic test frame is patent in figure 11.4.6; in this case for the bias paths made at ± 5 and $+10$ V no visible or measurable reaction was observed; whereas other bias paths resulted in a restricted mechanical deformation of the sample surface (with or without eventual electrochemical reaction), as observed in the topographic image, specially for the bias voltage $+20$ V (top lines), and for the succession $-10, -15$ and -20 V (bottom lines).

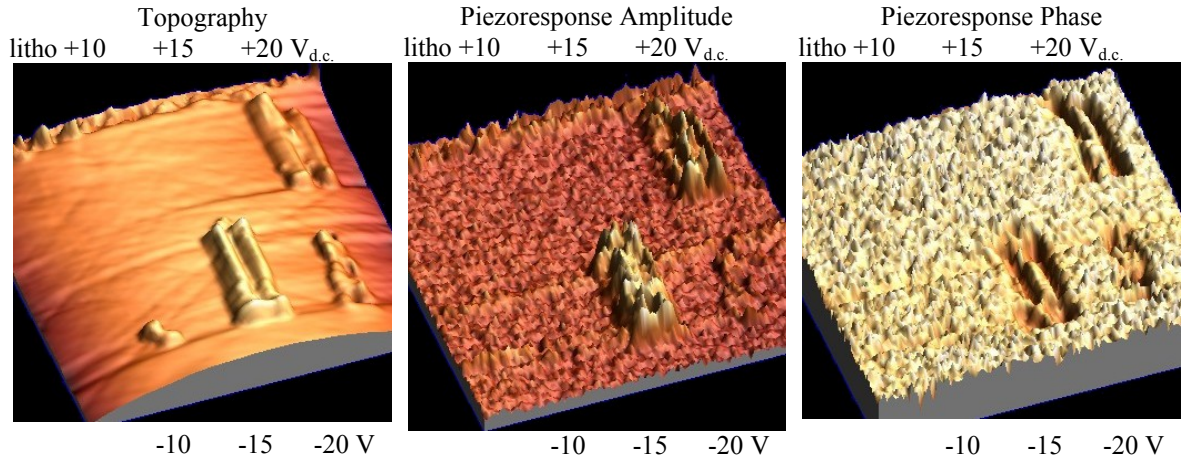


Fig. 11.4.6: Topographic (left), amplitude (center) and phase (right) PFM maps of a $5 \times 5 \mu\text{m}$ region of the $\text{Pr}_{0.60}\text{Ca}_{0.40}\text{MnO}_3$ monocrystalline sample after performing a lithographic frame of $\pm 10, \pm 15, \pm 20 \text{ V}_{\text{d.c.}}$.

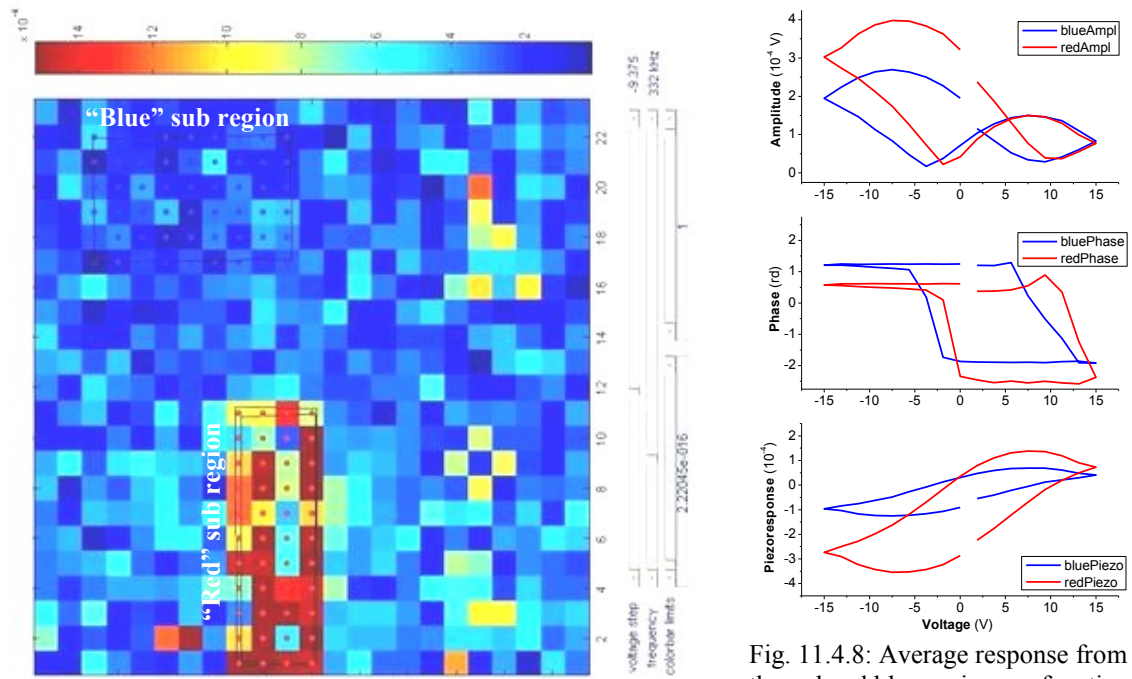


Fig. 11.4.7: BEPS Map section obtained at 332 kHz and -10V bias field.

Fig. 11.4.8: Average response from the red and blue regions as function of the bias voltage at 332 kHz

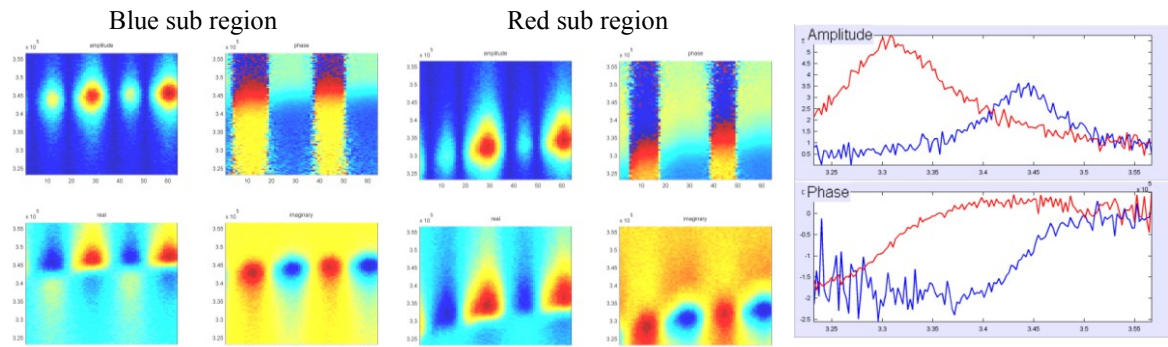


Fig. 11.4.9: Spectrograms of the blue (left) and red (center) sub regions: amplitude and phase (top), real and imaginary components (bottom). Profile of the average amplitude and phase spectral response at -10V bias.

As attest the sectional map acquired at 332 kHz and -10 bias of figure 11.4.7, the sub region stimulated with -15 V_{d.c.} (red like pixels) revealed in the subsequent BEPS measurements a particular enhanced piezoresponse both in amplitude and phase when compared to non-stimulated regions (blue like pixels) either as function of the applied modulated bias voltage (figure 11.4.8) and of the probing frequency (figure 11.4.9). The sub regions stimulated with ± 20 V_{d.c.} had more discrete FE performance.

From the extensive sequence of amplitude and phase data gathered for each pixel as function of the probing frequency and bias voltage, it becomes possible to trace the different sub regions having piezoresponse properties. Resulting BEPS maps, shown in figure 11.4.10, confirm the ferroelectric like response of the stimulated regions, configuring hysteresis cycles, nucleation sites, imprint and energy dissipation due to a finite polarization switching under inversion of the bias field. Subsequent PFM scans show no visible alteration of the sample surface after several hours or even after a second BEPS procedure using relatively high modulated voltage (>15 V).

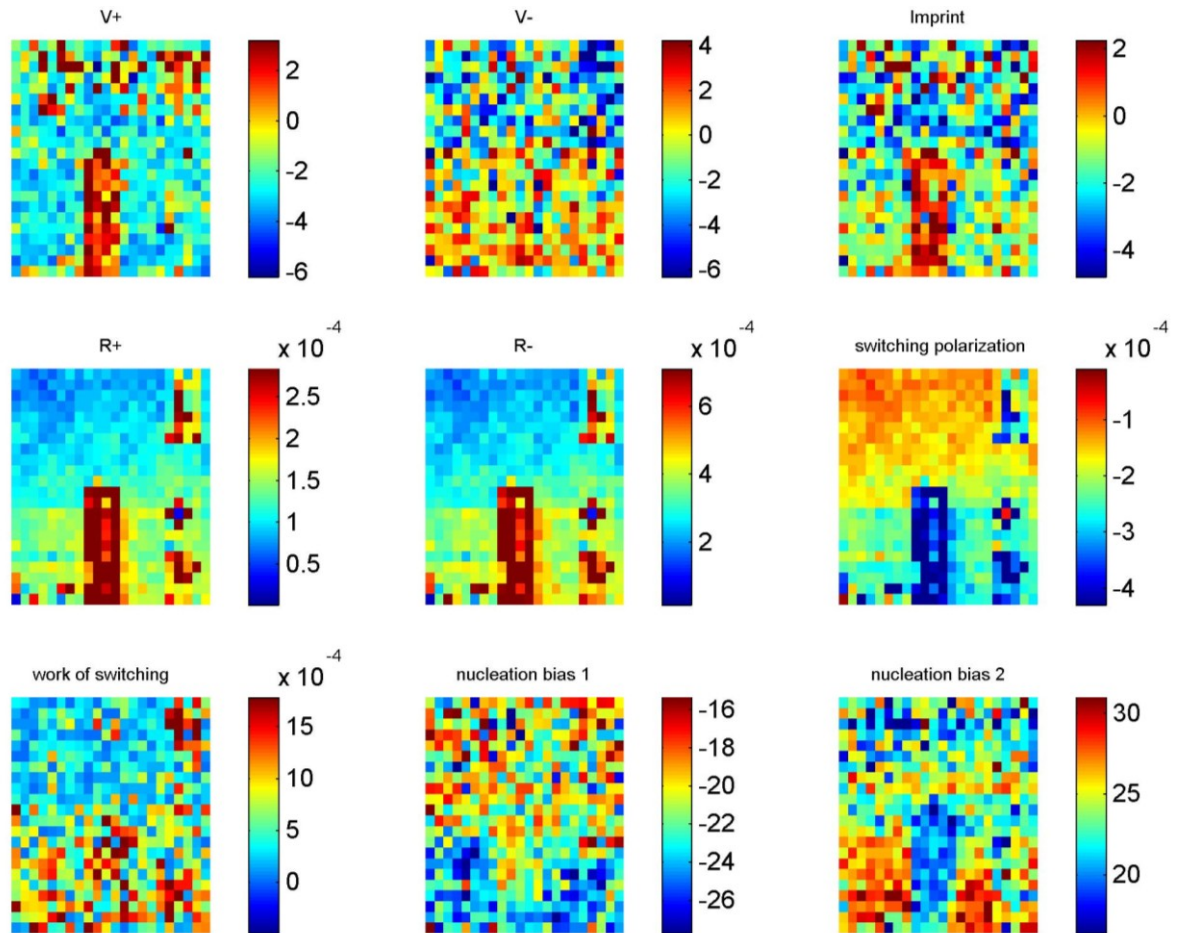
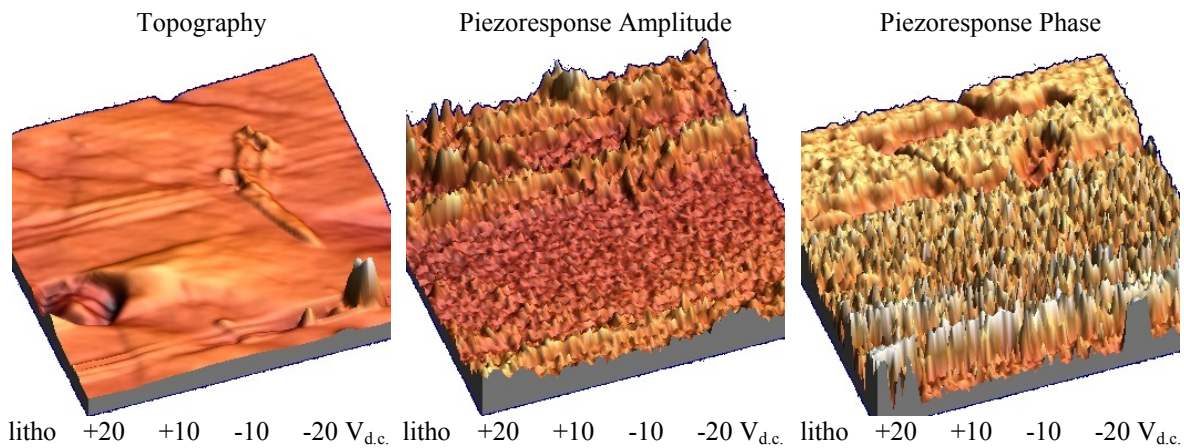


Fig. 11.4.10: BEPS maps $\text{Pr}_{0.60}\text{Ca}_{0.40}\text{MnO}_3$ monocrystalline sample after lithographic tests.

Similar PFM, lithographic and BEPS experiments were carried out in the several samples, subsequent to the d.c. lithographic tests it is usually observed very circumspect or even no mechanical deformation of the samples surface, as observed in figures 11.4.11, 11.4.13 and 11.4.15; some of piezoresponse amplitude signals are traceable to the respective lithographic paths without correspondence to modifications in the topological aspect; such results confirm that the ferroelectric character detected it is not due to cross-talk effects of the PFM scan and also lessen the likelihood of local electrochemical reaction.

In the case of the experiments performed in the $\text{Pr}_{0.60}\text{Ca}_{0.40}\text{MnO}_3$ polycrystalline sample the most relevant effect was detected in the lithographic path stimulated at +20 $V_{\text{d.c.}}$, although the amplitude and phase piezoresponse maps shown in figure 11.4.11 do not evidence such features, BEPS scans shown in figure 11.4.12 reveal a strong FE response.



litho +20 +10 -10 -20 $V_{\text{d.c.}}$ litho +20 +10 -10 -20 $V_{\text{d.c.}}$ litho +20 +10 -10 -20 $V_{\text{d.c.}}$
 Fig. 11.4.11: Topographic (left), piezo response amplitude (center) and phase (right) PFM maps of a $5 \times 5 \mu\text{m}$ region of the $\text{Pr}_{0.60}\text{Ca}_{0.40}\text{MnO}_3$ polycrystalline sample after performing lithographic paths of +10, 10 V.

Lithographic paths performed $\pm 10 V_{\text{d.c.}}$ bias had no impact in the sample, at -20 $V_{\text{d.c.}}$ a partial surface bulging was observed but it proven not to be associated to any FE response detected from the PFM or BEPS scans. The interpretation of this sample results must consider two experimental factors:

- A systematic drift in the $MFP-3D^{\text{®}}$ SPM system was detected in the sequence of this sample scans; this technical problem implied the recalibration of the $MFP-3D^{\text{®}}$ SPM system and was corrected for the remaining samples experiments. Although some accuracy limitations of the tip positioning, such disturbance translates the supposed original vertical bias lithographic lines into diagonal features to be distinctively read in the BEPS maps coefficients of figure 11.4.12.

- The fact that the sample has a polycrystalline ($>2\ \mu\text{m}$ size grains) structure leads to an anisotropic piezoresponse from each crystallite to the perpendicular bias field stimulation ($<100\ \text{nm}$ size resolution); hence additional noise can be observed in the amplitude and phase maps due to tip crossing through different crystalline orientations and grain boundaries, as can be observed in the maps of figures 11.4.11 and 11.4.12.

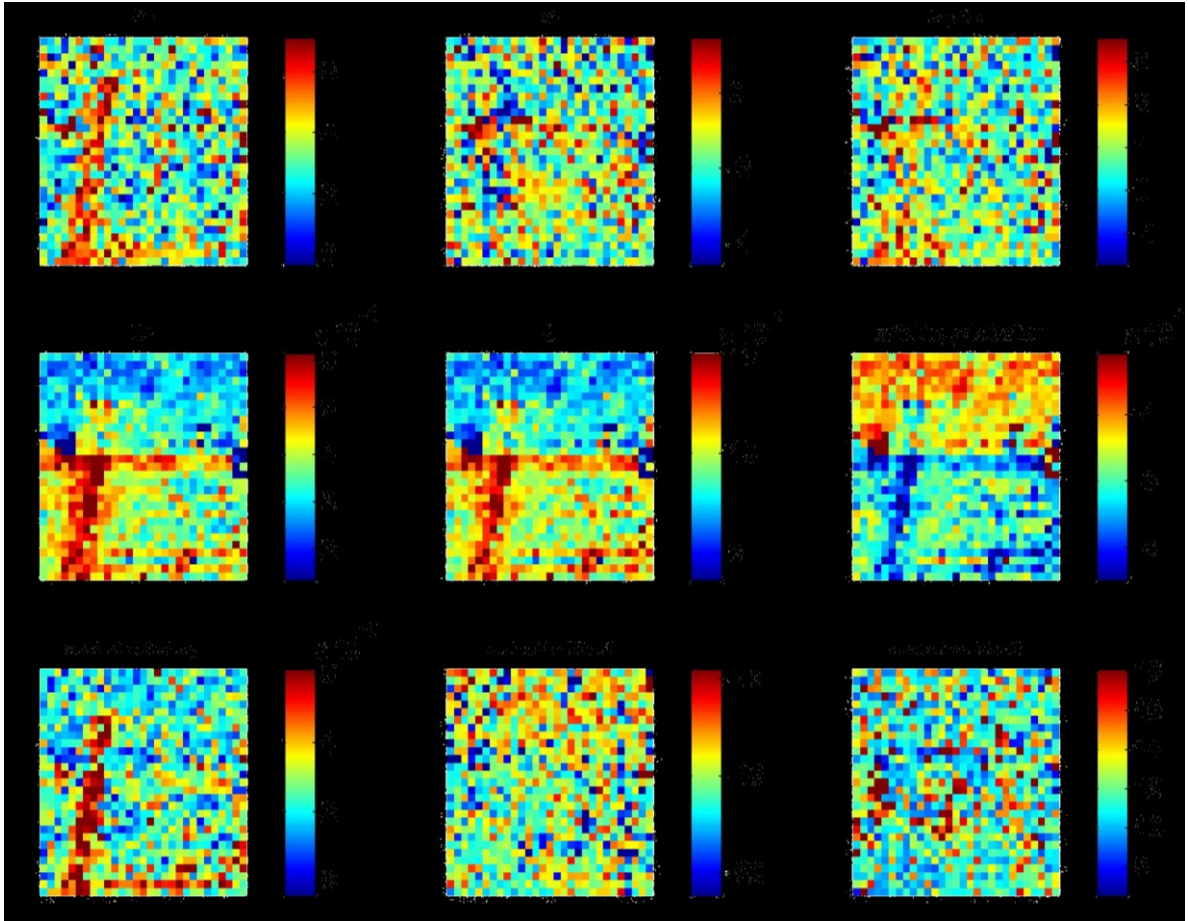


Fig. 11.4.12: BEPS Maps of the $\text{Pr}_{0.60}\text{Ca}_{0.40}\text{MnO}_3$ polycrystalline sample.

The researches presented in [11.4.12] to [11.4.15] give some indications of the polaronic mechanisms (modulated strain/electron/spin) leading to different C.O. ordering states and localized phase transitions, embedded in the host phase, that give rise to the formation of specific structural insulating domains which are susceptible to develop FE properties under the proper external bias field stimulation.

For the experiments performed in the $\text{La}_{0.89}\text{Sr}_{0.11}\text{MnO}_3$ mono crystalline sample, the PFM scans of figure 11.4.13 and BEPS maps of figure 11.4.14 testify how local piezo-response signals are directly traceable to the lithographic paths stimulated regions.

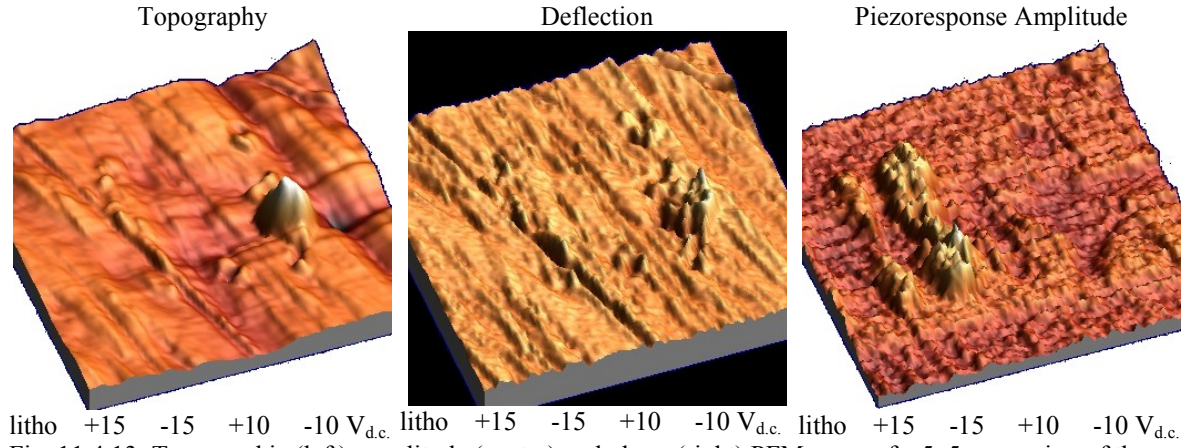


Fig. 11.4.13: Topographic (left), amplitude (center) and phase (right) PFM maps of a $5 \times 5 \mu\text{m}$ region of the $\text{La}_{0.89}\text{Sr}_{0.11}\text{MnO}_3$ monocrystalline sample after performing a lithographic frame of ± 15 and $\pm 10 V_{d.c.}$ lines.

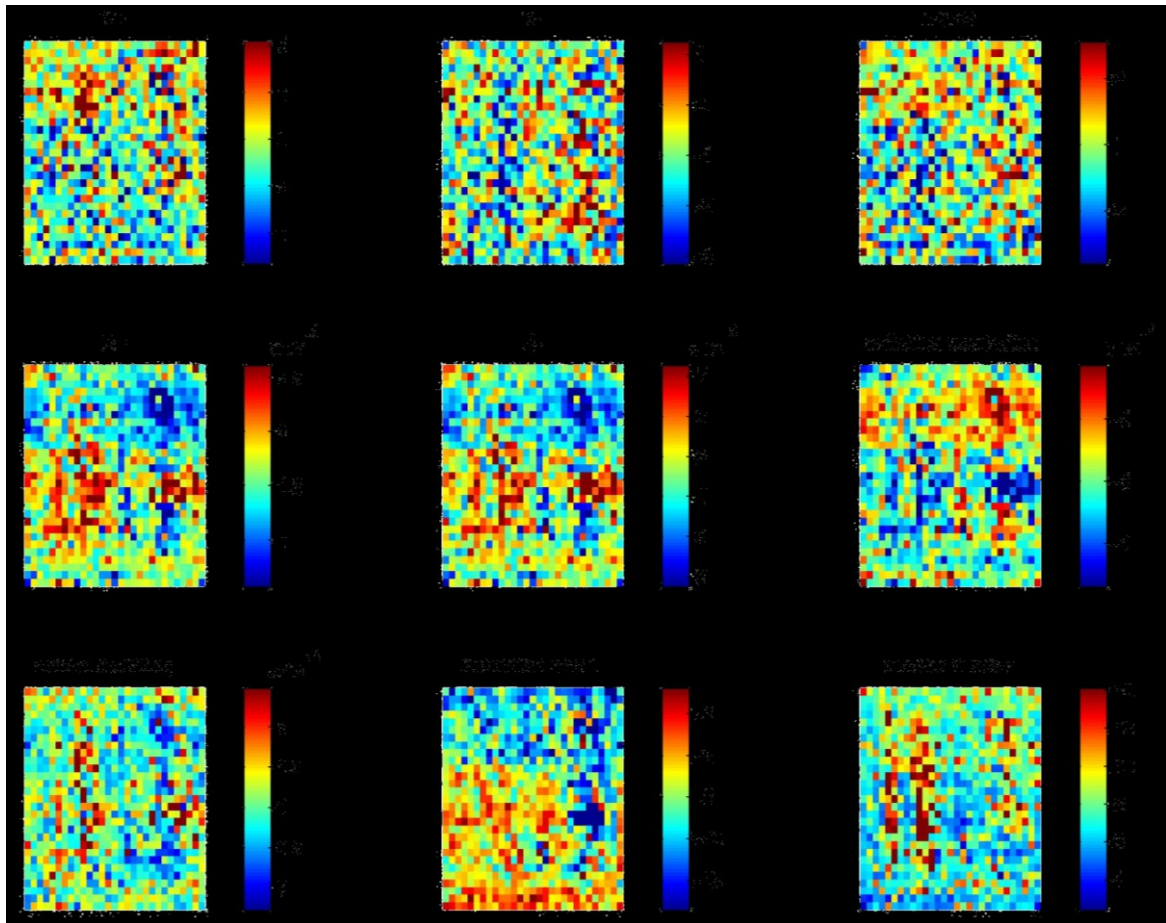


Fig. 11.4.14: BEPS maps results of $\text{La}_{0.89}\text{Sr}_{0.11}\text{MnO}_3$ monocrystalline sample after lithographic tests.

It is possible to observe that the lithographic paths made under negative bias voltage induce stronger piezoresponse behavior on the sample surface than the positive bias; such asymmetric response of the sample is visible in the remanence values found for the fitted narrow FE cycles (“+R” $\sim 2.5 \times 10^{-4}$ V and “-R” $\sim 7 \times 10^{-4}$ V) in particular for the path stimulated at $-15 \text{ V}_{\text{d.c.}}$ which also emerge distinctively in the BEPS parameters of nucleation, work ($\sim 2.5 \times 10^{-4}$ J) and polarization switching (-4 V). This bias dependent response is also detected in the i - V experiments described and analyzed further in this section.

No reaction was detected from the $+10 \text{ V}_{\text{d.c.}}$ litho path; a punctual surface alteration can be identified at the end of the path made at $-10 \text{ V}_{\text{d.c.}}$ due to a delayed positioning of the lithographic tip and should not be considered relevant, since the bulging is not extended to the rest of the line.

The results obtained from PFM and BEPS measurements over the surface of the $\text{La}_{0.95}\text{Ca}_{0.05}\text{MnO}_3$ polycrystalline sample are summarized in figures 11.4.15 and 11.4.16.

Even if the litho path performed at $+10 \text{ V}_{\text{d.c.}}$ resulted in a minor surface scratching, the relevant piezoresponse in amplitude and phase maps corroborate the material dielectric properties modification across the litho paths at -5 and $-10 \text{ V}_{\text{d.c.}}$; this last path promoted a subtle enhancement of the nucleation bias, however the hysteresis cycles turn to be too narrow to determine an inversion field, and in fact there is a finite range of the polarization remanence in relation to the ground level of the non stimulated regions, translated in $\sim 0.01 \text{ V}$ for R^+ and $\sim 0.03 \text{ V}$ for R^- and also changing the switching polarization by $\sim 0.03 \text{ V}$.

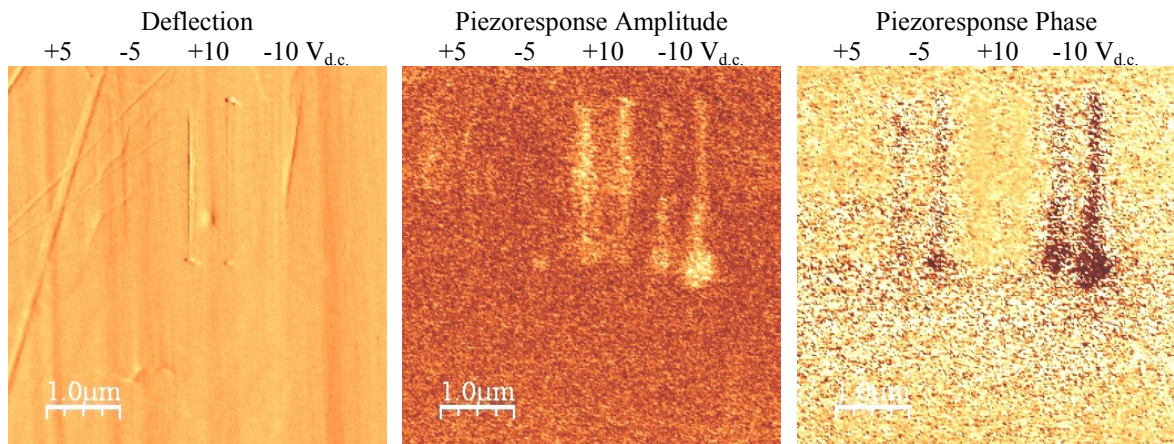


Fig. 11.4.15: Deflection (left), piezoresponse amplitude (center) and phase (right) PFM maps of a $5 \times 5 \mu\text{m}$ region of the $\text{La}_{0.95}\text{Ca}_{0.05}\text{MnO}_3$ polycrystalline sample after performing a lithographic frame of $\pm 5, \pm 10 \text{ V}_{\text{d.c.}}$.

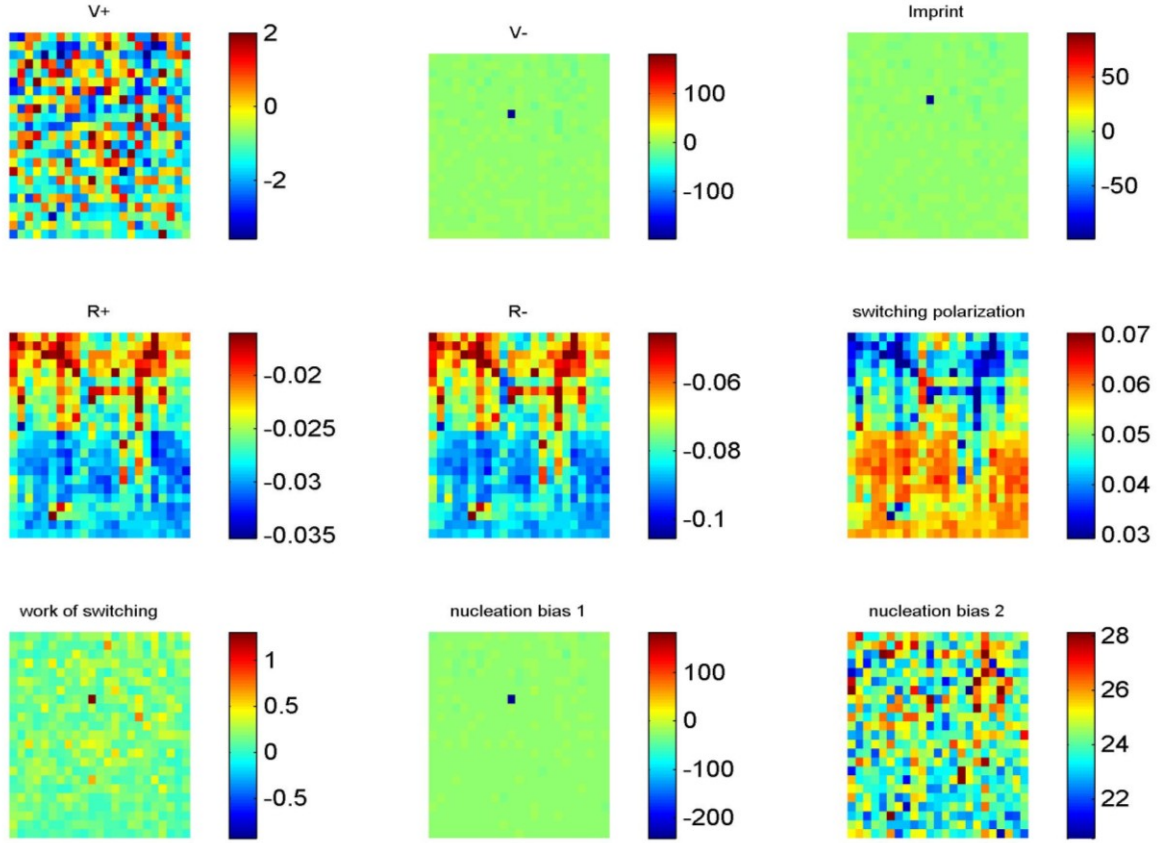


Fig. 11.4.16: BEPS maps results of $\text{La}_{0.95}\text{Ca}_{0.05}\text{MnO}_3$ polycrystalline sample after lithographic tests.

For the remaining manganite samples having compositions that also allow C.O. type states, namely a monocrystalline PrMnO_3 and another of $\text{Pr}_{0.65}\text{Ca}_{0.35}\text{MnO}_3$ and a polycrystalline $\text{Pr}_{0.15}\text{Ca}_{0.85}\text{MnO}_3$, it was not possible to perform complete or conclusive mapping measurements by the BEPS technique; nevertheless in figure 11.4.17 are respectively represented the most relevant results of the PFM scans obtained for each sample surface after the lithographic experiments; in general, these images reveal some piezoresponse amplitude contrast traceable to the negative lithographic paths.

In detail, the monocrystalline $\text{Pr}_{0.65}\text{Ca}_{0.35}\text{MnO}_3$ sample does not have significant reaction to lithographic bias fields smaller than $|\pm 20| \text{ V}_{\text{d.c.}}$; some scarce surface bulging from the tip passage at $-20 \text{ V}_{\text{d.c.}}$ can be observed; even if some cross talk is plausible, the piezoresponse amplitude contrast is homogeneous along all the path, attesting the correlation to a change in the dielectric properties and not due to mechanical features; for the $+20 \text{ V}_{\text{d.c.}}$ parallel litho path the piezoresponse amplitude contrast changes signal, pointing again to different effects on the material structure depending on the bias voltage signal.

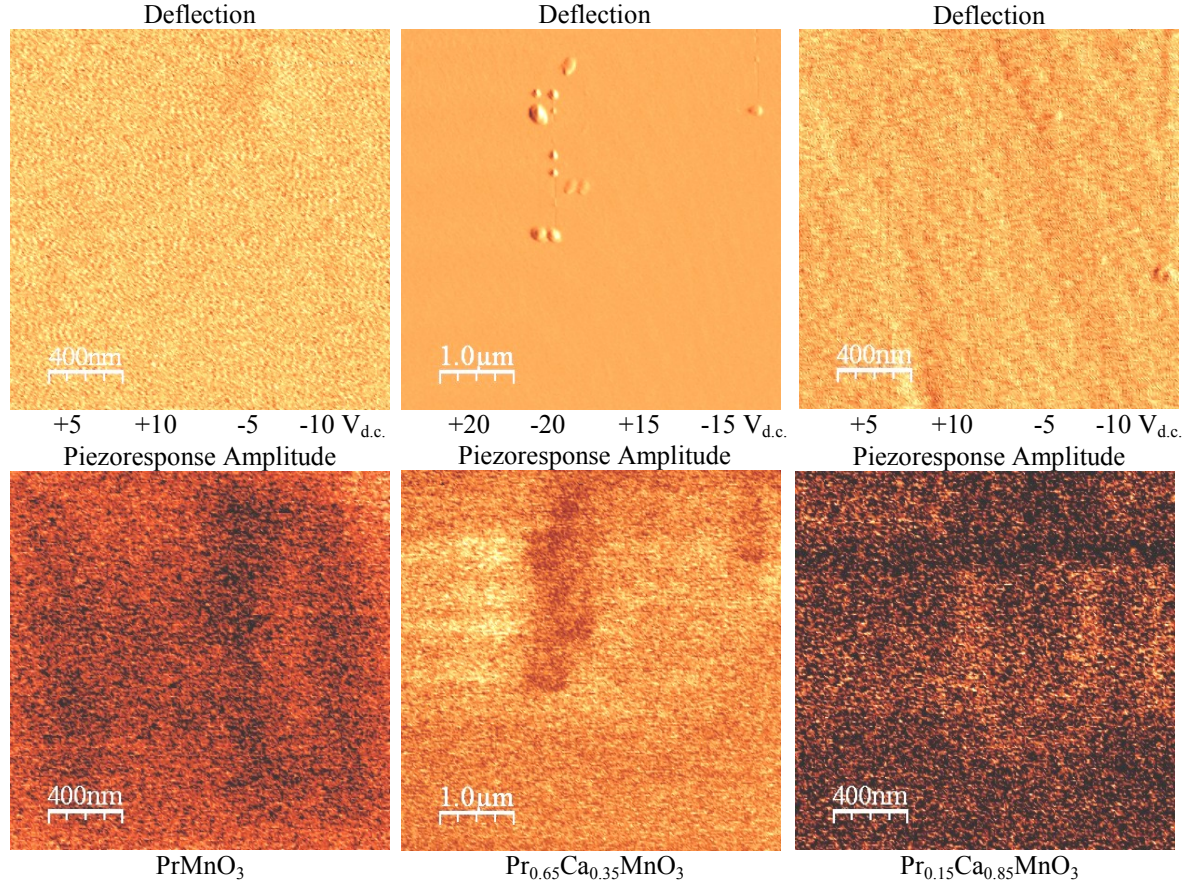


Fig. 11.4.17: PFM deflection (top) and respective piezoresponse amplitude (bottom) for monocrystalline samples PrMnO_3 (left) and $\text{Pr}_{0.65}\text{Ca}_{0.35}\text{MnO}_3$ (center) and polycrystalline $\text{Pr}_{0.15}\text{Ca}_{0.85}\text{MnO}_3$ (right) after performing lithographic experiments.

In comparison to the $\text{Pr}_{1-x}\text{Ca}_x\text{MnO}_3$ samples with $x = 0.45$, these manganite samples with $x = 0.00, 0.35, 0.85$ have a much weaker piezoresponse, since these compositions imply that the respective C.O. states lie at a much lower temperature (<120 K in contrast to ~ 235 K for $x = 0.40$). The eventual local bias induced polarization becomes easily dispersed by the room temperature thermodynamic conditions.

These reckonable alterations of the samples dielectric properties under the lithographic bias stimulation were definitively not possible (and very improbable) to obtain in control manganite samples such as the mono crystals of $\text{La}_{0.67}\text{Ca}_{0.33}\text{MnO}_3$ and $\text{La}_{0.60}\text{Sr}_{0.40}\text{MnO}_3$, due to their higher electric conductivity that renders any charge accumulation induced by the PFM tip to be rapidly dispersed through the material and dissipated to the system sample holder.

Besides the PFM and BEPS scans that enabled to recognize and characterize the local induced changes on the samples surface due to lithographic tests, it was also possible to implement some probing i - V measurements in order to bring some additional insight over the effect of the voltage signal on the nature of charge carriers injected into the samples' surface through the PFM tip.

The typical high resistivity found at the surface of the C.O. type manganites samples ($>10^3 \Omega \cdot \text{mm}$), imply that it was only possible to establish a quantifiable current ($0.1 \text{ nA} < i < 20 \text{ nA}$) within a distance of few μm between tip and sample holder electrode across the sample surface, Hence i - V measurements performed for most samples were not successful, besides many essays having nil current detection, it was also observed some inconsistent pA charge/discharge loops when the sample's dielectric behavior allowed established an equivalent capacitor circuit with the PFM system.

The samples surface generally have a non conductive barrier formed by an oxide and hydration adsorption layer, meaning that the tip contact must surpass this barrier, demanding a certain amount of over pressure besides the bias offset voltage in the tip contributing for its wearing. Due to the highly localized measures ($<50 \text{ nm}^2$) and eventual surface inhomogeneities it is also possible a localized or even a progressive degradation of the sample surface due to current leakage and eventual electrochemical reaction, making irreversible damage that prevent cycling through the i - V curve, therefore these tests are repeated in several different points of the sample surface; the data acquired is not reproducible and should be validated and interpreted according to the common trends detected in the i - V curves that became specific associated with each sample.

Although the point effect of the probe bias voltage on the sample surface may induce some localized FE phase transition (as previously described for some samples), this phenomena is not expected since a current is established and any charge carriers injection is dissipated through the electrodes. In figure 11.4.18 are only summarized the coherent and interesting results obtained.

The semi-dielectric nature of these manganites is patent in the delay of the current in relation to low bias in particular for negative voltages, as the electric potential difference grows between the tip and the holder electrode, more charge carriers can be injected in the material and a more conventional linear resistive behavior may develop.

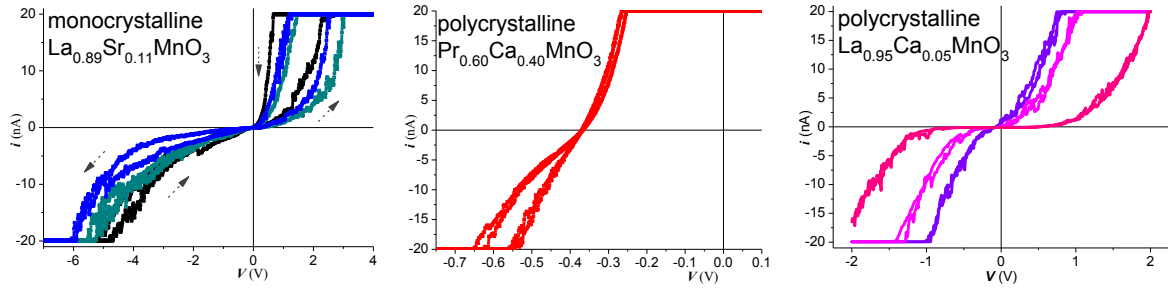


Fig. 11.4.18: surface i - V curves measurements at different surface points of the monocrystalline sample $\text{La}_{0.89}\text{Sr}_{0.11}\text{MnO}_3$ (left), polycrystalline samples $\text{Pr}_{0.60}\text{Ca}_{0.40}\text{MnO}_3$ (center) and $\text{La}_{0.95}\text{Ca}_{0.05}\text{MnO}_3$ (right).

An asymmetric shape and hysteresis of the current curve in relation to the bias voltage applied is observable in the three samples. These asymmetries can be related to the different availability and mobility of the charge carriers, polarons (electrons) or holes in the material. In its turn, the current inversion hysteresis can be associated to the FE domains inversion.

In Conclusion, for a particular class of manganites possessing C.O. properties, it is possible to induce localized FE metastable states corresponding to an extension of the phase diagram under additional thermodynamic variables that comprise bias voltage stimulation within restricted time and spatial frames. These non equilibrium thermodynamic conditions can be generated by means of PFM lithographic writing using contact mode and suitable bias voltage.

The bias induced C.O. state stimulated volume near the samples surface may vary from 1 μm to 100 nm across depending on the intensity and time interval of the lithographic impingement, for a point it's assumed a half sphere spreading of the electric field, which involves roughly 10^7 to 10^8 Mn ions which are subjected to a new (ordered) charge redistribution and assume a new metastable structural rearrangement. Local charge injection by the tip ($\sim 10 \text{ nm}^2$ contact area) is estimated of the order of 10^5 electrons (within a few ms) and such low current cannot be detected by the *ORCA* SPM system.

On the lithographic writing, the piezoresponse asymmetry on negative or positive bias voltage can be correlated to how the material's electronic structure accommodates additional charge built, locally injected through the PFM tip, respectively electrons or holes; and how these are locally and temporarily ordered and frozen within the network, taking advantage of the dielectric nature and C.O. mechanisms that stabilize this carriers as a redistribution of the $\text{Mn}^{3+}/\text{Mn}^{4+}$ ratio and Jahn-Teller distortions rearrangements

(polarons entrapment). Due to the correlated magnetic nature of the polarons, it leads to an intrinsic multiferroic behavior system.

The localized poling effect induces a transition to a metastable phase having a broken inversion symmetry structure distinctive by assuming a detectable self sustained FE state (slow decay time)

BEPS measurements are a useful tool to confirm and quantify the presence of locally induced piezo/ferroelectric parameters, mapping ferroelectric cycles and switching in the studied samples. The BE method described here when compared to single frequency SPM, enables data acquisition having unambiguous decoupling of the conservative and dissipative interactions, removing topographic cross-talk and allowing identification of non-linear responses. Local response can be probed as a function of variables such as electric potential, temperature, or time, giving rise to multidimensional spectroscopic SPM methods probing dynamic materials functionality beyond classical data acquisition.

Combined with other techniques, like PAC, hyperfine spectroscopy and theoretical modeling, it can bring new insights on correlated electrons systems, opening new pathways to study local scale multiferroic phenomena originated on complex charge/orbital ordering effects in materials particularly susceptible to phase transitions under localized bias electrical disturbance.

Further studies and measurements are in progress to obtain new clues to understand the mechanisms that underlie such complex process and optimize the technical procedures and materials design in order to reach room temperature stabilization of the modifications.

12. Thin Films deposited by RF Sputtering

12.1. (La,Sr)MnO₃ phase Thin Films deposited by RF Sputtering

Preceding research work performed on deposition of (La, Sr)MnO₃ films employing MOCVD method and samples characterization recurring to XRD, EDS-SEM, VSM, MR and MFM measurement techniques. Overall results shown that the adjustment of the organo-metallic precursors composition and the management of deposition conditions enabled to control and obtain polycrystalline thin films of the rhombohedral La_{0.7}Sr_{0.3}MnO₃ manganite phase into LaAlO₃ (100) and MgO (100) substrates, having average grain size $\sim 0.2 \mu\text{m}$, surface roughness $\sim 13 \text{ nm}$, $\rho \sim 0.1 \Omega\cdot\text{cm}$ at 300K and the distinctive $T_{\text{critical}} \sim 355 \text{ K}$. The unsatisfactory epitaxial growth of the film phase onto the substrates and the inadequacy of the MOCVD method to be employed in the deposition of multilayers and metallic alloys are the major limitations that compel the research to recur to PVD methods [12.1.1].

The experience gathered in the characterization and recognition of this manganite phase in the thin film form became an important asset that simplified the definition of technical objectives and interpretation of results of a new series of thin film depositions using Magnetron RF sputtering system.

The experimental thin films deposition of the (La,Sr)MnO₃ manganite (LSM) comprise some of the initial work performed with the updated RF sputtering system configured in section 7.2.

The deposition conditions and glass substrates selected for the 5th series of samples, as described in table 9.1.1, were found not to be suited to achieve proper growth of the (La, Sr)MnO₃ phase in the different substrates, as can be observed from the XR diffractograms examples of figure 12.1.1. Although it was observed a partial melting of these amorphous substrates, no relevant chemical reaction is evident from the spectrograms and the presence of a polycrystalline rhombohedral LSM phase can be recognized; another feature of these series is the insufficient annealing temperature, performed at 74° C that leads to deficient oxidation and presence of spurious SrO and Mn₃O₄ in the film.

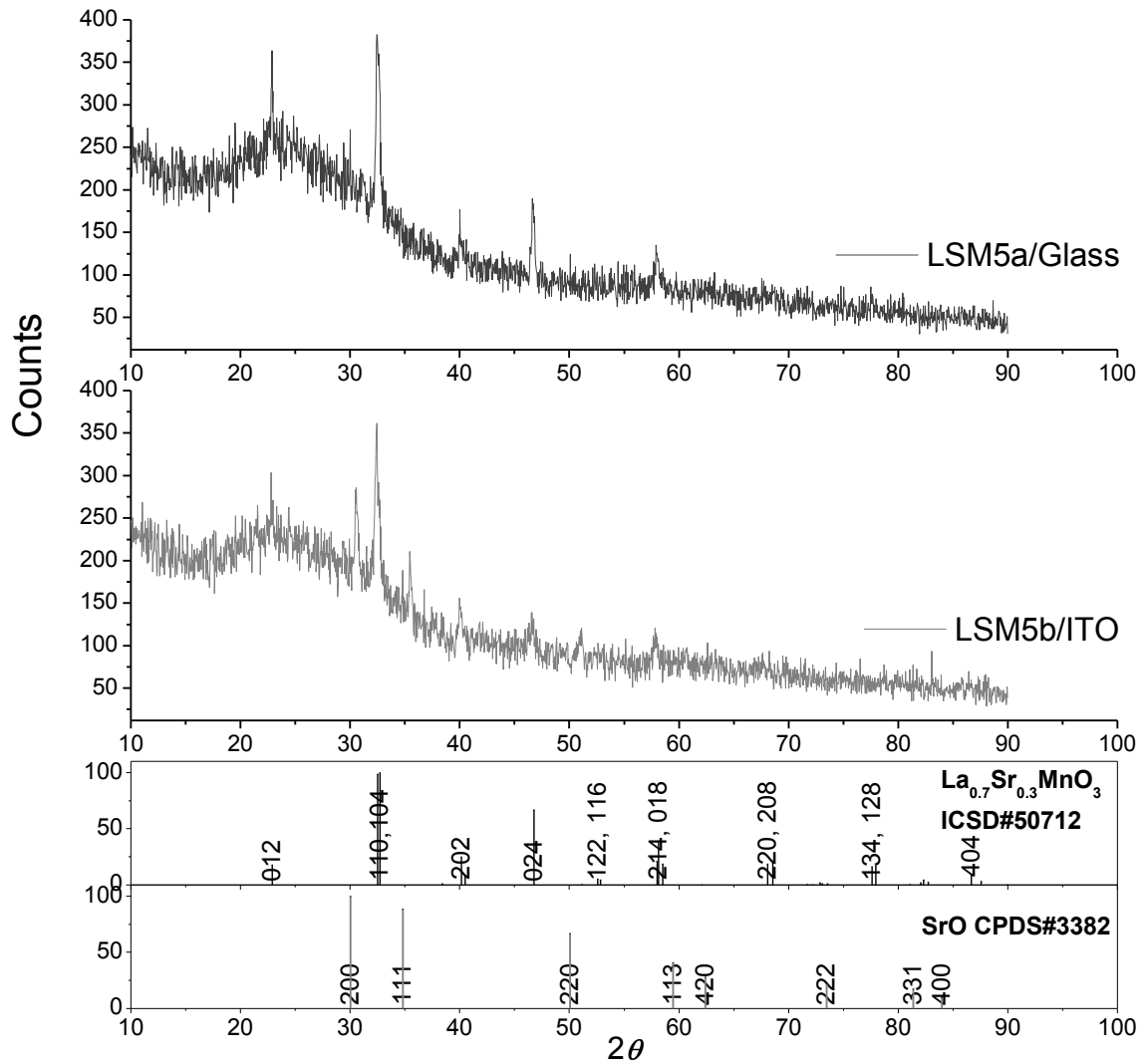


Fig.12.1.1: θ - 2θ XR Diffractograms for samples LSM5a/ITO, LSM5b/glass; XRD Data base patterns for $\text{La}_{0.7}\text{Sr}_{0.3}\text{MnO}_3$ [ICSD#50712] and SrO [CPDS#3382] (bottom)

Preliminary XRD measurements performed for the 3rd series of samples suggested homogeneous and epitaxial manganite films that grow in the rhombohedral phase justifying further characterization by High Resolution XRD.

For the sample LSM3b deposited onto MgO (100) substrate, indexing procedures enable to identify the rhombohedral $R\text{-}3c$ symmetry group common peaks like (012) at $2\theta \sim 22.8^\circ$ and (024) at $\sim 46.5^\circ$, as observed on top of in figure 12.1.2, giving a lattice parameter of $a = 5.52 \text{ \AA}$. The distinctive rhombohedral “double” pattern due to the diffraction of some particular planes like (110) and (104) should not be mistaken with the double peaks observed in the rocking curve at $2\theta \sim 46.5^\circ$, corresponding to a single (024) reflection.

Although the d_{024} remains the same, there are two slightly different alignment directions for the crystallites growth, revealed by the two peaks (with $\Delta\Omega \sim 1^\circ$) visible on the rocking curve of figure 12.1.2 centre right.

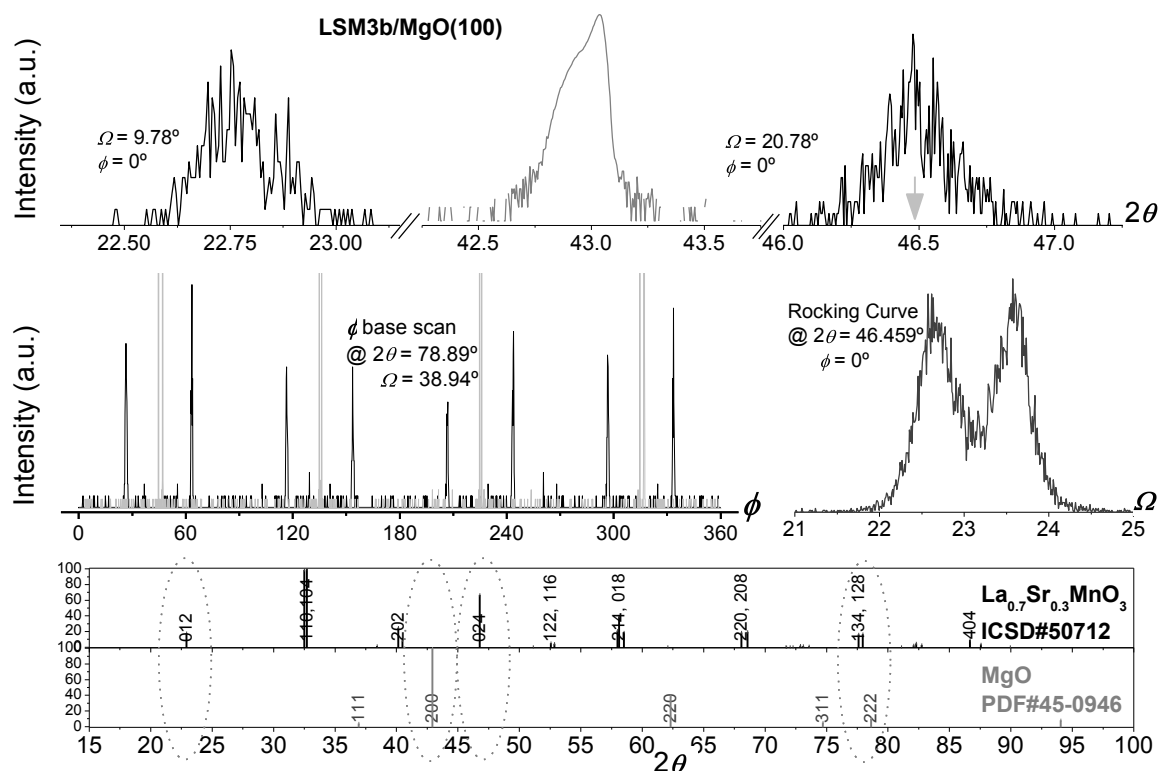


Fig. 12.1.2: HR-XRD of sample LSM3b/MgO(100); top: θ - 2θ scans details at 22.8° , 43.0° and 46.5° ; Φ scan at $2\theta = 78.89^\circ$, $\Omega = 38.94^\circ$; centre right: Rocking curve at $2\theta = 46.46^\circ$ (centre left); XRD Data base patterns for $\text{La}_{0.7}\text{Sr}_{0.3}\text{MnO}_3$ [ICSD#50712] and MgO [PDF#45-0946] (bottom).

This dual orientated growth feature is imposed to the LSM phase by epitaxial adjustments to the substrate lattice; it can also be traced in the Φ scan of figure 12.1.2 at centre left, where appears two sets of planes (134), rotated by $\Delta\Phi \sim 37^\circ$, resulting from the film 4 reflections at left, plus 4 reflections at right siding the MgO substrate (222) peaks. a)

Further confirmation is shown on the reciprocal space scan presented on figure 12.1.3, the lower peak is originated the (200) reflection from the MgO substrate while the film has a twined oriented growth in close directions.

a) Note: this scheme could also be valid to (128) planes, that have a reflection at $2\theta \sim 78.9^\circ$, rotated by $\sim 23^\circ$ in relation to the similar (134) planes, but that are not in the same ϕ axis.

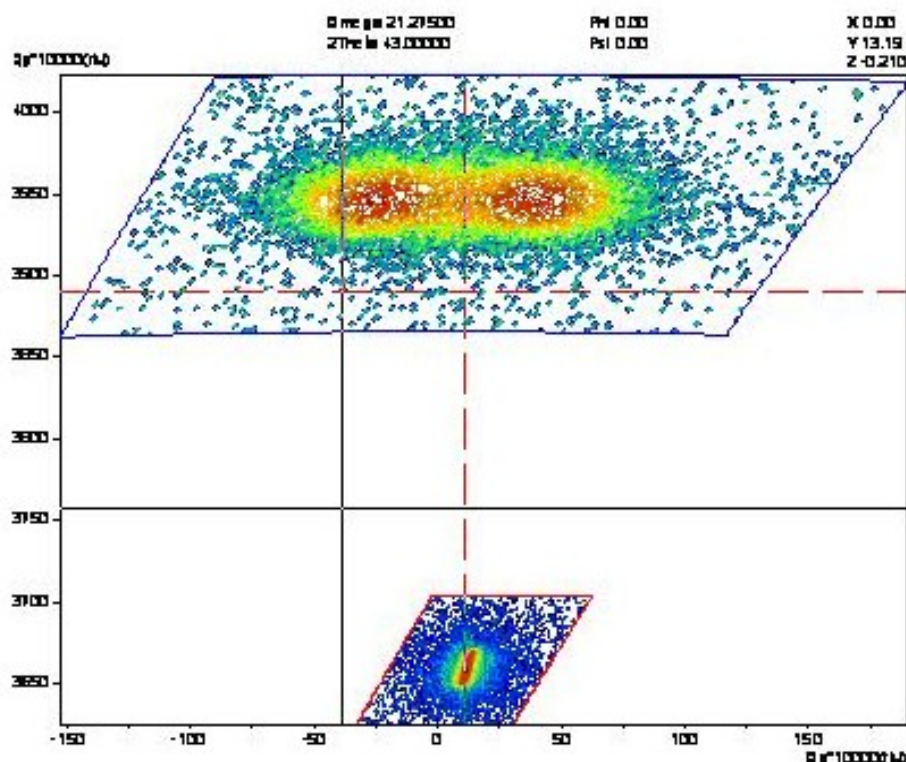


Fig.12.1.3: “Q_x,Q_y” HR-XRD of LSM3a/MgO(100)

Similar results and interpretation are recognizable in the θ - 2θ graphs and Rocking curves of sample LSM6a also deposited onto MgO (100) substrate as depicted in figure 12.1.4, giving a lattice parameter of $a = 5.51$ Å. For sample LSM6b, deposited onto LaAlO₃ (100), whose XRD graphs are depicted on figure 12.1.5, the lattice parameter a approaches ~ 5.57 Å.

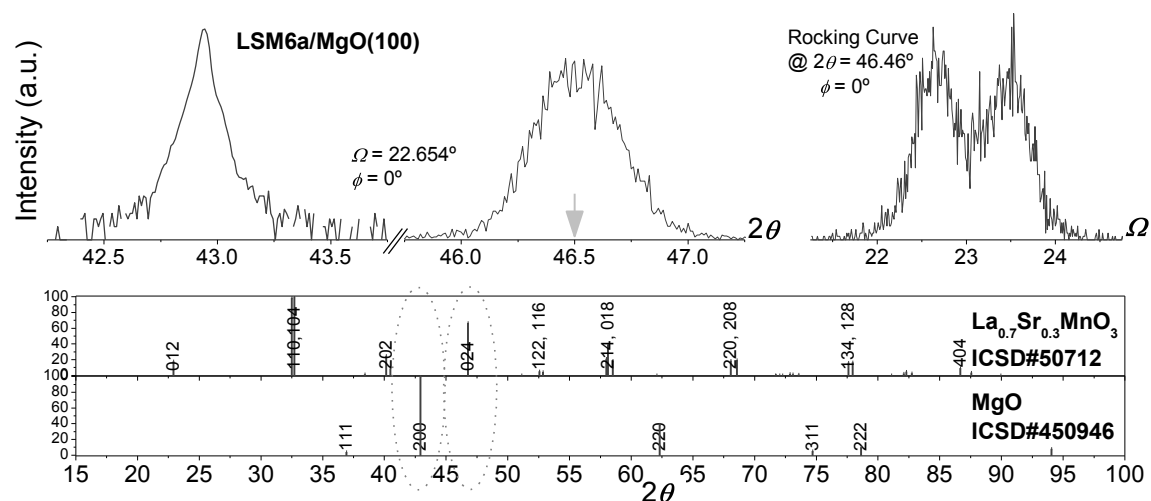


Fig.12.1.4: HR-XRD of sample LSM6a/MgO(100): θ - 2θ scans details at 43.0° and 46.5° (top); Rocking curve at $2\theta = 46.46^\circ$ (top right); XRD data base patterns for La_{0.7}Sr_{0.3}MnO₃ and MgO (bottom).

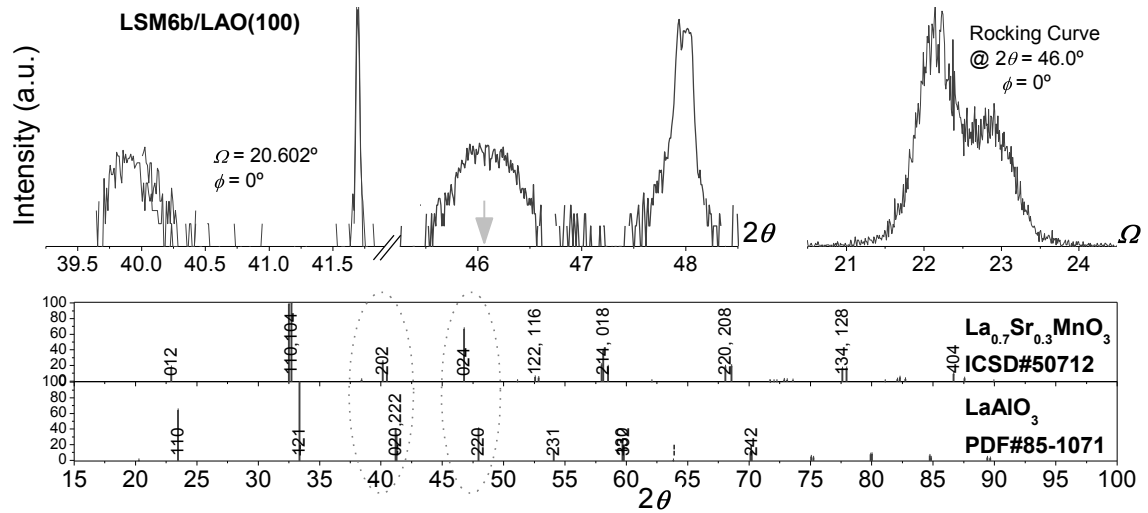


Fig.12.1.5: HR-XRD of sample LSM6a/LaAlO₃(100) (top): θ - 2θ scans details near 40° and 47° (left and centre); Rocking curve at $2\theta = 46.0^\circ$ (right); data base patterns for La_{0.7}Sr_{0.3}MnO₃ and LaAlO₃ (bottom).

For the sample LSM3a deposited onto SrTiO₃ (110) substrate, the HR-X-Ray diffractograms depicted on figure 12.1.6 may be identified once more to the SG $R\bar{3}c$ indexed to planes (110) and (104) at $2\theta \sim 32.49^\circ$, that became distinguishable by performing a rocking curve from 15 to 17° in Ω range, as observed in centre left graph.

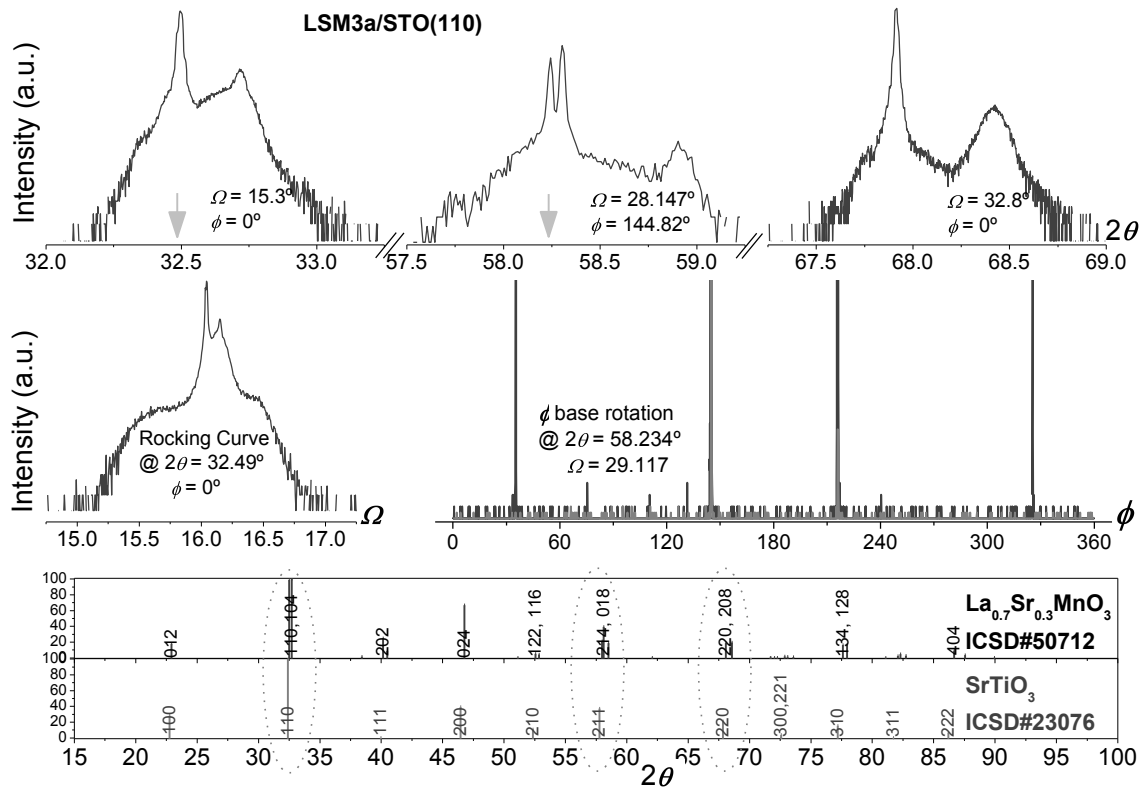


Fig.12.1.6: HR-XRD of LSM3b/SrTiO(110) top: θ - 2θ scans details (top): Rocking curve at $2\theta = 32.49^\circ$ (centre right); ϕ scan at $2\theta = 58.23^\circ$, $\Omega = 29.12^\circ$ (centre left); XRD Data base patterns for La_{0.7}Sr_{0.3}MnO₃ and SrTiO₃ (bottom).

The similarity between the rhombohedral planes of the LSM phase to the cubic substrate planes is also substantiated by Φ scans performed for the film and the substrate as shows the superposition of both diffractograms seen at centre right of figure 12.1.6, where the (214) planes from the film lay on the (211) planes from the substrate.

It is possible to observe a peculiar broadening of the SrTiO_3 peaks patent on the θ - 2θ diffractograms; a more detailed HR-XRD represented in the reciprocal space graph of figure 12.1.7 enable us to recognize that the substrate itself present some crystallites spreading from the main (110) orientation, certainly due to maculae in the surface, giving rise to a distribution of related satellite peaks from the epitaxial growth of LSM phase.

Despite of the uncertain quality of the substrate, the particular experimental deposition conditions lead to an effective epitaxial growth of the LSM phase, which follows even the minority of stray crystallites, revealing the preponderance of the substrate in the behavior of the film LSM phase formation.

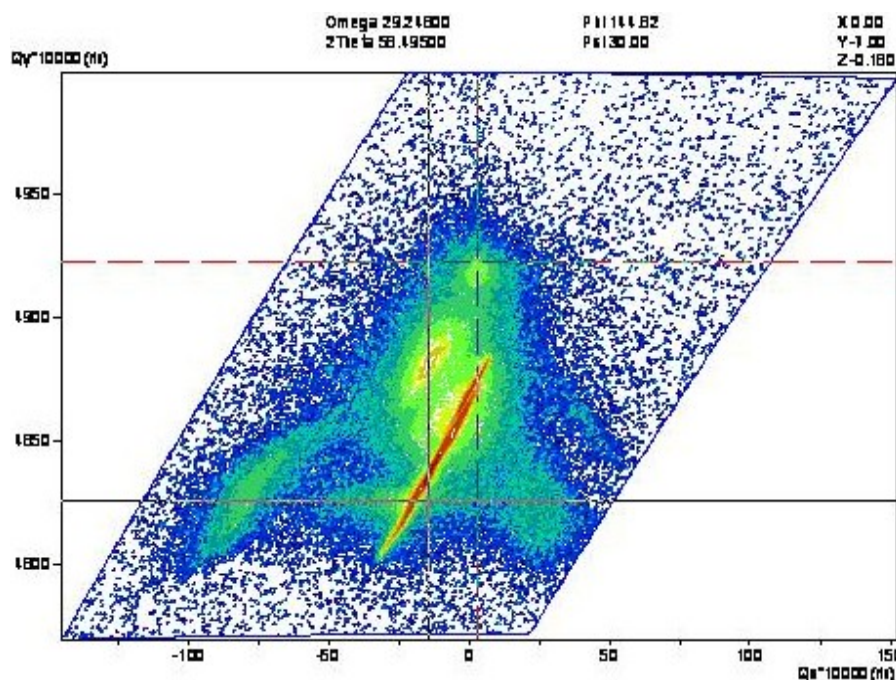


Fig.12.1.7: “Q_x.Q_y” HR-XRD of LSM3a/SrTiO(110)

From TEM pictures on figures 12.1.8 it's possible to observe on the film upper surface the presence of a ~20 nm jagged layer that justifies the polycrystalline diffraction rings in the TEM diffraction pattern of figure 12.1.9, obtained in the perpendicular direction to the film surface. The film seems to grow epitaxially near the substrate and becomes polycrystalline towards the surface.

Due to the substrate square lattice symmetry in the direction 110, the epitaxy of the LSM phase also presents $a = b \sim 5.48 \text{ \AA}$ in the plane parallel to the substrate surface, corroborating the previous two XRD Φ scans, showing the coincidence of the film and substrate peaks, as previously seen on figure 12.1.6.

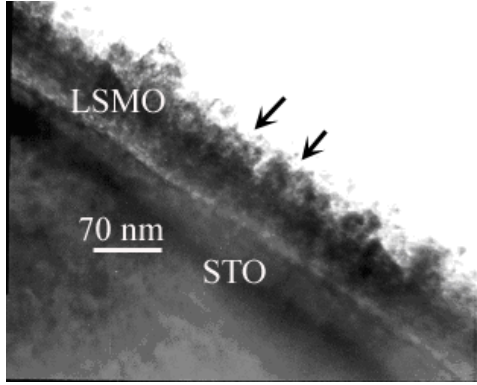


Fig.12.1.8: TEM Cross section image of sample LSM3a/SrTiO₃(110)

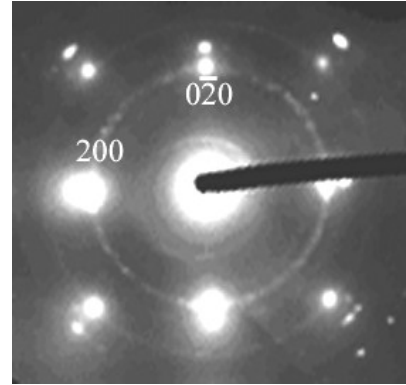


Fig.12.1.9: TEM Diffraction pattern of sample LSM3a/SrTiO₃(110)

SEM images from representative samples are presented in figures 12.1.10 to 13. It is patent from top surface images the tight reticulated arrangement of the film phase composed of $\sim 50 \text{ nm}$ grains. From the transverse fractures images it is possible to confirm the film surface higher rugosity of the 3rd series of samples while a clear improvement on the film uniformity and smoothness for the 6th series.

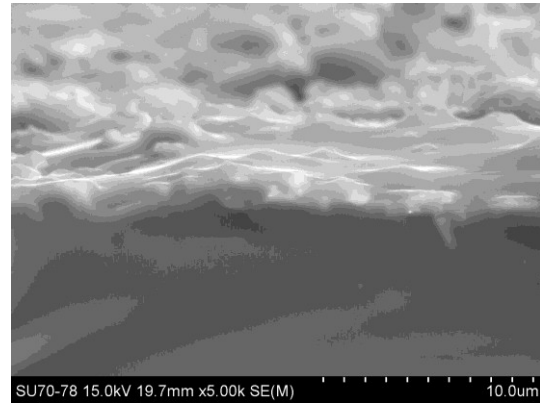
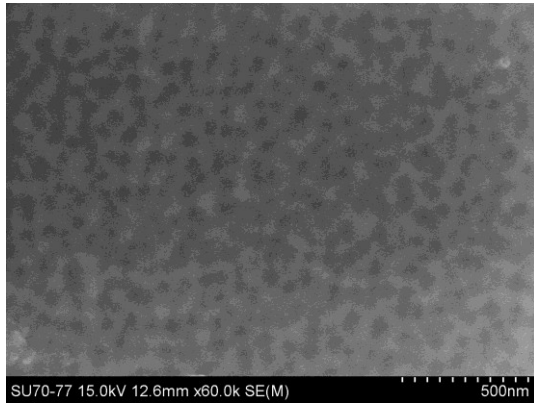


Fig.12.1.10: SEM images of sample LSM3a/MgO(100): top surface (right); transverse fracture (left).

Comparing the several samples film thickness for the same deposition conditions of the 6th series, it is observable that the film grown on SrTiO₃ substrate has $\sim 150 \text{ nm}$ thick, around 50% higher than the $\sim 100 \text{ nm}$ of film grown on MgO substrate, whereas the film grown on Al₂O₃ substrate has grown up to $\sim 1 \text{ }\mu\text{m}$ thick.

Further confirmation that the film phase growth rate noticeably depends on the nature of the substrate is also detected from the RBS measurements illustrated in figure 12.1.14 of the 3rd series of samples, sample LSM3a grown on SrTiO₃ is ~20% thicker and ~2% denser than sample LSM3a grown on MgO, even deposited simultaneously under same conditions and having similar La/Mn content.

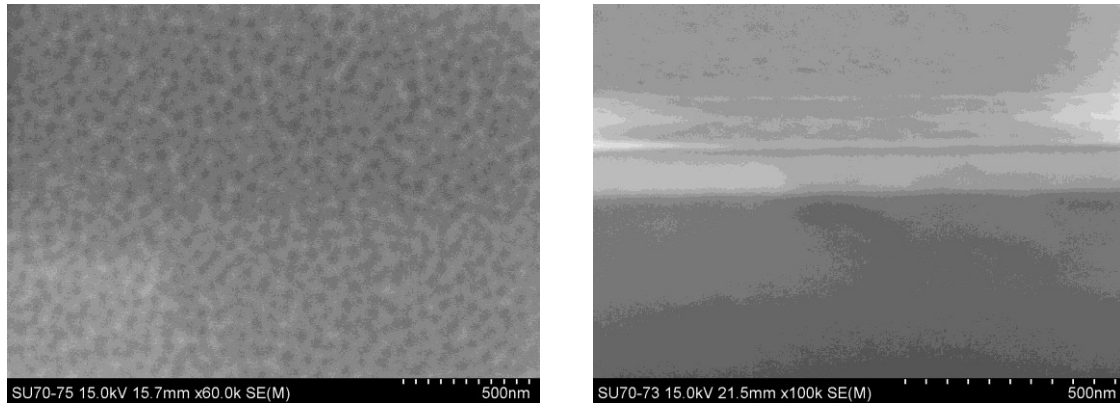


Fig.12.1.11: SEM images of sample LSM6a/MgO(100): top surface (right); cross section (left).

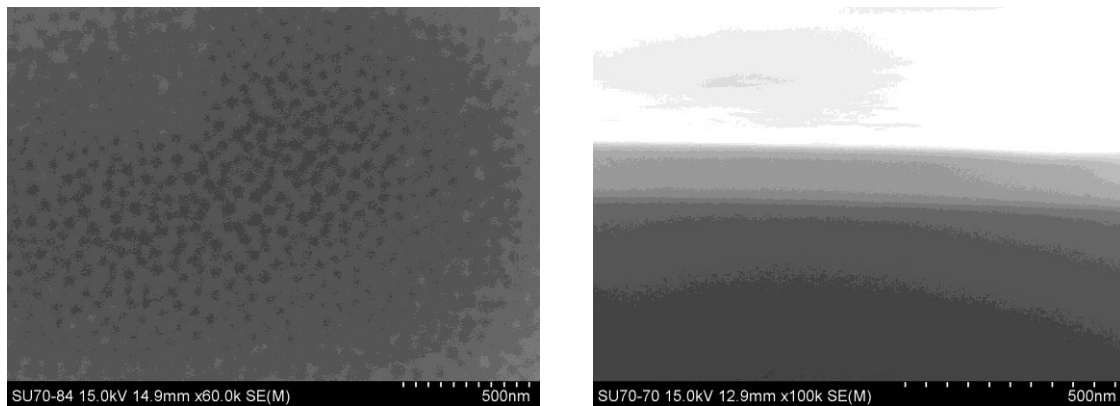


Fig.12.1.12: SEM images of sample LSM6c/SrTiO₃(100): top surface (right); cross section (left).

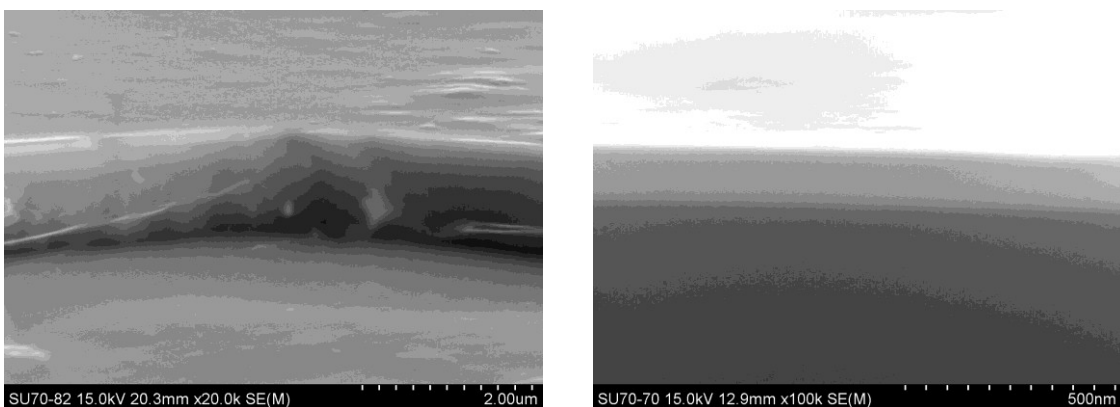


Fig.12.1.13: SEM images of sample LSM6d/Al₂O₃(0001): transverse fracture (left); cross section (right).

The RBS chemical composition results are presented in table 12.1.1 and 12.1.2, the elements ratio can be traced to the target composition, with some preponderance of the Lanthanum over Strontium and Manganese.

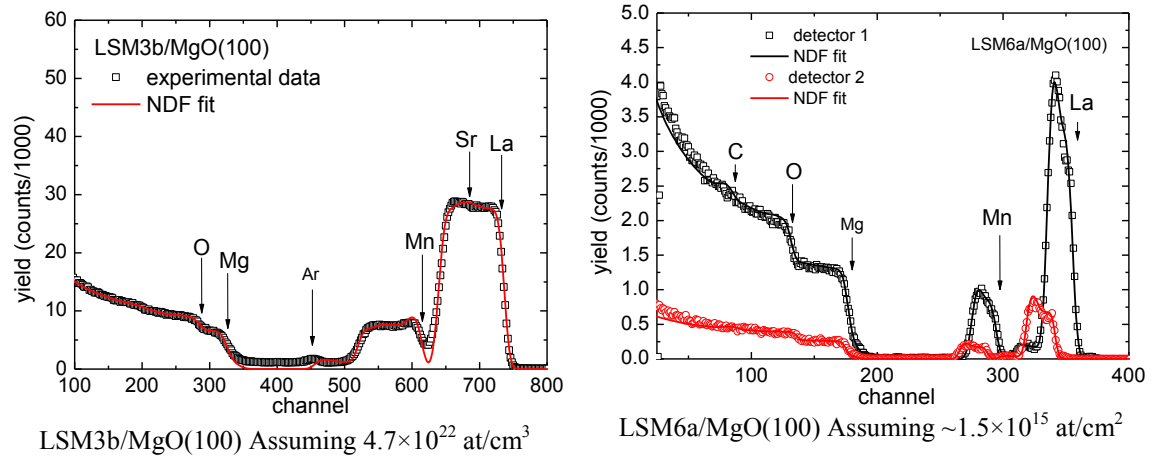


Fig 12.1.14: RBS measurements and fittings for samples LSM3b (left) and LSM6a (right) in MgO(100)

thick	MgO	La	Mn	O	Sr	La/Mn	Sr/Mn
90 nm	-	15.7	21.4	59.2	3.7	0.73	0.17
130 nm	-	16.4	21.7	56.4	5.5	0.76	0.26
115nm	-	14.9	18.3	59.8	7.0	0.81	0.38
>425 nm	100	-	-	-	-	-	-

layer	MgO	La	Mn	O	Sr	La/Mn	Sr/Mn
728 nm	0	6.5	8.4	55.9	0.8	0.77	0.1
114 nm	0	45.8	52.8	1.3	0.1	0.87	0.002
-	100	-	-	-	-	-	-

Table 12.1.1: Sample LSM3b/MgO(100) RBS results Table 12.1.2: Sample LSM6a/MgO(100) RBS results

In figures 12.2.15 and 12.2.16 are shown some illustrative graphs corresponding to EDS-SEM measurements summarized in table 12.1.3 for the pertinent thin film elements; overall results the percentage of Sr is bellow the expected 30% nominal from the target, pointing to a deficient incorporation of this element in the film phase.

Sample	EDS kV line:	La (% at.) <i>L</i>	Sr (% at.) <i>L</i>	Mn (% at.) <i>K</i>	La/Mn	Sr/Mn
LSM1a/STO(100)	20	3.97	n.a.	7.35	0.54	n.a.
LSM1b/MgO(100)	20	5.08	0.83	6.13	0.83	0.14
LSM2a/STO(100)	20	5.19	n.a.	8.96	0.58	n.a.
LSM2b/MgO(100)	20	7.06	0.98	8.22	0.86	0.12
LSM3a/MgO(100)	15	5.78 ± 0.8	0.58 ± 0.1	8.63 ± 0.5	0.67	0.07
LSM6a/MgO(100)	15	2.21 ± 0.4	0.25 ± 0.1	3.16 ± 0.3	0.70	0.08
LSM6b/LAO(100)	15	n.a.	0.17 ± 0.0	7.22 ± 0.3	n.a.	0.02
LSM6c/STO(100)	15	n.a.	n.a.	6.85 ± 0.3	n.a.	n.a.
LSM6d/AIO(0001)	15	2.99 ± 0.5	0.45 ± 0.2	4.72 ± 0.4	0.63	0.1

Table 12.1.3: Chemical composition of samples from EDS (SEM) measurements.

Only the composition of samples LSM3a and LSM6a were measured by both EDS and RBS methods; however, these results cannot be directly compared since RBS is depth sensitive while the EDS probes throughout the film thickness well into the substrate; in addition the composition accuracy is affected by additional factors related to the film surface roughness, thickness, density and the higher the electrons beam acceleration voltage the deeper it reaches the substrate; rendering meaningless the estimation of common elements both present in the substrates and films.

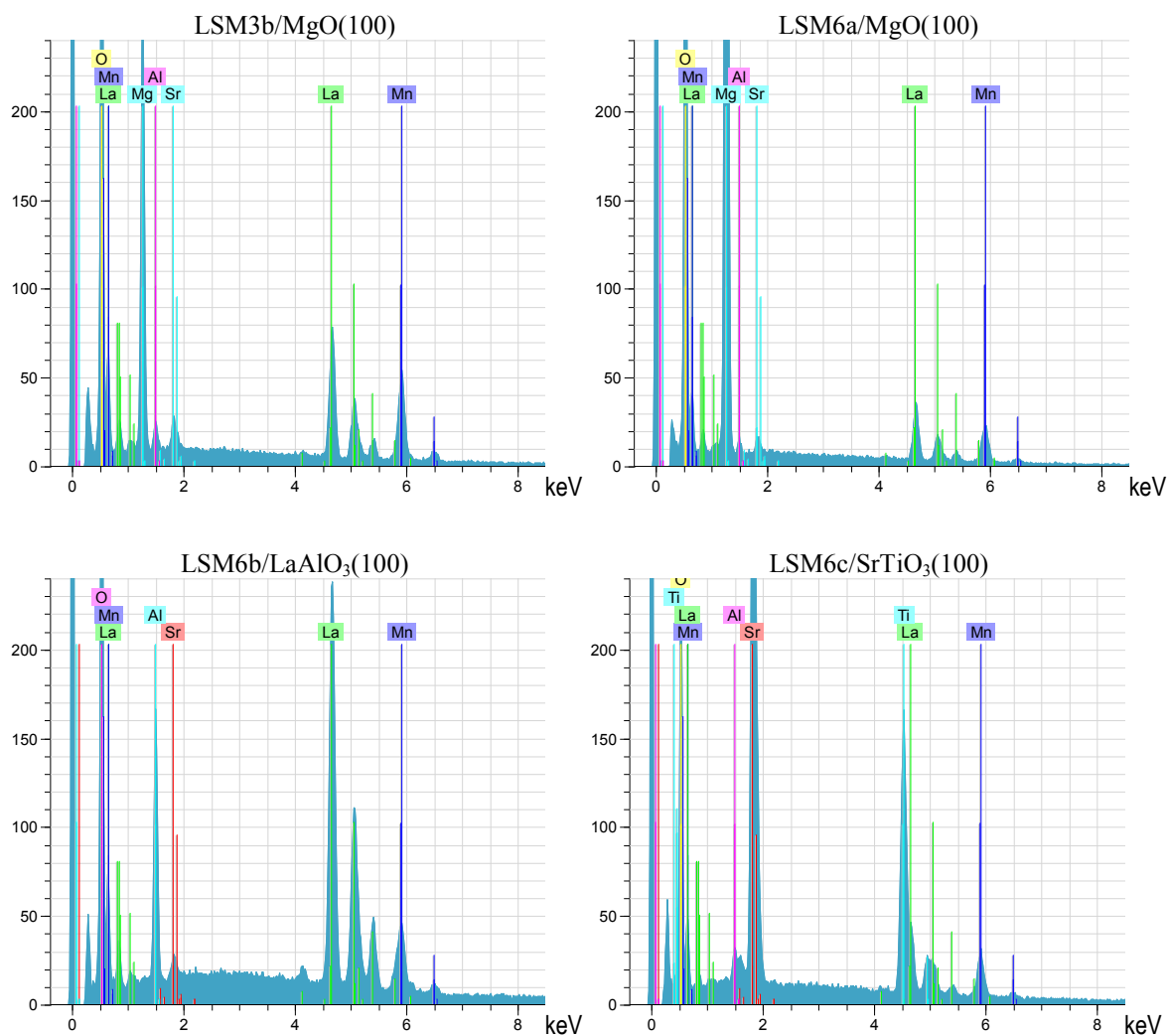


Fig.12.1.15: Examples of EDS acquisition graphs from the surface of samples identified; it is also possible to observe the different spectral contributions from the distinct substrates.

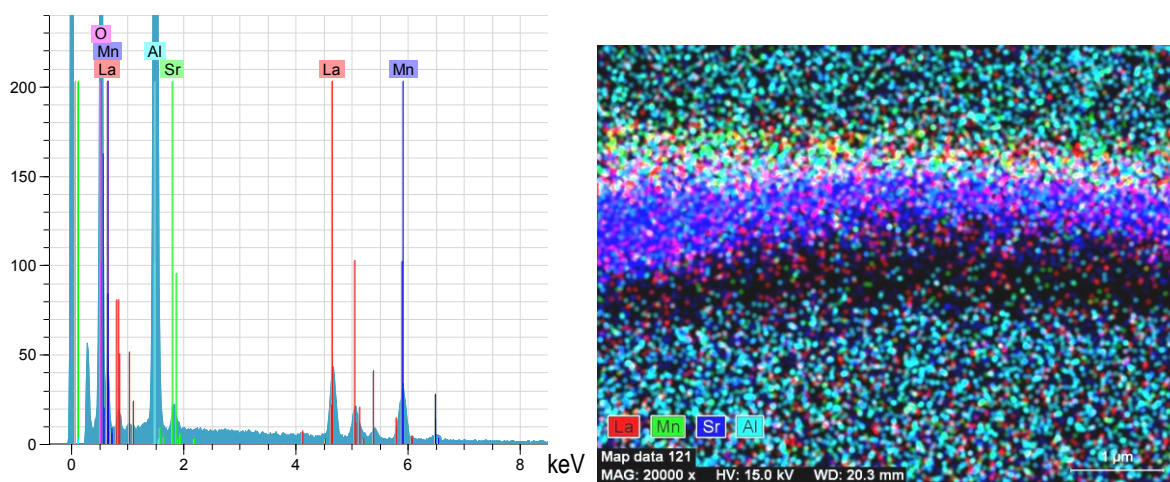


Fig.12.1.16: Surface EDS measurement (left); EDS map of LSM6d/Al₂O₃(0001) fracture point from respective SEM image in figure 12.2.14 (right).

Raman spectroscopy was performed in the 6th series of films in order to corroborate the identification of the LSM phase structure [12.1.2], because the XRD characterization does not exclude the possibility that the usual rhombohedral symmetry could suffer some partial orthorhombic or tetragonal distortion due to the epitaxial growth of the film onto the substrates. In fact these space groups have analogous distribution of main peaks, although indexed to different planes they lay within the analyzed regions $2\theta \sim 33^\circ$, $\sim 47^\circ$ and $\sim 58^\circ$ of the XRD diffractograms. As illustrated in the four examples of figure 12.1.17, the Raman spectra from the film phase (dark lines) conceals the original Raman response from the respective clean substrates (light lines), the intense peak detected at $\sim 320 \text{ cm}^{-1}$ cannot be interpreted as intrinsic to the LSM phase since it appears also in some of the distinct substrates, it rather results from the UV 325 nm laser line constructive interference with the sensor grid.

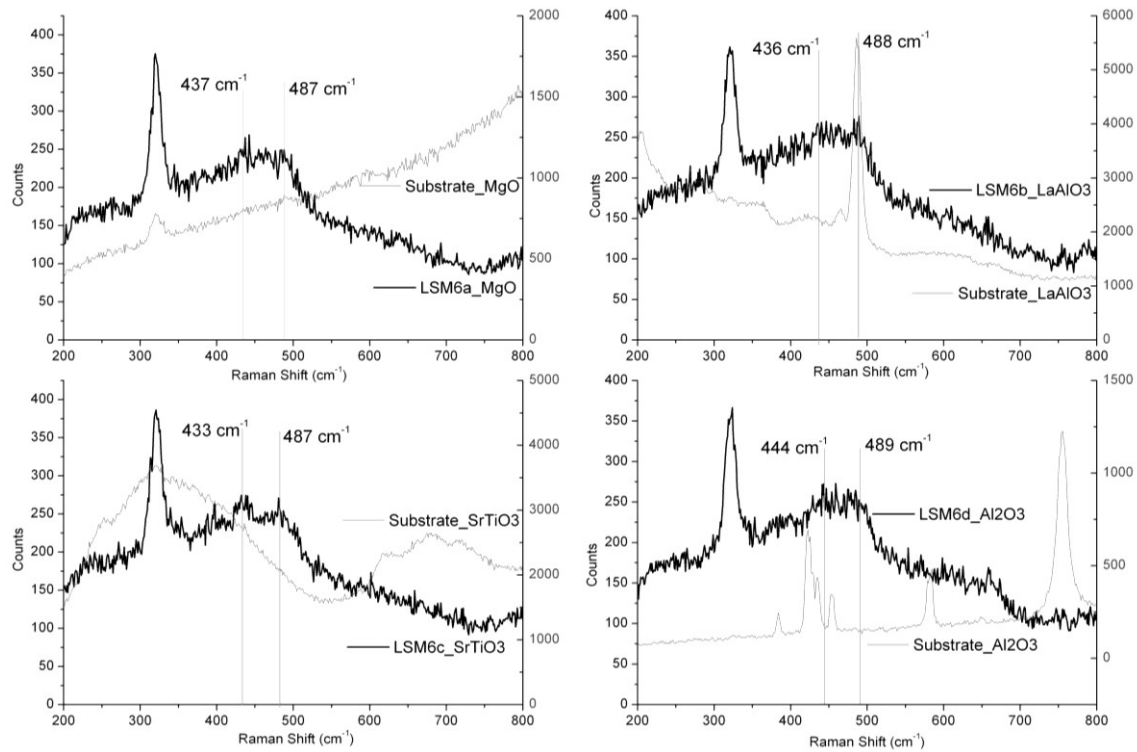


Fig.12.1.17: UV Raman spectroscopy diagrams for samples of the 6th series.

Eventual Raman peaks originated from the LSM phase to be considered are identified for each sample in the respective graphs of figure 12.1.17; the most significant are centered at 433 cm^{-1} and 487 cm^{-1} in sample LSM6c deposited onto SrTiO_3 substrate. These bands are usually assigned to the antisymmetric stretching (A_g) associated with the MnO_6 Jahn Teller distortion that are normally found in the $Pbnm$ orthorhombic manganites

structure; nevertheless, these modes are compatible with the $R-3c$ structure, particularly in case of the $\text{La}_{0.7}\text{Sr}_{0.3}\text{MnO}_3$ phase having a density of states that allow similarities between the bands [12.1.2], [12.1.3]. Hence, considering the lack of a more numerous and definitive peaks exclusive of the orthorhombic phase, it's assumed a dominant presence of the rhombohedral phase.

Representative magnetization measurements as function of temperature and magnetic field performed by VSM are presented in figure 12.1.18. The M vs. B Graphs clearly show the diamagnetic contribution from substrate, masking the small FM thin film contribution particularly above 3-4 Tesla external field. The M vs. T measurements had to be performed at a relatively high B of 0.5 Tesla in order to obtain an adequate VSM signal from the samples; as consequence the actual thin films magnetic moment has more $\sim 0.25 \times 10^{-3}$ emu than the observed in the respective graphs. The thin films are also approximately under magnetic saturation condition; hence the observed 230-240 K for the PM transitions can be slightly over estimated due to the imposed FM state.

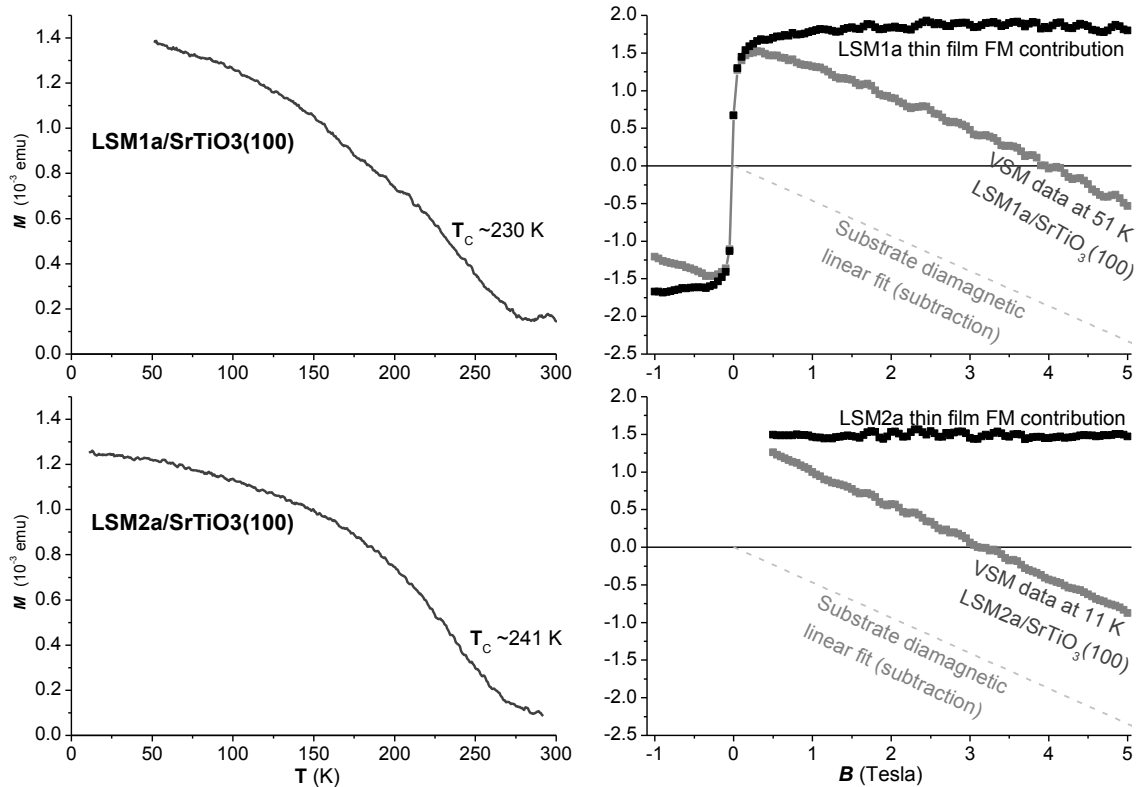


Fig.12.1.18: VSM measurements of magnetization as function of T (left) and B (right), for samples LSM1a (top) and LSM2a (low) deposited onto SrTiO_3 (100) substrates.

Figure 12.1.19 shows the magneto-resistance characterization performed only in the 6th series of samples, since they present the finest composition, structure and magnetic properties achieved. The temperature dependence of the resistivity without and under 0.8 Tesla magnetic field for the samples is presented in left and the correspondent MR% vs. T graphs are presented on the right of the same figure.

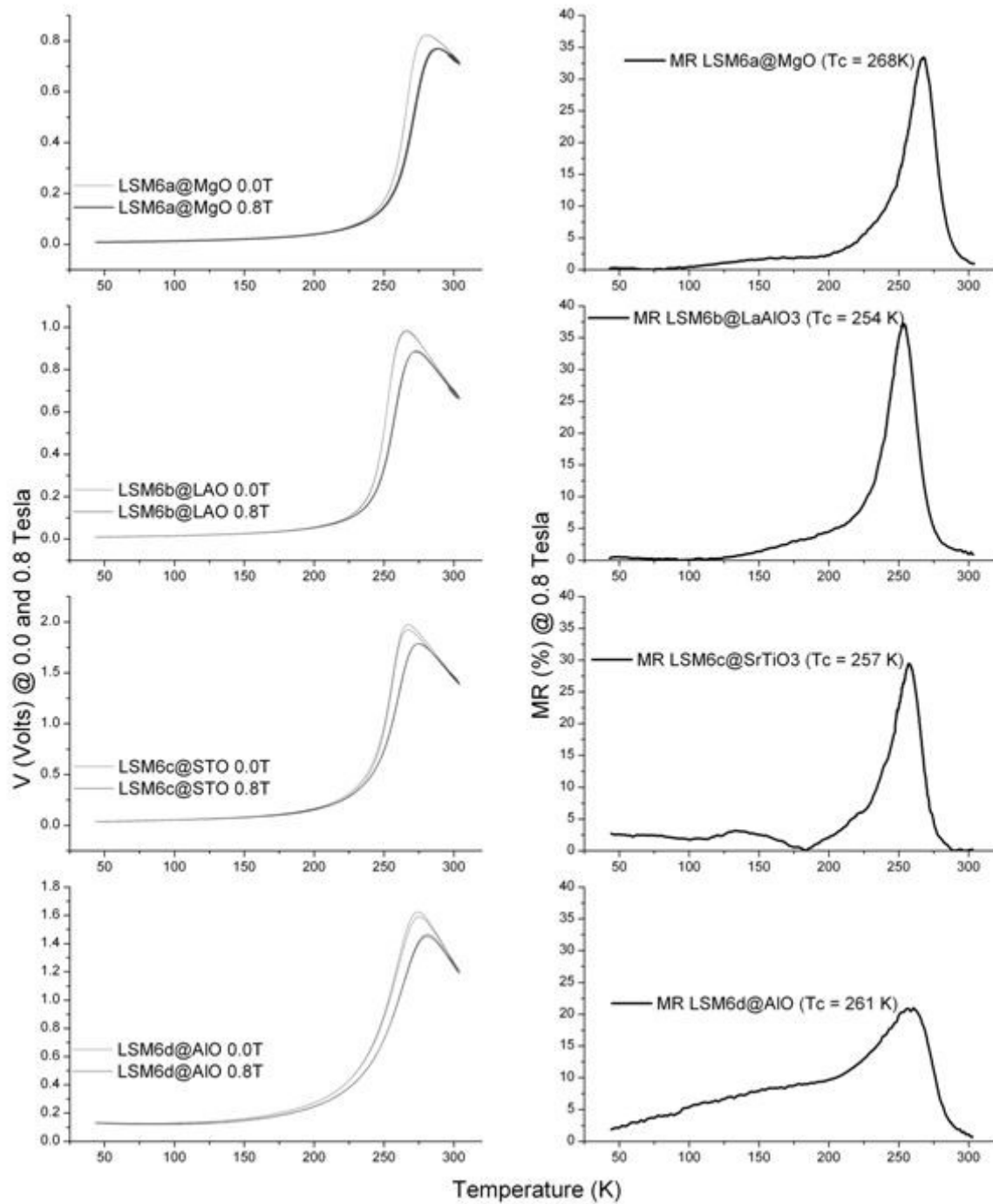


Fig.12.1.19: Magneto resistance measurements on the 6th series of LSM samples: Left Voltage vs. Temperature graphs at 0 and 0.8 Tesla and 1 mA dc; Right: respective MR percentage vs. temperature

graphs.

It is clear that the LSM phase growing epitaxially on MgO has better MR performance than on the SrTiO₃ substrate, both in critical temperature: 268 K compare to 257 K and maximum intensity: 33% to 29%; the LSM film deposited onto Al₂O₃ presents a significant MR response above 5% down to 100 K while the other samples drastically drop the MR response at 200 K, while onto the LaAlO₃ substrate the MR reaches the 37% maximum. In practical terms the 6th series of LSM phase thin films have a MR average critical temperature $\sim 260 \text{ K} \pm 5\%$ of an order of 10 to 30 % within a 50 K range and disappears above 300 K; these values should be compared to the polycrystalline La_{0.7}Sr_{0.3}MnO₃ bulk phase from the target that is characterized on previous section 11.1, whose MR performance is much lower, only of $\sim 6\%$ at 300 K, reducing to $\sim 4.5\%$ at 350 K and still active at 370 K with $\sim 3\%$ MR.

When evaluated whit the previous VSM magnetization measurements it is evident the progress of the ferromagnetic transition temperature (T_C) of the thin film LSM phase with the adjustments of the deposition conditions in order to improve the films' quality.

The magnetization is mostly dominated by the chemical composition and structural homogeneity of the films which dictate the ratio of Mn⁴⁺ to Mn³⁺ that in turn has a major influence in the magnetic ordering phase (FM/AFM); whereas the electric transport behavior depends strongly on the electrons transfer integral correlated to the manganite phase structure which, in its turn, is imposed by the epitaxy to the substrate lattice, in addition factors such as crystallographic defects, grain size and hopping effects between grains interfaces have also a direct role on resistivity.

Overall results analysis indicate that the epitaxial growth of the LSM phase is proven more efficient onto the SrTiO₃ than the other substrates, the lattices similarities both in planes distances and directions play a fundamental role in the film growth, as can attest the comparison between the respective data base diffractograms depicted on figure bottom of figure 12.1.6.

The MgO, LaAlO₃ and Al₂O₃ substrates are less suitable templates to the growth of epitaxial LSM phase due to the mismatch between lattices; consequently, part of the thermal energy of the vaporized elements from the sputtering process is channelled for compensate the higher Gibbs energy toll necessary to for nucleation and growth process of

the film phase onto the less matching substrates. Hence, less kinetic energy is available for diffusion of the film elements through the substrate surface and to balance the mechanical stress induced by the forced epitaxy to the substrate, as result the film grows in a more multifaceted structure having twined grains.

On the other hand, the less demanding Gibbs energy toll for formation of the LSM phase onto SrTiO_3 substrate means that a wider range of momentum distribution of elements from the plasma arriving to the substrate in will have prompt adhesion to the film phase, thus the superior growth rate when compared to the MgO , LaAlO_3 and Al_2O_3 substrates for which the distribution of species from the plasma with sufficient kinetic energy is reduced and more will rebound and cannot be incorporated in the film.

The best conditions to perform thin films deposition by magnetron RF sputtering of the LSM phase was found empirically in the 6th series of samples, where the film approaches the nominal composition of the target ($\text{La/Mn} \sim 0.7$ and $\text{Sr/Mn} \sim 0.3$), the surface presents a smooth and uniform aspect and the film grows epitaxially onto the substrate in a typical rhombohedral regular structure in particular with lattice compatible SrTiO_3 substrates.

The specific parameters were found by lowering the Argon pressure to 5×10^{-3} mbar, raising O_2 pressure to 2×10^{-3} mbar, setting the RF power to 73 Watt with 200 V bias, the substrate heater at $\sim 700^\circ \text{C}$ and ending by slow cooling in a 0.5 mbar of O_2 atmosphere. By implementing a proficient Magnetron RF sputtering system that enables a high degree of control of deposition parameters it was possible to achieve the successful deposition of high quality epitaxial thin films of the $\text{La}_{0.7}\text{Sr}_{0.3}\text{MnO}_3$ phase onto SrTiO_3 perovskite substrates, opening the perspectives to further research multiferroic multilayers systems namely using also the $\text{La}_{0.7}\text{Ba}_{0.3}\text{MnO}_3$ manganite and the FE BaTiO_3 .

12.2. Ni_2MnGa thin Films deposited by RF Sputtering (@ IENM)

The objectives of this experimental work section were: *i*) to prove the viability of achieving the Ni_2MnGa phase like Heusler alloy as thin films deposited by Magnetron RF sputtering near ambient temperatures conditions (~ 300 to ~ 400 K); *ii*) to determine the specific deposition conditions to achieve the most suited composition and crystalline phase of the Ni_2MnGa thin films grown into PZT buffers on Si substrates.

The first run of experimental depositions was based on a single 3" target available, with nominal composition $\text{Ni}_{0.5}\text{Mn}_{0.33}\text{Ga}_{0.17}$. The surface of this target appears non homogeneous, presenting a mosaic of relatively large grains in different gray shades and textures as shown in figure 12.2.1. Although the chemical composition of this target was far from the conventional $\text{Ni}_{0.5}\text{Mn}_{0.25}\text{Ga}_{0.25}$ stoichiometry for producing functional shape memory Heusler alloy films, it was possible to find the most adequate (relative) deposition parameters to obtain films onto Si (100) substrates having the similar crystalline phase like of the metallic Ni_2MnGa alloy. In this initial run of depositions, only basic XRD structural characterization was foreseen.



Fig. 12.2.1: Photograph of the single 3" target available for first run of depositions, having nominal $\text{Ni}_{0.5}\text{Mn}_{0.33}\text{Ga}_{0.17}$ composition.

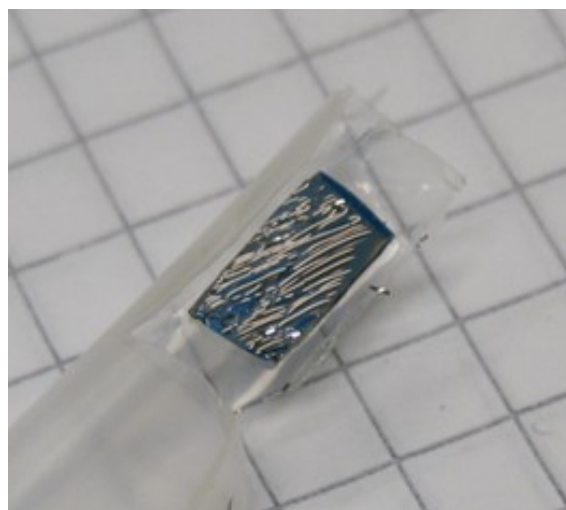


Fig. 12.2.2: Photograph of a film delaminating from substrate after being under temperatures above 400°C or high fields during magnetic measurements.

The deposition parameters to be studied included the magnetron power, Argon pressure, substrate temperature and position and how these influence the crystallization of the alloy thin films onto Si substrates.

The first sets of experimental results indicate that high pressure during sputtering reduces the plasma energy suppressing crystallization and leading to film detachment as exemplified in figure 12.2.2. On the other hand, the plasma becomes unstable under very low Ar pressure which results in the growth of inhomogeneous films. Some investigations were performed to study the film crystallization at different off-axis distances. Equivalent parameters were found for the films deposited at stabilized substrate temperature of 10° C, as well as around 100° C under plasma heating effect.

Basic θ - 2θ scans exemplified on figure 12.2.3 indicate the presence of a single Bragg peak between ≈ 42.5 to $\approx 43^\circ$ which can be indexed to the (220)_C [12.2.1] austenitic cubic phase of the alloy [12.2.2] or as (112)_T tetragonal setting of Ni_{2.16}Mn_{0.84}Ga [12.2.3].

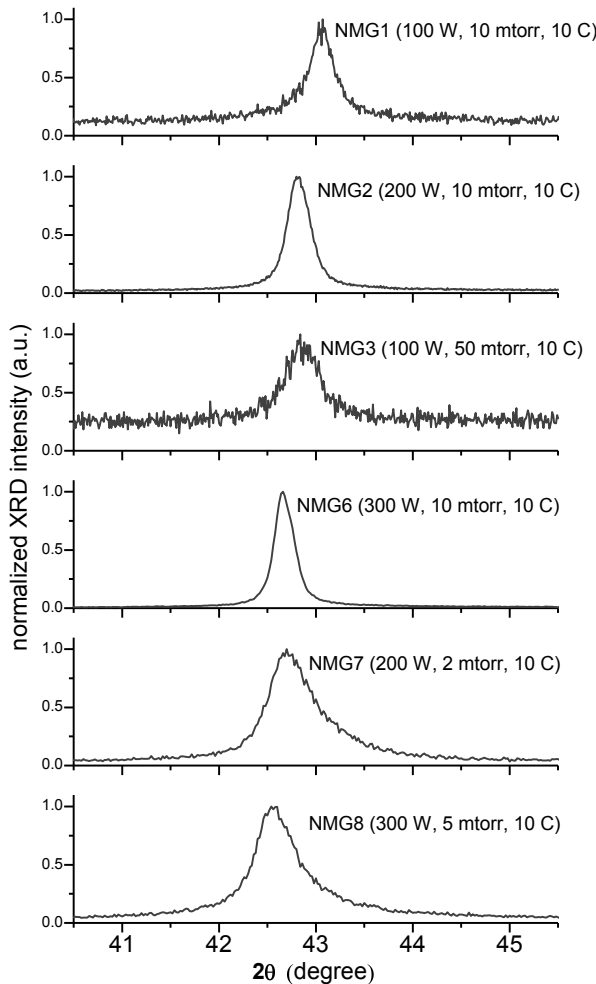


Fig. 12.2.3: Comparative diffractograms of Ni₂MnGa phase peak indexed to (220)_C or (112)_T.

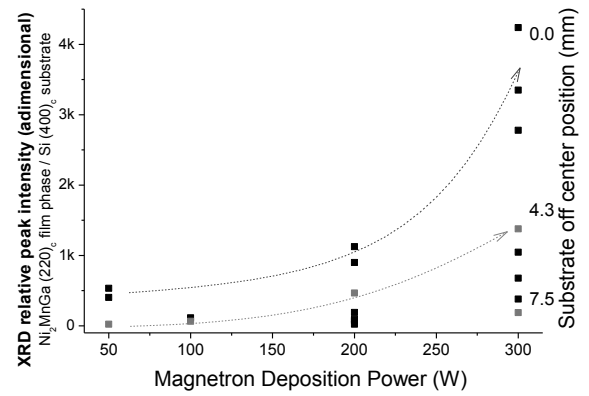


Fig. 12.2.4: Relative influence in the film crystallization of the substrate position and RF magnetron power during deposition.

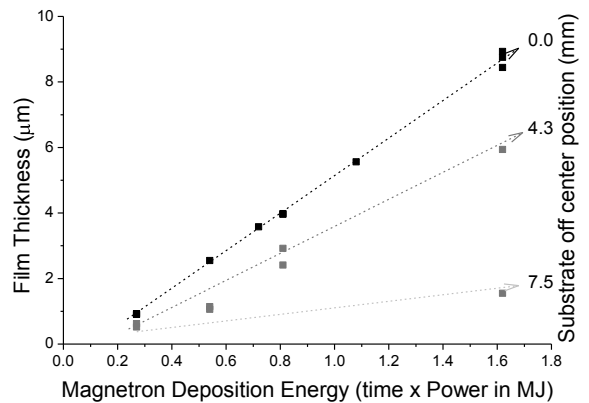


Fig. 12.2.5: Dependence of film thickness with deposition time x power and substrate position.

The cubic cell parameter estimated for these films between $a \approx 5.79$ to ≈ 5.94 Å cannot be attributed to the epitaxial effect of the smaller lattice parameter of the Si

substrate $a \approx 5.431 \text{ \AA}$ and in fact corroborates the higher concentration of Mn in relation to the stoichiometric Ni_2MnGa phase [12.2.4].

The peak intensity, sharpness and position depends mainly on the RF power suggesting that the additional energy of the plasma increases the crystallization of the film during sputtering and induces the formation of other phases. In fact, with a RF power of 300 W a Bragg peak appear at 49.5° which can be indexed as $(111)_C$ of the $\text{Mn}_{0.8}\text{Ni}_{0.2}$ alloy cubic phase [12.2.5]. It means that, in addition to the composition of the film, the structure and lattice parameters are strongly dependent on the RF power applied as depicted in graph from figure 12.2.4.

Films thickness was measured with a conventional profilometer, for an on-axis substrate position and under 300 W magnetron power the films have $\sim 8.5 \text{ \mu m}$ for a 90 min sputtering time under different Argon pressures, which indicates a deposition rate $\sim 95 \text{ nm/min}$. figure 12.2.5 film illustrates the decrease in the deposition rate as consequence of the relative off-axis position of substrate.

At a later time this experimental work was complemented with a more comprehensive analysis of some previously obtained samples; it was possible to perform HR-RXD, SEM, and EDS at the University of Aveiro, while SQUID measurements were made in Duisburg University, Germany.

A more in-depth characterization of one film was performed by HR-XRD, at a low angle measurement $\Omega = 2^\circ$, as represented in figure 12.2.6 curve (c). It indicates segregation of $\text{Mn}_{0.8}\text{Ni}_{0.2}$ alloy [12.2.5] and $\text{Mn}_{1.5}\text{Ni}_{1.5}\text{O}_4$ [12.2.6] at the surface of the film and even the presence of metallic gallium [12.2.7]. In an attempt to identify the Ni-Mn-Ga phases in one of the films deposited on bulk silicon substrate, more careful structure investigations were performed using high resolution four-circle diffractometer. The orientation of the films was investigated by Φ scans for an asymmetrical reflection ($\Psi = 45^\circ$) at $2\theta = 63.67^\circ$ which corresponds without any doubts to the $(400)_C$ peak of the cubic phase of the Ni_2MnGa phase. An example of such a 3D pole figure is given in Figure 12.2.7 for a film grown on Si (100). Four peaks are clearly observed at 90° from each other, indicating a fourfold symmetry as expected for the $(220)_C$ oriented cubic film of austenite Ni_2MnGa alloy. Overall XRD studies showed good crystallization and deduced cubic lattice parameters are presented on table 12.2.1.

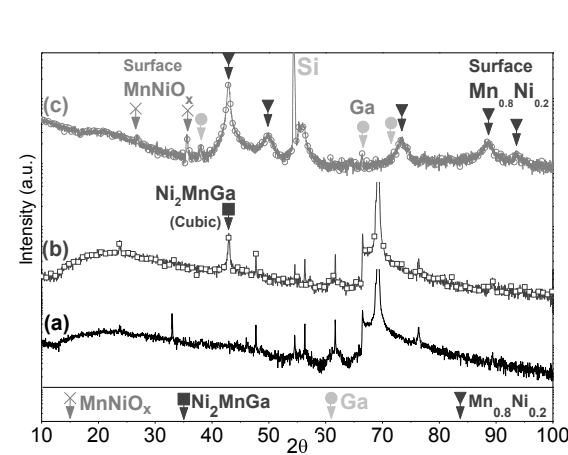


Fig. 12.2.6: XRD scans performed on NMG17 sample: (a) bare Si substrate, (b) film, (c) grazing incidence at $\Omega = 2^\circ$ to analyze film surface.

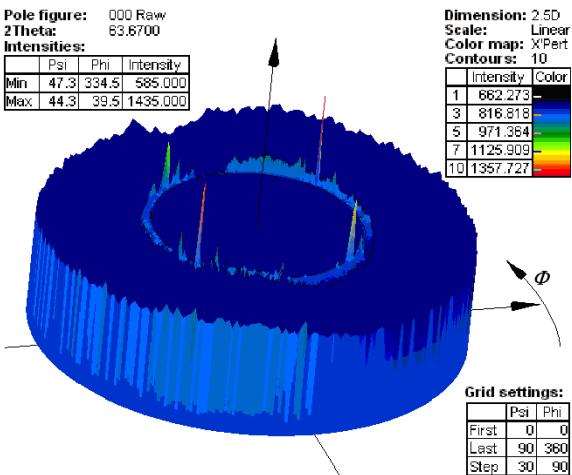


Fig. 12.2.7: Pole figure around the $(400)_c$ peak ($\psi = 44.3^\circ$ to 47.3° at $2\theta = 63.67^\circ$) confirming film cubic symmetry oriented in $(220)_c$ onto Si (100) substrate

SEM examination shows overall smooth and flat surface quality of deposited films, (figures 12.2.8 and 12.2.9) with a preferential and regular columnar growth of the metallic film; respective EDS measurements confirm the relatively higher Mn composition of film, as listed on table 12.2.1.

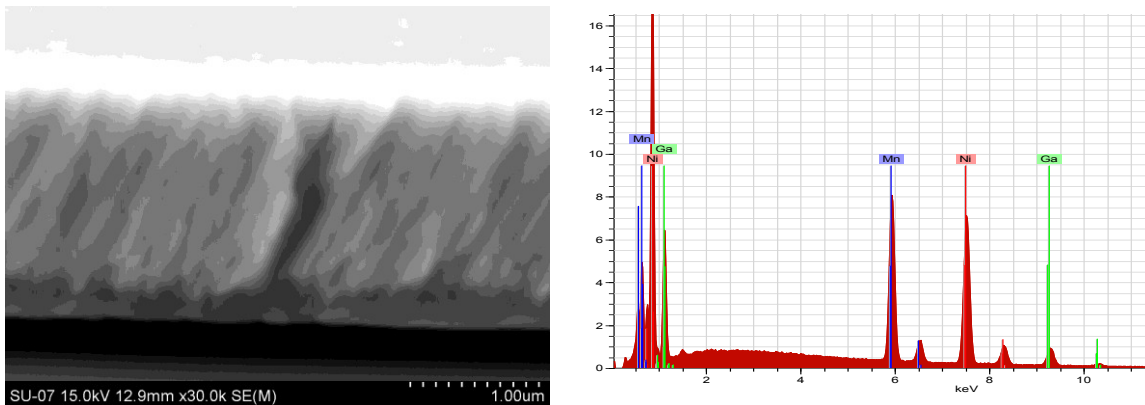


Fig. 12.2.8: SEM image of sample NMG14 cross section and respective surface EDS measurement.

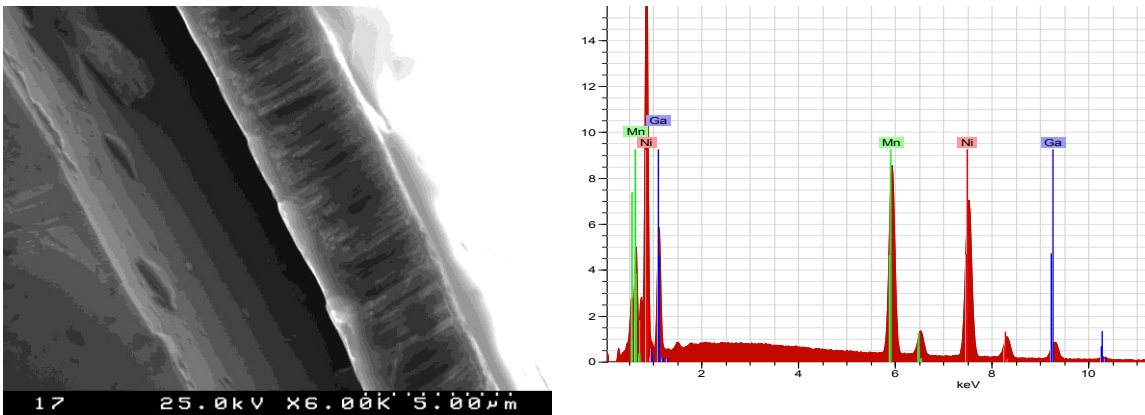


Fig. 12.2.9: SEM image of sample NMG17 cross section and respective surface EDS measurement.

Next step in this work was to study the growth, adhesion, and properties of the Ni-Mn-Ga films deposited onto a (100) oriented PZT thick film; this perovskite layer was previously deposited onto Si (100) substrates having a top LaNiO_3 (LNO) semiconductor thin film serving as epitaxial buffer and bottom electrode for the PZT film, as described in [12.2.8], using a dedicated magnetron sputtering *Addax* system.

The standard quality of these PZT films was verified using SEM and XRD analyses. The performed measurements confirmed that the thickness of this buffer layer is about $\sim 1 \mu\text{m}$. Good surface quality is patent in Figure 12.2.10. The films were deposited onto this perovskite type buffer applying the previously optimized sputtering parameters used for the deposition on Si (100) substrates. With the aim to compare the data with our previous results obtained on bare Si (100) substrates, extensive structural investigations were performed on NMGPZT6 sample.

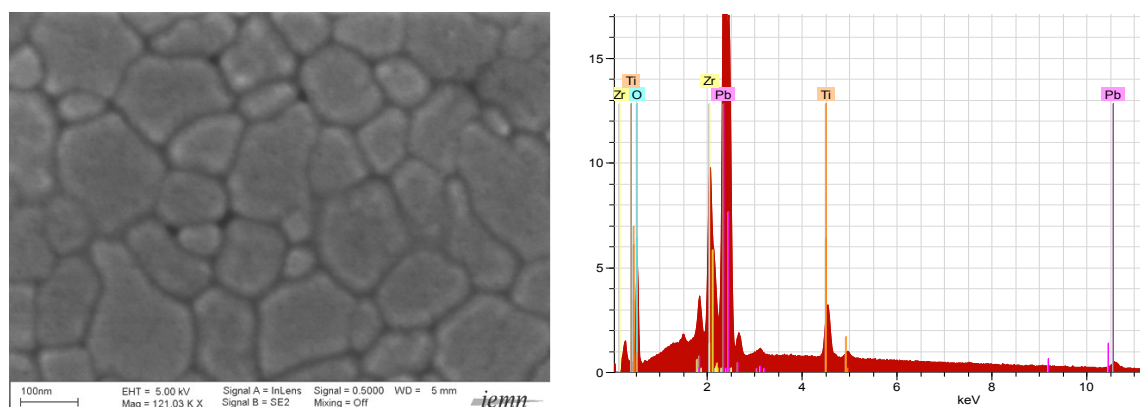


Fig. 12.2.10: SEM image of PZT buffer surface on Si substrate and respective EDS measurement.

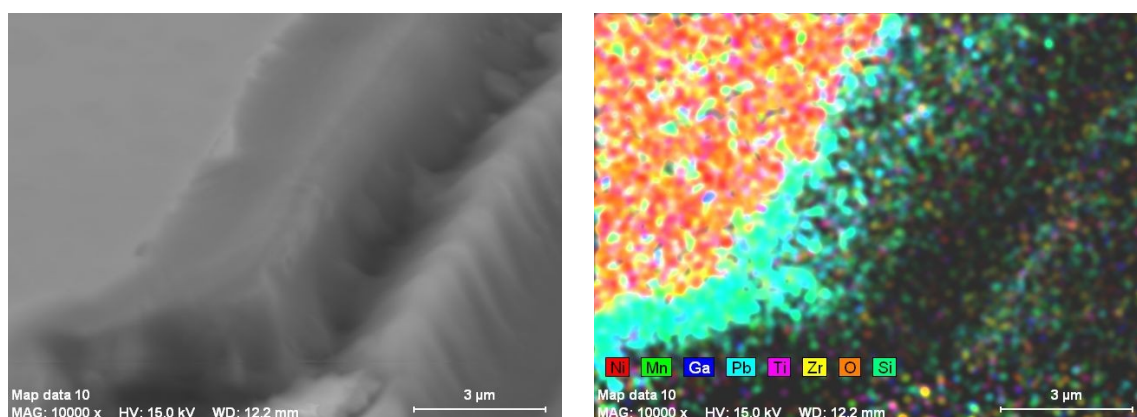


Fig. 12.2.11: SEM image of sample NMGPZT1 surface and respective EDS map showing the several layers.

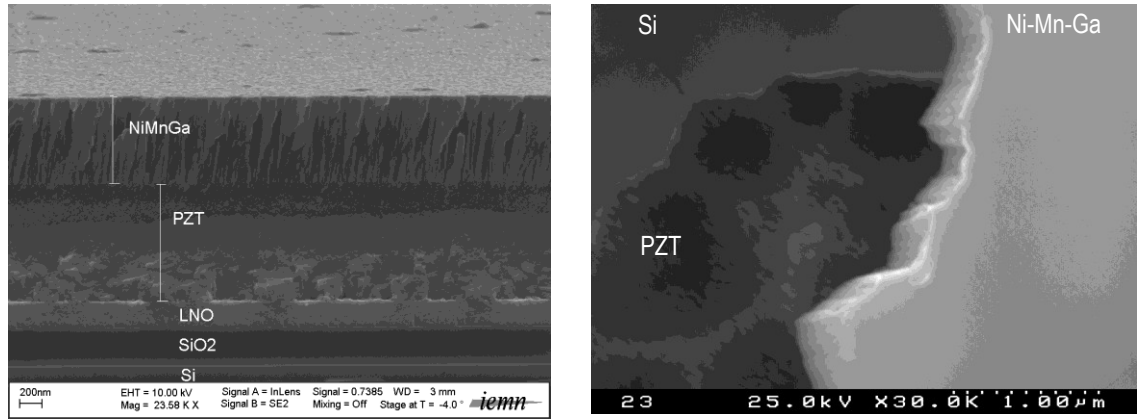


Fig. 12.2.12: SEM image of sample NMGPZT6 cross section and surface showing the layers stacking.

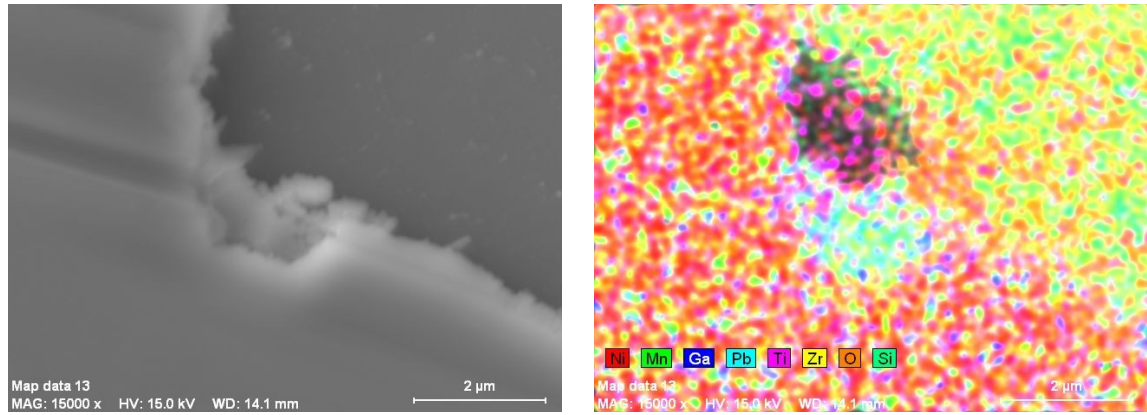


Fig. 12.2.13: SEM image of sample NMGPZT6 surface and respective EDS map showing the several layers.

Using high resolution four-circles diffractometer a θ - 2θ measurements of Ni-Mn-Ga films deposited on PZT buffer layer indicate the presence of both structures (cubic and tetragonal). The orientation of the films was also investigated by Φ scans for two different asymmetrical reflection $\Psi = 41$ to 50° at $2\theta = 62.71^\circ$ which corresponds to the (400) parameter of the cubic phase of the Ni_2MnGa phase alloy [12.2.2] (Figure 12.2.14 a) and $\Psi = 45^\circ$ to 50° at 68.38° which corresponds to the $(220)_T$ parameter of the tetragonal structure of $\text{Ni}_{2.16}\text{Mn}_{0.84}\text{Ga}$ [12.2.3] $(112)_T$ -oriented on the substrate (Figure 12.2.14 b). In both cases four peaks are observed separated at 90° , indicating the specific fourfold deconvolution expected for each kind of symmetry group. Thus a part of the film crystallizes in the martensitic phase with lattice parameters $a = 3.846 \text{ \AA}$ and $c = 6.672 \text{ \AA}$. This study shows that both structures are present in the films; however, this kind of measurements is not able to determine the predominant phase in the film.

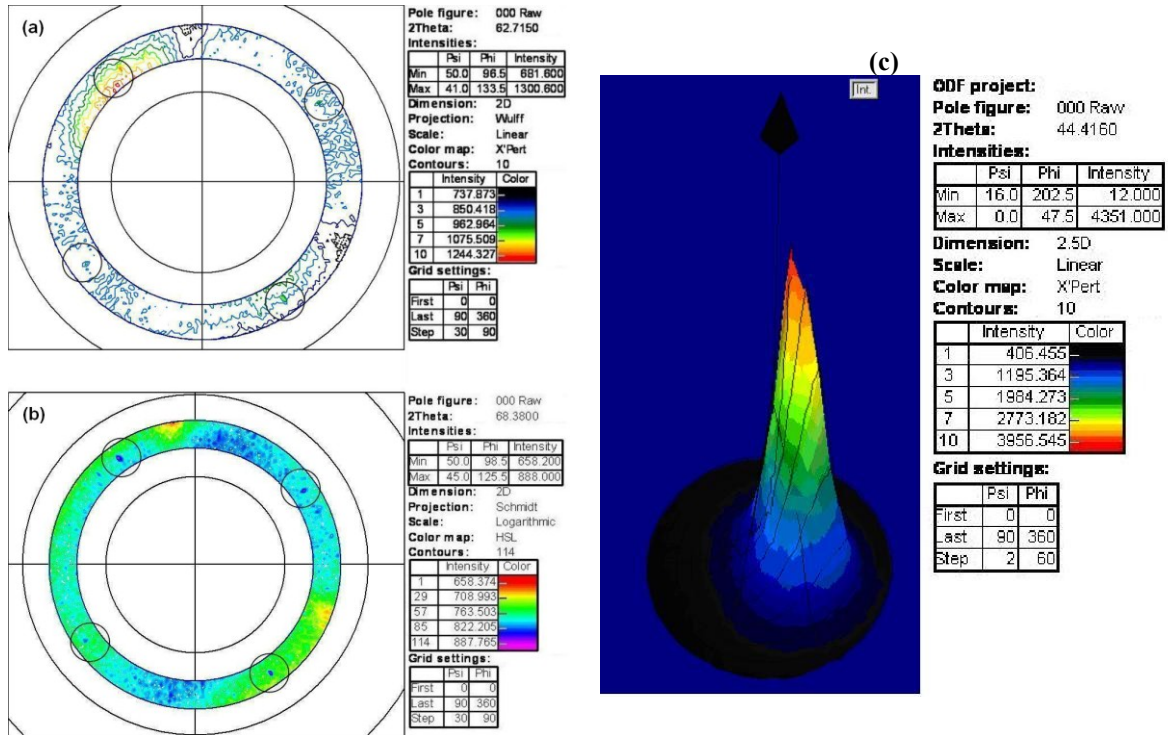


Fig. 12.2.14: (a) Pole figure recorded around the (400)_C peak ($\psi = 41$ to 50° at $2\theta = 62.71^\circ$) confirming cubic symmetry of the film (220) oriented on the PZT buffer Si (100) substrate. (b) Pole figure recorded around the (220)_T peak ($\psi = 45^\circ$ to 50° at $2\theta = 68.38^\circ$) confirming tetragonal symmetry of the film (112)-oriented on the PZT buffer. (c) 3D Pole figure detail of the (400)_C peak at $2\theta = 44.4^\circ$

In the sequence of the experimental depositions described in table 9.2.1, the most relevant composition and structural results are systematized on table 12.2.1. The thickness and roughness of the prepared films were also verified with a profilometer. The graphs of figure 12.2.15 enable to observe that the Argon atmosphere has some noteworthy discriminator effect on the elements travel from the target through the plasma; probably by an added screening effect over the dominant vapor of Ni atoms than that of the Mn and Ga; on the other hand, the effect of RF magnetron power in the 50 to 300 watt range has a negligible effect ($<0.5\%$) on the thin film composition.

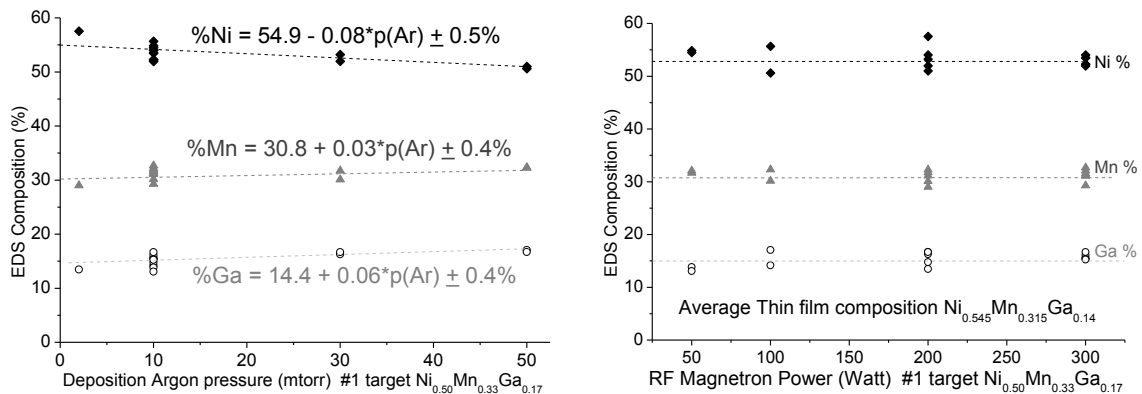


Fig. 12.2.15: Thin films composition dependence with Argon pressure and RF power during deposition.

Sample	Substrate	axis	Thickness (μm)	Composition (EDS)			Cubic lattice a (\AA)	XRD peak broadening @ 43° (2θ)	Area Ratio of NMG / Si XRD Peaks	Observations:
				Ni %	Mn %	Ga %				
NMG01	Si	(100)	2.55	55.66	30.18	14.16	5.917	0.450	113	
NMG02	Si	(100)	5.56	54.04	31.17	14.78	5.971	0.262	1124	
NMG03	Si	(100)	1.14	50.63	32.30	17.07	5.844	2.684	64	
NMG04	Si	(100)					n.a.			no crystallization
NMG05	Si	(100)					n.a.			no crystallization
NMG06	Si	(100)	8.44	52.22	32.09	15.63	5.987	0.358	2778	
NMG07	Si	(100)	3.58	57.54	29.02	13.45	5.970	0.642	899	
NMG08	Si	(100)	8.93				5.994	0.640	1045	
NMG09	Si	(100)					n.a.			no crystallization
NMG10	Si	(100)					n.a.			crushed
NMG11	Si	(100)	8.75	51.95	32.69	15.36	n.a.			no crystallization
NMG12	Si	(100)	5.94	52.32	31.56	16.12	n.a.			no crystallization
NMG13	Si	(100)	1.55	54.05	29.29	16.66	n.a.			no crystallization
NMG14	Si	(100)	2.41				5.936	1.440	1378	
NMG15	Si	(100)					n.a.			no crystallization
NMG16	Si	(100)					5.953	1.153	678	
NMG17	Si	(100)	3.96	53.54	31.09	15.37	5.959	1.122	4238	good crystallization
NMG18	Si	(100)					5.947	1.269	380	
NMG19	Si	(100)		51.02	32.28	16.69	5.956	0.788	91	
NMG20	Si	(100)					n.a.			no crystallization
NMG21	Si	(100)		51.99	31.73	16.28	5.961	0.589	73	
NMG22	Si	(100)					5.939	0.725	24	
NMG23	Si	(100)	0.93				5.944	0.318	533	
NMG24	Si	(100)	0.52	54.48	31.69	13.83	5.942	0.571	23	
NMGPZT1	Si/LNO/PZT	(100)	3.98	53.48	31.3	15.26	5.753	0.232	3350	0.50 μm PZT buffer
NMGPZT2	Si/LNO/PZT	(100)	2.92				5.769	0.194	188	
NMGPZT3	Si/LNO/PZT	(100)		53.22	30.1	16.68	5.772	0.174	191	
NMGPZT4	Si/LNO/PZT	(100)	1.06				5.772	0.196	465	
NMGPZT5	Si/LNO/PZT	(100)	0.90	54.85	32.10	13.07	5.770	0.194	403	
NMGPZT6	Si/LNO/PZT	(100)	0.62				5.763	0.239	8127	0.75 μm PZT buffer

Table 12.2.1: List of samples deposited by RF Magnetron Sputtering from $\text{Ni}_{0.50}\text{Mn}_{0.33}\text{Ga}_{0.17}$ target.

To improve the control of the film composition, the second step of investigation consisted of depositing Ni-Mn-Ga films by co-sputtering from three complementary targets: Ni, Mn, and Ni:Ga (50:50), which allowed to vary the elements ratio of the sputtered film in a wide range of concentrations. Since the physical properties of the Ni-Mn-Ga alloy depend strongly on composition, an extensive empirical calibration of deposition parameters is required to obtain the desired composition of the films. Several trial samples were deposited at different RF power ratios applied to each magnetron and the composition of the films grown was measured using EDS analysis.

Under these specific conditions, with three targets operating with respective magnetron power $P_{\text{Ni}} = 130$, $P_{\text{Mn}} = 244$, $P_{\text{NiGa}} = 300$ W, and Ar pressure of 10 mTorr, it was possible to achieve a film composition of $\text{Ni}_{2.16}\text{Mn}_{0.98}\text{Ga}_{0.98}$ as estimated by EDS.

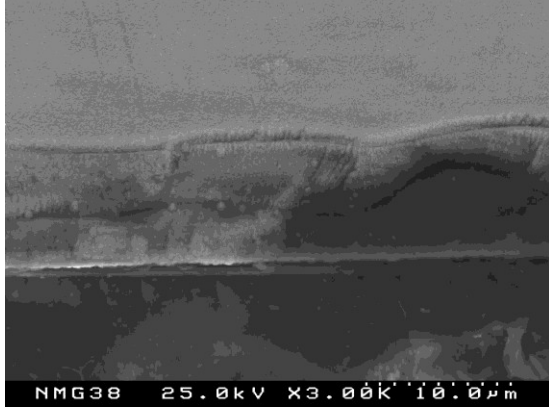


Fig. 12.2.16: SEM image of sample NMG38 over a fracture zone.



Fig. 12.2.17: SEM image of sample NMG44 over a fracture zone.

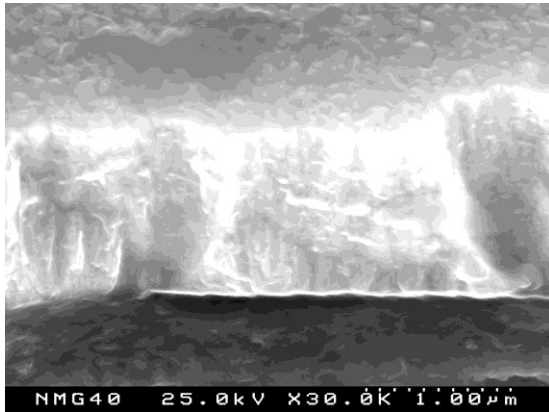


Fig. 12.2.18: SEM image of sample NMG40 over a fracture zone.

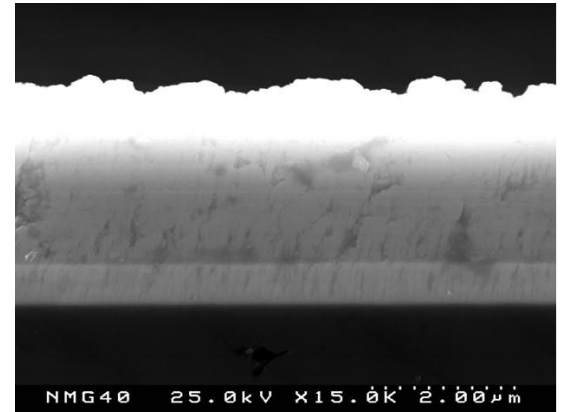


Fig. 12.2.19: SEM image of sample NMG40 over a polished cross section.

Examples of surface morphology, microstructure, and cross-section of such a near stoichiometric sample are presented in Figure 12.2.16 to 19. SEM images of the film cross-section show a thickness of ~ 3 μm for a deposition time of 30 min which indicates a sputtering rate of ~ 100 nm/min. Furthermore, XRD study also confirmed the presence of Ni_2MnGa phase with cubic structure.

All studied films demonstrated typical behavior of Ni-Mn-Ga alloy, even though the respective magnetization is very low in comparison with similar films deposited by other methods at much higher temperatures [12.2.9]. Figures 12.2.20 and 12.2.21 illustrate two examples of SQUID measurements of samples, after subtracting the diamagnetic contribution of substrates. Magnetization is lower than 0.1 emu/g for films grown on bare

Si substrate (inset of figure 12.2.20) and around 5 emu/g for the film grown on Si with LNO/PZT buffer layer (figure 12.2.21) while bulk Ni-Mn-Ga alloy magnetization can reach 70 emu/g [12.2.10]. This possibly means that the films are mostly composed of the cubic Ni_2MnGa alloy. However, no anomalies are observed in the temperature dependence of the magnetization in the range 10-300 K measured under sufficiently weak (1 kOe) magnetic field. (figure 12.2.20 and inset of figure 12.2.21). These measurements also confirmed that the transition to the paramagnetic phase is above room temperature.

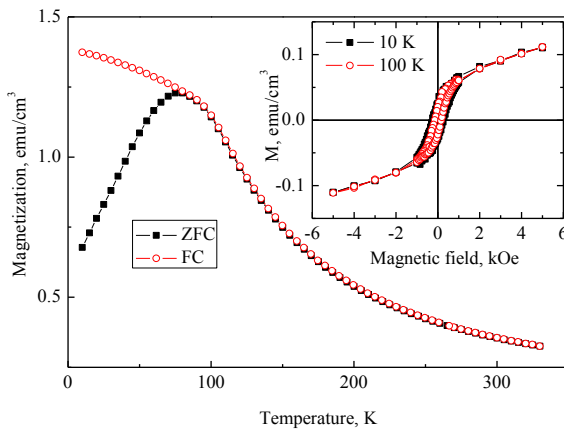


Fig. 12.2.20: Representative temperature dependence of magnetization of a Ni-Mn-Ga film on Si substrate; in Zero Field cooling (ZFC) and Field cooling (FC) modes under 1 kOe magnetic field. Inset: M vs. H hysteresis loops at 10 and 100 K.

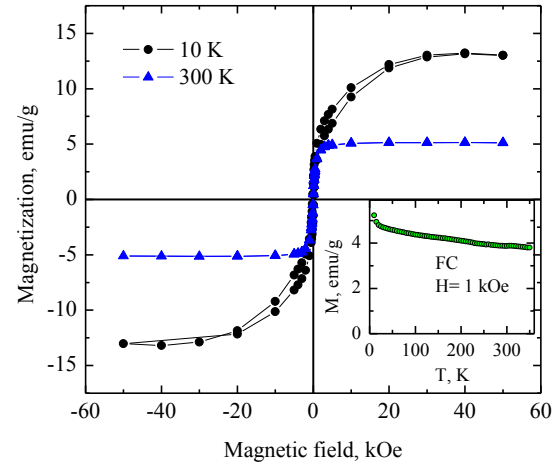


Fig. 12.2.21: Hysteresis loop of representative Ni-Mn-Ga film on Si/LNO/PZT substrate. Inset: M vs. T dependence under 1 kOe.

The weak magnetization of the films can be due to the fact that the film is mostly composed of the cubic Ni_2MnGa alloy phase, to significant disordering of Ni, Mn and Ga sublattices, or to partial segregation of $\text{Mn}_{0.8}\text{Ni}_{0.2}$ alloy that contributes to lower Mn content in the Ni-Mn-Ga phase. In spite of the low magnetization, the films still exhibit magnetostrictive deformation under elevated magnetic field (>1 Tesla) resulting in the visible delamination of the films from the substrate during measurements (Figure 12.2.2).

Annealing experiments performed on the films at $T \sim 300$ °C showed that films delaminate from the substrate. This behavior is probably induced by the expected martensite-austenite phase transition that occurs in the Ni_2MnGa phase-like film while the parameters of the substrate remain constant.

A mechanism of the film damage at magnetic measurements might be similar to that under heating described above. This behavior indicates a clear potential of such films for multiferroic applications in which high deformation (either with increasing temperature or with magnetic field) can be used in the cantilever-type structures or freestanding films.

Samples	Substrate	Orientation	Film Thick, (μm)	Composition (EDS)			Cubic Lattice a (Å)	XRD peak broadening @ 43° (2θ)	Area Ratio of NMG / Si XRD Peaks
				Ni (%)	Mn (%)	Ga (%)			
NMG25	Si	(100)	0.49	55.93	12.20	31.83	5.740	2.586	588
NMG26	Si	(100)	0.47	56.46	12.27	31.26			
NMG27	Si	(100)	1.34	58.01	14.63	27.36	5.831	1.954	2742
NMG28	Si	(100)	1.09	58.65	14.61	26.74			
NMG29	Si	(100)	1.63	60.01	13.91	26.09			
NMG30	Si	(100)	1.95	60.34	13.68	25.98			
NMG31	Si	(100)	1.73	58.78	23.17	18.06	5.884	1.464	1455
NMG32	Si	(100)	1.46	62.02	16.99	20.98			
NMG33	Si	(100)	0.30	47.76	2.75	49.49			
NMG34	Si	(100)		51.77	5.04	43.19			
NMG35	Si	(100)		47.56	32.00	20.45	5.813	0.740	1011
NMG36	Si	(100)							
NMG37	Si	(100)							
NMG38	Si	(100)		45.90	33.27	20.83	5.796	0.656	2367
NMG39	Si	(100)							
NMG40	Si	(100)		53.24	23.40	23.36	5.788	0.802	2172
NMG41	Si	(100)							
NMG42	Si	(100)					5.870	0.765	825
NMG43	Si	(100)							
NMG44	Si	(100)		49.74	8.68	41.58	5.827	0.953	143
NMG45	Si	(100)							
PZTNMG6	Si/LNO/PZT	(100)		59.24	13.96	26.8	5.775	0.214	2893
PZTNMG8	Si/LNO/PZT	(100)							
PZTNMG9	Si/LNO/PZT	(100)		50.39	25.7	23.9	5.770	0.218	3783
PZTNMG10	Si/LNO/PZT	(100)							

Table 12.2.2: Samples deposited by RF Magnetron co-sputtering from 3 targets: Ni, Mn and $\text{Ni}_{0.50}\text{Ga}_{0.50}$.

After comparing more than fifty samples prepared under different deposition conditions and primarily characterized by XRD and EDS analysis, it became possible to approach the desired composition and structure for the Ni-Mn-Ga films deposited on-axis geometry, and low Ar pressure (10 mTorr) at preferably high RF power (>200 W).

From the experimental depositions described in table 9.2.2, the resulting thin films' data is compiled on table 12.2.2. As can be observed in the graphs of figure 12.2.22 it is possible to relate the films composition to the ratio between each magnetron RF power and respective target: $[\text{Ni}]/[\text{Ga}] \sim 2.23 \cdot (P_{\text{Ni}}/P_{\text{NiGa}})$ and $[\text{Mn}]/[\text{Ga}] \sim 1.3 \cdot (P_{\text{Mn}}/P_{\text{NiGa}})$.

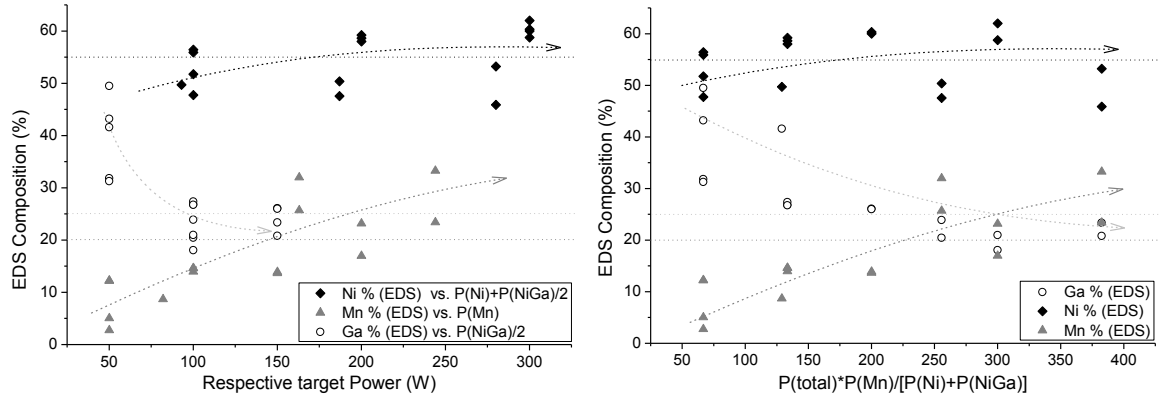


Fig. 12.2.22: Graphs of dependence of composition with RF magnetron power for three targets co-sputtering.

As the film/substrate adhesion is not yet optimized, the structural austenitic/martensitic transformation usually leads to the delaminating of the films, either in the cases when the crystallization takes place above T_M under annealing, and the structural phase transition occurs during cooling, or in the cases the intense magnetic field causes the transformation. The expansion of the unit cell along c -axis coming from this phase transition is compensated by a decrease of a and b lattice parameters which will result in a twinning of the Ni-Mn-Ga alloy [12.2.11] not accompanied by the rigid Si substrate.

An article [12.2.12] was published based on these experimental results and further research is carried out autonomously in the CNRS-IEMN center.

12.3. Ni₂MnGa thin films deposited by RF Sputtering (@ UA)

As listed in table 4.5.1 and table 12.3.1, most research performed so far on Ni_{2+x}Mn_{1-x}Ga Heusler alloy, either in bulk or thin film form, recurs to a variety of sample preparation methods that are generally chemically constrained to a single precursor or target composition and use synthesis or annealing temperatures above 800° C.

Composition (at. %)			Preparation method	Film thick Substrate	T _{annealing} ° C	T _{Martensitic} K	T _{Curie} K	M _{Sat} emu/cm ³	Ref.
Ni	Mn	Ga							
55.0	20.0	25.0	arc melting	ingot	827	334	334		[4.5.8]
58.0	16.8	25.6	arc melting	ingot	827	508	331		[4.5.8]
58.8	16.5	24.5	arc melting	ingot	827	537	320		[4.5.8]
53.6	23.4	23.0	1 target RF sputtering	0.1 µm, Al ₂ O ₃	800	377	354	438	[12.2.10]
53.6	23.4	23.0	1 target RF sputtering	0.4 µm, Al ₂ O ₃	800	343	346	500	[12.2.10]
53	22	25	arc-melting	ingot		275	318	410	[12.2.11]
55	20	25	arc-melting	ingot		319	306	352	[12.2.11]
54.9	23.8	21.3	solid state at 980° C	ingot	800	541	360		[12.3.10]
54.3	20.5	25.2	Induction melting	ingot		276	341		[12.3.11]
50	25	25	1 target DC sputtering	0.1 µm, Al ₂ O ₃	500	276	360	450	[12.3.12]
50	25	25	1 target DC sputtering	0.1 µm, MgO	500	220	360		[12.3.12]
56.4	21.8	21.8	1 target DC sputtering	0.1 µm, Mica	800	330	350	500	[12.3.13]
50	25	25	1 target MBE	0.5 µm, GaAs	585		350	200	[12.3.14]
55	23	22	1 target PLD	0.2 µm, Si	500	270	340	380	[12.3.15]

Table 12.3.1: Comparison of critical properties for similar Ni_{2+x+y}Mn_{1-x}Ga_{1-y} composition samples prepared by different methods.

In this new series of thin films samples, the experimental depositions, measurements and results analysis take advantage of the preceding work developed in the IENM labs described in the previous section, demonstrating that it is possible the formation of the Ni₂MnGa crystalline phase onto Si substrates and oriented PZT buffers close to room temperature. This new research path was carried out at the Dep. of Physics of Aveiro University, performing thin film deposition of the Ni_{2+x}Mn_{1-x}Ga phase magnetostrictive Heussler alloy by RF magnetron co-sputtering from two complementary targets, Ni₅₀Mn₅₀ and Ni₅₀Ga₅₀, onto a variety of substrates at relatively low temperatures (>100° to <550° C) as described in table 9.2.3. This investigation also intended to recognize the most suitable deposition conditions to achieve high quality epitaxial thin films of the Ni_{2+x}Mn_{1-x}Ga alloy within the composition 0.1 < x < 0.3 onto the different substrates in order to enhance the magnetostrictive properties and the martensitic transition temperature.

Experimental work first focused on SEM characterization and representative images of cross sections and upper surfaces are presented in figures 12.3.1 through 12.3.3. Comparison between overall surface and cross section of different samples series, identified in table 9.2.3, attest that films deposited onto substrates at relatively higher temperature (293° C for NM1g sample or 43° C for sample NM2g) reveal superior quality in terms of thickness uniformity, surface smoothness and crystallites growing; this temperature parameter has a more evident influence than the effect of the different substrates in the films texture, as can be seen when comparing samples within each series.

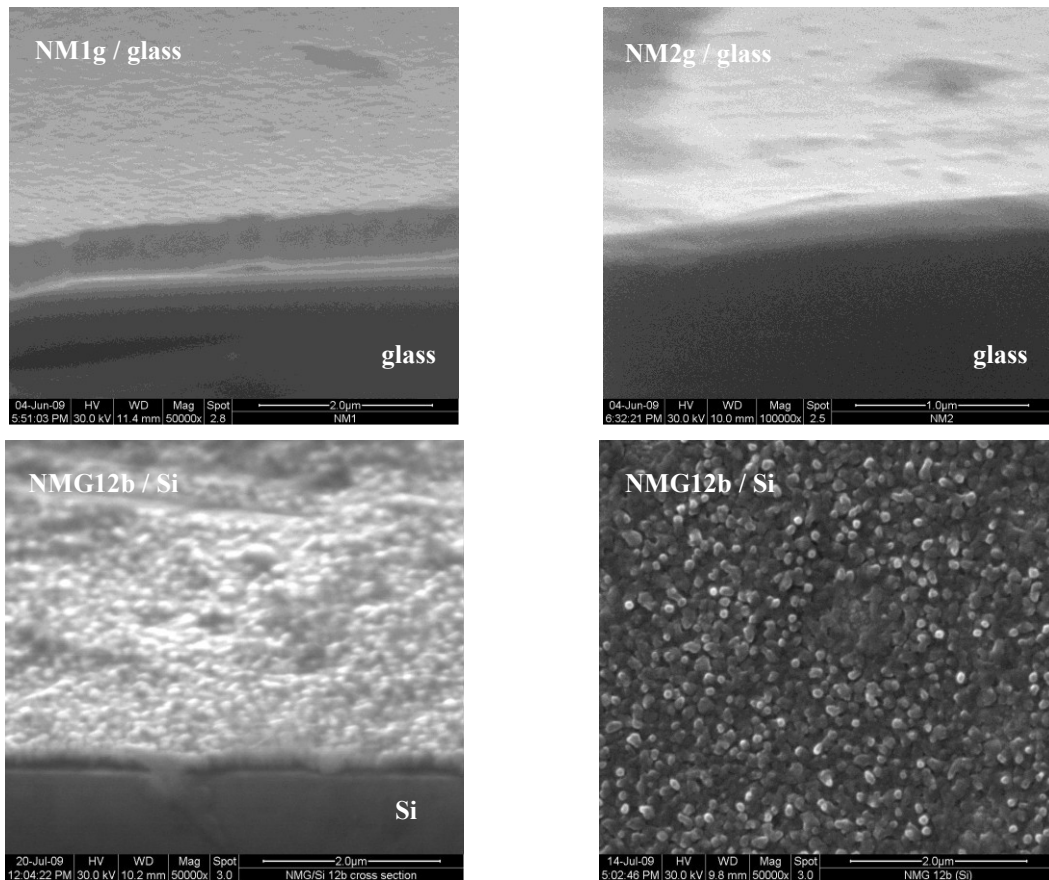


Fig. 12.3.1: SEM cross sections images of samples NM1g (top left) and NM2g (top right) onto glass substrate and of sample NMG12b onto Si(100) substrate.

In figure 12.3.2 it is possible to observe for the 10th series of films the effect of a small Oxygen contamination during deposition process at 420° C, leading to an amorphous microstructure and a visibly low gloss film; in figure 12.3.4 it is possible to compare the relevance of deposition time on layer thickness, crystallization and continuity of the film phase; insufficient exposure (<20 min, as in the case of series NMG13) leads to incomplete coverage of the substrate, as some 100-200 nm gaps in the film surface are visible.

Longer deposition time (>90 min) leads to nucleation of the Ni-Mn-Ga phase into crystallites <100 nm size.

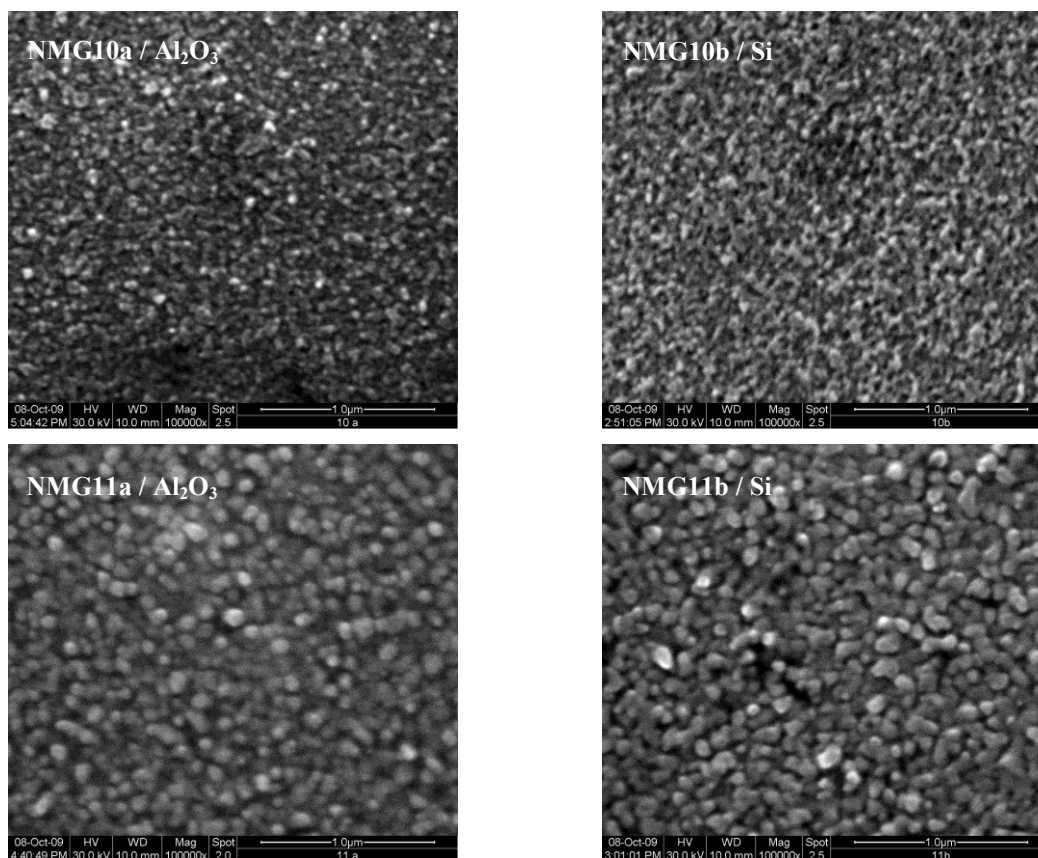


Fig. 12.3.2: SEM images comparison of samples surface deposited onto Al_2O_3 (0001) substrates: NMG10a (top left), NMG11a (down left) and onto Si (100) substrates: NMG10b (top right), NMG11b (down right).

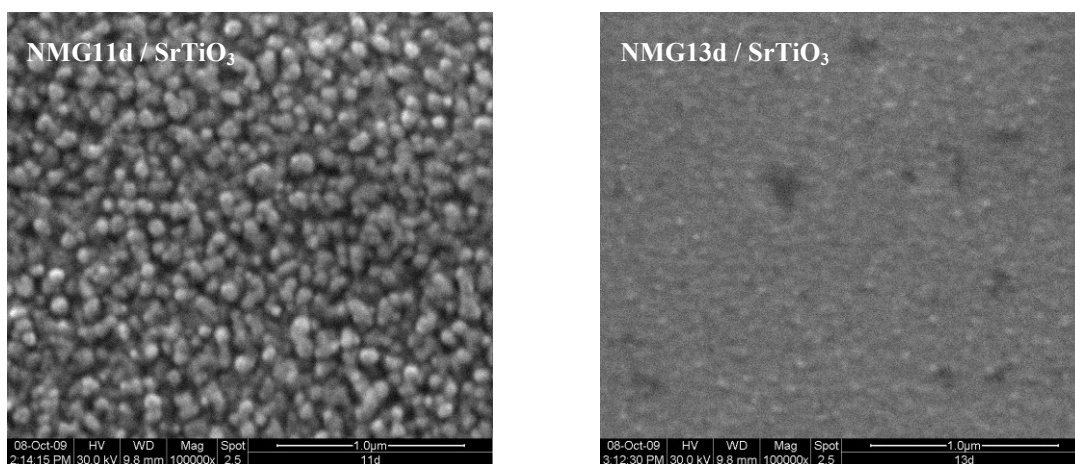


Fig. 12.3.3: SEM images comparison of samples surface deposited onto SrTiO_3 (100): NMG11d (left) and NMG13d (right)

Table 12.3.2 summarizes some relevant preliminary observations of the produced thin films samples. The chemical composition measured by EDS-SEM is displayed as function of the magnetrons power ratio applied to targets, as can be seen in figure 12.3.4:

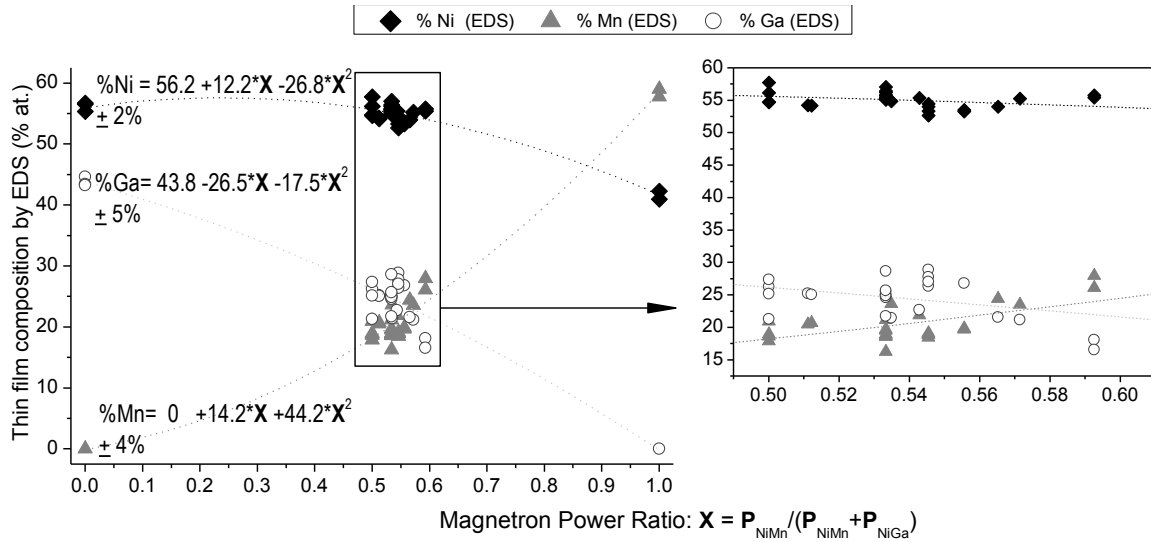


Fig. 12.3.4: Graph relating the thin film chemical composition with the co-deposition power ratio of the targets defined as $X = P_{\text{NiMn}} / (P_{\text{NiMn}} + P_{\text{NiGa}})$.

It is patent that the relation between films composition and the sputtering power applied to the respective targets is not linear; binary alloy films depositions performed at different power feed and temperatures made from single targets, either $\text{Ni}_{50\%}:\text{Ga}_{50\%}$ or $\text{Ni}_{50\%}:\text{Mn}_{50\%}$ (atomic ratio), result for the respective thin film composition outcome in a roughly $\sim 5\%$ excess of Mn over Ni and $\sim 5\%$ of Ni over Ga; furthermore, within the experimental parameters used ($0.5 < P_{\text{target}}/S_{\text{target}} < 1 \text{ W.cm}^{-2}$; $10^{-3} < P_{\text{Argon}} < 10^{-2} \text{ mbar}$; $40 < T_{\text{substrate}} < 540^\circ \text{ C}$) it became evident that the efficiency of the film deposition process in this co-focal horizontal on-axis geometry from the NiMn target was barely $\sim 65\%$ than that from the NiGa target.

These experimental results enable to effectively achieve a control over the stoichiometry of Ni-Mn-Ga thin films by managing the magnetrons feed the power ratio between targets defined as $X = P_{\text{NiMn}} / (P_{\text{NiGa}} + P_{\text{NiMn}})$; consequently, in order to achieve a composition near the intended $\text{Ni}_{55}\text{Mn}_{20}\text{Ga}_{25}$, this ratio was found within 0.50 to 0.52.

Sample	Substrate (orientation)	XRR Film Thick (nm)	Error \pm (nm)	Composition (EDS)			Observations
				Ni (%)	Mn (%)	Ga (%)	
NG1g	glass	45	1	55.4	0	44.6	Films appear uniform with shine metallic mirror like aspect
NG2g	glass	103	5	56.6	0	43.4	
NG3g	glass	36	3	56.8	0	43.2	
NM1g	glass	455	5	41.0	59.0	0	Film has semi gloss brown color
NM2g	glass	200	5	42.3	57.7	0	Films appear uniform with shine metallic mirror like aspect
NM3g	glass	103	7			0	
NM4g	glass	36	2			0	
NMG01g	glass	111	4	54.3	20.5	25.2	Sample heater oscillating ± 10 C and shut down.
NMG02g	glass	90	6	54.2	20.7	25.1	Films appear uniform with shine metallic mirror like aspect
NMG03g	glass			54.9	23.7	21.4	
NMG04g	glass	35	1	55.4	21.9	22.7	Sample heater shut off during deposition
NMG05g	glass			55.8	26.1	18.1	Films appear uniform with shine metallic mirror like aspect
NMG06g	glass			55.4	28.0	16.6	
NMG07g	glass	196	6	55.3	23.6	21.2	
NMG08g	glass			54.0	24.4	21.6	
NMG09a	Al ₂ O ₃ (0001)	80		53.5	19.7	26.8	Due to overload of magnetron, successive system power shut down occur. Plasma interruption and restart occur 5 times during deposition procedure.
NMG09b	Si (100)	80		53.3	19.9	26.8	
NMG09c	SrTiO ₃ (100)						
NMG09d	MgO (100)						
NMG10a	Al ₂ O ₃ (0001)			52.7	18.5	28.9	Error due to O ₂ gas leak into the chamber through mass flow controller. Resulting films show smooth surface but appear in a semi gloss brown color.
NMG10b	Si (100)			53.3	18.9	27.8	
NMG10c	SrTiO ₃ (100)			54.5	19.1	26.4	
NMG10d	MgO (100)			54.0	18.9	27.1	
NMG11a	Al ₂ O ₃ (0001)			56.4	18.9	24.6	Films appear uniform with shine metallic mirror like aspect
NMG11b	Si (100)			55.5	19.6	25.0	
NMG11c	SrTiO ₃ (100)			55.8	18.7	25.5	
NMG11d	MgO (100)			55.3	19.7	25.0	
NMG12a	Al ₂ O ₃ (0001)			56.2	18.9	24.9	Films appear uniform with shine metallic mirror like aspect Thickness interpolated by SEM cross section
NMG12b	Si (100)	120	10	55.7	18.6	25.7	
NMG12c	SrTiO ₃ (100)			55.1	16.3	28.7	
NMG12d	MgO (100)			57.1	21.2	21.7	
NMG13a	Al ₂ O ₃ (0001)	31	1	54.8	19.0	26.2	Power failure, deposition time limited to 17 min.
NMG13b	MgO (100)	24	1	57.8	20.9	21.3	Thinner films having a metallic semitransparent aspect
NMG13c	SrTiO ₃ (100)	35	1	56.2	18.6	25.2	
NMG13d	Si (100)	10 a)	1	54.7	17.9	27.4	

Table 12.3.2: List of samples and respective thickness estimated by XRR measurements; composition results obtained by EDS-SEM and observation of overall visual aspect and occurrences during deposition procedure.

a) Note: This thickness value corresponds most probably to the refraction bands originated from the common SiO₂ layer over Si substrate and not from the film itself.

Figure 12.3.5 gathers examples of XRR measurements performed in samples. Thin film thickness was estimated recurring to the software *X'Pert Epitaxy 4.1*[©] that performs a simple average of the distance corresponding by the Bragg Law to the angle pace between successive fringes identified in the diffractograms.

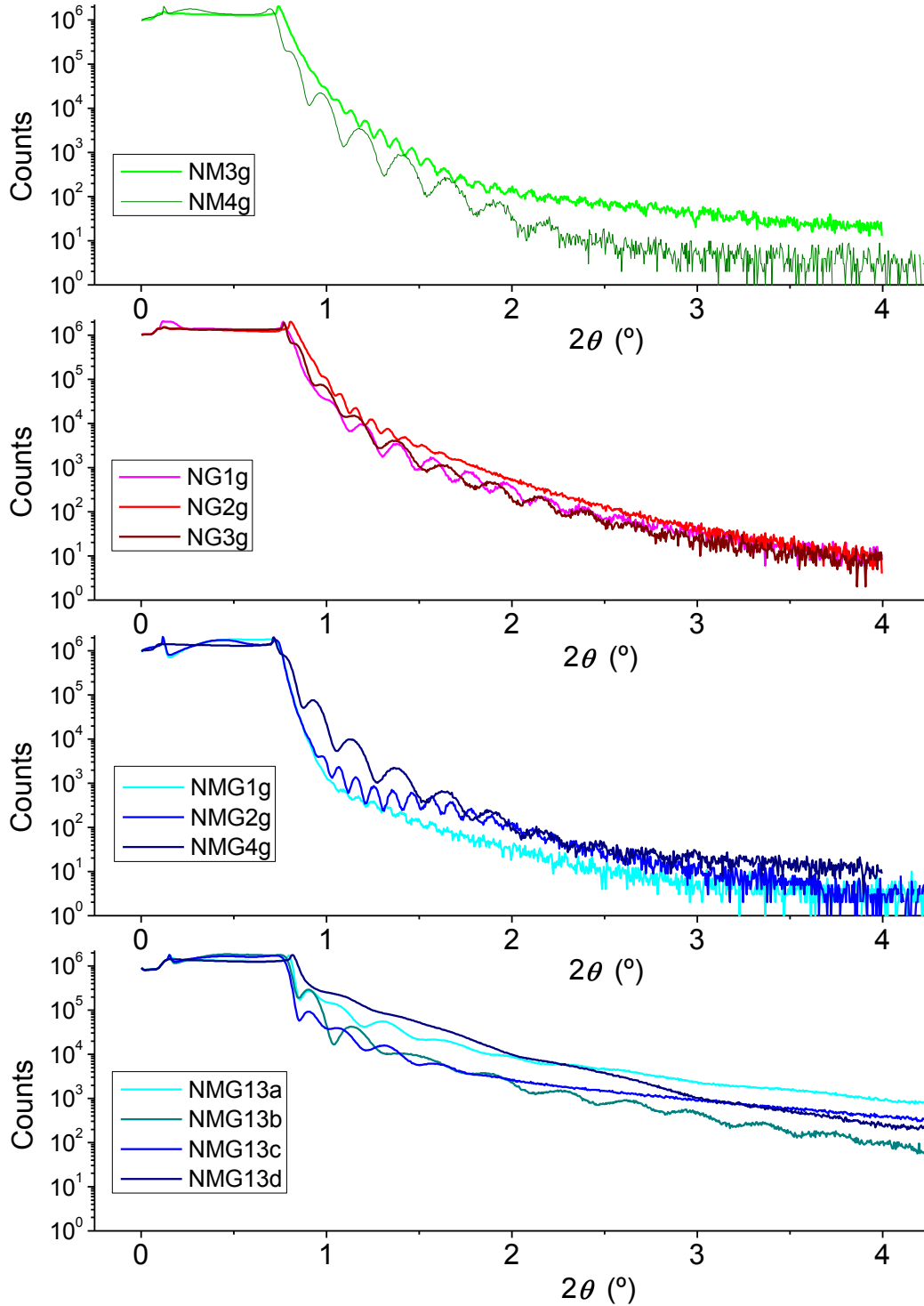


Fig. 12.3.5: X-Ray Reflectometry of some of the deposited thin film samples

Accurate estimation of thickness requires a simulation model that includes the film density and more precise XRR measurements with a rigorous alignment of the XRD goniometer in a grazing “low angle” with the thin film sample, this experimental condition is not always possible to achieve since the XRD systems used are not yet equipped with specific XRR auxiliary devices that allow automated measurements, thus results in table 12.3.2 are not successfully extended to all samples; nonetheless it is possible to recognize a trend between the film thickness and the key conditions used during deposition, namely, time x magnetron power feed and substrate temperature, as represented in figure 12.3.6. Typical rate of deposition for the conditions used for samples of the series 08 to 13 was ~ 1 nm/min.

Conventional XRD measurements of the samples enable a basic structural analysis of the deposited thin films and to recognize the eventual epitaxial effect of the respective substrate.

Figure 12.3.7 shows some of the diffractograms obtained from the first series of samples deposited in plain glass substrates. As expected, the amorphous structure of this substrate does not favour the ordered growth of the Ni-Mn-Ga phase.

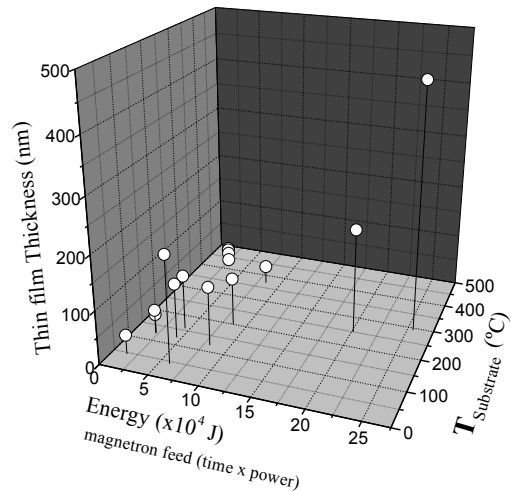


Fig. 12.3.6: 3D graph of thin films thickness in relation to deposition time, magnetron power and substrate temperature.

The deposition parameters ($T_{\text{substrate}} < 290^{\circ}\text{C}$, $\Delta t_{\text{deposition}} < 50$ min, $P_{\text{target}}/S_{\text{target}} > 2$ W.cm $^{-2}$) selected for samples NMG 01g, 02g and 03g were proven inadequate to allow any crystallization of the alloy phase. Once deposition conditions were adapted to $T_{\text{substrate}} > 370^{\circ}\text{C}$, $\Delta t_{\text{deposition}} > 60$ min, $P_{\text{target}}/S_{\text{target}} \sim 1$ W.cm $^{-2}$, it was possible to discriminate a couple of XRD peaks characteristic of the Ni $_2$ MnGa phase like alloy; the tetragonal (112) at $2\theta \approx 43^{\circ}$ [12.3.2] and the cubic (220) at $2\theta \approx 44^{\circ}$ [12.3.3]. Clearly the NMG06g and NMG08g films ($T_{\text{substrate}} \sim 450^{\circ}\text{C}$) present the concomitance of both phases, in comparison NMG07g film ($T_{\text{substrate}} \sim 150^{\circ}\text{C}$) present a dominance of the tetragonal phase, possibly influenced by the limited substrate temperature.

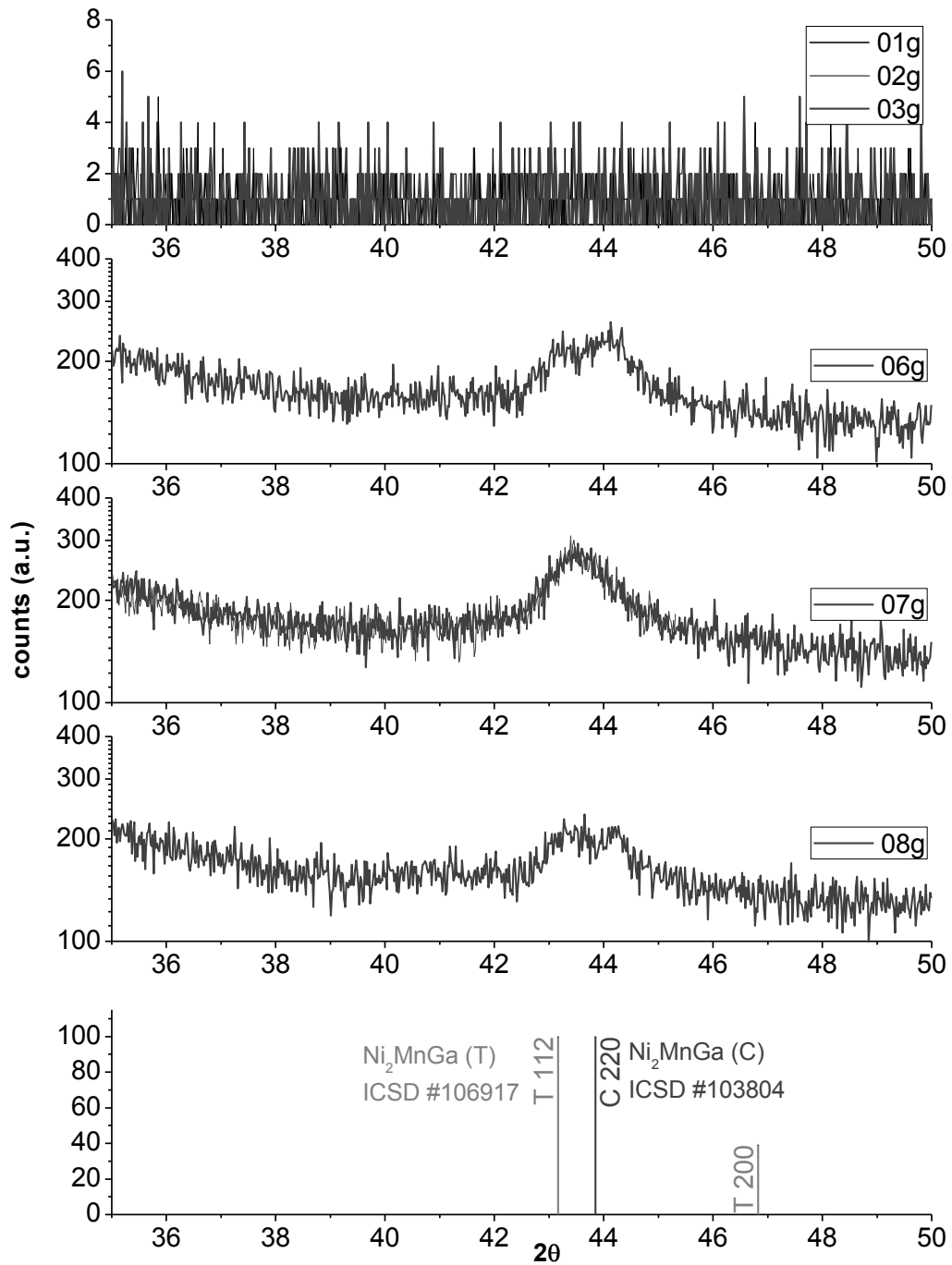


Fig. 12.3.7: XRD diffractograms of the series of samples deposited onto glass substrate.

XRD scans from the different series of films deposited onto Al_2O_3 (0001) substrates are shown in figure 12.3.8. The strong and sharp reflection distinctive of the (006) planes from the substrate can be observed at $2\theta \approx 41.7^\circ$ [12.3.4]; the broadening of the peak at $2\theta \approx 43.5^\circ$ observed in the diffractograms can be explained by the convolution of the reflections from the (220) cubic planes and the (112) tetragonal planes of the Ni_2MnGa phases.

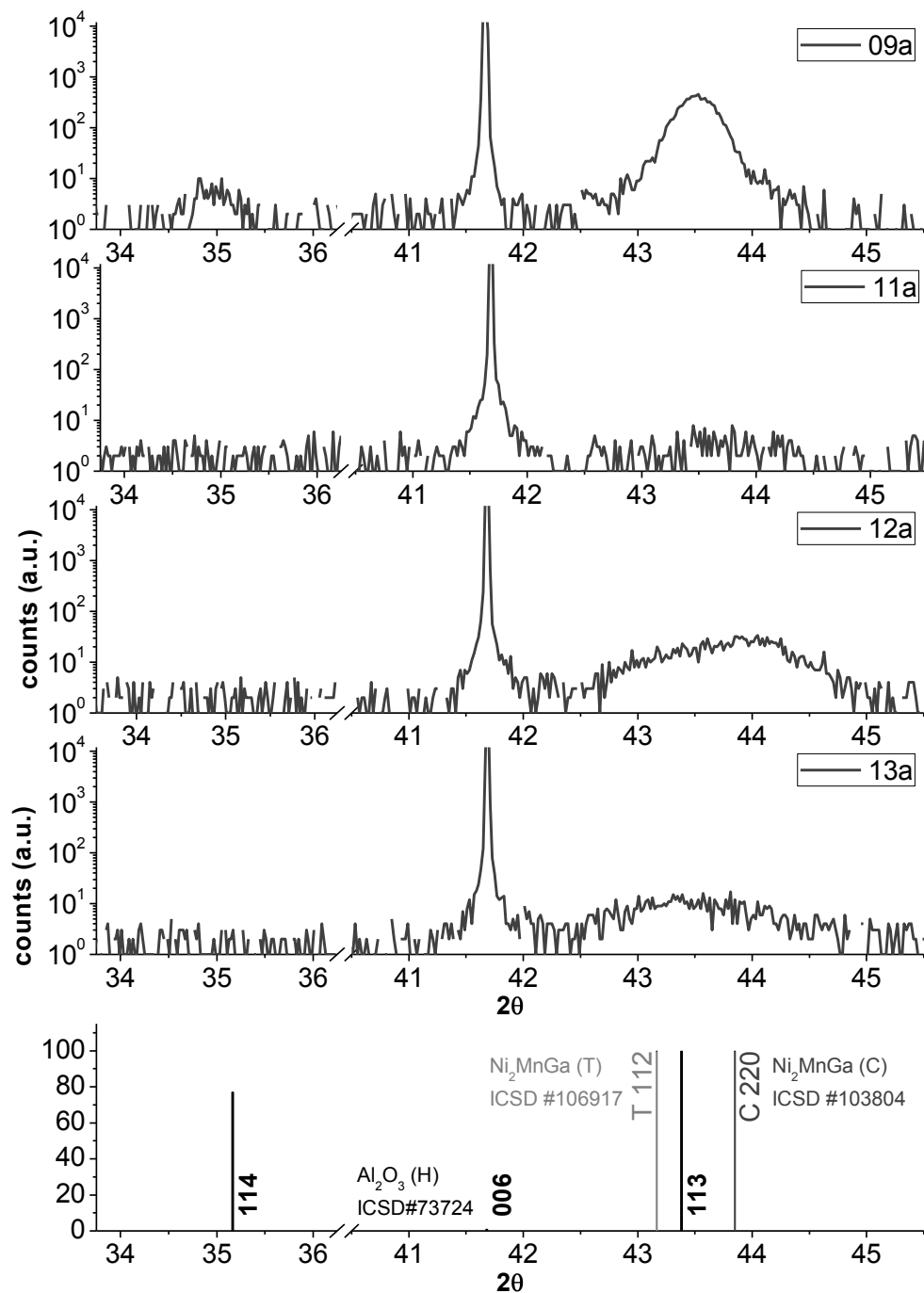
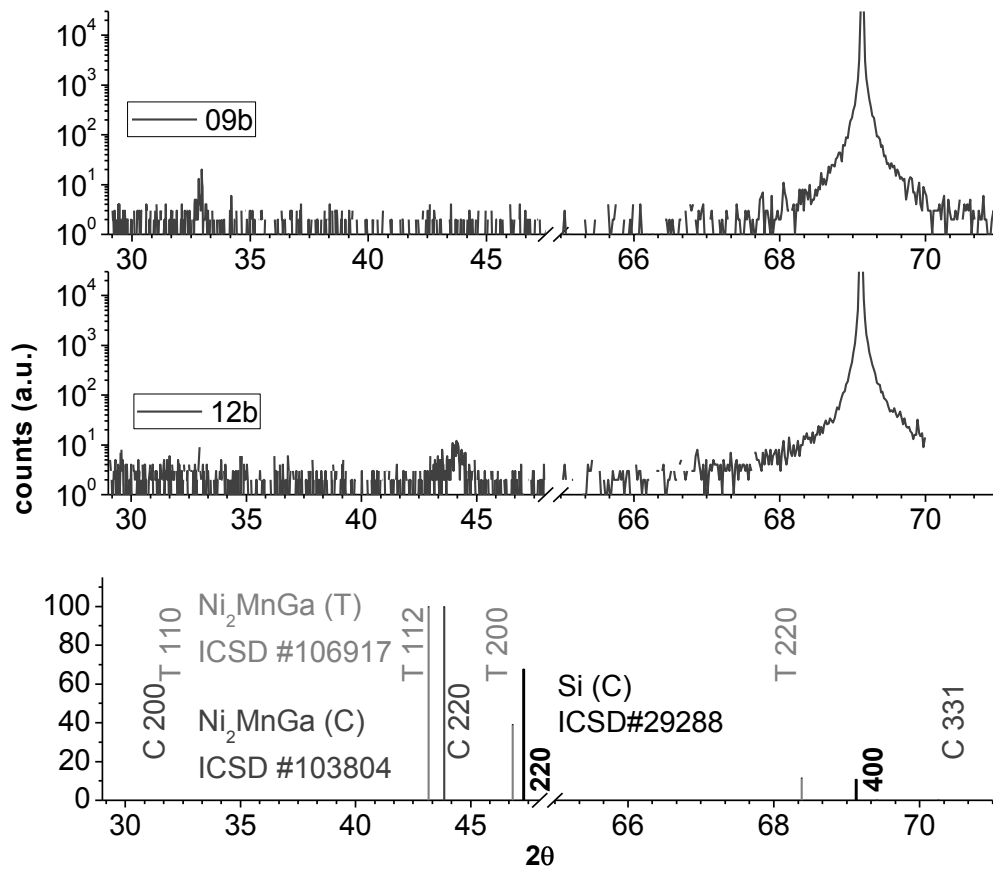


Fig. 12.3.8: XRD diffractograms of the series of samples deposited onto Al_2O_3 (0001) substrate.

In the case of sample NMG12a it is possible to observe a displacement of the reflections group centre, suggesting a larger contribution of the cubic Ni_2MnGa austenite phase, whereas on sample NMG09a and NMG13a the tetragonal martensitic phase seems more preponderant; the amount of each phase could be correlated to the area ratio between the peaks, however this information remains qualitative since it is expected that the films are only partially crystalline and contain a significant amount of amorphous alloy.

The deposition conditions selected for the NMG12 series of samples, namely lower substrate temperature ($\sim 400^\circ\text{C}$) and lowest Argon pressure ($\sim 5 \cdot 10^{-3}$ bar), seem to favour the growth of the cubic Ni_2MnGa austenite phase over the tetragonal phase. Under the described conditions the two phases do not seem to be concomitant in each sample; figure 12.3.9 compares the appearance of the (110) tetragonal reflection at $2\theta \approx 32.8^\circ$ in NMG09b sample while in NMG12b sample prevails a reflection at $2\theta \approx 44.1^\circ$ indexed to the (220) planes of the cubic phase. The equivalent planes orientation of both phases growth confirms the role of the Si [12.3.5] substrate structure in the epitaxial growth of the film leading to a $\sim 5\%$ tightening of the alloy cell parameters when compared to the bulk form.



12.3.9: XRD diffractograms of NMG09b and NMG12b samples deposited onto Si (100) substrates.

XRD diffractograms of the series of thin films deposited onto SrTiO_3 (100) or (110) substrates [12.3.6] are depicted in figure 12.3.10. Sample NMG13c diffractogram confirms the low amount of alloy deposited and poor crystalline formation by the presence of an insipient peak at $2\theta = 43.5^\circ$. The Oxygen contamination detected on sample NMG10c may justify the deficient spectra found.

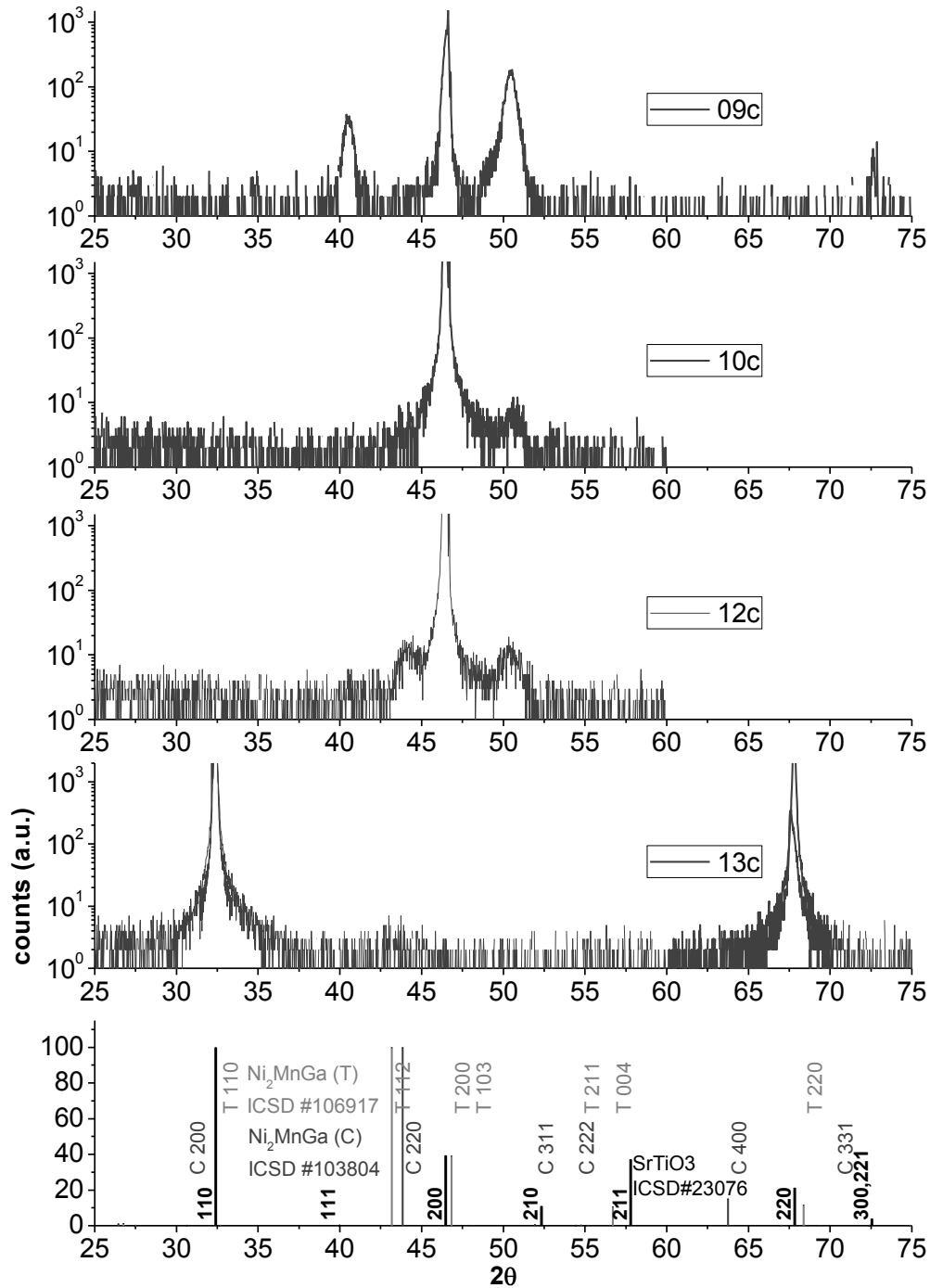


Fig. 12.3.10: XRD diffractograms of the series of samples deposited onto SrTiO_3 substrates.

Although indexation to the cubic or the tetragonal phases is not straightforward for the XRD diffractograms from samples NMG09c and NMG12c, the differences observed worth further analysis. A more distorted structure such as the monoclinic $I12/m1$ phase of the Ni-Mn-Ga alloy [12.3.7] could be associated as (112) peaks at $2\theta \approx 51^\circ$; for sample NMG09c it can also justify the reflections from (021) planes near $2\theta \approx 40^\circ$ and (222) or (113) at $2\theta \approx 73^\circ$.

As for sample NMG12c the peak found at $2\theta \approx 44^\circ$ could be related either to the (200) and (002) reflections or due to the concomitance with the previous referred cubic phase. It is not utterly clear if these two samples have equivalent monoclinic phases.

Finally for the thin films deposited onto MgO [12.3.8], the diffractogram present in figure 12.3.11 suggests the presence of the cubic Ni_2MnGa phase, although the overlap of the XRD reflections from the substrate (100) planes with the main peaks of the tetragonal and cubic SG difficulties the distinction and does not exclude the occurrence of both phases.

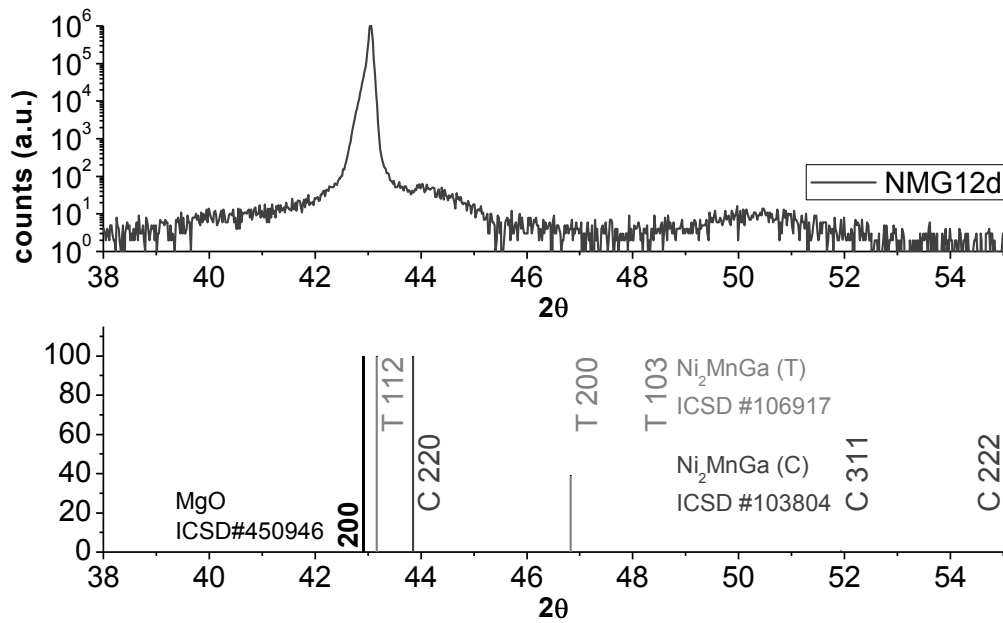


Fig. 12.3.11: XRD diffractograms of the NMG12d sample deposited onto MgO (100) substrate.

These collections of results reveal that the $\text{Ni}_{2+x}\text{Mn}_{1-x}\text{Ga}$ Heusler alloy can be deposited in thin film form via RF magnetron sputtering under the deposition conditions: $T_{\text{substrate}} \sim 450^\circ \text{C}$; $\Delta t_{\text{deposition}} \sim 90 \text{ min}$; $P_{\text{target}}/S_{\text{target}} \sim 1 \text{ W.cm}^{-2}$; $P_{\text{Argon}} \sim 5 \mu\text{bar}$. Depending on the epitaxial correlation to the substrate used the alloy can form initially amorphous, tetragonal or even monoclinic phases; as the film thickens the epitaxial effect of the substrate is attenuated and the alloy tends to stabilize in the FM austenite cubic phase, hence this cubic phase can be concomitant with previously formed phases.

Due to the small magnetic signal found in the samples, the magnetization measurements were performed via SQUID. Original data exemplified in figure 12.3.12 and 12.3.13 reveal that the substrates significant diamagnetic contribution subtracts to that of the alloy ferromagnetic signal below $\sim 340 \text{ K}$ and paramagnetic response beyond.

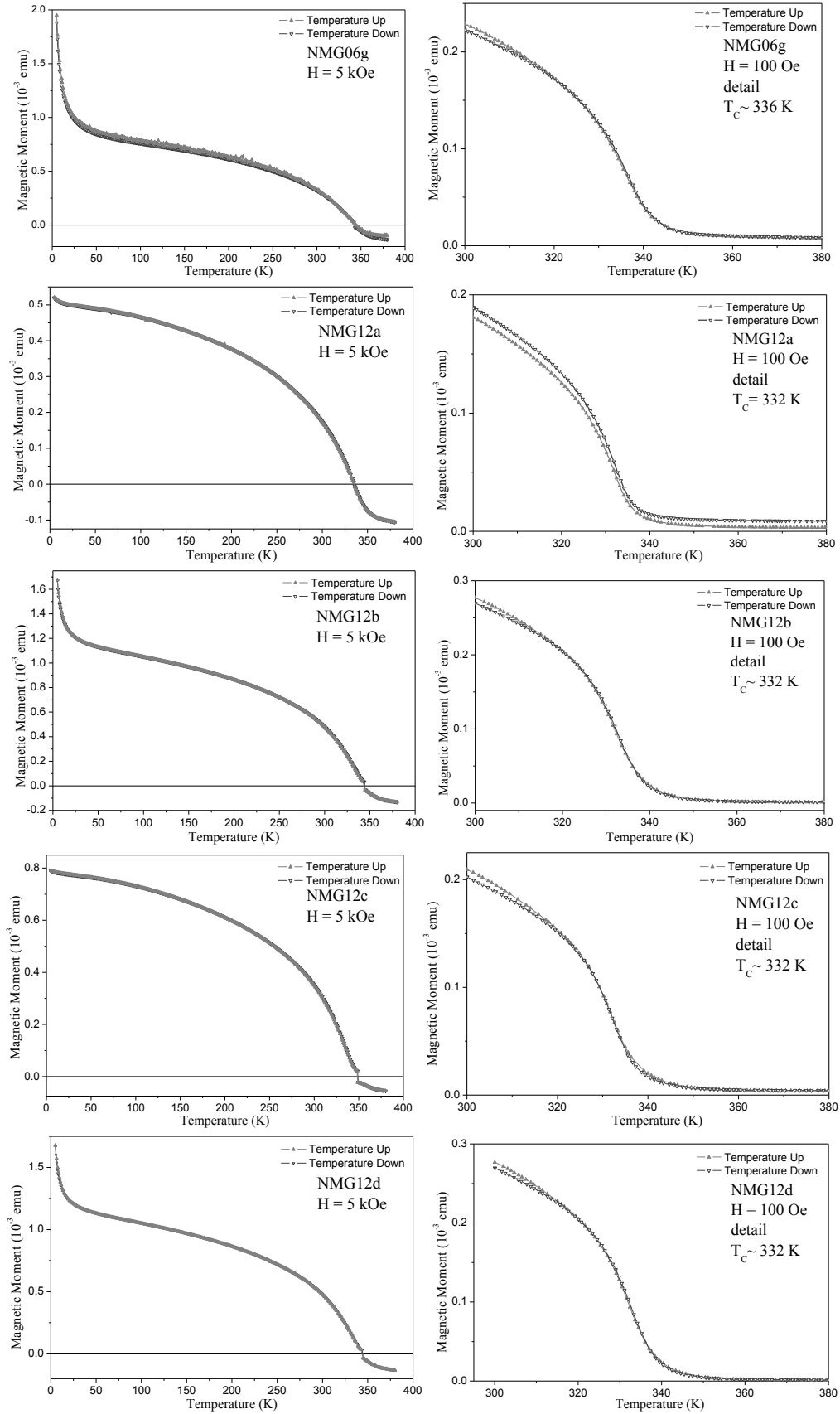


Fig. 12.3.12: Graphs of Magnetization vs. Temperature for samples NMG06g; and NMG12 series (left); respective detail showing the magnetic transition (right) once subtracted the diamagnetic contribution.

The similarity between the films phases, deposited under comparable conditions, within the NMG12 series and the NMG06g film is attested by the magnetization dependence in temperature, as can be observed in figure 12.3.12; the magnetization drops rapidly above ~ 335 K, and the films become paramagnetic above $T_C \sim 350$ K. The smooth magnetic increase detected below ~ 80 K for sample NMG06g and at ~ 64 K for samples NMG12b and NMG12d could be related to the formation of modulated superstructures with orthorhombic symmetry [4.5.1] justifying the strong enhancement of the FM signal at 5 K.

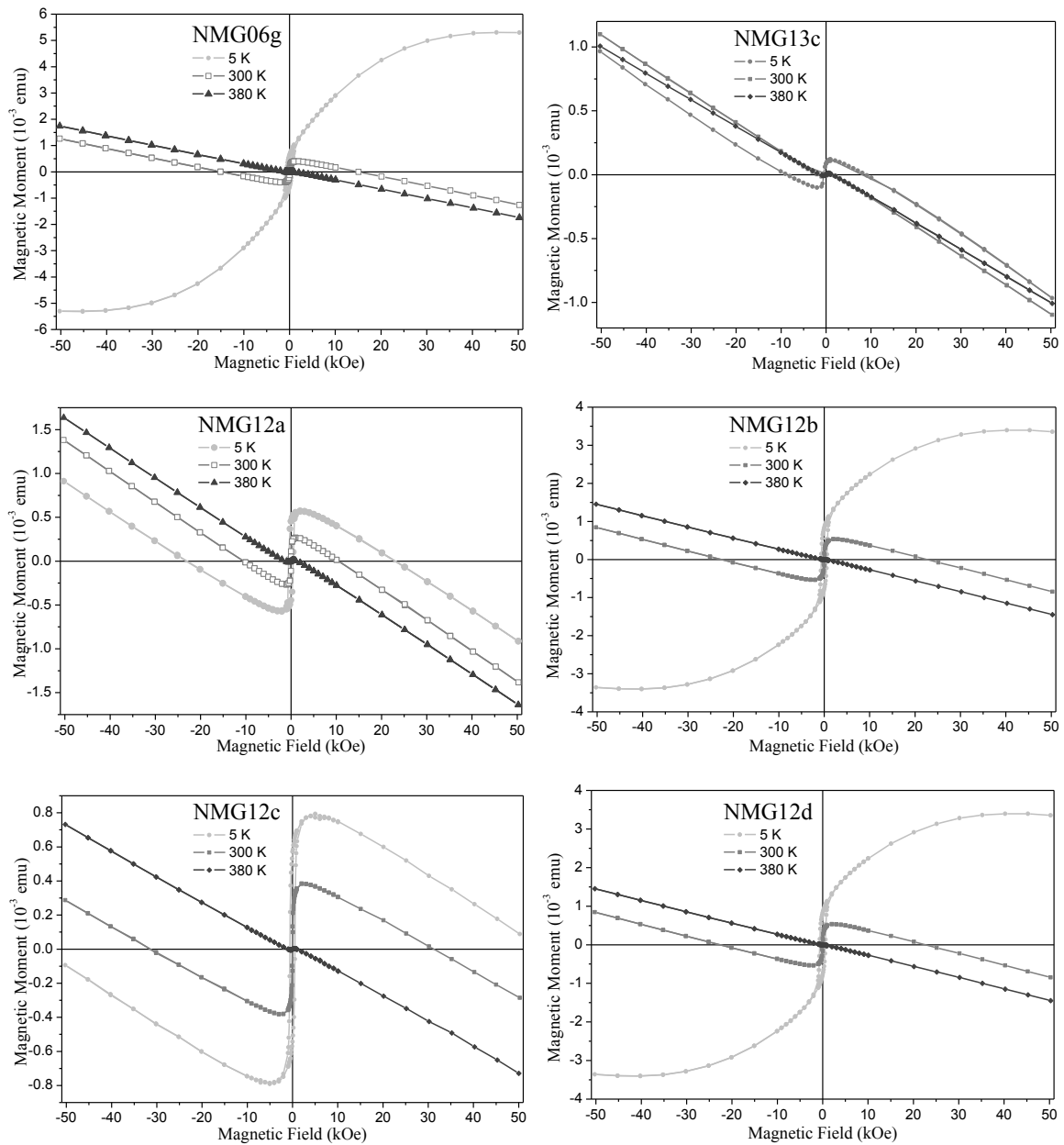


Fig. 12.3.13: SQUID measurements M vs. H for samples NMG06g; 13c and 12a, b, c, d.

Figure 12.3.13 also confirm the distinct behavior of the magnetization at very low temperatures (curves at 5 K) for samples NMG06g, NMG12b and NMG12d where the magnetization of these films surpass the diamagnetic response of the substrate.

Figure 12.3.14 presents detailed graphs of isothermal magnetization as function of field obtained for the NMG12 series, normalized to each sample film volume and excluding the substrate effect. Aside subtle differences, these hysteresis loops have an overall similarity, having at room temperature, $M_{\text{saturation}} \sim 200 \text{ emu.cm}^{-3}$, $M_{\text{remanence}} \sim 100 \text{ emu.cm}^{-3}$ and $B_{\text{coercive}} \sim 0.015 \text{ Tesla}$. These values are double at 150 K.

Assuming an alloy density of $\sim 8.16 \text{ g.cm}^{-3}$, the ferromagnetic behaviour of these films correspond to $\sim 25 \text{ emu.g}^{-1}$, which is near half the magnetization of the bulk stoichiometric Ni_2MnGa martensitic phase [12.3.9]. This result is most likely due to the lower FM contribution of the amorphous fraction formed in the films resulting from the low temperature deposition.

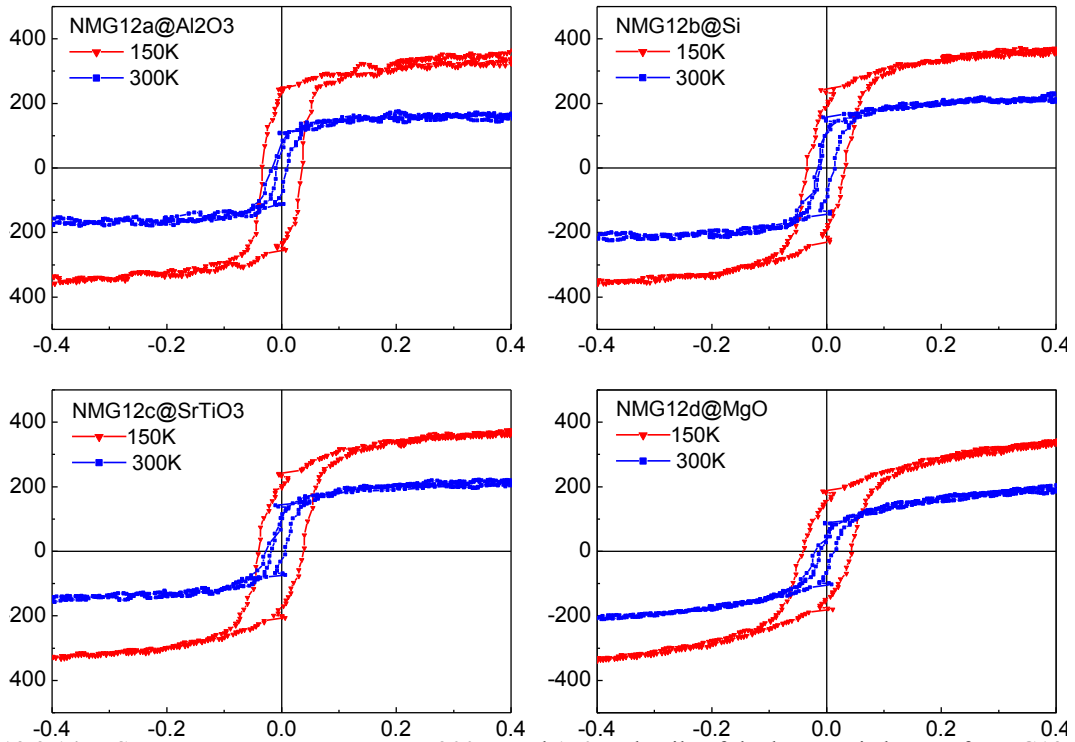


Fig. 12.3.14: VSM M vs. B measurements at 300 K and 150 K details of the hysteresis loops of NMG12 samples series between -0.4 to 0.4 T, subtracted from the diamagnetic contribution from substrates.

Magnetic Force Microscopy scan are exemplified in figure 12.3.15, the phase contrast images clearly presents magnetic domain patterns common of a large perpendicular magnetocrystalline anisotropy in films. The configuration of domains wide and contrast is much larger than the expected from similar films [12.2.10]; the observed domains clearly reoriented and grow in the direction of an external magnetic field.

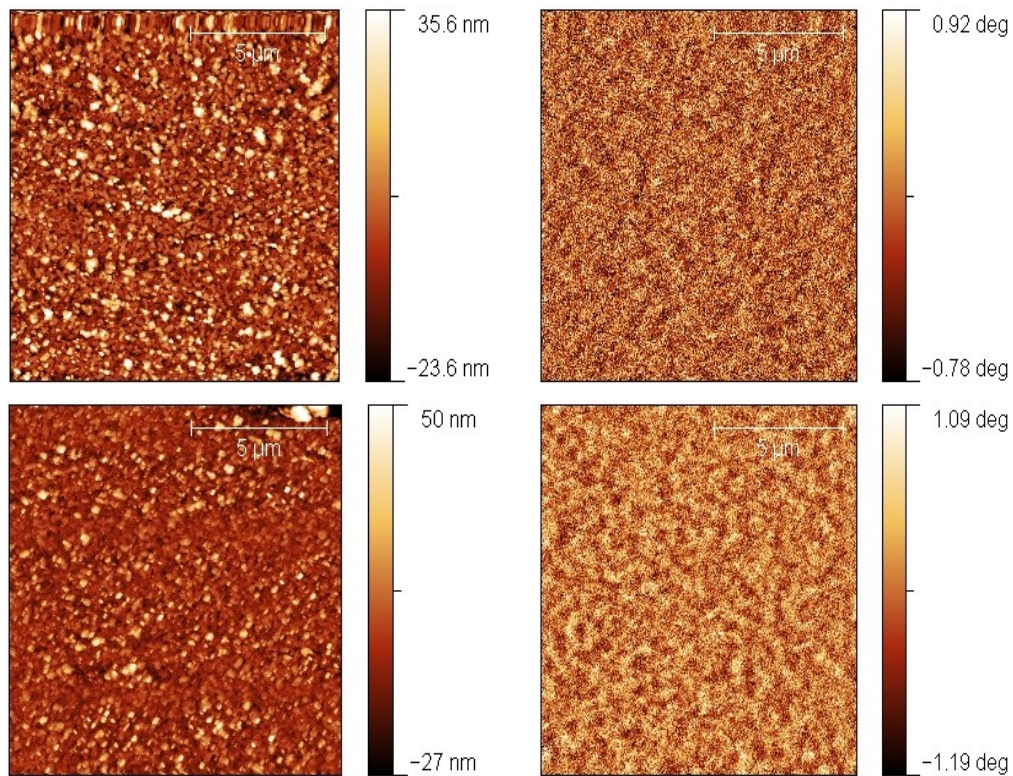


Fig. 12.3.15: Representative topographic (left) and MFM phase images (right) of sample NMG12a surface, before (top) and after (down) application of a ~ 1 kOe stimulation field

In comparison to previous films obtained at IENM labs from 3 independent targets (Ni, Mn and Ni:Ga) which allowed a good control of the composition of the deposited films, but generally resulted in the formation of the Ni_2MnGa alloy in an incipient amorphous phase, as described in previous 12.2 section, we conclude that the films obtained from 2 targets sputtering (Ni:Mn and Ni:Ga) prove the advantage of departing from the two semi-alloy precursors in order to obtain thin films deposited at relatively low temperature forming a viable Heusler crystalline phase that exhibits ferromagnetic properties.

The interpretation seems rather simple; since the bond energy necessary for the formation of the three elements alloy is partially present in each of the binary precursor targets, the sputtering process allows to transfer and to use this energy on the alloy

formation into the substrate. However when performing sputtering from single element targets, the indispensable energy for the alloy formation is redirected from the kinetics of the elements arriving to substrate, hence less thermal energy is available for diffusion and suitable crystallization of the alloy.

In conclusion, the process hereby described confirms that it is feasible to deposit the $\text{Ni}_{2+x}\text{Mn}_{1-x}\text{Ga}$ Heusler alloy onto a variety of substrates at low temperature by RF co sputtering method from binary targets, with good control of the phase composition and thermodynamic conditions to achieve the suitable crystalline structure (austenitic phase), resulting functional ferromagnetic properties at room temperature; without need for post-deposition annealing or any further thermal treatment, enabling a relevant requirement for device fabrication onto sensitive oxide materials.

Hence this experimental deposition process can be safely extended onto active substrates like PZT or PMN-PT [12.3.16] avoiding the deterioration of this piezoelectric materials, with good perspectives to achieve some magnetoelectric coupling effect.

Page intentionally left blank

IV CONCLUSIONS

The multiferroic materials research area has recently gathered international momentum within the field of R&D of Materials Science and Engineering, having nonetheless already showed an enormous potential for scientific and technological development. Under this scope the research of materials with strong electronic correlations, namely magnetic oxides like manganites has been, for quite some time, the subject of several international projects in which have been involved CICECO, the Physics Dep. of UA and the Chemistry Centre of UTAD, also in close collaborations with IFIMUP, ITN and ISOLDE at CERN. The experience gathered through participation in many of these projects and institutions and the know-how acquired during a Master's course in Materials Science and Engineering at UA were proven fundamental and fully applied in the present thesis work.

The aim of the present thesis included preparing potential multiferroic samples. A two-prong approach was taken: on one hand, studying the manganite-type oxides either intrinsically exhibiting multiferroic/magneto-electric effects (although this behavior can be better observed at low temperatures), or through materials' modification by conventional chemical doping or a more sophisticated phase induced transitions by means of biased lithography; on the other hand, studying materials that might exhibit such effects at room temperature constructed as composites containing extrinsic ferroelectric and ferromagnetic phases, whether these are in a bulk form or as multilayered thin films.

The samples surface, structural, magnetic and electric properties characterization was performed using several different tools, from state of the art SEM, XRD, SQUID, SPM, recurring to prototype stage systems like VSM and BEPS, or even implementing new MR and ME measuring systems. The way the samples preparation conditions and measured properties correlate and can develop magnetoelectric effects were studied and interpreted, making use of the relevant theoretical models.

Hence this multiferroic materials' study initiated with several different approaches as the experimental work and relevance of each preparation method, characterization technique and samples results progressed, some of the research themes deserve more focused interested, having a potential scientific and technological interest that ensures further research continuity in upcoming projects. The most relevant conclusions are summarized below.

13.1. Bulk Ceramics Synthesis and proprieties

Preceding researches results attained with prospective multiferroic composites of $\text{La}_{0.675}\text{Sr}_{0.325}\text{MnO}_3 + \text{LuMnO}_3$ and $\text{BaFe}_{12}\text{O}_{19} + \text{BaTiO}_3$ prepared by solid state route have confirmed that the high temperatures ($>1200^\circ \text{C}$) required for sintering the precursors oxides and carbonates into the final ceramic phases give rise to a deficient Oxygen stoichiometry and extensive grain growth to the order of μm size, implying reduced surface to volume ratio and fade of an eventual magneto-elastic-electric interaction via interface of distinct grains. In its turn, some *Sol-Gel* synthesis methods based on a slow nucleation/precipitation chemical reaction stage of the ceramic phases may give rise to inhomogeneities in the grains compositions due to the different reaction velocities of each metallic ion and the progressive deviation of the solution concentration during the reaction process.

Therefore the above methods demonstrated not to be the most adequate to prepare composites with the required grain size or chemical quality for propose of studying multiferroic interactions between combining phases. Hence the *Urea* combustion route was successful elected to perform the chemical synthesis of nano-powder oxides of $\text{La}_{0.6}\text{Sr}_{0.3}\text{MnO}_3$, $\text{La}_{0.6}\text{Ba}_{0.3}\text{MnO}_3$ and $\text{LuMn}_{1-z}\text{O}_{3-d}$. This method was proven to be more suitable for achieving single and composite ceramics with high chemical purity and nanometric grain size distribution ($\ll 100 \text{ nm}$) when compared to the conventional solid state sintering or the *Pechini* and co-precipitation Sol-Gel routes.

Reducing the grain size to nanometer scale becomes fundamental to achieve a better densification of the ceramic samples and enable further control of the grains growth

according to the sintering or thermal treatments temperature. The relative increase in the available surface of grains facilitates the thermodynamic diffusion of ions, thus yielding a better chemical homogeneity within a phase and consequently a more effective segregation of immiscible phases, greater interconnectivity between grains that will promote the interaction between functionalities of the different crystalline phases. For this reason a limited sintering temperature between 800° and 900° C was implemented since it avoids prominent grain growth while promoting oxygen incorporation in the phase.

Special consideration must be taken to avoid the percolation of the conductive phase, keeping the FM manganite phase below the 30 % volume of the sample; otherwise the charge accumulation between electrodes and the ferroelectric response of the sample would be neutralized through electric current loss. This is valid even when using FM ferrites (like $\text{BaFe}_{12}\text{O}_{19}$) which have much lower conductivity than the manganites.

The bulk composites based in manganites involving one ferromagnetic (rhombohedral $\text{La}_{0.7}\text{Sr}_{0.3}\text{MnO}_3$) and another ferroelectric (hexagonal LuMnO_3) took advantage of the immiscibility of the two structural/compositional phases; therefore the conditions for forming intimate mechanical contact between phases are implemented by spontaneous segregation mechanisms from precursors in solution, afterward controlling the nucleation and particles size by thermal treatments.

The most pertinent result comes from the ME effect measurements performed in sample Lu78LSM, confirming the effective (mechanical and eventually chemical) connection between the two different phases giving rise to a ME effect at room temperature reaching $\sim 150 \text{ mV/m.Oe}$ under 1 Tesla bias field and 10^5 Hz 10 Oe a.c. field.

The observation of extraordinary Raman modes at the composites Lu78LSM and Lu89LSM suggests the presence of extraordinary atomic arrangements structures having a strong non-centro-symmetric geometry giving rise to a series of new Raman active modes not present in the pure phases. A tight interconnectivity between the manganites hexagonal and the rhombohedral phases may lead to the formation of a perfusion of $\text{O}_4\text{Mn—O—MnO}_5$ (Octahedra connecting bipyramid) molecular arrangements along the grain boundaries which can justify such modes; besides configuring new polaronic states and extending accessible angles for the $\text{Mn}^{3+}\text{—O}^{2-}\text{—Mn}^{4+}$ transfer integral, such metastable structures also suggest a high multiferroic functional potential. Further experiments and

simulation will be required to identify the actual atomic/molecular arrangements that originate such modes and inherent FE and FM properties; for example, to prepare a sample based on thin film deposition of a bilayer LuMnO_3 onto $\text{La}_{0.7}\text{Sr}_{0.3}\text{MnO}_3$ having epitaxial growth and perform TEM diffraction measurements in the interlayer boundary.

Bulk composites based in perovskites materials may take advantage of using typical ferroelectric oxides like BaTiO_3 and the ferromagnetic manganite $\text{La}_{0.7}\text{Ba}_{0.3}\text{MnO}_3$; some degree of miscibility was expected and ensures better interface connection of the functional grains, however, in order to prevent excessive diffusion of atomic species between the two phases and avoid chemical reaction of spurious phases, a more innocuous mechanical mixture and hot pressing of the independent powders was chosen.

The observed FM character of the BaTiO_3 phase grain boundaries enables to establish an additional and direct coupling route with the magnetic moment orientation of neighboring $\text{La}_{0.7}\text{Ba}_{0.3}\text{MnO}_3$ phase grains, besides the strictive interaction between the two phases.

Composites recurring to high performance piezoelectric PZT or PMN-PT oxides imply additional safety procedures since dealing with Pb based materials, usually demanding dedicated synthesis equipment like crucibles and furnaces.

The results obtained from the series of nano powder samples $\text{LuMn}_{1-z}\text{O}_{3-\delta}$ from NPD, VSM and PFM measurements point in the direction that intrinsic multiferroics based on the RMnO_3 ($\text{R} = \text{Er, Ho, Y, Lu...}$) hexagonal manganites, which exhibit ferroelectric and antiferromagnetic order in the same phase below the respective critical Néel temperature are candidate materials to perform selective nonstoichiometry doping, either by anionic or cationic vacancies, generating a limited amount of Mn^{4+} ions within the structure and promoting a break in the AFM spin frustration geometry, promoting a partial FM state, while keeping FE proprieties, and converting the material into a proper multiferroic.

An interesting tool was found of particular relevance in the study of multiferroic phenomena, the case of Raman active modes shifts due to the appearance of an ordered magnetic spins state and how this additional periodicity affects the lattice vibrations within the onset of electric polarization, The detailed analysis of the Raman spectra of the single phase LuMnO_3 sample revealed the presence of the shift in the trend of the A_1 mode

frequency with temperature correlated with phonon anomalies across the magnetic phase transition near 90 K.

The most promising experimental breakthrough may come from the PFM studies performed in several C.O. manganite samples and the possibility to induce localized FE phases by means of surface bias lithography. The innovative BEPS scan procedure proved to be a useful and versatile measurement method to identify the formation of ferroelectric domains traceable to previous lithographic paths (stimulated with d.c. voltage up to ± 20 V); revealing a piezoresponse enhancement in relation to the non stimulated dielectric regions of the order of 500 % for the $\text{La}_{0.89}\text{Sr}_{0.11}\text{MnO}_3$ and $\text{Pr}_{0.60}\text{Ca}_{0.40}\text{MnO}_3$ samples and of the order of 50 % for the $\text{La}_{0.50}\text{Ca}_{0.50}\text{MnO}_3$ sample.

Lithographic bias induced structural/magnetic/electro/chemical phase transitions is a promising alternative technological process for manufacturing permanent or temporary localized FE and or FM single domains paths onto nano circuit's chips made from a single material base, widening the possibilities for high density signal processing or storage applications.

The extent of differentiated states and functionalities can range:

- 2 opposing ferromagnetic polarizations,
- 2 due to antiferromagnetic or paramagnetic state,
- 2 opposing electric polarizations,
- 2 conduction behaviors: metallic or as paraelectric insulator
- In addition to this multiferroic diversity of states, such manganites offer the possibility to select charge carriers from polarons or non polarized electrons and also vacancies;

Such broad phenomenological possibilities make these manganites materials a potential test ground to design spintronics devices and even explore the new fields of magnonics [13.1.1].

13.2. Thin Films deposited by Magnetron RF Sputtering

Magnetron RF sputtering proved to be an exceptional technique for deposition of high quality single thin films or multilayers, due to the high degree of control and precision of fabrication parameters, being able to manipulate targets to substrate distance and geometry; to perform single target sputtering or two targets co-sputtering with independent magnetron feeding power (affecting plasma acceleration); to select from a wide range of possible substrate temperature; to choose chamber atmosphere gas and pressure and also in-situ thermal treatments. Once established the targets and substrates to be employed, by performing a limited number of deposition essays and the respective samples thorough characterization, it becomes possible an empirical assessment of the system capabilities and/or limitations to achieve the desired thin film characteristics. The choice of the most adequate conditions for the subsequent depositions result from interpolations assessment, enabling to manage the rate of deposition, thin film composition, adhesion to substrate, layer thickness, epitaxy, preferred orientation, degree of crystallization and surface texture, that will ultimately dictate the sample properties. In order to produce high quality films particularly for multiferroic materials R&D, the experimental work implemented included both the installation of auxiliary devices to improve the management of the RF sputtering system and an extensive inventory of thin films produced using a variety of targets, substrates and depositions conditions.

Under this scope the best conditions to achieve high quality epitaxial thin films of the rhombohedral $\text{La}_{0.7}\text{Sr}_{0.3}\text{MnO}_3$ phase onto SrTiO_3 perovskite substrates, were found to be: Argon pressure 5×10^{-3} mbar; O_2 pressure 2×10^{-3} mbar; RF power 73 Watt with 200 V bias; substrate heater at $\sim 700^\circ \text{C}$ and finalizing with slow cooling in 0.5 mbar O_2 atmosphere.

Most relevant and successful results were obtained at U.A. with the series of thin films of the Ni_2MnGa phase like shape memory Heusler alloy deposited by magnetron RF co-sputtering from $\text{Ni}_{50}\text{Mn}_{50}$ and $\text{Ni}_{50}\text{Ga}_{50}$ targets using moderate power of 16 and 14 Watt respectively, onto a variety of substrates at $\sim 400^\circ \text{C}$; achieving a film phase composition of $\text{Ni}_{56}\text{Mn}_{19}\text{Ga}_{25}$ ($\pm 1\%$ for each element), with good adhesion and epitaxial growth; crystallization in the austenite phase; a martensitic transition temperature of $\sim 350 \text{ K}$ and a

magnetic remanence of $\sim 25 \text{ emu.g}^{-1}$, in the same order of magnitude of the similar bulk phase prepared by melting methods which needs temperatures of $\sim 1000^\circ \text{C}$.

To be able to prepare the Ni_2MnGa Heusler alloy functional phase at such relatively low temperatures offers new opportunities for the fabrication of multiferroic layered structures onto ferroelectric PZT or PMN-PT substrates, taking advantage from the combination of the enhanced functional magnetostriction and piezoelectric properties of each material while avoiding eventual Oxygen migration or Pb contamination from the substrate ceramics, resulting degradation of both materials.

13.3. Characterization Systems

This research work employed an extensive list of characterization methods, some of which benefited from previous knowhow, while some others were subject of new and comprehensive study taken as crucial for the study of multiferroic materials.

The implement of an autonomous MR and ME measuring systems in the CICECO and Physics Dep. of Aveiro University are factual accomplishments in the technical and operational point of view, an indispensable team work was essential to implement such systems hardware and software, gathering the necessary tools from each researcher in these common objectives. Generally both systems make possible to perform a high precision voltage measurements in samples as function of bias magnetic field, temperature and radial orientation of the sample in relation to the d.c. field; specifically the MR measurements depend on the d.c. current applied to the samples terminals, whereas the ME depends on a stimulation a.c. magnetic field.

In addition to the widespread EDS-SEM compositional analysis, it was possible to explore some of the specific advantages of the XPS technique particularly to distinguish some cations oxidation state; in it's turn, RBS probing allowed to trace composition and gradients in thin films within few tenths nm thickness.

Standard powders crystallographic XRD analysis can be complemented with NPD for an additional insight of the magnetic structure of the sample: In the case of thin film

samples, the practical XRR grazing angle scan enables a highly precise measure of the thin films thickness (within nm range up to $\sim 0.2 \mu\text{m}$); whereas recurring to a HRXRD it becomes possible to identify epitaxial effects of substrates and to uncover layers crystallographic orientation.

VSM and SQUID magnetometers are indispensable tools to access the magnetic states and phase transition temperatures of samples; parallel results acquired from methods like MZ, MR and ME measurements involving magnetic or temperature dependences have been proven valuable to compare, and confirm samples transitions and correlate properties trends

Scanning probe microscopy in the PFM version also enabling lithography, BEPS and $\mathbf{I-V}$ modes or in the MFM variant; were proven fundamental tools to investigate the sample's surface features that are both an outcome of the material bulk properties and localized boundary phenomena. With these tools it became possible to identify surface textures, distinguish grain boundary's and most important, to trace FE or FM domains allocation and evolution.

V FURTHER STUDIES

The work performed for the deposition of $\text{La}_{0.7}\text{Sr}_{0.3}\text{MnO}_3$ and Ni_2MnGa phase like thin films was fundamental in establishing the magnetron RF sputtering system capabilities to further implement the experimental deposition of multiferroic perovskite systems based on multilayers of $\text{La}_{0.7}\text{Sr}_{0.3}\text{MnO}_3$ or $\text{La}_{0.7}\text{Ba}_{0.3}\text{MnO}_3$ manganite and FE BaTiO_3 buffers or PMN-PT substrates.

These researches are still in progress under the scope of the *R&D* project “*Multiceral*”, and intends to design and development a micro chip architecture based on the integration of FE and FM complementary functional materials (either bulk composites or thin films multilayers) in order to demonstrate a proof of concept magneto electric functional device that is able to operate as a sensor/transducer or composing a memory element.

Further research is planned to be carried in collaboration with CNMS ONRL, TN-USA labs, namely to perform additional PFM and BEPS experiments, to perform low temperature PFM scans in high vacuum environment in order to understand the role of the C.O. phase transitions and reduce the probability of electrochemical reaction or Oxygen adsorption at samples surface. Another experiments also planned are to micro-Raman spectroscopy on the FE regions generated by the bias lithography stimulation and comparison to the regular phase.

So far the SPM equipment suppliers separate the MFM and PFM variants by means of independent data acquisition modes, cantilever holders and selection of adequate tips; the act of replacing these subsystems renders very difficult to retrieve the previous analyzed area of the sample. It is most pertinent for the study of multiferroic materials to develop a new common system able to operate consecutively in the MFM (non contact) and in the PFM mode (tapping), performing alternate modes scans without the need to replace the scanning subsystems. By matching the piezoresponse and magnetic domain maps it would become possible to observe unequivocally localized magnetoelectric effects (either in intrinsic or composite materials), moreover by comparing the FE and FM domains co-evolution resulting from a external electric or magnetic field stimulus or if

possible taking advantage of the more precise biased lithographic writing and BEPS analysis.

Since single phase compounds can hardly combine strong spontaneous ferroelectric and ferromagnetic properties (due to the ruling out of the polarizable *pd* hybridization with the 3*d* magnetic ions), future research will certainly be concentrated to improve efficiency of the contact and to establish the best nano-geometry between the piezoelectric and magnetostrictive constituents of composite structures. Special attention should be devoted to progress to nano-structures manufacture procedures and develop techniques for self-assembled materials growth.

Microwave devices, sensors, transducers and heterogeneous read/write devices are among the suggested technical implementations of the composite ME effect.

14. Closure Note

Although the rapid evolution of science and technology will render any research work obsolete in a few decades or years, I hope the broad-spectrum description of fundamental and experimental concepts present in this thesis can be useful for future reference and the experimental work and results may contribute to spawn new knowledge, even if in a small measure help, it will serve a useful function.

“To open new windows even where there are no walls”

Fábio Gabriel Nazário Figueiras

VI REFERENCES

- [0.0.1] G. Lövestam, H. Rauscher, G. Roebben, B. S. Klüttgen, N. Gibson, J.-P. Putaud and H. Stamm "Considerations on a Definition of Nanomaterial for Regulatory Purposes", (2010) J R C Reference Reports.
- [0.0.2] E. Alves et al., "Studies of Colossal Magnetoresistive Oxides with Radioactive Isotopes", ISOLDE/CERN IS390 (2005) Add I.
- [0.0.3] B. M. Moskowitz, "A Handbook of Physical Constants", (1995) American Geophysical Union.
- [1.0.1] D. Shi, B. Aktas, L. Pust, F. Mikailov, "Nanostructured Magnetic Materials and Applications", (2002) Springer.
- [1.0.2] Mark Johnson, "Magnetoelectronics", (2004) Elsevier Academic Press.
- [1.0.3] J. J. Welser, George I. Bourianoff, Victor V. Zhirnov, Ralph Keary Cavin III "The quest for the next information processing technology", J. Nanopart. Res. **10** (2008), 1–10.
- [1.0.1] P. W. Atkins, "Physical Chemistry", (1990) Oxford.
- [1.0.2] W. F. Smith, "Principles of Materials Science and Engineering", (1996) McGraw-Hill.
- [1.0.3] C. Giacovazzo; H. L. Monaco, D. Viterbo, F. Scordari, G. Gilli, G. Zanotti, and M. Catti, "Fundamentals of Crystallography", (1992) Oxford University Press.
- [1.0.4] R. E. Newnham, D. P. Skinner, and L. E. Cross, Mater. Res. Bull. **13** (1978) 525.
- [2.0.1] J. A. Edminster, "Electromagnetism", (1980) Shaum Mc Graw Hill.
- [2.0.2] G. W. C. Kaye and T. H. Laby, "Tables of physical and chemical constants", (1993) Longman.
- [2.1.1] W. N. W. Ashcroft, D.N. Mermin, "Solid State Physics", (1976) Harcourt.
- [2.2.1] S. O. Kasap, "Principles of Electrical Engineering Materials Devices", (1997) Irwin.
- [2.3.1] A. J. Moulson and J. M. Herbert, "Electroceramics - Materials, Properties, Applications", (2003) Wiley.
- [2.3.2] K. C. Kao, "Dielectric Phenomena in Solids", (2004) Elsevier.
- [3.0.1] R. Skomski, "Simple Models of Magnetism", (2008) Oxford.
- [3.0.2] K. H. J. Buschow, F. R. de Boer, "Physics of Magnetism and Magnetic Materials", (2004) Kluwer Ac. Pub.
- [3.1.1] R. L. Stamps, "Mechanisms for exchange bias", J. Phys. D: Appl. Phys. **33** (2000) R247–R268.
- [3.1.2] P. Panissod and M. Drillon "Magnetic Ordering due to Dipolar Interaction in Low Dimensional Materials" Magnetism: Molecules to Materials **IV** (2002) Wiley.
- [3.1.3] E. T. Lacheisserie, D. Gignoux, M. Schlenker, "Magnetism Fundamentals", (2005) Springer.
- [4.1.1] W. Eerenstein, N. D. Mathur and J. F. Scott, "Multiferroic and magnetoelectric materials", Nature **442** 17 (2006) 759.
- [4.1.2] W. F. Brown Jr., R. M. Hornreich and S. Shtrikman, "Upper bound on the magnetoelectric susceptibility", Phys. Rev. **168** (1968) 574-577.
- [4.1.3] N. A. Hill, "Why Are There so Few Magnetic Ferroelectrics?", J. Phys. Chem. B **104** (2000) 6694-6709.
- [4.1.4] S. W. Cheong & M. Mostovoy "Multiferroics: a magnetic twist for ferroelectricity", Nature Materials **6** (2007) 13–20.
- [4.1.5] J Wang et al., "Epitaxial BiFeO₃ Multiferroic Thin Film Heterostructures", Science **299** (2003) 1719.
- [4.1.6] B. Dabrowski, O. Chmaissem, J. Mais and S. Kolesnik, "Design Rules for Manganites with Novel Magnetic and Electronic Properties" Acta Physica Polonica A Vol. **105** (2004) 1-2.
- [4.1.7] D. V Efremov, J. Van Den Brink and D. I. Khomskii, "Bond- versus site-centred ordering and possible ferroelectricity in manganites", Nature Materials Vol **3** (2004) 853-856.

- [4.1.8] C. Ederer and N. Spalding, "A new route to magnetic ferroelectrics", *Nature Materials* Vol. **3** (2004) 849-851.
- [4.1.9] M. Fiebig, Th. Lottermoser, Th. Lonkai, A.V. Goltsev, R.V. Pisarev, "Magnetoelectric effects in Manganites" *Journal of Magnetism and Magnetic Materials* **290–291** (2005) 883–890.
- [4.1.10] N. Hur, S. Park, P. A. Sharma, J. S. Ahn, S. Guha and S-W. Cheong, "Electric polarization reversal and memory in a multiferroic material induced by magnetic fields", *Nature* **429** (2004) 392-395.
- [4.1.11] Y. Noda, H. Kimura, M. Fukunaga, S. Kobayashi, I. Kagomiya and K Kohn, "Magnetic and ferroelectric properties of multiferroic RMn_2O_5 " *J. Phys.: Condens. Matter* **20** (2008) 434206.
- [4.1.12] I. Kagomiya, and K. Kohn, "Ferroelectric transitions of LuMn_2O_5 ", *Ferroelectrics* **219**, 1 (1998) 169-176.
- [4.1.13] J. Hemberger, P. Lunkenheimer, R. Fichtl, H.-A. Krug von Nidda, V. Tsurkan and A. Loidl, "Relaxor ferroelectricity and colossal magnetocapacitive coupling in ferromagnetic CdCr_2S_4 ", *Nature* **434** (2005) 364-367.
- [4.1.14] A. Loidl, H. von Loehneysen and G. M. Kalvius (guest editors), "Multiferroics Special issue", *J. Phys. Condens. Matter* **20**, 434201–434220 (2008).
- [4.1.15] S. Q. Ren, L. Q. Weng, S.-H. Song, F. Li, J. G. Wan, M. Zeng, " $\text{BaTiO}_3/\text{CoFe}_2\text{O}_4$ particulate composites with large high frequency magnetoelectric response", *J. Mat. Sci.* **40** (2005) 4375 – 4378 Letters.
- [4.1.16] M. I. Bichurin, D. Viehland and G. Srinivasan, "Magnetoelectric interactions in ferromagnetic-piezoelectric layered structures: Phenomena and devices", *J. Electroceramics* (2007) **19**: 243–250.
- [4.1.17] N. Hur S.-W. Cheong, S. N. Kale, S. B. Ogale, R. Choudhary, S. R. Shinde, and T. Venkatesan, "Substrate-induced epitaxial mixing of bulk-immiscible $\text{La}_{5/8}\text{Sr}_{3/8}\text{MnO}_3$ / LuMnO_3 films", *App. Phys. Lett.* **86**, 112507 (2005).
- [4.1.18] M. Fiebig, "Revival of the magnetoelectric effect", *J. Phys. D: Appl. Phys.* **38** (2005) R123.
- [4.1.19] F. Figueiras, et al., "Study of $\text{Ni}_2\text{–Mn–Ga}$ phase formation by magnetron sputtering film deposition at low temperature onto Si substrates and $\text{LaNiO}_3/\text{Pb}(\text{Ti,Zr})\text{O}_3$ buffer", *J. Vac. Sci. Technol. A* **28** 1 (2010).
- [4.2.1] J. M. D. Coey, M. Viret and S. von Molnar, "Mixed-Valence Manganites" *Adv. In Phys.* Vol. **48**, 2 (1999) 167.
- [4.2.2] Y. Tokura, "Critical Features of Colossal Magnetoresistive Manganites" *Rep. Prog. Phys.* **69** (2006) 797.
- [4.2.3] P. G. Radaelli, M. Marezio, H. Y. Hwang, and S-W. Cheong, "Structural Phase Diagram of Perovskite $\text{A}_{0.7}\text{A}'_{0.3}\text{MnO}_3$ ($\text{A} = \text{La, Pr}$; $\text{A}' = \text{Ca, Sr, Ba}$): A New Imma Allotype", *J. Sol. St. Chem.* **122** (1996) 444.
- [4.2.4] A. Urushibara et al., "I-M transition and GMR in $\text{La}_{1-x}\text{Sr}_x\text{MnO}_3$ ", *Phys. Rev. B* Vol. **51** No. 20 (1995) 14103.
- [4.2.5] H. L. Ju, , Y. S. Nam, J. E. Lee and H. S. Shin, "Anomalous magnetic properties and magnetic phase diagram of $\text{La}_{1-x}\text{Ba}_x\text{MnO}_3$ ", *Journal of Magnetism and Magnetic Materials* Vol. **219**, Issue 1, 2 (2000) 1.
- [4.3.1] G. H. Kwei, A. C. Lawson, S. J. L. Billinge and S. W. Cbeong, "Structures of the Ferroelectric Phases of BaTiO_3 ", *J. Phys. Chem.* **97** (1993) 2368.
- [4.3.2] T. S. Low and W. Guo, "Modeling of a three-layer piezoelectric bimorph beam with hysteresis" *Journal of Microelectromechanical Systems* Vol. **4**, No. **4** (1995) 234.
- [4.3.3] R. Blinc, "Order and Disorder in Perovskites and Relaxor Ferroelectrics", *Struct. Bond* **124** (2007) 51–67.
- [4.3.4] I-W. Chen, P. Li and Y. Wang, "Structural origin of relaxor perovskites", *J. Phys. Chem. Sol.* V **57**, 10 (1996) 1525.
- [4.3.5] Y. M. Poplavko, "The nature of large dielectric constant of relaxors", *iee* 01418357 (2004) 143.
- [4.3.6] "TRIS Electrostrictors", <http://www.trstechnologies.com/pdf/Electrostrictors.pdf>
- [4.4.1] S. Lee, et al., "Giant magneto-elastic coupling in multiferroic hexagonal manganites" *Nature Letters* **451** (2008).
- [4.4.2] Bas B. van Aken, A. Meetsma, T. T. M. Palstra, "Hexagonal LuMnO_3 revisited", *Acta Cryst.* **E57** (2001) 101-103.
- [4.4.3] Bas B. Van Aken, and T. T. M. Palstra, "Influence of magnetic on ferroelectric ordering in LuMnO_3 ", *Phys. Rev. B* **69** (2004) 134113.
- [4.4.4] M. Fiebig, Th. Lottermoser, Th. Lonkai, A.V. Goltsev, R.V. Pisarev, "Magnetoelectric effects in multiferroic manganites", *Journal of Magnetism and Magnetic Materials* **290–291** (2005) 883–890.
- [4.4.5] D. G. Tomuta, S. Ramakrishnan, G. J. Nieuwenhuys and J. A. Mydosh, "The magnetic susceptibility, specific heat and dielectric constant of hexagonal YMnO_3 , LuMnO_3 and ScMnO_3 ", *J. Phys.: Condens. Matter* **13** (2001) 4543.

- [4.5.1] P. J. Brown, J. Crangle, T. Kanomata, M. Matsumoto, K. U. Neumann, B. Ouladdiaf and K. R. A. Ziebeck "The crystal structure and phase transitions of the magnetic shape memory compound Ni_2MnGa ", J. Phys.: Condens. Matter **14** (2002) 10159–10171.
- [4.5.2] A. Ayuela, J. Enkovaara, K. Ullakko, and R. M. Nieminen, "Structural properties of magnetic Heusler alloys", J. Phys.: Condens. Matter **11** (1999) 2017–2026.
- [4.5.3] A. Sozinov, A. A. Likhachev, N. Lanska, and K. Ullakko, "Giant magnetic-field-induced strain in NiMnGa seven-layered martensitic phase", Appl. Phys. Lett., Vol. **80**, No. 10, (2002) 1746–1748.
- [4.5.4] S. Banik, et al. "Structural studies of by powder x-ray diffraction and total energy calculations $\text{Ni}_{2+x}\text{Mn}_{1-x}\text{Ga}$ ", Phys. Rev. B **75** (2007) 104107.
- [4.5.5] A. N. Vasil'ev, V. D. Buchel'nikov, T. Takagi, V. V. Khovailo, E. I. Estrin, "Shape memory ferromagnets", Phys. Uspekhi **46** (2003) 559.
- [4.5.6] R. C. O'Handley, S. J. Murray, M. Marioni, H. Nembach, and S. M. Allen, "Phenomenology of magnetic & strain in FM shape memory material", J. Appl. Phys. Vol. **87**, No. 9 (2000) 4712–4717.
- [4.5.7] M. Wuttig and L. Liu, K. Tsuchiya, R. D. James, "Occurrence of ferromagnetic shape memory alloys", J. Appl. Phys., Vol. **87**, No. 9 (2000) 4707.
- [4.5.8] P. Entel et al., "Fundamental Aspects of Magnetic Shape Memory Alloys", Materials Science Forum Vol. 635 (2010) 3–12.
- [4.5.9] J. Enkovaara, "Magnetically driven shape memory alloys", Matt. Sci. Eng. A **V378**, 1–2 (2004) 52–60.
- [4.5.10] V. V. Khovailo, V. Novosad, T. Takagi, D. A. Filippov, R. Z. Levitin, and A. N. Vasil'ev, "Magnetic properties and magnetostructural phase transitions in $\text{Ni}_{2+x}\text{Mn}_{1-x}\text{Ga}$ shape memory alloys" Phys. Rev. B **70** (2004) 174413.
- [5.1.1] W. F. Smith, "Principles of Materials Science Engineering", (1996) McGrawHill.
- [5.1.2] A. Staneva, J. M. Vieira, Y. Ivanova, M. Kostova, L. Yang, E. Gattf, Y. Dimitriev, "Preparation of nanosized $\text{La}_{1-x}\text{Sr}_x\text{MnO}_3$ powders" Nanoscience and nanotechnology **3** (2003) Heron Press.
- [5.1.3] M. P. Pechini, US Patent No 3 330, 695, July 1967.
- [5.1.4] T. T. Carvalho and P. B. Tavares, "Synthesis and thermodynamic stability of multiferroic BiFeO_3 ", Materials Letters Vol. **62**, Issue. 24 (2008) 3984–3986.
- [5.1.5] D. A. Fumo, J. R. Jurado, A. M. Segadães, and J. R. Frade, "Combustion Synthesis of Fe-substituted SrTiO_3 perovskites", Materials Research Bulletin, Vol. **32**, No. 10 (1997) 1459–1470.
- [5.2.1] M. Ohring, "Materials Science of Thin Films (Deposition and Structure)", 2nd Edition (2002) Academic Press.
- [5.2.2] I. B. Freund, S. Suresh, "Thin Film Materials: Stress, Defect Formation and Surface Evolution", (2003) Cambridge University Press.
- [6.0.1] C. R. Brundle and C. A. Evans Jr., "Materials Characterization Series, Surfaces, Interfaces, Thin Films", (1992) Butxetworch-Heinemann.
- [6.3.1] D. A. Bonnell, S. V. Kalinin, A. L. Kholkin, and A. Gruverman, "Piezoresponse Force Microscopy: A Window into Electromechanical Behavior at the Nanoscale", MRS Bulletin Vol **34** (2009) 648–657.
- [6.3.2] S. Jesse, S. Kalinin, R. Proksch, A. P. Baddorf, B. J. Rodriguez; "The BE method in SPM ...", Nanotechnology **18** (2007) 435503.
- [6.5.1] J. R. D. Copley, "The Fundamentals of Neutron Powder Diffraction", Materials Science and Engineering Laboratory, NIST Recommended Practice Guide Special Publication **960-2** (2001).
- [6.6.1] B. A. Hunter and C. J. Howard, "LHPM Rietica Manual", Lucas Heights Research Laboratories (2000) <http://www.ccp14.ac.uk/>
- [6.7.1] A. E. Pantoja, H. J. Trodahl, A. Fainstein, R. G. Pregliasco, R. G. Buckley, G. Balakrishnan, M. R. Lees, And D. McK. Paul, "O(Mn) vibrational bands in double-layered manganites: First and second order Raman scattering", Phys. Rev. B, Vol. **63** (2001) 132406.
- [6.7.2] M. N. Iliev and M. V. Abrashev, "Raman phonons and Raman Jahn–Teller bands in perovskite-like manganites", J. Raman Spectrosc. **32** (2001), 805–811

- [6.8.1] T. Shinjo, "Nanomagnetism and spintronics", (2009) Elsevier.
- [6.8.2] E. Velu, C. Dupas, D. Renard, J. P. Renard and J. Seiden, "Enhanced magnetoresistance of ultrathin $(\text{Au/Co})_n$ multilayers with perpendicular anisotropy", Phys. Rev. B **37** (1988) 668-671.
- [6.8.3] M. N. Baibich, et al., "Giant Magnetoresistance of $(001)\text{Fe}/(001)\text{Cr}$ Magnetic Superlattices", J. Phys. Rev. Lett. **61** (1988) 2472-2475.
- [6.8.4] P. Grünberg, R. Schreiber, Y. Pang, M. B. Brodsky and H. Sowers, "Layered Magnetic Structures: Evidence for Antiferromagnetic Coupling of Fe Layers across Cr Interlayers", Phys. Rev. Lett. **57** (1986) 2442-2445.
- [6.8.5] N. Tezuka and T. Miyazaki, "Magnetic tunneling effect in $\text{Fe}/\text{Al}_2\text{O}_3/\text{Ni}_{1-x}\text{Fe}_x$ junctions", J. Appl. Phys. **79** (1996) 6262-6265.
- [6.9.1] G. V. Duong, R. Groessinger, M. Schoenhardt and D. Bueno-Basques, "The lock-in technique for studying magnetoelectric effect", Journal of Magnetism and Magnetic Materials **316**, Issue 2, (2007) 390-393.
- [6.10.1] V. M. Prida, P. Gorria, G. V. Kuryandskaya, M. L. Sánchez, B. Hernando and M. Tejedor, "Magneto-impedance effect in nanostructured soft ferromagnetic alloys", Nanotechnology **14** (2003) 231-238.
- [6.11.1] <http://web.mit.edu/newsoffice/2007/obits-tt1128.html>
- [6.12.1] Van Dozer, T. Turner, C. W. "Principles of Superconductive Devices and Circuits", (1999) Prentice Hall.
- [8.2.1] N. Sama, R. Herdier, D. Jenkins, C. Soyer, D. Remiens, M. Detalle, and R. Bouregba, "On the influence of the top and bottom electrodes—A comparative study between Pt and LNO electrodes for PZT thin films" J. Cryst. Growth **310** (2008) 3299.
- [9.1.1] P. Sum, H. P. Lang and H. J. Guntherodt, "Scanning force microscopy study of single-crystal substrates used for thin-film growth of high-temperature superconductors", Physica C242, Issue 1-2 (1995), 174-182.
- [9.1.2] C. J Howard, B. J Kennedy and B. C Chakoumakos, "Neutron powder diffraction study of rhombohedral rare-earth aluminates and the rhombohedral to cubic phase transition", J. Phys.: Condens. Matter **12** (2000) 349–365.
- [10.0.1] J. Rodriguez-Carvajal, "Recent Advances in Magnetic Structure Determination by Neutron Powder Diffraction", Physica B **192** (1993) 55-69.
- [10.0.2] J. F. Moulder, W. F. Stikle, P. E. Sobol and K. D. Bomben, Physical Electronics Inc, (1995) USA.
- [10.0.3] J.A.F. Gamelas, H.M. Carapuça, M.S. Balula, D.V. Evtuguin, W. Schlindwein, F.G. Figueiras, V.S. Amaral and A.M.V. Cavaleiro, "Synthesis and characterisation of novel ruthenium multi-substituted polyoxometalates: α,β - $[\text{SiW}_9\text{O}_{37}\text{Ru}_4(\text{H}_2\text{O})_3\text{Cl}_3]^{7-}$ ", Polyhedron Vol. **29**, 16, (2010) 3066-3073; <http://dx.doi.org/10.1016/j.poly.2010.08.002>
- [10.0.4] N. P. Barradas, C. Jeynes, R. P. Webb, "Simulated annealing analysis of Rutherford backscattering data", Appl. Phys. Lett. **71** (1997) 291.
- [10.0.5] J. F. Ziegler, J. P. Biersack, U. Littmark, "Stopping and Ranges of Ions in Solids" (1985) Pergamon, New York.
- [11.0.1] F. Figueiras, J.M. Veira, M.E. Guzik, J. Legendziewicz, P.B. Tavares, V.S. Amaral "The effects of Ca and Mn excess co-doping in CMR manganites solid solution structures", Materials 2005 Conference, Advanced Materials Forum III Vol. **514-516** (2006), 294-298 Trans Tech.
- [11.0.2] G. B. Song, J. S. Amaral, V.S. Amaral, A.L. Kholkin, "Processing and phase separation of LSMO-based multiferroic composite ceramics", Journal of the European Ceramic Society **27** (2007) 3941.
- [11.0.3] S. Park, N. Hur, S. Guha, and S.-W. Cheong, "Percolative Conduction in the Half-Metallic-Ferromagnetic and Ferroelectric Mixture of $(\text{La,Lu,Sr})\text{MnO}_3$ ", Phys. Rev. Lett. **92** (2004) 167206.
- [11.0.4] J. Lee, J. Park, A. Kim, K. Chara, S. Park, N. Hur, and S.-W. Cheong, "Phase separation in $\text{La}_{5/8}\text{Sr}_{3/8}\text{MnO}_3$ (30%)+ LuMnO_3 (70%) bulk sample studied by scanning microwave microscopy", App. Phys. Letters **86**, 012502 (2005).
- [11.0.5] E. Selesneva, "Magnetoelectric Composites Based on Hexagonal Ferrites", M.Sc Thesis research work in Materials Science, Univ. Aveiro (2008).
- [11.0.6] A. L. Kholkin, D. V. Karpinsky, E. K. Selezneva, Igor Bdikin, F. Figueiras, K. E. Kamentsev, Yuri Fetisov, R. C. Pullar, J. Krebbs, N. M. Alford, "Development of Novel Multiferroic Composites Based on BaTiO_3 and Hexagonal Ferrites", MRS Proceedings **1161E** (2009) 1161.

- [11.0.7] D. V. Karpinsky, R. C. Pullar, Y. K. Fetisov, K. E. Kamentsev and A. L. Kholkin, "Local probing of magnetoelectric coupling in multiferroic composites of $\text{BaFe}_{12}\text{O}_{19}$ – BaTiO_3 " J. Appl. Phys. **108**, 042012 (2010).
- [11.0.8] F. Figueiras, J. Agostinho Moreira, M. Kostadinova, "Characterization studies of doped YMnO_3 hexagonal manganites", Poster presentation at Conference Dyproso 2007.
- [11.0.9] M. Chen, B. Hallstedt, L. J. Gauckler, "Thermodynamic assessment of the Mn–Y–O system", Journal of Alloys and Compounds **393** (2005) 114–121.
- [11.1.1] A. N. Petrov, V. I. Voronin, T. Norby, P. Kofstad, "Crystal structure of the mixed oxides $\text{La}_{0.7}\text{Sr}_{0.3}\text{Co}_{(1-z)}\text{Mn}_{(z)}\text{O}_{(3+y)}$ ($0 \leq z \leq 1$)", Journal of Solid State Chemistry **143** (1999) 52–57.
- [11.1.2] I. Kagomiya, K. Kohn, T. Uchiyama, "Structure and ferroelectricity of RMn_2O_5 ", Ferroelectrics **280** (2002) 131–143. (ICSD #97050)
- [11.1.3] A. Saiki, N. Ishizawa, N. Mizutani and M. Kato, "Structural change of C-type rare earth oxides, ytterbium oxide and erbium oxide at high temperatures", Journal of the Ceramic Society of Japan **93** (1985) 649–654 (ICSD #40471)
- [11.1.4] L. B. Vedmid, V. F. Balakirev, A. M. Yankin, and Yu. V. Golikov, "P–T–x Phase Diagram of the Lu–Mn–O System", Doklady Physical Chemistry, Vol. **389**, Nos. 4–6 (2003) 87–89.
- [11.1.5] G. De Marzia, H. J. Trodahl, J. Bok, A. Cantarero, F. Sapiña, "The effect of Cu substitution on the A_{1g} mode of $\text{La}_{0.7}\text{Sr}_{0.3}\text{MnO}_3$ manganites", Solid State Communications **127** (2003) 259–264.
- [11.1.6] J. Vermette, S. Jandl, A. A. Mukhin, V. Y. Ivanov, A. Balbashov, M. M. Gospodinov and L. P.-Gaudart, "Raman study of the antiferromagnetic phase transitions in hexagonal YMnO_3 and LuMnO_3 ", J. Phys.: Condens. Matter **22** (2010) 356002.
- [11.1.7] J. A. Moreira, et al., "Coupling between phonons and magnetic excitations in orthorhombic $\text{Eu}_{1-x}\text{Y}_x\text{MnO}_3$ ", Phys. Rev. B **81** (2010) 054447.
- [11.1.8] A. F. García-Flores, et al., "Anomalous phonon shifts in the paramagnetic phase of multiferroic RMn_2O_5 ($R=\text{Bi, Eu, Dy}$): Possible manifestations of unconventional magnetic correlations", Phys. Rev. B **73** (2006) 104411.
- [11.1.9] B. Mihailova, M. M. Gospodinov, B. Güttler, F. Yen, A. P. Litvinchuk and M. N. Iliev, "Temperature-dependent Raman spectra of HoMn_2O_5 and TbMn_2O_5 ", Phys. Rev. B **71**, 172301 (2005).
- [11.1.10] I. Kagomiya, K. Kohn, "Ferroelectric transitions of LuMn_2O_5 ", Ferroelectrics **219**, (1998) 169–176.
- [11.1.11] R. Tackett, G. Lawes, B. C. Melot, M. Grossman, E. S. Toberer, and R. Seshadri, "Magnetodielectric coupling in Mn_3O_4 ", Physical Review B **76**, 024409 (2007).
- [11.1.12] Y.-H. Huang, et al., "Soft chemical synthesis and transport properties of $\text{La}_{0.7}\text{Sr}_{0.3}\text{MnO}_3$ granular perovskites", Solid State Communications **114** (2000) 43–47.
- [11.1.13] R. Mahendiran, R. Mahesh, A.K. Raychaudhuri and C.N.R. Rao, "Resistivity, GMR and Thermopower in $\text{La}_{0.7}\text{Sr}_{0.3}\text{MnO}_3$ showing large difference in Temperature corresponding to the FM transition and the I-M transition", Solid State Communications **99**, No. 3 (1996), 149–152.
- [11.1.14] R. Mahendiran, S. K. Tiwary, A. K. Raychaudhuri, T. V. Ramakrishnan, R. Mahesh, N. Rangavittal, and C. N. R. Rao, "Structure, electron-transport properties, and giant magnetoresistance of hole-doped LaMnO_3 systems", Physical Review B **53**, 6 (1996) 3348–3358.
- [11.1.15] A. L. Millis, P.B. Littlewood and B.I. Shaiman, "Double Exchange Alone Does Not Explain the Resistivity of $\text{La}_{1-x}\text{Sr}_x\text{MnO}_3$ ", Physical Review Letters **74** (1995), 5144–5147.
- [11.1.16] P. Raychaudhuri, T. K. Nath, A. K. Nigam, and R. Pinto, "A phenomenological model for magnetoresistance in granular polycrystalline colossal magnetoresistive materials: The role of spin polarized tunnelling at the grain boundaries", Journal of Applied Physics **54**, 4 (1998) 2048–2052.
- [11.1.17] B. Z. Sun, L. L. He, F. Luo, C. H. Yan, "Lu-induced orthorhombic phase in polycrystalline $\text{La}_{0.7}\text{Sr}_{0.3}\text{MnO}_3$ ", Physica B **367** (2005) 249–254.
- [11.1.18] B. Z. Sun, L. L. He, F. Luo, C. H. Yan, "Microstructural evolution of bulk polycrystalline $\text{La}_{0.7-x}\text{Lu}_x\text{Sr}_{0.3}\text{MnO}_3$ ($x = 0.2, 0.45, 0.6$) compounds", Materials Chemistry and Physics **98** (2006) 415–418.
- [11.1.19] Y.-H. Huang, F. Luo, Y. Li, Z.-M. Wang, C.-S. Lião and C.-H. Yan, "Abnormal lattice effect on magnetic-transport phase diagram in $\text{La}_{0.7-x}\text{Lu}_x\text{Sr}_{0.3}\text{MnO}_3$ perovskites", Journal of Applied Physics **91**, 12 (2002) 10218–10220.

- [11.1.20] P. Mandal, P. Choudhury, and B. Ghosh, "Electronic transport in ferroelectric-ferromagnetic composites $La_{5/8}(Ba,Ca)_{3/8}MnO_3:LuMnO_3$ ", *Physical Review B* **74** (2006) 094421.
- [11.2.1] F. Figueiras, "Composição, Estrutura e Propriedades de Manganites Cerâmicas – Efeitos da Substituição de La por Ca e Lacunas", Thesis Defense Work, Master Degree course on Materials Science and Engeneering (2004), Aveiro University.
- [11.2.2] L. N. Bulaevskii, C. D. Batista, M. V. Mostovoy and D. I. Khomskii, "Electronic orbital currents and polarization in Mott insulators", *Phys. Rev. B* **78** (2008) 024402.
- [11.2.3] T. Katsufuji, S. Mori, M. Masaki, Y. Moritomo, N. Yamamoto, and H. Takagi, "Dielectric and magnetic anomalies and spin frustration in hexagonal $RMnO_3$ ($R=Y, Yb$, and Lu)", *Phys. Rev. B* **64** (2001) 104419.
- [11.2.4] A. Ghosh, J. R. Sahu, S. V. Bhat and C.N.R. Rao, "A Raman study of multiferroic $LuMnO_3$ ", *Solid State Sciences* **11** (2009) 1639–1642.
- [11.2.5] K. Yoshii and H. Abe, "Magnetic Properties of $LnMnO_3$ ($Ln=Ho, Er, Tm, Yb$, and Lu)", *Journal of Solid State Chemistry* **165** (2002) 131–135.
- [11.2.6] H. J. Lewtas, et al., "Magnetic excitations in multiferroic $LuMnO_3$ studied by inelastic neutron scattering", arXiv: cond-mat.str-el 1007.5490v2 (2010).
- [11.2.7] C. T. Wu, B. N. Lin, H. C. Ku and Y. Y. Hsu, "Variation of Triangular Antiferromagnetic Order in Ferromagnetic $Sc_{1-x}Lu_xMnO_3$ Manganites", *Chinese Journal of Physics* **41**, no.6 (2003) 652-662.
- [11.2.8] K. Uusi-Esko, J. Malm, N. Imamura, H. Yamauchi, M. Karppinen, "Characterization of $RMnO_3$ ($R = Sc, Y, Dy-Lu$): High-pressure synthesized metastable perovskites and their hexagonal precursor phases", *Materials Chemistry and Physics* **112** (2008) 1029–1034.
- [11.2.9] T. Katsufuji, et al., "Crystal structure and magnetic properties of hexagonal $RMnO_3$ ($R= Y, Lu$ and Sc) and the effect of doping", *Phys. Rev. B* **66** (2002) 134434.
- [11.2.10] H. L. Yakel, W. C. Koehler, E. F. Bertaut, E. F. Forrat, "On the crystal structure of the manganese(III) trioxides of the heavy lanthanides and yttrium" *Acta Crystallographica* **16** (1963) 957.
- [11.2.11] F.C. Tsao, et al., "Mn magnetic ordering in fully oxygenated $LuMnO_3$ ", *Journal of Magnetism and Magnetic Materials* **272–276** (2004) 1778–1779.
- [11.2.12] N. Imamura, M. Karppinen, H. Fjellvag, H.Yamauchi, "Hole doping into the metastable $LuMnO_3$ perovskite", *Solid State Communications* **140** (2006) 386-390.
- [11.2.13] G. Zhu, P. Liu, Y. Liu, H. Miao and J. Zhou, "Hydrothermal Synthesis $YbMnO_3$ and $LuMnO_3$ Platelets", *J. Am. Ceram. Soc.* **91** [10] (2008) 3423–3427.
- [11.2.14] R. Das, A. Jaiswal, S. Adyanthaya, and P. Poddar, "Origin of Magnetic Anomalies below the Neel Temperature in Nanocrystalline $LuMnO_3$ ", *J. Phys. Chem. C* **114** (2010) 12104–12109.
- [11.2.15] V. F. Balakirev, L. B. Vedmid, A. M. Yankin, and Yu. V. Golikov, "P–T–x Phase Diagram of the Lu–Mn–O System", *Doklady Physical Chemistry*, Vol. **389**, Nos. 4–6 (2003) 87–89.
- [11.2.16] L. B. Vedmid, V. F. Balakirev, A. M. Yankin, Yu. V. Golikov, and O. M. Fedorova, "Effect of Oxygen Pressure on Phase Equilibria in the Lu–Mn–O System", *Doklady Physical Chemistry*, Vol. **389**, Nos. 4–6 (2003), 87–89.
- [11.2.17] S. Lee, M. Kanga, C. Lee, A. Hoshikawa, M. Yonemura, T. Kamiyama, J.-G. Parka, "Multiferroic behavior and two-dimensional magnetism of hexagonal manganites", *Physica B* **385–386** (2006) 405–407.
- [11.2.18] X. Fabreges, S. Petit, I. Mirebeau, S. Pailhes, L. Pinsard, A. Forget, M. T. Fernandez-Diaz, and F. Porcher, "Spin-Lattice Coupling, Frustration, and Magnetic Order in Multiferroic $RMnO_3$ ", *Phys. Rev. Lett.* **103** (2009) 067204.
- [11.3.1] C. A. F. Vaz, J. Hoffman, C. H. Ahn, and R. Ramesh, "Magnetoelectric Coupling Effects in Multiferroic Complex Oxide Composite Structures", *Adv. Mater.* **22** (2010), 2900-2918.
- [11.3.2] K. Ban, M. Gomi, T. Shundo, and N. Nishimura, "Giant M-E effect of multiferroic $BaTiO_3$ - $LaMnO_3$ ceramic composites" *IEEE transactions on magnetics*, **41** (2005), 2793-2795.
- [11.3.3] N. G. Kim, Y. S. Koo, C. J. Won, N. Hur, J. H. Junga, J. Yoon, Y. Jo, and M. H. Jung, "Magnetodielectric effect in $BaTiO_3$ - $LaMnO_3$ composites", *Journal of Applied Phys.* **102**, 014107 (2007).

- [11.3.4] V. A. Cherepanov, E. A. Filonova, V. I. Voronin, I. F. Berger, "Phase equilibria in the (LaCoO₃)-(LaMnO₃)-(BaCoO₃) (BaMO₃) system", Journal of Solid State Chemistry **153** (2000), 205-211
- [11.3.5] R. J. Zollweg, "X-Ray lattice constant of Barium Oxide" Phys Rev **100**, no. 2 (1955), 671-673.
- [11.3.6] S. Moehr, H. Mueller-Buschbaum, "Eine neue Hochtemperaturform von TiO: H-TiO", Zeitschrift fuer Anorganische und Allgemeine Chemie **620** (1994) 1175-1178 (file ICSD#74849).
- [11.3.7] C. J. Howard, T. M. Sabine, F. Dickson, "Structural and Thermal Parameters for Rutile and Anatase", Acta Crystallographica B **47** (1991) 462-468.
- [11.3.8] E. P. Meagher, G. A. Lager, "Polyhedral thermal expansion in the TiO₂ polymorphs. Refinement of the crystal structures of Rutile and Brookite", Canadian Mineralogist **17** (1979) 77-85. (file ICSD#36408).
- [11.3.9] C. E. Rice, W. R. Robinson, "Structural changes in the solid solution (Ti_{1-x}V_x)₂O₃ as x varies from zero to one", Journal of Solid State Chemistry **21** (1977). 145-154 (file ICSD#1462).
- [11.3.10] B. Boucher, R. Buhl, M. Perrin, "Proprietes et structure magnetique de Mn₃O₄", Journal of Physics and Chemistry of Solids **32** (1971) 2429-2437. (file ICSD#76088).
- [11.3.11] R. Pazik, D. Kaczorowski, D. Hreniak, W. Stręk and W. Łojkowski, "Synthesis, structure and magnetic properties of BaTiO₃ nanoceramics", Chemical Physics Letters Vol. 452, Is. 1-3, (2008), 144-147.
- [11.3.12] R. V. K. Mangalam, M. Chakrabarti, D. Sanyal, A. Chakrabati and A. Sundaresan, "Identifying defects in multiferroic nanocrystalline BaTiO₃ by positron annihilation techniques", J. Phys.: Condens. Matter **21** (2009) 445902.
- [11.3.13] R.V.K. Mangalam, N. Ray, U. V. Waghmare, A. Sundaresan, C.N.R. Rao, "Multiferroic properties of nanocrystalline BaTiO₃", Solid State Communications **149** (2009) 1-5.
- [11.3.14] R. Tripathi, V. P. S. Awana, H. Kishan, S. Balamurugan and G. L. Bhalla "Impact of Silver Addition on Room Temperature Magneto-Resistance in La_{0.7}Ba_{0.3}MnO₃ (LBMO): Ag_x (x = 0.0, 0.1, 0.2, 0.3, 0.4)", J Supercond. Nov. Magn. (2008).
- [11.3.15] H. L. Ju, J. Gopalakrishnan, J. L. Peng, Qi Li, G. C. Xiong, t. Venkatesan and R. L. Greene, "Dependence of GMR on Oxygen stoichiometry and magnetization in polycrystalline La_{0.67}Ba_{0.33}MnO₃", Phys. Rev. B **51**, 9 (1995).
- [11.3.16] B. M. Nagabhushana, R. P. S. Chakradhar, K. P. Rameshb, V. Prasad, C. Shivakumara, G. T. Chandrappa, "Magnetoresistance studies on barium doped nanocrystalline manganite", Journal of Alloys and Compounds **450** (2008) 364-368.
- [11.3.17] B. Dabrowski, K. Rogacki, X. Xiong, P. W. Klamut, R. Dybziński, J. Shaffer and J. D. Jorgensen, "Synthesis and properties of the vacancy-free La_{1-x}Ba_xMnO₃", Phys. Rev. B **58**, 5 (1998) 2716-11.23.
- [11.3.18] S. M. Bhagat, S. E. Lofland, P. H. Kim, D. C. Schmadel, C. Kwon, R. Ramesh and S. D. Tyagi, "Ferromagnetic antiresonance in La_{0.7}Ba_{0.3}MnO₃ traced out by temperature variation of temperature", J. Appl. Phys. **81**, 8 (1997), 5157-5158.
- [11.3.19] W. Eerenstein, M. Wiora, J. L. Prieto, J. F. Scott and N. D. Mathur, "Giant sharp magnetoelectric switching in multiferroic epitaxial heterostructures La_{0.67}Sr_{0.33}MnO₃ on BaTiO₃", Nature Materials **6**, (2007) 348-351.
- [11.3.20] K. Dörr and C. Thiele, "Multiferroic bilayers of manganites and titanates", Phys. Stat. Sol. (b) **243**, No. 1 (2006) 21-28.
- [11.3.21] M. P. Singh and W. Prellier, "Oxide superlattices for multiferroics: opportunities, issues, and challenges", Philosophical Magazine Letters, Vol. **87**, Nos. 3-4, (2007), 211-222.
- [11.3.22] S. A. Solopan, O. I. V'yunov, A. G. Belous, A. I. Tovstolytkin, L.L. Kovalenko, "Magnetoelectric effect in composite structures based on ferroelectric-ferromagnetic perovskites", Journal of the European Ceramic Society **30** (2010) 259-263.
- [11.3.23] B. T. Cong, N. N. Dinh, D. V. Hien, N. L. Tuyen, "Study of La_{0.7}Sr_{0.3}Mn_{0.96}Co_{0.04}O₃, La_{0.7}Sr_{0.3}MnO₃ and BaTiO₃ composites", Physica B **327** (2003) 370-373.
- [11.4.1] J. Van Den Brink and D I. Khomskii, "Multiferroicity due to charge ordering", J. Phys.: Condens. Matter **20** (2008) 434217.
- [11.4.2] A. Asamitsu, Y. Tomioka, H. Kuwahara and Y. Tokura, "Current switching of resistive states in magnetoresistive manganites", Nature Vol. **388** (3 July 1997), 50-52

- [11.4.3] C. Martin, A. Maignan, M. Hervieu, and B. Raveau, "Magnetic phase diagrams of $L_{1-x}A_x\text{MnO}_3$ manganites ($L=\text{Pr,Sm}$; $A=\text{Ca,Sr}$)", *Phys. Rev. B* **60**, no. 17 (1999).
- [11.4.4] E. Dagotto, T. Hotta, A. Moreo, "Colossal magnetoresistant materials: the key role of phase separation", *Physics Reports* **344** (2001) 1-153.
- [11.4.5] Y. Tomioka, A. Asamitsu, H. Kuwahara, Y. Moritomo and Y. Tokura, "Magnetic-field-induced metal-insulator phenomena in $\text{Pr}_{1-x}\text{Ca}_x\text{MnO}_3$ with controlled charge-ordering instability", *Phys. Rev. B* **53**, 4 (1996) R1689-R1692.
- [11.4.6] Ch. Jooss, et al, "Polaron melting and ordering as key mechanisms for colossal resistance effects in manganites", *PNAS* **104**, no. 34 (2007) 13597–13602.
- [11.4.7] A. M. L. Lopes, J. P. Araújo, V. S. Amaral, J. G. Correia, Y. Tomioka and Y. Tokura, "New Phase Transition in the $\text{Pr}_{1-x}\text{Ca}_x\text{MnO}_3$ System: Evidence for Electrical Polarization in Charge Ordered Manganites", *Phys. Rev. Lett.* **100** (2008) 155702.
- [11.4.8] R. F. Mamin, I. K. Bdikin and A. L. Kholkin, "Locally induced charged states in $\text{La}_{0.89}\text{Sr}_{0.11}\text{MnO}_3$ single crystals", *App. Phys. Lett.* **94** (2009) 222901.
- [11.4.9] M. Hennion, F. Moussa, J. Rodriguez-Carvajal, L. Pinsard and A. Revcolevschi, "New dynamical features in $\text{La}_{0.95}\text{Ca}_{0.05}\text{MnO}_3$ ", *Physica B* **234-236** (1997) 851-853.
- [11.4.10] M. Roy, J. F. Mitchell, A. P. Ramirez, P. Schiffer, "Doping-induced transition from double exchange to charge order in $\text{La}_{1-x}\text{Ca}_x\text{MnO}_3$ near $x=0.50$ ", *Phys. Rev. B* **58**, 9 (1998) 5185-5188.
- [11.4.11] S.V. Kalilin et al., "Local bias-induced phase transitions", *Mat. Today V.* **11**, no. 11 (2008) 16-27.
- [11.4.12] D. D. Sarma, et al., "Direct Observation of Large Electronic Domains with Memory Effect in Doped Manganites", *Phys. Rev. B* **93**, 9 (2004).
- [11.4.13] K. H. Ahn, T. Lookman and A. R. Bishop, "Strain-induced metal-insulator phase coexistence in perovskite manganites", *Nature* **428** (2004) 401-404.
- [11.4.14] L. Wu, R. F. Klie, Y. Zhu and Ch. Jooss "Experimental confirmation of Zener-polaron-type charge and orbital ordering in $\text{Pr}_{1-x}\text{Ca}_x\text{MnO}_3$ ", *Phys. Rev. B* **76** (2007) 174210.
- [11.4.15] I. A. Sergienko, C. Sen and E. Dagotto, "Ferroelectricity in the Magnetic E-Phase of Orthorhombic Perovskites", *Phys. Rev. Lett.*, **97**, (2006) 227204.
- [12.1.1] Project POCTI/CTM/40063/2001: "Energy transfer from electro luminescent polymers to phosphorescent sources"
- [12.1.2] L. Martín-Carrón, A. de Andrés, M. J. Martínez-Lope, M. T. Casais and J. A. Alonso, "Raman phonons as a probe of disorder, fluctuations, and local structure in doped and undoped orthorhombic and rhombohedral manganites", *Phys. Rev. B* **66** (2002) 174303
- [12.2.1] V. Chernenko, M. Kohl, S. Doyle, P. Mullner, and M. Ohtsuka, "Texture dependence of the martensitic transformation in Ni-Mn-Ga films deposited on alumina", *Scripta Materialia* **54** (2006) 1287-1291.
- [12.2.2] F. A. Hames, *J. Appl. Phys.* **31** (1960) 370S. (PDF File No. 04-006-2515).
- [12.2.3] B. Wedel, M. Suzuki, Y. Murakami, C. Wedel, T. Suzuki, D. Shindo and K. J. Itagaki, *Alloys Compds.* **290** (1999) 137. (PDF File No. 04-008-1270).
- [12.2.4] V. A. Chernenko, V. V. Kokorin, O. M. Babii and I. K. Z asimchuk, "Phase diagrams in the Ni---Mn---Ga system under compression", *Intermetallics* **6** Is. 1, (1998), 29-34
- [12.2.5] H. Uchishiba, *J. Phys. Soc. Jpn.* **31** (1971) 436. (PDF File No. 04-006-6410).
- [12.2.6] J. Jarrige and J. Bull Mexmain, *Soc. Chim. Fr.* **1-419** (1980). (PDF File No. 04-006-4866).
- [12.2.7] C. E. Weir, G. J. Piermarini and S. J. Block, *Phys. Chem.* **54** (1971)2768. (PDF File No. 01-070-2615).
- [12.2.8] N. Sama, R. Herdier, D. Jenkins, C. Soyer, D. Remiens, M. Detalle, and R. Bouregba, "On the influence of the top and bottom electrodes—A comparative study between Pt and LaNiO_3 electrodes for PZT thin films" *Journal of Crystal Growth* **310**, Is. 14, (2008), 3299-3302.
- [12.2.9] F. J. Castano, B. Nelson-Cheeseman, R. C. O'Handley, C. A. Ross, C. Redondo and F. Castano, "Structure and thermomagnetic properties of polycrystalline Ni-Mn-Ga thin films", *Journal of Applied Physics* **93**, (2003) 8492-8494.

- [12.2.10] V. A. Chernenko, V. A. L'vov, V. V. Khovailo, T. Takagi, T. Kanomata, T. Suzuki, and R. Kainuma, *J. Phys: Condens. Matter* **16**, (2004) 8345.
- [12.2.11] I. Babita, M. M. Raja, R. Gopalan, V. Chandrasekaran and S. Ram, *J. Alloys and Comp.* **423** (2007) 23.
- [12.2.12] F. Figueiras, et al., "Study of Ni₂-Mn-Ga phase formation by magnetron sputtering film deposition at low temperature onto Si substrates and LaNiO₃/Pb(Ti,Zr)O₃ buffer", *J. Vac. Sci. Technol. A* **28** Issue 1 (2010), 6.
- [12.3.1] A. C. Lourenço, F. Figueiras, S. Das, et. al., "Low Temperature Deposition of Ferromagnetic Ni-Mn-Ga Thin Films from Two Different Targets via RF Magnetron Sputtering", *Mater. Res. Soc. Symp. Proc.* **1250** (2010), G08-02.
- [12.3.2] B. Wedel, M. Suzuki, Y. Murakami, C. Wedel, T. Suzuki, D. Shindo, K. Itagaki, "Low temperature crystal structure of Ni-Mn-Ga alloys", *Journal of Alloys Compd.* **290** (1999) 137-143. (File ICSD #106917), (PDF File No. 01-072-9053)
- [12.3.3] K. H. J. Buschow, P. G. van Engen, R. Jongebreur, "Magneto-optical properties of metallic ferromagnetic materials", *Journal of Magnetism and Magnetic Materials* **38** (1983) 1-22. (File ICSD #103804)
- [12.3.4] E. N. Maslen, V. A. Streltsov, N. R. Streltsova, N. Ishizawa and Y. Satow, "Synchrotron X-ray study of the electron density in -Al₂O₃", *Acta Cryst.* **B49** (1993) 973-980. (File ICSD #73724)
- [12.3.5] W. L. Bond and W. Kaiser, "Interstitial versus substitutional Oxygen in Silicon", *Journal of Physics and Chemistry of Solids* **16** (1960), 44-45. (File ICSD #29288)
- [12.3.6] G. M. Meyer, R. J. Nelmes, J. Hutton, "High-resolution (direct space) studies of anharmonic motion associated with the structural phase transition in SrTiO₃", *Phase Transition* **38** (1992) 127-220 (File ICSD#23076).
- [12.3.7] L. Righi, F. Albertini, L. Pareti, A. Paoluzi, G. Calestani, "Commensurate and incommensurate "5M" modulated crystal structures in Ni-Mn-Ga martensitic phases", *Acta Mater.* **55** (2007) 5237-5245 (File ICSD#158167).
- [12.3.8] A. Kern, R. Doetzer, W. Eysel, *Moscow University Geology Bulletin* **47** 80 (1992) (File ICSD#450946).
- [12.3.9] A. Sozinov, A. A. Likhachev, and K. Ullakko, "Crystal Structures and Magnetic Anisotropy Properties of Ni-Mn-Ga Martensitic Phases With Giant Magnetic-Field-Induced Strain", *IEEE Transactions on Magnetics*, Vol. **38**, no. 5 (2002) 2814-2816.
- [12.3.10] N. Lanska, O. Soderberg, A. Sozinov, Y. Ge, K. Ullakko, V. K. Lindroos, "Composition and temperature dependence of the crystal structure of Ni-Mn-Ga alloys", *Journal of Applied Physics* **95**, 12 (2004), 8074-8078.
- [12.3.11] V. A. Chernenko, E. Cesari, V. V. Kokorin, I. N. Vitenko, "The Development of new Ferromagnetic Shape Memory Alloys in Ni-Mn-Ga System", *Scripta Metalurgica et Materialia* **33**, 8 (1995), 1239-1244
- [12.3.12] G. Jakob, T. Eichhorn, M. Kallmayer, and H. J. Elmers, "Correlation of electronic structure and martensitic transition in epitaxial Ni₂MnGa films", *Physical Review B* **76** (2007) 174407.
- [12.3.13] J. Dubowik, I. Goscianska, "Martensitic transformations in Ni-Mn-Ga sputtered films", *Journal of Magnetism and Magnetic Materials* **316** (2007) e599-e602
- [12.3.14] M. Kohl, A. Agarwal, V.A. Chernenko, M. Ohtsuka, K. Seemann, "Shape memory effect and magnetostriction in polycrystalline Ni-Mn-Ga thin film microactuators", *Materials Science and Engineering A* **438-440** (2006) 940-943
- [12.3.15] V. O. Golub, A. Ya. Vovk, L. Malkinski, C. J. O'Connor, Z. Wang and J. Tang, "Anomalous magnetoresistance in NiMnGa thin films", *Journal of Applied Physics* **96**, 7 1 (2004), 3865-3869.
- [12.3.16] M. Y. Teferi, "Developments of Multiferroic Heterostructures of Thin Films of Ni-Mn-Ga Alloys and PMN-PT", Master Thesis in Materials Science, Univ Aveiro, Physics Dep. (2010).
- [13.1.1] V. V. Kruglyak, S. O. Demokritov, and D Grundler, "Magnonics", *J. Phys. D: Appl. Phys.* **43** (2010) 264001.

VII COMMUNICATIONS AND PUBLICATIONS LIST

In the following are listed the communications and presentations related to the present thesis work:

14.1. Articles

Article: A. L. Kholkin, D. V. Karpinsky, E. K. Selezneva, Igor Bdikin, F. Figueiras, K. E. Kamentsev, Yuri Fetisov, R. C. Pullar, J. Krebs, N. M. Alford, “*Development of Novel Multiferroic Composites Based on BaTiO₃ and Hexagonal Ferrites*”, MRS Proceedings **1161E** (2009) I 01-06.

Article: F. Figueiras, et al., “*Study of Ni₂-Mn-Ga phase formation by magnetron sputtering film deposition at low temperature onto Si substrates and LaNiO₃/Pb(Ti,Zr)O₃ buffer*”, J. Vac. Sci. Technol. A **28** Issue 1 (2010), 6.

Article: J.A.F. Gamelas, H.M. Carapuça, M.S. Balula, D.V. Evtuguin, W. Schlindwein, F.G. Figueiras, V.S. Amaral and A.M.V. Cavaleiro, “*Synthesis and characterisation of novel ruthenium multi-substituted polyoxometalates: α,β -[SiW₉O₃₇Ru₄(H₂O)₃Cl₃]⁷⁻*”, Polyhedron Vol. **29**, 16, (2010) 3066-3073.

Article: A. L. Kholkin, A. C. Lourenço, F. Figueiras, S. Das, et. al., “*Low Temperature Deposition of Ferromagnetic Ni-Mn-Ga Thin Films from Two Different Targets via RF Magnetron Sputtering*”, Mater. Res. Soc. Symp. Proc. **1250** (2010), G08-02.

14.2. Communications Abstracts

Presentation Abstract: F. Figueiras, Armando Lourenço, Sérgio Pereira, Mário Reis, Vitor Amaral, Joaquim Vieira, Pedro Tavares, “*RF Sputtering thin film deposition system at the Physics Department, Aveiro University*”, International School on Structural characterization of nanostructures, (2007), Department of Physics of the University of Aveiro and I3N - Portugal.

Poster Abstract: F. Figueiras, Armando Lourenço, Sérgio Pereira, Mário Reis, Vitor Amaral, Joaquim Vieira, Pedro Tavares, “*RF Sputtering thin film deposition system at the Physics Department, Aveiro University*”, IV CICECO meeting (2007), University of Aveiro - Portugal.

Poster Abstract: F. Figueiras, J. A. Moreira, M. Kostadinova, “*Characterization studies of doped YMnO₃ hexagonal manganites*”, ‘DyProSo XXXI’, 31st International Symposium on the Dynamic Properties of Solids September 25th – 29th, 2007, University of Porto - Portugal.

Poster Abstract: F. Figueiras, N. P. Vyshatko, H. Romain, C. Soyer, D. Remiens, V. V. Shvartsman, P. Borisov, W. Kleemann, V. S. Amaral, A. L. Kholkin, “*Thin film devices of layered Ni₂MnGa and PZT prepared by RF sputtering*”, FAMEnoe Summer School on Inorganic Functional Materials, 6th-11th July 2008, São Pedro do Sul, Aveiro - Portugal.

Poster Abstract: F. Figueiras, N. P. Vyshatko, H. Romain, C. Soyer, D. Remiens, V. V. Shvartsman, P. Borisov, W. Kleemann, V. S. Amaral, A. L. Kholkin, “*Thin Film Deposition of Ni-Mn-Ga Alloy onto Si and PZT buffer substrates by RF Magnetron Sputtering at Room Temperature*”, JEMS’08, Joint European Magnetic Symposia, Sept. 14-19, 2008, Dublin – Ireland.

Poster Abstract: F. Figueiras, V. S. Amaral, A.L. Kholkin, S. V. Kalinin, “*SPM study of charge ordered multiferroic manganites*”, VII CICECO Meeting, January 28-29th, 2010, Department of Physics, University of Aveiro – Portugal.

Presentation Abstract: F. Figueiras, I. K. Bdikin, V. S. Amaral, A. L. Kholkin, S. V. Kalinin, “*SPM study of charge ordered multiferroic manganites*”, XVIth Workshop on Magnetism and Intermetallics, 4-6 March 2010, Science Faculty of University of Porto - Portugal.

Poster Abstract: A. C. Lourenço, F. Figueiras, S. Das, M. Peres, N. Soares, M. J. Pereira, N. M. Santos, N. A. Sobolev, V. S. Amaral, A. Kholkin, “*As-deposited ferromagnetic Ni-Mn-Ga thin films by co-deposition of two different targets using rf-magnetron sputtering*”, MRS Spring 2010 Meeting, April 5-9, 2010, San Francisco, CA-USA

14.1. Oral Communications

Presentation: F. Figueiras, I. K. Bdikin, V. S. Amaral, A. L. Kholkin, S. V. Kalinin, “*SPM study of charge ordered multiferroic manganites*”, XVIth Workshop on Magnetism and Intermetallics, 4-6 March 2010, Science Faculty of University of Porto - Portugal.

Presentation: F. Figueiras, et al., “*Thin Film Deposition by RF Sputtering at the Physics Dep. of Aveiro Univ.*”, International School on Structural characterization of nanostructures, 25th January 2007, Department of Physics of the University of Aveiro and I3N - Portugal.

14.1. Poster Communications

Poster: F. Figueiras, A. Lourenço, Sérgio Pereira, Mário Reis, Vitor Amaral, Joaquim Vieira, Pedro Tavares, “*RF Sputtering thin film deposition system at the Physics Department, Aveiro University*”, IV CICECO meeting (2007), University of Aveiro – Portugal.

Poster: F. Figueiras, J. A. Moreira, M. Kostadinova, “*Characterization studies of doped YMnO₃ hexagonal manganites*”, ‘DyProSo XXXI’, 31st International Symposium on the Dynamic Properties of Solids September 25th – 29th, 2007, University of Porto - Portugal.

Poster: F. Figueiras, N. P. Vyshatko, H. Romain, C. Soyer, D. Remiens, V. V. Shvartsman, P. Borisov, W. Kleemann, V. S. Amaral, A. L. Kholkin, “*Thin film devices of layered Ni₂MnGa and PZT prepared by RF sputtering*”, FAMEnoe Summer School on Inorganic Functional Materials, 6th-11th July 2008, São Pedro do Sul, Aveiro - Portugal.

Poster: F. Figueiras, N. P. Vyshatko, H. Romain, C. Soyer, D. Remiens, V. V. Shvartsman, P. Borisov, W. Kleemann, V. S. Amaral, A. L. Kholkin, “*Study of Ni-Mn-Ga Phase Formation by Low Temperature RF Sputtering Film Deposition onto Si Substrates and LNO/PZT Buffer*”, JEMS’08, Joint European Magnetic Symposia, Sept. 14-19, 2008, Dublin – Ireland.

Poster: F. Figueiras, V. S. Amaral, A.L. Kholkin, S. V. Kalinin, “*SPM study of charge ordered multiferroic manganites*”, VII CICECO Meeting, January 28-29th, 2010, Department of Physics, University of Aveiro – Portugal.

Poster: A. C. Lourenço, F. Figueiras, S. Das, M. Peres, N. Soares, M. J. Pereira, N. M. Santos, N. A. Sobolev, V. S. Amaral, A. Kholkin, “*As-deposited ferromagnetic Ni-Mn-Ga thin films by co-deposition of two different targets using rf-magnetron sputtering*”, MRS Spring 2010 Meeting, April 5-9, 2010, San Francisco, CA-USA.

Poster: F. Figueiras, I. K. Bdikin, V. S. Amaral, A. L. Kholkin, S. V. Kalinin “*Modification and Study of Multiferroic Manganites by Scanning Probe Microscopy*”, “Encontro com a Ciência e Tecnologia Em Portugal”, 4 a 7 Jul. 2010, Centro de Congressos de Lisboa - Portugal.

Page intentionally left blank

VIII ATTACHMENTS

The preceding comprehensive list of publications and communications abstracts is hereby presented as attachments alongside the respective images of posters and oral presentations illustrating some of the complementary work performed in the context of PhD project.

MRS – Materials Research Society

Symposium I: Engineered Multiferroics - Magnetoelectric Interactions, Sensors and Devices

MRS Proceedings Volume 1161E (2009) I01-06

Development of Novel Multiferroic Composites Based on BaTiO₃ and Hexagonal Ferrites

A. L. Kholkin, D. V. Karpinsky, E. K. Selezneva, Igor Bdikin, F. Figueiras, K. E. Kamentsev, Yuri Fetisov, R. C. Pullar, J. Krebbs, N. M. Alford

Abstract

A new multiferroic composite ceramics with the general formula (x)Ba(Sr)Fe₁₂O₁₉-(1-x)BaTiO₃ (x =0.1, 0.5) was synthesized via a simple solid-state reaction technique. Crystal structure analysis performed for both materials revealed the presence of two crystalline phases pertinent to the initial composite components. X-ray diffraction (XRD), scanning electron microscopy (SEM) and atomic force microscopy (AFM) were used to testify the crystallinity, microstructure, and local magnetoelectric interactions between ferroelectric and ferromagnetic grains. Magnetic measurements revealed that the saturation magnetization is proportional to the volume fraction of ferrite phase. Dielectric studies demonstrated strong frequency relaxation due to space charge polarization and high conductivity loss making macroscopic magnetoelectric measurements difficult. Novel nanoscale magnetoelectric effect observed by AFM is discussed.

DOI: 10.1557/PROC-1161-I01-06

http://www.mrs.org/s_mrs/sec_subscribe.asp?CID=18429&DID=243469&action=detail

J. Vac. Sci. Technol. A 28, 6 (2010)

© 2010 American Vacuum Society

Study of Ni₂–Mn–Ga phase formation by magnetron sputtering film deposition at low temperature onto Si substrates and LaNiO₃/Pb(Ti,Zr)O₃ buffer

F. Figueiras, E. Rauwel, V. S. Amaral, N. Vyshatko, A. L. Kholkin, C. Soyer, D. Remiens, V. V. Shvartsman, P. Borisov, and W. Kleemann

Abstract

Film deposition of Ni₂MnGa phaselike alloy by radio frequency (rf) magnetron sputtering was performed onto bare Si(100) substrates and LaNiO₃/Pb(Ti,Zr)O₃ (LNO/PZT) ferroelectric buffer layer near room temperature. The prepared samples were characterized using conventional x-ray diffraction (XRD), superconducting quantum interference device, and electron dispersive x-ray spectroscopy from scanning electron microscope observations. The optimized films deposited under high rf power and low argon pressure present good surface quality and highly textured phase crystallization. The positioning distance between the substrate and the target-holder axis has some limited effect on the film's composition due to the specific diffusion behavior of each element in the sputtering plasma. Extended four pole high resolution XRD analysis allowed one to discriminate the intended Ni–Mn–Ga tetragonal martensitic phase induced by the (100) LNO/PZT oriented buffer. This low temperature process appears to be very promising, allowing separate control of the functional layer's properties, while trying to achieve high electromagnetoelastic coupling.

Acknowledgments

The work was performed within the EC-funded project “Multiceral” (Grant No. NMP3-CT-2006-032616). Partial financial support from FCT under Grant Nos. SFRH/BD/25011/2005 and SFRH/BPD/45136/2008, Marie Curie EIF (Grant No. MEIF-CT2006-041632), and collaborative projects FLAD/NSF 600-06/2006 and DFG/SFB 491 is acknowledged. The authors are thankful to L. W. Martin for magnetic measurements.

DOI: 10.1116/1.3256200 (5 pages)

http://avspublications.org/jvsta/resource/1/jvtad6/v28/i1/p6_s1?isAuthorized=no

Synthesis and characterisation of novel ruthenium multi-substituted polyoxometalates:

α, β -[SiW₉O₃₇Ru₄(H₂O)₃Cl₃]⁷⁻

J.A.F. Gamelas^a, H.M. Carapuça^a, M.S. Balula^a, D.V. Evtuguin^a, W. Schlindwein^b, F.G. Figueiras^c, V.S. Amaral^c and A.M.V. Cavaleiro^a.

^a CICECO, Department of Chemistry, University of Aveiro, 3810-193 Aveiro, Portugal

^b Leicester School of Pharmacy, De Montfort University, Leicester, LE1 9BH, UK

^c CICECO, Department of Physics, University of Aveiro, 3810-193 Aveiro, Portugal

Abstract

Novel ruthenium multi-substituted polyoxometalate compounds of general formulae K₆Na[SiW₉O₃₇Ru^{III}₄(H₂O)₃Cl₃] \cdot nH₂O (α - and β -SiW₉O₃₄ isomers) were synthesised via the reactions of the trilaunary Keggin α - and β -[SiW₉O₃₄]¹⁰⁻ anions with RuCl₃ in aqueous solution. Characterisation was performed by analytical, spectroscopic, magnetic, and electrochemical techniques. The results are in accordance with the new polyoxometalates having the trivacant Keggin anion (α or β isomer) linked to a cubane-type Ru₄O₄ cluster. The co-ordination sphere of ruthenium is completed with water molecules and chloride anions. Magnetic measurements showed that the majority of the molecules have the Ru ions cluster in a compensated configuration constrained to an antiferromagnetic alignment at very low temperature and following a Curie-Weiss like behaviour. For both isomers, cyclic voltammetry revealed quasi-reversible redox processes at the ruthenium centres, namely Ru^{IV/III} and Ru^{III/II}, which were found to be pH dependent. The novel polyoxotungstates incorporate the highest content of ruthenium (W:Ru = 2.25:1) ever reported for Keggin-, Dawson or sandwich-type transition metal-substituted polyoxometalates and may find promising applications as oxidative catalysts.

Acknowledgments

Authors wish to thank the University of Aveiro and the Portuguese Foundation for the Science and Technology (FCT) for funding. The authors also thank Dr. N.J.O. Silva for additional magnetic measurements performed at Zaragoza University, Spain and Dr. C.P. Moreira de Sá, CEMUP Porto-Portugal, for XPS analysis. J.A.F. Gamelas thanks FCT for the award of a postdoctoral research grant (SFRH/BPD/11571/2002).

Received 30 November 2009; accepted 7 August 2010. Available online 17 August 2010.

DOI: 10.1016/j.poly.2010.08.002

<http://dx.doi.org/10.1016/j.poly.2010.08.002>

MRS – Materials Research Society

Symposium G: Materials and Physics for Nonvolatile Memories II

MRS Proceedings Volume 1250 (2010) G08-02

Low Temperature Deposition of Ferromagnetic Ni-Mn-Ga Thin Films from Two Different Targets via rf Magnetron Sputtering

Andrei L. Kholkin, A. C. Lourenço, F. Figueiras, S. Das, J. S. Amaral, G. N. Kakazei, D. V. Karpinsky, N. Soares, M. Peres, M. J. Pereira, P. B. Tavares, N. Sobolev, V. Amaral, N. M. Santos

Abstract

Low temperature (400°C) deposition of ferromagnetic Ni-Mn-Ga thin films is successfully performed via rf magnetron sputtering technique using co-deposition of two targets Ni₅₀Mn₅₀ and Ni₅₀Ga₅₀ on sapphire (0001) and Si (100) substrates. The films are in part amorphous with significant degree of crystallinity. The obtained crystallographic structure is shown to be substrate-dependent. Films on both substrates are ferromagnetic at room temperature (Curie temperature ~332.5K) with well-defined hysteresis loops, low coercivity (~100 Oe) and a saturation magnetization of ~200 emu/cc. At low temperature (5 K), both films show increased magnetization value with wider hysteresis loops having higher coercivity and remanent magnetization. The process is therefore effective in achieving the appropriate thermodynamic conditions to deposit thin films of the Ni-Mn-Ga austenitic phase (highly magnetic at room temperature) at relatively low substrate temperature without the need for post-deposition annealing or further thermal treatment, which is prerequisite for the device fabrication.

DOI: 10.1557/PROC-1250-G08-02

http://www.mrs.org/s_mrs/sec_subscribe.asp?CID=26215&DID=325790&action=detail

Abstract: Fábio Figueiras, et al., “*Thin Film Deposition by RF Sputtering at the Physics Dep. of Aveiro Univ.*”, International School on Structural characterization of nanostructures, 25th January 2007, Department of Physics of the University of Aveiro and I3N

RF Sputtering thin film deposition system at Physics Department, Aveiro University

Fábio Figueiras¹, Armando Lourenço¹, Sérgio Pereira¹, Mário Reis¹, Vitor Amaral¹, Joaquim Vieira¹, Pedro Tavares²

(1) University of Aveiro, Department, CICECO, 3810-193 Aveiro, Portugal

(2) University of Trás-os-Montes e Alto Douro, Centro de Química, 5001-801 Vila Real

E-mail: ffigueiras@ua.pt, alourenco@ua.pt

Since March 2006 the RF Sputtering [1] system of the Physics Department at Aveiro University became operational. This custom made RF Sputtering system consists on a spherical UHV chamber, 3 magnetron guns in a confocal configuration operating at 13.56 MHz RF up to 300 Watt. The substrate heater is able to operate up to 950 C in a Oxygen atmosphere; mounted on-axis, it can also adopt off-axis geometry if required. Full pressure control of Oxygen and Argon can be obtained from 10^{-5} mbar up to 1 atm; there is also provision for additional gas entrances and mass flow controllers, 0.5 sccm minimum flux.

Characterizations of the first thin films of $\text{La}_{0.7}\text{Sr}_{0.3}\text{MnO}_3$ deposited in different substrates are made by several complementary techniques [2], like RXD [3], EDS-SEM, RBS, VSM, and Raman spectroscopy.

Based on the results attain by this first series of thin films structural, chemical and physical properties, further optimization of the RF Sputtering system deposition conditions is still under development.

Future work will be developed in several different targets, for the management of the deposition rates according to the target/substrate distance, Argon partial pressure and RF power.

References

- [1] H.S. Butler and G.S. Kino, *Phys. Fluids* (1963) no.6, 1346, "Plasma Sheath Formation by Radio-Frequency Fields"
- [2] Fábio G.N. Figueiras, PhMs Thesis, Universidade de Aveiro (2004), “Composição, estrutura e propriedades de manganites cerâmicas: Efeito da substituição de Lantânio por Cálcio e lacunas”
- [3] D.K. Bowen and B.K. Tanner, *High Resolution X-ray Diffractometry and Topogtaphy*, (2001)

Acknowledgments

Project: POCTI/CTM/35462/2000

FCT Scholarship: SFRH/BD/25011/2005

Presentation: Fábio Figueiras, et al., “Thin Film Deposition by RF Sputtering at the Physics Dep. of Aveiro Univ.”, International School on Structural characterization of nanostructures, 25th January 2007, Department of Physics of the University of Aveiro and I3N

Thin Film Deposition RF Sputtering System at the Physics Department, Aveiro University

Fábio Figueiras^{1,2,3}
Armando Lourenço^{1,2}
Sérgio Pereira^{1,2}
Vitor Amâncio^{1,2}
Joaquim Vieira^{1,3}
Pedro Tavares⁴

Project: This unit has been mainly funded by project PEP/01/00000/2002 (FCT).

1: CICECO
2: Physics Department
3: Ceramics and Glass Engineering Department Aveiro University
Campus Universitario Santiago, 301, 4813 Aveiro, Portugal
4: Chemical Centre of Materials, Universidade Nova de Lisboa
Campus Capucho, 2749-016, Vila Nova de Poiares, Portugal

ISSCN'07 – Poster # 218

Thin Film Deposition RF Sputtering System at the Physics Department, Aveiro University

RF Sputtering is an essential tool in thin film R&D of new functional materials; it offers high control over the deposition process:

- deposition and growth rate,
- composition homogeneity,
- adhesion and epitaxy,
- surface quality,
- thickness,
- grain size,
- step coverage,
- overall properties,
- ...

RF Sputtering deposition systems operate using a Radio Frequency field to generate an plasma (1) in a low pressure gas, while the electrons (2) loop in the permanent magnetic field (3), the positive ions (4) are accelerated towards the target (5) and dislodge the target atoms (sputter) (6) that condenses in the substrate (7) to form a thin film (8).

ISSCN'07 – Poster # 218

Thin Film Deposition RF Sputtering System at the Physics Department, Aveiro University

This versatile custom made system is optimized for oxide and magnetic materials thin film deposition, it consists of:

- spherical UHV chamber (can reach 10^{-6} mbar up to 1 atm)
- mass flow controllers (full pressure control of O₂ and Argon) (0.5 sccm minimum flux)
- provision for additional gas entrances
- 3 magnetron guns in a confocal configuration (2 with special high field magnets) (operating at 13.56 MHz RF) (up to 300 Watt)
- 2 inch substrate heater (up to 950 C in a O₂ atmosphere) (can adopt on-axis or off-axis geometry) (in situ annealing for epitaxial growth)

ISSCN'07 – Poster # 218

Thin Film Deposition RF Sputtering System at the Physics Department, Aveiro University

Characterization of La_{0.7}Sr_{0.3}MnO₃ (LSM) thin films: HRXRD

▲ Rhombo. R-3c LSM thin film grows with [211] direction over (110) SrTiO₃ substrate.
▲ HR-XRD symmetric reciprocal space map of LSM (R-3c) thin film shows tilted growth of (10-2) planes relatively to the (100) direction of MgO substrate.

ISSCN'07 – Poster # 218

Thin Film Deposition RF Sputtering System at the Physics Department, Aveiro University

Characterization of La_{0.7}Sr_{0.3}MnO₃ (LSM) thin films: SEM

▲ LSM @ MgO ▲ LSM @ SrTiO₃

25 KV SEM images of 50 µm film surface.

EDS-SEM measures show highly uniform chemical composition over all the thin films surface and no contaminants. Thin films grown in SrTiO₃ substrates have almost no surface defects, while on MgO exhibit higher rugosity and defects.

ISSCN'07 – Poster # 218

Thin Film Deposition RF Sputtering System at the Physics Department, Aveiro University

Characterization of La_{0.7}Sr_{0.3}MnO₃ (LSM) thin films: RBS

RBS/PIXE measures show a relative raise in Lanthanum composition and confirms a better growth of the LSM film on SrTiO₃ substrate compared to MgO.

Substrate	Film	Mn	La	Sr	O	Atoms/cm ³
SrTiO ₃	520 nm	1.00	0.87	---	2.8	~4.8 x 10 ²²
MgO	425 nm	1.00	0.75	0.25	2.6	~4.7 x 10 ²²

ISSCN'07 – Poster # 218

Thin Film Deposition RF Sputtering System at the Physics Department, Aveiro University

- ✓ Preliminary results confirm the versatility of the RF sputtering system, allowing a fine control of deposition conditions: targets and substrate selection, Argon/Oxygen pressure and flux, time and temperature deposition, plasma intensity and focusing and in situ annealing.
- ✓ Optimization of the RF Sputtering system deposition conditions is still under development, based on the results attain by the first series of thin films structural, chemical and physical properties.
- ✓ Further work will be developed for the management of the deposition rates according to the target / substrate distance, Argon partial pressure and RF power.

ISSCN'07 – Poster # 218

Thin Film Deposition RF Sputtering System at the Physics Department, Aveiro University

Thanks for Your Attention!

ISSCN'07 – Poster # 218

Abstract: Fábio Figueiras, Armando Lourenço, Sérgio Pereira, Mário Reis, Vitor Amaral, Joaquim Vieira, Pedro Tavares, “*RF Sputtering thin film deposition system at the Physics Department, Aveiro University*”, IV CICECO Meeting (2007)

RF Sputtering thin film deposition system at Physics Department, Aveiro University

Fábio Figueiras¹, Armando Lourenço¹, Sérgio Pereira¹, Mário Reis¹, Vitor Amaral¹, Joaquim Vieira¹, Pedro Tavares²

(1) University of Aveiro, Physics Department, CICECO, 3810-193 Aveiro, Portugal

(2) University of Trás-os-Montes e Alto Douro, Centro de Química, 5001-801 Vila Real

E-mail: ffigueiras@cv.ua.pt, alourenco@fis.ua.pt

Since March 2006 the RF Sputtering [1] system of the Physics Department at Aveiro University became operational. This custom made RF Sputtering system consists on a spherical UHV chamber, 3 magnetron guns in a confocal configuration operating at 13.56 MHz RF up to 300 Watt. The substrate heater is able to operate up to 950 C in a Oxygen atmosphere; mounted on-axis, it can also adopt off-axis geometry if required. Full pressure control of Oxygen and Argon can be obtained from 10^{-5} mbar up to 1 atm; there is also provision for additional gas entrances and mass flow controllers, 0.5 sccm minimum flux.

Characterizations of the first thin films of $\text{La}_{0.7}\text{Sr}_{0.3}\text{MnO}_3$ deposited in different substrates are made by several complementary techniques [2], like RXD [3], EDS-SEM, RBS, VSM, and Raman spectroscopy.

Based on the results attain by this first series of thin films structural, chemical and physical properties, further optimization of the RF Sputtering system deposition conditions is still under development.

Future work will be developed in several different targets, for the management of the deposition rates according to the target/substrate distance, Argon partial pressure and RF power.

References




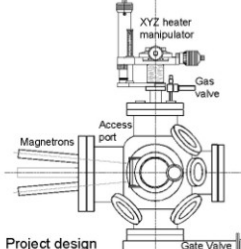
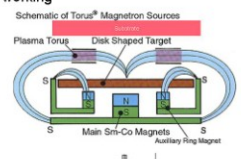

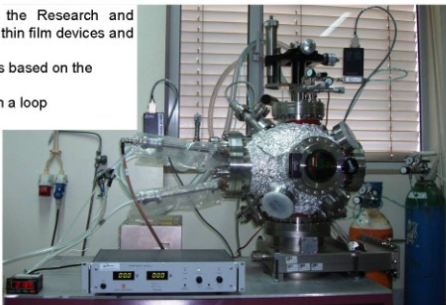
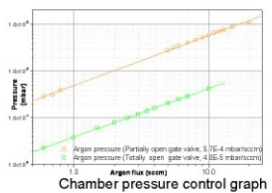
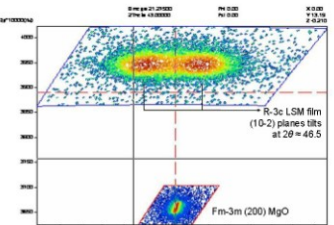
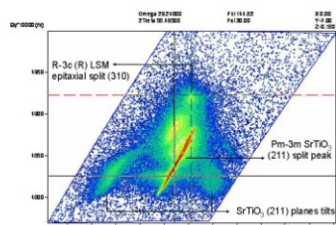

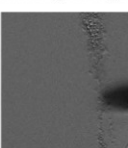
- [1] H.S. Butler and G.S. Kino, *Phys. Fluids* (1963) no.6, 1346, "Plasma Sheath Formation by Radio-Frequency Fields"
- [2] Fábio G.N. Figueiras, PhMs Thesis, Universidade de Aveiro (2004), “Composição, estrutura e propriedades de manganites cerâmicas: Efeito da substituição de Lantânio por Cálcio e lacunas”
- [3] D.K. Bowen and B.K. Tanner, *High Resolution X-ray Diffractometry and Topogtaphy*, (2001)

Acknowledgments

Project: POCTI/CTM/35462/2000

FCT Scholarship : SFRH/BD/25011/2005

Poster: Fábio Figueiras, Armando Lourenço, Sérgio Pereira, Mário Reis, Vitor Amaral, Joaquim Vieira, Pedro Tavares, "RF Sputtering thin film deposition system at the Physics Department, Aveiro University", IV CICECO Meeting (2007)

AUTHORS	<div></div> <div>Fábio Figueiras ^{1,2, (e)} Armando Lourenço ^{1,2} Sérgio Pereira ^{1,2}</div> <div></div> <div>Vitor Amaral ^{1,2} Joaquim Vieira ^{1,3} Pedro Tavares ⁴</div> <div></div>	AUTHORS
TITLE	Thin Film Deposition RF Sputtering system at the Physics Department, Aveiro University	TITLE
INTRODUCTION	<p>RF Sputtering is an essential tool in the Research and Development of new functional materials, thin film devices and granular or multilayer nanostructures. The physical principle behind this device is based on the Radio frequency electrical field generated. The magnetic field entraps the electrons in a loop working</p> <div></div> <div></div> <div><p>The RF Sputtering system now operational at the Physics Department at Aveiro University has been optimized for the deposition of thin films oxides and magnetic materials in clean conditions and <i>in situ</i> annealing for epitaxial growth. This custom made RF Sputtering system consists on a spherical UHV chamber, 3 magnetron guns in a confocal configuration operating at 13.56 MHz RF up to 300 Watt (two with special high field magnets). The substrate heater is able to operate up to 950 C in a Oxygen atmosphere; mounted on-axis, it can also adopt off-axis geometry if required. Full pressure control of Oxygen and Argon can be obtained from 10⁻⁵ mbar up to 1 atm; there is also provision for additional gas entrances and mass flow controllers, 0.5 sccm minimum flux.</p></div>	SYSTEM
RESULTS	<p style="text-align: center;">Characterization of La_{0.7}Sr_{0.3}MnO₃ (LSM) thin films includes: HR-XRD, EDS-SEM, RBS, VSM, Raman spectroscopy</p> <div></div> <div><p>EDS-SEM measures show no contaminants and highly uniform chemical composition over all the thin films surface. Thin films grown in SrTiO₃ substrates have almost no surface defects, while on MgO exhibit higher rugosity and defects.</p></div> <div><p>LSM @ MgO LSM @ SrTiO₃ 25 KV SEM images of 50 μm film surface.</p></div> <p>Rhombohedral R-3c LSM thin film grows with {211} direction over {110} SrTiO₃ substrate. HR-XRD asymmetric reciprocal space map at $\phi=30^\circ$ confirms coherent growth of film in {310} planes relatively to the substrate' (211).</p> <p>HR-XRD symmetric reciprocal space map of LSM (R-3c) thin film shows tilted growth of {10-2} planes relatively to the {100} direction of MgO substrate.</p>	RESULTS
CONCLUSIONS	<p>Preliminary results confirm the versatility of the RF sputtering system, allowing a fine control of deposition conditions: targets and substrate selection, Argon/Oxygen pressure and flux, time and temperature deposition, plasma intensity and focusing and <i>in situ</i> annealing.</p> <p>Optimization of the RF Sputtering system deposition conditions is still under development, based on the results attain by the first series of thin films structural, chemical and physical properties.</p> <p>Further work will be developed for the management of the deposition rates according to the target / substrate distance, Argon partial pressure and RF power.</p>	CONCLUSIONS
ACKNOWLEDGMENTS	<p>Project: The unit has been mainly funded by project POCTI/CTM/35462/2000 and CICECO.</p> <p>1: CICECO – L.C.A., Campus Universitário de Santiago, 3810 – 193 Aveiro, Portugal</p> <p>2: Physics Department of Aveiro University – Campus Universitário de Santiago, 3810 – 193 Aveiro, Portugal</p> <p>3: Ceramics and Glass Engineering Department of Aveiro University– Campus Universitário de Santiago, 3810 – 193 Aveiro, Portugal</p> <p>4: Chemical Centre of Trás-os-Montes e Alto-Douro University - Apartado 1013, 5001-801 Vila Real, Portugal</p> <p>(e): ffigueiras@cv.ua.pt ; FCT Scholarship : SFRH/BD/25011/2005 and POCTI/CTM/40063/2001</p>	ACKNOWLEDGMENTS

Abstract: F. Figueiras, J. Agostinho Moreira, M. Kostadinova, “*Characterization studies of doped YMnO₃ hexagonal manganites*”, ‘DyProSo XXXI’, 31st International Symposium on the Dynamic Properties of Solids September 25th – 29th, 2007, University of Porto, Porto, Portugal.

Characterization studies of doped YMnO₃ hexagonal manganites

F. Figueiras^{1,2,a}, J. Agostinho Moreira³, M. Kostadinova⁴

¹ CICECO, Universidade de Aveiro, 3810-193 Aveiro, Portugal

² Departamento de Física, Universidade de Aveiro, 3810-193 Aveiro, Portugal

³ Dep. De Física, Fac. De Ciências da Universidade do Porto, 5001-911 Porto, Portugal

⁴ Silicates Technology Department, UTQM Sofia, Bulgária.

^a Contact author: ffigueiras@ua.pt

Keywords: YMnO₃, Hexagonal Manganites, doping, structural characterization, Raman

Abstract.

The structural characterization of doped hexagonal manganites is an essential part of the research and development of new functional magnetoelectric materials, with potential applications in sensors, memory storing and reading, as well data processing. The identical chemical formula of the manganites, AMnO₃, can present different crystalline structures, corresponding to different properties: hexagonal (P6₃/mmc), with A = Y, Ho to Lu, are mainly ferroelectric, while Orthorhombic (Pmna) or Rhombohedral (R-3c) with A = La to Dy, Ba, Sr, Ca,... are ferro or antiferromagnetic. A reference YMnO₃ hexagonal ceramic powder and two other derived samples, doped with 14 % Ca and with 16% Mn excess, were produced by the co-precipitation method and treated in air at 900°C for more than 48 h. Our aim is to partially form Mn⁴⁺ and point defects to promote locally modify structural arrangements with potential intrinsic magnetoelectric properties. Samples were analyzed by XRD and Raman spectroscopy. Besides the expected structural hexagonal symmetry and some secondary phase formation like Y₂O₃, we report the effects of the chemical doping.

References:

[1] M.N. Iliev, et.al., Phys. Rev. B 67, 212301 (2003)

[2] P.A. Salvador, et.al., Chem. Mater. 1998, 10, 2592

Acknowledgments:

PhD Research work done under FCT scholarship SFRH/BD/25011/2005

Poster: F. Figueiras, J. Agostinho Moreira, M. Kostadinova, “Characterization studies of doped YMnO₃ hexagonal manganites”, ‘DyProSo XXXI’, 31st International Symposium on the Dynamic Properties of Solids September 25th – 29th, 2007, University of Porto, Porto, Portugal.

Study of Structural and Dynamic Effects of Ca and Mn Doping in Hexagonal YMnO₃

Authors:

F.Figueiras^{1, (e)}, J. A. Moreira², P.B. Tavares³, M. Kostadinova⁴

Introduction

➤ Following previous studies over the effect of Ca and Mn excess doping in Orthorhombic and Rhombohedral CMR Manganites [1], we now turn our attention to Hexagonal Manganites.

➤ YMnO₃ and other Hexagonal Manganites like, (Ho,...,Lu)MnO₃, present dielectric properties with potential Magneto-electric effects for fundamental studies and applications [2].

Experimental

➤ Nano powders of Y_{1-x}A_xMn_{1+2x/3}O_{3+δ} with x=0 or x=0.14 and A= Ca or Vacancies, were synthesized using pH controlled reverse-solution coprecipitation method [3]

➤ Annealing in air at 800°C for 48 for enhancing Oxygen incorporation in the ceramic compound [1]

➤ The structure and dynamics of the processed samples were studied by using EDS-SEM and XRD and Raman spectroscopy.

Results

➤ EDS-SEM results do not reveal significant deviations of the correspondent composition to nominal synthesis process. Particles size is typically between 10 to 20 nm.

➤ The crystal structure of the samples at room temperature is described by the space group P6₃cm.

➤ Contamination with Y₂O₃ was detected; partial indexation to the S.G.: I₂₁₃ (199) was found.

➤ Mn excess or Ca doping do not show significant effect in the cell parameters.

➤ Due to the presence of unreacted Y₂O₃ in all samples, it is expected some contribution to A site vacancies in the Hexagonal Manganite phases.

➤ Raman spectroscopy from 10 to 300 K shows for the doped samples a smaller anomaly in the temperature dependence of the phonons near the transition temperature T_N of YMnO₃ [4].

➤ Ca doping is expected to generate Mn⁴⁺ ions and eventual interfere in the antiferromagnetic arrangement of the conventional YMnO₃ Mn³⁺ ions.

Further work:

➤ Additional Magnetic and Dielectric characterization of the sample will enable to confirm the presence and coupling contribution of Mn⁴⁺.

References:

- [1] F. Figueiras, J.M.M.M. Vol. 272-276 Part 3 (2004) 1753, Structural and magnetic study of self-doped La_{1-x}Ca_xO₃MnO₃
 - [2] Bas B. van Aken, cond-mat/0106298 (2001) Structural view of hexagonal non-perovskite AMnO₃
 - [3] A. Staneva, NanoSc.& NanoTech. no.3 (2004), Preparation of nanosized La_{1-x}Sr_xMnO₃ powders
 - [4] M.N. Iliev, Phys Rev. B 56, No.5, 1997, Raman and IR phonons in Hex. YMnO₃
- 1: Physics Department of Aveiro University**
Campus Universitário de Santiago, 3810 – 193 Aveiro, Portugal
2: IFIMUP - Rua do Campo Alegre, 4169 - 007 Porto, Portugal
3: Chemical Centre of Trás-os-Montes e Alto-Douro University
Apartado 1013, 5001-801 Vila Real, Portugal
4: University of Chemical Technology and Metallurgy -
8St. Kliment Ohridski blvd. 1756 Sofia, Bulgaria
(e): ffigueiras@ua.pt ; FCT Scholarship : SFRH/BD/25011/2005

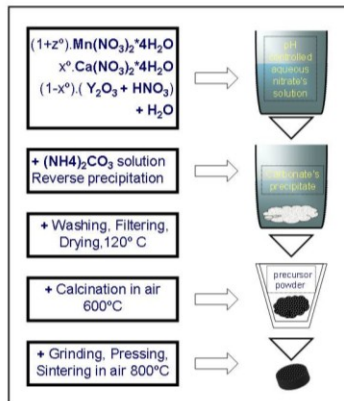


Fig. 1: Coprecipitation synthesis process diagram



Fig. 2: YMnO₃ Hexagonal P6₃cm representation

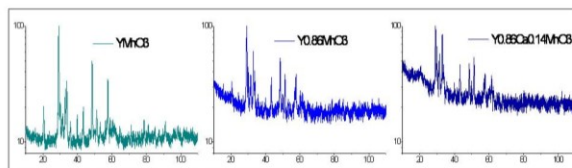


Fig. 3: XRD diffractograms of samples

Nominal Sample:	YMnO ₃	Y _{0.88} MnO ₃	Y _{0.88} Ca _{0.14} MnO ₃
SG	P6 ₃ cm (185)	P6 ₃ cm (185)	P6 ₃ cm (185)
a	6.1769	6.1592	6.1567
b	6.1769	6.1592	6.1567
c	11.4968	11.3871	11.3829
Y ₂ O ₃ traces	Yes	Yes	Yes

Table 1: XRD lattice parameters of samples

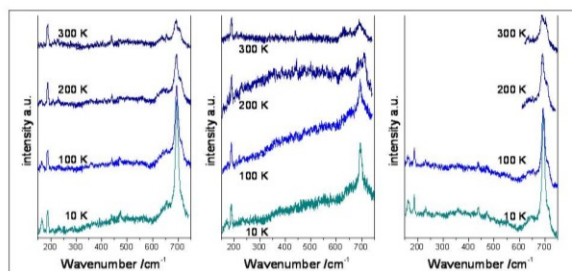


Fig. 4: Partial Raman spectroscopy results of samples

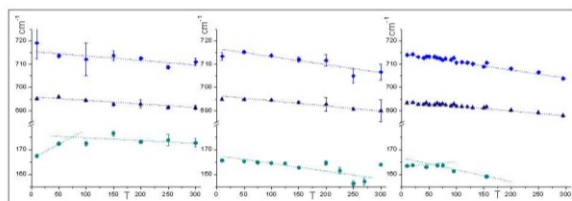


Fig. 5: Main Raman modes of samples

Abstract: F. Figueiras, N. P. Vyshatko, H. Romain, C. Soyer, D. Remiens, V. V. Shvartsman, P. Borisov, W. Kleemann, V. S. Amaral, A. L. Kholkin, “*Thin film devices of layered Ni₂MnGa and PZT prepared by RF sputtering*”, FAMEnoe Summer School on Inorganic Functional Materials, 6th-11th July 2008, São Pedro do Sul, Aveiro - Portugal.

THIN FILM DEPOSITION OF NI-MN-GA ALLOY ONTO SI AND PZT BUFFER SUBSTRATES BY RF MAGNETRON SPUTTERING AT ROOM TEMPERATURE

F. Figueiras¹, N.P.Vyshatko², H. Romain³, C. Soyer³, D. Remiens³, V. V. Shvartsman⁴, P. Borisov⁴, W. Kleemann⁴, V. S. Amaral¹, A.L.Kholkin²

¹Department of Physics, & CICECO, University of Aveiro, Aveiro, Portugal

²Department of Ceramics and Glass Engineering & CICECO, University of Aveiro, Aveiro, Portugal

³IEMN-DOA-MIMM, CNRS, Villeneuve d'Ascq, France

⁴Department of Physics, University of Duisburg-Essen, Duisburg, Germany

RF Sputtering deposition of Ni-Mn-Ga ferromagnetic shape memory films alloy onto plain Si substrates and Si with LNO/PZT ferroelectric buffer was performed. The controlling parameters RF power ratio and Argon pressure in the chamber were varied to establish the most favourable parameters to perform a successful film deposition at low temperature conditions (near room temperature).

Extensive characterization by SEM, EDS, AFM and XRD of the NMG films show good surface quality and crystallization of the film in high textured (110)_c martensitic tetragonal phase. Compositions of the films were varied according to the relative position of the substrate to deposition axis. SQUID and magneto-optic measurements showed a typical hysteresis, anisotropy and a spin glass like behaviour with low magnetization in comparison with a bulk NMG alloy.

This low temperature fabrication is very promising in order to minimize oxygen diffusion effects between NMG and PZT interfacing surface, to improve magnetoelectric applications [1] [2]: ferromagnetism and shape memory effect characteristic of the martensitic phase transition coupling to a ferroelectric layer. The work was performed within EC-funded project “Multiceral” (NMP3-CT-2006-032616).

[1] H. Zeng et al., Science 303, 661 (2004).

[2] W. Eerenstein et al., Nature Materials 6, 348 (2007).

Poster: F. Figueiras, N. P. Vyshatko, H. Romain, C. Soyer, D. Remiens, V. V. Shvartsman, P. Borisov, W. Kleemann, V. S. Amaral, A. L. Kholkin, "Thin film devices of layered Ni₂MnGa and PZT prepared by RF sputtering", FAMEnoe Summer School on Inorganic Functional Materials, 6th-11th July 2008, São Pedro do Sul, Aveiro, Portugal

Ni-Mn-Ga Alloy Thin Film Deposition by RF Sputtering at Room Temperature onto Si substrates and PZT buffers

F. Figueiras^{1,3}, N.P.Vyshatko^{2,3}, H. Romain⁴, C. Soyer⁴, D. Remiens⁴, V. V. Shvartsman⁵, P. Borisov⁵, W. Kleemann⁵, V. S. Amaral^{1,3}, A.L.Kholkin^{2,3}

INTRODUCTION

Multiferroics have significant potential in scientific research and technological applications such as sensors, memory devices, highly sensitive transducers and microactuators that can be driven by both electric and magnetic fields. The magnetoelectric effect can be achieved by interacting ferromagnetism and ferroelectric properties in materials, either in intrinsic, composites, thin films or multilayer form. A suitable combination is to have Ni-Mn-Ga ferromagnetic alloy, with shape memory effect coupled to high piezoelectric response materials, such as PZT.

OBJECTIVES

This work investigates the conditions and properties of RF Sputtered thin films of Ni-Mn-Ga deposited on PZT buffer layers/ Si substrates at room temperature.

Low temperature fabrication is relevant in order to minimize oxygen diffusion effects between the metallic alloy NMG and the PZT interface.

EXPERIMENTAL

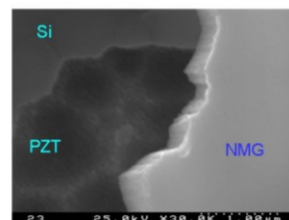
The RF power ratio and Argon pressure in the chamber were varied to establish the most favorable parameters to achieve typical Ni₂MnGa FM phase. The used deposition temperature were in the range from 10 to 60°C.

Extensive characterization of the Ni-Mn-Ga films was performed by SEM, EDS, AFM, XRD, magnetic (SQUID) and magneto-optic measurements.

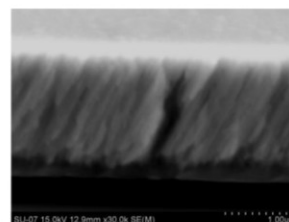
RESULTS

The composition of the films could be controlled by magnetron power ratio, both in single target and in simultaneous co-sputtering of Ni, GaNi, Mn targets. The relative position of the substrate to deposition axis also has an significant effect in the film composition. This allows the tuning of the magnetic and structural transitions of Ni-Mn-Ga. The NMG films show good surface quality and crystallization presenting high textured (110)c martensitic tetragonal phase.

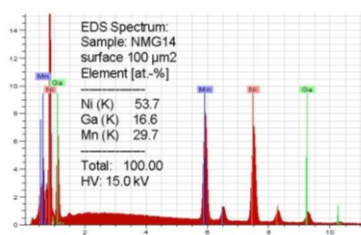
Magnetic measurements showed a typical hysteresis, anisotropy and a spin glass like behavior with low magnetization in comparison with a bulk NMG alloy.



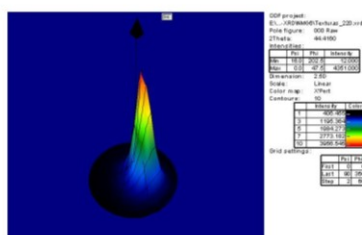
SEM image of sample showing Si substrate, PZT buffer and Ni-Mn-Ga film.



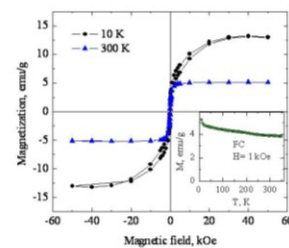
SEM Scanning of fracture showing columnar tilted growth of Ni-Mn-Ga film



EDS-SEM Scanning of Ni-Mn-Ga film sample confirms suitable composition for T_C and T_M tuning.



HR-XRD confirms tilted growth of Ni-Mn-Ga film on PZT.



SQUID measurement of Ni-Mn-Ga film

CONCLUSIONS

Successful Ni-Mn-Ga ferromagnetic shape memory alloy thin films deposition by RF Sputtering onto plain Si substrates and Si with LNO/PZT ferroelectric buffer was performed at near room temperature conditions. This low temperature fabrication is very promising, allowing partial control of the functional layers properties, seeking for a high electromagnetoelastic coupling.

ACKNOWLEDGEMENTS

The work was performed within EC-funded project "Multiceral" (NMP3-CT-2006-032616), and FCT grant (SFRH/BD/25011/2005)



¹Department of Physics, University of Aveiro, Portugal

²Department of Ceramics and Glass Engineering, University of Aveiro, Portugal

³CICECO, University of Aveiro, Portugal

⁴IEMN-DOA-MIMM, CNRS, Villeneuve d'Ascq, France

⁵Department of Physics, University of Duisburg-Essen, Germany



Abstract: F. Figueiras, N. P. Vyshatko, H. Romain, C. Soyer, D. Remiens, V. V. Shvartsman, P. Borisov, W. Kleemann, V. S. Amaral, A. L. Kholkin, “*Study of Ni-Mn-Ga Phase Formation by Low Temperature RF Sputtering Film Deposition onto Si Substrates and LNO/PZT Buffer*”, JEMS’08, Joint European Magnetic Symposia, Sept. 14-19, 2008, Dublin – Ireland

Thin Film Deposition of Ni-Mn-Ga Alloy onto Si and PZT buffer substrates by RF Magnetron Sputtering at Room Temperature

F. Figueiras¹, N.P.Vyshatko², H. Romain³, C. Soyer³, D. Remiens³, V. V. Shvartsman⁴, P. Borisov⁴, W. Kleemann⁴, V. S. Amaral¹, A.L.Kholkin²

¹Department of Physics, & CICECO, University of Aveiro, Aveiro, Portugal

²Department of Ceramics and Glass Engineering & CICECO, University of Aveiro, Aveiro, Portugal

³IEMN-DOA-MIMM, CNRS, Villeneuve d’Ascq, France

⁴Department of Physics, University of Duisburg-Essen, Duisburg, Germany

Abstract

The deposition of RF Sputtering film of Ni-Mn-Ga ferromagnetic shape memory alloy onto plain Si substrates and Si with LNO/PZT ferroelectric buffer was performed. The controlling parameters RF power ratio and Argon pressure in the chamber were varied to establish the most favourable parameters to perform a successful film deposition at low temperature conditions (near room temperature).

Extensive characterization by SEM, EDS, AFM and XRD of the NMG films show good surface quality and crystallization of the film in high textured (110)_c martensitic tetragonal phase. Composition of the films were varied according to the relative position of the substrate to deposition axis. SQUID and magneto-optic measurements showed a typical hysteresis, anisotropy and a spin glass like behaviour with low magnetization in comparison with a bulk NMG alloy. This low temperature fabrication is very promising in order to minimize oxygen diffusion effects between NMG and PZT interfacing surface, to improve magnetoelectric applications [1] [2]: ferromagnetism and shape memory effect characteristic of the martensitic phase transition coupling to a ferroelectric layer.

The work was performed within EC-funded project “Multiceral” (NMP3-CT-2006-032616).

References

- [1] H. Zeng et al., Science 303, 661 (2004).
- [2] W. Eerenstein et al., Nature Materials 6, 348 (2007).

Full Address of Contact Author:

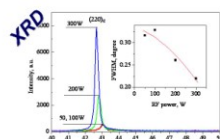
Fábio Gabriel Nazário Figueiras
Departamento de Física & CICECO
Universidade de Aveiro
3810 Aveiro, Portugal
Phone: +351 234 378 110
e-mail: ffigueiras@ua.pt

Proposed Symposium: FM

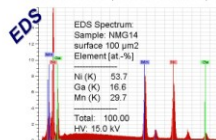
Poster: F. Figueiras, N. P. Vyshatko, H. Romain, C. Soyer, D. Remiens, V. V. Shvartsman, P. Borisov, W. Kleemann, V. S. Amaral, A. L. Kholkin, “Study of Ni-Mn-Ga Phase Formation by Low Temperature RF Sputtering Film Deposition onto Si Substrates and LNO/PZT Buffer”, JEMS’08, Joint European Magnetic Symposia, Sept. 14-19, 2008, Dublin – Ireland

Study of Ni-Mn-Ga Phase Formation by Low Temperature RF Sputtering Film Deposition onto Si Substrates and LNO/PZT Buffer.

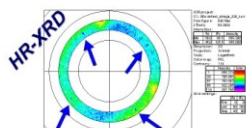
*F. Figueiras^{1,3}, N.P. Vyshatko^{2,3}, E. Rauwel^{1,3},
C. Soyer⁴, D. Remiens⁴,
V. V. Shvartsman⁵, P. Borisov⁵, W. Kleemann⁵,
V. S. Amaral^{1,3}, A.L. Kholkin^{2,3}



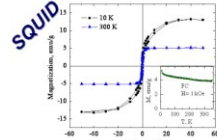
▲ XRD peaks of films deposited at 10mTorr Ar pressure and RF power in the range 50-300W. (Insert: Width of Bragg peak as a function of RF power at the same Ar pressure).



▲ EDS-SEM Scanning of Ni-Mn-Ga film sample confirms suitable composition for T_c and T_m tuning.



▲ HR-XRD confirms tilted growth of Ni-Mn-Ga film on PZT. Pole figure recorded around the 220 (88.38°) confirming tetragonal symmetry of the 112-oriented film on the substrate.



▲ SQUID Hysteresis loop of Ni-Mn-Ga film on PZT/LNO/Si substrate. (Insert: M-T dependence at 0.1 T)

High Textured Film

Composition of the films can be controlled by magnetron power ratio, both in single target as in simultaneous co-sputtering of Ni, GaNi, Mn targets, also the relative position of the substrate to deposition axis has a partial effect in the film composition.

The Ni-Mn-Ga films show good surface quality and crystallization of the film in high textured (110)₂ martensitic tetragonal phase.

Magnetic measurements showed a typical hysteresis, anisotropy, with low magnetization in comparison with a bulk Ni-Mn-Ga alloy.

Promising Method

Successful Ni-Mn-Ga ferromagnetic shape memory alloy thin films deposition by RF Sputtering onto plain Si substrates and Si with LNO/PZT ferroelectric buffer was performed at near room temperature conditions.

This low temperature fabrication is very promising in order to minimize oxygen diffusion effects between the metallic alloy Ni-Mn-Ga and the PZT ceramic interface, allowing partial control of the functional layers properties while enhancing electromagnetoelectric coupling.

MULTIFERROICS

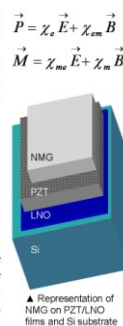
The Magneto-electric effect can be achieved by interacting ferromagnetism and ferroelectric properties in materials, either in intrinsic phase, composites, thin films or multilayer form. These Multiferroics materials, have significant potential in scientific research and technological applications such as sensors, memory devices, highly sensitive transducers and microactuators that can be driven by both electric and magnetic fields.

Ni₂MnGa Thin Film on PZT

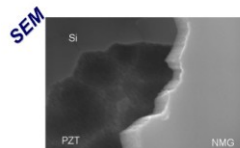
This work researches the combination of RF Sputtered thin films of Ni-Mn-Ga ferromagnetic alloy, with shape memory effect, and high piezoelectric response PZT ceramic.

RF Sputtering

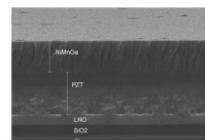
The RF power ratio and Argon pressure in the chamber were varied to establish the most favorable parameters to achieve typical Ni₂MnGa FM phase. Extensive characterization of the Ni-Mn-Ga films was performed by SEM, EDS, AFM, XRD, HR-XRD, SQUID and magneto-optic measurements.



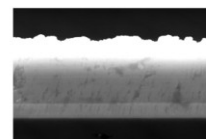
▲ Representation of Ni-Mn-Ga on PZT/LNO films and Si substrate



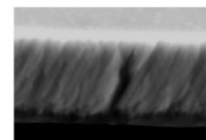
▲ SEM image of sample showing Si substrate, PZT buffer and Ni-Mn-Ga film.



▲ cross section SEM Scanning of Ni-Mn-Ga film on PZT/LNO/Si, shows layers and interfaces



▲ SEM Scanning of Ni-Mn-Ga film on Si, cross section shows an intermediate layer growth.



▲ SEM Scanning of fracture showing textured columnar tilted growth of Ni-Mn-Ga film in PZT.

FURTHER WORK

- Improving the RF power ratio, Argon pressure and temperature control in the chamber to achieve better Ni₂MnGa FM phase and achieve the electromagnetoelectric coupling with the PZT active layer.
- Implementing Magneto-dielectric characterization of the Ni-Mn-Ga/PZT composite films
- Development of Prototypes

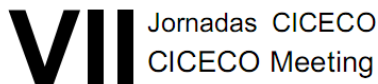
ACKNOWLEDGEMENTS

The work was performed within :

- EC-funded project “Multiceral” (NMP3-CT-2006-032616),
- Marie Curie EIF (MEIF-CT2006-041632),
- FCT grant (SFRH/BD/25011/2005),
- project FLAD/NSF 600-06/2006.

¹ Physics' Department, University of Aveiro, Portugal
² Ceramics' and Glass Engineering Department, University of Aveiro, Portugal
³ CICECO, Villeneuve d'Ascq, France
⁴ IEMN-DOA-MIMM, CNRS, University of Duisburg-Essen, Germany
⁵ Physics' Department, ffigueiras@ua.pt
 * Author's contact: <http://multiceral.web.ua.pt/index.htm>
 * References and Project URL:

Abstract: F. Figueiras, V. S. Amaral, A.L. Kholkin, S. V. Kalinin, “SPM study of charge ordered multiferroic manganites”, VII CICECO Meeting, January 28-29th, 2010, Department of Physics, University of Aveiro – Portugal.



JANUARY 28-29th, 2010

SPM study of charge ordered multiferroic manganites

***F. Figueiras^{1,3}, V. S. Amaral^{1,3}, A.L. Kholkin^{2,3}, S. V. Kalinin⁴,**

¹ Physics' Department, University of Aveiro, Portugal

² Ceramics' and Glass Eng. Department, University of Aveiro, Portugal

³ CICECO, University of Aveiro, Portugal

⁴ CNMS ORNL, Oak Ridge, TN, USA

The manganites present a wide spectra of structural and functional phases, Besides doping and thermal manipulation. Localized Magnetic/Electrical induced phase transitions have a potential use for materials modification. Under certain circumstances Charge Order mechanisms can induce Ferroelectricity in magnetic material [1].

A set of mono and polycrystalline manganites samples of $\text{La}_{1-x}\text{Sr}_x\text{MnO}_3$ ($x=0.11, 0.40$) [2] and $\text{Pr}_{1-x}\text{Ca}_x\text{MnO}_3$ ($x=0.11, 0.35, 0.40, 0.85$) [3] was selected for their potential CO multiferroic properties Although the finite conductivity of these material renders difficult to observe directly its FE response, preliminary results demonstrated a clear piezocontrast at room temperature, which may be associated with the presence of nanoscopic CO regions (above the CO transition). We believe that the bias-induced ferroelectricity studied via PFM may also be an important for creating artificial multiferroic materials and memory cells.

With collaboration of CNMS at ORNL, TN USA, experimental AFM scans were performed on samples using *Asylum MFP-3D SPM* system. Selecting a $5 \times 5 \mu\text{m}$ region with regular topology, perform a lithographic frame based on $1 \mu\text{m}$ length vertical lines $0.5 \mu\text{m}$ apart at different dc bias voltages ($\pm 5, \pm 10, \pm 15, \dots$); further PFM scan enable to trace the sample surface reaction to the electrical stimulus. A representative area within the stimulated region is selected to performing Band Excitation (BEPS) [4] grid measurements in a $\sim 100 \text{ kHz}$ window of the respective resonance frequency and maximum applied ac voltage up to 20 V.

Some samples show local piezo-response traceable to the stimulated regions by the DC lithographic tests; the BEPS maps confirm partial ferroelectric behavior of these regions with configuration of nucleation sites and energy dissipation in polarization switching. No sample surface electrochemical reaction to the AC voltage after the BEPS process was detected.


[1] Ch. Joss et al, PNAS V. 104, no. 34 (Aug 2007)

[2] R. F. Mamian et al, APL 94, 222901 (2009)

[3] A.M.L. Lopes et al, PRL 100, 155702 (2008)

[4] S.V. Kalilin et al, Mat. Today V. 11, no. 11 (Nov. 2008)

Poster: F. Figueiras, V. S. Amaral, A.L. Kholkin, S. V. Kalinin, “SPM study of charge ordered multiferroic manganites”, VII CICECO Meeting, January 28-29th, 2010, Department of Physics, University of Aveiro – Portugal.



Scanning Probe Microscopy study of charge ordered multiferroic manganites

F. Figueiras^{1,3}, V. S. Amaral^{1,3}, A. L. Kholkin^{2,3}, S. V. Kalinin⁴

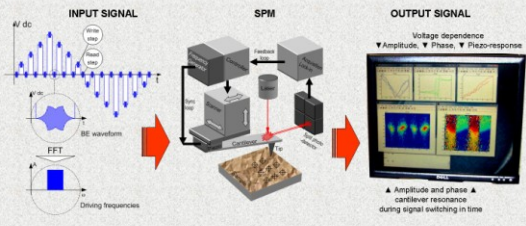
¹ Physics' Department,
² Ceramics' and Glass Eng. Department,
³ CICECO,
⁴ CNMS ORNL,
Author's contact:

University of Aveiro, Portugal
University of Aveiro, Portugal
University of Aveiro, Portugal
Oak Ridge, TN, USA
ffigueiras@ua.pt

BEPS measurements:


- Conventional Piezo-Response Force Microscopy has single frequency and phase-lock limitations.
- Band Excitation Piezo-Response Spectroscopy mode collects broad response-frequency at each point.
- BEPS mode requires a modulated waveform, high-speed data acquisition and FFT signal processing.
- The resulting data array for each surface point has terms of Amplitude-Frequency-Voltage response.
- Data analysis yields Resonance, Dissipation and Amplitude dependence at each mapped point.

Matt. Today 11, 11 (2008)

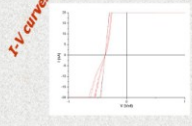


Results: $\text{Pr}_{0.60}\text{Ca}_{0.40}\text{MnO}_3$ poly crystalline sample


Topography



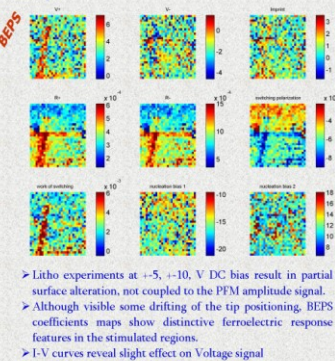
Amplitude



I-V curves



BEPS



- Litho experiments at +5, +10, V DC bias result in partial surface alteration, not coupled to the PFM amplitude signal.
- Although visible some drifting of the tip positioning, BEPS coefficients maps show distinctive ferroelectric response features in the stimulated regions.
- I-V curves reveal slight effect on Voltage signal

Multiferroic Manganites:

- Manganites present a wide spectra of structural and functional phases, both magnetic and electric. Besides doping and thermal manipulation, localized Magnetic/Electrical induced phase transitions associated with structural/doping modifications have a potential use for materials properties tailoring. This work focuses on inducing ferroelectric behavior.
- In order to understand the mechanisms and properties of these induced phases, SPM, BEPS and I-V experiments were performed in manganites possessing a combined site- and bond-centered charge ordering, particularly susceptible to C.O. phase transitions under localized bias electrical disturbance and potentially present multiferroic phenomena.

PRL 100, 155702 (2008)
APL 94, 222901 (2009)

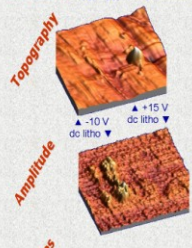
▲ The rich phase diagram of $\text{Pr}_{1-x}\text{Ca}_x\text{MnO}_3$ has regions with potential multiferroicity.

Experimental:

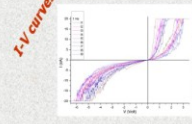
- The experiments were performed in mono and poly crystalline bulk manganites presenting Charge Order phase and also non-C.O. control samples: $\text{Pr}_{1-x}\text{Ca}_x\text{MnO}_3$ ($x=0.00; 0.35; 0.40; 0.85$), $\text{La}_{1-x}\text{Sr}_x\text{MnO}_3$ ($x=0.11; 0.40$), $\text{La}_{1-x}\text{Ca}_x\text{MnO}_3$ ($x=0.05; 0.33$)
- Experiments use a *Asylum MFP-3D/SPM* system.
- From a PFM survey a $5 \times 5 \mu\text{m}$ region with regular topology is selected;
- Perform $1 \mu\text{m}$ long lithograph paths at different DC bias voltages ($\pm 5, \pm 10, \pm 15, \dots$);
- Further PFM scan enable to trace the sample surface reaction to the electrical stimulus.
- Perform BEPS scan in a representative area.
- Current-Voltage curves are measured with *Asylum ORCA* sample mount and cantilever holder.
- Data acquisition and processing comprise *Igor Pro*, *Nanotec WSxM* and *MathLab* software

Results: $\text{La}_{0.90}\text{Sr}_{0.10}\text{MnO}_3$ mono crystalline sample

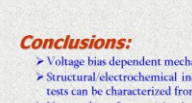
Topography



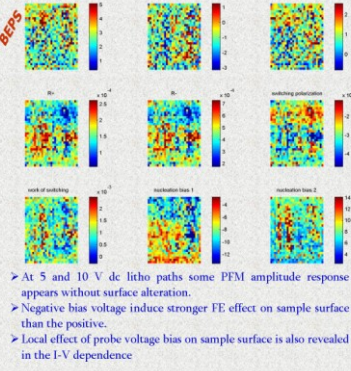
Amplitude



I-V curves



BEPS



- At 5 and 10 V dc litho paths some PFM amplitude response appears without surface alteration.
- Negative bias voltage induce stronger FE effect on sample surface than the positive.
- Local effect of probe voltage bias on sample surface is also revealed in the I-V dependence

Conclusions:

- Voltage bias dependent mechanisms can induce local temporary polarization dynamics on samples.
- Structural/electrochemical induced changes on samples surface resulting from lithographic dc bias tests can be characterized from the piezo/ferroelectric parameters shifts obtained by BEPS scans.
- No sample surface reaction is observed after BEPS procedure even at high a.c. voltage ($\sim 20 \text{ V}$)
- BEPS enables to probe ferroelectric switching even in samples with limited piezo-response.
- Localized holes or electrons concentration has different effects on structure and transport properties.
- Lithographic induced Structural Electro-chemical phase transitions can be an alternative for manufacturing permanent or temporary nano circuits chips from a single material base.

Further Work:

- BEPS measurement system is still under development stage.
- To investigate the time dependence of charge injection/dissipation of the induced FE phases.
- SPM experiments planned to be performed across C.O. transition temperature of samples using a low temperature UHV SPM system at CNMS-ORNL.

Acknowledgments:

The Author wish to thank the technical support of: Senli Guo, Petro Maksymovych, Katayani Seal, Stephan Jesse, Nina Balke, Maxim Nikiforov and CNMS-ORNL staff. Work performed within:

- CNMS Proposal: CNMS2009-083
- EC-funded project "Multicore" (NMP3-CT-2006-032616).
- FCT grant (SFRH/BD/25011/2005).
- Project FLAD/NSF 600-06/2006.

Abstract: F. Figueiras, I. K. Bdikin, V. S. Amaral, A. L. Kholkin, S. V. Kalinin, “SPM study of charge ordered multiferroic manganites”, XVIth Workshop on Magnetism and Intermetallics, 4-6 March 2010, Science Faculty of University of Porto - Portugal.

XVIth Workshop on Magnetism and Intermetallics

SPM study of charge ordered multiferroic manganites

F. Figueiras^{1,2,*}, I. K. Bdikin^{2,3,4}, V. S. Amaral^{1,3}, A. L. Kholkin^{2,3}, S. V. Kalinin⁵

¹ Physics' Department, University of Aveiro, Portugal

² CICECO, University of Aveiro, Portugal

³ Ceramics' & Glass Eng. Department, University of Aveiro, Portugal

⁴ Department of Mechanical Eng., University of Aveiro, Portugal

⁵ CNMS, ORNL, Oak Ridge, TN, USA

*ffigueiras@ua.pt

The manganites present a wide spectra of structural and functional phases, Besides doping and thermal manipulation. Localized Magnetic/Electrical induced phase transitions have a potential use for materials modification. Under certain circumstances Charge Order mechanisms can induce Ferroelectricity in magnetic material [1].

A set of mono and polycrystalline manganites samples of $\text{La}_{1-x}\text{Sr}_x\text{MnO}_3$ ($x=0.11, 0.40$) [2] and $\text{Pr}_{1-x}\text{Ca}_x\text{MnO}_3$ ($x=0.11, 0.35, 0.40, 0.85$) [3] was selected for their potential CO multiferroic properties Although the finite conductivity of these material renders difficult to observe directly its FE response, preliminary results demonstrated a clear piezocontrast at room temperature, which may be associated with the presence of nanoscopic CO regions (above the CO transition). We believe that the bias-induced ferroelectricity studied via PFM may also be an important for creating artificial multiferroic materials and memory cells.

With collaboration of CNMS at ORNL, TN USA, experimental AFM scans were performed on samples using Asylum MFP-3D SPM system. Selecting a $5 \times 5 \mu\text{m}$ region with regular topology, perform a lithographic frame based on $1 \mu\text{m}$ length vertical lines $0.5 \mu\text{m}$ apart at different dc bias voltages ($\pm 5, \pm 10, \pm 15, \dots$); further PFM scan enable to trace the sample surface reaction to the electrical stimulus. A representative area within the stimulated region is selected to performing Band Excitation (BEPS) [4] grid measurements in a $\sim 100 \text{ kHz}$ window of the respective resonance frequency and maximum applied ac voltage up to 20 V.

Some samples show local piezo-response traceable to the stimulated regions by the DC lithographic tests; the BEPS maps confirm partial ferroelectric behavior of these regions with configuration of nucleation sites and energy dissipation in polarization switching. No sample surface electrochemical reaction to the AC voltage after the BEPS process was detected.

[1] Ch. Joss et al, PNAS V. 104, no. 34 (Aug 2007)

[2] R. F. Mamian et al, APL 94, 222901 (2009)

[3] A.M.L. Lopes et al, PRL 100, 155702 (2008)

[4] S.V. Kalilin et al, Mat. Today V. 11, no. 11 (Nov. 2008)

Presentation: F. Figueiras, I. K. Bdikin, V. S. Amaral, A. L. Kholkin, S. V. Kalinin, “SPM study of charge ordered multiferroic manganites”, XVIth Workshop on Magnetism and Intermetallics, 4-6 March 2010, Science Faculty of University of Porto - Portugal.

Scanning Probe Microscopy study of Charge Ordered Multiferroic Manganites
F. Figueiras^{1,2,*}, I.K. Bdikin^{2,3,4}, V.S. Amaral^{1,3}, A.L. Kholkin^{2,3}, S.V. Kalinin⁵

¹Physic Department, ²Corrosion & Glass Eng. Department, ³CICECO, ⁴Mechanical Eng. Department, ⁵CNMS ORNL, * ffigueira@ua.pt

University of Aveiro, Portugal
University of Aveiro, Portugal
University of Aveiro, Portugal
University of Aveiro, Portugal
Oak Ridge, TN, USA

Scanning Probe Microscopy:
The underlying principle of the Piezoresponse Force Microscopy (PFM) is the measurement of deformation of the cantilever between the tip and the sample under applied electric field.

Domain imaging, Domain writing, Temperature dynamics and phase transitions, PFM spectroscopy, Spectroscopy Mapping, PFM spectroscopy

Experimental:

- To performed PFM, BEPS scans and I-V test in order to characterize possible FE response of the localized field induced phases.
- The experiments were performed in single- and poly- crystalline bulk manganites presenting Charge Order phase and also non-CO control samples: $\text{Pr}_{0.5}\text{Ca}_{0.5}\text{MnO}_3$ ($x=0.00, 0.25, 0.40, 0.85$), $\text{La}_{0.5}\text{Sr}_{0.5}\text{MnO}_3$ ($x=0.11, 0.40$), $\text{La}_{0.5}\text{Ca}_{0.5}\text{MnO}_3$ ($x=0.05, 0.30$)
- Experiments use a 4-tuple AFM-SPM system.
- From a PFM survey a 5x5 μm region with regular topography is selected.
- Perform a 1 μm long lithography paths at different DC bias voltages ($\pm 5, \pm 10, \pm 15, \dots$).
- Further PFM scan enable to trace the sample surface reaction to the electrical stimulus.
- Perform BEPS scan in a representative area.
- Current-Voltage curves are measured with Asylum ORC sample mount and cantilever holder.
- Data acquisition and processing comprise Igor Pro, Nanoscope IIIa/M and Matlab software.

Conclusions:

- Localized lithographic dc Voltage tests can induce local temporary polarization effects on particular CO Manganite samples.
- PFM and BEPS scans enable to characterize the local induced changes on the samples surface.
- BEPS mapping of piezo-ferroelectric parameters confirm the presence of locally induced ferroelectric cycles and switching in the studied samples.
- No sample surface reaction is observed after BEPS procedure even at high a.c. voltage (± 20 V).
- Asymmetry of positive and negative electric fields either in poling, lithography or bias current point to a process of charge injection that locally change the hole concentration ($\text{Mn}^{3+}/\text{Mn}^{4+}$ ratio and Jahn-Teller ordering) hence transitioning to a metastable structure, corresponding to a novel situation on the phase diagram.
- Lithographic induced Structural/Electro-chemical phase transitions can be an alternative technological process for manufacturing permanent or temporary nano circuits chips from a single material base.

Manganites:
Manganites present a wide spectra of structural and magnetic/electric functional phases

- Conventional bulk ceramics can be straightforwardly modified by Cationic chemical doping or influencing Oxygen content by means of thermal treatments
- Thin films samples can be additionally structural modified by substrate induced epitaxial pressure.
- Besides temperature, phase transitions can be induced by external pressure and/or Magnetic/Electrical fields.

Preceding Work
"Scanning probe microscopy was used to create and to detect local bias induced charged states in $\text{La}_{0.5}\text{Sr}_{0.5}\text{MnO}_3$ single crystal at room temperature. The lifetime of these non-equilibrium states exceeds 100 h. These bias induced states display also a ferroelectric like hysteresis with piezoelectric contrast reversed by the applied field."

SPM images of the electric field induced contrast on a 500 nm lateral surface of the $\text{La}_{0.5}\text{Sr}_{0.5}\text{MnO}_3$ single crystal obtained after the applying of ± 10 V (left) and ± 15 V (right) steps to the tip.

Topographic images before and after poling shows no change.
a) kFM image immediately after poling.
b) kFM image several minutes after poling.
c) AFM image after prolonged aging $\sim 10^3$ h.

Dispersively acquired force (piezo)-response hysteresis loops

Results: $\text{La}_{0.5}\text{Sr}_{0.5}\text{MnO}_3$ mono crystalline sample

Topography, BEPS, Amplitude, I-V curves

- At 5 and 10 V dc litho paths some PFM amplitude response appears without surface alteration.
- Negative bias voltage induce stronger FE effect on sample surface than the positive, as observed in the measured parameters.
- Point effect of pulse voltage bias on sample surface is also revealed in the I-V behavior.

Further Work:

- BEPS measurement system is still under improvement stage.
- To investigate the time dependence of charge injection/disipation of the induced FE phases.
- To develop advanced SPM for Multiferroic Materials combining MFM and PFM measurements.
- SPM experiments planned to be performed across CO transition temperature of samples using Ultrahigh vacuum variable temperature AFM/SPM system at CNMS-ORNL.
- To unveil multiferroic states in the studied manganite systems and extend the respective phase diagram in terms of field induced phases.

Acknowledgments:
The author wish to thank the technical support of CNMS-ORNL staff: Benk Gao, Peter Makarewicz, Karyn Seal, Stephen Jones, Nina Balke, Masim Sukhorov.
Work performed within:
CNMS Proposal: CNMS2009-083
EU-funded project "Makrotop" (NSRF-CT-2006-032816).
FCT grant (SFRH/BQ/26011/2005).
Project FLAD/NSF 600-06/2006.

Multiferroic Manganites:
Localized Magnetic/Electrical bias fields may induce Permanent/temporary metapases within a single chemical specie, having a potential use for materials properties tailoring.

This work focuses on inducing ferroelectric behavior in insulating manganites possessing relatively sensitive structure and a combined size- and bond- controlled charge ordering, particularly susceptible to CO phase transitions under localized bias electrical disturbance and potentially present multiferroic phenomena.

Phase diagrams of Manganites showing regions sensitive to phase transitions obtained by localized external fields

BEPS measurements:

- Conventional PFM operates with single frequency and phase lock limitations.
- Band Excitation Piezo-Response Spectroscopy mode collects broad response-frequency at each point.
- BEPS mode requires a modulated waveform, high-speed data acquisition and FFT signal processing.
- The resulting data array for each surface point has terms of Amplitude-Frequency-Voltage response.
- Data analysis yields Resonance, Disipation and Amplitude dependence at each mapped point.

Input Signal, SPM, Output Signal

Results: $\text{La}_{0.5}\text{Sr}_{0.5}\text{MnO}_3$ poly crystalline sample

Topography, BEPS, Amplitude, I-V curves

- Litho experiments at $\pm 5, \pm 10, \pm 15$ V dc bias result in partial surface alteration, not coupled to the PFM amplitude signal.
- Although visible some drifting of the tip positioning, BEPS coefficients maps show distinctive ferroelectric response features in the stimulated regions.
- I-V curves reveal slight effect on Voltage signal

Abstract: A. C. Lourenço, F. Figueiras, S. Das, M. Peres, N. Soares, M. J. Pereira, N. M. Santos, N. A. Sobolev, V. S. Amaral, A. Kholkin, "*As-deposited ferromagnetic Ni-Mn-Ga thin films by co-deposition of two different targets using rf-magnetron sputtering*", MRS Spring 2010 Meeting, April 5-9, 2010, San Francisco, CA-USA

As-deposited ferromagnetic Ni-Mn-Ga thin films by co-deposition of two different targets using rf-magnetron sputtering

A. C. Lourenço^{1,2}(alourenco@ua.pt), F. Figueiras^{1,2}(ffigueiras@ua.pt), S. Das^{1,2} (soma@ua.pt), M. Peres^{1,4}(marco.peres@ua.pt), N. Soares^{1,2}(narciso.soares@ua.pt), M. J. Pereira^{1,2}(mjsapereira@hotmail.com), N. M. Santos^{1,4}(nsantos@ua.pt), N. A. Sobolev^{1,4}(sobolev@ua.pt), V. S. Amaral^{1,2}(vamaral@fis.ua.pt), A. Kholkin^{2,3} (kholkin@ua.pt)

1-Departamento de Física, Universidade de Aveiro, 3810-193 Aveiro, Portugal

2- CICECO, Universidade de Aveiro, 3810-193 Aveiro, Portugal

3-Departamento de Engenharia Cerâmica e do Vidro, Universidade de Aveiro, 3810-193 Aveiro, Portugal

4- I3N, Universidade de Aveiro, 3810-193 Aveiro, Portugal

Ferromagnetic shape memory alloy thin films were prepared by rf sputtering co-deposition of two targets of Ni₅₀Mn₅₀ and Ni₅₀Ga₅₀ on (0001) sapphire and (100) Si substrates at 400 °C. SEM (scanning electron microscopy) cross-section of the films reveals a thickness of approximately 120 nm and a columnar type structural growth. Energy dispersive X-ray spectroscopy confers an atomic composition of the films of Ni₅₆Mn₁₉Ga₂₅.

Conventional XRD (x-ray diffraction) analysis at room temperature shows for both films the co-existence of a significant amorphous structure along with a low degree of crystalline structure. However, we can clearly identify both cubic and tetragonal phases on sapphire whereas film on Si shows mainly the tetragonal phase.

Magnetic measurements (in-plane M-H hysteresis loops) using VSM (Vibrating Sample Magnetometer) showed highly ferromagnetic behavior with well-defined hysteresis loops of similar shape either at room temp (300 K) or at low temperature (150 K). Both the films possess narrow hysteresis loops, low coercivity (~100 Oe) and high saturation magnetization of ~200 emu/cc.

Ferromagnetic resonance measured in the X-band (~9.47 GHz) in the temperature range from 280 K to 400 K revealed a Curie temperature of approx. 350 K for both the cases. In-plane and out-of-plane angular dependences of the FMR spectra were measured. No in-plane anisotropy was detected. The absence of in-plane anisotropy and the similarity in magnetic behavior indicates that the as-deposited structure is independent of substrate and is completely governed by the co-deposition procedure and corresponding conditions.

This study also reveals that co-sputtering of the complementary targets enables to manage the Mn/Ga composition by the ratio of magnetron power during the co-deposition. The process is effective in achieving the thermodynamic conditions to deposit at relatively low substrate temperature thin films of the Ni-Mn-Ga austenitic phase (highly magnetic at room temperature) without need for post-deposition annealing or further thermal treatment, which is a relevant requirement for processing device fabrication.

Work performed within EC-funded project "Multiceral" (NMP3-CT-2006-032616).

Keywords:

Shape memory alloys, Thin films, RF Magnetron sputtering, Magnetic materials. (depends on what is required in the submission)

Symposium **G8.2: [Materials and Physics of Nonvolatile Memories](#)**

Poster: A. C. Lourenço, F. Figueiras, S. Das, M. Peres, N. Soares, M. J. Pereira, N. M. Santos, N. A. Sobolev, V. S. Amaral, A. Kholkin, "As-deposited ferromagnetic Ni-Mn-Ga thin films by co-deposition of two different targets using rf-magnetron sputtering", MRS Spring 2010 Meeting, April 5-9, 2010, San Francisco, CA-USA

Low Temperature Deposition of Ferromagnetic Ni-Mn-Ga Thin Films From Two Different Targets via RF Magnetron Sputtering



A.C. Lourenço¹, F. Figueiras¹, Soma Das¹, M. Peres², N. Soares¹, M.J. Pereira¹, B.N.M. Santos², D. Karpinsky³, N.A. Sobolev², V.S. Amaral¹ and A.L. Kholkin³

¹Dept. of Physics, CICECO, University of Aveiro, Aveiro, Portugal

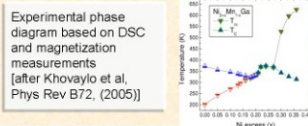
²Dept. of Physics, I3N, University of Aveiro, Aveiro, Portugal

³Dept. of Ceramics and Glass Engineering, CICECO, University of Aveiro, Aveiro, Portugal.

CICECO
centre for research
in ceramics &
composite materials
I3N
institute for
nanostructures,
nanomodelling and
nanofabrication

Motivation

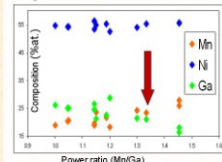
- Ferromagnetic shape memory alloy films have great potential for multifunctional applications due to a multitude of useful multifunctional properties, especially when combined with ferroelectrics.
- Thin film composition control and low temperature deposition can be achieved by co-sputtering from two different targets.



Ni-Mn-Ga phase diagram

- Structural martensitic transition from high-T austenitic phase to low-T martensitic phase takes place in ferromagnetically ordered state.
- The combination of ferromagnetism of the martensite phase and thermoelastic nature of the martensitic transformation in this material allows controlling its shape and dimensions via both magnetic field and temperature

Experiments



Equipments: RF sputtering
Magnetron type: 2" planar
Targets: $\text{Ni}_{50}\text{Ga}_{50}$ & $\text{Ni}_{50}\text{Mn}_{50}$
Substrates: Al_2O_3 , Si, MgO, STO
Temperature: ~400°C
Thickness: ~120nm
Power of targets:
 $\text{Ni}_{50}\text{Mn}_{50}$: $\text{Ni}_{50}\text{Ga}_{50}$ = 16:14
Deposition rate: ~2 nm/min
Target-substrate distance: 125 mm.

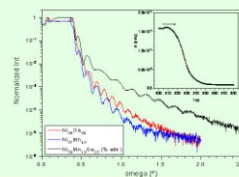
Conclusions

- The co-sputtering of two complementary targets enables to control the Mn/Ga composition by adjusting the magnetron power during the co-deposition.
- The process is effective in achieving the thermodynamic conditions to deposit thin films of the Ni-Mn-Ga austenitic phase (highly magnetic at room temperature) at relatively low substrate temperature without need for post-deposition annealing or any further thermal treatment.
- These as-grown thin films without additional heat treatment are prerequisite for device fabrication.

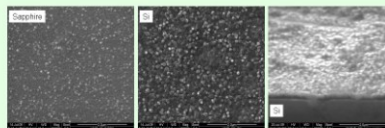
On-going work

Electrical characterization (resistivity/magneto-resistance).
Temperature dependence (and hysteresis) of the structural transformation.
Deposition on active substrates for magneto-electric coupling studies.

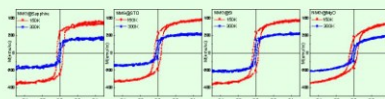
Results



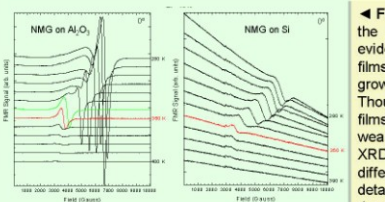
▲ Co-sputtering of two different targets ($\text{Ni}_{50}\text{Ga}_{50}$ and $\text{Ni}_{50}\text{Mn}_{50}$) in a co-focal geometry allows for the low temperature (400 °C) deposition of NiMnGa films. X-Ray reflectometry (XRR) is used for the evaluation of growth rates: ~2 nm/min



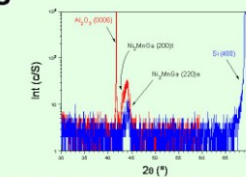
▲ SEM cross-section of the films reveals a columnar type structural growth and a thickness of approximately 120 nm. Energy dispersive X-ray spectroscopy confers an atomic composition of the films of $\text{Ni}_{48}\text{Mn}_{18}\text{Ga}_{34}$.



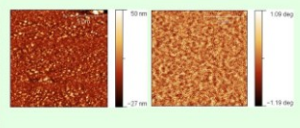
▲ Magnetic Measurements (in-plane M-H hysteresis loops) using vibrating sample magnetometry revealed strongly ferromagnetic behavior with well-defined hysteresis loops of similar shape both at room (300 K) and at low temperatures (150 K). The films exhibited narrow hysteresis loops, low coercivity (~100 Oe) and high saturation magnetization of ~200 emu/cc.



▲ Ferromagnetic Resonance (FMR) measured in the X-band (~9.77 GHz) from 280 K to 400 K evidenced a Curie temperature ~350 K for both films. We observe two magnetic phases in the film grown on Al_2O_3 and only one in that grown on Si. Though the magnetization is similar in the two films, the FMR signal in the latter one is much weaker. These results corroborate the SQUID, XRD and SEM data: the obtained films on very different substrates are magnetic, however, the details of the magnetic and structural properties depend on the substrate.



▲ X-Ray Diffraction (XRD) patterns of two $\text{Ni}_{50}\text{Mn}_{50}\text{Ga}_{50}$ films under study: 12a (red) on Al_2O_3 (0001) and 12b (blue) on Si (100) substrates. A significant portion of the film is in an amorphous state.




▲ Topography (left) & MFM contrast (right) images of NMG film on STO substrate. MFM image shows magnetic domain pattern inherent for perpendicular magnetic anisotropy. Domains configuration is characteristic of large magnetocrystalline anisotropy.

Acknowledgments

This work is partly supported by the EC-funded project "Multiceral" (NMP3-CT-2006-032616) and by FCT (Fundação para a Ciência e a Tecnologia).

Poster: F. Figueiras, I. K. Bdikin, V. S. Amaral, A. L. Kholkin, S. V. Kalinin "Modification and Study of Multiferroic Manganites by Scanning Probe Microscopy", "Encontro com a Ciência e Tecnologia Em Portugal", 4 a 7 Jul. 2010, Centro de Congressos de Lisboa - Portugal.


university of aveiro
theoria poiesis praxis



ciceco
centre for research in ceramics & composite materials

Modification and Study of Multiferroic Manganites by Scanning Probe Microscopy


F. Figueiras^{1,3,*}, I. K. Bdikin^{2,3,4}, V. S. Amaral^{1,3}, A. L. Kholkin^{2,3}, S. V. Kalinin⁵



¹ Physics' Department,
² Ceramics' & Glass Eng. Department,
³ CICECO,
⁴ Mechanics' Eng. Department,
⁵ CNMS ORNL,
*ffigueiras@ua.pt

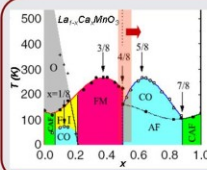
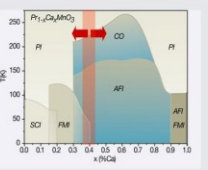
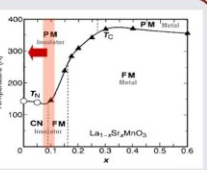
University of Aveiro, Portugal
University of Aveiro, Portugal
University of Aveiro, Portugal
University of Aveiro, Portugal
Oak Ridge, TN, USA

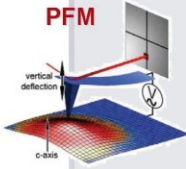
www2.fis.ua.pt/
www.cv.ua.pt/
www.ciceco.ua.pt/
www.mec.ua.pt/
www.cnms.ornl.gov/



Manganites

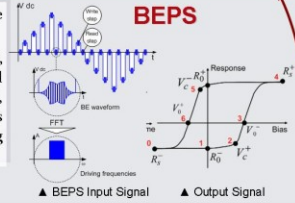
Manganites present a wide spectra of structural magnetic and electric functional phases [RPP 69, 797 (2006)] leading to Colossal Magneto Resistance or Charge Order Phenomena. Ferroelectric behavior can be induced in insulating manganites possessing relatively sensitive structure and combined site-bond-centered charge ordering, particularly susceptible to phase transitions under localized bias electrical disturbance [JPCM 20 (2008) 434217].



PFM

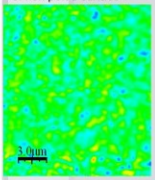
Piezoresponse Force Microscopy is based in the measurement of deformation of the cantilever between the tip and the sample under applied electric field. Conventional PFM operates with single frequency and phase-lock limitations, whereas Band Excitation Piezo-Response Spectroscopy measurements collects broad response-frequency from the surface. BEPS mode requires a modulated waveform, high-speed data acquisition and FFT signal processing, the resulting data array has terms of Amplitude-Frequency-Voltage response at each mapped point yielding Resonance, Dissipation and Amplitude dependencies [MT 11, 11 (2008)].



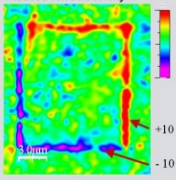
BEPS

Results on Pr_{0.6}Ca_{0.4}MnO₃ single crystal

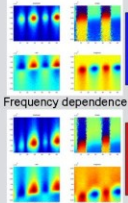
Conventional PFM map of non poled surface



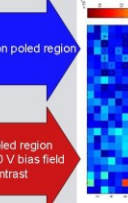
Poling dependence of Bias-field induced ferroelectricity



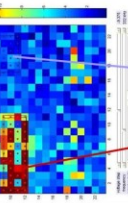
Frequency dependence



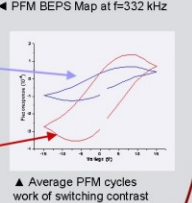
Non poled region



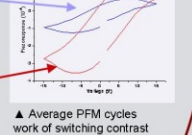
Polled region -10 V bias field contrast



BEPS BEPS Map at f=332 kHz

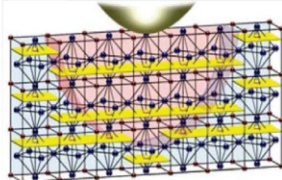


Average PFM cycles work of switching contrast

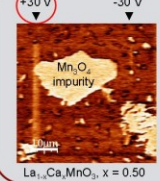
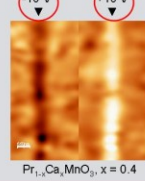
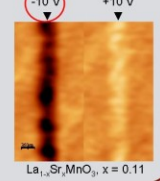


Poling Asymmetries

Asymmetry of positive and negative electric fields either in poling, lithography or bias current point to a process of charge injection that locally change the hole concentration (Mn³⁺/Mn⁴⁺ ratio and Jahn-Teller ordering) hence transiting to a metastable structure, corresponding to a novel situation on the phase diagram.



Positive poling leads to increased hole doping (Mn⁴⁺) whereas a negative poling injects electrons (Mn³⁺)

Conclusions

- Induced metaphases within a single chemical specie, can present Multiferroic phenomena and has a technological potential to be use for materials properties tailoring.
- Lithographic induced Structural/Electro-chemical phase transitions can be an alternative technological process for manufacturing permanent or temporary nano circuits chips from a single material base.

FCT funded:
CERN/FP/109357/2009,
PTDC/FIS/105416/2008 "Multifox"
SFRH/BD/25011/2005

CNMS Proposal:
CNMS2009-083

EC-funded project:
NMP3-CT-2006-032616 "Multicera"